A THESIS
FOR THE DEGREE OF DOCTOR OF PHILOSOPHY

Development of Advanced Nanostructured Electrode Materials for High-Performance Supercapacitors and Self-Charging Power Cell

Parthiban Pazhamalai

DEPARTMENT OF MECHATRONICS ENGINEERING

GRADUATE SCHOOL
JEJU NATIONAL UNIVERSITY

2018.12

Development of Advanced Nanostructured Electrode Materials for High-Performance Supercapacitors and Self-Charging Power Cell

Parthiban Pazhamalai

(Supervised by Professor Sang-Jae Kim)

A thesis submitted in partial fulfilment of the requirement for the degree of

Doctor of Philosophy

2018.12

The thesis has been examined and approved.

Prof. Young Sun Mok Thesis Director	Professor, Department of Chemical & Biological Engineering, College of Engineering, Jeju National University.
Prof. Woo Young Kim Thesis Committee Member	Assistant Professor, Department of Electronic Engineering, College of Engineering, Jeju National University.
Prof. Hyomin Lee Thesis Committee Member	Assistant Professor, Department of Chemical & Biological Engineering, College of Engineering, Jeju National University.
Dr. Karthikeyan Krishnamoorthy Thesis Committee Member	Contract Professor, Department of Mechanical Engineering, College of Engineering, Jeju National University.
Prof. Sang-Jae Kim Thesis Committee Member and Supervisor	Professor, Department of Mechatronics Engineering, College of Engineering, Jeju National University.

December, 2018

DEPARTMENT OF MECHATRONICS ENGINEERING

GRADUATE SCHOOL

JEJU NATIONAL UNIVERSITY

REPUBLIC OF KOREA

Dedicated to

my family

Acknowledgement

"எந்நன்றி கொன்றார்க்கும் உய்வுண்டாம் உய்வில்லை
செய்ந்நன்றி கொன்ற மகற்கு"
"There is salvation for faltering on any virtue
but not for ingratitude"

-Thiruvalluvar

First of all, I thank GOD for showering me his abundant blessings, strength and wisdom to achieve this task successfully. It is my great pleasure to thank so many people who have made this thesis possible. I sincerely acknowledge all the people who helped and supported me during my doctoral course.

It gives me pride and pleasure to express my deep sense of gratitude to my research supervisor Prof. Sang -Jae Kim, for his supervision, advice and guidance as well as giving me extraordinary moral support throughout the work. He has been supportive since the day I began working on this project. He always tells us to try continuously to achieve the higher goals in our life and gives more motivation for achieving the goal. During some of my initial critical times in the research, he is the real guardian for me to overcome the issues.

I would like to say my sincere gratitude to Prof. Gunasekaran Venugopal for recommending me to this lab for the doctoral course. Without his help, I couldn't get such a great opportunity to work in this lab. I also thank him for his support and guidance during my doctoral course.

I feel great pleasure and gratitude to thank Dr. Karthikeyan Krishnamoorthy, who not only gave his continuous support and guidance in the research but also outside the lab as a brother and a well-wisher. I also want to thank my colleagues and friends Dr S. Radhakrishnan, Dr. Sakthivel Thangavel, Dr. Kaliannan Thiyagarajan, Dr. Nagamalleswara Rao Alluri, Dr. Arunkumar Chandrasekhar, Dr. Sophia Selvarajan, Mrs. Saipriya

Ramalingam, Ms. Yuvasree Purusothaman, Mr. Surjit Sahoo, Mr. Vivek Venkateswaran, Ms. Kausalya Ganesan, Mr. Vimal Kumar Mariappan, Ms. Sindhuja Manoharan, Mr. Rajagopal Pandey, Mr. Gaurav Khandelwal, Mr. Nirmal, Mr. Divakar, Mr. Abisek, Mr. Dhanasekar kesavan, Mr. Swapnil, Mr. Prashanth, Mr. Woo Joong Kim, Mr. Kim Taehyun, and Mr. Seong Mingeon for their timely help and support in the lab during the course of time.

I would also thank the friends outside the lab, Dr. MSP Sudhakaran, Dr. Srikanth, Ms. Karthika Muthuramalingam, Mr. Dharanibalan, Mr. Gnanselvan, Dr. Raj Mogre, Mr. Sravan Kumar, Mr. Rajveer, and Ms. Jayalakshmi giving me so many wonderful memories to cherish during my stay in Jeju.

I would like to thank all the family persons who made homely environment during my stay in Korea for the last 4 years. I also thank all the JISO members and my international country friends who have been very co-operative and support during my stay in Jeju. I am very much thankful to the Research Instrument Center at JNU for providing the instrumental facilities during my study.

Last but certainly not least, I would like to express my deepest gratitude to my parents Mr. Pazhamalai Durairajan and Mrs. Thillaiammalle Pazhamalai who have sacrificed their today for the betterment my tomorrow with love and gratitude. I also thank my sister Ms. Paarkavi Pazhamalai who have love and support for me. My thanks are bountiful for their wholehearted love and care.

Words can hardly substitute the indebted that I owe to my inspiring friends who stood behind in all possible ways to complete this work successfully. Without the above, I might not complete this research work as great full one.

Finally, my thanks are due to all those who have helped me directly and indirectly for the successful completion of my research work.

Parthiban Pazhamalai

Table of contents

CHAPTER – 4

SYNTHESIS OF LAYERED TRANSITION METAL COMPOUNDS (TiO_2, SILOXENE, AND HT-SILOXENE) AND FABRICATION OF SYMMETRIC CAPACITOR USING ORGANIC/IONIC LIQUID ELECTROLYTE

CHAPTER 6

SELF-CHARGING SUPERCAPACITOR POWER CELL: ENERGY CONVERSION AND STORAGE

A High Efficacy Self-Charging $MoSe_2$ Solid-State Supercapacitor Using Electrospun Nanofibrous Piezoelectric Separator with Ionogel Electrolyte

Nomenclature

AC	Activated carbon
BET	Brunauer-Emmet-Teller
CV	Cyclic voltammetry
CNT	Carbon nanotube
CT	Conductive textile
DI	De-ionized
DRR	Dry reforming reaction
ECD	Electrochemical deposition
ECs	Electrochemical capacitors
EDLC	Electrochemical double layer capacitor
EES	Energy storage systems
EDS	Energy dispersive X-ray Spectroscopy
EIS	Electrochemical Impedance spectroscopy
ESR	Equivalent series resistance
FE-SEM	Field-emission scanning electron microscopy
FT-IR	Fourier transform-infrared
GC	Gas chromatography
GCD	Galvanostatic charge discharge
GO	Graphene oxide
HK	Horvath-Kawazae
HT	Heat tratment
HR-TEM	High resolution transmission electron microscope

HSCs	Hybrid supercapacitors
JCPDS	Joint committee on powder diffraction standard
LEDs	Light emitting diodes
PANI	Polyaniline
PC	Porous carbon
RGO	Reduced graphene oxide
SAED S	elected area electron diffraction
SCs	Supercapacitors
SCE	Saturated calomel electrode
SEM	Scanning electron microscope
SS	Stainless steel
TEM	Transmission electron microscope
XRD	X-ray diffraction
XPS	X-ray photo electron spectroscopy

LIST OF TABLES

LIST OF FIGURES

Figure 6.12. Schematic illustration for the working mechanism of the self-charging of $MoSe_2$ SCSPC device. (A) The initial state of the $MoSe_2$ SCSPC device with no applied compressive force. (B) With an applied compressive force to the $MoSe_2$ SCSPC device, the $NaNbO_3$/PVDF creates a piezoelectric potential which drives the migration of electrolyte ions. (C) the electrolyte ions drive towards the electrode and electrochemical intercalation of ions in the $MoSe_2$ electrode. (D) An equilibrium state has been reached between the piezoelectric potential created and the electrochemical reaction of the $MoSe_2$ SCSPC device. (E) Completion of one self-charging cycle with the compressive force applied is released, and the piezoelectric potential disappeared, and the electrolyte ions reach the equilibrium state.

361

ABSTRACT - HANGUL

신산업의 급속한 발전과 더불어 재생 가능한 에너지의 필요성은 다양한 분야 (주거, 산업, 방위 보안 및 연구부문 등)에서 일상 생활에서의 사용을 위한 대체 에너지 변환/저장 시스템의 개발을 위한 연구가 활발히 진행되고 있다. 특히, 다양한 유형의 에너지 저장 장치 중에서도 전기화학적 커패시터 (슈퍼커패시터)는 높은 고유전력 밀도, 보통수준의 고유에너지 밀도, 빠른 충전-방전 속도, 환경 안전성 등의 다양한 장점을 가지고 있어, 많은 관심을 끌고 있다. 슈퍼커패시터의 주요 단점은 기존의 배터리 기술에 비해 보통수준의 고유에너지를 가지고 있지만, 다른 우수한 초고속 충전-방전 특성 등은 슈퍼커패시터를 고전력 전자장치, 하이브리드-전기차량 등과 같은 잠재적인 응용분야를 가지고 있으며, 슈퍼커패시터의 성능 지표를 높이기 위해 많은 연구그룹에 의해 수행되고 있다. 일반적으로, 슈퍼커패시터의 성능지표는 주로 전극재료, 분리막 및 전해액 시스템에 의존한다. 전극재료의 경우, 고려해야 될 주요 측면은 우수한 전기전도성, 특정 고유표면적과 우수한 전기화학적 특성을 갖는 나노 구조 형태이다. 전극물질의 다양한 유형의 유효성 가운데, 표면적이 큰 새로운 나노 구조의 전 재료는 전기화학적 특성을 높일 수 있으며, 이러한 나노 재료들은 슈퍼커패시터 전극의 잠재적인 후보가 될 수 있다. 또한, (i) 하이브리드-이온 커패시터/비대칭성 수퍼커패시터 (동작 전압 창 (operating voltage window, OPW)을 2.0 V까지 증가시키기 위해) 와 (ii) 이온/유기성 전해액(OPW를 3.5 V까지 증가시키기 위해)의 제작은 슈퍼커패시터의 고유에너지 지표를 높이기 위해 사용된다.

슈퍼커패시터의 또 다른 흥미로운 응용은 자가충전 슈퍼커패시터 전력 소자(self-charging supercapacitor power cell, SCSPC)라고 부를 수 있는 일체형 에너지 변환 및 저장 시스템의 개발이 가능한 압전기 개념과 통합하는 능력이다. SCSPC 장치는 에너지원으로써 사람의 생체역학적 에너지를 이용하여 착용 가능한 전자 장치들을 구동하거나 동력을 공급하는 것이 가능한 중요한 일체형 자가구동 시스템이다. SCSPC 시스템은 (i)에너지 수확기, 그리고 (ii) 에너지 저장 장치를 하나의 장치에 통합한다. SCSPC 장치의 에너지 변환효율은 현재 단계에서는 매우 낮으므로, SCSPC의 성능 개선이 필요하다. 본 논문에서는 소자의 성능지표 향상을 위한 나노가공 전극 재료와 피에조-폴리머 분리기로 상업적 폴리머 분리기를 대체한 자가 충전 전력장치의 개발에 중점을 둔 연구를 수행하였다.

수용성 전해액 시스템을 사용한 성능 지표 개선을 위하여 제작한 하이브리드-이온 수퍼커패시터(HSCs)/비대칭 수퍼커패시터(ASC)는 배터리 형태의 유도전류성 나노구조 전극재료($LiMn_2O_4$, CuHCF, MnHCF & Cu_2WS_4/Ni) 및 용량형 전극 재료 (그래핀 및 흑연 카본)을 이용하여 제작하였다. $LiMn_2O_4$‖그래핀, CuHCF‖GC 및 MnHCF‖그래핀 같은 제작된 장치는 각각 약 39, 42 및 44 Wh/kg의 고유 에너지를 특성을 보였으며, 상응하는 고유 전력은 각각 440, 523, 588 W kg^{-1}이다. 마찬가지로, CWS/Ni‖그래핀 ASC 장치 또한 전기화학적 공정 중에 전자-이온을 빠르게 운송하는 Ni폼과 전극 물질의 직접결합에 의한 고에너지 (48Wh/kg) 및 전력 (321W/kg) 특성을 보였다.

성능지표를 개선을 위한 또 다른 체계적인 방법으로써, 이온/유기 전해액을 사용한 우수한 전기화학적 활성영역을 제공할 수 있는 층/시트 같은 구조로 만들어진 전극재료의 개발을 시도하였으며, 층간소재의 준비는 열수반응 (파란 TiO_2, $MoSe_2$, ReS_2), 지리화학적 반응 (2D 실리콘 시트), 그리고 기계가공 박리 공정 (MoS_2)와 같은 다양한 제작방법을 사용하였다. 금속산화물(블루TiO_2), 2차원 전이금속 칼코게나이드 (MoS_2, ReS_2, $MoSe_2$), 층간 실록신 및 그 파생물 (실록신, 열처리된 실록신, 실리콘옥시카바이드막)과 같은 서로 다른 층간소재는 유기 전해액 ($TEABF_4$)을 사용하는 대칭성 슈퍼커패시터 (SSCs)를 위해 새로운 전극 재료를 사용하였다. 면적 성능지표는 실리콘 물질 및 SSCs기반의 TiO_2 물질을 이용해 널리 사용되는 반면 중력 성능 지표는 SSCs기반의 TMC 물질을 이용하였다. SSCs기반의 TiO_2 및 2D 실리콘의 면적 지표에서 고유 에너지 및 고유 전력의 상대적인 비교 값은 i) 고유 에너지 TiO_2 (3.22 μWh cm^{-2}) < 실록신 (2.52 μWh cm^{-2}) > HT-실록신 (4.31 μWh cm^{-2}) 및 ii) 고유 전력 TiO_2 (8.06 mW cm^{-2}) > 실록신 (9.75 mW cm^{-2}) > HT-실록신 (9.75 mW cm^{-2}) 순이었다. 실리콘 옥시카바이드 (SiC_xO_y) SSC 장치의 전기화학적특성은 최대 고유전력 (15 kW/kg)과 함께 고유 에너지(~20.8 Wh/kg)를 보였다. 이 SSCs의 성능지표 분석은 높은 고유 에너지는 MoS_2 (18.43 Wh/kg) > $MoSe_2$ (20.31 Wh/kg) > ReS_2 (28.55 Wh/kg)순이고 고유 전력은 MoS_2 (7.5 kW/kg) > $MoSe_2$ (7.5 kW/kg) > ReS_2 (10 kW/kg) 순임을 보여 주었다. 이 결과들을 바탕으로, $MoSe_2$ 전극 및 슈퍼커패시터는 높은 고유 에너지(20.31 Wh/kg)와 전력 밀도(7.5 kW/kg)와 함께 높은 OPW(3.0V)라는 이점을 갖고 있다. 또한, 큰 음이온 분극률의 이점 (그리고 높은 이온화 열확산성)을

가진 $MoSe_2$시트의 전기 전도도는 MoS_2 및 ReS_2시트보다 높으며 MoS_2 및 ReS_2의 S^{2-}와 비교하여 Se^{2-}에서 발생 하였다. 따라서, $MoSe_2$ SSC는 최초로 이온젤화 전해질 및 전기방사된 PVDF 섬유를 사용하는 자가충전 수퍼커패시터소자(SCSPC)의 제작 및 성능 평가를 위한 추가 연구에 사용하였다. SCSPC 장치는 $MoSe_2$ 전극(에너지 저장 전극), 전기방사된 나노섬유 PVDF/$NaNbO_3$ 매트(다공성 피에조-폴리머 분리기), 그리고 PVDF-co-HFP/$TEABF_4$ (이온젤화 전해질)를 사용하여 제작하였다. SCSPC의 개별 전기화학적 성능은 2.0V이상의OPW에서 작동하는 능력을 보였고 이것은 높은 고유 에너지 (37900 μJcm^{-2}) 및 고유전력(2685 μWcm^{-2})특성을 보여 주었다. 전기방사된 나노섬유 PVDF/$NaNbO_3$ 매트의 개별 전기화학적 성능은 기계적 힘 (30N)이 가해졌을 때 높은 전압(~12V)을 보여 주었다. $MoSe_2$ SCSPC의 자가충전성능은 넓은 범위의 힘(압력)에서 SCSPC에 저장된 전하를 모니터링 하였다. SCSPC는 최대 30N의 힘을 받을 때 705mV까지 충전되었으며, $MoSe_2$ SCSPC의 달성된 성능 지표는 기존 SCSPCs의 성능과 비교하여 5배 이상 높은 소자의 제작에 성공 하였으며, $MoSe_2$ SCSPC 장치를 이용하여 기계적 에너지를 유용한 에너지로 변환할 수 있는 유연/휴대가능/착용 가능한 차세대 자체충전전력원의 개발을 위한 기반연구성과를 제공하였다.

ABSTRACT

In the advent of the modern era, the need for global renewable energy is on great demand owing to the depletion of renewable energy resources which initiates the development of alternative energy conversion/storage systems for day-to-day life usage in various sectors (including residential sector, industrial sector, defence security and institutional research sectors). Amongst various types of energy-storage devices, electrochemical capacitors/supercapacitors have gained much more interest due to its high-specific power density, moderate specific energy density, fast charge-discharge rate, extended cycle with environmental safety. The main drawback in a supercapacitor is their moderate specific energy compared to the existing battery technology. Even though supercapacitors lack in terms of specific energy, the other fascinating properties of supercapacitors (ultrafast charge-discharge properties) makes them as an ideal choice for the potential application in high power electronics, hybrid-electric vehicles and so on. The progressive research has been carried by many research groups to enhance the performance metrics of electrochemical capacitors. Usually, the performance metrics of supercapacitors mainly depend upon electrode materials and electrolyte system. In the case of electrode materials, the main aspects need to be taken into consideration are good electrical conductivity, nanostructures morphology with the high specific surface area and superior electrochemical properties. Amidst the availability of various types of electrode materials, novel nanostructured electrode materials with the high surface area can lead to enhanced electrochemical properties, and these nanomaterials become a potential candidature for the supercapacitor electrodes. The fabrication of (i) hybrid-ion capacitor/asymmetric supercapacitor (to increase the operating voltage window (OPW) up to 2.0 V) and (ii) the use of ionic/organic electrolytes ((to increase the OPW up to 3.5 V), are used to boost the specific energy metrics of supercapacitors.

Another interesting application of supercapacitor is their ability to integrate with the concept of piezoelectric to develop all-in-one energy conversion and storage system which can be termed as self-charging supercapacitor power cell (SCSPC). The SCSPC devices are of great interest for driving or powering wearable electronics via utilizing the biomechanical energy from human as an energy source. The SCSPC system integrates two compartments viz, (i) energy harvester, and (ii) energy storage compartments together in a single device. The energy-conversion-efficiency of SCSPC devices are very low at this stage, which needs to be improved via engineering each compartment of SCSPC. Therefore, the development of highly-efficient SCSPC device attract much attention considering the depletion of renewable energy sources. Considering all the aspects regarding the energy storage device, this thesis is mainly focused on the engineering nano-structured electrode materials for improving the performance metrics and their application towards self-charging power cell devices via replacing the commercial polymeric separator by piezo-polymer separator.

In the view of improving performance metrics using aqueous electrolyte system, the hybrid-ion supercapacitors (HSCs) / asymmetric supercapacitor (ASC) are fabricated using battery-type faradaic nanostructured electrode materials ($LiMn_2O_4$, CuHCF, MnHCF & Cu_2WS_4/Ni) and capacitive type electrode materials (graphene and graphitic carbon). The fabricated device such as $LiMn_2O_4$‖graphene, CuHCF‖GC and MnHCF‖graphene delivers specific energy of about 39, 42, and 44 Wh/kg with the corresponding specific power of 440, 523, and 588 W kg^{-1} respectively. Likewise, the CWS/Ni‖graphene ASC device also possesses high energy (48 Wh/kg) and power (321 W/kg), due to the direct integration of the electrode material on to the Ni foam which makes the electron-ion transport fast during the electrochemical process.

Another systematic way to improve the performance metric is to develop electrode materials made of layered/sheet-like structures which can provide superior electrochemical

active sites with the use of the ionic/organic electrolyte. In this aspect, the preparation of layered materials involved various methodologies such as hydrothermal preparation (blue TiO_2, $MoSe_2$, ReS_2), topochemical de-intercalation reaction (2D silicon sheets), and mechanomilling assisted exfoliation process (MoS_2). Different layered materials such as metal oxide (blue TiO_2), two-dimensional transition metal chalcogenides (MoS_2, ReS_2, $MoSe_2$), layered siloxene and their derivatives (siloxene, heat-treated siloxene, silicon oxy carbide lamellas) were examined as novel electrode materials for symmetric supercapacitors (SSCs) using organic electrolyte ($TEABF_4$). Areal performance metrics are widely used for silicon- and TiO_2- based SSCs whereas gravimetric performance metrics are used for TMC-based SSCs. The specific energy and specific power in areal metrics of TiO_2 and 2D silicon based SSCs were in the order of TiO_2 (3.22 μWh cm^{-2}) < siloxene (2.52 μWh cm^{-2}) > HT-siloxene (4.31 μWh cm^{-2}) for specific energy and TiO_2 (8.06 mW cm^{-2}) > siloxene (9.75 mW cm^{-2}) > HT-siloxene (9.75 mW cm^{-2}) for specific power. The electrochemical analysis of silicon oxy carbide SSC device possesses specific energy (~20.8 Wh/kg) with a maximum specific power (15 kW/kg). The analysis of performance metrics of these SSCs demonstrated that the high specific energy is in the order of MoS_2 (18.43 Wh/kg) > $MoSe_2$ (20.31 Wh/kg) > ReS_2 (28.55 Wh/kg) and the specific power is in the order of MoS_2 (7.5 kW/kg) > $MoSe_2$ (7.5 kW/kg) > ReS_2(10 kW/kg). Based on these findings, $MoSe_2$ electrodes and supercapacitors possess the advantage of high OPW (3.0V) with high specific energy (20.31 Wh/kg) and power density (7.5 kW/kg). Further, electrical conductivity of $MoSe_2$ sheets is higher than MoS_2, and ReS_2 sheets with the advantage of large anionic polarizability (and high ionic diffusivity) arise from the Se^{2-} as compared to that of S^{2-} in MoS_2 and ReS_2. Thus, $MoSe_2$ SSC is used for further studies for the fabrication and performance evaluation of self-charging supercapacitor cell (SCSPC) device using ionogel electrolyte and electrospun PVDF fibres for the first time. The SCSPC device was fabricated using $MoSe_2$ electrodes (as energy

storage electrode), electrospun nanofibrous PVDF/$NaNbO_3$ mats (porous piezo-polymer separator), and PVDF-co-HFP/$TEABF_4$ (ionogel electrolyte). The individual electrochemical performance of SCSPC showed their ability to work over an OPW of 2.0 V and delivered high specific energy (37900 μJ cm^{-2}) and specific power (2685 μW cm^{-2}). The individual electromechanical performance of electrospun nanofibrous PVDF/$NaNbO_3$ mats showed a high voltage (~12 V) when subjected to a mechanical force (30 N). The self-charging properties of the $MoSe_2$ SCSPC was examined via monitoring the charge stored in the SCSPC under various range of applied force (compressive). The SCSPC was charged up to 705 mV subjected to a maximum force of 30 N. The achieved performance metrics of $MoSe_2$ SCSPC is five- fold higher compared to state of art of SCSPCs. The key experimental findings ensure the conversion of mechanical energy into useful energy using the $MoSe_2$ SCSPC device, thus highlighting their impact towards the development of future-generation self-powered devices for flexible/portable/wearable electronics.

CHAPTER 1

INTRODUCTION

1.1. Background

In the advent of modern era and the increased demand in the need of global renewable energy due to rapid consumption of available energy resources paves the way to the development of alternative energy conversion and storage system for the human availability in various sectors such as residential, transportation, industry, military and space exploration[1–3]. The energy demand increases day-to-day steadily in domestic applications and industries but the available conventional energy resources not enough to meet out our necessities[4]. This factor is due to the reason that the available energy resources such as solar, hydro and wind cannot produce energy for the upcoming years and the non-renewable (fossil fuels) sources of energy are not utilized to the thorough potential due to their own demerits. At the same extent is that the demolitions of environmental hazards like nuclear waste from non-renewable sources from the nuclear plants. Furthermore, over the last few years the cost of liquid fuels has enormously increasing day by day which makes more stress on economic development of the developing and growing countries[5]. These problems can be solved by the development of effective electrical energy storage systems which can promote efficient energy storage and utilization of the power for the electronic applications. The development in the electrochemical energy storage can reduce the dependence of the available resources and move towards the next generation electrical energy storage resources.

1.2. Importance of electrochemical energy storage devices

To overcome the deficiency in the energy resources, the alternative energy storage devices which can reduce are the electrochemical energy storage devices (batteries and supercapacitors). Electrochemical energy storage systems (EES) play an important role in storing electrical energy in terms of transforming chemical into electrical energy. The EES

has captivated among other classes of energy storage systems because of its several advantages which includes high efficiency of energy conversion, portable, reduction in size, easy to commercialize and minimum pollution[6,7]. However, the EES system are nowadays reinvigorated as representative as the energy resources for the electronics gadgets. However, the essential tasks and problem headed for the commercialization of EES system, have been extensively deliberate in different fields of technology essentially on electrode materials and electrolyte[8,9]. Subsequently, there yet continue numerous problems interconnected for the development of prototype such as materials synthesis cost, life cycle, and so on. Along with some practical issues and when considering the EES, the utilization with lower cost electrode material is a major issue.

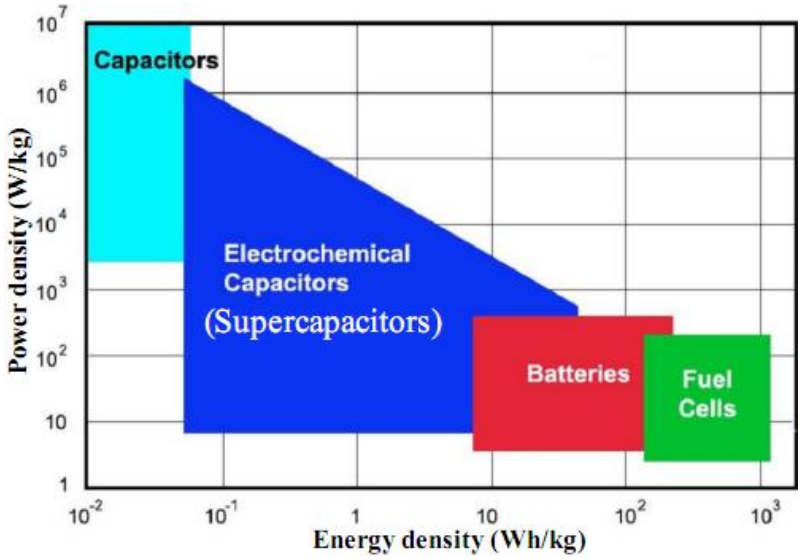

Figure 1.1 Comparison of energy storage devices by Ragone plot

Amidst the EES systems, supercapacitors (SC) have attracted as the alternative energy storage device compared to the battery system. This is due to the fact that the SCs posses higher power density, long cycle life, rapid charge discharge compared to the batteries which have high energy and low cycle life. Practically, SCs have high power in the range of KW kg^{-1} , than batteries which are theoretically very low as seen in Fig. 1.1.

Hence, the SCs are considered alternative energy system with longer life time and lighter weight than the other energy storage devices[10]. In addition, due to its high-power density, nowadays SCs are mostly used in various applications. SCs are also used in various electronic applications which includes smart phones, watches, health band, camera, communication sector and other industrial gadgets[11].

1.3 CLASSIFICATION OF SUPERCAPACITORS

Based upon current R&D trends, supercapacitors can be divided into three types: electrochemical double-layer capacitors (EDLC), pseudocapacitors, and hybrid capacitors. Each class is characterized by its unique mechanism for storing charge. These are non-Faradaic, Faradaic, and a combination of the two processes are shown in the Fig.1.2[12].

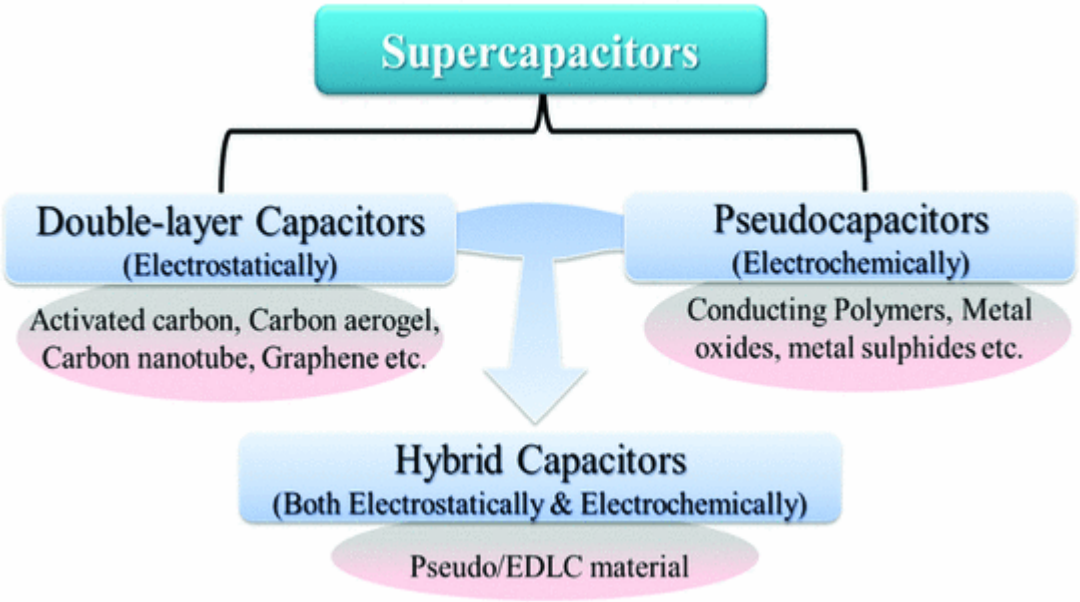

Fig.1.2 Classification of Supercapacitors

1.3.1 ELECTROCHEMICAL DOUBLE- LAYER CAPACITORS (EDLC)

EDLCs store charge electrostatically, or non-Faradaic, and there is no transfer of charge between electrode and electrolyte interface.

In EDLCs, the capacitance is related to accumulation of charge as double layer, between the electrode and electrolyte interface via non-Faradaic process. Here, different types of carbon materials (activated carbon, carbon nanotubes and graphene) have been used to store charges in EDLCs. However, the amount of charge accumulation is estimated by using the following equation to that of parallel-plate capacitor, therefore[13]

$$C = \varepsilon_o \varepsilon_r \frac{A}{D}$$

Where, ε_o is the permittivity of free space and ε_r the relative dielectric constant of the electrolyte as liquid or solid, A is the surface area of the electrodes (m^2 g^{-1}) and d is the thickness of the electrical double-layer (EDL) or Debye length (DL) [14]. Moreover, an energy storage mechanism in EDLC is based on the electric double layer (EDL) theory. This EDL theory was firstly proposed by Helmholtz in 1853 as similar to that of parallel plate capacitor therefore this model tells that two layers of opposite charges build up at the electrode-electrolyte interface with some atomic distance (**Figure. 1.3**). Although, this presented model does not examine the adsorption of counter ions and water molecules. In the earlier 1900's, it is further modified by Gouy and Chapman, thus theory sates that distribution of electrolyte ions in the electrolyte medium due to the thermal motion, named as a diffuse layer[14] (**Figure. 1.3**).

But this modified theory exhibits an overestimation of EDL capacitance. Afterwards, in 1924 Stern developed a modified theory by combined the Helmholtz and Gouy-Chapman model. Therefore, explains that possibility of two layers of ion distribution. First is compact layer or Stern layer or Helmholtz layer which is formed by absorbed ions and non-specifically adsorbed counter ions on electrode where these two types of adsorbed ions are distinguished as outer Helmholtz plane (OHP) and inner Helmholtz plane (IHP) (Figure. 1.3). Second is diffuse layer which is same as what the Gouy-Chapman model describes. So, total capacitance (C_t) is build up by both layers i.e., compact layer (Helmholtz layer) and the

diffuse layer and stored capacitance termed as compact/Helmholtz double layer capacitance (C_H) and diffusion layer capacitance (C_{diff}). So, therefore the total capacitance is expressed as follow[14],

$$1/C_t = 1/C_H + 1/ C_{diff}$$

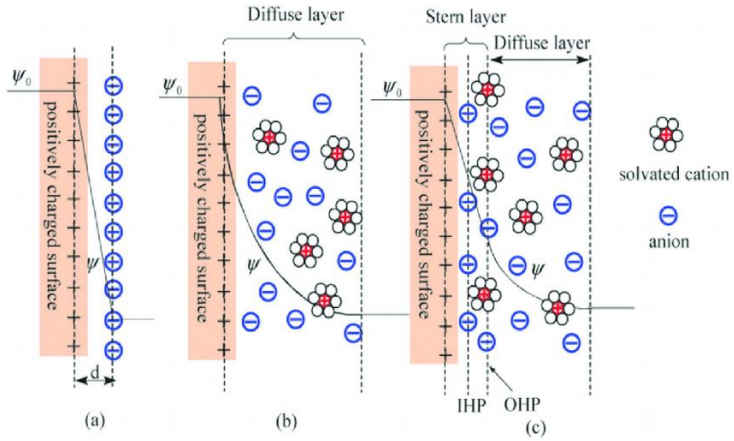

Figure 1.3 Models of the electrical double layer at a positively charged surface: (a) the Helmholtz model, (b) the Gouy–Chapman model, and (c) the Stern model, showing the inner Helmholtz plane (IHP) and outer Helmholtz plane (OHP)[14].

1.3.2 PSEUDOCAPACITORS

It involves the transfer of charge between electrode and electrolyte interface resulting in bulk oxidation in anode and reduction in cathode i.e. oxidation-reduction reactions or redox reaction. The amount of chemical reaction is proportional to the charge storage[15,16].

Energy storage in pseudocapacitors due to Faradaic process through the transfer of charge between electrode and electrolyte interface. This is accomplished through electrosorption, reduction-oxidation reactions, and intercalation processes. These Faradaic processes may allow pseudocapacitors to achieve greater capacitances and energy densities than EDLCs. The source of "pseudocapacitance" can be established in the association of the prefix "pseudo" and capacitance. It can be applied to define something that is fake or false, illusive, a sham (example: pseudoscience, methodology, a theory, or practice that is referred to be without scientific base)[17]. In other words, (i) not actually but having the appearance

of; (ii) nearly, more or less, approaching, or trying to be (example: pseudo-classicism, the imitative utilization of classicism in art and literature, widespread during the 18th century). Because the word “pseudocapacitance” was created in order to confine the properties of an electrode that behaves like a capacitor in its electrochemical signature, this second definition of “pseudo” is the more correct use in the present case.

In the field of electrochemical capacitors, the word “pseudocapacitance” is used to indicate the electrode materials (MnO_2 and RuO_2)[18,19] that have the electrochemical signature of a capacitive electrode (such as noticed with activated carbon)[20,21], i.e., exhibiting a linear dependence of the charge stored with the wideness of the potential window, but where charge storage arises from different reaction mechanisms. Pseudocapacitance arises at the surface of the electrodes where a totally distinct charge storage mechanism occurs. It is faradaic in nature, undergoing the passing of charge crossing the double layer, as in battery charging or discharging, but capacitance arises in account of the appropriate relation that can originate for thermodynamic reasons between the extent of charge acceptance and the change in potential so that the derivative charge acceptance to the change in potential, which is equivalent to a capacitance, can be formulated and experimentally measured by dc, ac, or transient methods. In addition, the average capacitance of redox electrodes is denoted as, $C = C_{dl} + C_{\Phi}$, where, C_{dl} is double layer capacitance and C_{Φ} is pseudocapacitance.

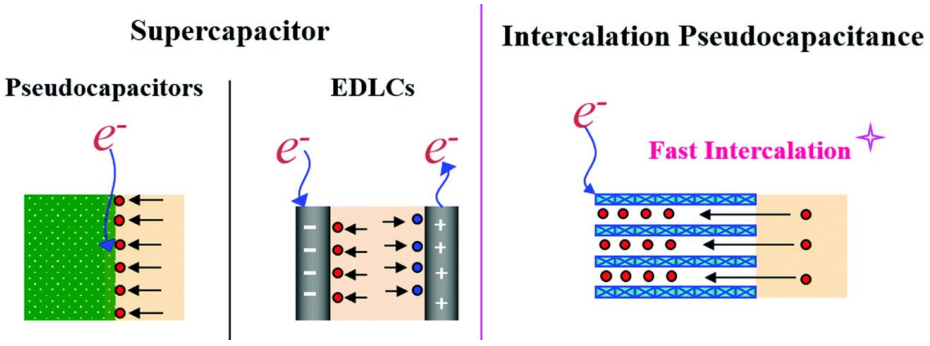

Figure 1.4 Schematic representation of the EDLC and pseudocapacitors

The principle difference of pseudocapacitors and EDLCs are that there is no net ion-exchange involving along with the electrode and electrolyte in EDLCs which implies that the electrolyte concentration remains stable all through the charge-discharge process[22]. But notably the EDL capacitance in such system always co-exists with pseudocapacitance. However, the number of ions to build an EDL formation is normally slighter than the number of protons exchanged between the electrodes. The values of pseudocapacitance are usually few times higher than EDL capacitance, results in both rapid adsorptions/desorption obvious reaction or multi-electron-transfer reaction through fast charge/discharge properties[23].

1.3.3 HYBRID CAPACITORS

Both Faradaic and non-Faradaic processes to store charge in hybrid capacitors to achieved a higher energy and power densities. Hybrid supercapacitors can combine the advantages of both EDLC and pseudocapacitor to meet the requirements of high energy density, high power density and high stability. Based upon the electrode configuration hybrid capacitors are classified as: composite, asymmetric and battery-type, respectively[24,25].

The term “hybrid” supercapacitor (is quite different from the “asymmetric” supercapacitor) which should be used when pairing two electrodes with different charge storage behavior, i.e., one faradaic and one capacitive, and the resulting device is in between a supercapacitor and a battery. Whereas, “asymmetric” supercapacitor covers a wider range of electrode combinations because it can be used for supercapacitors use electrodes of the same nature but with various mass loading, or two electrodes using different materials. Brousse et al, recently suggested the term “asymmetric” should be used only when pseudocapacitive or capacitive electrodes are involved in order to avoid confusion with true “hybrid” devices[26]. There are many literatures on the usage of faradaic electrode materials for electrochemical capacitor applications including our published reports. Unfortunately, some of these materials are denoted as “pseudocapacitive” materials although the reason that

their electrochemical signature (i.e., charge/discharge curve and cyclic voltammogram) is akin to that of “battery electrodes”. Generally, positive electrodes for hybrid supercapacitors are based on same faradaic reaction as we discussed in previous section. But it is potential independent charge storage behaviour which should be denoted as “battery like electrodes” of faradaic electrodes. Hybrid devices constitute a special case of asymmetric cells. In hybrid devices, various charge storage mechanisms are implemented in the positive and negative electrode materials. For instance, one electrode uses the double-layer storage mechanism (that is, porous carbon) while the other charge storage by means of faradaic reactions, that is, as occurs in transition metal oxides, except MnO_2, RuO_2 (which is called as asymmetric device as named by Brousse et al). Thus, the possible way to boosting the specific energy of the supercapacitor is to congregating the EDLC material as one electrode and faradaic material (ex, NiO) as another electrode.

1.3.4 Electrode materials

The capacitance and charge storage of supercapacitor mainly depend on the electrode materials and the electrolyte/device configurations. Therefore, further developing new electrode materials with high capacitance and improved performance relative to existing electrode materials is the most important method to overcome these challenges. In general, the electrode materials of supercapacitor can be classified as: (1) carbon materials with high specific surface area, (2) conducting polymers, (3) metal oxides, and (4) transition metal dichalcogenides.

1.3.4.1 Carbon based electrode materials

Carbon and carbon derivatives are the generally, the electrode materials for the electrical double layer capacitors. The various types of carbon materials used for the electrochemical double layer capacitors are activated carbon, carbon black, carbon nanotubes, graphene, and their derivates.

(A) Activated carbon : Activated carbon (AC) is a non-graphitic (disordered carbon) carbon and it has maximum amount of porous nature[20,27]. Similarly, the interplanar spacing (0.335 nm) of activated carbon is smaller than the graphite (0.34-0.35 nm) and this AC is composed of many numbers of disorder graphene layers or basal layer which is known as turbostatic carbon. Currently, ACs is mainly used as electrode material in commercial SCs because of their high surface area, good electrochemical stability, electrically conductive properties and better porous nature. Therefore, the conventional raw materials such as petroleum coke, tar pitches and coal could not meet our demand for the large-scale production of ACs due to their less availability as well as they are not renewable in nature and cost effective. Therefore, biomass is considered as the suitable precursor for the preparation of ACs, due to its availability and renewable in nature, waste management and cost effective.

(B) Carbon nanotube: CNTs show advantages of unique inter-connected mesoporous structure, high electronic conductivity, good mechanical and thermal stability[28–30]. These excellent properties of CNTs make them an interesting electrode material for EDLCs. The open and accessible network of mesopores in CNTs compared to other carbon materials provides a continuous charge distribution[31,32]. CNTs also have low ESR than activated carbon; the ESR can be further decreased by using suitable fabrication technique. Aligned CNTs is more efficient than tangled CNTs, due to the fast-ionic transportation. However, due to contact resistance at the interface between electrode and electrolyte, CNT-based supercapacitors show lower electrochemical performances.

(C) Graphene: Graphene, a 2D monolayer of sp^2 -hybridized carbon atoms, has much considered in recent years due to its exceptional mechanical, optical, thermal properties, outstanding electrical properties, and extreme large specific surface area (over 2600 $m^2 g^{-1}$)[33–35]. It is contributing stupendous new advances in the various fields, such as field-

effect transistors, biological/chemical sensors, transparent conductors, and energy storage and conversion devices. The merit of graphene in energy storage devices is quite large due to its interesting properties. Many methods such as thermal reduction, chemical reduction, electrochemical reduction, microwave assisted reduction and multistep reduction methods etc. have been used to synthesize graphene-based materials. Graphene based EDLCs was first reported by Stoller et al. They have prepared graphene by chemical modification and showed a capacitance of 135 F g^{-1} in aqueous electrolyte[36,37]. The energy density of EDLCs is still unsatisfactory with the severe requirements and development of EES devices.

1.3.4.2 CONDUCTING POLYMERS (CPs)

CPs are promising electrode materials for supercapacitors for three main reasons: (i) high specific capacitance because the doping process involves the entire polymer mass (ii) high conductivity in the charged state and (iii) doping/undoping process is generally fast[38–42], so that devices with low ESR and high specific power are feasible, in addition conventional CPs are low-cost[43–45]. The conducting polymer negatively charged (n-doped) and positively charged (p-doped) polymer electrode have the greatest potential energy and power densities. However, the polymer electrode materials do not have long term stability and cycle life during charge- discharge cycle due to swelling and shrinking of electro-active of the conducting polymers leads to degradation of the carbon backbone chain[46].

1.3.4.3 METAL OXIDES

Metal oxides are electrode material due high conductivity, cheaper transition metal oxide candidates with good capacitive values have attracted much attention[47–51]. The cyclic voltammogram (CV) of metal oxides such as RuO_2 and IrO_2 electrodes have an almost rectangular shape. However, the shape of the CV is a sequence of redox reactions occurring in the metallic oxide. Hydrous ruthenium oxides are used for supercapacitors because of their

high theoretical specific capacitance (1358 F/ g) and high electrical conductivity (3 * 10^2 S /cm), specific capacitance (750 F/ g). 90% of the cost involved in the preparation of the electrode material. However, despite this potential are limited by its prohibitive cost. Now the low-cost metal oxides such as MnO_2, MoO_3, VO_x, and WO_3 are used for supercapacitor[52,53].

1.3.4.4 Transition metal chalcogenides

Recently, two-dimensional (2D) nanomaterials, particularly layered transition metal dichalcogenides (TMDs), are emerging as a class of key materials in chemistry and electronics due to their intriguing chemical and electronic properties and therefore hold great promise for a variety of applications including electrocatalysts, electronics devices and energy storage[54–56]. Metal sulfides are also known to be electrochemically active materials for supercapacitor applications, but to date very few metal sulfides such as WS_2, ReS_2, MoS_2, have been employed to fabricate supercapacitor electrodes due to their high conductivity and high surface area. Among the TMDs layered compounds, MoS_2, $MoSe_2$, MnSe, WS_2, and WSe_2 are semiconductors; VS_2 and VSe_2 are metallic[57–61]. Therefore, developing a TMDs materials by a cost effective, simple method for energy storage and energy conversion devices is extremely urgent[62–65]. However, TMDs with very few layered shows extensive properties compared the bulk counterpart, Therefore, much more efforts must be made to apply layered TMDs to supercapacitors, using organic/ionic electrolyte for the energy storage system.

1.4. Energy harvesting: Nanogenerator

In recent years, searching and developing for sustainable**,** renewable and green energy has been one of the most important tasks for the researchers to address the rapidly increasing global warming and energy crisis in the world[66,67]. As for energy harvesting from ambient environment such as solar, wind, thermal, chemical and mechanical energy has attracted huge

attention in the researcher due to the independent and sustainable operating of such systems without the use of a battery[68,69]. Among them, harvesting mechanical energy from our living environment (include sound, friction, motion, wind, and noise) is widely considered to be one of the promising approaches to provide a clean and green energy source for self powered devices, such as wireless sensor networks, implanted medical devices, nanorobotics, security applications and portable/wearable personal electronics. The mechanical energy directly converts into electrical energy using piezoelectric, triboelectric, electromagnetic, and electrostatic principles[70–72].

Among the conversion methods, nanogenerator (NG) has been developed for converting low frequency mechanical energy into electricity though piezoelectric and tribo-electrification processes and they have been demonstrated to power small electronic devices[73]. The vibration energy is enormous and available everywhere at any time. The harvesting energy is small but it has the potential to operate wearable and portable devices with the asset of power source without external power. Basically, piezoelectric nanogenerator (PNG) depends on the piezoelectric potential which created by an externally applied force in the piezoelectric material for driving the flow of electrons to the external load. Since, PNG have been developed to efficiently convert small scale mechanical energy into electricity and used as power source for diverse applications[68,74].

1.4.1. Mechanism of piezoelectric nanogenerator

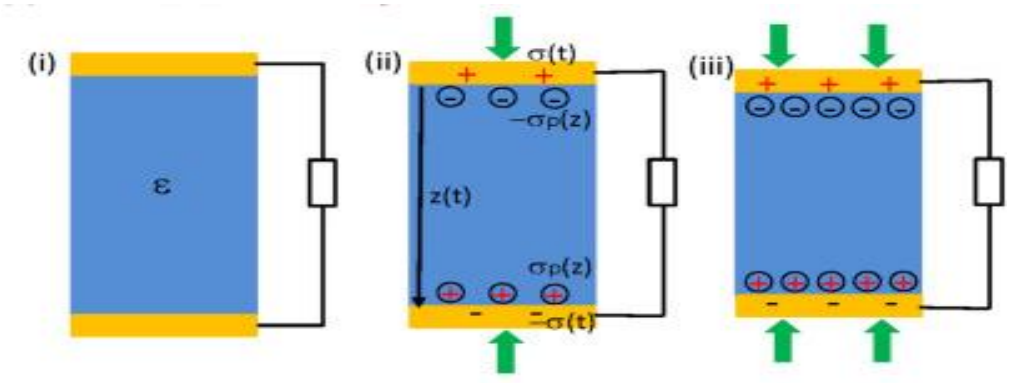

Figure 1.5 Mechanism of the piezoelectric nanogenerator.

The mechanism of the nanogenerator was explained through the piezoelectric effect. At the initial state, there is no piezoelectric potential generation in device, as shown in Figure 1.5. When a compressive force is applied to the device, the piezoelectric potential is generated inside the piezo-materials abruptly and the electric dipoles align strongly in a single direction due to stress-induced poling effect, which creates a significant potential across the electrodes, as shown Figure 1.5. In order to screen the piezoelectric potential, positive and negative charges are accumulated at the top and bottom electrodes, respectively, resulting in voltage and current output signals from the device. Further, when the compressive force is removed, the piezoelectric potential is diminished, and the accumulated charges move back to the opposite direction (Figure 1.5). Therefore, continuous application and releasing of the compressive force results in AC-type voltage and current output signals from the nanogenerator.

1.4.2. Piezo-materials

Many research groups have attempted to fabricate high performance nanogenerators using different materials and architectural forms. A variety of nanostructured piezoelectric materials such as zinc oxide, lead zirconium titanate (PZT)[75], cadmium sulfide, barium titanate[76], gallium nitride, AlGaN nanocones, poly (vinylidene fluoride)[77] and polytetrafluoroethylene, and piezoelectric polymers in the form of nanorods, wires, fibers, micro belts and thin films were utilized for self-driven power source applications[78,79]. Among the various piezoelectric materials studied for nanogenerator, many of the researches have focused on the materials with wurtzite structure such as ZnO, CdS and GaN. The greatest advantage of these material arises from the facile and cost-effective fabrication techniques[80].

1.5. Objectives and scope of thesis

To develop high-performance supercapacitors, the key shortcoming of supercapacitors, such as low energy density, and cost of electrode materials must be addressed. The inadequate charge accumulation in the electrical double layer limits the specific capacitance and energy density of EDLCs (carbon electrodes). In contrast, pseudocapacitors (metal oxide or conducting polymer electrodes) generally have higher specific capacitance and energy density which gradually decrease due to the poor electrical conductivity. Therefore, metal oxides and carbon materials may not be employed alone as the supercapacitor electrodes for practical purpose. There is an urgent demand to improve the electrochemical performance of supercapacitor electrode materials. Thus, to exploit advanced electrode materials is the key to develop high-performance supercapacitors. Therefore, significant efforts have been devoted to develop various electrode materials such as battery type electrodes ($LiMn_2O_4$, Cu-HCF, Mn-HCF, copper tungsten sulfide), transition metal compounds (TiO_2, Siloxene, HT-siloxene, Siloxy carbide) and transition metal chalcogenides (MoS_2, $MoSe_2$, ReS_2) materials for high performance supercapacitor application. It is one of the most significant ongoing research in the field of energy storage systems in recent times.

With these considerations, this thesis aimed to design and prepare novel electrode materials that simultaneously possess high power density, high energy density as well as good rate capability, cyclic stability, low cost and environmentally free. The specific research activities in this thesis aim to:

- Construct complex nanoscale architectures with a combination of battery type and capacitive type electrodes for high-performance supercapacitors.
- Investigate the mechanical properties including bending/folding strength as well as excellent flexibility of 2D nanomaterials by preparing MoS_2, $MoSe_2$, ReS_2, Siloxene,

blue TiO_2 and siloxy carbide as high-performance supercapacitor electrodes using organic/ionic electrolyte.

- Design novel nanostructured materials and identify the proficiency and efficiency of the fabricated all-solid-state supercapacitors, to construct an energy module by integrating supercapacitor with nanogenerator, for self-powered devices operation.
- Lastly, the thesis aimed to develop new self-charging supercapacitor power cell for directly converting mechanical energy into electrochemical energy. Such a device hybridizes a piezoelectric nanogenerator, a supercapacitor, and a power-management system, and can be directly used as a power source.

The results presented in this thesis may provide simple and effective approaches to preparing two-dimensional nanomaterials as supercapacitor electrodes. In addition, the development of SCSPC provide a new promising direction in the field supercapacitor research for the development of next generation self-powered sustainable power source for wearable and flexible electronic devices.

1.6. Structure of this thesis

This thesis is systematized into eight chapters,

Chapter - 1 describes that the detailed introduction about the energy storage systems, electrochemical capacitors, mechanism of the different types of electrochemical capacitors, materials used in the different electrochemical capacitors and energy harvesting system.

Chapter - 2 provides details of the chemicals and reagents, experimental setups and methods used in the thesis. Also, it accords with the different characterization performed in the analysis of properties of the materials like structural, optical, composition, morphological and electrochemical properties. The details about the device and working electrodes preparation, electrolyte preparation, electrochemical measurement techniques and equations used for linear and non-liner profiles are presented.

Chapter – 3 presents the synthesis of battery type electrodes ($LiMn_2O_4$, Cu-HCF, Mn-HCF, copper tungsten sulfide) and their structural and electrochemical properties as a positive electrode material for supercapacitor applications.

Chapter – 4 presents the synthesis of layered transition metal compounds (Siloxene, blue TiO_2 and siloxy carbide) and their structural and electrochemical properties as electrode material for supercapacitor applications using ionic liquid electrolyte.

Chapter – 5 emphasizes the improved electrochemical performances of 2D TMCS for electrochemical energy storage system suing ionic liquid as electrolyte.

Chapter – 6 describes the fabrication and self-charging performance of Self-Charging Supercapacitor Power Cell (SCSPC) using electrospun PVDF-$NaNbO_3$ as a piezoelectric as well as a separator and electrochemically active materials as positive and negative electrodes, respectively for the first time. The fabrication and working mechanism of a SCSPC was discussed in detail. The SCSPC provide a new promising direction in the supercapacitor research for the development of next generation self-powered sustainable power source for wearable and flexible electronic devices.

Chapter 7 summarizes the salient features of the present study and outlined some suggestions for future work.

1.7. References:

[1] G. Ren, G. Ma, N. Cong, Review of electrical energy storage system for vehicular applications, Renew. Sustain. Energy Rev. 41 (2015) 225–236. doi:10.1016/j.rser.2014.08.003.

[2] W.K. Chee, H.N. Lim, Z. Zainal, N.M. Huang, I. Harrison, Y. Andou, Flexible Graphene-Based Supercapacitors: A Review, J. Phys. Chem. C. 120 (2016) 4153–4172. doi:10.1021/acs.jpcc.5b10187.

[3] A. González, E. Goikolea, J.A. Barrena, R. Mysyk, Review on supercapacitors: Technologies and materials, Renew. Sustain. Energy Rev. 58 (2016) 1189–1206. doi:10.1016/j.rser.2015.12.249.

[4] M. Höök, X. Tang, Depletion of fossil fuels and anthropogenic climate change—A review, Energy Policy. 52 (2013) 797–809. doi:10.1016/j.enpol.2012.10.046.

[5] Y.-Z. Zhang, Y. Wang, T. Cheng, W.-Y. Lai, H. Pang, W. Huang, Flexible supercapacitors based on paper substrates: a new paradigm for low-cost energy storage, Chem. Soc. Rev. 44 (2015) 5181–5199. doi:10.1039/C5CS00174A.

[6] S.J. Patil, A.C. Lokhande, J.S. Park, J.H. Kim, Y.B. Kim, B.C. Choi, S.H. Park, S.H. Jung, D.W. Lee, Towards high performance unique microstructures of Co_9S_8//$CoFe_2O_4$ for asymmetric supercapacitor, J. Ind. Eng. Chem. (2017). doi:10.1016/j.jiec.2017.12.018.

[7] B. Mendoza-Sánchez, Y. Gogotsi, Synthesis of Two-Dimensional Materials for Capacitive Energy Storage, Adv. Mater. 28 (2016) 6104–6135. doi:10.1002/adma.201506133.

[8] C. Zhong, Y. Deng, W. Hu, J. Qiao, L. Zhang, J. Zhang, A review of electrolyte materials and compositions for electrochemical supercapacitors., Chem. Soc. Rev. 44 (2015) 7484–7539. doi:10.1039/c5cs00303b.

[9] G. Wang, L. Zhang, J. Zhang, A review of electrode materials for electrochemical supercapacitors, Chem. Soc. Rev. 41 (2012) 797–828. doi:10.1039/C1CS15060J.

[10] S. Peng, L. Li, H. Bin Wu, S. Madhavi, X.W.D. Lou, Controlled Growth of $NiMoO_4$ Nanosheet and Nanorod Arrays on Various Conductive Substrates as Advanced Electrodes for Asymmetric Supercapacitors, Adv. Energy Mater. 5 (2015) 1401172. doi:10.1002/aenm.201401172.

[11] S. Gao, J. Zhao, Y. Zhao, Y. Wu, X. Zhang, L. Wang, X. Liu, Y. Rui, J. Xu, Na_2CoSiO_4 as a novel positive electrode material for sodium-ion capacitors, Mater. Lett. 158 (2015) 300–303. doi:10.1016/j.matlet.2015.06.038.

[12] A.K. Samantara, S. Ratha, Components of Supercapacitor, in: Springer, Singapore, 2018: pp. 11–39. doi:10.1007/978-981-10-7263-5_3.

[13] A. Borenstein, O. Hanna, R. Attias, S. Luski, T. Brousse, D. Aurbach, Carbon-based composite materials for supercapacitor electrodes: a review, J. Mater. Chem. A. 5 (2017) 12653–12672. doi:10.1039/C7TA00863E.

[14] L.L. Zhang, X.S. Zhao, Carbon-based materials as supercapacitor electrodes, Chem. Soc. Rev. 38 (2009) 2520. doi:10.1039/b813846j.

[15] T.N.Y. Khawula, K. Raju, P.J. Franklyn, I. Sigalas, K.I. Ozoemena, Symmetric pseudocapacitors based on molybdenum disulfide (MoS_2)-modified carbon nanospheres: Correlating physicochemistry and synergistic interaction on energy storage, J. Mater. Chem. A. 4 (2016) 6411–6425. doi:10.1039/c6ta00114a.

[16] V. Augustyn, P. Simon, B. Dunn, Pseudocapacitive oxide materials for high-rate electrochemical energy storage, Energy Environ. Sci. 7 (2014) 1597. doi:10.1039/c3ee44164d.

[17] K. Krishnamoorthy, S. Thangavel, J. Chelora Veetil, N. Raju, G. Venugopal, S.J. Kim, Graphdiyne nanostructures as a new electrode material for electrochemical

supercapacitors, Int. J. Hydrogen Energy. 41 (2016) 1672–1678. doi:10.1016/j.ijhydene.2015.10.118.

[18] J. Ni, W. Lu, L. Zhang, B. Yue, X. Shang, Y. Lv, Low-Temperature Synthesis of Monodisperse 3D Manganese Oxide Nanoflowers and Their Pseudocapacitance Properties, J. Phys. Chem. C. 113 (2009) 54–60. doi:10.1021/jp806454r.

[19] J.P. Zheng, Hydrous Ruthenium Oxide as an Electrode Material for Electrochemical Capacitors, J. Electrochem. Soc. 142 (1995) 2699. doi:10.1149/1.2050077.

[20] H. Kim, K.-Y. Park, M.-Y. Cho, M.-H. Kim, J. Hong, S.-K. Jung, K.C. Roh, K. Kang, High-Performance Hybrid Supercapacitor Based on Graphene-Wrapped $Li_4Ti_5O_{12}$ and Activated Carbon, ChemElectroChem. 1 (2014) 125–130. doi:10.1002/celc.201300186.

[21] Z. Ye, F. Wang, C. Jia, Z. Shao, Biomass-based O, N-codoped activated carbon aerogels with ultramicropores for supercapacitors, J. Mater. Sci. 53 (2018) 12374–12387. doi:10.1007/s10853-018-2487-x.

[22] A. Laheäär, P. Przygocki, Q. Abbas, F. Béguin, Appropriate methods for evaluating the efficiency and capacitive behavior of different types of supercapacitors, Electrochem. Commun. 60 (2015) 21–25. doi:10.1016/j.elecom.2015.07.022.

[23] G.K. Veerasubramani, A. Chandrasekhar, S. M. S. P., Y.S. Mok, S.J. Kim, Liquid electrolyte mediated flexible pouch-type hybrid supercapacitor based on binderless core–shell nanostructures assembled with honeycomb-like porous carbon, J. Mater. Chem. A. 5 (2017) 11100–11113. doi:10.1039/C7TA01308F.

[24] S.N. Guo, Y. Zhu, Y.Y. Yan, Y.L. Min, J.C. Fan, Q.J. Xu, H. Yun, (Metal-Organic Framework)-Polyaniline sandwich structure composites as novel hybrid electrode materials for high-performance supercapacitor, J. Power Sources. 316 (2016) 176–182. doi:10.1016/j.jpowsour.2016.03.040.

[25] P. Pazhamalai, K. Krishnamoorthy, M.S.P. Sudhakaran, S.J. Kim, Fabrication of High-Performance Aqueous Li-Ion Hybrid Capacitor with $LiMn_2O_4$ and Graphene, ChemElectroChem. 4 (2017) 396–403. doi:10.1002/celc.201600550.

[26] T. Brousse, D. Belanger, J.W. Long, To Be or Not To Be Pseudocapacitive?, J. Electrochem. Soc. 162 (2015) A5185–A5189. doi:10.1149/2.0201505jes.

[27] W. Qian, F. Sun, Y. Xu, L. Qiu, C. Liu, S. Wang, F. Yan, Human hair-derived carbon flakes for electrochemical supercapacitors, Energy Environ. Sci. 7 (2014) 379–386. doi:10.1039/c3ee43111h.

[28] Y. Dall'Agnese, P. Rozier, P.L. Taberna, Y. Gogotsi, P. Simon, Capacitance of two-dimensional titanium carbide (MXene) and MXene/carbon nanotube composites in organic electrolytes, J. Power Sources. 306 (2016) 510–515. doi:10.1016/j.jpowsour.2015.12.036.

[29] E.A. Nagelli, L. Huang, A.Q.Z. Dai, F. Du, L. Dai, 3D Vertically Aligned CNT/Graphene Hybrids from Layer-by-Layer Transfer for Supercapacitors, Part. Part. Syst. Charact. 34 (2017) 1700131. doi:10.1002/ppsc.201700131.

[30] S. Chen, Q. Wu, M. Wen, C. Wang, Q. Wu, J. Wen, M. Zhu, Y. Wang, A Tubular Sandwich-Structured CNT@Ni@$Ni_2(CO_3)(OH)_2$ with High Stability and Superior Capacity as Hybrid Supercapacitor, J. Phys. Chem. C. 121 (2017) 9719–9728. doi:10.1021/acs.jpcc.7b01551.

[31] J.P. Alper, M. Vincent, C. Carraro, R. Maboudian, Silicon carbide coated silicon nanowires as robust electrode material for aqueous micro-supercapacitor, Appl. Phys. Lett. 100 (2012) 163901. doi:10.1063/1.4704187.

[32] B. Pan, J. Xiao, J. Li, P. Liu, C. Wang, G. Yang, Carbyne with finite length: The one-dimensional sp carbon, Sci. Adv. 1 (2015) e1500857–e1500857. doi:10.1126/sciadv.1500857.

[33] H.J. Kim, S.Y. Lee, L.H. Sinh, C.S. Yeo, Y.R. Son, K.R. Cho, Y.K. Song, S. Ju, M.K. Shin, S.J. Park, S.Y. Park, Maximizing volumetric energy density of all-graphene-oxide-supercapacitors and their potential applications for energy harvest, 2017. doi:10.1016/j.jpowsour.2017.02.040.

[34] K. Krishnamoorthy, S.J. Kim, Mechanochemical preparation of graphene nanosheets and their supercapacitor applications, J. Ind. Eng. Chem. 32 (2015) 39–43. doi:10.1016/j.jiec.2015.09.012.

[35] K. Wang, L. Li, T. Zhang, Z. Liu, Nitrogen-doped graphene for supercapacitor with long-term electrochemical stability, Energy. 70 (2014) 612–617. doi:10.1016/j.energy.2014.04.034.

[36] M.D. Stoller, R.S. Ruoff, Best practice methods for determining an electrode material's performance for ultracapacitors, Energy Environ. Sci. 3 (2010) 1294. doi:10.1039/c0ee00074d.

[37] M.D. Stoller, S. Park, Y. Zhu, J. An, R.S. Ruoff, Graphene-Based Ultracapacitors, Nano Lett. 8 (2008) 3498–3502. doi:10.1021/nl802558y.

[38] S.K. Simotwo, V. Kalra, Polyaniline-carbon based binder-free asymmetric supercapacitor in neutral aqueous electrolyte, Electrochim. Acta. 268 (2018) 131–138. doi:10.1016/j.electacta.2018.01.157.

[39] A. Afzal, F.A. Abuilaiwi, A. Habib, M. Awais, S.B. Waje, M.A. Atieh, Polypyrrole/carbon nanotube supercapacitorsTechnological advances and challenges, J. Power Sources. 352 (2017) 174–186. doi:10.1016/j.jpowsour.2017.03.128.

[40] D. Aradilla, F. Gao, G. Lewes-Malandrakis, W. Müller-Sebert, P. Gentile, M. Boniface, D. Aldakov, B. Iliev, T.J.S. Schubert, C.E. Nebel, G. Bidan, Designing 3D Multihierarchical Heteronanostructures for High-Performance On-Chip Hybrid Supercapacitors: Poly(3,4-(ethylenedioxy)thiophene)-Coated Diamond/Silicon

Nanowire Electrodes in an Aprotic Ionic Liquid, ACS Appl. Mater. Interfaces. 8 (2016) 18069–18077. doi:10.1021/acsami.6b04816.

[41] X.F. Qiao, J. Bin Wu, L. Zhou, J. Qiao, W. Shi, T. Chen, X. Zhang, J. Zhang, W. Ji, P.H. Tan, Polytypism and unexpected strong interlayer coupling in two-dimensional layered ReS_2, Nanoscale. 8 (2016) 8324–8332. doi:10.1039/c6nr01569g.

[42] S.R.P. Gnanakan, N. Murugananthem, A. Subramania, Organic acid doped polythiophene nanoparticles as electrode material for redox supercapacitors, Polym. Adv. Technol. 22 (2011) 788–793. doi:10.1002/pat.1578.

[43] A. Chellachamy Anbalagan, S.N. Sawant, Brine solution-driven synthesis of porous polyaniline for supercapacitor electrode application, Polymer (Guildf). 87 (2016) 129–137. doi:10.1016/j.polymer.2016.01.049.

[44] A. Shanmugavani, S. Kaviselvi, K.V. Sankar, R.K. Selvan, Enhanced electrochemical performances of PANI using redox additive of $K_4[Fe(CN)_6]$ in aqueous electrolyte for symmetric supercapacitors, Mater. Res. Bull. 62 (2015) 161–167. doi:10.1016/j.materresbull.2014.10.075.

[45] K.J. Huang, L. Wang, Y.J. Liu, H.B. Wang, Y.M. Liu, L.L. Wang, Synthesis of polyaniline/2-dimensional graphene analog MoS_2 composites for high-performance supercapacitor, Electrochim. Acta. 109 (2013) 587–594. doi:10.1016/j.electacta.2013.07.168.

[46] W. Lin, K. Xu, J. Peng, Y. Xing, S. Gao, Y. Ren, M. Chen, Hierarchically structured carbon nanofiber-silsesquioxane-polyaniline nanohybrids for flexible supercapacitor electrodes, J. Mater. Chem. A. 3 (2015) 8438–8449. doi:10.1039/c4ta06806h.

[47] W. Zeng, G. Zhang, S. Hou, T. Wang, H. Duan, Facile synthesis of graphene@NiO/MoO_3 composite nanosheet arrays for high-performance supercapacitors, Electrochim. Acta. 151 (2015) 510–516.

doi:10.1016/j.electacta.2014.11.088.

[48] A. Pathak, A.S. Gangan, S. Ratha, B. Chakraborty, C.S. Rout, Enhanced Pseudocapacitance of MoO_3-Reduced Graphene Oxide Hybrids with Insight from Density Functional Theory Investigations, J. Phys. Chem. C. 121 (2017) 18992–19001. doi:10.1021/acs.jpcc.7b04478.

[49] S. Ardizzone, G. Fregonara, S. Trasatti, "Inner" and "outer" active surface of RuO_2 electrodes, Electrochim. Acta. 35 (1990) 263–267. doi:10.1016/0013-4686(90)85068-X.

[50] X. Lu, M. Yu, G. Wang, T. Zhai, S. Xie, Y. Ling, Y. Tong, Y. Li, H-TiO_2@MnO_2//H-TiO_2@C core-shell nanowires for high performance and flexible asymmetric supercapacitors, Adv. Mater. 25 (2013) 267–272. doi:10.1002/adma.201203410.

[51] Z. Liu, H. Zhang, Q. Yang, Y. Chen, Graphene/V_2O_5 hybrid electrode for an asymmetric supercapacitor with high energy density in an organic electrolyte, Electrochim. Acta. 287 (2018) 149–157. doi:10.1016/j.electacta.2018.04.212.

[52] S.M. Cha, G. Nagaraju, S. Chandra Sekhar, J.S. Yu, A facile drop-casting approach to nanostructured copper oxide-painted conductive woven textile as binder-free electrode for improved energy storage performance in redox-additive electrolyte, J. Mater. Chem. A. 5 (2017) 2224–2234. doi:10.1039/C6TA10428B.

[53] S. Ratha, C.S. Rout, Supercapacitor Electrodes Based on Layered Tungsten Disulfide-Reduced Graphene Oxide Hybrids Synthesized by a Facile Hydrothermal Method, ACS Appl. Mater. Interfaces. 5 (2013) 11427–11433. doi:10.1021/am403663f.

[54] M. Rahman, K. Davey, S.Z. Qiao, Advent of 2D Rhenium Disulfide (ReS_2): Fundamentals to Applications, Adv. Funct. Mater. 27 (2017) 1606129. doi:10.1002/adfm.201606129.

[55] P. Miró, M. Audiffred, T. Heine, An atlas of two-dimensional materials, Chem. Soc.

Rev. 43 (2014) 6537–6554. doi:10.1039/C4CS00102H.

[56] H.T. Tan, W. Sun, L. Wang, Q. Yan, 2D Transition Metal Oxides/Hydroxides for Energy-Storage Applications, ChemNanoMat. 2 (2016) 562–577. doi:10.1002/cnma.201500177.

[57] A. Ambrosi, Z. Sofer, M. Pumera, 2H → 1T phase transition and hydrogen evolution activity of MoS_2 , $MoSe_2$, WS_2 and WSe_2 strongly depends on the MX_2 composition, Chem. Commun. 51 (2015) 8450–8453. doi:10.1039/C5CC00803D.

[58] M. Jiang, J. Zhang, M. Wu, W. Jian, H. Xue, T.-W. Ng, C.-S. Lee, J. Xu, Synthesis of 1T-$MoSe_2$ ultrathin nanosheets with an expanded interlayer spacing of 1.17 nm for efficient hydrogen evolution reaction, J. Mater. Chem. A. 4 (2016) 14949–14953. doi:10.1039/C6TA07020E.

[59] M. Acerce, D. Voiry, M. Chhowalla, Metallic 1T phase MoS_2 nanosheets as supercapacitor electrode materials, Nat. Nanotechnol. 10 (2015) 313–318. doi:10.1038/nnano.2015.40.

[60] A.L. Friedman, A.T. Hanbicki, F.K. Perkins, G.G. Jernigan, J.C. Culbertson, P.M. Campbell, Evidence for Chemical Vapor Induced 2H to 1T Phase Transition in MoX_2 (X = Se, S) Transition Metal Dichalcogenide Films, Sci. Rep. 7 (2017) 3836. doi:10.1038/s41598-017-04224-4.

[61] B. Jariwala, D. Voiry, A. Jindal, B.A. Chalke, R. Bapat, A. Thamizhavel, M. Chhowalla, M. Deshmukh, A. Bhattacharya, Synthesis and Characterization of ReS_2 and $ReSe_2$ Layered Chalcogenide Single Crystals, Chem. Mater. 28 (2016) 3352–3359. doi:10.1021/acs.chemmater.6b00364.

[62] S.B. Patil, K. Adpakpang, S.M. Oh, J.M. Lee, S.-J. Hwang, Reductive hybridization route with exfoliated graphene oxide and MoS_2 nanosheets to efficient electrode materials, Electrochim. Acta. 176 (2015) 188–196.

doi:10.1016/j.electacta.2015.06.133.

[63] X. Fu, P. Ilanchezhiyan, G. Mohan Kumar, H.D. Cho, L. Zhang, A.S. Chan, D.J. Lee, G.N. Panin, T.W. Kang, Tunable UV-visible absorption of SnS_2 layered quantum dots produced by liquid phase exfoliation, Nanoscale. 9 (2017) 1820–1826. doi:10.1039/C6NR09022B.

[64] J. Xiao, D. Choi, L. Cosimbescu, P. Koech, J. Liu, J.P. Lemmon, Exfoliated MoS_2 nanocomposite as an anode material for lithium ion batteries, Chem. Mater. 22 (2010) 4522–4524. doi:10.1021/cm101254j.

[65] T. Fujita, Y. Ito, Y. Tan, H. Yamaguchi, D. Hojo, A. Hirata, D. Voiry, M. Chhowalla, M. Chen, Chemically exfoliated ReS_2 nanosheets, Nanoscale. 6 (2014) 12458–12462. doi:10.1039/c4nr03740e.

[66] M. Choi, G. Murillo, S. Hwang, J.W. Kim, J.H. Jung, C.-Y. Chen, M. Lee, Mechanical and electrical characterization of PVDF-ZnO hybrid structure for application to nanogenerator, Nano Energy. 33 (2017) 462–468. doi:10.1016/j.nanoen.2017.01.062.

[67] Y. Chen, Y. Zhang, Z. Wang, T. Zhan, Y.-C. Wang, H. Zou, H. Ren, G. Zhang, C. Zou, Z.L. Wang, Dynamic Electronic Doping for Correlated Oxides by a Triboelectric Nanogenerator, Adv. Mater. (2018) 1803580. doi:10.1002/adma.201803580.

[68] K. Parida, V. Bhavanasi, V. Kumar, J. Wang, P.S. Lee, Fast charging self-powered electric double layer capacitor, J. Power Sources. 342 (2017) 70–78. doi:10.1016/j.jpowsour.2016.11.083.

[69] R. Liu, J. Wang, T. Sun, M. Wang, C. Wu, H. Zou, T. Song, X. Zhang, S.-T. Lee, Z.L. Wang, B. Sun, Silicon Nanowire/Polymer Hybrid Solar Cell-Supercapacitor: A Self-Charging Power Unit with a Total Efficiency of 10.5%, Nano Lett. 17 (2017) 4240–4247. doi:10.1021/acs.nanolett.7b01154.

[70] H. Parangusan, D. Ponnamma, M.A.A. Al-Maadeed, Stretchable Electrospun PVDF-

HFP/Co-ZnO Nanofibers as Piezoelectric Nanogenerators, Sci. Rep. 8 (2018) 754. doi:10.1038/s41598-017-19082-3.

[71] A. Ramadoss, B. Saravanakumar, S.W. Lee, Y.-S. Kim, S.J. Kim, Z.L. Wang, Piezoelectric-Driven Self-Charging Supercapacitor Power Cell, ACS Nano. 9 (2015) 4337–4345. doi:10.1021/acsnano.5b00759.

[72] Y.-S. Kim, Y. Xie, X. Wen, S. Wang, S.J. Kim, H.-K. Song, Z.L. Wang, Highly porous piezoelectric PVDF membrane as effective lithium ion transfer channels for enhanced self-charging power cell, Nano Energy. 14 (2015) 77–86. doi:10.1016/j.nanoen.2015.01.006.

[73] X. Cao, Y. Jie, N. Wang, Z.L. Wang, Triboelectric Nanogenerators Driven Self-Powered Electrochemical Processes for Energy and Environmental Science, Adv. Energy Mater. 6 (2016) 1600665. doi:10.1002/aenm.201600665.

[74] X. Xiao, T. Li, P. Yang, Y. Gao, H. Jin, W. Ni, W. Zhan, X. Zhang, Y. Cao, J. Zhong, L. Gong, W.-C. Yen, W. Mai, J. Chen, K. Huo, Y.-L. Chueh, Z.L. Wang, J. Zhou, Fiber-Based All-Solid-State Flexible Supercapacitors for Self-Powered Systems, ACS Nano. 6 (2012) 9200–9206. doi:10.1021/nn303530k.

[75] Y. Zhang, Y. Zhang, X. Xue, C. Cui, B. He, Y. Nie, P. Deng, Z. Lin Wang, PVDF-PZT nanocomposite film based self-charging power cell., Nanotechnology. 25 (2014) 105401. doi:10.1088/0957-4484/25/10/105401.

[76] T.G. Mofokeng, A.S. Luyt, V.P. Pavlović, V.B. Pavlović, D. Dudić, B. Vlahović, V. Djoković, Ferroelectric nanocomposites of polyvinylidene fluoride/polymethyl methacrylate blend and $BaTiO_3$ particles: Fabrication of β-crystal polymorph rich matrix through mechanical activation of the filler, J. Appl. Phys. 115 (2014) 084109. doi:10.1063/1.4866694.

[77] E.J. Ko, E.J. Lee, M.H. Choi, T.H. Sung, D.K. Moon, PVDF based flexible

piezoelectric nanogenerators using conjugated polymer:PCBM blend systems, Sensors Actuators A Phys. 259 (2017) 112–120. doi:10.1016/j.sna.2017.03.013.

[78] A.C. Wang, C. Wu, D. Pisignano, Z.L. Wang, L. Persano, Polymer nanogenerators: Opportunities and challenges for large-scale applications, J. Appl. Polym. Sci. 135 (2018) 45674. doi:10.1002/app.45674.

[79] M.S. Sorayani Bafqi, R. Bagherzadeh, M. Latifi, Fabrication of composite PVDF-ZnO nanofiber mats by electrospinning for energy scavenging application with enhanced efficiency, J. Polym. Res. 22 (2015) 130. doi:10.1007/s10965-015-0765-8.

[80] J. Briscoe, N. Jalali, P. Woolliams, M. Stewart, P.M. Weaver, M. Cain, S. Dunn, Measurement techniques for piezoelectric nanogenerators, Energy Environ. Sci. 6 (2013) 3035. doi:10.1039/c3ee41889h.

CHAPTER 2

MATERIALS, METHODS OF PREPARATION, CHARACTERIZATION AND FABRICATION TECHNIQUES

This chapter explains the detailed information regarding the materials, preparation, characterization and the fabrication technique which are adapted for the present investigation of this work. To accomplish the research objective, experimental work was done in the laboratory, followed by physicochemical characterization and evaluation of the electrochemical properties of the obtained materials. This chapter describes the experimental details including the materials, chemicals and apparatus used in the research project. The typical materials synthesis methods such as sol-gel combustion, hydrothermal, sonication, electrospinning, topotactic extraction, mechano-milling and modified hummers method for the preparation of graphene oxide synthesis was used in this investigation. The basic materials characterization techniques for structure, morphology, composition, surface area and optical properties are also used in this investigation. The electrode fabrication, cell assembly, and electrochemical measurement is discussed in detail.

2.1 Materials and Apparatus

The materials in this thesis experiments were of research grade and used without any further purification. The list materials used in this thesis are given in Table 2.1.

Table 2.1 Materials and chemicals used in this thesis.

Chemicals	Formula	Purity	Supplier
Lithium nitrate	$LiNO_3$	98%	Daejung Chemicals & Metals Co. Ltd, South Korea
Manganese nitrate	$Mn(NO_3)_2$	97%	
Glycine	$C_2H_5NO_2$	99%	
Potassium permanganate	$KMnO_4$	99.3%	
Sodium hydroxide	NaOH	98%	
Carbon black	C	99.9%	
Sodium tungstate	Na_2WO_4	98%	
Copper chloride	$CuCl_2$	97%	
Lithium sulfate	Li_2SO_4	99%	
Thioacetamide	C_2H_5NS	98%	
Sodium molybdate	Na_2MoO_4	98.5%	
Selenium	Se	99%	
Sodium borohydride	$NaBH_4$	98%	
Copper nitrate	$Cu(NO_3)_2$	98%	
Potassium ferricyanide	$K_3[Fe(CN)_6]$	99%	
Thiourea	CH_4N_2S	98%	
Hydrogen peroxide	H_2O_2	30%	
Hydrazine hydrate	$N_2H_4.H_2O$	80%	
N-Methyl-2-pyrrolidone	NMP	99.7%	

Sulphuric acid	H_2SO_4	98%	
Hydrochloric acid	HCl	35%	
Hydrofluoric acid	HF	98%	
Hydroxylamine hydrochloride	$HONH_3Cl$	-	
Graphite powder	C	75%	Sigma Aldrich Ltd, South Korea
Calcium silicide	$CaSi_2$	-	
Polyvinylidene fluoride	PVDF	-	
1-Ethyl-3-methylimidazolium tetrafluoroborate	$EMIMBF_4$	98%	Alfa Aesar Chemicals, South Korea
Tetraethylammonium tetrafluoroborate	$TEABF_4$	99%	
Titanium boride	TiB_2	99.5%	
Ammonium perrhenate	NH_4ReO_4	99%	
Molybdenum disulfide	MoS_2	-	Asbury carbon, USA

The general equipment's used for materials preparation, characterization and electrochemical measurements are given **Table 2.2.**

Table. 2.2 Apparatus used in the research project

Apparatus	Model or Specification	Manufacturer
Hot plate & Magnetic stirrer	MS300HS	M TOPS
Autoclave	PTFE container	XI ' AN FENG YU INDUSTRY CO,.LTD
Oven	OF-02 GW	JEIO Tech
Microwave	MW-202BG	LG
Furnace	CRF-M15	Ceber
Centrifuge	GYROZEN -1580 MG	Gyrozen
Ultrosonicator	SONIC VCX 500 model (20 kHz, 500 W)	Sonics Materials, Inc.
Ultrasonic cleaner	Elmasonic P 30H	ELMA
Balance	AUW220D	Shimadzu
Electrochemical work station	AUTOLAB PGSTAT302N	Eco Chemie
Keithley Nano voltmeter& picoammeter	2182A & 6485	Keithley
Spin coater	SPIN-1200	Midas System
Glove box	KK-011AS	Korea Kiyon
Coin cell crimping and disassembling machine	MSK-160D	MTI, Korea
Electrospinning	ESR200R2	NanoNC, Korea

2.2 Material preparation

The preparation of nanomaterials with controlled size and shape have attracted rapidly growing interest for many practical and technological applications. To fulfil the research tasks, the materials were mainly synthesized using following methods such as sol-gel combustion, sonochemical, hydrothermal, electrospinning, topotactic extraction, mechano-milling, thermal treatment, etc.,

2.2.1 Sol-gel combustion method

Sol-gel combustion methods is an effective preparation method for the synthesis of bulk production of nanoscale materials. Sol-gel combustion methods makes use of metal precursor salts (such as nitrates) as oxidants and reducing reagents and glycine/urea as fuels for the reaction. Nitrate acts as an oxidizer for the fuel during the combustion process[1]. The obtained powder can be a pyrolyzed product of a single-phase metal oxides and in some cases the by-product needs subsequent heat treatment to form single-phase products. The principle of combustion method is that once the reaction is heated, an exothermic reaction occurs which initiated the self-sustaining within a certain time interval, resulting in formation of powder product. The exothermic reaction begins at the ignition temperature of the fuel and generates a certain amount of heat that is manifested in the maximum temperature or temperature of combustion. The advantage of sol-gel combustion methods is the rapid production of fine and homogeneous powders[2]. Hence, it is an exothermic, auto-propagated process, and with a high heat release rate, it can be explosive and should be undertaken with extra precautions. $LiMn_2O_4$ nanostructure is prepared using sol-gel combustion method and provided in chapter 3.

2.2.2 Sonochemical method

Sonochemical method has been used widely used to prepare novel materials with unusual properties because this method results in the formation of particles with

exceptionally smaller size and higher surface area compared to the other conventional methods of preparation[3,4]. The formation of particle with such properties is due to the chemical effects of ultrasound raised from acoustic cavitation which results in the formation, growth, and implosive collapse of bubbles in a liquid medium. The formed implosive collapse of the bubbles produces a confined hotspot through adiabatic compression or shock wave formation with transient temperatures of ~5000 K, pressures of 1800 atm, and cooling rates in excess of 1010 K s^{-1}. These enabled reaction conditions result in the formation of particles with unique properties. Cu-HCF, Mn-HCF nanostructures and the reduction of graphene oxide are performed using sonochemical method and presented in chapter 3.

2.2.3 Hydrothermal method

Hydrothermal approach is one important technique that has many advantages such as low cost, environmentally friendly, excellent morphology, and the possibility of achieving high accessible active sites. This method has been considered as one of the popular promising approaches for preparing nanomaterials with different morphologies and also direct of materials on the substrate[5,6]. The synthesis process utilizes homo- or heterogeneous or metastable precursors in aqueous medium at the pressure more than 1 atm and at the temperature above 90 °C and the precursors undergo recrystallization of metastable precursors (RMP) process due to the effect of temperature and pressure inside the hydrothermal reactor which leads to the formation of crystallize nanostructured materials directly from precursor solution. The reduced graphene oxide, molybdenum selenide, rhenium disulfide, blue titanium oxide, and binder-free copper tungsten sulfide on Ni foam, were prepared through hydrothermal technique as presented in this thesis.

2.2.4 Electrospinning method

Electrospinning is a fiber production method which uses electric force to draw charged threads of polymer solutions up to fiber diameters in the order of nanometers[7,8].

Electrospinning shares characteristics of both electro-spraying and conventional solution dry spinning of fibers. The mechanism is that, when a sufficiently high voltage is applied to a liquid droplet, the body of the liquid becomes charged, and electrostatic repulsion counteracts the surface tension and the droplet is stretched; at a critical point a stream of liquid erupts from the surface known as the Taylor cone. As the jet dries in flight, the mode of current flow changes from ohmic to convective as the charge migrates to the surface of the fiber. The jet is then elongated by a whipping process caused by electrostatic repulsion initiated at small bends in the fiber, until it is finally deposited on the grounded collector. The elongation and thinning of the fiber leads to the formation of uniform fibers with nanometer-scale diameters. The normal electrospinning consists of a spinneret (typically a hypodermic syringe needle) connected to a high-voltage (5 to 50 kV) direct current power supply, a syringe pump, and a grounded collector. A polymer solution, sol-gel or particulate suspension is loaded into the syringe and this liquid is extruded from the needle tip at a constant rate by a syringe pump. The piezo-polymer separator (PVDF/$NaNbO_3$) was fabricated using electrospinning technique and discussed in chapter 6

2.2.5 Topochemical extraction method

Topochemical extraction method is a method which is used to selectively extract/remove the metal from the layered materials in acidic medium[9,10]. For example, MXenes (layered transition metal carbides or nitrides) can be obtained by the selective extraction of aluminium from MAX phase compounds (where “M” is transition metal, “A” represents Al or Si and “X” represents carbides or carbonitrides) in HF solution. This method can also be applied to form 2D siloxene sheets by removing Ca from $CaSi_2$ in an ice-cold hydrochloric acid[11]. After the extraction of the metal, the product was washed with distilled water many times to remove the trace of metal impurities.

2.2.6 Mechanical exfoliation method

Among the several methods applied for the exfoliation of few layered materials, mechanical exfoliation method (Ball milling) is considered as the effective technique for the large-scale production of few layered materials[12–14]. Mechanical exfoliation (using ball milling) is one of the methods used for exfoliating layered materials from their bulk via the mechanical shock forces. Ball milling is a versatile technique used for the preparation of nanopowders, composites, and paint industries. The effectiveness of ball milling approach for the production of graphene platelets, functionalized graphene's, and reduced graphene oxide sheets shows the bulk production compared to the conventional methods of exfoliation and preparation of nanomaterials. MoS_2 was exfoliated in this work and discussed in chapter 5.

2.2.7 Graphene oxide synthesis by modified Hummer's method

Graphene oxide was successfully synthesized from graphite powder using modified Hummer's method[15]. Initially, 2g of graphite powder was stirred in 40 mL H_2SO_4 (98%) for 2 h. After 2 h of stirring, 6 g of $KMnO_4$ was gradually added to the stirring solution in a time period of 1 h. The reaction bath should be maintained at 15 °C during the addition of $KMnO_4$ to reduce the excess heat generation. Followed by addition of $KMnO_4$ the solution is allowed to stir for 1 h and then the resulting solution was diluted by adding 90 mL of water. The suspension was further treated by adding 30% H_2O_2 solution (10 mL) and 150 mL of distilled water. The resulting suspension solution was washed by repeated centrifugation with 5% HCl aqueous solution and then with distilled water until the pH of the solution became neutral. The obtained GO nanosheets were obtained by adding 150 mL of water to the resulting graphite oxide precipitate and were subjected to ultrasound irradiation for 1 h with the aid of a probe type sonicator for the exfoliation of the graphitic oxide into a GO monolayer. The prepared GO was used for the synthesis of reduced graphene oxide (rGO) which is used as negative and positive electrode which are presented in in **Chapter 3.**

2.3. Materials characterization

The prepared nanomaterials were analyzed using several characterizations techniques to identify the phase, morphology, microstructure, size, chemical composition and specific surface area. The detailed experimental conditions are given below.

2.3.1. X-ray diffraction (XRD)

X-ray diffractometer (XRD) is an important analysis to determine the phase purity, phase of the crystal, structure, and crystal size[16]. The synthesized samples were performed by using Rigaku X-ray diffractometer (XRD) operated at the power of 40 kV and current of 40 mA with Cu-kα radiation in the range 2θ angle of 10-80° with a step of 0.02°.

2.3.2. Laser Raman spectroscopy

The Raman spectrum is a non-destructive tool towards and sensitive technique the structural defects and disorders, crystallization in nanostructures. Further, it is also used to study the bonding nature of various materials and to analyze the number layers in the two-dimensional materials such as MoS_2. Raman spectra for the prepared samples in this thesis were studied using a LabRam HR800 micro Raman spectroscope (manufacturer: Horiba Jobin-Yvon, France). The Raman spectrum was operated at an excitation wavelength of 514 nm at the different laser power using Ar^+ ion laser. The spectral region of 100–3500 cm^{-1} was used to collect the data were using an acquisition time of 10-s data point.

2.3.3. Fourier transform infrared (FT-IR) spectrometer

FT-IR spectroscopy is an important technique for the direct monitoring of interaction between adsorbed molecules and the material. FT-IR spectra were measured at room temperature with an FT-IR spectrometer (Thermo Scientific Systems, Nicolet- 6700) using the KBr pellet technique in the range of 4000 to 400 cm^{-1}.

2.3.4. Field-emission scanning electron microscopy

The morphology and particle size of the prepared material is very important to

investigate the electrochemical reaction and it was easily identified using the Field emission scanning electron microscope. Here we used FE-SEM, JSM-6700F, JEOL Ltd and TESCAN – MIRA3 for the morphological measurement of the prepared sample. Prior to measurement, the as-prepared samples were fixed onto a double-face conducted tape mounted on a metal stud and coated with platinum with a sputter coater.

2.3.5. High-resolution transmission electron microscopy

The particle size, microstructure, and crystalline phase of the nanomaterials were studied by the high-resolution transmission electron microscopy (HR-TEM, JEOL–JEM 200CX) with an accelerating voltage of 200 kV, The samples used for TEM observations were prepared by dispersing the NPs in ethanol followed by ultrasonic vibration for 5 min, and then placing a drop of the dispersion onto a copper grid before loading in to the instrument.

2.3.6. Energy dispersive X-ray spectroscopy analysis (EDS)

The elemental composition of the prepared samples was measured using Energy Dispersive X-ray Spectroscopy (EDS). The EDS analysis was done with the Field-emission Scanning Electron Microscopy (FE-SEM) instrument (TESCAN – MIRA3) with a separate EDS detector (INCA) connected to that instrument.

2.3.7. X-ray photoelectron spectroscopy (XPS)

The chemical composition and the state of elements present in the outermost part of samples was obtained by X-ray photoelectron spectroscopy (XPS) techniques using ESCA-2000, VG Microtech Ltd and Theta Probe AR-XPS system (Thermo Fisher Scientific, U.K). Here a monochromatic X-ray beam source at 1486.6 eV (Aluminum anode) and 14 kV was used to scan upon the sample surface. A high flux X-ray source with Aluminum anode was used for X-ray generation, and a quartz crystal monochromatic was used to focus and scan the X-ray beam on the sample.

2.3.8. Brunauer, Emmett and Teller (BET) surface area analysis

The nitrogen (N_2) adsorption-desorption isotherm measurement was carried out to determine the surface area, pore-volume and pore-size distribution of the as-prepared samples. The Brunauer-Emmett-Teller (BET) analysis was performed with Quantachrome RASiQwin™ c 1994-2012, Quantachrome Instruments v2.02 and nitrogen (N_2) gas was used as an adsorptive for the determination of the above parameters. The specific surface area of the samples was calculated by using the multiple-point BET model. The pore size distributions were obtained from the adsorption/ desorption branch of the isotherm by the Horvath-Kawazae (HK) method. The total pore volume was calculated from the volume of nitrogen adsorbed at a relative pressure of P/Po =0.95.

2.3.9 UV-Vis spectrophotometer (UV-Vis)

The optical properties of the NPs were studied using UV–Vis spectroscopy (UV/VIS/NIR spectrophotometer (Cary 5G)) with a quartz cuvette path length of 1 cm. The data was collected in the range of wavelength 200 to 850 nm.

2.3.10 Photoluminescence

Photoluminescence spectrum for the prepared sample were analyzed with an excitation wavelength of 266 nm at an applied laser power of 20 mW using photoluminescence analysis system (SPEX1403.

2.3.11 Electron spin resonance (ESR)

The magnetic properties of the prepared sample was analyzed using ESR spectroscopy via CW/Pulse EPR system (EMX-plus) at a temperature of 77 K.

2.4 Fabrication of electrode

The working electrodes were prepared by a simple slurry coating method and doctor blade method. Briefly, the as-prepared samples, carbon black, and polyvinylidene difluoride (PVDF) were mixed in an appropriate mass ratio of 80:15:5 or 85:10:5 using N-methyl

pyrrolidone (NMP) as solvent and grinded well to form uniform homogeneous paste/slurry. The resulting slurry was coated on to the current collector substrate using brush coating or doctor blade method and dried in the oven at 80 °C for 12 h. For hierarchical grow of nanostructures, the active material is directly grown on the Ni foam. The electroactive mass of the active material on the stainless-steel/Al current collector was determined from the difference between the mass of the current collector before and after loading of sample using a dual-range semi microbalance (AUW-220D, Shimadzu) with an approximation to five decimal places.

2.5 Device fabrication

This study mainly focusses on the improvement of the energy storage performance metrics, we developed both the fabrication of asymmetric/hybrid ion capacitor using aqueous electrolyte and also the fabrication of symmetric supercapacitor using ionic/organic electrolyte.

2.5.1 Asymmetric/hybrid ion supercapacitor

For the fabrication of asymmetric/hybrid ion capacitor, one battery type electrode ($LiMn_2O_4$, Cu-HCF, Mn-HCF and CWS/Ni foam) and the capacitive type electrode (graphitic carbon, and graphene) was used to form the asymmetric device with celgard as the separator. In this we fabricated the device in the form of a sandwich-type electrode, with an electrolyte-immersed Celgard as the separator[17].

2.5.2 Coin-cell symmetric supercapacitor

The symmetric supercapacitor was fabricated in CR2032 coin cell configuration using active material coated stainless-steel substrates with an area of 1.86/1.54 cm^{-2} as electrodes separated by a Celgard membrane and $TEABF_4$ /AN or $EMIMBF_4$ as the electrolyte[18,19]. The fabricated SSC device was crimped using an electric coin cell crimping and disassembling

machine (MTI, Korea). Electrolyte handling and device fabrication were carried out in a glove box with less than 1 ppm of moisture and oxygen.

2.6 Electrochemical characterization

To confirm the capacitive behavior and quantify the specific capacity, specific capacitance of the fabricated electrodes, cyclic voltammetry (CV), and galvanostatic charge/discharge (GCD) and electrochemical impedance spectroscopy (EIS) tests were performed. All of the electrochemical experiments were investigated using an AUTOLAB PGSTAT302N electrochemical work station. A typical three-electrode configuration was equipped with a working electrode, platinum foil as a counter electrode, and an Ag/AgCl or SCE reference electrode, was used. Three electrode configurations are common in fundamental research where it allows one electrode to be studied in isolation, without complications from the electrochemistry of the other electrodes. For measuring packaged supercapacitors (two electrode cell configuration), both reference and counter electrode leads are connected to the negative (-) terminal of the capacitor. The working electrode and working sense leads are connected to the positive (+) terminal.

2.6.1 Cyclic voltammetry (CV)

CV measurement is popularly known to be a suitable tool for evaluating the difference between capacitor type EDLC behaviors, battery like faradaic nature in an electrochemical reaction. In CV measurement, the ranges of voltage scan rates have been given from a lower to an upper limit at constant voltage. The evolution of current was measured as voltage function. The characteristics of the linear sweep voltammogram recorded depend on a rate of the electron transfer reaction, chemical reactivity of the active species and the voltage scan rate. The CV data of the electrodes were received by using the changing of scan rates: 5 to 1000 mV s^{-1}.

2.6.2 Galvanostatic charge/discharge (GCD)

The GCD technique are the most essential and direct strategy to investigate the applicability of energy storage devices. A repetitive loop of charge and discharge is denoted as a cycle. Principally, charge and discharge are measured at constant current density until the reach of set potential. The GCD curves were produced at the various current densities.

2.6.3 Electrochemical impedance spectroscopy (EIS)

EIS is a most powerful and non-destructive tool to evaluate the capacitive behavior and resistance for the surface of the electrode material. This makes the possibility for further electrochemical measurements. EIS is the most common method for measuring the equivalent series resistance of energy storage devices. It also permits developing models to annotate, underlying reaction mechanisms. Using these models, capacitor non-idealities can be found. A sinusoidal alternate current (AC) excitation signal is applied during an EIS experiment to the investigated system and AC response is measured. Scanning of frequency in a wide range from lower to higher creates the reaction steps with different rate constants, such as charge transfer, mass transport, and chemical reaction. In the study, EIS experiment for prepared electrodes was conducted between the frequency ranges of 0.1 Hz and 100 kHz. Nyquist plot was used to analyze the data and, are the plotted with the real component (Z') against imaginary component ($-Z''$) which show the response of frequency for the electrode/electrolyte system.

2.6.4. Calculation of electrochemical parameters

The electrochemical parameters, such as the specific capacitance, Coulombic efficiency (η), energy (E), and power density (P) are important parameters for the investigation of the capacitive behavior of electrochemical cells.

2.6.4.1 Determination of specific capacitance from CV analysis:

The specific capacitance owas calculated from the CV profiles using the relation[20]:

$$C_G = [\int IdV / (s \times \Delta V \times M)] \quad \text{..... (1)}$$

$$C_A = [\int IdV / (s \times \Delta V \times A)] \quad \text{..... (2)}$$

Here "C_A and C_G" represents the specific areal capacitance (F cm^{-2}) and gravimetric capacitance (F g^{-1}), "∫ IdV" is the integral area, "s" is the scan rate, "A" is the area of the electroactive material, "M" is the electroactive mass, and "ΔV" is the potential window.

2.6.4.2 Determination of specific capacitance from CD analysis:

The specific capacitance was calculated from the CD profiles using the relation[18,21]:

$$C_A = (I \times T_d) / (A \times \Delta V) \quad \text{..... (3)}$$

$$C_G = (I \times T_d) / (M \times \Delta V) \quad \text{..... (4)}$$

Here "C_A and C_G" represents the specific areal capacitance (F cm^{-2}) and gravimetric capacitance (F g^{-1}), "I" is the discharge current, "T_d" is the time required for discharge, "A" is the area of the electroactive material, "M" is the electroactive mass, and "ΔV" is the potential window.

2.6.4.3 Determination of Columbic efficiency (η%), Energy and power density:

The energy and power density are calculated in terms of using the relations given below[14]:

$$\eta\% = T_d / T_c \times 100 \quad \text{……. (5)}$$

$$E = [C \times \Delta V^2] / 2 \quad \text{..... (6)}$$

$$P = E / T_d \quad \text{..... (7)}$$

Here "E" and "P" are the energy and power density of the device, "C" is the specific capacitance, "ΔV" is the potential window, and "T_c" is the charging time and "T_d" is the discharge time

2.6.4.4 Determination of specific capacitance from EIS analysis:

The specific capacitance with respect to applied frequency obtained from the EIS analysis using the relation[22]:

$$C = 1/ (2\pi f z'')\ldots\ldots\ldots\ldots\ldots\ldots(8)$$

Here "C" is the specific capacitance of the device, and "f" is the applied frequency, and "z''" is the imaginary part of impedance.

2.6.4.5 Determination of real and imaginary components of capacitance from EIS analysis

The variation of real and imaginary capacitance with respect to the applied range of frequencies was obtained using the relation (9) and (10) respectively[22]:

$$C'_{\omega} = -Z''_{\omega} /(\omega|Z_{\omega}|^2)\ldots\ldots\ldots (9)$$

$$C''_{\omega} = Z'_{\omega} /(\omega|Z_{\omega}|^2)\ldots\ldots\ldots (10)$$

Here, "C'_{ω}" and "C''_{ω}" represents the real and imaginary components of capacitance that corresponds to the stored energy and irreversible energy loses, respectively.

2.6.4.6 Analysis for the fabrication of asymmetric supercapacitor device:

Prior to the fabrication of the asymmetric supercapacitor (ASC) device, the mass of the negative and positive electrodes needs to be balanced to equate the charge accumulation in the individual electrodes. To balance the charges accumulated at the both electrodes (i.e., $Q^+ = Q^-$), the mass ratio of positive electrode and negative for the ASC device was calculated using the relation[23]:

$$m^+ / m^- = [C^- \times \Delta V^-] / [C^+ \times \Delta V^+] \ldots\ldots\ldots\ldots\ldots (11)$$

where m^- and m^+ represent the mass of the negative and positive electrodes, C^- and C^+ denote the specific capacitance of the negative and positive electrodes, and, ΔV^- and ΔV^+ are the potential window of the negative and positive electrodes obtained using the three-electrode system, respectively.

2.7 References:

[1] P. Yu, X. Zhang, Y. Chen, Y. Ma, Solution-combustion synthesis of ε-MnO_2 for supercapacitors, Mater. Lett. 64 (2010) 61–64. doi:10.1016/j.matlet.2009.10.007.

[2] S. Chitra, P. Kalyani, T. Mohan, Characterization and electrochemical studies of $LiMn_2O_4$ cathode materials prepared by combustion method, J. …. 3 (1999) 433–441. doi:10.1023/A:1009982301437.

[3] P. Veluswamy, S. Sathiyamoorthy, S. P., G. Karunakaran, C.W. Lee, D. Kuznetsov, J. Kadarkaraithangam, H. Ikeda, Sono-synthesis approach of reduced graphene oxide for ammonia vapour detection at room temperature, Ultrason. Sonochem. 48 (2018) 555–566. doi:10.1016/j.ultsonch.2018.07.012.

[4] K. Krishnamoorthy, G.-S. Kim, S.J. Kim, Graphene nanosheets: Ultrasound assisted synthesis and characterization, Ultrason. Sonochem. 20 (2013) 644–649. doi:10.1016/j.ultsonch.2012.09.007.

[5] S. Ratha, C.S. Rout, Supercapacitor Electrodes Based on Layered Tungsten Disulfide-Reduced Graphene Oxide Hybrids Synthesized by a Facile Hydrothermal Method, ACS Appl. Mater. Interfaces. 5 (2013) 11427–11433. doi:10.1021/am403663f.

[6] G. Wang, X.P. Gao, P.W. Shen, Hydrothermal synthesis of Co_2SnO_4 nanocrystals as anode materials for Li-ion batteries, 2009. doi:10.1016/j.jpowsour.2009.02.074.

[7] S. Vijayan, B. Kirubasankar, P. Pazhamalai, A.K. Solarajan, S. Angaiah, Electrospun Nd^{3+} -Doped $LiMn_2O_4$ Nanofibers as High-Performance Cathode Material for Li-Ion Capacitors, ChemElectroChem. 4 (2017) 2059–2067. doi:10.1002/celc.201700161.

[8] X. Wang, C. Gong, G. Fan, Preparation and mechanical properties of silicon oxycarbide fibers from electrospinning/sol–gel process, Mater. Res. Bull. 46 (2011) 2398–2402. doi:10.1016/j.materresbull.2011.08.052.

[9] Y. Dall'Agnese, P. Rozier, P.L. Taberna, Y. Gogotsi, P. Simon, Capacitance of two-

dimensional titanium carbide (MXene) and MXene/carbon nanotube composites in organic electrolytes, J. Power Sources. 306 (2016) 510–515. doi:10.1016/j.jpowsour.2015.12.036.

[10] R.B. Rakhi, B. Ahmed, M.N. Hedhili, D.H. Anjum, H.N. Alshareef, Effect of Postetch Annealing Gas Composition on the Structural and Electrochemical Properties of Ti_2CT_x MXene Electrodes for Supercapacitor Applications, Chem. Mater. 27 (2015) 5314–5323. doi:10.1021/acs.chemmater.5b01623.

[11] H. Nakano, M. Ishii, H. Nakamura, Preparation and structure of novel siloxene nanosheets, Chem. Commun. 2 (2005) 2945. doi:10.1039/b500758e.

[12] V. León, A.M. Rodriguez, P. Prieto, M. Prato, E. Vázquez, Exfoliation of graphite with trriazine derivatives under ball-milling conditions: Preparation of few-layer graphene via selective noncovalent interactions, ACS Nano. 8 (2014) 563–571. doi:10.1021/nn405148t.

[13] K. Krishnamoorthy, S.J. Kim, Mechanochemical preparation of graphene nanosheets and their supercapacitor applications, J. Ind. Eng. Chem. 32 (2015) 39–43. doi:10.1016/j.jiec.2015.09.012.

[14] K. Krishnamoorthy, P. Pazhamalai, G.K. Veerasubramani, S.J. Kim, Mechanically delaminated few layered MoS_2 nanosheets based high performance wire type solid-state symmetric supercapacitors, J. Power Sources. 321 (2016) 112–119. doi:10.1016/j.jpowsour.2016.04.116.

[15] K. Krishnamoorthy, M. Veerapandian, K. Yun, S.J. Kim, The chemical and structural analysis of graphene oxide with different degrees of oxidation, Carbon N. Y. 53 (2013) 38–49. doi:10.1016/j.carbon.2012.10.013.

[16] J.R. Dahn, B.M. Way, E.W. Fuller, W.J. Weydanz, J.S. Tse, D.D. Klug, T. Van Buuren, T. Tiedje, X-ray diffraction and x-ray absorption studies of porous silicon,

siloxene, heat-treated siloxene, and layered polysilane, J. Appl. Phys. 75 (1994) 1946–1951. doi:10.1063/1.356342.

[17] P. Pazhamalai, K. Krishnamoorthy, M.S.P. Sudhakaran, S.J. Kim, Fabrication of High-Performance Aqueous Li-Ion Hybrid Capacitor with $LiMn_2O_4$ and Graphene, ChemElectroChem. 4 (2017) 396–403. doi:10.1002/celc.201600550.

[18] K. Krishnamoorthy, P. Pazhamalai, S.-J. Kim, Two-dimensional siloxene nanosheets: novel high-performance supercapacitor electrode materials, Energy Environ. Sci. 11 (2018) 1595–1602. doi:10.1039/C8EE00160J.

[19] P. Pazhamalai, K. Krishnamoorthy, S. Manoharan, S.-J. Kim, High energy symmetric supercapacitor based on mechanically delaminated few-layered MoS_2 sheets in organic electrolyte, J. Alloys Compd. 771 (2019) 803–809. doi:10.1016/j.jallcom.2018.08.203.

[20] M.D. Stoller, R.S. Ruoff, Best practice methods for determining an electrode material's performance for ultracapacitors, Energy Environ. Sci. 3 (2010) 1294. doi:10.1039/c0ee00074d.

[21] K. Krishnamoorthy, P. Pazhamalai, S. Sahoo, S.-J. Kim, Titanium carbide sheet based high performance wire type solid state supercapacitors, J. Mater. Chem. A. 5 (2017) 5726–5736. doi:10.1039/C6TA11198J.

[22] K. Krishnamoorthy, P. Pazhamalai, S.J. Kim, Ruthenium sulfide nanoparticles as a new pseudocapacitive material for supercapacitor, Electrochim. Acta. 227 (2017) 85–94. doi:10.1016/j.electacta.2016.12.171.

[23] P. Pazhamalai, K. Krishnamoorthy, V.K. Mariappan, S.-J. Kim, Fabrication of high energy Li-ion hybrid capacitor using manganese hexacyanoferrate nanocubes and graphene electrodes, J. Ind. Eng. Chem. 64 (2018) 134–142. doi:10.1016/j.jiec.2018.03.009.

CHAPTER – 3

Aqueous hybrid-ion/asymmetric supercapacitor using battery type faradaic electrodes ($LiMn_2O_4$, Cu-HCF, Mn-HCF and copper tungsten sulfide) and capacitive type electrodes (graphene and graphitic carbon)

CHAPTER 3.1: Fabrication of High-Performance Aqueous Li-Ion Hybrid Capacitor with $LiMn_2O_4$ and Graphene

Highlights

- A facile glycine-assisted combustion method was adopted to prepare the spinel $LiMn_2O_4$ and sonochemical method was used to prepare graphene nanosheets has been reported.
- The physicochemical characterization of the prepared $LiMn_2O_4$ and Graphene analyzed using XRD, Raman, FT-IR, FE-SEM and surface area analysis.
- The prepared $LiMn_2O_4$ and graphene delivered a specific capacitance of 217.42 F g^{-1} and 289.5 F g^{-1} ,respectively.
- The fabricated $LiMn_2O_4$‖graphene LHC operates over the potential window of 2.2 V and delivered a high specific capacitance of 59.45 F/g with high specific energy of 39.96 Wh/kg.

3.1.1 Introduction

The need for high performance, cost-effective, and environmentally benign energy storage devices for driving electrical vehicles and other products are increasing rapidly due to the decrease in the fossil fuel production globally[1]. Electrochemical energy storage devices become an ideal candidate for overcoming the above issues. The electrochemical energy storage devices are widely classified into batteries and supercapacitors in which the former is known for high energy density, whereas the later provides better power density[2–4]. Efforts have been taken to increase the power and energy outputs of batteries and supercapacitors for making them viable for commercial applications. Batteries work in the principle of Li-ion intercalation and de-intercalation during the charging and discharging process which makes them to provide higher energy density, as well as slow charging and discharging rates[5]. On the other hand, supercapacitors are known for high power density with rapid charging and discharging process compared to batteries[6,7]. Even though these two systems possess independent merits, the current findings are not enough to use them in the view of practical applications. A combination of battery and supercapacitor circuit is developed for utilizing in the hybrid electric vehicles. However, the high energy and power requirements of the current world made much attention to increase the energy and power outputs of these devices. In the recent decade, extensive works have been performed by various researchers to increase the device efficiency of batteries and supercapacitors[8,9]. Developing high specific area materials, one or two dimensional nanostructures, hierarchical structures, binder free electrodes and use of redox additives have been examined to increase the energy and power density of these systems[10–12].

In this regard, Li-ion hybrid capacitors become an important class of energy storage devices which can bridge the energy and power density of batteries and supercapacitors. The Li-ion hybrid capacitor uses a battery type as well as capacitive type electrode materials in

the system which results in significant improvements in the overall electrochemical energy storage properties. The advantage of Li-ion hybrid capacitors over conventional batteries and supercapacitors is that it can provide the fast charging and discharging rate of the supercapacitor together the high energy density of a battery [13–15]. Further, charge storage mechanism in the Li-ion capacitors relies on the formation of electrical double layer at the capacitive type electrode and ion intercalation/de-intercalation occurs at the battery type electrode[16]. Recently, some studies demonstrated the usefulness of Li-ion hybrid capacitors in which they used organic electrolytes, thus providing higher operating potential, larger specific capacitance, high energy and power density[17]. Most of these research works are ongoing currently as the need for developing and utilizing aqueous electrolyte for ion capacitors is high important due to the safety issues[18]. Further, the successful evaluation of use of aqueous electrolytes for ion capacitors can be beneficial for the future applications in flexible, wearable and portable electronic device applications [19]. There are some efforts taken by the researchers on the use of aqueous electrolytes Li-ion hybrid capacitors. Considering the efforts taken until now, Wang et al reported the fabrication and properties of aqueous electrochemical hybrid capacitor using $LiMn_2O_4$ and carbon[20]. Following the previous study, Wang also compared the use of other lithium based positive electrodes such as $LiMn_2O_4$, $LiCo_{1/3}Ni_{1/3}Mn_{1/3}O_2$ and $LiCoO_2$ in aqueous electrolyte[21]. Following this, Luo et al demonstrated the electrochemical properties of Li-ion capacitors using $LiTi_2(PO_4)_3 \| MnO_2$ with a energy density of about 25 Wh/kg[22]. Xu et al reported $Li_4Ti_5O_{12}$-G‖AC Li-ion capacitors with energy density of about 30 Wh/Kg has been achievable using aqueous electrolyte[23]. Herein, we focused to develop Li-ion hybrid capacitors (LHC) using $LiMn_2O_4$ and graphene as positive and negative electrodes. The positive electrode $LiMn_2O_4$ is a well-known battery type material with excellent Li-ion chemistry and possess several advantages such as low cost, environmentally benign, natural

abundance, and good safety compared with commercialized $LiCoO_2$[24,25]. The negative electrode graphene is one of the best EDLC material reported until now compared to the other carbon based materials such as carbon, activated carbon, carbon nanotubes, and so on[26]. We expect that the combination of these two electrode materials can provide new insights in the hybrid ion capacitors.

3.1.2 Experimental section

3.1.2.1 Preparation of lithium manganese oxide

The lithium manganese oxide was prepared via glycine-assisted combustion method [27]. Briefly, appropriate molar ratios of $LiNO_3$ and $Mn(NO_3)_2$ were dissolved in distilled water to get homogeneous clear solution. To this solution, the appropriate molar ratio of glycine was added which act as the fuel for the combustion process. In this reaction the oxidant to fuel ratio was maintained as 1. The resulting solution was placed on hot plate at 200 ºC until the formation of a gel followed by self-combustion reaction which results in the formation of black colored ash. After that, the resulting black colored ash is ground in an agate mortar and calcined at 500 ºC for 5 h to achieve the $LiMn_2O_4$ nanoparticles.

3.1.2.2 Preparation of graphene nanosheets

At first, GO sheets was synthesized according to the modified Hummers method as reported in our earlier study[28]. The graphene nanosheets were prepared using a fast and facile sonochemical reaction using graphene oxide as a starting precursor[28]. Briefly, the pH of the as exfoliated GO solution (0.2 g in 200 mL) was adjusted to reach 10 by NaOH solution followed by the addition of 2 mL of hydrazine and the entire reaction is subjected to ultrasound irradiation for 2 h. The experiment was performed under atmospheric conditions. The obtained graphene nanosheets were washed thoroughly with distilled water and centrifuged in order to remove the residuals. The procedure was repeated for several times until the synthesized product becomes free from trace amount of impurities. Further, the

synthesized graphene nanosheets were dried in a hot air oven and were used for further characterization.

3.1.2.3 Preparation of the working electrodes and electrochemical analysis

The working electrodes were prepared using the following procedure. The active material ($LiMn_2O_4$ or graphene) were ground with carbon black and polyvinylidene difluoride (PVDF) with the mixture ratio of 80:15:5 using N-methyl pyrrolidone (NMP) as solvent to form the slurry. Then, the slurry was coated on to the pre-cleaned stainless steel substrate (1×1 cm^2), and allowed to dry at 80 ºC overnight. The mass loading of the $LiMn_2O_4$ nanostructures and graphene nanosheets on the electrode was 2.3 and 0.8 mg respectively. A solution containing 1 M Li_2SO_4 was used as the electrolyte. The electrochemical behavior of the positive and negative electrodes was examined at room temperature using a three-electrode system: $LiMn_2O_4$ and graphene as the working electrode, saturated calomel electrode (SCE) as the reference electrode, and platinum as the counter electrode. Finally, the $LiMn_2O_4$‖graphene LHC was fabricated in the form of a sandwich-type electrode, with an electrolyte-immersed Celgard as the separator. All of the electrochemical properties of the working electrodes and the $LiMn_2O_4$‖graphene LHC were examined via cyclic voltammetry (CV), electrochemical impedance spectroscopy (EIS) and galvanostatic charge–discharge (CD) measurements using an Autolab PGSTAT302N electrochemical workstation.

3.1.3 Results and discussion

3.1.3.1 Physicochemical characterization

Figure 3.1.1(a) shows the XRD pattern of the prepared $LiMn_2O_4$ nanoparticles. The XRD pattern of the prepared $LiMn_2O_4$ matched well the spinel $LiMn_2O_4$ structure with strong intensities of (111), (311) and (400) planes and is in close agreement with the standard JCPDS file number: 89-8321 [29]. This confirmed the formation of single phase spinel $LiMn_2O_4$ with a space group of *Fd3m*. There are no peaks related to lithium oxide,

manganese oxide and any hydroxides in the XRD pattern was observed, thus suggesting the formation of $LiMn_2O_4$ with high purity. The average crystallite size of the $LiMn_2O_4$ was calculated as 80 nm using the Debye Scherer equation. Figure 3.1.1(b) shows the FT-IR spectrum

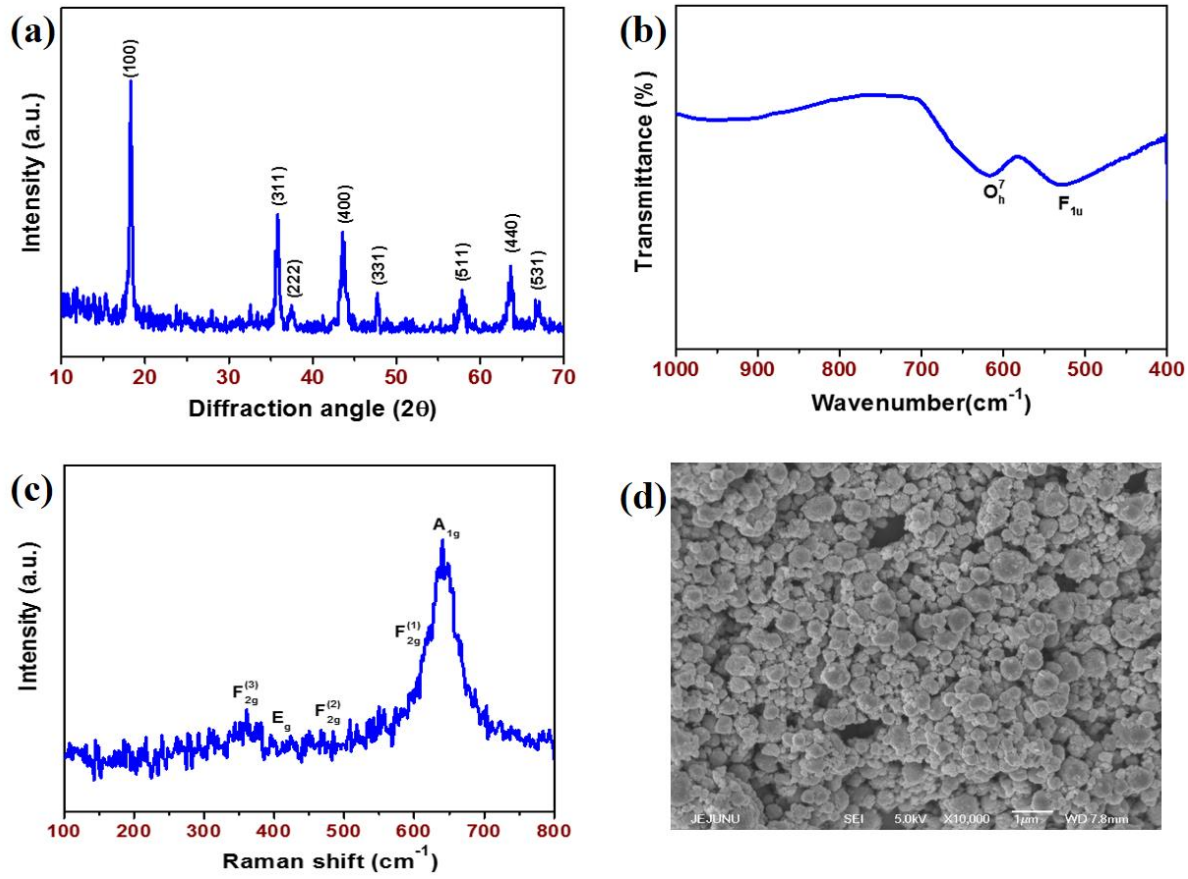

Fig. 3.1.1 Characterization of $LiMn_2O_4$ nanoparticles. (a) X-ray diffraction pattern confirmed the formation of spinel $LiMn_2O_4$ with *Fd3m* space group, (b) Fourier-transform infra-red spectrum reveals the strong stretching modes of MnO_6 octahedral structure, (c) laser Raman spectrum shows a strong vibrational band of symmetric Mn-O stretching of MnO_6 and (d) Field emission scanning electron micrograph depicts the formation of spherical $LiMn_2O_4$ with a particle size of 100 nm.

of the $LiMn_2O_4$ which revealed the presence of two strong bands at 520 and 617 cm^{-1} corresponded to modes of the F_{1u} species in the O_h^7 symmetry[30]. These two strong

absorption bands mainly involved in the displacement of the oxide ions and primarily attributed to the asymmetric stretching modes of MnO_6 octahedral structure. The characteristic bands after 1000 cm^{-1} is due to the metal oxygen vibrational frequencies. Figure 3.1.1(c) shows the Raman spectra for the $LiMn_2O_4$ nanoparticles. The Raman spectrum of the $LiMn_2O_4$ shows a broad peak at the 638 cm^{-1} with a small shoulder peak at the 610 cm^{-1} which corresponds to the A_{1g} and $F^{(1)}_{2g}$ mode of strong vibrational band of symmetric Mn-O stretching in MnO_6. The remaining small intensity peaks at 480, 419 and 364 cm^{-1} corresponds to the $F^{(2)}_{2g}$, E_g and $F^{(3)}_{2g}$ respectively[31]. The surface morphology of the prepared $LiMn_2O_4$ particles was examined using FE-SEM and the corresponding micrograph is shown in Fig. 3.1.1(d) which revealed the formation of spherical shaped particles with size in the range of 100 nm.

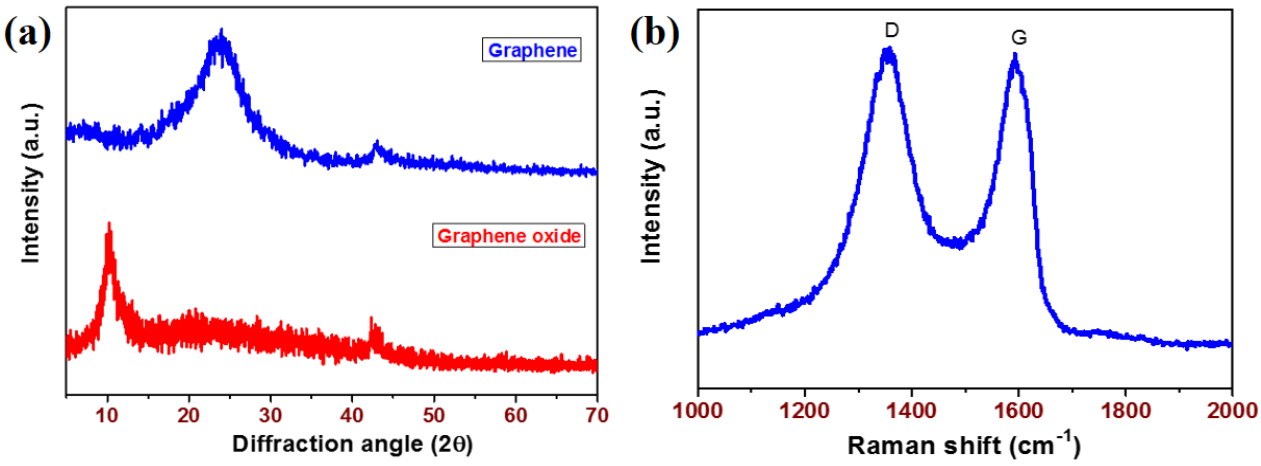

Fig. 3.1.2 Characterization of graphene nanosheets (a) X-ray diffraction pattern of GO and graphene sheets confirms the formation of graphene from GO via ultra-sonication process and (b) laser Raman spectrum of graphene sheets reveals the high crystalline nature of the graphene with better I_D/I_G ratio.

The XRD pattern of the GO and graphene sheets are shown in Fig. 3.1.2(a). The diffraction peaks of the GO sheets showed a predominant peak at 10.21º which was assigned

to (001) reflection with an interlayer distance of 0.89 nm. After the ultrasound irradiation of the graphene oxide in presence of NaOH and hydrazine, the peak at 10.21º is fully disappeared and a strong broad peak arise at diffraction angle of 24.12 º which was assigned to (002) plane with an interlayer spacing of 0.365 nm[28]. The observed change in the diffraction angle is due to the removal of oxygenated functional groups in GO sheets[28]. This confirmed the formation of graphene sheets via sonochemical reduction of GO sheets. Figure 3.1.2(b) shows the Raman spectra of graphene nanosheets depicting the presence of G and D band at 1591.17 and 1358.95 cm^{-1}, respectively[32]. The I_D/I_G ratio of the graphene sheets is found to be 0.82, suggesting the high order of crystallinity in the prepared graphene sheets [28]. These studies suggested the high crystalline nature of the prepared electrode materials in this study.

It is well known that the specific surface area of the electrode materials plays a crucial role on their electrochemical properties. The specific surface area of the prepared $LiMn_2O_4$ and graphene materials has been evaluated by N_2 adsorption/desorption isotherm and is shown in Fig. 3.1.3 (a) and (b), respectively.

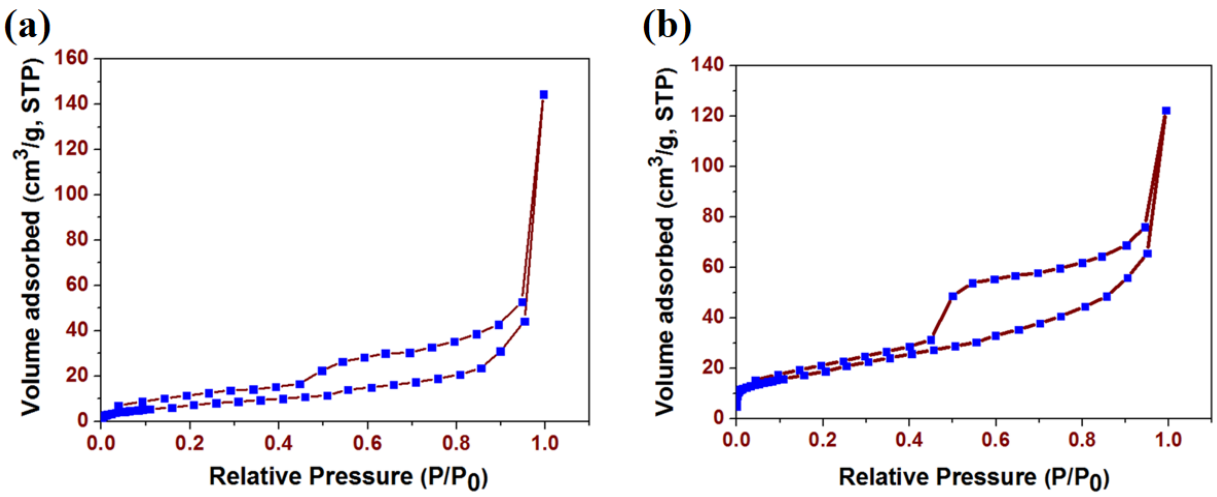

Fig. 3.1.3 Nitrogen adsorption/desorption isotherm of (a) $LiMn_2O_4$ nanoparticles which shows a specific surface area of 28.71 m^2/g and (b) graphene sheets exhibits a specific surface area of 211.59 m^2/g.

From this, the specific surface area of $LiMn_2O_4$ nanoparticles and graphene sheets were calculated to be 28.78 and 211.596 m^2/g, respectively[33]. The N_2 adsorption/desorption isotherm of $LiMn_2O_4$ nanoparticles (shown in Fig. 3.1.3(a)) revealed the presence of hysteresis in the relative partial pressure region (0.45 to 0.9) and the obtained surface area of the $LiMn_2O_4$ nanoparticles is higher than bulk $LiMn_2O_4$ (3.8 m^2/g) and $LiMn_2O_4$ microspheres (24.7 m^2/g) [34] which is due to the nanosized powders. Similarly, the N_2 adsorption/desorption isotherm of graphene sheets (shown in Fig. 3.1.3(b)) can be categorized as type IV curves according to the IUIPAC definition with the presence of hysteresis in the relative partial pressure region of about 0.4 to 0.9 range, suggesting the mesoporous nature. This increased surface area of the electrodes can effectively increase the effective electrode contact area with the electrolytes and might result in superior electrochemical performance.

3.1.3.2 Electrochemical characterization

The electrochemical properties of the prepared $LiMn_2O_4$, and graphene nanosheets electrodes were investigated via CV and EIS analyses using a three-electrode configuration prior to the fabrication of the device. At first, the CV profiles of the $LiMn_2O_4$ electrode were recorded in the potential window of 0 to 1.4 V at different scan rates. Figure 3.1.4(a) shows the CV profile of the $LiMn_2O_4$ electrode obtained at a low scan rate (5 mV/s) which indicated the presence of a pair of redox peaks 0.65 and 1.15 V respectively. The observed peaks are related to the lithium ion intercalation and de-intercalation in the spinel host structure of $LiMn_2O_4$. The possible mechanism of charge storage occurred at the positive ($LiMn_2O_4$) electrode can be explained using the equation[15]:

$$Li^+ [Mn^{3+} Mn^{4+}] O^{4-} \Leftrightarrow Li_{1-x} + [Mn^{3+} Mn^{4+}] O^{4-} + x\, Li^+ + x\, e^- \quad \text{---------- (1)}$$

Figure 3.1.4(b) represents the CV behavior of the $LiMn_2O_4$ electrode at different scan rates. The shape of the CV profiles is not distorted with an increase in scan rate, thus

suggesting the better electrochemical stability of $LiMn_2O_4$. Further, the current density increased with increase in scan rates suggesting the better capacitive nature of the $LiMn_2O_4$ electrode.

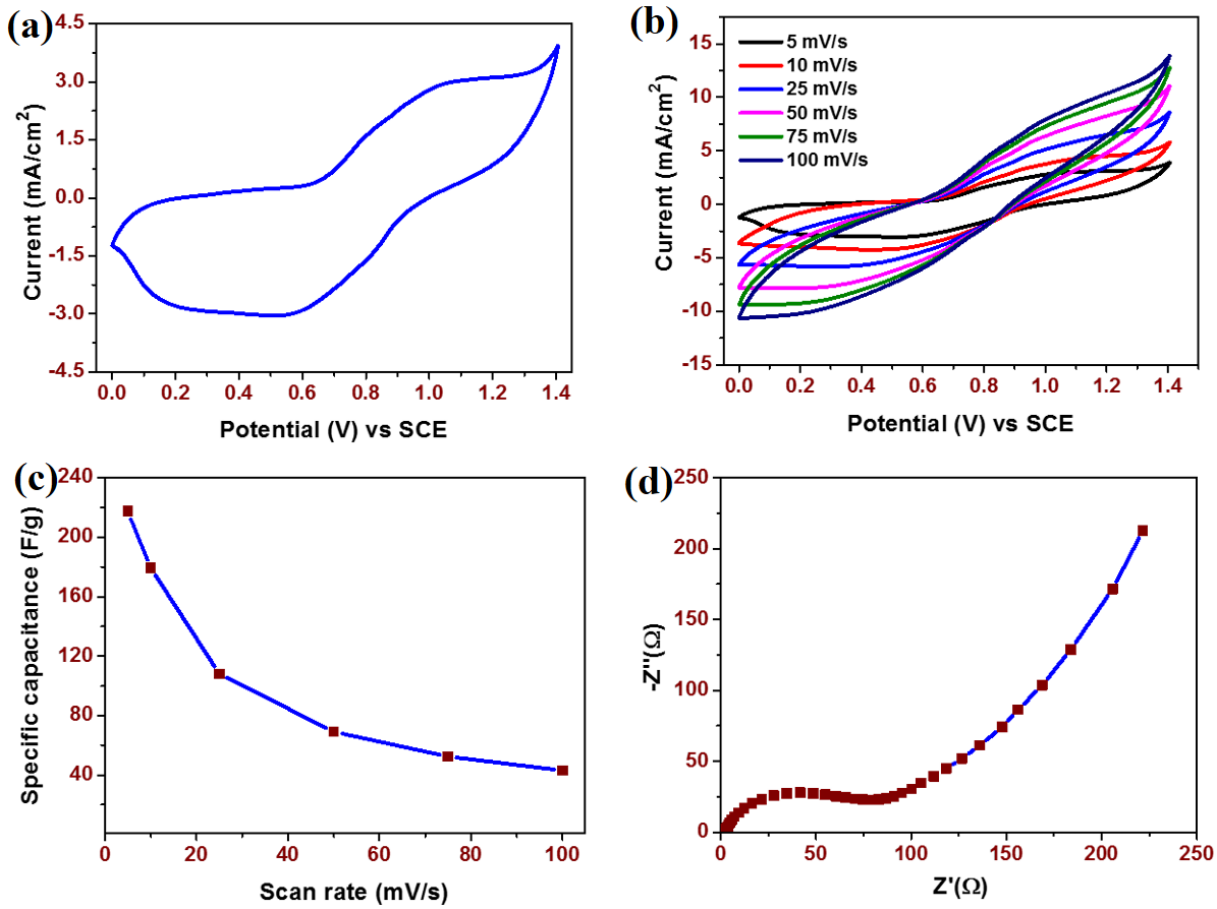

Fig. 3.1.4 Electrochemical properties of $LiMn_2O_4$ electrode measured using three electrode system. (a) Cyclic voltammetric profile of $LiMn_2O_4$ measured at a scan rate of 5 mV/s, (b) Cyclic voltammetric profile of $LiMn_2O_4$ measured at different scan rates (5-100 mV/s) delivered a high specific capacitance of 217.42 F/g at a scan rate of 5mV/s, (c) effect of scan rate on specific capacitance of $LiMn_2O_4$ electrode, and (d) Nyquist plot of $LiMn_2O_4$ electrode.

The specific capacitance of the $LiMn_2O_4$ electrode was calculated from the CV curves using the relation[35]:

$$Csp = [\int IdV / (s \times \Delta V \times m)] \quad F/g \ldots\ldots\ldots\ldots\ldots (2)$$

where "*Csp*" is the specific capacitance(F/g), "*I*" is the current (*A*), "s" is the scan rate (mV/s), "Δ*V*" is the potential window (V), and "*m*" is the active mass of the electrode (g). The effect of scan rate on the specific capacitance is shown in Fig. 3.1.4(c) which highlights that the specific capacitance is higher at a low scan rate and vice versa. This is due to the variation in time constraints of the electrolyte ion to access the electroactive material at different scan rates[36]. A specific capacitance of 217.42 F/g was obtained for the $LiMn_2O_4$ electrode using the CV analysis measured at a low scan rate of 5 mV/s. The prepared $LiMn_2O_4$ exhibits a high specific capacitance compared to the nano porous $LiMn_2O_4$ by Wang et al[37]. The Nyquist plot of the $LiMn_2O_4$ electrode is shown in Fig. 3.1.4(d) which represents the real and imaginary component of the impedance as function of applied frequency. The Nyquist plot revealed the presence of semi-circle region at high frequency region corresponding to the charge-transfer resistance of the $LiMn_2O_4$ electrode. The observed straight line in the low frequency region indicates the diffusion of electrolyte ions into the active material[38].

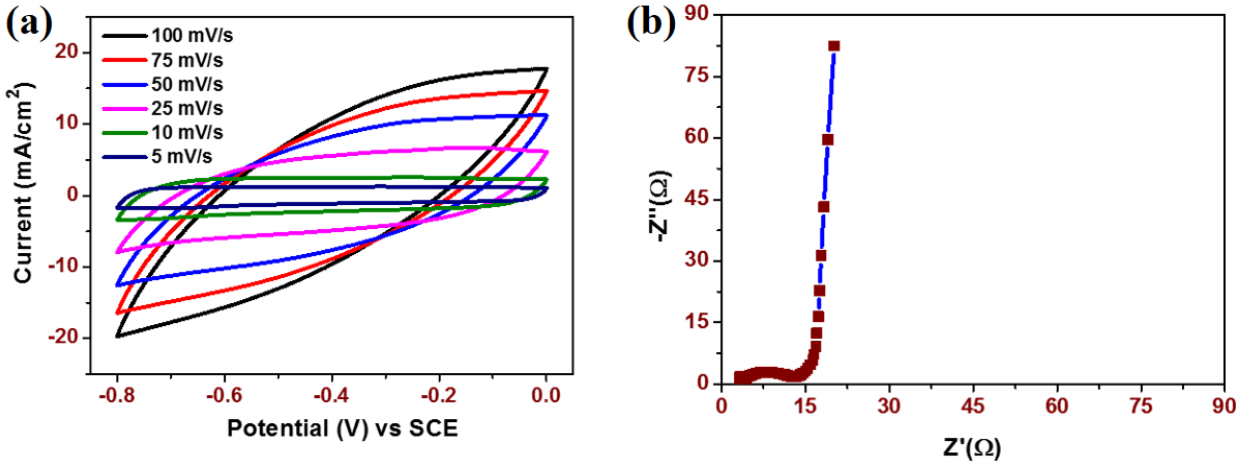

Fig. 3.1.5 Electrochemical properties of graphene electrode measured using three electrode system. (a) Cyclic voltammetric profile of graphene electrode measured at different scan rates (5-100 mV/s) delivered a high specific capacitance of 289.5 F/g at a scan rate of 5mV/s, and (b) Nyquist plot of the graphene electrode.

The electrochemical properties of the negative electrode (sonochemically derived graphene) are provided in Fig. 3.1.5. The CV profiles of the graphene electrode were recorded over the potential window of -0.8 to 0 V at different scan rates as shown in Fig. 3.1.5 (a). The CV profiles revealed the presence of ideal rectangular behavior, thus confirming the mechanism of charge storage is due to the presence of electrochemical double layers capacitance. Moreover, the shape of the CV curves is nearly rectangular at all scan rates (5 to 100 mV/s) with little distortion at high scan rates which might be due to the presence of residual oxygenated functional groups in the sonochemically prepared graphene nanosheets[39]. Further, the current density is increasing with an increase in scan rate, thus suggesting an ideal capacitive behavior. The specific capacitance of the graphene electrode was calculated as 289.5 F/g from the CV curve measured at a scan rate of 5 mV/s. The obtained specific capacitance of the prepared graphene is high and comparable with the some of the chemically derived graphene[40]. The Nyquist plot of graphene electrode is shown in Fig. 3.1.5(b) which is significantly different from the $LiMn_2O_4$ electrode. Herein, the charge-transfer resistance is low and the Warburg line is almost parallel to the imaginary component of the impedance, thus suggesting the better EDLC nature of graphene electrodes.

Further, asymmetric Li-ion capacitors were fabricated using $LiMn_2O_4$ as a positive electrode and graphene as the negative electrode for practical applications. The electrochemical properties of the $LiMn_2O_4$ and graphene studied using three electrode system shows that these materials can work in the potential of 1.4 and 0.8 V, respectively. Hence, it is quite satisfactory to achieve an operating window of about 2.2 V for the $LiMn_2O_4$‖graphene LHC using neutral $LiSO_4$ electrolyte. The main advantage of using neutral Li_2SO_4 over alkaline LiOH electrolyte is that in alkaline electrolytes the maximum full cell voltages is limited within 1.3 V whereas for neutral electrolytes, the highest cell voltage can be reached up to 2.2 V[41,42]. The CV profiles of $LiMn_2O_4$ and graphene

electrodes measured at a scan rate of 5 mV/s is shown in Fig. 3.1.6(a) and the corresponding specific capacitance of the materials is about 217.42, and 289.5 F/g, respectively.

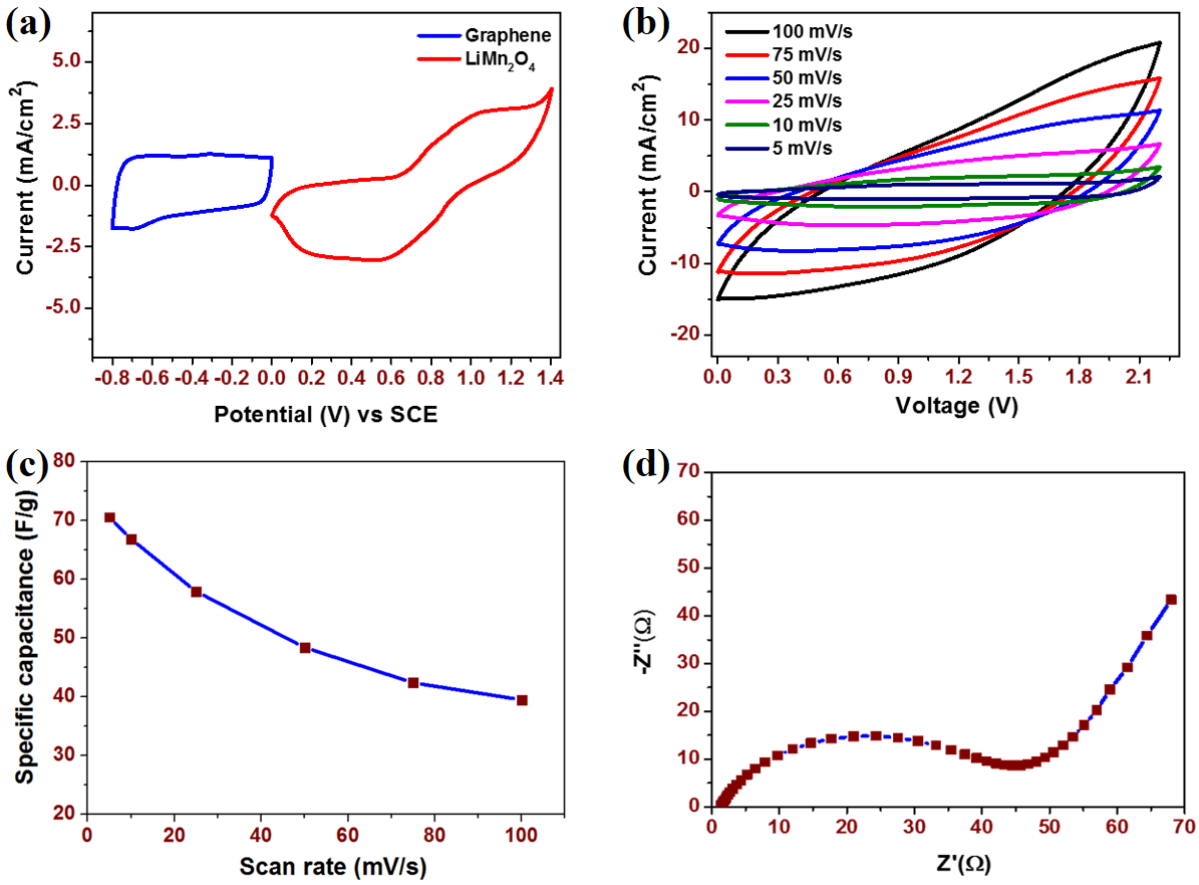

Fig. 3.1.6 (a) Cyclic voltammetric profiles of $LiMn_2O_4$ and graphene electrodes measured at a scan rate of 5 mV/s, (b) Cyclic voltammetric profiles of $LiMn_2O_4$‖graphene LHC measured at different scan rates (5-100 mV/s) reveals the linear behavior at all scan rates and delivered a maximum specific capacitance of 70.60 F/g at a low scan rate of 5 mV/s at a scan rate of 5mV/s, (c) Effect of scan rate on the specific capacitance of $LiMn_2O_4$‖graphene LHC, and (d) Electrochemical impedance spectrum of $LiMn_2O_4$‖graphene LHC.

In order to achieve the maximum device output, the mass of the negative and positive electrodes should be balanced to equate the charge accumulation in the individual electrodes[43]. Since, the charge accumulation and the operational potential window of the

positive and negative electrodes are different; the charge storage capacities of both electrodes should be balanced by fine-tuning the mass loading between these electrodes[43]. In order to balance the charges accumulated at the both electrodes (i.e., $Q^+=Q^-$), the mass ratio of $LiMn_2O_4$ and graphene for the $LiMn_2O_4$‖graphene LHC device was calculated using the relation[43]:

$$m^- \times C^- \times \Delta V^- = m^+ \times C^+ \times \Delta V^+ \ldots\ldots\ldots\ldots\ldots\ldots (3)$$

where *"m^-"* and *"m^+"* represent the mass of the negative and positive electrodes, *"C^-"* and "C^+" denotes the specific capacitance of the negative and positive electrodes, and, "ΔV^-" and "ΔV^+" are the potential window of the negative and positive electrodes obtained using the three-electrode system, respectively. Afterwards, the asymmetric $LiMn_2O_4$‖graphene LHC was fabricated with $LiMn_2O_4$ and graphene as the positive and negative electrode with a polypropylene as separator in 1 M Li_2SO_4 aqueous electrolyte. Figure 3.1.6(b) shows the CV curves of the asymmetric $LiMn_2O_4$‖graphene LHC measured over the potential window of up to 0 to 2.2 V at various scan rates from 5-100 mV/s. A quasi rectangular CV profiles were obtained for the fabricated $LiMn_2O_4$‖graphene LHC suggesting the better capacitive nature of the device. Further, the current density increases with an increase in scan rate from 5 to 100 mV/s and the there is no distortion in the shape of the curves observed even at higher scan rates demonstrating the better rate capability of the fabricated $LiMn_2O_4$‖graphene LHC device. The effect of scan rate on the specific capacitance of the fabricate $LiMn_2O_4$‖graphene LHC device is shown in Fig. 3.1.6(c), which revealed an increase in specific capacitance with a corresponding decrease in scan rate. A specific capacitance of about 70.60 F/g has been observed for the fabricated $LiMn_2O_4$‖graphene LHC device. The Nyquist plot of the fabricated $LiMn_2O_4$‖graphene LHC is shown in Fig. 3.1.6(d) which revealed the presence of solution resistance (R_s = 1.36

Ω), charge-transfer resistance (R_{ct} = 43.61 Ω), and the Warburg line at the low frequency region.

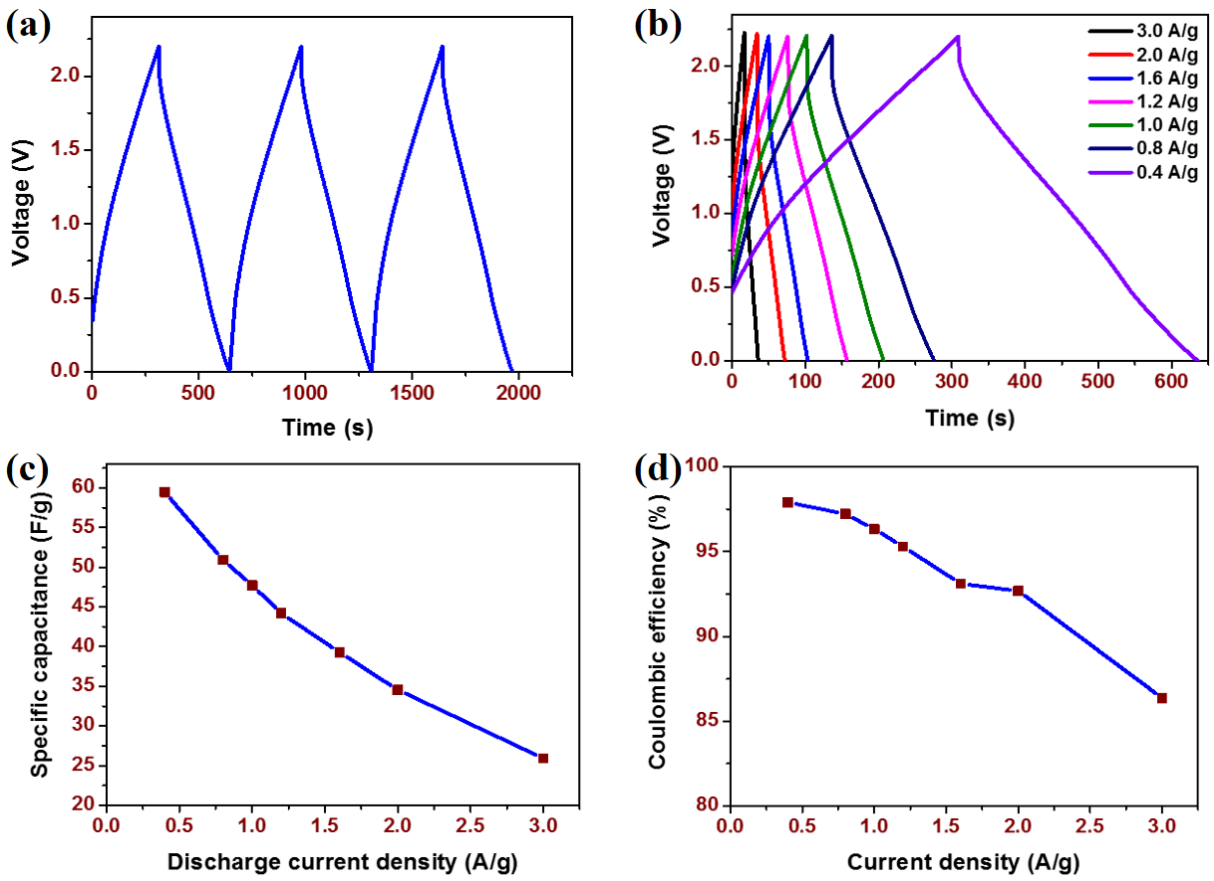

Fig. 3.1.7 (a) Galvanostatic charge-discharge profile of $LiMn_2O_4$‖graphene LHC measured at a current density of 0.4 A/g, (b) galvanostatic charge-discharge profiles measured at different current densities (0.4-3 A/g) reveals symmetric GCD profiles with a high specific capacitance of 59.45 F/g at low current density of 0.4 A/g, (c) Effect of current density on the specific capacitance of $LiMn_2O_4$‖graphene LHC, and (d) Coulombic efficiency of $LiMn_2O_4$‖graphene LHC obtained at different current densities.

Figure 3.1.7(a) shows the galvanostatic CD profile of the fabricated $LiMn_2O_4$‖graphene LHC measured at a constant current density of 0.4 to 3 A/g. It revealed the presence of symmetric CD profiles, thus indicating the better capacitive properties of the fabricated $LiMn_2O_4$‖graphene LHC device. With an increase in current density, the

symmetric nature of the CD profiles is retained (as shown in Fig. 3.1.7(b)) which highlights the better capacitive nature of the $LiMn_2O_4$‖graphene LHC device[44]. The time taken for the charging and discharging process is low at a high current density, whereas, lower current densities resulted in a longer charging and discharging process. The specific capacitance of the $LiMn_2O_4$‖graphene LHC was calculated from the discharge profile using the relation[35]:

$$C_{sp} = [(I \times \Delta t) / (\Delta V \times m)] \quad F/g \ldots\ldots\ldots\ldots\ldots\ldots (4)$$

where *"I"* is the current (A), *"*Δt*"* is the discharge time(s), *"*ΔV*"* is the potential window (V), and *"m"* is the active mass of the electrode (g). The effect of current density on the specific capacitance of the fabricated $LiMn_2O_4$‖graphene LHC is summarized in Fig. 3.1.7(c). The device delivered a specific capacitance of 59.45 F/g measured at a current density of 0.4 A/g. The important parameters which determines the practical applications of the fabricated $LiMn_2O_4$‖graphene LHC devices are columbic efficiency (η%), energy density (E), power density (P), and cyclic stability. The ratio of the time required for discharging to the time required for charging is the coulombic efficiency and the plot of coulombic efficiency against various current densities is provided in the Fig. 3.1.7(d). A high coulombic efficiency of 97.9 % at a low current density (0.4 A/g) was obtained for the fabricated $LiMn_2O_4$‖graphene LHC device. The energy density (E) and power density (P) of the $LiMn_2O_4$‖graphene LHC were calculated from the galvanostatic discharge cycles as follows[35]:

$$E = (I \times t \times V)/ (7.2 \times m) \ Wh/kg \ldots\ldots\ldots\ldots\ldots\ldots (5)$$

$$P = (3.6 \times E) / t \quad W/kg \ldots\ldots\ldots\ldots\ldots\ldots\ldots\ldots (6)$$

where *"I"* is the current, *"t"* is the time of discharge, *"V"* is the potential and "*m*" is the electroactive mass of the electrodes. The Ragone plot of the fabricated $LiMn_2O_4$‖graphene LHC device shown in Fig. 3.1.8(a) demonstrates that the energy density

of the device is about 39.96 Wh/kg at a corresponding power density of 440 W/kg measured at a constant current of 0.4 A/g. The obtained energy density of the asymmetric $LiMn_2O_4$‖graphene LHC is better compared to the recently reported aqueous Li-ion capacitors [LMO-NH‖AC hybrid capacitor (24 Wh/kg), $Li_2Mn_4O_9$‖activated carbon (29 Wh/kg), $LiMn_2O_4$‖RHC (29.5 Wh/kg)][45–47], Na ion capacitor [AC‖Na_2CoSiO_4 (12.4 Wh/kg), $Na_3V_2(PO_4)_3$‖C (15.9 Wh/kg), MnHCF‖Fe_3O_4/rGO (27.9 Wh/kg), $NiCo_2O_4$‖AC (13.8 Wh/kg)][48–51] and asymmetric hybrid capacitor ($CoMoO_4$‖$NiMoO_4$ (33 Wh/kg), rGO‖$CoMoO_4$ (8.17 Wh/kg), $Cu_{1.79}Co_{0.21}CH$/NF‖graphene/NF (21.5 Wh/kg)] [43,52,53] and high compared with the hydrothermally derived $LiMn_2O_4$ from MnO_2 (44.3 Wh/kg)[54].

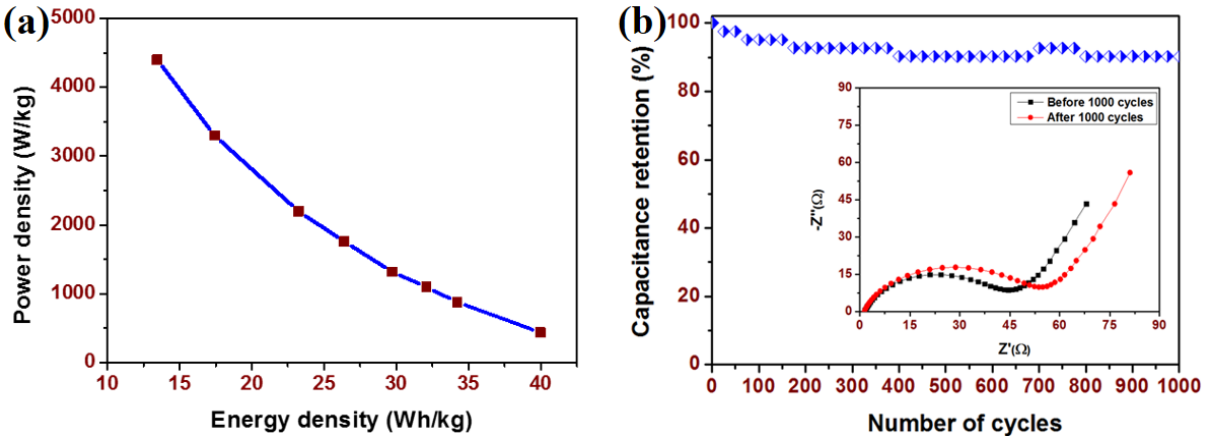

Fig. 3.1.8 (a) Ragone plot of $LiMn_2O_4$‖graphene LHC elucidate the high energy density of 39 Wh/kg at constant current density of 0.4 A/g, (b) Cyclic stability analysis of $LiMn_2O_4$‖graphene LHC measured at a constant current density of 2 A/g. The inset in Fig. 8(b) shows the Nyquist plot of $LiMn_2O_4$‖graphene LHC before and after cyclic test.

The cyclic stability for the fabricated $LiMn_2O_4$‖graphene LHC was performed for 1000 cycles using the charge discharge analysis under the constant current density of 2 A/g is shown in Fig. 3.1.8(b). The fabricated device shows good stability and retained its initial capacitance of about 90.24 % even after 1000 cycles. This decrease in the initial capacitance is due to the nature of the $LiMn_2O_4$ which undergoes Jahn-Teller distortion and also due to

the dissolution of electrodes into the electrolyte over prolonged cycles[15]. In order to understand this, the Nyquist plot of the fabricated $LiMn_2O_4$‖graphene LHC device after cyclic tests was measured and is shown in inset of Fig. 3.1.8(b). It showed an increase in charge transfer resistance of the device from 43.61 Ω (initial) to 56.92 Ω after 1000 cycles of continuous charge-discharge measurement which resulted in the observed capacitance decay in Fig 3.1.8(b).

3.1.4 Conclusions

The collective findings of this study demonstrate the high performance of LHC fabricated using $LiMn_2O_4$ and graphene as positive and negative electrodes. The fabricated $LiMn_2O_4$‖graphene LHC showed excellent electrochemical performances with a device operating window (of about 2.2 V), high specific capacitance (of about 59.45 F/g), and a better coulombic efficiency (97.9 %) with good cyclic stability. The fabricated $LiMn_2O_4$‖graphene LHC delivered excellent energy density of 39.96 Wh/kg and power density of 440 W/kg using aqueous electrolyte which can be an alternative to the use of organic electrolytes, thus it possess great potential in the use of cost-effective and high performance energy storage devices.

3.1.5 References

[1] X. Luo, J. Wang, M. Dooner, J. Clarke, Overview of current development in electrical energy storage technologies and the application potential in power system operation, Appl. Energy. 137 (2015) 511–536. doi:10.1016/j.apenergy.2014.09.081.

[2] M.K. Devaraju, T. Tomai, I. Honma, Supercritical hydrothermal synthesis of rod like Li_2FeSiO_4 particles for cathode application in lithium ion batteries, Electrochim. Acta. 109 (2013) 75–81. doi:10.1016/j.electacta.2013.07.056.

[3] A. Rose, N. Raghavan, S. Thangavel, B. Uma Maheswari, D.P. Nair, G. Venugopal, Investigation of cyclic voltammetry of graphene oxide/polyaniline/polyvinylidene fluoride nanofibers prepared via electrospinning, Mater. Sci. Semicond. Process. 31 (2015) 281–286. doi:10.1016/j.mssp.2014.10.051.

[4] H. Kim, K.-Y. Park, M.-Y. Cho, M.-H. Kim, J. Hong, S.-K. Jung, K.C. Roh, K. Kang, High-Performance Hybrid Supercapacitor Based on Graphene-Wrapped $Li_4Ti_5O_{12}$ and Activated Carbon, ChemElectroChem. 1 (2014) 125–130. doi:10.1002/celc.201300186.

[5] M.K. Devaraju, I. Honma, Hydrothermal and Solvothermal Process Towards Development of $LiMPO_4$ (M = Fe, Mn) Nanomaterials for Lithium-Ion Batteries, Adv. Energy Mater. 2 (2012) 284–297. doi:10.1002/aenm.201100642.

[6] K. Krishnamoorthy, P. Pazhamalai, G.K. Veerasubramani, S.J. Kim, Mechanically delaminated few layered MoS_2 nanosheets based high performance wire type solid-state symmetric supercapacitors, J. Power Sources. 321 (2016) 112–119. doi:10.1016/j.jpowsour.2016.04.116.

[7] D.P. Nair, T. Sakthivel, R. Nivea, J.S. Eshow, V. Gunasekaran, Effect of Surfactants on Electrochemical Properties of Vanadium-Pentoxide Nanoparticles Synthesized via Hydrothermal Method, J. Nanosci. Nanotechnol. 15 (2015) 4392–4397.

doi:10.1166/jnn.2015.9786.

[8] G. Wang, L. Zhang, J. Zhang, A review of electrode materials for electrochemical supercapacitors, Chem. Soc. Rev. 41 (2012) 797–828. doi:10.1039/C1CS15060J.

[9] M.K. Devaraju, Q.D. Truong, T. Tomai, I. Honma, Supercritical fluid methods for synthesizing cathode materials towards lithium ion battery applications, RSC Adv. 4 (2014) 27452–27470. doi:10.1039/c4ra01772b.

[10] S.-E. Chun, B. Evanko, X. Wang, D. Vonlanthen, X. Ji, G.D. Stucky, S.W. Boettcher, Design of aqueous redox-enhanced electrochemical capacitors with high specific energies and slow self-discharge, Nat. Commun. 6 (2015) 7818. doi:10.1038/ncomms8818.

[11] C.X. Guo, C.M. Li, A self-assembled hierarchical nanostructure comprising carbon spheres and graphene nanosheets for enhanced supercapacitor performance, Energy Environ. Sci. 4 (2011) 4504–4507. doi:10.1039/c1ee01676h.

[12] P. Pazhamalai, K. Krishnamoorthy, S.J. Kim, Hierarchical copper selenide nanoneedles grown on copper foil as a binder free electrode for supercapacitors, Int. J. Hydrogen Energy. 41 (2016) 14830–14835. doi:10.1016/j.ijhydene.2016.05.157.

[13] L. Ye, Q. Liang, Y. Lei, X. Yu, C. Han, W. Shen, Z.-H. Huang, F. Kang, Q.-H. Yang, A high performance Li-ion capacitor constructed with $Li_4Ti_5O_{12}$/C hybrid and porous graphene macroform, J. Power Sources. 282 (2015) 174–178. doi:10.1016/j.jpowsour.2015.02.028.

[14] P. Sennu, V. Aravindan, M. Ganesan, Y.-G. Lee, Y.-S. Lee, Biomass-Derived Electrode for Next Generation Lithium-Ion Capacitors, ChemSusChem. 9 (2016) 849–854. doi:10.1002/cssc.201501621.

[15] Y. Liu, D. Zhang, Y. Shang, Y. Liu, J. Zhang, Synthesis of Nitrogen-Doped Graphene as Highly Effective Cathode Materials for Li-Ion Hybrid Supercapacitors, J.

Electrochem. Soc. 162 (2015) A2123–A2130. doi:10.1149/2.0721510jes.

[16] Y.G. Lim, D. Kim, J.M. Lim, J.S. Kim, J.S. Yu, Y.J. Kim, D. Byun, M. Cho, K. Cho, M.S. Park, Anti-fluorite Li_6CoO_4 as an alternative lithium source for lithium ion capacitors: An experimental and first principles study, J. Mater. Chem. A. 3 (2015) 12377–12385. doi:10.1039/c5ta00297d.

[17] M.K. Devaraju, T. Tomai, A. Unemoto, I. Honma, Novel processing of lithium manganese silicate nanomaterials for Li-ion battery applications, RSC Adv. 3 (2013) 608–615. doi:10.1039/c2ra22409g.

[18] J. Yan, Y. Sun, L. Jiang, Y. Tian, R. Xue, L. Hao, W. Liu, B. Yi, Electrochemical performance of lithium ion capacitors using aqueous electrolyte at high temperature, J. Renew. Sustain. Energy. 5 (2013) 021404. doi:10.1063/1.4798432.

[19] B. Liu, D. Kong, Z.X. Huang, R. Mo, Y. Wang, Z. Han, C. Cheng, H.Y. Yang, Three-dimensional hierarchical $NiCo_2O_4$ nanowire@Ni_3S_2 nanosheet core/shell arrays for flexible asymmetric supercapacitors, Nanoscale. 8 (2016) 10686–10694. doi:10.1039/c6nr02600a.

[20] Y. Wang, Y. Xia, A new concept hybrid electrochemical surpercapacitor: Carbon/$LiMn_2O_4$ aqueous system, Electrochem. Commun. 7 (2005) 1138–1142. doi:10.1016/j.elecom.2005.08.017.

[21] Y. Wang, Y. Xia, Hybrid Aqueous Energy Storage Cells Using Activated Carbon and Lithium-Intercalated Compounds, J. Electrochem. Soc. 153 (2006) A450. doi:10.1149/1.2140678.

[22] J.Y. Luo, J.L. Liu, P. He, Y.Y. Xia, A novel $LiTi_2(PO_4)_3/MnO_2$ hybrid supercapacitor in lithium sulfate aqueous electrolyte, Electrochim. Acta. 53 (2008) 8128–8133. doi:10.1016/j.electacta.2008.05.080.

[23] N. Xu, X. Sun, X. Zhang, K. Wang, Y. Ma, A two-step method for preparing

$Li_4Ti_5O_{12}$-graphene as an anode material for lithium-ion hybrid capacitors, RSC Adv. 5 (2015) 94361–94368. doi:10.1039/c5ra20168c.

[24] C.G. Han, C. Zhu, G. Saito, T. Akiyama, Improved electrochemical performance of $LiMn_2O_4$ surface-modified by a Mn^{4+}-rich phase for rechargeable lithium-ion batteries, Electrochim. Acta. 209 (2016) 225–234. doi:10.1016/j.electacta.2016.05.075.

[25] Z. Zhang, T. Zeng, Y. Lai, M. Jia, J. Li, A comparative study of different binders and their effects on electrochemical properties of $LiMn_2O_4$ cathode in lithium ion batteries, J. Power Sources. 247 (2014) 1–8. doi:10.1016/j.jpowsour.2013.08.051.

[26] W.K. Chee, H.N. Lim, Z. Zainal, N.M. Huang, I. Harrison, Y. Andou, Flexible Graphene-Based Supercapacitors: A Review, J. Phys. Chem. C. 120 (2016) 4153–4172. doi:10.1021/acs.jpcc.5b10187.

[27] Y. Zhang, H.C. Shin, J. Dong, M. Liu, Nanostructured $LiMn_2O_4$ prepared by a glycine-nitrate process for lithium-ion batteries, Solid State Ionics. 171 (2004) 25–31. doi:10.1016/j.ssi.2004.04.008.

[28] K. Krishnamoorthy, G.-S. Kim, S.J. Kim, Graphene nanosheets: Ultrasound assisted synthesis and characterization, Ultrason. Sonochem. 20 (2013) 644–649. doi:10.1016/j.ultsonch.2012.09.007.

[29] S. Chitra, P. Kalyani, T. Mohan, Characterization and electrochemical studies of $LiMn_2O_4$ cathode materials prepared by combustion method, J. …. 3 (1999) 433–441. doi:10.1023/A:1009982301437.

[30] A. Rougier, K.A. Striebel, S.J. Wen, T.J. Richardson, R.P. Reade, E.J. Cairns, Characterization of pulsed laser-deposited $LiMn_2O_4$ thin films for rechargeable lithium batteries, Appl. Surf. Sci. 134 (1998) 107–115. doi:10.1016/S0169-4332(98)00234-7.

[31] C. V. Ramana, M. Massot, C.M. Julien, XPS and Raman spectroscopic characterization of $LiMn_2O_4$ spinels, Surf. Interface Anal. 37 (2005) 412–416.

doi:10.1002/sia.2022.

[32] E. Manikandan, G. Kavitha, J. Kennedy, Epitaxial zinc oxide, graphene oxide composite thin-films by laser technique for micro-Raman and enhanced field emission study, Ceram. Int. 40 (2014) 16065–16070. doi:10.1016/j.ceramint.2014.07.129.

[33] S. Liu, W. Peng, H. Sun, S. Wang, Physical and chemical activation of reduced graphene oxide for enhanced adsorption and catalytic oxidation, Nanoscale. 6 (2014) 766–771. doi:10.1039/C3NR04282K.

[34] H. Zhang, Y. Xu, D. Liu, Novel nanostructured $LiMn_2O_4$ microspheres for high power Li-ion batteries, RSC Adv. 5 (2015) 11091–11095. doi:10.1039/C4RA13041C.

[35] K. Krishnamoorthy, G.K. Veerasubramani, P. Pazhamalai, S.J. Kim, Designing two dimensional nanoarchitectured MoS_2 sheets grown on Mo foil as a binder free electrode for supercapacitors, Electrochim. Acta. 190 (2016) 305–312. doi:10.1016/j.electacta.2015.12.148.

[36] M.-X. Guo, S.-W. Bian, F. Shao, S. Liu, Y.-H. Peng, Hydrothermal synthesis and electrochemical performance of MnO_2/graphene/polyester composite electrode materials for flexible supercapacitors, Electrochim. Acta. 209 (2016) 486–497. doi:10.1016/j.electacta.2016.05.082.

[37] F.X. Wang, S.Y. Xiao, Y. Shi, L.L. Liu, Y.S. Zhu, Y.P. Wu, J.Z. Wang, R. Holze, Spinel $LiNi_xMn_{2-x}O_4$ as cathode material for aqueous rechargeable lithium batteries, Electrochim. Acta. 93 (2013) 301–306. doi:10.1016/j.electacta.2013.01.106.

[38] F.X. Wang, S.Y. Xiao, Y.S. Zhu, Z. Chang, C.L. Hu, Y.P. Wu, R. Holze, Spinel $LiMn_2O_4$ nanohybrid as high capacitance positive electrode material for supercapacitors, J. Power Sources. 246 (2014) 19–23. doi:10.1016/j.jpowsour.2013.07.046.

[39] S. Rasul, A. Alazmi, K. Jaouen, M.N. Hedhili, P.M.F.J. Costa, Rational design of

reduced graphene oxide for superior performance of supercapacitor electrodes, Carbon N. Y. 111 (2017) 774–781. doi:10.1016/j.carbon.2016.10.066.

[40] K.V. Sankar, R. Kalai Selvan, Improved electrochemical performances of reduced graphene oxide based supercapacitor using redox additive electrolyte, Carbon N. Y. 90 (2015) 260–273. doi:10.1016/j.carbon.2015.04.023.

[41] C. Zhong, Y. Deng, W. Hu, J. Qiao, L. Zhang, J. Zhang, A review of electrolyte materials and compositions for electrochemical supercapacitors, Chem. Soc. Rev. 44 (2015) 7484–7539. doi:10.1039/C5CS00303B.

[42] K. Fic, G. Lota, M. Meller, E. Frackowiak, Novel insight into neutral medium as electrolyte for high-voltage supercapacitors, Energy Environ. Sci. 5 (2012) 5842–5850. doi:10.1039/C1EE02262H.

[43] G.K. Veerasubramani, K. Krishnamoorthy, S.J. Kim, Electrochemical performance of an asymmetric supercapacitor based on graphene and cobalt molybdate electrodes, RSC Adv. 5 (2015) 16319–16327. doi:10.1039/C4RA15070H.

[44] S. Chitra, P. Kalyani, T. Mohan, R. Gangadharan, B. Yebka, S. Castro-Garcia, M. Massot, C. Julien, M. Eddrief, No Title, J. Electroceramics. 3 (1999) 433–441. doi:10.1023/A:1009982301437.

[45] F.X. Wang, S.Y. Xiao, X.W. Gao, Y.S. Zhu, H.P. Zhang, Y.P. Wu, R. Holze, Nanoporous $LiMn_2O_4$ spinel prepared at low temperature as cathode material for aqueous supercapacitors, J. Power Sources. 242 (2013) 560–565. doi:10.1016/j.jpowsour.2013.05.115.

[46] Y.J. Hao, Q.Y. Lai, L. Wang, X.Y. Xu, H.Y. Chu, Electrochemical performance of a high cation-deficiency $Li_2Mn_4O_9$/active carbon supercapacitor in $LiNO_3$ electrolyte, Synth. Met. 160 (2010) 669–674. doi:10.1016/j.synthmet.2009.12.025.

[47] C. Rong, S. Chen, J. Han, K. Zhang, D. Wang, X. Mi, X. Wei, Hybrid supercapacitors

integrated rice husk based activated carbon with $LiMn_2O_4$, J. Renew. Sustain. Energy. 7 (2015) 023104. doi:10.1063/1.4913965.

[48] S. Gao, J. Zhao, Y. Zhao, Y. Wu, X. Zhang, L. Wang, X. Liu, Y. Rui, J. Xu, Na_2CoSiO_4 as a novel positive electrode material for sodium-ion capacitors, Mater. Lett. 158 (2015) 300–303. doi:10.1016/j.matlet.2015.06.038.

[49] S. Wang, J. Zhao, L. Wang, X. Liu, Y. Wu, J. Xu, High performance $Na_3V_2(PO_4)_3$/C composite electrode for sodium-ion capacitors, Ionics (Kiel). 21 (2015) 2633–2638. doi:10.1007/s11581-015-1428-9.

[50] K. Lu, D. Li, X. Gao, H. Dai, N. Wang, H. Ma, An advanced aqueous sodium-ion supercapacitor with a manganous hexacyanoferrate cathode and a Fe_3O_4/rGO anode, J. Mater. Chem. A. 3 (2015) 16013–16019. doi:10.1039/C5TA04244E.

[51] R. Ding, L. Qi, H. Wang, An investigation of spinel $NiCo_2O_4$ as anode for Na-ion capacitors, Electrochim. Acta. 114 (2013) 726–735. doi:10.1016/j.electacta.2013.10.113.

[52] X. Xu, J. Shen, N. Li, M. Ye, Microwave-assisted synthesis of graphene/$CoMoO_4$ nanocomposites with enhanced supercapacitor performance, J. Alloys Compd. 616 (2014) 58–65. doi:10.1016/j.jallcom.2014.07.047.

[53] S. Liu, K.N.K.S. Hui, K.N.K.S. Hui, V. V. Jadhav, Q.X. Xia, J.M. Yun, Y.R. Cho, R.S. Mane, K.H. Kim, Facile Synthesis of Microsphere Copper Cobalt Carbonate Hydroxides Electrode for Asymmetric Supercapacitor, Electrochim. Acta. 188 (2016) 898–908. doi:10.1016/j.electacta.2015.12.018.

[54] X. Yang, F. Qu, H. Niu, Q. Wang, J. Yan, Z. Fan, High-performance aqueous asymmetric supercapacitor based on spinel $LiMn_2O_4$ and nitrogen-doped graphene/porous carbon composite, Electrochim. Acta. 180 (2015) 287–294. doi:10.1016/j.electacta.2015.08.128.

CHAPTER 3.2: High-energy aqueous Li-ion hybrid capacitor based on metal-organic-framework-mimicking insertion-type copper hexacyanoferrate and capacitive-type graphitic carbon electrodes

Highlights

- Copper hexacyanoferrate (Cu-HCF) was synthesized via a sonochemical method and graphitic carbon was prepared via carbonization reaction of sodium alginate,
- Aqueous Li-ion capacitor was assembled using Cu-HCF and graphitic carbon electrodes and the fabricated LHC device operates in a wide voltage window of 2.2 V.
- The aqueous LHC device delivered a high specific capacitance of 63.64 F g^{-1} with a high energy density of 42.78 Wh kg^{-1}.

3.2.1 Introduction

The rising demand for energy storage for electric vehicles and portable electronics is increasing the requirement for incorporating renewable energy sources into various practical applications [1,2]. Hence, there is a need to develop high-performance, cost-effective and eco-friendly energy storage devices [3,4]. Electrochemical energy storage devices, such as supercapacitors and batteries, are ideal choices for facing this increasing energy supply demand. Supercapacitors are of particular interest because of their high power, fast charging-discharging rate, and long cycle life. Although supercapacitors have a higher power density than do batteries, their drawback is their low energy density, which limits their practical applications [5]. To overcome this energy density ($E = 0.5\ CV^2$) deficiency in a supercapacitor, the operating voltage window (V) and specific capacitance (C) must both be improved by choosing appropriate electrodes and electrolytes, which will enhance the energy density [6–8]. Extensive research has focused on developing novel electrodes with high surface areas to enhance the specific capacitance and on the fabrication of symmetric/asymmetric supercapacitors using an organic electrolyte, which allows for an increase in the voltage window and thereby the energy density [9]. Among supercapacitors, ion hybrid capacitors have great potential for improving energy density [10,11]. The high energy density of ion capacitors is due to the effectiveness of the corresponding electrode materials, viz., intercalative and capacitive electrodes. The former can store energy via intercalation/deintercalation processes, and the latter stores energy via double-layer capacitance. Due to the dual charge storage mechanism exhibited in the ion capacitor, it is likely that an exceptional energy density and a good rate capability will be achieved [12,13].

Li-ion- and Na-ion-based hybrid capacitors in both aqueous and organic electrolytes have been studied by several research groups [14–17]. In this context, Li-ion intercalating electrode materials ($LiMn_2O_4$, $LiCoO_2$ or $LiFePO_4$) and/or Na-ion intercalating materials

($NaVPO_4F$, $NaFePO_4$ or $NaTi_2(PO_4)_3$) are used to form intercalative electrodes, with capacitive electrodes based on carbon materials [18–20]. Furthermore, extensive research has been carried out over the past decade to explore the ion intercalation properties of transition metal oxides (MnO_2 and RuO_2), transition metal chalcogenides (MoS_2, VS_2, and TiS_2) and layered materials (e.g., M'Xene and graphdyine) for use as intercalative electrodes [21,22]. Additionally, various carbon-based materials such as activated carbon (AC), graphite, porous carbon, carbon nanotubes, and graphene have been examined as a capacitive electrode materials for ion capacitors [23,24]. It is known that the selection of an electrode for an ion capacitor plays an important role in the performance of the fabricated ion capacitor. In this scenario, the Prussian blue analogue metal hexacyanoferrate (with the chemical formula $A_xPR(CN)_6$) possesses an open framework with a large interstitial space that can facilitate the ion intercalation/deintercalation of a variety of ions, such as Li^+ and Na^+, in the cyano-bridged network [25]. Recently, the research of Wessells et al. on nanostructured hexacyanoferrate-type materials has opened a gateway for the material's potential use in non-aqueous Li-ion and Na-ion batteries [26,27]. Among the various metal hexacyanoferrates available, copper hexacyanoferrate (Cu-HCF) has been examined as a potential electrode material for Li-ion and Na-ion batteries using organic electrolytes [28–30]. However, only limited reports are available on the effectiveness of these electrode materials in aqueous ion capacitors, which are more promising than organic electrolytes due to the high ionic conductivity of aqueous electrolytes and offer the advantages of being inexpensive and environmentally benign.

In this work, we fabricated an aqueous Li-ion hybrid capacitor (LHC) based on Cu-HCF and sodium alginate-derived graphitic carbon (GC) that can serve as intercalative and capacitive electrodes. Compared with widely used AC or other carbon materials, GC particles derived from the pyrolysis of biomolecules have a low surface area and high capacitance due

to the presence of heteroatoms in the derived graphitic carbon [31]. The electrochemical properties of the fabricated LHC device were examined for its potential applications in electrochemical energy storage devices.

3.2.2 Experimental section

3.2.2.1 Preparation of copper hexacyanoferrate (Cu-HCF) nanoparticles

Copper hexacyanoferrate (Cu-HCF) was synthesized via a sonochemical method [26]. Briefly, two separate aqueous solutions containing 1 M $Cu(NO_3)_2$ and 0.5 M $K_3[Fe(CN)_6]$ were prepared. The copper nitrate solution and potassium ferricyanide solution were gradually added dropwise to distilled water (50 mL), which was kept under ultrasound irradiation. The sonication process proceeded for 2 h, and the resulting Cu-HCF precipitates were washed with distilled water and ethanol by centrifugation. Finally, the Cu-HCF particles were dried at 80 °C overnight.

3.2.2.2 Preparation of graphitic carbon (GC) nanoparticles

Graphitic carbon was derived from the carbonization reaction of sodium alginate [32]. Briefly, the sodium alginate was ground to a fine powder and annealed at 200 °C for 2 h; next, the temperature was increased to 900 °C, and the sample was kept for 6 h in an Ar atmosphere for the carbonization of the precursor material, followed by cooling to room temperature. A solid, black powder was formed as a result of the carbonization reaction. The black powder was collected and washed with distilled water several times to remove any residue, followed by drying at 80 °C overnight.

3.2.2.3 Preparation of the working electrodes and electrochemical analysis

The Cu-HCF and GC working electrodes for the electrochemical studies were according to the slurry coating method [33]. Briefly, the active material (Cu-HCF or GC), carbon black and polyvinylidene difluoride (PVDF) were mixed the ratio of 80:15:5 using N-methyl pyrrolidone (NMP) as solvent and ground well to form the slurry. Then, the prepared

slurry was coated on to the pre-cleaned stainless-steel substrate (1×1 cm^2) and allowed to dry at 80 ºC overnight. The mass loading on the stainless-steel substrate was calculated as 2.0 and 1.0 mg cm^{-2} for the Cu-HCF and GC, respectively. An aqueous solution containing 1 M $LiNO_3$ was used as an electrolyte. The electrochemical characterization of the Cu-HCF and GC electrodes were examined using a three-electrode system. Here, Cu-HCF or GC electrode was used as the working electrode, silver/silver chloride as the reference electrode, and platinum as the counter electrode. Finally, the Cu-HCF‖GC Li-ion hybrid capacitors were fabricated in the form of a sandwich-type electrode, with an electrolyte-immersed Celgard as the separator. The electrochemical properties of the working electrodes and the Cu-HCF‖GC LHC were examined via cyclic voltammetry (CV), electrochemical impedance spectroscopy (EIS) and galvanostatic charge-discharge (CD) measurements using an Autolab PGSTAT302N electrochemical workstation. The specific capacity of Cu-HCF and GC electrodes were calculated from the CV curves using the relation[34]:

$$Q_s = [\int IdV / (s \times m)] \quad \ldots\ldots\ldots\ldots\ldots\ldots (1)$$

where *"Q_s"* is the specific capacity (C g^{-1}), *"I"* is the current (A), *"s"* is the scan rate (mV s^{-1}), and *"m"* is the active mass of the electrode (g). In order to balance the charges accumulated at both electrodes (i.e., $Q^+=Q^-$), the mass ratio of Cu-HCF and GC for the Cu-HCF‖GC LHC device was calculated using the relation[34]:

$$m^- = (m^+ \times Q_s^+ \times \Delta V^+) / (Q_s^- \times \Delta V^-) \quad \ldots\ldots\ldots\ldots\ldots\ldots (2)$$

where *"m^-"* and *"m^+"* represent the mass of the negative and positive electrodes, *"Q_s^-"* and *"Q_s^+"* denotes the specific capacity of the negative and positive electrodes, *"ΔV^-"* and *"ΔV^+"* are the potential windows of the negative and positive electrodes obtained using the three-electrode system, respectively.

3.2.3. Results and discussion

3.2.3.1 Physicochemical characterization

Figure 3.2.1(A) shows the X-ray diffraction (XRD) pattern of the Cu-HCF. The observed diffraction peaks correspond to the face-centred cubic structure of Prussian blue, which belongs to space group $Fm\bar{3}m$ (JCPDS card no. 86-0513)[26]. The calculated lattice parameter was 10.10 Å, and the crystallite size calculated from the Debye–Scherer equation was 33 nm.

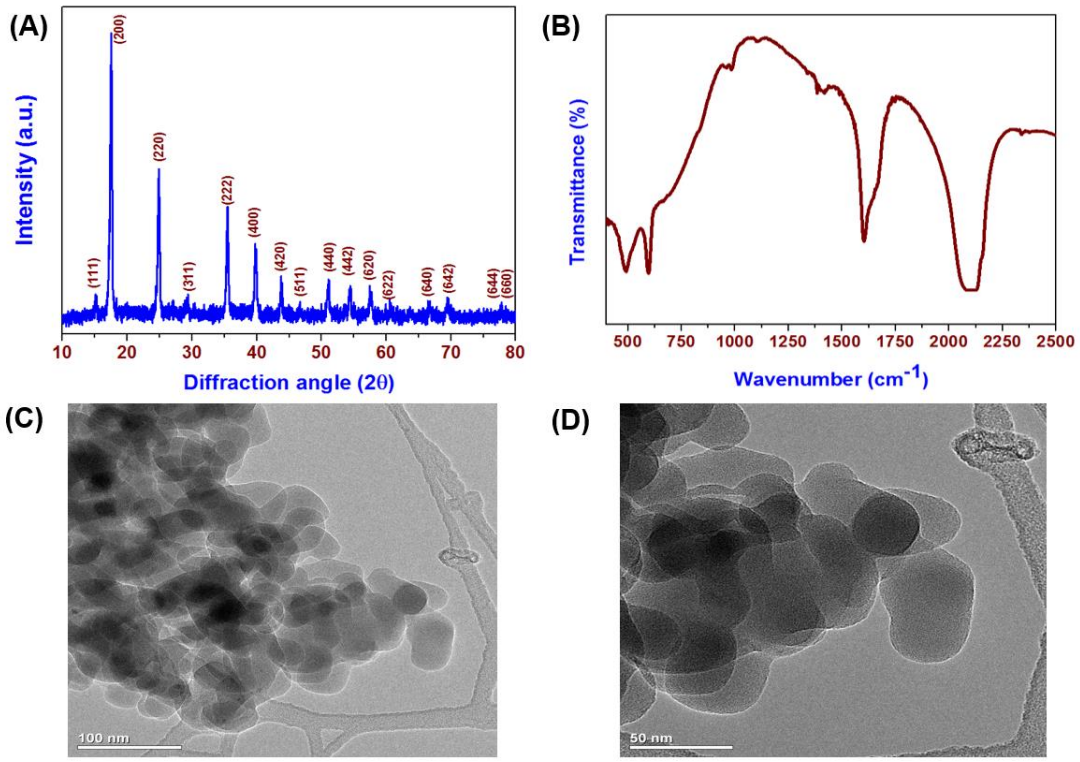

Figure 3.2.1. (A) X-ray diffraction (XRD) pattern of the copper hexacyanoferrate (Cu-HCF) nanoparticles. (B) Fourier-transformed infrared spectrum of the Cu-HCF nanoparticles. High-resolution transmission electron microscopy (HR-TEM) micrographs of Cu-HCF: (C) low resolution and (D) high resolution.

The Fourier transform-infrared (FT-IR) spectrum of the Cu-HCF nanoparticles (Figure 3.2.1(B)) displayed absorption bands at 492, 592, 1600, and 2100 cm^{-1}. The bands observed at 492 and 592 cm^{-1} were assigned to the skeletal vibrations of Cu–C and $Cu(CN)_6$,

which are commonly associated with metal hexacyanoferrate, and the band at 1,604 cm^{-1} corresponded to the adsorbed water molecules bonded within the metal organic framework [35]. The band observed from 2080 to 2137 cm^{-1} corresponds to the strong stretching vibrations of -CN groups bridging two metals [35,36]. The bands observed from 2080 to 2137 cm^{-1} correspond to the stretching vibrations of CN groups in the Cu-HCF nanoparticles [6]. The surface morphology of the Cu-HCF was investigated high-resolution transmission electron microscopy (HR-TEM) (Fig. 3.2.1(C and D)).The HR-TEM micrographs of Cu-HCF (Figure 3.2.1(C)) reveal well-defined sphere-like particles, and the high-magnification micrograph (Figure 3.2.1(D)) shows the presence of uniform 30- to 60-nm particles.

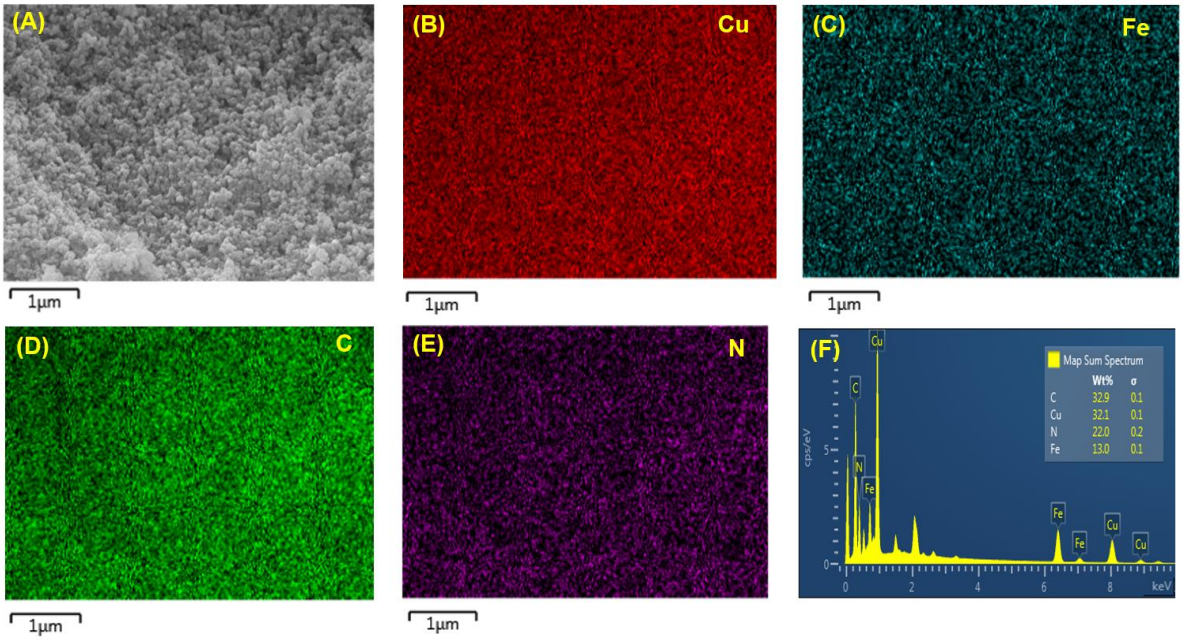

Figure 3.2.2. Elemental mapping analysis of Cu-HCF nanostructures (A) Field-emission scanning electron image of the Cu-HCF nanoparticles. (B) Elemental mapping of Cu in Cu-HCF nanoparticles. (C) Elemental mapping of Fe in Cu-HCF nanoparticles. (D) Elemental mapping of C in Cu-HCF nanoparticles. (E) Elemental mapping of N in Cu-HCF nanoparticles. (F) Mass sum spectrum of elements present in Cu-HCF.

The elemental mapping analysis of the Cu-HCF nanoparticles is shown in Fig. 3.2.2(A-E), which confirms the presence of elements such as Cu, Fe, C, and N in the Cu-HCF. The summed mass spectrum of the elements present in the Cu-HCF nanostructure is presented in Fig. 3.2.2(F), confirming the formation of stoichiometric Cu-HCF.

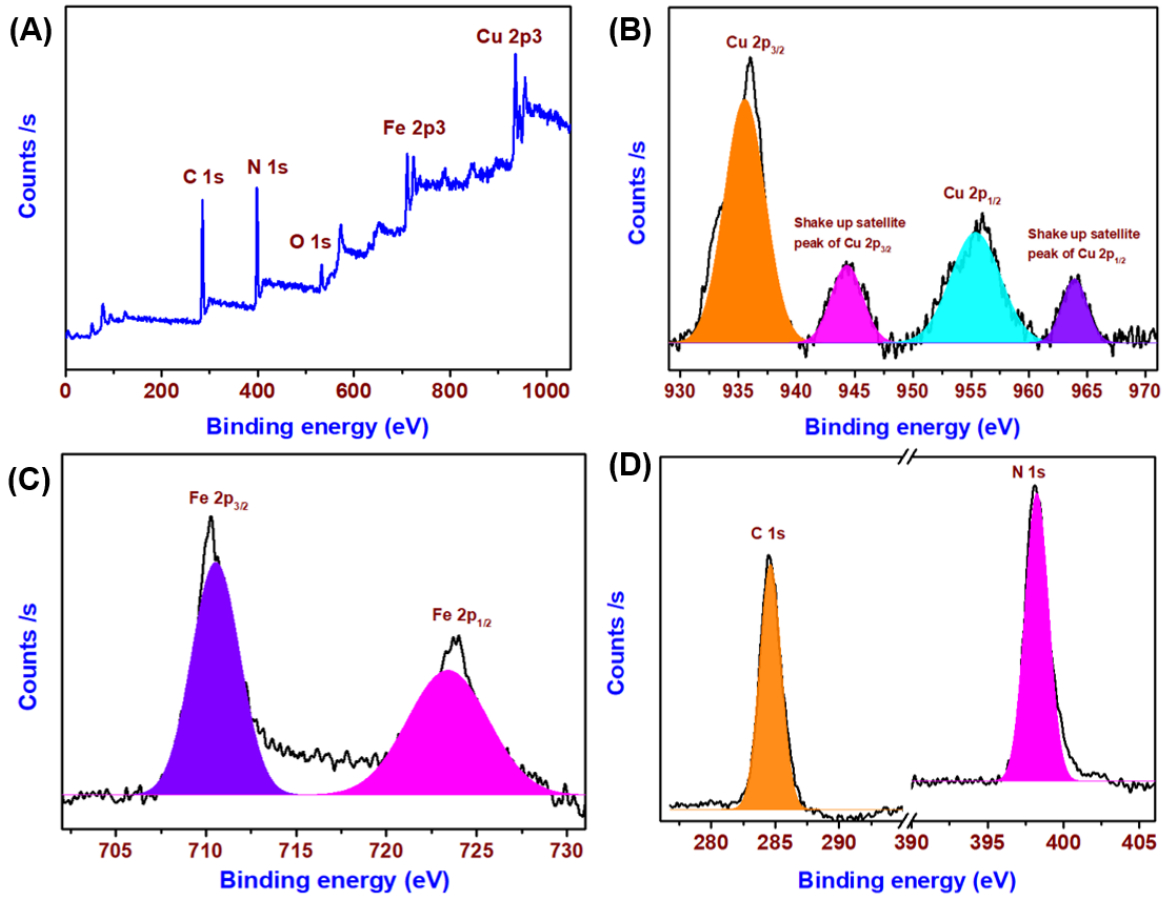

Figure 3.2.3. X-ray photoelectron spectroscopy of the Cu-HCF nanoparticles. (A) Survey spectrum for Cu-HCF, (B) core-level spectrum of copper in Cu-HCF, (C) core-level spectrum of iron in Cu-HCF and (D) core-level spectra of carbon and nitrogen present in Cu-HCF nanoparticles.

The XPS survey spectrum depicts the presence of copper, iron, carbon and nitrogen elements in the prepared Cu-HCF, as shown in Fig. 3.2.3(A). The core-level spectrum of the copper present in the Cu-HCF (Fig. 3.2.3(B)) shows two main peaks at 936.7 and 956 eV, corresponding to the Cu $2p_{3/2}$ and Cu $2p_{1/2}$ states, respectively [37]. In addition to the two

major peaks, strong satellite peaks of Cu^{2+} are also observed in the spectrum, which confirms that the oxidation state of copper is +2 in the prepared Cu-HCF. The core-level spectrum of Fe (Fig. 3.2.3 (C)) signifies the presence of two peaks centred at binding energies of 710 and 723 eV, corresponding to the Fe $2p_{3/2}$ and Fe $2p_{1/2}$ states, respectively [37,38]. The core-level spectra of C 1s and N 1s suggest the presence of C and N components in the cyano bridged framework of Cu-HCF nanostructures (Fig. 3.2.3(D)).

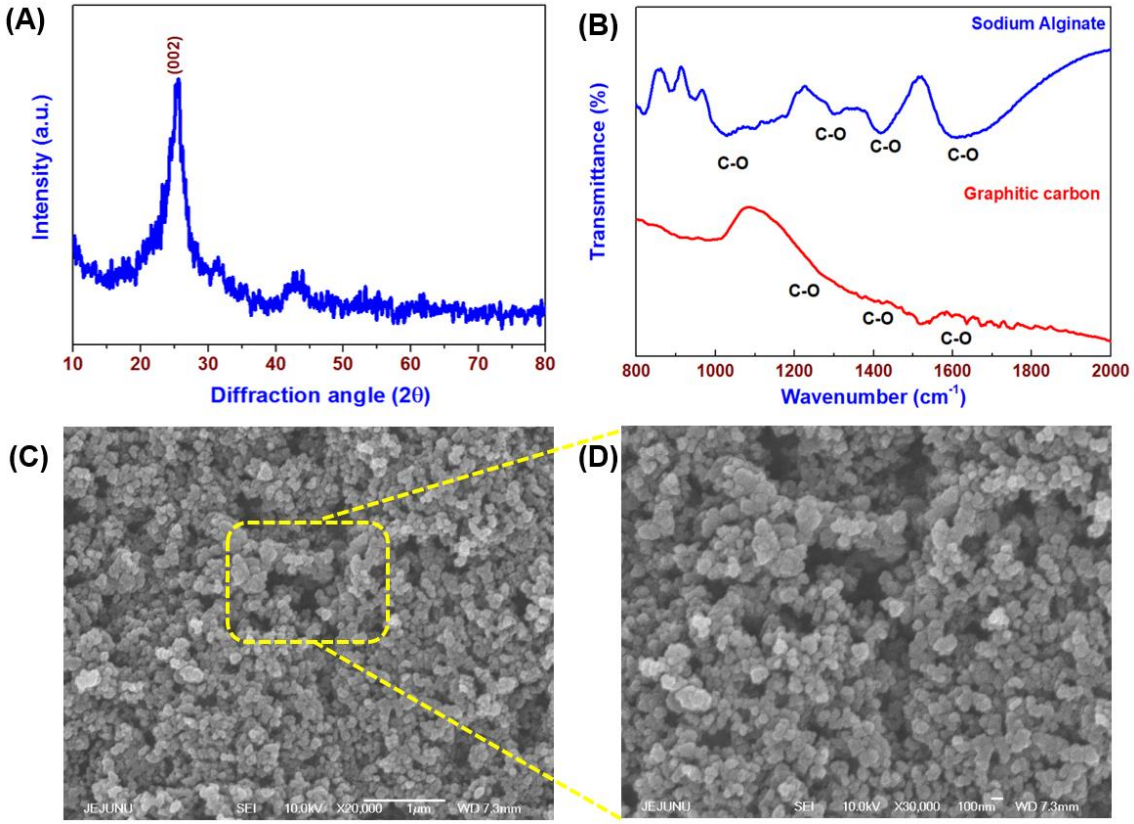

Figure 3.2.4. (A) XRD pattern of the GC nanoparticles. (B) Fourier-transform infrared (FT-IR) spectra of sodium alginate and GC nanoparticles. Field-emission scanning electron microscopy (FE-SEM) micrographs of (C) GC nanoparticles and (D) the enlarged portions of the square regions marked (C).

The XRD pattern of the sodium alginate-derived GC nanoparticles (Figure 3.2.4(A)) shows diffraction peaks at 25.73° and 43.8°, which confirm the formation of GC nanoparticles [32]. The broadened peaks at 43.8° indicate the presence of low crystallinity

and loosely packed z-axis stacking in the GC compared with that in graphite [39]. The FT-IR spectra of sodium alginate and the GC nanoparticles are shown in Figure 3.2.4(B). After the graphitization reaction, the disappearance of characteristic absorption bands for sodium alginate at 1027, 1305, 1423, and 1614 cm^{-1} corresponding to the carbonyl (C–O) stretching vibrations of the carboxyl anions and carboxyl groups, respectively was consistent with the formation of GC nanoparticles [40]. The weak band at 1014 cm^{-1} was attributed to the presence of carbonyl groups on the GC nanoparticles [40].

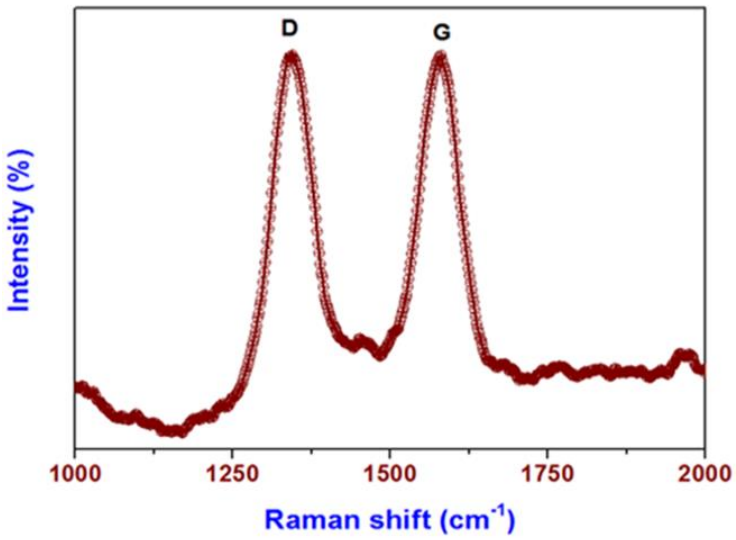

Figure 3.2.5. Raman spectrum of GC nanostructures.

The laser Raman spectrum of the GC nanoparticles (shown in Fig. 3.2.5) depicts two prominent bands at 1354 and 1586 cm^{-1}. The band observed at 1354 cm^{-1} can be termed a defect (D) band, which is due to the presence of defects (formed due to the high-temperature thermal treatment of the alginate) in the GC nanoparticles [41]. The G band observed at 1586 cm^{-1} corresponds to the first-order scattering of the E_{2g} (high) mode of the graphitic structure [39]. Furthermore, the shift in the peak position to higher wavenumbers compared with the peak position observed for graphite (G band at approximately 1570 cm^{-1} [42]) indicates the low crystallinity of the material. The I_D/I_G value of the GC particles is approximately 1.03, which also suggests the lower crystallinity of the GC compared with that of pyrolytic

graphite, and these values are close to those of chemically prepared GO and rGO [43]. The observed Raman data are in good agreement with values reported in the literature [32,39,42]. FE-SEM micrographs of the GC at low and high magnifications are shown in Figure 3.2.4(C, D). The images clearly reveal the presence of spherical carbon nanoparticles with sizes ranging from 40 to 50 nm.

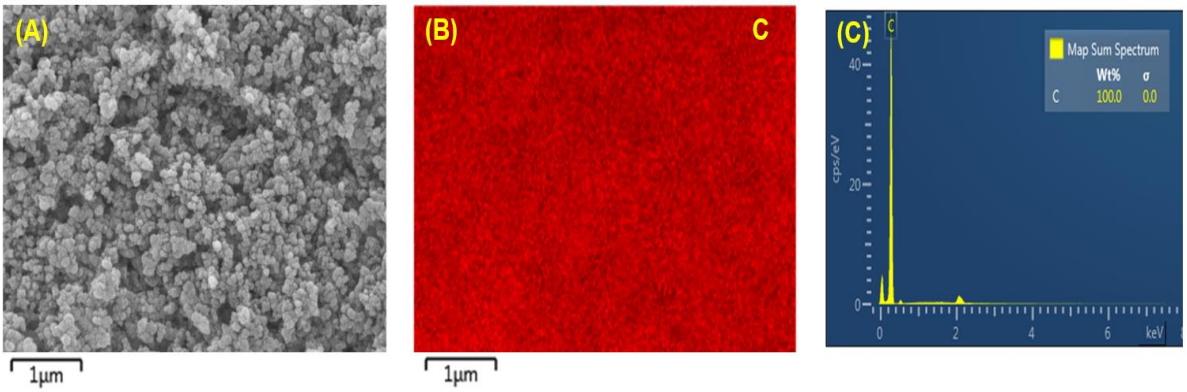

Figure 3.2.6. Elemental mapping analysis of GC nanostructures (A) Field-emission scanning electron image of the GC nanoparticles. (B) Elemental mapping of C in GC nanoparticles. (C) Mass sum spectrum of C present in GC.

Figure 3.2.6(A and B) shows the overlay and carbon mapping of the GC nanoparticles. The summed mass spectrum of the elements present in the GC nanostructure is presented in Fig. 3.2.6(C), confirming the formation of GC with a high carbon content.

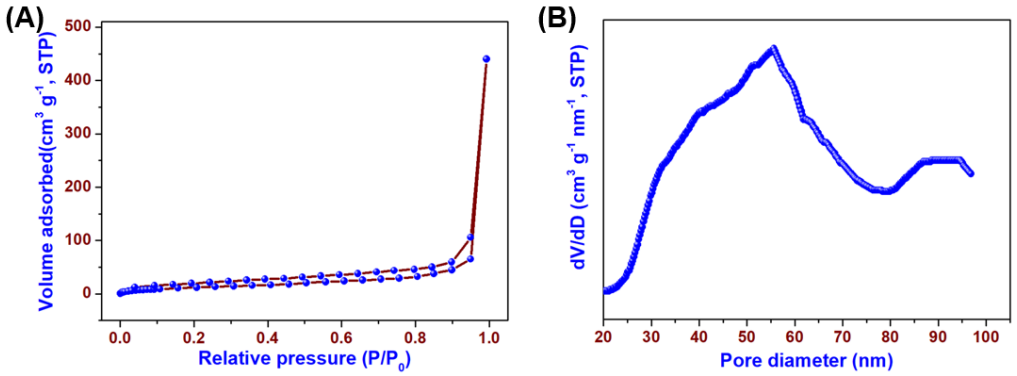

Figure 3.2.7. (A) N_2 adsorption/desorption isotherm of Cu-HCF and (B) pore volume distribution calculated via HK method.

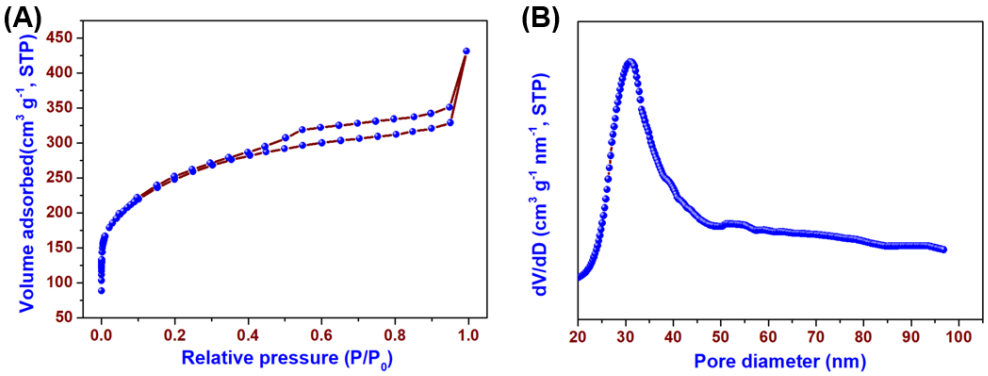

Figure 3.2.8. (A) N_2 adsorption/desorption isotherm of GC and (B) pore volume distribution calculated via HK method.

The N_2 adsorption/desorption curves of the Cu-HCF and GC nanoparticles (Fig. 3.2.7(A) and 3.2.8(A)) exhibit Type II isotherms, which is indicative of a non-porous nature or the presence of a very small fraction of micropores [44]. The specific surface areas of the Cu-HCF and GC nanoparticles were calculated to be 48 and 802 $m^2\ g^{-1}$, respectively. The pore volume distributions for the Cu-HCF and GC calculated via the HK method are shown in Fig. 3.2.7(B) and 3.2.8(B). The Cu-HCF has a wide pore diameter distribution in the range of 40-60 nm, whereas in the GC, the pore volume range is 30-40 nm.

3.2.3.2 Electrochemical characterization

The electrochemical properties of the Cu-HCF and GC electrodes were first analysed using a three-electrode configuration (Fig. 3.2.9). The cyclic voltammetry (CV) profiles of the Cu-HCF electrodes were recorded over the potential window of 0 to 1.4 V at scan rates ranging from 5 to 100 mV s^{-1} (Fig. 3.2.9(A)). The CV profiles displayed a pair of pronounced redox peaks (at 0.96 and 0.75 V), which arose due to the transformation of the Fe^{3+}/Fe^{2+} redox couple in the Cu-HCF and the intercalation/deintercalation of Li^+ ions into the cyano-bridged framework of the Cu-HCF [25]. The anodic and cathodic peak currents increased with the scan rate according to a power law (Fig. 3.2.10(A)), suggesting an improvement in the capacitive properties of the Cu-HCF electrodes. Fig. 3.2.10(B) shows that the anodic and cathodic peak potentials moved towards higher and lower potentials, respectively, with a

corresponding increase in the scan rate, and the peak separation potential (ΔE) increased with the scan rate, as shown in Fig. 3.2.10(C).

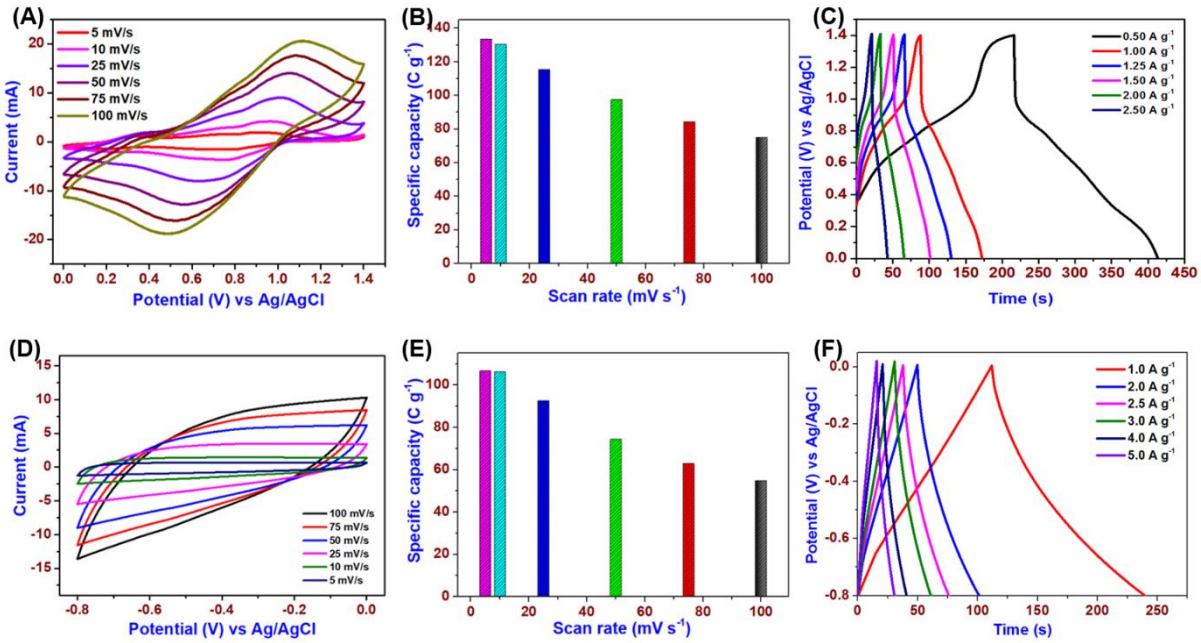

Figure 3.2.9. Electrochemical characterization of Cu-HCF and GC electrodes measured using a three-electrode configuration. Cyclic voltammetry (CV) profiles of the (A) Cu-HCF electrode measured at different scan rates, (B) effect of the scan rate on the specific capacity of the Cu-HCF electrode, and (C) CD profiles of the Cu-HCF electrode measured at different current densities. Cyclic voltammetry (CV) profiles of the (D) GC electrode measured at different scan rates, (E) effect of the scan rate on the specific capacity of the GC electrode, and (F) CD profiles of the GC electrode measured at different current densities.

This variation is due to the quasi-reversible electrochemical reversibility of the Cu-HCF electrode [45]. The possible charge storage mechanism of the Cu-HCF in aqueous $LiNO_3$ can be explained as follows [46]:

$$Cu_3^{II}[Fe^{III}(CN)_6] + xLi^+ + xe^- \longleftrightarrow Li_x Cu_3^{II}[Fe^{III}(CN)_6] \quad \ldots\ldots\ldots\ldots\ldots (7)$$

The Cu-HCF electrode showed a maximum specific capacity of 133.43 C g^{-1} at a scan rate of 5 mV s^{-1}. A specific capacity retention rate of 56.22 % was obtained for the Cu-HCF electrode when the scan rate was increased 20-fold (Fig. 3.2.9(B)).

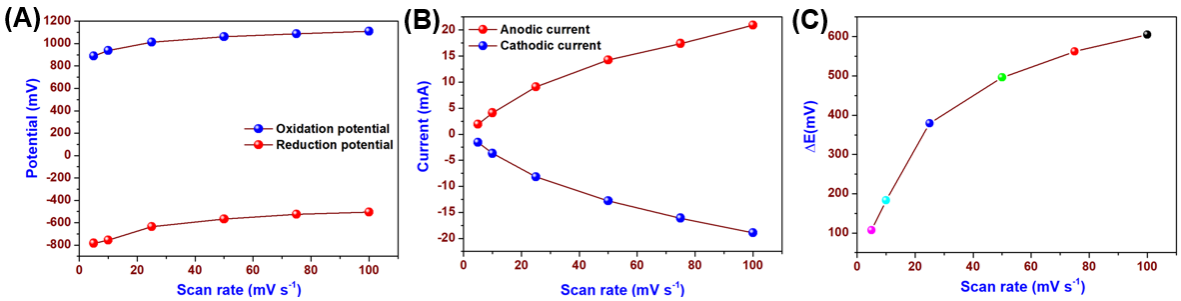

Figure 3.2.10. (A) Plot of anodic and cathodic peak current (maximum) against the scan rates of Cu-HCF electrode, (B) Plot of anodic and cathodic peak potential (maximum) against the scan rates of Cu-HCF electrode, and (C) Plot of peak to peak separation potential (ΔE) against the scan rates of Cu-HCF electrode.

Furthermore, the contributions of surface and intercalative capacitance to the overall capacitance of the Cu-HCF electrode were determined using the Trasatti method [47]. Commonly, the total amount (q^*_{total}) of charge stored in an electrode is the sum of the charge storage contributions from the inner (q^*_{in}) and outer (q^*_{out}) surfaces of the electrode. The y-intercept of the linear fit of $1/q^*$ vs. $v^{1/2}$ at $v = 0$ represents the total amount of charge stored in the Cu-HCF electrode (Fig. 3.2.11(A)). The y-intercept of the linear fit of q^* vs. $v^{-1/2}$ at $v = \infty$ represents the amount of charge stored at the outer surface of the electrode (Fig 3.2.11(B)). The values were derived from the intercept for the maximum or total charge stored and charge stored in the outer surface of the Cu-HCF electrode. According to the Trasatti method, the percentages of charge stored in the outer and inner surfaces of the Cu-HCF electrode are 52.1 % and 47.9 %, respectively.

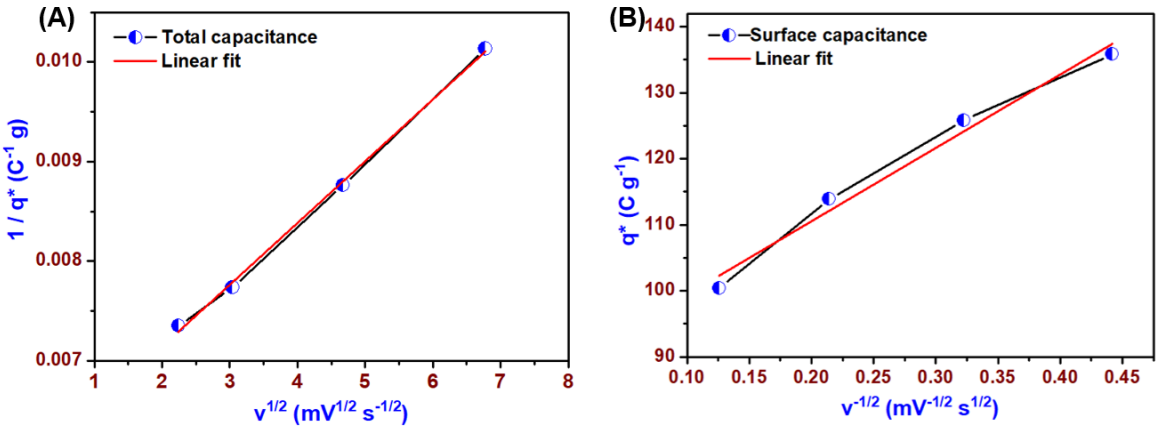

Figure 3.2.11. The trasatti plot for Cu-HCF electrode. (A) Dependence of $1/C_{total}$ against $v^{1/2}$ and (B) dependence of C_{out} on $v^{-1/2}$ for Cu-HCF electrode in the $LiNO_3$ electrolyte.

The galvanostatic charge-discharge (CD) profiles of the Cu-HCF electrode (Fig. 3.2.9(C)) were measured at current densities ranging from 0.5 to 2.5 A g^{-1}. The CD profiles indicate the presence of peaks at 0.96 and 0.75 V, which correspond to the transformation of Fe^{3+}/Fe^{2+}, suggesting the intercalation capacitance of the electrode. Figure 3.2.9(D) shows the CV profiles of the GC electrode measured at various scan rates (5 to 100 mV s^{-1}) measured over a potential window of –0.8 to 0 V. The profiles exhibited ideal rectangular behaviour and showed little distortion when the scan rate was increased from 5 to 100 mV s^{-1}. The storage of charge in the GC electrode is due to the combination of double-layer capacitance and pseudocapacitance from the residual functional groups and heteroatoms present in the material [48]. The GC electrode delivered a specific capacity of 106.69 C g^{-1}, measured at a CV scan rate of 5 mV s^{-1}. The effect of the scan rate on the specific capacity of the GC electrode (Fig. 3.2.9(E)) shows that a capacity retention of 51.50 % is obtained with a 20-fold increase in scan rate. Figure 3.2.9(F) shows the CD profiles of the GC electrode obtained for current densities ranging from 1 to 5 A g^{-1}. The charge-discharge profiles for the GC electrode displayed quasi-triangular curves, suggesting that the charge storage resulted from the combination of electrical double-layer capacitance and pseudocapacitance arising from the heteroatoms present in the GC nanoparticles. This result is in agreement with the findings

of Enacarnocian et al. regarding the supercapacitive properties of alginate-derived GC particles [31]. The electrochemical results revealed the presence of Li-ion intercalation/de-intercalation in the Cu-HCF electrode within the operating window (0.0 to1.4 V) and double-layer capacitance in the GC electrode within the operating window (0.0 to -0.8 V).

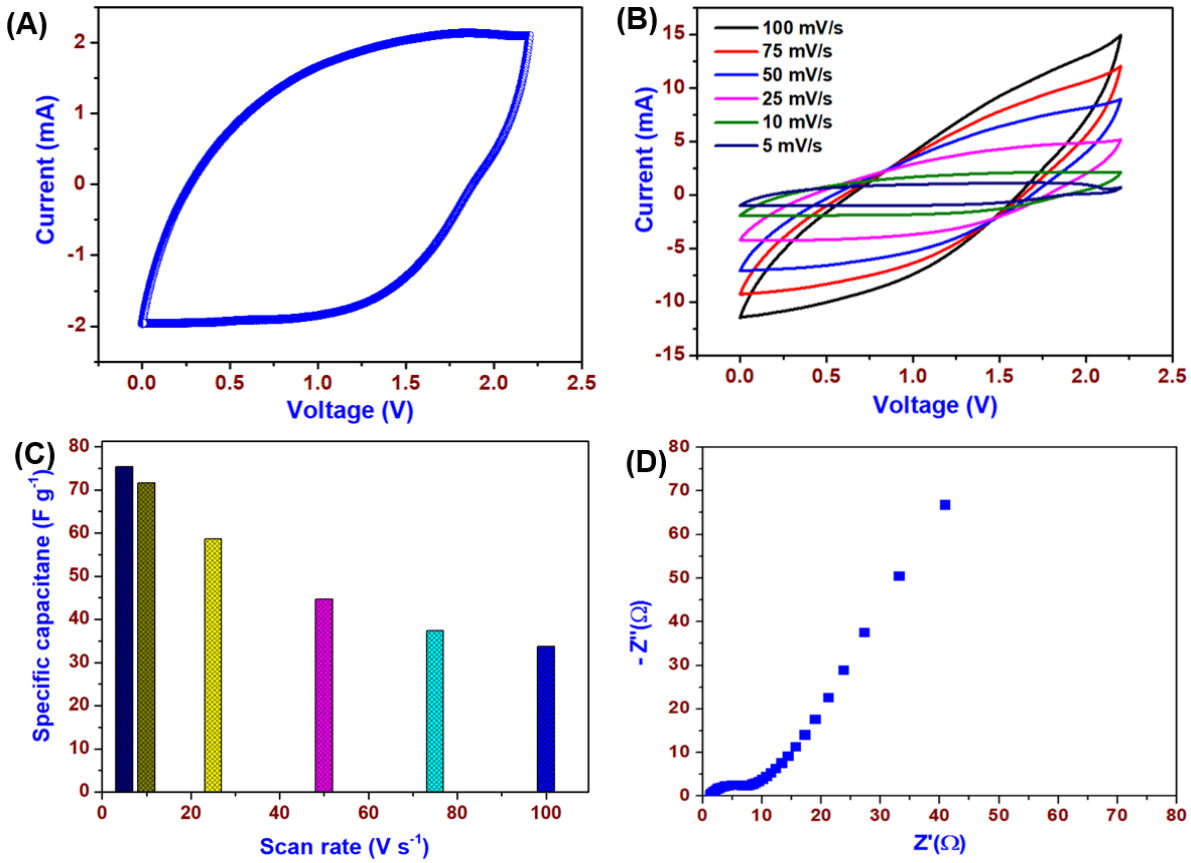

Figure 3.2.12. Electrochemical characterization of the Cu-HCF‖GC Li-ion hybrid capacitor (LHC) device. (A) CV profile measured at a scan rate of 10 mV s^{-1}. (B) CV profiles measured at scan rates ranging from 5 to 100 mV s^{-1}. (C) Effect of the scan rate on the specific capacitance of the device. (D) Electrochemical impedance spectrum (Nyquist plot).

Hence, it is possible to achieve an overall operating potential of 2.2 V for the fabricated LHC device in a neutral electrolyte ($LiNO_3$). The CV profiles of the Cu-HCF‖GC LHC device were measured over a voltage window ranging from 0 to 2.2 V at scan rates ranging from 5 to 100 mV s^{-1}. The CV profile measured at a scan rate of 10 mV s^{-1} (Fig. 3.2.12(A)) displayed

quasi-rectangular curves without any sign of evolution. Figure 3.2.12(B) shows the increasing scan rate (from 5 to 100 mV s^{-1}) of the CV profiles; the current density increased with increasing scan rate. The specific capacitance of the device was obtained from the CV profiles and the effect of the scan rate on the specific capacitance (Fig. 3.2.12(C)). Thee device delivered a specific capacitance of 75.31 F g^{-1} at a scan rate of 5 mV s^{-1}, while a capacitance retention of 44.71 % was obtained with a 20-fold increase in the scan rate. The corresponding Nyquist plot (Fig. 3.2.12(D)) showed a semi-circle in the high-frequency region and a sloped line in the low-frequency region, with a solution resistance (R_s) of 1.16 Ω and charge transfer resistance (R_{ct}) of 8.84 Ω. The Warburg line in the low-frequency region corresponded to the diffusion of electrolyte ions onto the surfaces of the electrodes [49].

A CD analysis of the fabricated Cu-HCF‖GC LHC device was performed at a constant current density ranging from 1 to 5 mA cm^{-2}. The CD profile measured at a current density of 1 mA cm^{-2} (Fig. 3.2.13(A)) showed triangular quasi-symmetric curves, which suggested improved capacitive properties. The CD profiles measured at different current densities are provided in Fig. 3.2.13(B). The symmetry of the CD curve was retained even at a high current density, indicating good capacitive performance. The Cu-HCF‖GC LHC device delivered a specific capacitance of 63.64 F g^{-1} at a constant discharge current density of 1 mA cm^{-2}. The obtained specific capacitance was higher than the capacitances reported for asymmetric/hybrid capacitors such as $Na_3V_2(PO_4)_3$‖carbon (37.33 F g^{-1}), MnHCF‖Fe_3O_4/rGO (51.8 F g^{-1}), $NiCo_2O_4$‖AC (18.8 F g^{-1}), $Cu_{1.79}Co_{0.21}$CH/NF‖graphene/NF (61 F g^{-1}), and $LiMn_2O_4$‖AC (30 F g^{-1})[50–54]. The change in specific capacitance of the fabricated Cu-HCF‖GC LHC with an increase in current density is shown in Fig. 3.2.13(C). A capacitance retention rate of 58.72 % was obtained with a five-fold increase in the current density. The obtained results suggested a good rate capability

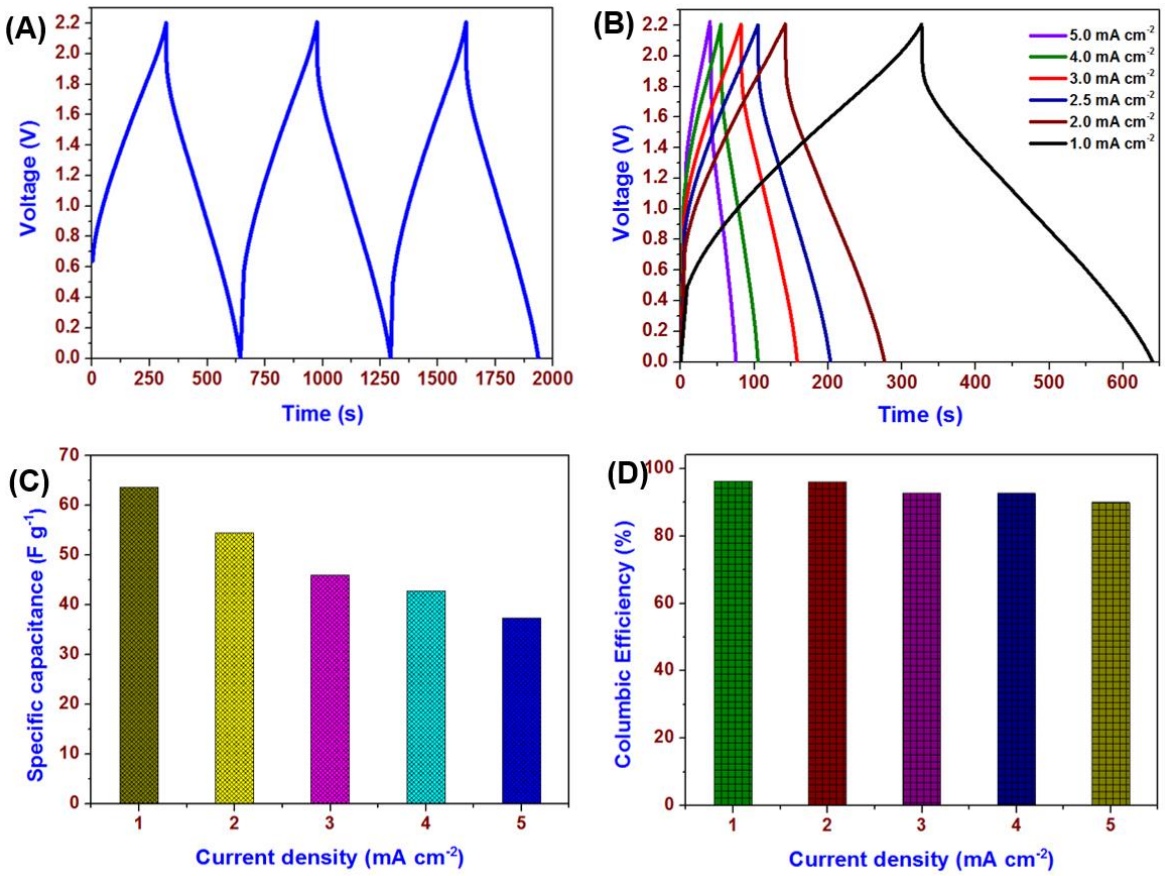

Figure 3.2.13. Electrochemical characterization of the Cu-HCF‖GC LHC device. (A) CD profile measured at a constant current density of 1 mA cm^{-2}. (B) CD profiles measured at constant current densities ranging from 1 to 5 mA $cm^{-2.}$ (C) Effect of the current density on the specific capacitance. (D) Coulombic efficiency (%) as a function of the current density.

for the fabricated Cu-HCF‖GC LHC device. The most important parameters determining the practical applications of the fabricated Cu-HCF‖GC LHC device are the coulombic efficiency, energy density (E), power density (P) and cyclic stability [55]. The coulombic efficiency ($\eta\%$) is the ratio of the time required for discharging (T_d) to that required for charging (T_c) i.e., $\eta\% = [(T_d/T_c) * 100]$; a plot of columbic efficiency versus current density for the Cu-HCF‖GC LHC is provided in Fig. 3.2.13(D). A coulombic efficiency of 96.33 % was obtained at a current density of 1 mA cm^{-2}, indicating good capacitive properties. Figure

3.2.13(D) shows that the coulombic efficiency exceeded 90 % for all of the CD profiles measured at the different current densities. The Ragone plot of the fabricated Cu-HCF‖GC LHC device (Fig. 3.2.14(A)) indicated an energy density of 42.78 Wh kg^{-1}, with a power density of 523.89 W kg^{-1} obtained at a constant current of 1 mA cm^{-2}. With a five-fold increase in current density, the obtained energy density of 26.91 Wh kg^{-1} with a corresponding power density of 2,619 W kg^{-1} indicated an improved rate capability. The energy density is higher than that of other reported hybrid and asymmetric capacitors (Table 3.2.1), such as the LMO‖graphene LHC (39 Wh kg^{-1})[33],

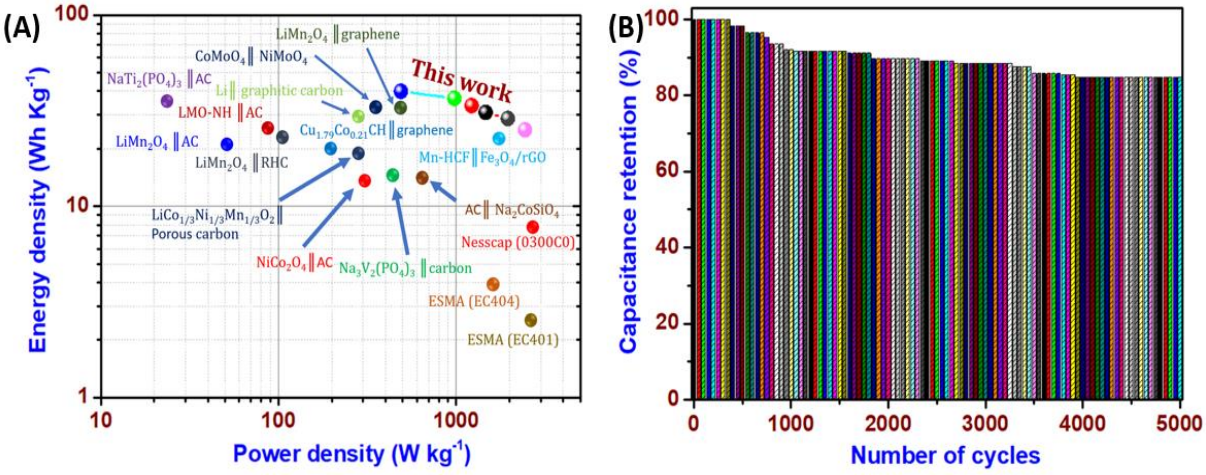

Figure 3.2.14. (A) Ragone plot of the Cu-HCF‖GC LHC device and (B) its cyclic stability over 5000 charge-discharge cycles.

MnHCF‖Fe_3O_4/rGO (27.9 Wh kg^{-1}) [51], $Cu_{1.79}Co_{0.21}$CH/NF‖graphene/NF (21.5 Wh kg^{-1}) [53], $LiMn_2O_4$‖AC (23.4 Wh kg^{-1}) [54], LMO-NH‖AC hybrid capacitor (29.8 Wh kg^{-1}) [56], $LiMn_2O_4$‖RHC (29.5 Wh kg^{-1}) [57], $NaTi_2(PO_4)_3$‖activated carbon (31.6 Wh kg^{-1}) [58], CoHCFe‖mRGO (34.4 Wh kg^{-1}) [59], and $NiMoO_4$||$FeMoO_4$ (29 Wh kg^{-1}) [60].

Table 3.2.1. Comparison on energy density of Cu-HCF‖graphitic carbon LHC with recently reported aqueous asymmetric capacitors, Li-ion capacitors, and Na-ion capacitors

S. No	Device	Energy density (Wh/kg)	Power density (Wh/kg)	Ref
1	LMO-NH‖AC hybrid capacitor	29.8	90	[56]
2	$LiMn_2O_4$‖RHC	29.5	100	[57]
3	$Na_3V_2(PO_4)_3$‖Carbon	15.9	490	[50]
4	MnHCF‖Fe_3O_4/rGO	27.9	2183	[51]
5	$NiCo_2O_4$‖AC	13.8	308	[52]
6	$CoMoO_4$‖$NiMoO_4$	33	375	[61]
7	$Cu_{1.79}Co_{0.21}$CH/NF‖graphene/NF	21.5	200	[53]
8	AC‖Na_2CoSiO_4	12.4	782.7	[62]
9	$LiMn_2O_4$ and activated carbon	23.4	50	[54]
10	$LiMn_2O_4$ and graphene	39	440	[33]
11	CoHCFe‖mRGO	34.4	2500	[59]
12	Graphitic carbon sphere‖Li	36	300	[15]
13	$LiCo_{1/3}Ni_{1/3}Mn_{1/3}O_2$‖ Porous carbon	20	264	[16]
14	$NaTi_2(PO_4)_3$‖activated carbon	31.6	23	[58]
15	Cu-HCF‖ graphitic carbon	42.78	523.89	This work

The obtained energy density of the device is also higher than that of commercial supercapacitors such as the NESCAP-0300C0 (8.7 Wh kg^{-1}), ESMA-401(2.8 Wh kg^{-1}) and ESMA-404 (4.2 Wh kg^{-1}). The cyclic stability of the fabricated Cu-HCF‖GC LHC device was assessed over 5,000 charge-discharge cycles at a constant current density of 5.0 mA cm^{-2} (Fig. 3.2.14(B)), and a retention rate of approximately 84.8 % of its initial capacitance suggested the superior stability of the device.

3.2.4 Conclusions

We successfully prepared Cu-HCF via a sonication process and GC nanostructures via a carbonization process and utilized them for the fabrication of hybrid ion capacitors. Physicochemical characterization, namely, X-ray diffraction, FT-IR, and HR-TEM analysis, confirmed the formation of Cu-HCF and GC nanostructures. Electrochemical characterization revealed that charge storage in the Cu-HCF occurs via intercalation/deintercalation of electrolyte ions, whereas in the GC electrode, charge storage proceeds via the adsorption/desorption of ions at the electrode/electrolyte interface. The Cu-HCF‖GC aqueous LHC device operated over an operating potential window of 2.2 V and delivered a high specific capacitance of 63.64 F g^{-1}. The Cu-HCF‖GC LHC device demonstrated a high energy density (42.78 Wh kg^{-1}) and a better cycle life, retaining approximately 84.8 % of its initial capacitance. Our findings suggest that the Cu-HCF‖GC LHC device has great potential as a high-performance energy storage device.

3.2.5 References:

[1] Y.-Z. Zhang, Y. Wang, T. Cheng, W.-Y. Lai, H. Pang, W. Huang, Flexible supercapacitors based on paper substrates: a new paradigm for low-cost energy storage, Chem. Soc. Rev. 44 (2015) 5181–5199. doi:10.1039/C5CS00174A.

[2] T. Cheng, Y.-Z. Zhang, J.-D. Zhang, W.-Y. Lai, W. Huang, High-performance free-standing PEDOT:PSS electrodes for flexible and transparent all-solid-state supercapacitors, J. Mater. Chem. A. 4 (2016) 10493–10499. doi:10.1039/C6TA03537J.

[3] X.-C. Li, Y. Zhang, C.-Y. Wang, Y. Wan, W.-Y. Lai, H. Pang, W. Huang, Redox-active triazatruxene-based conjugated microporous polymers for high-performance supercapacitors, Chem. Sci. 8 (2017) 2959–2965. doi:10.1039/C6SC05532J.

[4] R. Subbiah, M. Veerapandian, K. S. Yun, Nanoparticles: Functionalization and Multifunctional Applications in Biomedical Sciences, Curr. Med. Chem. 17 (2010) 4559–4577. doi:10.2174/092986710794183024.

[5] S. Vijayan, B. Kirubasankar, P. Pazhamalai, A.K. Solarajan, S. Angaiah, Electrospun Nd^{3+}-Doped $LiMn_2O_4$ Nanofibers as High-Performance Cathode Material for Li-Ion Capacitors, ChemElectroChem. 4 (2017) 2059–2067. doi:10.1002/celc.201700161.

[6] H. Pang, Y. Zhang, T. Cheng, W.-Y. Lai, W. Huang, Uniform manganese hexacyanoferrate hydrate nanocubes featuring superior performance for low-cost supercapacitors and nonenzymatic electrochemical sensors, Nanoscale. 7 (2015) 16012–16019. doi:10.1039/C5NR04322K.

[7] H. Pang, X. Li, Q. Zhao, H. Xue, W.-Y. Lai, Z. Hu, W. Huang, One-pot synthesis of heterogeneous Co_3O_4 -nanocube/$Co(OH)_2$ -nanosheet hybrids for high-performance flexible asymmetric all-solid-state supercapacitors, Nano Energy. 35 (2017) 138–145. doi:10.1016/j.nanoen.2017.02.044.

[8] K. Lu, B. Song, X. Gao, H. Dai, J. Zhang, H. Ma, High-energy cobalt hexacyanoferrate and carbon micro-spheres aqueous sodium-ion capacitors, J. Power Sources. 303 (2016) 347–353. doi:10.1016/j.jpowsour.2015.11.031.

[9] X. Wang, Y. Xiao, D. Su, S. Xu, L. Zhou, S. Wu, L. Han, S. Fang, S. Cao, Hierarchical porous cobalt monoxide nanosheet@ultrathin manganese dioxide nanosheet core-shell arrays for high-performance asymmetric supercapacitor, Int. J. Hydrogen Energy. 41 (2016) 13540–13548. doi:10.1016/j.ijhydene.2016.06.133.

[10] J. Ding, H. Wang, Z. Li, K. Cui, D. Karpuzov, X. Tan, A. Kohandehghan, D. Mitlin, Peanut shell hybrid sodium ion capacitor with extreme energy–power rivals lithium ion capacitors, Energy Environ. Sci. 8 (2015) 941–955. doi:10.1039/C4EE02986K.

[11] Y.-Z. Zhang, T. Cheng, Y. Wang, W.-Y. Lai, H. Pang, W. Huang, A Simple Approach to Boost Capacitance: Flexible Supercapacitors Based on Manganese Oxides@MOFs via Chemically Induced In Situ Self-Transformation, Adv. Mater. 28 (2016) 5242–5248. doi:10.1002/adma.201600319.

[12] Y. Yang, Y. Hao, J. Yuan, L. Niu, F. Xia, In situ co-deposition of nickel hexacyanoferrate nanocubes on the reduced graphene oxides for supercapacitors, Carbon N. Y. 84 (2015) 174–184. doi:10.1016/j.carbon.2014.12.005.

[13] Q. Zhao, M. Zhao, J. Qiu, H. Pang, W.-Y. Lai, W. Huang, Facile synthesis of $Mn_3[Co(CN)_6]2{\cdot}nH_2O$ nanocrystals for high-performance electrochemical energy storage devices, Inorg. Chem. Front. 4 (2017) 442–449. doi:10.1039/C6QI00595K.

[14] H. Song, J. Fu, K. Ding, C. Huang, K. Wu, X. Zhang, B. Gao, K. Huo, X. Peng, P.K. Chu, Flexible Nb_2O_5 nanowires/graphene film electrode for high-performance hybrid Li-ion supercapacitors, J. Power Sources. 328 (2016) 599–606. doi:10.1016/j.jpowsour.2016.08.052.

[15] S. Jayaraman, S. Madhavi, V. Aravindan, High energy Li-ion capacitor and battery

using graphitic carbon spheres as an insertion host from cooking oil, J. Mater. Chem. A. 6 (2018) 3242–3248. doi:10.1039/C7TA09905C.

[16] B. Ramkumar, S. Yuvaraj, S. Surendran, K. Pandi, H.V. Ramasamy, Y.S. Lee, R. Kalai Selvan, Synthesis and characterization of carbon coated $LiCo_{1/3}Ni_{1/3}Mn_{1/3}O_2$ and bio-mass derived graphene like porous carbon electrodes for aqueous Li-ion hybrid supercapacitor, J. Phys. Chem. Solids. 112 (2018) 270–279. doi:10.1016/j.jpcs.2017.09.012.

[17] S. Jayaraman, A. Jain, M. Ulaganathan, E. Edison, M.P. Srinivasan, R. Balasubramanian, V. Aravindan, S. Madhavi, Li-ion vs. Na-ion capacitors: A performance evaluation with coconut shell derived mesoporous carbon and natural plant based hard carbon, Chem. Eng. J. 316 (2017) 506–513. doi:10.1016/j.cej.2017.01.108.

[18] M.K. Devaraju, Q.D. Truong, I. Honma, One pot synthesis of in situ Au decorated LiNiPO4 nanoplates for Li-ion batteries, Appl. Mater. Today. 1 (2015) 95–99. doi:10.1016/j.apmt.2015.11.003.

[19] A.J. Fernández-Ropero, D. Saurel, B. Acebedo, T. Rojo, M. Casas-Cabanas, Electrochemical characterization of $NaFePO_4$ as positive electrode in aqueous sodium-ion batteries, J. Power Sources. 291 (2015) 40–45. doi:10.1016/j.jpowsour.2015.05.006.

[20] H. Kim, K.-Y. Park, M.-Y. Cho, M.-H. Kim, J. Hong, S.-K. Jung, K.C. Roh, K. Kang, High-Performance Hybrid Supercapacitor Based on Graphene-Wrapped $Li_4Ti_5O_{12}$ and Activated Carbon, ChemElectroChem. 1 (2014) 125–130. doi:10.1002/celc.201300186.

[21] H.T. Tan, W. Sun, L. Wang, Q. Yan, 2D Transition Metal Oxides/Hydroxides for Energy-Storage Applications, ChemNanoMat. 2 (2016) 562–577.

doi:10.1002/cnma.201500177.

[22] M. Pumera, Z. Sofer, A. Ambrosi, Layered transition metal dichalcogenides for electrochemical energy generation and storage, J. Mater. Chem. A. 2 (2014) 8981–8987. doi:10.1039/C4TA00652F.

[23] J. Wang, P. Nie, B. Ding, S. Dong, X. Hao, H. Dou, X. Zhang, Biomass derived carbon for energy storage devices, J. Mater. Chem. A. 5 (2017) 2411–2428. doi:10.1039/C6TA08742F.

[24] L.L. Zhang, X.S. Zhao, Carbon-based materials as supercapacitor electrodes, Chem. Soc. Rev. 38 (2009) 2520. doi:10.1039/b813846j.

[25] C.D. Wessells, S. V. Peddada, M.T. McDowell, R.A. Huggins, Y. Cui, The Effect of Insertion Species on Nanostructured Open Framework Hexacyanoferrate Battery Electrodes, J. Electrochem. Soc. 159 (2012) A98. doi:10.1149/2.060202jes.

[26] C.D. Wessells, R.A. Huggins, Y. Cui, Copper hexacyanoferrate battery electrodes with long cycle life and high power, Nat. Commun. 2 (2011) 550. doi:10.1038/ncomms1563.

[27] X.Y. Wu, M.Y. Sun, Y.F. Shen, J.F. Qian, Y.L. Cao, X.P. Ai, H.X. Yang, Energetic aqueous rechargeable sodium-ion battery based on $Na_2CuFe(CN)_6$-$NaTi_2(PO_4)_3$ intercalation chemistry, ChemSusChem. 7 (2014) 407–411. doi:10.1002/cssc.201301036.

[28] P. Jiang, H. Shao, L. Chen, J. Feng, Z. Liu, Ion-selective copper hexacyanoferrate with an open-framework structure enables high-voltage aqueous mixed-ion batteries, J. Mater. Chem. A. 5 (2017) 16740–16747. doi:10.1039/C7TA04172A.

[29] W. Li, F. Zhang, X. Xiang, X. Zhang, Nickel-Substituted Copper Hexacyanoferrate as a Superior Cathode for Aqueous Sodium-Ion Batteries, ChemElectroChem. 5 (2018) 350–354. doi:10.1002/celc.201700958.

[30] A. Paolella, C. Faure, V. Timoshevskii, S. Marras, G. Bertoni, A. Guerfi, A. Vijh, M. Armand, K. Zaghib, A review on hexacyanoferrate-based materials for energy storage and smart windows: challenges and perspectives, J. Mater. Chem. A. 5 (2017) 18919–18932. doi:10.1039/C7TA05121B.

[31] E. Raymundo-Pi?ero, F. Leroux, F. B?guin, A High-Performance Carbon for Supercapacitors Obtained by Carbonization of a Seaweed Biopolymer, Adv. Mater. 18 (2006) 1877–1882. doi:10.1002/adma.200501905.

[32] W. Cui, N. Cheng, Q. Liu, C. Ge, A.M. Asiri, X. Sun, Mo_2C Nanoparticles Decorated Graphitic Carbon Sheets: Biopolymer-Derived Solid-State Synthesis and Application as an Efficient Electrocatalyst for Hydrogen Generation, ACS Catal. 4 (2014) 2658–2661. doi:10.1021/cs5005294.

[33] P. Pazhamalai, K. Krishnamoorthy, M.S.P. Sudhakaran, S.J. Kim, Fabrication of High-Performance Aqueous Li-Ion Hybrid Capacitor with $LiMn_2O_4$ and Graphene, ChemElectroChem. 4 (2017) 396–403. doi:10.1002/celc.201600550.

[34] S. Dsoke, B. Fuchs, E. Gucciardi, M. Wohlfahrt-Mehrens, The importance of the electrode mass ratio in a Li-ion capacitor based on activated carbon and $Li_4Ti_5O_{12}$, J. Power Sources. 282 (2015) 385–393. doi:10.1016/j.jpowsour.2015.02.079.

[35] N. Karikalan, M. Velmurugan, S.M. Chen, K. Chelladurai, A copper hexacyanocobaltate nanocubes based dopamine sensor in the presence of ascorbic acid, RSC Adv. 6 (2016) 48523–48529. doi:10.1039/C6RA05810H.

[36] J.T.R. Dunsmuir, A.P. Lane, The infrared spectra (40–3000 cm^{-1}) of potassium hexacyanoferrate and potassium hexacyanocobaltate, J. Chem. Soc. A. (1971) 776–780. doi:10.1039/J19710000776.

[37] Z. Jia, J. Wang, Y. Wang, H.H. Xu, Z. Li, Y. Shen, L.X. Yuan, X.L. Hu, X. Dai, Y.H. Huang, L.Q. Chen, Electrochemical sodium storage of copper hexacyanoferrate with a

well-defined open framework for sodium ion batteries, RSC Adv. 4 (2014) 22768. doi:10.1039/c4ra02559h.

[38] K. Krishnamoorthy, P. Pazhamalai, S. Sahoo, J.H. Lim, K.H. Choi, S.J. Kim, A High-Energy Aqueous Sodium-Ion Capacitor with Nickel Hexacyanoferrate and Graphene Electrodes, ChemElectroChem. 4 (2017) 3302–3308. doi:10.1002/celc.201700690.

[39] P. Atienzar, A. Primo, C. Lavorato, R. Molinari, H. García, Preparation of graphene quantum dots from pyrolyzed alginate, Langmuir. 29 (2013) 6141–6146. doi:10.1021/la400618s.

[40] K. Govindaraju, K. Krishnamoorthy, S.A. Alsagaby, G. Singaravelu, M. Premanathan, K. Govindaraju, M. Premanathan, K. Krishnamoorthy, S.A. Alsagaby, G. Singaravelu, M. Premanathan, Green synthesis of silver nanoparticles for selective toxicity towards cancer cells, IET Nanobiotechnology. 9 (2015) 325–330. doi:10.1049/iet-nbt.2015.0001.

[41] M. Veerapandian, M.-H. Lee, K. Krishnamoorthy, K. Yun, Synthesis, characterization and electrochemical properties of functionalized graphene oxide, Carbon N. Y. 50 (2012) 4228–4238. doi:10.1016/j.carbon.2012.05.004.

[42] C. Lavorato, A. Primo, R. Molinari, H. García, Natural alginate as a graphene precursor and template in the synthesis of nanoparticulate ceria/graphene water oxidation photocatalysts, ACS Catal. 4 (2014) 497–504. doi:10.1021/cs401068m.

[43] S. Thangavel, G. Venugopal, Understanding the adsorption property of graphene-oxide with different degrees of oxidation levels, Powder Technol. 257 (2014) 141–148. doi:10.1016/j.powtec.2014.02.046.

[44] F. Wu, A. Magasinski, G. Yushin, Nanoporous Li2S and MWCNT-linked Li_2S powder cathodes for lithium-sulfur and lithium-ion battery chemistries, J. Mater. Chem. A. 2 (2014) 6064–6070. doi:10.1039/c3ta14161f.

[45] H. Liu, H. Zhang, H. Xu, T. Lou, Z. Sui, Y. Zhang, Influence of the Concentration of Electrolyte on the Capacitive Properties of Vanadium Nitride Electrode for Electrochemical Capacitors, J. Electrochem. Soc. 165 (2018) A97–A103. doi:10.1149/2.0461802jes.

[46] S.T. Senthilkumar, Y. Wang, H. Huang, Advances and prospects of fiber supercapacitors, J. Mater. Chem. A. 3 (2015) 20863–20879. doi:10.1039/C5TA04731E.

[47] M. Sathiya, A.S. Prakash, K. Ramesha, J. Tarascon, A.K. Shukla, V_2O_5 -Anchored Carbon Nanotubes for Enhanced Electrochemical Energy Storage, J. Am. Chem. Soc. 133 (2011) 16291–16299. doi:10.1021/ja207285b.

[48] R. Ramachandran, M. Saranya, V. Velmurugan, B.P.C. Raghupathy, S.K. Jeong, A.N. Grace, Effect of reducing agent on graphene synthesis and its influence on charge storage towards supercapacitor applications, Appl. Energy. 153 (2015) 22–31. doi:10.1016/j.apenergy.2015.02.091.

[49] X. Liu, J.-Z. Zhang, K.-J. Huang, P. Hao, Net-like molybdenum selenide–acetylene black supported on Ni foam for high-performance supercapacitor electrodes and hydrogen evolution reaction, Chem. Eng. J. 302 (2016) 437–445. doi:10.1016/j.cej.2016.05.074.

[50] S. Wang, J. Zhao, L. Wang, X. Liu, Y. Wu, J. Xu, High performance $Na_3V_2(PO_4)_3$/C composite electrode for sodium-ion capacitors, Ionics (Kiel). 21 (2015) 2633–2638. doi:10.1007/s11581-015-1428-9.

[51] K. Lu, D. Li, X. Gao, H. Dai, N. Wang, H. Ma, An advanced aqueous sodium-ion supercapacitor with a manganous hexacyanoferrate cathode and a Fe_3O_4/rGO anode, J. Mater. Chem. A. 3 (2015) 16013–16019. doi:10.1039/C5TA04244E.

[52] R. Ding, L. Qi, H. Wang, An investigation of spinel $NiCo_2O_4$ as anode for Na-ion

capacitors, Electrochim. Acta. 114 (2013) 726–735. doi:10.1016/j.electacta.2013.10.113.

[53] S. Liu, K.N.K.S. Hui, K.N.K.S. Hui, V. V. Jadhav, Q.X. Xia, J.M. Yun, Y.R. Cho, R.S. Mane, K.H. Kim, Facile Synthesis of Microsphere Copper Cobalt Carbonate Hydroxides Electrode for Asymmetric Supercapacitor, Electrochim. Acta. 188 (2016) 898–908. doi:10.1016/j.electacta.2015.12.018.

[54] H. Liu, L. Liao, Y.-C. Lu, Q. Li, High Energy Density Aqueous Li-Ion Flow Capacitor, Adv. Energy Mater. 7 (2017) 1601248. doi:10.1002/aenm.201601248.

[55] G.K. Veerasubramani, K. Krishnamoorthy, S.J. Kim, Electrochemical performance of an asymmetric supercapacitor based on graphene and cobalt molybdate electrodes, RSC Adv. 5 (2015) 16319–16327. doi:10.1039/C4RA15070H.

[56] F.X. Wang, S.Y. Xiao, Y.S. Zhu, Z. Chang, C.L. Hu, Y.P. Wu, R. Holze, Spinel $LiMn_2O_4$ nanohybrid as high capacitance positive electrode material for supercapacitors, J. Power Sources. 246 (2014) 19–23. doi:10.1016/j.jpowsour.2013.07.046.

[57] C. Rong, S. Chen, J. Han, K. Zhang, D. Wang, X. Mi, X. Wei, Hybrid supercapacitors integrated rice husk based activated carbon with $LiMn_2O_4$, J. Renew. Sustain. Energy. 7 (2015) 023104. doi:10.1063/1.4913965.

[58] S. Zhang, Y. Liu, Q. Han, S. He, N. Zhang, J. Yang, Development and characterization of aqueous sodium-ion hybrid supercapacitor based on $NaTi_2(PO_4)_3$//activated carbon, J. Alloys Compd. 729 (2017) 850–857. doi:10.1016/j.jallcom.2017.08.256.

[59] F. Zhao, Y. Wang, X. Xu, Y. Liu, R. Song, G. Lu, Y. Li, Cobalt Hexacyanoferrate Nanoparticles as a High-Rate and Ultra-Stable Supercapacitor Electrode Material, ACS Appl. Mater. Interfaces. 6 (2014) 11007–11012. doi:10.1021/am503375h.

[60] B. Senthilkumar, R. Kalai Selvan, Hydrothermal synthesis and electrochemical

performances of 1.7 V $NiMoO_4.xH_2O||FeMoO_4$ aqueous hybrid supercapacitor, J. Colloid Interface Sci. 426 (2014) 280–286. doi:10.1016/j.jcis.2014.04.010.

[61] Z. Yin, Y. Chen, Y. Zhao, C. Li, C. Zhu, X. Zhang, Hierarchical nanosheet-based $CoMoO_4$–$NiMoO_4$ nanotubes for applications in asymmetric supercapacitors and the oxygen evolution reaction, J. Mater. Chem. A. 3 (2015) 22750–22758. doi:10.1039/C5TA05678K.

[62] S. Gao, J. Zhao, Y. Zhao, Y. Wu, X. Zhang, L. Wang, X. Liu, Y. Rui, J. Xu, Na_2CoSiO_4 as a novel positive electrode material for sodium-ion capacitors, Mater. Lett. 158 (2015) 300–303. doi:10.1016/j.matlet.2015.06.038.

CHAPTER 3.3 Fabrication of high energy Li-ion hybrid capacitor using manganese hexacyanoferrate nanocubes and graphene electrodes

Highlights

- Manganese hexacyanoferrate (Mn-HCF) prepared via facile sonochemical method.
- X-ray diffraction, HR-TEM, and XPS analyses revealed the formation of Mn-HCF cubes.
- The Mn-HCF electrode shows ion-intercalation pseudocapacitance with a specific capacity of 81.59 mAh g^{-1}.
- Aqueous Li-ion hybrid capacitor was assembled using Mn-HCF and graphene.
- A high energy density of 44.18 Wh kg^{-1} was obtained for the fabricated LHC device.

3.3.1. Introduction

The exponential increase in the use of fossil fuels and renewable energy leads to the energy crisis and adulterated situation in day to day life [1,2]. The consumption of energy from the industries has been increased, and the release of organic pollutants from the industries have a direct detrimental effect on the depletion of fuels and to the environment [3]. To overcome the energy crisis and the environmental effect, the researchers are focusing towards the development of sustainable and environmentally friendly energy devices [4,5]. Energy storage devices are classified as the batteries and supercapacitors in which the former possess high energy density whereas the later has high power density[6]. Out of energy storage devices, supercapacitors have been considered because of its high power density and long cycle life[7]. The supercapacitors have been classified into double layer capacitor which stores energy via electrostatic separation of charges whereas the pseudocapacitors stores charges via faradaic redox reaction[8,9]. The double layer capacitors use carbon-based materials such as graphene, graphdyine, CNT as electrode materials whereas the pseudocapacitors use metal oxides and dichalcogenides such as RuO_2, RuS_2, VS_2, TiS_2 as the electrode materials[10–16]. Even though the supercapacitors have high power density, its use for practical applications is limited due to its poor energy density[17]. To improve the energy density of the supercapacitors, the working potential window should be increased, since energy density is 0.5 CV^2 (where 'C' is the specific capacitance, and 'V' is the operating voltage window) which implies that working potential is directly proportional to the energy density of the supercapacitor device[18–20]. For this concept to increase the potential window, the researchers used the organic electrolyte instead of aqueous electrolyte, and then towards asymmetric and hybrid capacitors, but the practical use of the device is limited since the organic electrolyte is hazardous and expensive compared to the aqueous electrolyte[21,22]. Several other research groups have investigated to enhance the

electrochemical properties of energy storage device with tailoring the working potential of the device, low-cost electrode material, works at wide temperature conditions and thus to enhance the energy density of the energy storage device, the researchers have developed the ion hybrid capacitors[23]. The ion hybrid capacitors have the combined properties of both batteries and supercapacitor since it uses one battery type electrode and one capacitive type electrode. The enhanced performance of the ion hybrid capacitor is due to the combination of intercalation/deintercalation occurred at the battery type electrode and the electrostatic absorption/desorption occurred at the capacitive type electrode which increases the energy density of the device [24].

Recently, Li-ion hybrid capacitors (LHC) using lithium-based intercalating materials such as $LiMn_2O_4$, $LiCoO_2$ and carbon-based capacitive materials such as activated carbon has been reported using both aqueous and non-aqueous electrolyte[25–27]. The low ionic radii (0.60 Å) and higher ionic conductivity (38.69 S cm^2 mol^{-1}) of Li^+ ions in aqueous solutions provides reversible ion intercalation/de-intercalation process at the interior of the electroactive surfaces with better ion diffusion kinetics compared with other aqueous electrolytes based on Na^+, and K^+ ions, respectively[28,29]. Recently, Shobana et al. reported the use of the rare earth element doped $LiMn_2O_4$ and pearl carbon as the electrode for the Li-ion capacitor with the energy density of 17 Wh kg^{-1} using aqueous electrolyte [30]. A Chaturvedi et al. studied the lithium insertion in the 2D metal chalcogenides as the electrode for the Li-ion capacitor[13]. Further, the researchers are exploring the other possible intercalative materials which can be used as the electrode for the Li-ion capacitors[31]. The selection of an electrode material plays a major role in the performance of an ion capacitor, and hence the appropriate materials with the intercalative properties must be chosen as the intercalation electrode with the enhanced surface area and large internal pore volume [32,33]. Later on, Wessells and co-researchers have reported the use of the nanostructured metal

hexacyanoferrate material as their potential use in the Li-ion and Na-ion batteries which paves the gateway of new series of intercalation material[32,34]. The metal hexacyanoferrate is a Prussian blue analog which possesses an open framework with a large interstitial space that can facilitate the ion intercalation/deintercalation of a variety of ions, such as Li+ and Na+ in the cyano-bridged network[29,32]. Several metal hexacyanoferrates have been investigated for the Li and Na ion batteries using organic electrolytes, and there are very limited reports for the use of metal hexacyanoferrate for the ion capacitors using aqueous neutral electrolytes [35,36]. The usage of aqueous electrolyte for the ion capacitors is more prominent, safe and eco-friendly compared to organic electrolytes due to the high ionic conductivity of aqueous electrolytes with the advantage of being low cost and environmentally benign nature[24]. In this work, we focused on fabricating the Li-ion hybrid capacitor using sonochemically prepared Mn-HCF as the intercalative-type positive electrode and hydrothermally reduced graphene nanosheets as the capacitive-type negative electrode with neutral $LiNO_3$ as the electrolyte. The fabricated Mn-HCF‖graphene LHC works over the wide potential window of 0.0 – 2.0 V with an exceptionally high energy density which paves the pathway for the growth of next-generation storage devices.

3.3.2. Experimental section

3.3.2.1 Preparation of Mn-HCF nanocubes

A facile sonochemical assisted method has been adopted for the preparation of Mn-HCF[37]. Briefly, an aqueous solution of 1 M manganese nitrate and 0.5 M potassium ferricyanide were prepared separately before the start of the experiment. A beaker containing DI water was kept under constant ultrasonication, and then the prepared manganese nitrate and potassium ferricyanide solutions were gradually added simultaneously to the DI water which kept under ultrasound irradiation. After complete addition of the precursor solution, the ultrasonication was preceded for 3 h. On completion of the sonication process, the

obtained precipitate was washed with DI and ethanol several times using centrifugation process. The washed precipitate was dried in hot air oven at 80 ºC overnight to obtain Mn-HCF nanocubes. The obtained Mn-HCF is used for further characterizations.

3.3.2.2 Preparation of graphene oxide and graphene nanosheets

Initially, graphene oxide (GO) sheets were prepared according to the modified Hummers method as reported in our earlier study[38]. The hydrothermal reduction of GO was employed for the preparation of graphene nanosheets[38]. Briefly, 0.05 g of as-synthesized GO nanosheets was dispersed in 50 mL of deionized water and was irradiated by ultrasound for 30 min to achieve uniform dispersion of GO. Then the solution pH was adjusted to reach 10 by the addition of NaOH followed by the addition of 2 mL of hydrazine hydrate. Then the final solution is transferred into 100 mL Teflon-lined stainless-steel autoclave, and the hydrothermal reaction was carried out at 90 °C for 24 h. Upon completion of the reaction, the hydrothermal is made to cool naturally, and then the obtained graphene nanosheets were washed several times using ethanol and doubly distilled water to remove the trace amount of impurities. The obtained graphene nanosheets were dried in hot air oven overnight and used for the further characterizations.

3.3.2.3 Fabrication of electrodes and electrochemical analysis

The working electrodes for the electrochemical characterization were prepared using slurry coating method as reported in our previous report[39]. Briefly, the electroactive material, carbon black and polyvinylidene difluoride were mixed using N-methyl pyrrolidone with the weight ratios of 80:15:5 and grounded well to form a slurry. The obtained slurry was coated on to the precleaned stainless steel collector (area of 1×1 cm^2) and dried at 70 ºC for 12 h. A 1 M $LiNO_3$ was used as an electrolyte throughout the electrochemical characterization. The use of $LiNO_3$ as an electrolyte for the electrochemical characterization in this work is because of the fact that among the various aqueous electrolytes, neutral

electrolytes can operate over a wide potential window (above 1.3 V), whereas acidic and basic electrolytes cannot operate over 1.3 V[28]. Similarly, the ionic conductivity of Li^{+} and NO^{3-} ions are about 38.69 and 71.42 S cm^2 mol^{-1} which is higher than that of other aqueous neutral electrolytes such as Li_2SO_4, Na_2SO_4 and etc.[28]. The electrochemical characterization was performed in both three-electrode and two-electrode configuration. In three-electrode configuration, Mn-HCF or graphene is used as the working electrode, silver/silver chloride and platinum as reference and counter electrode, respectively. Furthermore, the LHC was fabricated using Mn-HCF and graphene electrode by sandwiching the electrode with Celgard immersed in the electrolyte as the separator. The electrochemical characterization of the working electrodes and the fabricated LHC were examined via cyclic voltammetry (CV), galvanotactic charge-discharge analyses and Electrochemical impedance spectroscopy (EIS) using an Autolab PGSTAT302N electrochemical workstation.

3.3.3 Results and discussion

3.3.3.1 Physicochemical characterization

In this work, we employed a simple and rapid sonochemical route for the preparation of Mn-HCF and hydrothermal route for graphene electrodes. Fig 3.3.1 (A) represents the X-ray diffraction pattern of the prepared Mn-HCF and graphene. In Fig.3.3.1 (A), the X-ray diffraction peaks obtained at 14.76°, 16.81°, 24.06°, 29.62°, 34.23°, 38.40°, 42.3° 49.2°, 52.4°, 55.53°, 58.6°, 63.8°, and 66.77° corresponds to (111), (202), (220), (222), (400), (420), (422), (440), (600), (620), (622), (640), and (642) planes which confirms the formation of face-centered cubic Prussian blue structure of the Mn-HCF[40]. The broad diffraction peaks of the Mn-HCF indicates the formation of crystalline and small-sized nanoparticles of Mn-HCF cubes. Figure 3.3.1 (B) shows the HR-TEM micrograph of the Mn-HCF with the average lateral dimension of 400-600 nm.

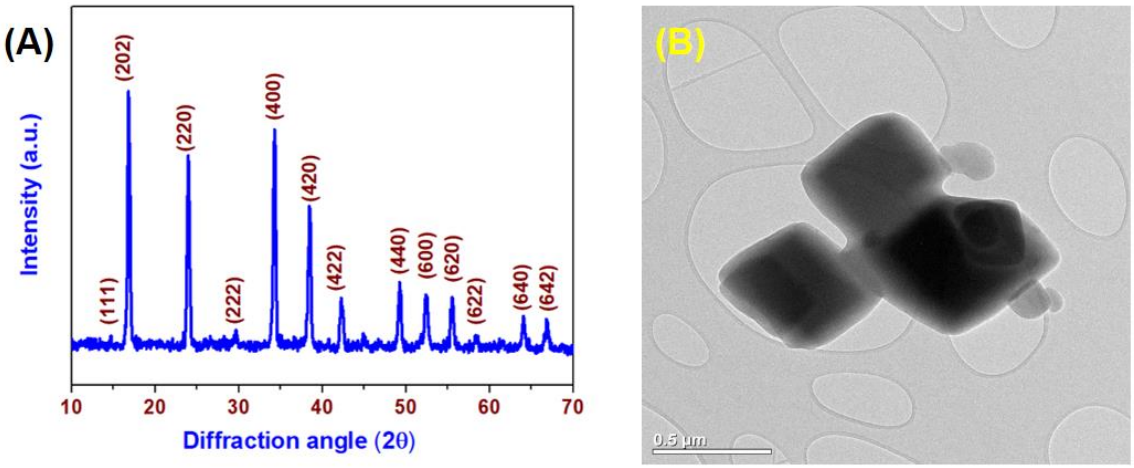

Figure 3.3.1. Physicochemical characterization of the Mn-HCF. (A) X-ray diffraction pattern of the Mn-HCF nanocubes. (B) HR-TEM micrograph of the prepared Mn-HCF nanocubes.

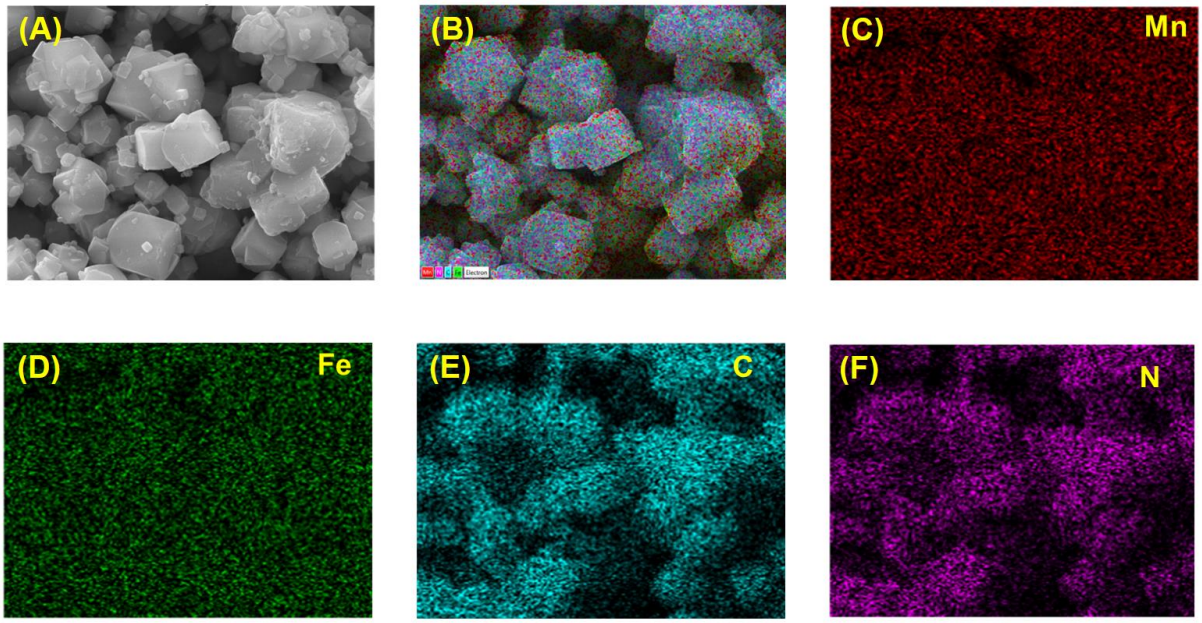

Figure 3.3.2. (A) FE-SEM micrograph of Mn-HCF nanocubes, (B) Overlay field-emission scanning electron micrograph of Mn-HCF nanocubes, elemental mapping showing the distribution of (C) Mn element, (D) Fe element (E) C element, (F) N element present in the Mn-HCF.

In addition to HR-TEM analysis, FE-SEM with EDS mapping analysis were analyzed to confirm the presence of various elements in the Mn-HCF. Figure 3.3.2 (A) shows the FE-SEM micrograph of Mn-HCF which clearly indicated the formation of nanocubes structure and Fig. 3.3.2(B) shows the overlay field-emission scanning electron micrograph of Mn-HCF nanocubes. Figure 3.3.2 (C-F) suggested the presence of Mn, Fe, C and N elements in the prepared Mn-HCF nanocubes[41].

X-ray photoelectron spectroscopy is used to analyze the chemical and state of the element present in the Mn-HCF nanostructures. The XPS survey spectrum is shown in Fig. 3.3.3(A), reveals the presence of manganese, iron, carbon and nitrogen element in the Mn-HCF.

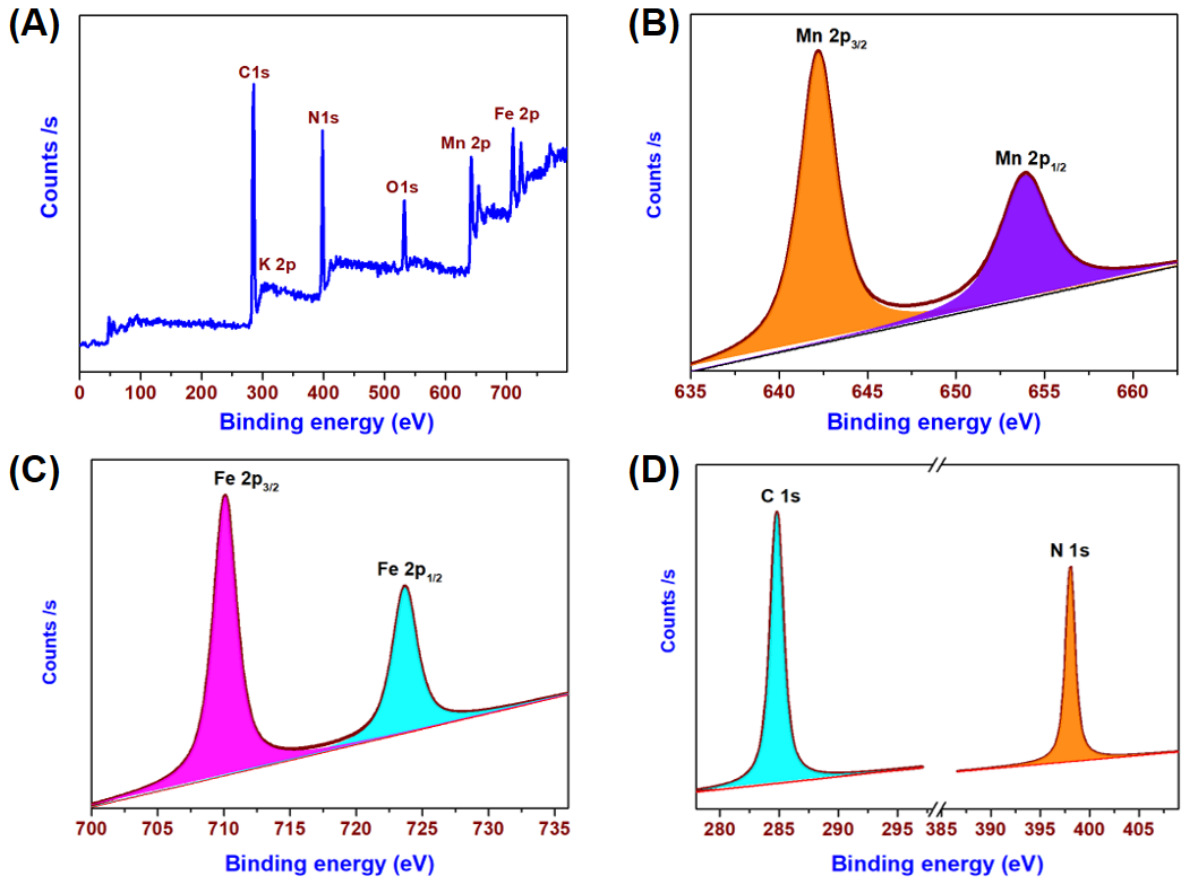

Figure 3.3.3. X-ray photoelectron spectroscopy of the Mn-HCF. (A) XPS survey spectrum of Mn-HCF. (B) Mn core level spectrum (C) Fe core level spectrum and (D) Core level spectrum of N and C

Figure 3.3.3(B) shows the core level spectrum of manganese present in the Mn-HCF with two prominent peaks at 641 and 654 eV corresponding to the Mn $2p_{3/2}$ and Mn $2p_{1/2}$ states[42]. Figure 3.3.3 (C) shows the core level spectrum of Fe element represents the presence of two peaks centered at binding energies 710 and 723 eV corresponding to the Fe $2p_{3/2}$ and Fe $2p_{1/2}$ states respectively[42]. Figure 3.3.3 (D) shows the core level spectrum of C 1s and N 1s which reveals the presence of C and N components in cyano bridged network frame of Mn-HCF nanostructures[42].

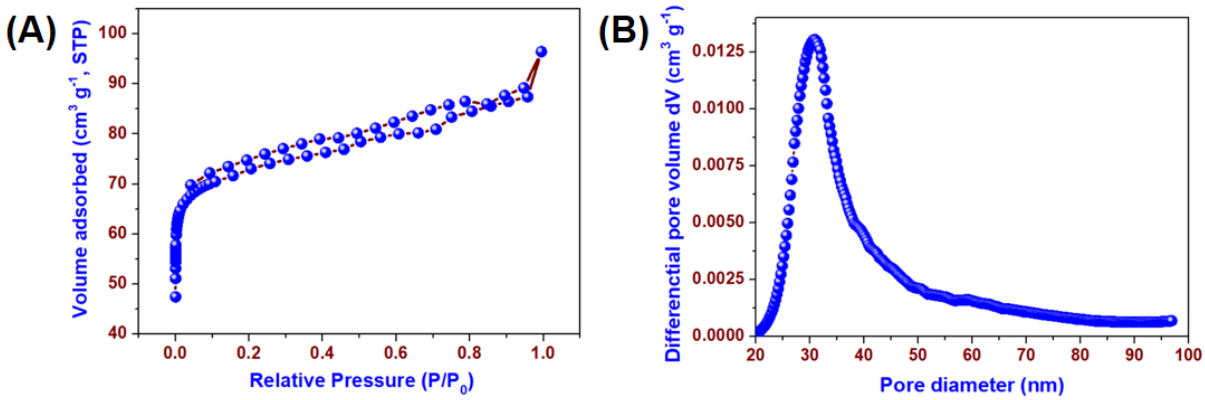

Figure 3.3.4. (A) The N_2 adsorption-desorption isotherm of the Mn-HCF and (B) Pore size distribution in the Mn-HCF calculated by HK method.

The electrochemical properties of the electrode materials depend upon the surface area and the pores present in it and hence we performed surface area and pore size analysis for the Mn-HCF electrode. The Nitrogen adsorption-desorption isotherm and pore size distribution curves of Mn-HCF nanostructures was examined, and the data is shown in Figure 3.3.4(A & B). The N_2 adsorption-desorption isotherm is shown in Fig 3.3.4 (A) reveals the presence of hysteresis loop which is similar to the type IV curve as per the IUPAC standard suggesting the presence of mesopores in the prepared Mn-HCF nanostructures with the surface area of 212.766 m^2 g^{-1} [40]. The pore volume of the Mn-HCF nanostructures was calculated using HK method and the average pore diameter is calculated as 30 nm.

3.3.3.2 Electrochemical characterization

The electrochemical characterization for the Mn-HCF and graphene nanosheets were examined using cyclic voltammetry, galvanostatic charge-discharge, and electrochemical impedance spectroscopy via three electrode configurations using an aqueous solution containing 1 M $LiNO_3$. Figure 3.3.5(A) shows the cyclic voltammetry profiles of the Mn-HCF over a potential window of -0.2 to 1.4 V measured at various scan ranging from 5 – 100 mV s^{-1}.

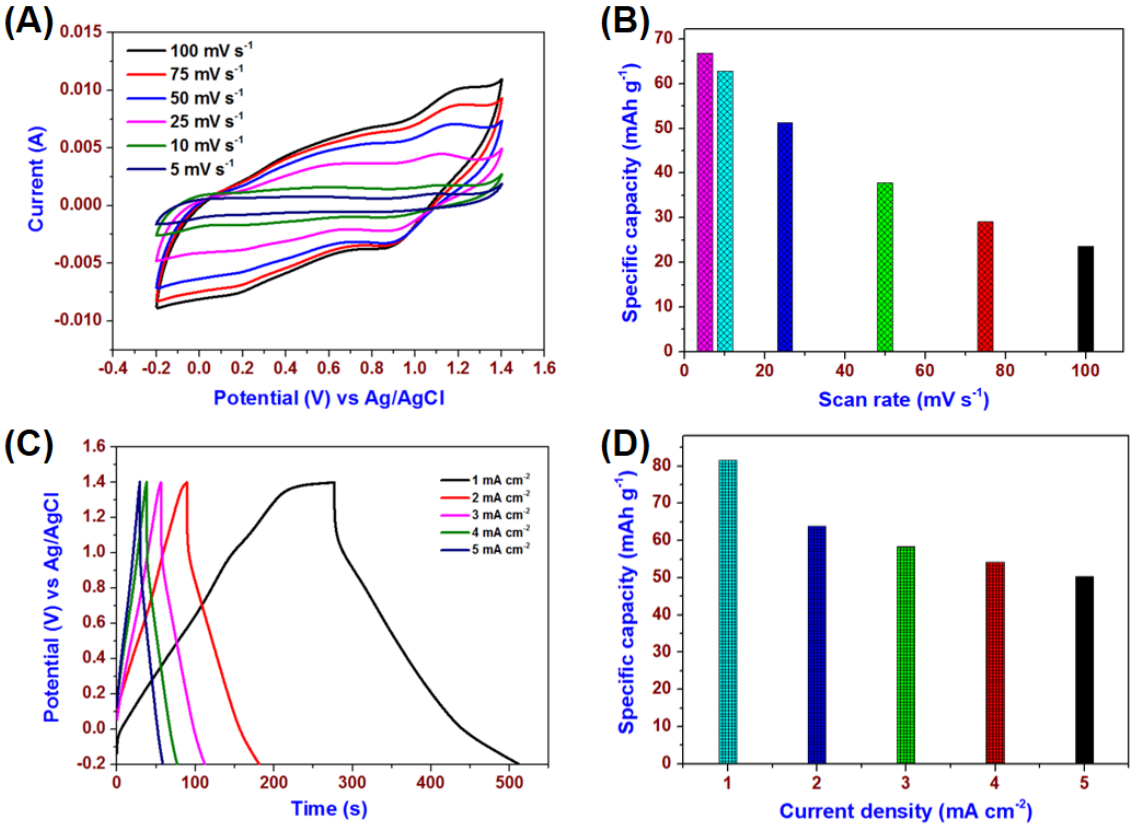

Figure 3.3.5. Electrochemical performances of Mn-HCF in 1 M $LiNO_3$ electrolyte. (A) cyclic voltammetric profiles measured at potential window (-0.2 to 1.4 V) at various scan rate ranging from 5 to 100 mV s^{-1}, (b) Effect of specific capacity of the Mn-HCF electrode with the change in scan rate. (C) galvanostatic charge-discharge profile measured at potential window (-0.2 to 1.4 V) at various current densities ranging from 1 to 5 mA cm^{-2}, (b) Effect of specific capacity of the Mn-HCF electrode with respect to current density.

The CV analysis of Mn-HCF electrode shows that it can operate over a wide potential window of -0.2 to 1.4 V without any sign of evolution. The CV profiles of the Mn-HCF electrode exhibits the quasi-rectangular shape with the presence of redox peaks suggesting the intercalation pseudocapacitance of Mn-HCF electrode. The pronounced redox peaks in the CV profiles of the Mn-HCF electrode arises from the Fe^{3+}/Fe^{2+} redox couple at 1.2 V and 0.8 V, and it is behavior is associated with the intercalation/deintercalation of Li^+ ions with the cyano-bridged framework of the hexacyanoferrate[32,43]. The peak current increases with the increase in scan rate and the shape of the CV profiles retain the shape even at higher scan rate suggesting the quasi-reversible behavior of the Mn-HCF electrode[37]. This indicates that the redox process of Mn-HCF electrode is related to the intercalation-deintercalation of Li^+ ions in electrode framework[32]. The specific capacity of the Mn-HCF electrode calculated from the CV analysis is 66.87 mAh g^{-1} obtained at a scan rate of 5 mV s^{-1}. The specific capacity of the Mn-HCF electrode decreases with increase in scan rate and is shown in Fig. 3.3.5 (B). This decrease is specific capacity is due to the mass transport of electrolyte ions is hindered to the interior part of the electrode material limits the electrochemical reaction and is agreement with the other reported works on supercapacitors[44]. Figure 3.3.5 (C) shows the galvanostatic charge-discharge profiles of the Mn-HCF electrode measures at the various current densities ranging from 1 to 5 mA cm^{-2} over the potential window of -0.2 to 1.4 V. The CD profiles shows the quasi-triangular shaped profiles which in agreement with the CV profiles of the Mn-HCF electrode[45]. The CD curves show semi-symmetric behavior over all the current ranges measured for the Mn-HCF electrode suggesting the better rate capability of the electrode[46]. From the Fig. 3.3.5(C), it is evident that the high current results in fast charging and discharging time whereas at the lower current produced better charging and discharging profiles in the Mn-HCF electrode. The specific capacity of the Mn-HCF electrode is 81.59 mAh g^{-1} measured at

a constant current density of 1 mA cm^{-2}. The effect of current density on the specific capacity of the Mn-HCF electrode s shown in Fig. 3.3.5 (D). At a higher current density of 5 mA cm^{-2}, Mn-HCF electrode delivered a specific capacity of 50.35 mAh g^{-1} which almost retained 61.69 % of the initial capacity with an increase in 5-fold in current density suggesting the better rate capability of the Mn-HCF electrode.

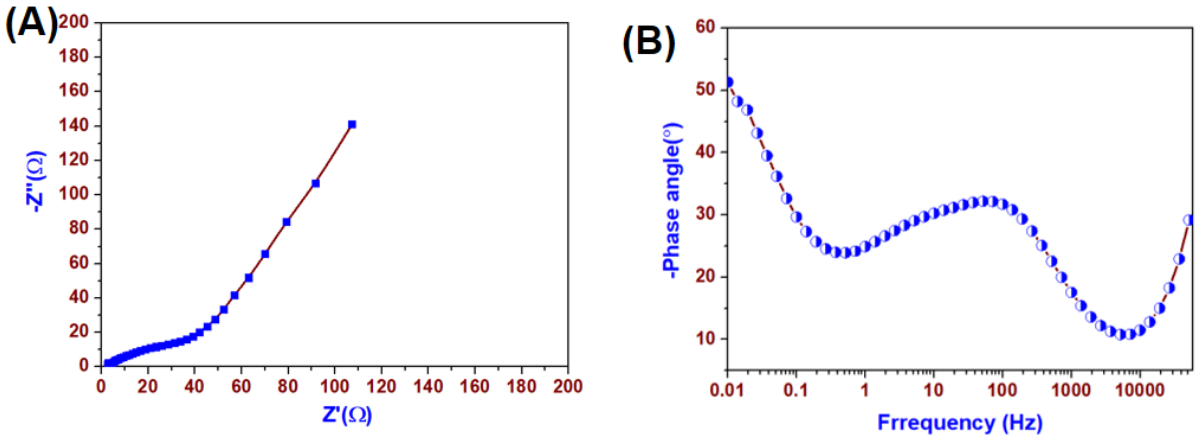

Figure 3.3.6 (A) Nuquist plot and (B) Bode phase angle plot for the Mn-HCF electrode

The electrochemical impedance spectroscopy of the Mn-HCF electrode was analyzed using Nyquist and Bode phase angle plot. The Nyquist plot of the Mn-HCF electrode is shown in Fig. 3.3.6 (A), shows the presence of a small semicircle arises due to the charge transfer resistance at the higher frequency region followed by a straight line or Warburg line at the low-frequency region almost parallel to the imaginary axis which is related to the frequency dependent ion diffusion kinetics of the Mn-HCF electrode[39]. Figure 3.3.6(B) shows the Bode phase angle plot which tails at -51.32º which highlight the pseudocapacitive nature of the Mn-HCF electrode[47].

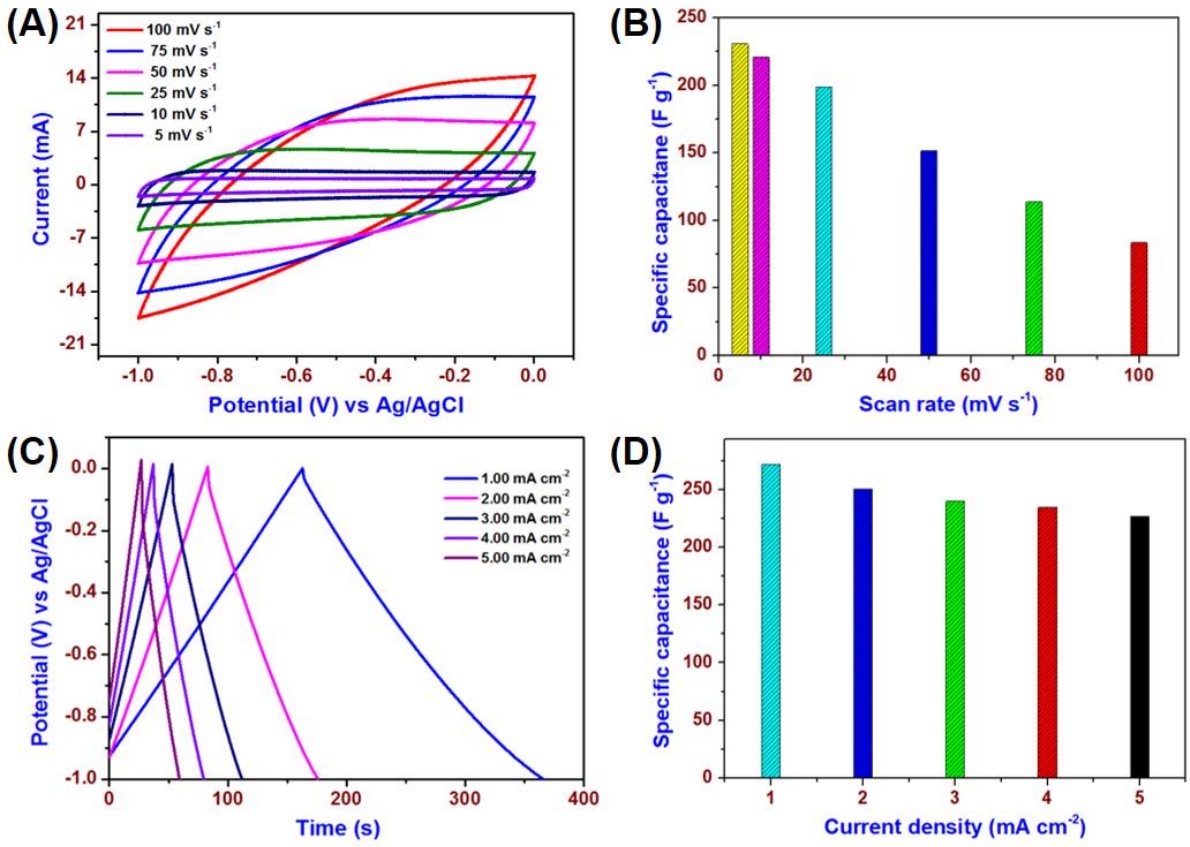

Figure 3.3.7. Electrochemical performances of graphene nanosheets in 1 M $LiNO_3$ electrolyte. (A) cyclic voltammetric profiles of graphene electrode measured at an operating potential window (-1 to 0 V) at various scan rate ranging from 5 to 100 mV s^{-1}, (b) Effect of specific capacitance of the graphene electrode with the change in scan rate. (C) galvanostatic charge-discharge profile of graphene electrode measured at an operating potential window (-1 to 0 V) at various current densities ranging from 1 to 5 mA cm^{-2}, (b) Effect of specific capacitance of the graphene electrode with respect to current density.

The electrochemical characterization such as cyclic voltammetry and galvanostatic charge-discharge analysis for the graphene electrode is provided in Fig. 3.3.7. The CV profiles of the graphene electrode were recorded over the potential window of -1.0 to 0.0 V at different scan rates from 5 to 100 mV s^{-1} as shown in Fig. 3.3.7 (A). The CV profiles showed the presence of ideal rectangular behavior of the graphene electrode suggesting the charge storage mechanism is due to the presence of electrochemical double layers capacitance[29].

Furthermore, the shape of the CV curves is rectangular at all scan rates, and the current density is increasing with an increase in scan rate, thus suggesting an ideal capacitive behavior [48]. The specific capacitance of the graphene electrode was calculated as 230.75 F g^{-1} from the CV curve measured at a scan rate of 5 mV s^{-1}. The effect of scan rate on the specific capacitance of the graphene electrode is shown in Fig. 3.3.7(B). With an increase in scan rate, the decrease in specific capacitance is due to the limitation of the electrochemical reactions at higher scan rates. Figure 3.3.7 (C) shows the galvanostatic charge-discharge analysis of the graphene electrode over the potential window -1 to 0 V measured at the current density ranging from 1 to 5 mA cm^{-2}. The CD profiles show the triangular, symmetric behavior which is in agreement with the CV profiles of the graphene electrode. The CD curves show symmetric behavior over all the current ranges measured for the graphene electrode suggesting the better rate capability of the electrode [23]. The specific capacitance of the graphene electrode is calculated from the GCD analysis is 272 F g^{-1} measured at a constant current density of 1 mA cm^{-2}.

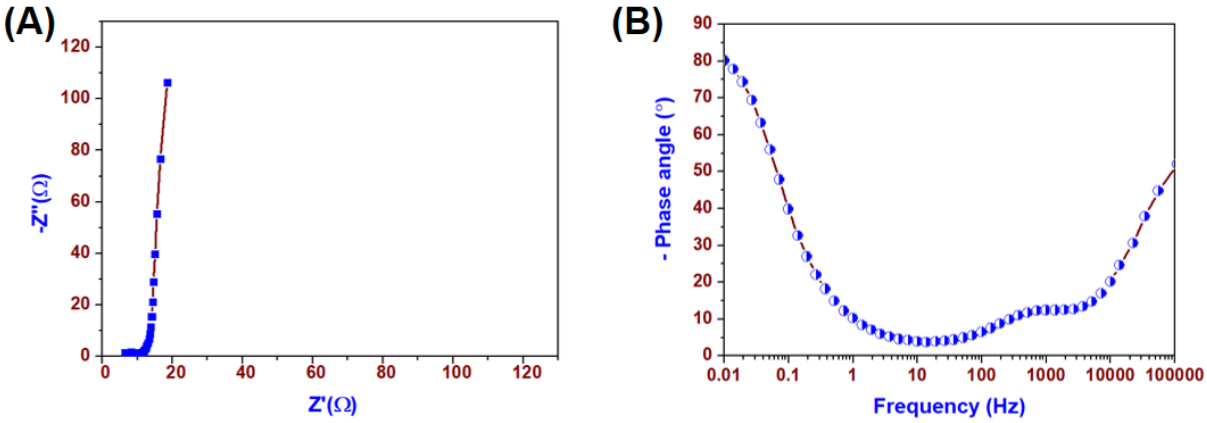

Figure 3.3.8 (A) Nuquist plot and (B) Bode phase angle plot for the graphene electrode

The effect of current density on the specific capacitance of the graphene electrode is shown in Fig. 3.3.7 (D). At a higher current density of 5 mA cm^{-2}, graphene electrode delivered a specific capacitance of 226.6 F g^{-1} which almost retained 83.3 % of the initial capacitance with an increase in 5-fold in current density suggesting the better rate capability of the

graphene electrode. The Nyquist plot of graphene electrode is shown in Fig. 3.3.8(A) reveals a small solution resistance (Rs) and a small semi-circle at higher frequency corresponds to the charge-transfer region and the Warburg line is almost parallel to the imaginary component of the impedance, thus signifying the better EDLC nature of graphene electrodes[49]. The Bode phase angle plot (Fig. 3.3.8(B)) tails at -80.13º suggesting the EDLC behavior of the graphene electrode[49] .

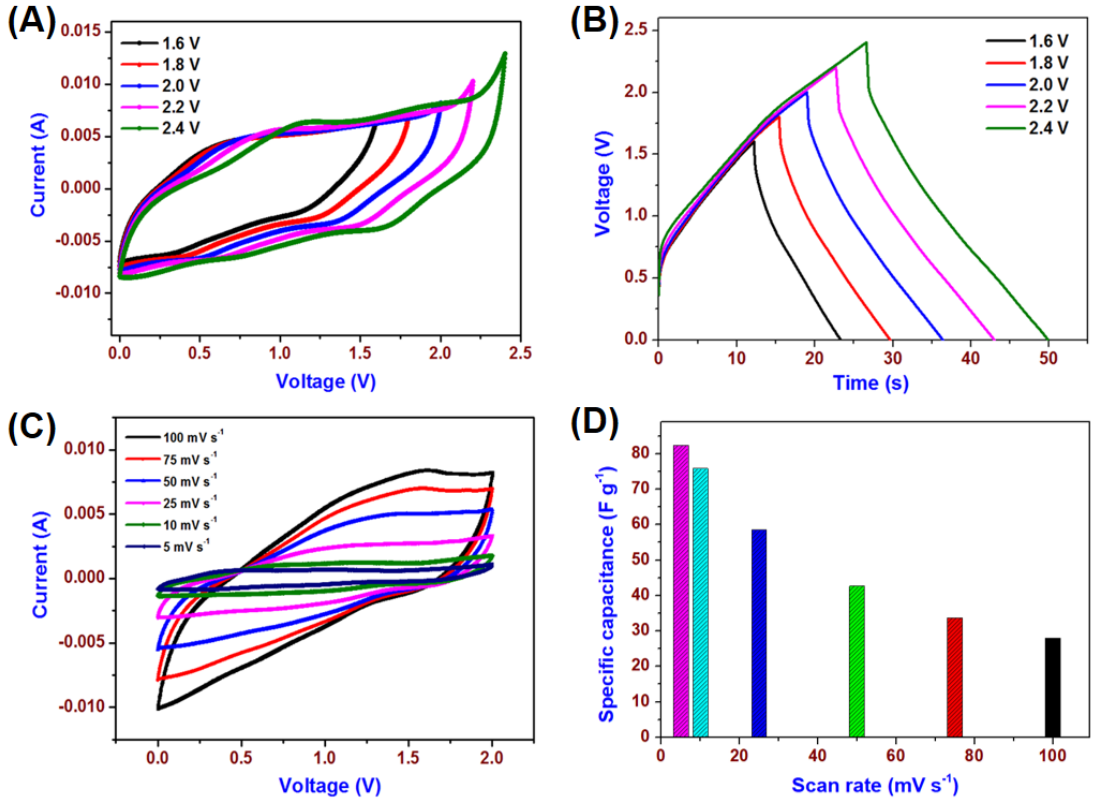

Figure 3.3.9. Electrochemical performances of Mn-HCF‖graphene LHC device in 1 M $LiNO_3$ electrolyte. (A) cyclic voltammetric profiles of LHC device measured at different operating potential window (0 to + 2.4 V) at a scan rate of 100 mV s^{-1}, (B) galvanostatic charge-discharge profiles of LHC device measured at different operating potential window (0 to + 2.4 V) at a constant current density of 5 mA cm^{-2}, (C) cyclic voltammetric profiles of Mn-HCF‖graphene LHC device measured at an operating potential window (0 to + 2.0 V) at various scan rate ranging from 5 to 100 mV s^{-1}, (D) Effect of scan rate on the specific capacitance of Mn-HCF‖graphene LHC device

Furthermore, the electrochemical studies of the Mn-HCF and graphene electrode suggest the intercalation and deintercalation of Li-ions in the Mn-HCF electrode with an operating potential of -0.2 to 1.4 V and the double layer capacitance of the graphene electrode with working potential window of -1 to 0 V, respectively. Henceforth, the fabricated device using Mn-HCF and graphene will able to achieve an operating voltage of 2.4 V using $LiNO_3$ as the electrolyte. Prior to the fabrication of the asymmetric hybrid ion capacitor, the charge accumulation on each electrode must be balanced for the better performance, and the mass balance for the Mn-HCF and graphene electrode is calculated. The obtained mass ratio for the fabrication of the Mn-HCF‖graphene LHC is approximately 0.926. Figure 3.3.9 (A and B) shows the CV and CD profiles of the fabricated Li-ion capacitor measured at a various operating voltage from 1 to 2.4 V. The CV profiles shown in Fig. 3.3.9 (A) shows the cyclic voltammetry profiles of the fabricated device measured at a scan rate of 100 mV s^{-1} can work up to 2.4 V with little evolution at the higher window. Fig. 3.3.9(B) shows the charge-discharge profiles of the device measured at a constant current density of 5 mA cm^{-2} and the profile is consistent with the CV profiles of the fabricated device measured at the various potential window. Hence, the operating potential window for the fabricated device is fixed to 0.0 – 2.0 V for further electrochemical characterization. The CV profiles of the Mn-HCF‖graphene LHC device were measured over the voltage window of 0.0 to 2.0 V at different scan rates ranging from 5 to 100 mV s^{-1} (shown in Fig. 3.3.9 (C)). The CV profiles show that the increasing scan rate from 5 to 100 mV s^{-1}; the current density increased with increasing scan rate. The specific capacitance of the device was obtained from the CV profiles and the effect of scan rate on the specific capacitance (Figure 3.3.9 (D)). The fabricated Mn-HCF‖graphene LHC device delivered a specific capacitance of 82.41 F g^{-1} at a scan rate of 5 mV s^{-1}; with the increase in the scan rate, the CV profiles retains the shape which suggests the better rate capability of the fabricated Li-ion capacitor.

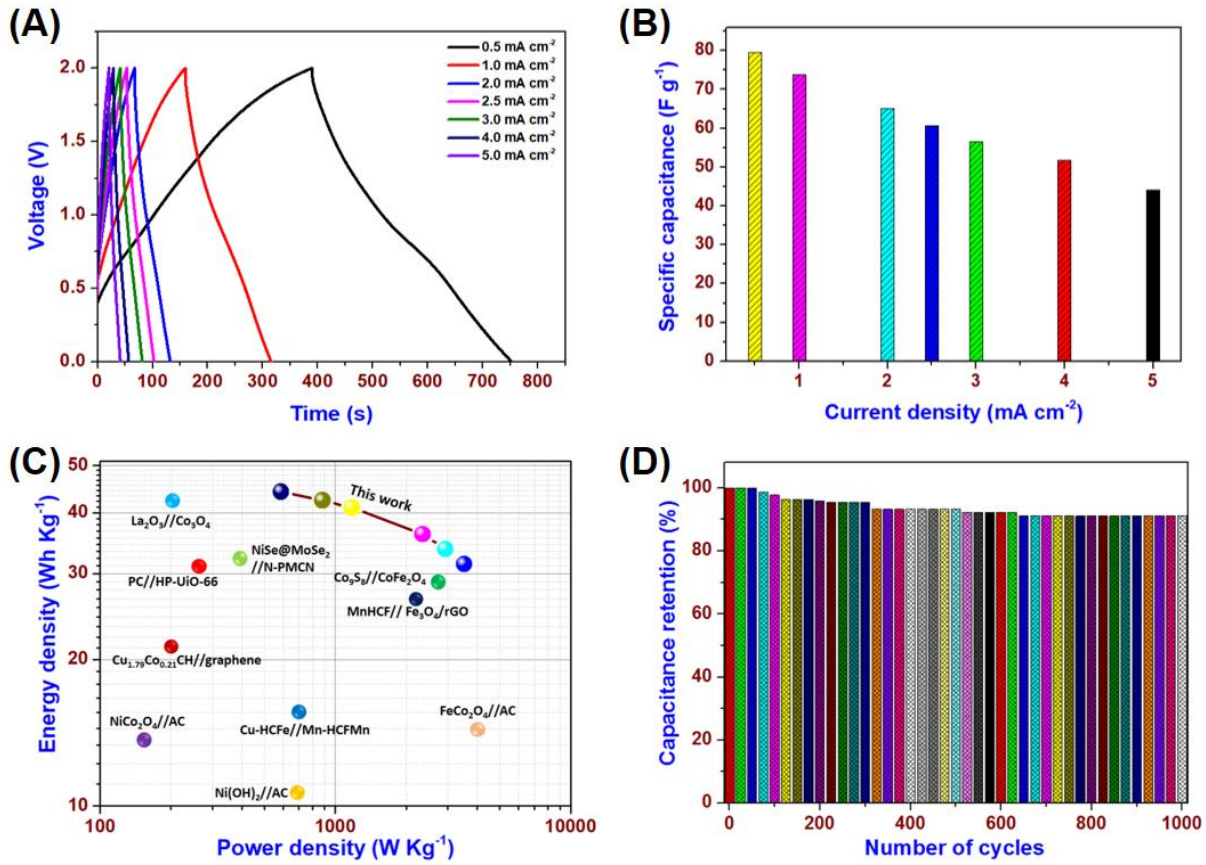

Figure 3.3.10. (A) Galvanostatic CD profiles of Mn-HCF‖graphene LHC device measured at an operating potential window (0 to + 2.0 V) at various current densities ranging from 0.5 to 5 mA cm^{-2}. (B) Effect of current densities on the specific capacitance of Mn-HCF‖graphene LHC device (C) shows the Ragone plot of Mn-HCF‖graphene LHC device, (D) Cyclic stability of Mn-HCF‖graphene LHC device over 1000 cycles of charge-discharge using cyclic voltammetry analysis.

Figure 3.3.10 (A) shows the galvanostatic charge-discharge profiles of the fabricated Mn-HCF‖graphene LHC device was recorded at a constant current density ranging from 0.5 to 5 mA cm^{-2}. The CD profiles showed the presence of triangular-shaped quasi-symmetric curves, which suggested a better capacitive property[50]. The symmetric nature of the CD curve was retained even at a high current density which indicated a good capacitive nature of the fabricated device[29]. The Mn-HCF‖graphene LHC device delivered a specific capacitance of 79.52 F g^{-1} at a constant discharge current density of 0.5 mA cm^{-2}. The effect

of change in current density is provide in the Fig. 3.3.10 (B). With the increase of ten-fold in the current density, the device retains 55.47% of its initial capacitance shows the excellent rate capability of the device. The electrochemical impedance spectroscopic analysis of the fabricated Mn-HCF‖graphene LHC device were analysed using Nyquist and Bode phase angle plot (shown in Fig. 3.3.11(A) and 3.3.11(B)). The Nyquist plot (Figure 3.3.11(A)) showed a semi-circle in the high frequency region and a sloped line in the low frequency region with the solution resistance (R_s) of 1.35 Ω and the charge transfer resistance (R_{ct}) of 10.5 Ω. The Warburg line in the low frequency region corresponded to the diffusion of electrolyte ions into the surface of the electrodes[47].

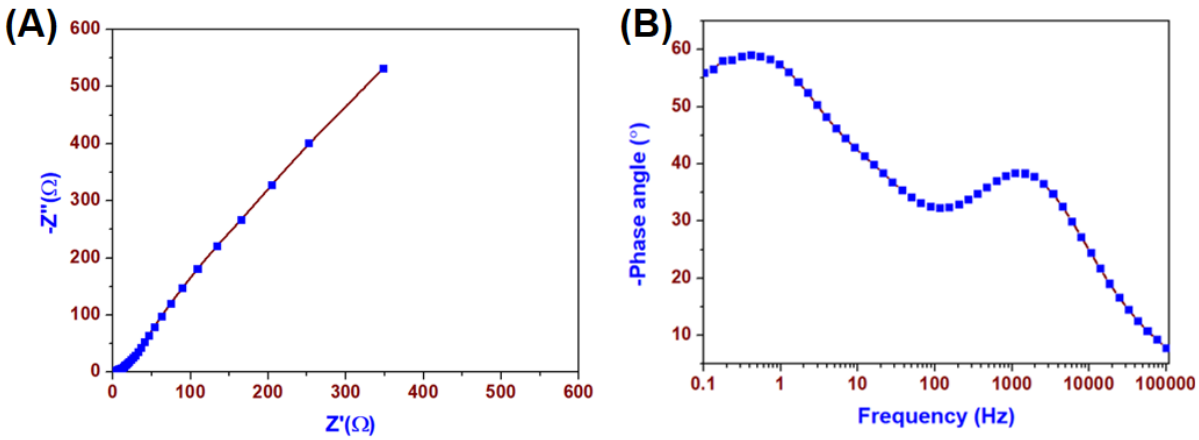

Figure 3.3.11 (A) Nuquist plot and (B) Bode phase angle plot for the Mn-HCF ‖ graphene LHC device

Figure 3.3.10 (C) represents the Ragone plot of the fabricated Mn-HCF‖graphene LHC device which delivered an energy density of 44.18 Wh kg^{-1} with a power density of 588.23 W kg^{-1} measured at a constant current density of 0.5 mA cm^{-2}. Further, the Ragone plot also evidenced the better energy density of Mn-HCF‖graphene LHC device compared with the recently reported ion and asymmetric capacitors such as $Cu_{1.79}Co_{0.21}CH$/NF‖graphene/NF (21.5 Wh kg^{-1})[51], $Ni(OH)_2$‖AC (10.5 Wh kg^{-1})[52], Co_2O_4‖AC (14.7 Wh kg^{-1})[53], MnHCF‖Fe_3O_4/rGO (27.9 Wh kg^{-1})[40], CuHCFe‖MnHCFMn (15 Wh kg^{-1})[54], La_2O_3‖Co_3O_4 (42.9 Wh kg^{-1})[55], Co_9S_8‖$CoFe_2O_4$ (28.8 Wh kg^{-1})[56], $FeCo_2O_4$‖AC (14

Wh kg $^{-1}$)[57], NiSe@$MoSe_2$‖N-PMCN (32.6 Wh kg $^{-1}$)[58], and PC‖HP-UiO-66 (32 Wh kg $^{-1}$)[59]. Figure 3.3.10 (D) represents the cyclic stability of the Mn-HCF‖graphene LHC device over 1000 cycles, which showed that a specific capacitance of 91.12 % (compared to its initial capacitance) was retained after the cyclic tests. Altogether, these studies suggested the better energy storage capacitive properties of the Mn-HCF‖graphene LHC device.

3.3.4 Conclusion

In this work, we successfully prepared Mn-HCF via simple, cost-effective and rapid sonochemical method and demonstrated their potential application as intercalative-type electrode material for the LHCs using graphene sheets as capacitive electrode. The presence of intercalation capacitance and double layer capacitance in the Mn-HCF and graphene electrodes were confirmed by the electrochemical studies performed using three-electrode configuration. The Mn-HCF nanocubes delivered a maximum specific capacity of about 81.59 mAh g^{-1} from the CV analysis obtained at a constant current density of 1 mA cm^{-2}. Further, the fabricated Mn-HCF‖graphene LHC device operates over the voltage window of 0.0 – 2.0 V and delivers a specific capacitance of 79.52 F g^{-1} with an energy density of 44.18 Wh kg^{-1} and long cycle life (~ 91.12 % capacitance retention). The experimental findings show that the potential use of Mn-HCF as an intercalative type electrode material for designing high energy aqueous Li-ion hybrid capacitor.

3.3.5 References

[1] M. Höök, X. Tang, Depletion of fossil fuels and anthropogenic climate change—A review, Energy Policy. 52 (2013) 797–809. doi:10.1016/j.enpol.2012.10.046.

[2] K. Jeyasubramanian, T.S. Gokul Raja, S. Purushothaman, M.V. Kumar, I. Sushmitha, Supercapacitive performances of MnO 2 nanostructures grown on hierarchical Cu nano leaves via electrodeposition, Electrochim. Acta. 227 (2017) 401–409. doi:10.1016/j.electacta.2017.01.044.

[3] P.M. Shafi, R. Dhanabal, A. Chithambararaj, S. Velmathi, A.C. Bose, α-MnO 2 /h-MoO 3 Hybrid Material for High Performance Supercapacitor Electrode and Photocatalyst, ACS Sustain. Chem. Eng. 5 (2017) 4757–4770. doi:10.1021/acssuschemeng.7b00143.

[4] C. Zhou, Y. Zhang, Y. Li, J. Liu, Construction of high-capacitance 3D CoO@Polypyrrole nanowire array electrode for aqueous asymmetric supercapacitor, Nano Lett. 13 (2013) 2078–2085. doi:10.1021/nl400378j.

[5] S. Vijayakumar, S. Nagamuthu, K.-S. Ryu, CuCo 2 O 4 flowers/Ni-foam architecture as a battery type positive electrode for high performance hybrid supercapacitor applications, Electrochim. Acta. 238 (2017) 99–106. doi:10.1016/j.electacta.2017.03.178.

[6] X. Lu, M. Yu, G. Wang, T. Zhai, S. Xie, Y. Ling, Y. Tong, Y. Li, H-TiO2@MnO2//H-TiO2@C core-shell nanowires for high performance and flexible asymmetric supercapacitors, Adv. Mater. 25 (2013) 267–272. doi:10.1002/adma.201203410.

[7] B. Zhao, D. Chen, X. Xiong, B. Song, R. Hu, Q. Zhang, B.H. Rainwater, G.H. Waller, D. Zhen, Y. Ding, Y. Chen, C. Qu, D. Dang, C.P. Wong, M. Liu, A high-energy, long cycle-life hybrid supercapacitor based on graphene composite electrodes, Energy Storage Mater. 7 (2017) 32–39. doi:10.1016/j.ensm.2016.11.010.

[8] Y. Wang, Y. Song, Y. Xia, Electrochemical capacitors: mechanism, materials, systems, characterization and applications, Chem. Soc. Rev. 45 (2016) 5925–5950. doi:10.1039/C5CS00580A.

[9] K. Jeyasubramanian, V.S. Prabhin, G.S. Hikku, A.V.M. Preethi, Investigation of super-capacitive nature of reduced graphene oxide nano mesh grown over 18 k gold foil using wings of Parides iphidamas as biological template, Mater. Res. Bull. 98 (2018) 25–33. doi:10.1016/j.materresbull.2017.09.051.

[10] P. Pazhamalai, K. Krishnamoorthy, S.J. Kim, Hierarchical copper selenide nanoneedles grown on copper foil as a binder free electrode for supercapacitors, Int. J. Hydrogen Energy. 41 (2016) 14830–14835. doi:10.1016/j.ijhydene.2016.05.157.

[11] V.K. Mariappan, K. Krishnamoorthy, P. Pazhamalai, S. Sahoo, S.-J. Kim, Electrodeposited molybdenum selenide sheets on nickel foam as a binder-free electrode for supercapacitor application, Electrochim. Acta. 265 (2018) 514–522. doi:10.1016/j.electacta.2018.01.075.

[12] J. Feng, X. Sun, C. Wu, L. Peng, C. Lin, S. Hu, J. Yang, Y. Xie, Metallic Few-Layered VS 2 Ultrathin Nanosheets: High Two-Dimensional Conductivity for In-Plane Supercapacitors, J. Am. Chem. Soc. 133 (2011) 17832–17838. doi:10.1021/ja207176c.

[13] A. Chaturvedi, P. Hu, V. Aravindan, C. Kloc, S. Madhavi, Unveiling two-dimensional TiS 2 as an insertion host for the construction of high energy Li-ion capacitors, J. Mater. Chem. A. 5 (2017) 9177–9181. doi:10.1039/C7TA01594A.

[14] H. Wang, H. Yi, X. Chen, X. Wang, Asymmetric supercapacitors based on nano-architectured nickel oxide/graphene foam and hierarchical porous nitrogen-doped carbon nanotubes with ultrahigh-rate performance, J. Mater. Chem. A. 2 (2014) 3223–3230. doi:10.1039/C3TA15046A.

[15] S. Saha, P. Samanta, N.C. Murmu, N.H. Kim, T. Kuila, J.H. Lee, Electrochemical

functionalization and in-situ deposition of the SAA@rGO/h-BN@Ni electrode for supercapacitor applications, J. Ind. Eng. Chem. 52 (2017) 321–330. doi:10.1016/j.jiec.2017.04.005.

[16] G.K. Veerasubramani, K. Krishnamoorthy, R. Sivaprakasam, S.J. Kim, Sonochemical synthesis, characterization, and electrochemical properties of MnMoO4 nanorods for supercapacitor applications, Mater. Chem. Phys. 147 (2014) 836–842. doi:10.1016/j.matchemphys.2014.06.028.

[17] D. Mohapatra, S. Badrayyana, S. Parida, Designing binder-free, flexible electrodes for high-performance supercapacitors based on pristine carbon nano-onions and their composite with CuO nanoparticles, RSC Adv. 6 (2016) 14720–14729. doi:10.1039/C5RA23700A.

[18] S. Nagamuthu, S. Vijayakumar, K.-S. Ryu, Cerium oxide mixed LaMnO 3 nanoparticles as the negative electrode for aqueous asymmetric supercapacitor devices, Mater. Chem. Phys. 199 (2017) 543–551. doi:10.1016/j.matchemphys.2017.07.050.

[19] M.E. Lee, S.Y. Cho, H.J. Yoon, Y.S. Yun, H.-J. Jin, High-performance Li-ion hybrid supercapacitors based on microporous pyropolymer nanoplates and orthorhombic Nb 2 O 5 nanocomposites, J. Ind. Eng. Chem. 57 (2018) 284–289. doi:10.1016/j.jiec.2017.08.034.

[20] Z. Fan, J. Yan, T. Wei, L. Zhi, G. Ning, T. Li, F. Wei, Asymmetric Supercapacitors Based on Graphene/MnO2 and Activated Carbon Nanofiber Electrodes with High Power and Energy Density, Adv. Funct. Mater. 21 (2011) 2366–2375. doi:10.1002/adfm.201100058.

[21] F. Wang, X. Wu, X. Yuan, Z. Liu, Y. Zhang, L. Fu, Y. Zhu, Q. Zhou, Y. Wu, W. Huang, Latest advances in supercapacitors: from new electrode materials to novel device designs, Chem. Soc. Rev. 46 (2017) 6816–6854. doi:10.1039/C7CS00205J.

[22] K. Fic, G. Lota, M. Meller, E. Frackowiak, Novel insight into neutral medium as electrolyte for high-voltage supercapacitors, Energy Environ. Sci. 5 (2012) 5842–5850. doi:10.1039/C1EE02262H.

[23] B. Xie, C. Yang, Z. Zhang, P. Zou, Z. Lin, G. Shi, Q. Yang, F. Kang, C.-P. Wong, Shape-Tailorable Graphene-Based Ultra-High-Rate Supercapacitor for Wearable Electronics, ACS Nano. 9 (2015) 5636–5645. doi:10.1021/acsnano.5b00899.

[24] J. Yan, Y. Sun, L. Jiang, Y. Tian, R. Xue, L. Hao, W. Liu, B. Yi, Electrochemical performance of lithium ion capacitors using aqueous electrolyte at high temperature, J. Renew. Sustain. Energy. 5 (2013) 021404. doi:10.1063/1.4798432.

[25] F.X. Wang, S.Y. Xiao, Y.S. Zhu, Z. Chang, C.L. Hu, Y.P. Wu, R. Holze, Spinel LiMn2O4 nanohybrid as high capacitance positive electrode material for supercapacitors, J. Power Sources. 246 (2014) 19–23. doi:10.1016/j.jpowsour.2013.07.046.

[26] N. Wu, Y. Zhang, Y. Wei, H. Liu, H. Wu, Template-Engaged Synthesis of 1D Hierarchical Chainlike LiCoO 2 Cathode Materials with Enhanced High-Voltage Lithium Storage Capabilities, ACS Appl. Mater. Interfaces. 8 (2016) 25361–25368. doi:10.1021/acsami.6b09159.

[27] C. Rong, S. Chen, J. Han, K. Zhang, D. Wang, X. Mi, X. Wei, Hybrid supercapacitors integrated rice husk based activated carbon with LiMn 2 O 4, J. Renew. Sustain. Energy. 7 (2015) 023104. doi:10.1063/1.4913965.

[28] C. Zhong, Y. Deng, W. Hu, J. Qiao, L. Zhang, J. Zhang, A review of electrolyte materials and compositions for electrochemical supercapacitors., Chem. Soc. Rev. 44 (2015) 7484–7539. doi:10.1039/c5cs00303b.

[29] K. Krishnamoorthy, P. Pazhamalai, S. Sahoo, J.H. Lim, K.H. Choi, S.J. Kim, A High-Energy Aqueous Sodium-Ion Capacitor with Nickel Hexacyanoferrate and Graphene

Electrodes, ChemElectroChem. 4 (2017) 3302–3308. doi:10.1002/celc.201700690.

[30] S. Vijayan, B. Kirubasankar, P. Pazhamalai, A.K. Solarajan, S. Angaiah, Electrospun Nd 3+ -Doped LiMn 2 O 4 Nanofibers as High-Performance Cathode Material for Li-Ion Capacitors, ChemElectroChem. 4 (2017) 2059–2067. doi:10.1002/celc.201700161.

[31] P. Sennu, V. Aravindan, M. Ganesan, Y.-G. Lee, Y.-S. Lee, Biomass-Derived Electrode for Next Generation Lithium-Ion Capacitors, ChemSusChem. 9 (2016) 849–854. doi:10.1002/cssc.201501621.

[32] C.D. Wessells, S. V. Peddada, M.T. McDowell, R.A. Huggins, Y. Cui, The Effect of Insertion Species on Nanostructured Open Framework Hexacyanoferrate Battery Electrodes, J. Electrochem. Soc. 159 (2012) A98. doi:10.1149/2.060202jes.

[33] V. Aravindan, J. Gnanaraj, Y.S. Lee, S. Madhavi, Insertion-type electrodes for nonaqueous Li-ion capacitors, Chem. Rev. 114 (2014) 11619–11635. doi:10.1021/cr5000915.

[34] C.D. Wessells, R.A. Huggins, Y. Cui, Copper hexacyanoferrate battery electrodes with long cycle life and high power, Nat. Commun. 2 (2011) 550. doi:10.1038/ncomms1563.

[35] F. Zhao, Y. Wang, X. Xu, Y. Liu, R. Song, G. Lu, Y. Li, Cobalt Hexacyanoferrate Nanoparticles as a High-Rate and Ultra-Stable Supercapacitor Electrode Material, ACS Appl. Mater. Interfaces. 6 (2014) 11007–11012. doi:10.1021/am503375h.

[36] S. Liu, G.L. Pan, G.R. Li, X.P. Gao, Copper hexacyanoferrate nanoparticles as cathode material for aqueous Al-ion batteries, J. Mater. Chem. A. 3 (2015) 959–962. doi:10.1039/C4TA04644G.

[37] H. Pang, Y. Zhang, T. Cheng, W.-Y. Lai, W. Huang, Uniform manganese hexacyanoferrate hydrate nanocubes featuring superior performance for low-cost supercapacitors and nonenzymatic electrochemical sensors, Nanoscale. 7 (2015)

16012–16019. doi:10.1039/C5NR04322K.

[38] K. Krishnamoorthy, M. Veerapandian, L.-H. Zhang, K. Yun, S.J. Kim, Antibacterial Efficiency of Graphene Nanosheets against Pathogenic Bacteria via Lipid Peroxidation, J. Phys. Chem. C. 116 (2012) 17280–17287. doi:10.1021/jp3047054.

[39] K. Krishnamoorthy, P. Pazhamalai, S. Sahoo, S.-J. Kim, Titanium carbide sheet based high performance wire type solid state supercapacitors, J. Mater. Chem. A. 5 (2017) 5726–5736. doi:10.1039/C6TA11198J.

[40] K. Lu, D. Li, X. Gao, H. Dai, N. Wang, H. Ma, An advanced aqueous sodium-ion supercapacitor with a manganous hexacyanoferrate cathode and a Fe 3 O 4 /rGO anode, J. Mater. Chem. A. 3 (2015) 16013–16019. doi:10.1039/C5TA04244E.

[41] M. Pasta, R.Y. Wang, R. Ruffo, R. Qiao, H.-W. Lee, B. Shyam, M. Guo, Y. Wang, L.A. Wray, W. Yang, M.F. Toney, Y. Cui, Manganese–cobalt hexacyanoferrate cathodes for sodium-ion batteries, J. Mater. Chem. A. 4 (2016) 4211–4223. doi:10.1039/C5TA10571D.

[42] R. Agarwal, M.K. Sharma, K. Bhattacharyya, Prussian Blue-Manganese Hexacyanoferrate Nanocomposite as Multifunctional High Performance Electrode Material, ChemistrySelect. 1 (2016) 3562–3568. doi:10.1002/slct.201600796.

[43] X. Wang, Y. Xiao, D. Su, S. Xu, L. Zhou, S. Wu, L. Han, S. Fang, S. Cao, Hierarchical porous cobalt monoxide nanosheet@ultrathin manganese dioxide nanosheet core-shell arrays for high-performance asymmetric supercapacitor, Int. J. Hydrogen Energy. 41 (2016) 13540–13548. doi:10.1016/j.ijhydene.2016.06.133.

[44] S.R. Marri, S. Ratha, C.S. Rout, J.N. Behera, 3D cuboidal vanadium diselenide embedded reduced graphene oxide hybrid structures with enhanced supercapacitor properties, Chem. Commun. 53 (2017) 228–231. doi:10.1039/C6CC08035A.

[45] Y. Moritomo, S. Urase, T. Shibata, Enhanced battery performance in manganese

hexacyanoferrate by partial substitution, Electrochim. Acta. 210 (2016) 963–969. doi:10.1016/j.electacta.2016.05.205.

[46] H.-W. Lee, R.Y. Wang, M. Pasta, S. Woo Lee, N. Liu, Y. Cui, Manganese hexacyanomanganate open framework as a high-capacity positive electrode material for sodium-ion batteries, Nat. Commun. 5 (2014) 5280. doi:10.1038/ncomms6280.

[47] R.B. Rakhi, B. Ahmed, M.N. Hedhili, D.H. Anjum, H.N. Alshareef, Effect of Postetch Annealing Gas Composition on the Structural and Electrochemical Properties of Ti 2 CT x MXene Electrodes for Supercapacitor Applications, Chem. Mater. 27 (2015) 5314–5323. doi:10.1021/acs.chemmater.5b01623.

[48] M.-X. Guo, S.-W. Bian, F. Shao, S. Liu, Y.-H. Peng, Hydrothermal synthesis and electrochemical performance of MnO2/graphene/polyester composite electrode materials for flexible supercapacitors, Electrochim. Acta. 209 (2016) 486–497. doi:10.1016/j.electacta.2016.05.082.

[49] P. Pachfule, D. Shinde, M. Majumder, Q. Xu, Fabrication of carbon nanorods and graphene nanoribbons from a metal–organic framework, Nat. Chem. 8 (2016) 718–724. doi:10.1038/nchem.2515.

[50] Y. Wang, Q. Chen, Dual-Layer-Structured Nickel Hexacyanoferrate/MnO 2 Composite as a High-Energy Supercapacitive Material Based on the Complementarity and Interlayer Concentration Enhancement Effect, ACS Appl. Mater. Interfaces. 6 (2014) 6196–6201. doi:10.1021/am5011173.

[51] S. Liu, K.N.K.S. Hui, K.N.K.S. Hui, V. V. Jadhav, Q.X. Xia, J.M. Yun, Y.R. Cho, R.S. Mane, K.H. Kim, Facile Synthesis of Microsphere Copper Cobalt Carbonate Hydroxides Electrode for Asymmetric Supercapacitor, Electrochim. Acta. 188 (2016) 898–908. doi:10.1016/j.electacta.2015.12.018.

[52] J. Huang, P. Xu, D. Cao, X. Zhou, S. Yang, Y. Li, G. Wang, Asymmetric

supercapacitors based on β-Ni(OH)2 nanosheets and activated carbon with high energy density, J. Power Sources. 246 (2014) 371–376. doi:10.1016/j.jpowsour.2013.07.105.

[53] R. Ding, L. Qi, M. Jia, H. Wang, Facile and large-scale chemical synthesis of highly porous secondary submicron/micron-sized NiCo2O4 materials for high-performance aqueous hybrid AC-NiCo2O4 electrochemical capacitors, Electrochim. Acta. 107 (2013) 494–502. doi:10.1016/j.electacta.2013.05.114.

[54] M. Pasta, C.D. Wessells, N. Liu, J. Nelson, M.T. McDowell, R.A. Huggins, M.F. Toney, Y. Cui, Full open-framework batteries for stationary energy storage, Nat. Commun. 5 (2014) 3007. doi:10.1038/ncomms4007.

[55] A.A. Yadav, A.C. Lokhande, J.H. Kim, C.D. Lokhande, High electrochemical performance asymmetric supercapacitor based on La 2 O 3 //Co 3 O 4 electrodes, J. Ind. Eng. Chem. 56 (2017) 90–98. doi:10.1016/j.jiec.2017.06.051.

[56] S.J. Patil, A.C. Lokhande, J.S. Park, J.H. Kim, Y.B. Kim, B.C. Choi, S.H. Park, S.H. Jung, D.W. Lee, Towards high performance unique microstructures of Co 9 S 8 //CoFe 2 O 4 for asymmetric supercapacitor, J. Ind. Eng. Chem. (2017). doi:10.1016/j.jiec.2017.12.018.

[57] A. Pendashteh, J. Palma, M. Anderson, R. Marcilla, Nanostructured porous wires of iron cobaltite: novel positive electrode for high-performance hybrid energy storage devices, J. Mater. Chem. A. 3 (2015) 16849–16859. doi:10.1039/C5TA02701B.

[58] H. Peng, J. Zhou, K. Sun, G. Ma, Z. Zhang, E. Feng, Z. Lei, High-Performance Asymmetric Supercapacitor Designed with a Novel NiSe@MoSe 2 Nanosheet Array and Nitrogen-Doped Carbon Nanosheet, ACS Sustain. Chem. Eng. 5 (2017) 5951–5963. doi:10.1021/acssuschemeng.7b00729.

[59] W. Gao, D. Chen, H. Quan, R. Zou, W. Wang, X. Luo, L. Guo, Fabrication of Hierarchical Porous Metal-Organic Framework Electrode for Aqueous Asymmetric

Supercapacitor, ACS Sustain. Chem. Eng. 5 (2017) 4144–4153. doi:10.1021/acssuschemeng.7b00112.

CHAPTER 3.4: Copper tungsten sulfide anchored on Ni-foam as a high-performance binder free negative electrode for asymmetric supercapacitor

Highlights

- Copper tungsten sulfide was grown on Ni foam via hydrothermal process.
- X-ray diffraction, HR-TEM, and XPS analyses revealed the formation of CWS on Ni foam.
- CWS/Ni electrode exhibits type-B curves indicating the presence of charge-storage due to the ion-intercalation/de-intercalation (between the interlayers of CWS) capacitance with partial redox process occurred at the electrode
- Aqueous Li-ion hybrid capacitor was assembled using CWS/Ni and graphene.

3.4.1 Introduction

Electrochemical capacitors or supercapacitors becomes the promising energy storage device technology to compensate the energy demands due to the increased depletion of energy resources from fossil fuels and renewable resources[1,2]. Additional benefits of supercapacitor devices rely on their fast charge-discharge properties, high power, and long cycle life compared to the batteries[3]. Electrode materials and their structure play a vital role in achieving high performance metrics (such as specific capacitance, energy and power density) of a supercapacitor device[4–6]. Recent works on supercapacitors has been focused on the use of various electrode materials such as layered materials such as transition metals (phosphorene, boron, antimonene)[7–9], transition metal chalcogenides (TMCs) (MoS_2, $MoSe_2$, VS_2)[10–12], layered metal carbides and nitrides (Ti_3C_2, Ti_2C, TiN, VN)[13,14], siloxene sheets[15], and layered transition metal oxides/hydroxides[16]. On the other hand, research on tailoring the surface area and morphology of the electrode materials via suitable chemical/physical/electrochemical methods gained much attention to enhance the energy storage properties of the electrode material as well as device[17,18]. Among these electrode materials, layered TMCs have attracted much attention due to their low-dimensional structures with covalently bounded layers of metal atoms bridged by chalcogens separated by weak van der Waals interactions between the inter-layers[19]. Recently, the research on layered TMCs was expanded to binary/ternary/multiple component TMCs which possess rich electronic structures with better physical, chemical and electrochemical properties[20,21]. The multicomponent TMCs possess the advantage of high electrical conductivity and enhanced electrochemical activity over their single component counterparts[22,23]. Thus, more studies have been focused on the use of binary metal sulfides ($CoNi_2S_4$, $NiCo_xS_y$, amorphous $CoMoS_4$) towards high performance electrode materials supercapacitors during this decade[24–26].

In this scenario, copper tungsten sulfide (CWS) is one of the layered ternary transition metal sulfides possesses high electrical conductivity with wide band gap which makes them a suitable for electrocatalytic hydrogen evolution reaction, visible-light driven photocatalysis, and biological applications [27,28]. Jia et al. reported the catalytic properties of copper tungsten sulfide for the aqueous Cr ion reduction[29]. The photocatalytic hydrogen evolution reaction of copper tungsten sulfide was reported by Jing et al.[30] Recently, Kannan et al. studied the superior antibacterial properties of the copper tungsten sulfide (prepared via a hydrothermal process) compared with other metal chalcogenides[31]. The energy storage properties of the CWS materials are recently demonstrated by Hu et al. in which they demonstrated the use of hydrogenated layered copper tungsten sulfide as a potential electrode (with a specific capacitance of 583 F cm^{-3}) for flexible solid-state supercapacitor application[27]. These studies highlighted the significance of CWS electrodes towards the electrochemical energy storage devices and additional efforts are essential to improve their energy performance. Further, a careful review on the supercapacitive properties of copper and tungsten sulfide shows the presence of battery-type charge-storage in the former (copper sulfide)[32] and pseudo-capacitive type charge-storage in the later (tungsten sulfide)[33]. Being a binary metal sulfide based on copper- and tungsten- transition metals, it is expected that electrochemical performance of CWS will be exception compared to the single component copper and tungsten sulfide-based electrodes.

In this scenario, the chemical engineering of electrode materials allows us to develop novel electrodes with a hierarchical structure, thus, leading to a higher electrochemical performance[34]. In general, the electrochemical properties of a material can be enhanced via various strategies such as (i) tailoring the electrical conductivity via physical or chemical methods, (ii) increasing high-surface area via various synthetic routes, and (iii) fabrication of binder-free electrodes[35]. Among these, the binder-free electrodes possess the merits such as

(i) low mass loading, (ii) direct integration of active material with the current collector and (iii) the absence of insulating binder in the electrode[36,37]. The improved electrochemical properties of binder-free electrodes are due to the sufficient exposure of active sites, enhanced ion/electron transport kinetics and complete utilization of the electroactive material compared to the binder-based electrodes in which majority of the electroactive materials are blocked from the contact with the electrolyte[38]. The significance of binder-free electrodes over binder-based electrodes were recently compared by Xu et al. [35]. They demonstrated the specific capacitance of Ti_3C_2 electrodes (48 F g^{-1}) was increased upto 140 F g^{-1} for the binder-free Ti_3C_2-nickel foam electrodes. In our recent study, we have demonstrated the improved supercapacitive properties of copper molybdenum sulfide (CMS) based binder free electrode with almost 20-fold higher specific capacity over the conventional binder- based electrode[39]. Binder-free electrodes can be fabricated via several methods such as physical/chemical vapour deposition, electrochemical deposition, and hydrothermal methods, etc.[40] Among these, hydrothermal reaction holds the advantage of being a cost-effective method, low-temperature reaction conditions, and good adherence of active material on the current collectors[39]. In this study, we aimed to develop the CWS based binder-free electrodes grown on nickel (Ni) foam and explored their electrochemical properties in comparison with conventional binder based electrodes (CWS+carbon+PVDF binder). Further, the use of CWS-binder free electrodes as a negative electrode for high performance asymmetric supercapacitors (utilizing graphene as a positive electrode)) was also demonstrated in this work.

3.4.2 Experimental section

3.4.2.1 Hydrothermal growth of copper tungsten sulfide nanostructures on Ni foam

The copper tungsten sulfide nanostructures were grown on the surface of Ni foam via the hydrothermal method. Briefly, the precursor solution containing 0.005 mol of Na_2WO_4,

0.01 mol of CuCl, and 0.025 mol of C_2H_5NS was dissolved in a solution containing water (20 mL) and ethanol (20 mL) until the formation of a clear homogeneous solution. Initially, the bare Ni foam was sonicated in dilute HCl solution for 10 min to remove the native oxide layers present in the Ni foam. This process was followed by thorough washing of the Ni foam using DI water for several times and dried at 70 ℃ for 1 h in an oven. The pre-cleaned Ni foam (2×4 cm^2) was kept in the 80 mL stainless steel autoclave and filled with the precursor solution for hydrothermal reaction at a temperature of 180 ℃ and kept for 15 h. After completion of the reaction, the reactor was allowed to cool down to room temperature naturally. Then, the black coloured copper tungsten sulfide grown on Ni foam was taken and cleaned with acetone, ethanol and dried at 80 ℃ for 6 h in an oven. The obtained copper tungsten sulfide grown on Ni foam (CWS/Ni) was used for further characterizations. The bare copper tungsten sulfide powders were prepared using similar experimental conditions without the use of Ni foam.

Two additional control reactions were also performed in this study as follows: (1) The Ni_3S_2/Ni foam was prepared via hydrothermal reaction between bare Ni foam with thioacetamide using the similar experimental conditions without Cu and W precursors. (2) The CWS/Ni_3S_2/Ni foam was prepared using the similar experimental conditions by replacing Ni foam substrate by Ni_3S_2/Ni foam.

3.4.2.2 Preparation of graphene nanosheets

The graphene sheets were prepared by the reduction of graphene oxide (GO) according to our earlier work[41]. Initially, GO was prepared using modified hummers method followed by sonochemical reduction of GO nanosheets to graphene. Briefly, as prepared GO nanosheets were dissolved in water and the GO dispersed solution pH was adjusted to pH 10 with the aid of NaOH followed by the addition of 2 mL of hydrazine. The final solution was subjected to ultrasound irradiation for 4 h without any cooling under the

atmospheric conditions. The graphene nanosheets obtained as the result of ultrasonication was washed thoroughly with DI water and ethanol several times to remove the residuals until it is free from trace amount of impurities. The washed sample was dried at 70 ℃ for overnight and used for further characterization.

3.4.2.3 Electrochemical measurement using three-electrode configuration

The as grown CWS/Ni electrode is used for the electrochemical studies and the electroactive mass of the CWS/Ni electrode is calculated from the difference between the mass of the Ni foam before and after growing of the CWS using Dual-range Semi-micro Balance (AUW-220D, SHIMADZU) is approximately ~ 0.7 mg cm^{-2}. The planar type CWS and/or graphene on stainless steel current collector was fabricated using slurry coating method as reported in our earlier work [42]. The electrochemical characterization of the CWS/Ni electrode, planar type CWS and planar type graphene working electrodes were examined using a three-electrode system using silver/silver chloride as the reference electrode, and platinum as the counter electrode.

3.4.2.4 Fabrication and electrochemical analysis of CWS-Ni‖graphene asymmetric supercapacitor device:

For the fabrication of asymmetric supercapacitor device (ASC), CWS/Ni electrode is used as the negative electrode and the graphene is used as the positive electrode. Prior to the fabrication of the asymmetric supercapacitor (ASC) device, the mass of the negative and positive electrodes needs to be balanced to equate the charge accumulation in the individual electrodes. To balance the charges accumulated at the both electrodes (i.e., $Q^+ = Q^-$), the mass ratio of CWS/Ni electrode and graphene for the CWS/Ni‖graphene ASC device was calculated using the relation[42]:

$$m^+ / m^- = [C^- \times \Delta V^-] / [C^+ \times \Delta V^+] \ldots\ldots\ldots\ldots\ldots\ldots (1)$$

where m^- and m^+ represent the mass of the negative and positive electrodes, C^- and C^+ denote the specific capacitance of the negative and positive electrodes, and, ΔV^- and ΔV^+ are the potential window of the negative and positive electrodes obtained using the three-electrode system, respectively.

The CWS/Ni‖graphene ASC were fabricated in the form of a sandwich-type electrode, with an electrolyte-immersed Celgard as the separator. The overall mass loading of the electroactive materials in the fabricated ASC is about 2.1 mg cm^{-2} (comprising 0.7 mg of CMS/Ni and 1.4 mg of graphene). The electrochemical properties were examined via cyclic voltammetry (CV), electrochemical impedance spectroscopy (EIS) and galvanostatic charge–discharge (CD) measurements using an Autolab PGSTAT302N electrochemical workstation. An aqueous solution containing 1 M Li_2SO_4 was used as an electrolyte.

3.4.3 Results and discussion

3.4.3.1 Physicochemical characterization

In this study, the CWS nanostructures were grown on the surface of Ni foam via a facile hydrothermal method and the mechanism for the formation of CWS nanostructures anchored on Ni foam can be explained as follows: The precursor was prepared by mixing the aqueous solutions of Na_2WO_4, CuCl and C_2H_5NS which results in the formation of precursor solution (Figure 3.4.1(A)) comprising amorphous colloids or ultra-small size nanocrystals of Cu-W-S in heterogeneous stoichiometry. During the hydrothermal reaction at a temperature of 180 °C, the precursors undergo recrystallization of metastable precursors (RMP) process[43] due to the effect of temperature and pressure inside the hydrothermal reactor which leads to the formation of crystalline CWS anchored on the surface of Ni foam (Figure 3.4.1(B-D)). In our previous study, we demonstrated the formation of Ni_3S_2 on the surface of Ni foam via direct hydrothermal reaction between Ni foam and thiourea as a sulfur

source[44]. Other studies also demonstrated the reaction between metallic nickel with sulfur ions from thioacetamide and L-cysteine under hydrothermal conditions[24,45,46].

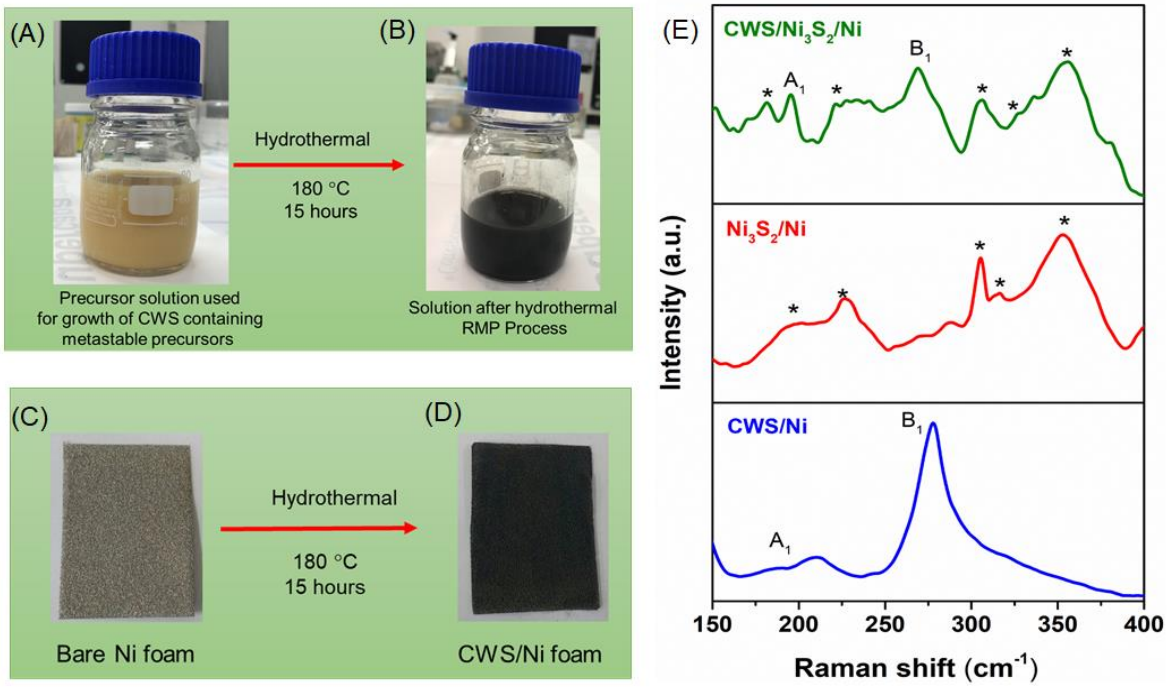

Figure 3.4.1. (A) Precursor used for the preparation of CWS/Ni foam before hydrothermal reaction and (B) final product obtained from the hydrothermal vessel after 15 h. (C-D) shows the change in colour from grey (Ni foam (C)) into black coloured Ni foam (D) after hydrothermal process indicating the formation of CWS on the surface of Ni foam. (E) represents the laser Raman spectrum of CWS anchored Ni foam in comparison with Ni_3S_2/Ni foam and CWS/Ni_3S_2/Ni foam.

Thus, there might be a possibility for the formation of Ni_3S_2 along with CWS on the Ni foam during the hydrothermal process. To verify either any formation of Ni_3S_2 along with CWS on the surface occurred or not, we have performed two control experiments with similar conditions but different precursors viz. (i) formation of Ni_3S_2/Ni foam via similar hydrothermal reaction between Ni foam and thioacetamide, and (ii) formation of CWS/Ni_3S_2/Ni using hydrothermal reaction between the Ni_3S_2/Ni foam and precursor

solution given in Figure 3.4.1(A). The hydrothermal product obtained in these two solutions are black in colour similar to that of Figure 3.4.1(D). The laser Raman spectra of the three hydrothermally prepared products were analysed to determine whether any nickel sulfides are formed along with CWS/Ni foam or not. Figure 3.4.1 (E) shows the comparative laser Raman spectra of (i) CWS/Ni, (ii) Ni_3S_2/Ni, and (iii) CWS/Ni_3S_2/Ni samples respectively. The laser Raman spectrum of CWS/Ni shows the presence of two main Raman bands observed at 210.5 and 277.6 cm^{-1} which correspond to the A_1, and B_1 mode of Cu_2WS_4, thus highlighting the formation of CWS/Ni foam [27,47]. The Raman spectrum of Ni_3S_2/Ni (using control reaction 1) shows the presence of Raman bands at 194, 227, 305, 319, and 352 cm^{-1} which matched well with the characteristic Raman bands of Ni_3S_2 [48]. The Raman spectra of CWS/Ni_3S_2/Ni ((using control reaction 2) shows the presence of bands arised from both CWS and Ni_3S_2 grown on the Ni foam. The comparison between Raman spectrum of CWS/Ni and CWS/Ni_3S_2/Ni samples further confirms that there was no growth of Ni_3S_2 occurred in the formation of CWS/Ni which is mainly due to the RMP process in the formation of CWS/Ni foam.

Figure 3.4.2 (A) shows the X-ray diffraction pattern of the Cu_2WS_4 (scratched from the surface of CWS/Ni foam) prepared via the hydrothermal process. The presence of major diffraction peaks of Cu_2WS_4 observed at 17.56°, 18.48°, 23.1°, 29.12°, 31.22°,32.78°, 37.45°,37.9°, 46.07°, 46.5°, 48.18°, 49.39°, 50.68°, 52.73°, 56.59°, 57.83° and 59.67° corresponding to (002), (101), (110), (112), (103), (200), (202), (211), (213), (220), (105), (204), (222), (006), (312), (303) and (215) planes of I-Cu_2WS_4 structure[49]. This confirmed the formation of body centred tetragonal I-Cu_2WS_4 with a space group of *I-42m* [50,51]. The presence of Cu 2p, W 4f, S 2p, Ni 2p, C 1s and O 1s states of elements in the prepared CWS/Ni foam has been confirmed by XPS analysis. The presence of Ni 2p is due to the Ni current collector used as the template for the growth of CWS nanostructures.

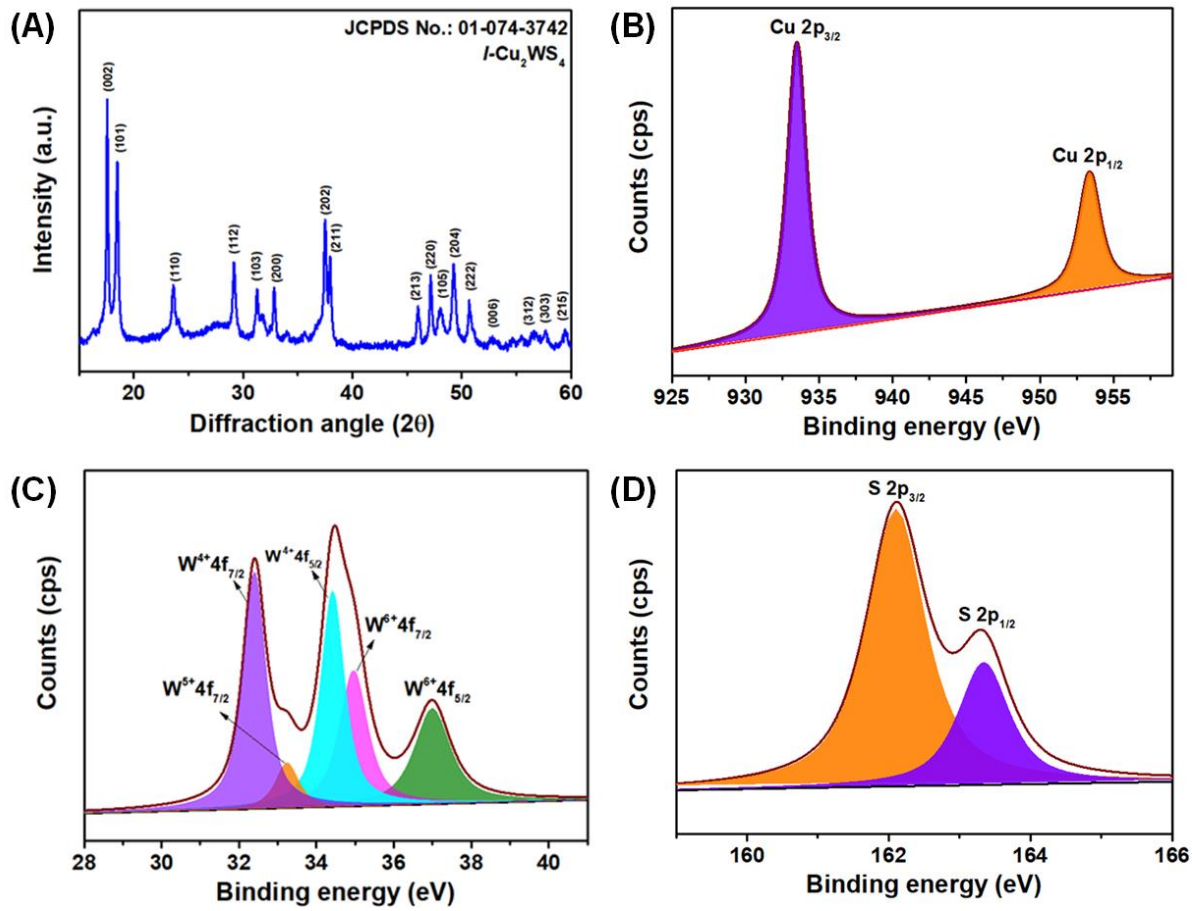

Figure 3.4.2. (A) X-ray diffraction pattern of CWS powders (scratched from Ni foam), (B-C) represents the core-level spectrum of (B) Cu 2p, (C) W 4f, and (D) S 2p states of elements present in the CWS/Ni foam.

The core-level spectrum of Cu 2p states (Figure 3.4.2 (B)) shows the presence of two major peaks at 953.41 eV and 933.49 eV corresponding to the Cu $2p_{1/2}$ and Cu $2p_{3/2}$ states present in the CWS/Ni foam which confirms the formation of +2 oxidation state[29]. The core-level spectrum of W (Figure 3.4.2(C)) indicates the presence of three strong peaks observed at 32.38, 34.60, and 37.12 eV corresponding to the W 4f state in the prepared CWS/Ni foam. The deconvoluted W 4f spectra shows the doublets peaks corresponds to W^{4+} $4f_{5/2}$, W^{4+} $4f_{7/2}$,W^{5+} $4f_{7/2}$, W^{6+} $4f_{5/2}$ & W^{6+} $4f_{7/2}$. The presence of +4 and +5 oxidation state in the XPS spectra denotes the amorphous nature of the WS_x, and the presence of +6 oxidation state is more obvious in CWS, which might be due to the WS_4^{2-} interaction with the Cu^{2+} ions

[52,53]. Figure 3.4.2(D) represents the core-level spectrum of S 2p state, which indicated the presence of a major peak around 162.14 and 163.31 eV corresponds to the S $2p_{3/2}$ and S $2p_{1/2}$ state[29]. The observed peaks are well matched with a previous report on the XPS analysis of copper tungsten sulfide[29]. The N_2 adsorption-desorption isotherm of CWS which is like that of type IV hysteresis loop according to IUPAC standard[54] and the estimated surface area of CWS nanostructures is found to be 14.12 m^2 g^{-1}. The surface area of the CWS nanostructures (grown without Ni foam) using hydrothermal method is found to be 10.06 m^2 g^{-1}.

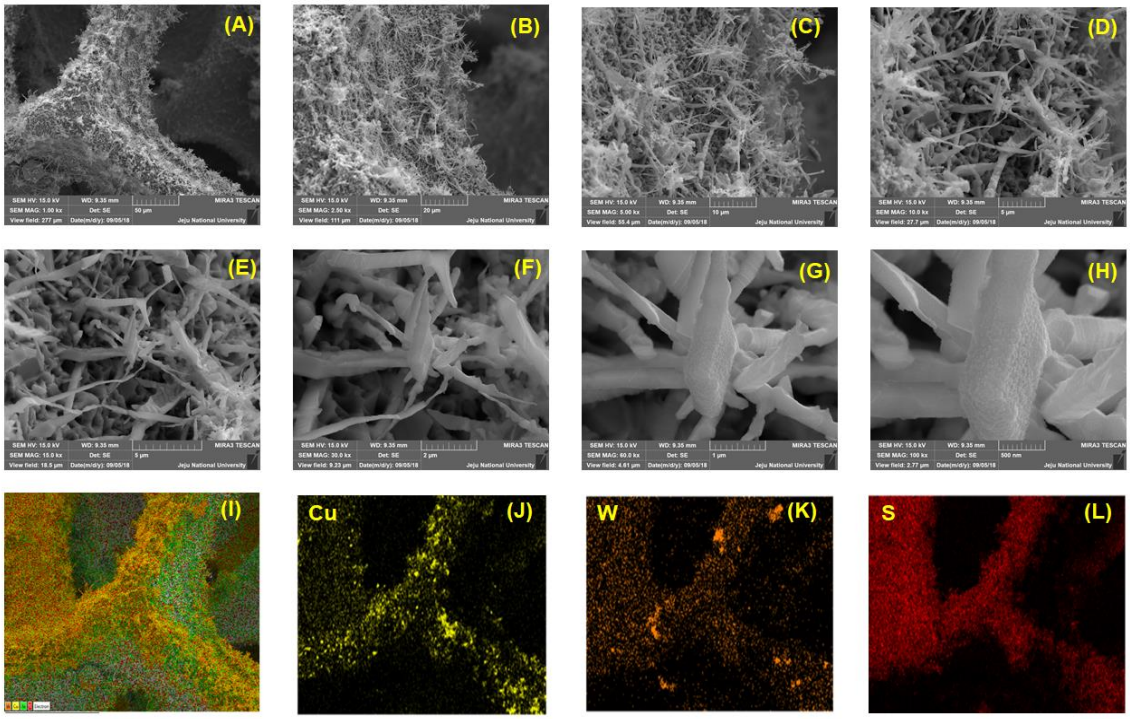

Figure 3.4.3. (A-H) Field emission- scanning electron micrographs (FE-SEM) of CWS/Ni foam obtained using various levels of magnifications (A) 50 µm & 1.0 Kx, (B) 20 µm & 2.5 Kx, (C) 10 µm & 5.0 Kx, (D) 5 µm & 10.0 Kx, (E) 5 µm & 15.0 Kx, (F) 2 µm & 30.0 Kx, (G) 1 µm & 60.0 Kx and (H) 500 nm & 100.0 Kx, respectively. (I) represents the elemental mapping analysis of CWS/Ni foam overlay image and (J-L) represents the mapping of (J) Cu, (K) W, and (L) S elements present in the CWS/Ni.

The surface morphology and elemental analysis of the CWS/Ni foam were examined by FE-SEM and HR-TEM analyses equipped with energy dispersive X-ray spectroscopy (EDAX) as shown in Figure 3.4.3(A-L) and Figure 3.4.4 (A-H). The FE-SEM micrograph shown in Figure 3.4.3(A) shows the uniform growth of CWS nanostructures on the surface of Ni foam via the hydrothermal process. Figure 3.4.3(B-D) clearly evidenced that the morphology of the CWS nanostructures comprises of both rods- and plates- like structures with almost vertically oriented on the surface of Ni foam. Figure 3.4.3 (B-H) shows the various levels of magnifications of CWS nanostructures grown on Ni-foam indicating the formation of hierarchical nanoclusters of CWS with nanoplate-like morphology with different lateral sizes.

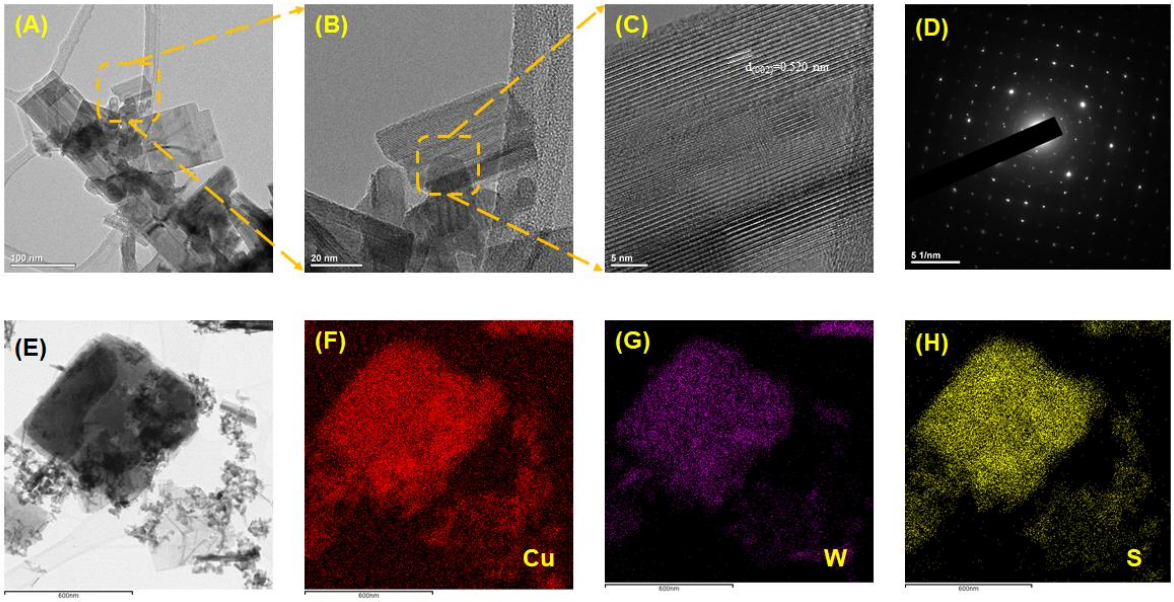

Figure 3.4.4. High resolution- transmission electron micrographs (HR-TEM) of CWS. (A) low resolution and (B) high resolution micrograph of CWS, (C) lattice fringes and (D) SAED pattern of CWS nanostructures. (E) represents the elemental mapping analysis of CWS overlay image and (F-H) represents the mapping of (F) Cu, (G) W, and (H) S elements present in the CWS.

Further, the FE-SEM micrographs also show the presence of gaps in between the adjacent CWS nanostructures and these structural merits are highly useful for the fast ion intercalation and diffusion kinetic reactions during the charge-discharge process[44,55]. The elemental mapping images for the CWS/Ni foam are provided in Figure 3.4.3 (I-L) which confirms the uniform distribution of copper, tungsten and sulfur element present in the CWS/Ni foam and the corresponding EDAX spectrum for the CWS/Ni is provided. The atomic percentage ratio of Cu:W:S is measured to be 2.02:0.96:4.12, which is very close to the expected stoichiometric ratio of CWS[31]. Figure 3.4.4 (A-B) shows the HR-TEM micrograph of CWS scratched from the Ni foam which represents the presence of rod- and plate-like structures of CWS with heterogeneous dimensions like that of the FE-SEM micrographs given in Figure 3.4.3. The HR-TEM micrograph (Figure 3.4.4 (C)) representing the lattice fringes with an interplanar spacing of d=0.520 nm, corresponds to the (002) plane of *I*-Cu_2WS_4 and the selected area diffraction (SAED) pattern (Figure 3.4.4(D)) shows clear spots indicating the crystalline nature of CWS[47]. The elemental mapping images for the CWS are provided in Figure 3.4.4 (E-H) which confirms the uniform distribution of copper, tungsten and sulfur element present in the CWS.

3.4.3.2 Electrochemical characterization

At first, we examined the electrochemical energy storage performance of the CWS/Ni electrode using a three-electrode configuration with the aid of cyclic voltammetry (CV) and galvanostatic charge-discharge (GCD) analysis respectively. A 1 M aqueous solution of Li_2SO_4 was used as the electrolyte. Figure 3.4.5 (A) shows the (CV) profiles of CWS/Ni electrode recorded using various scan rate ranging from 5–50 mV s^{-1} over the operating potential window of -0.8 to 0.4 V.

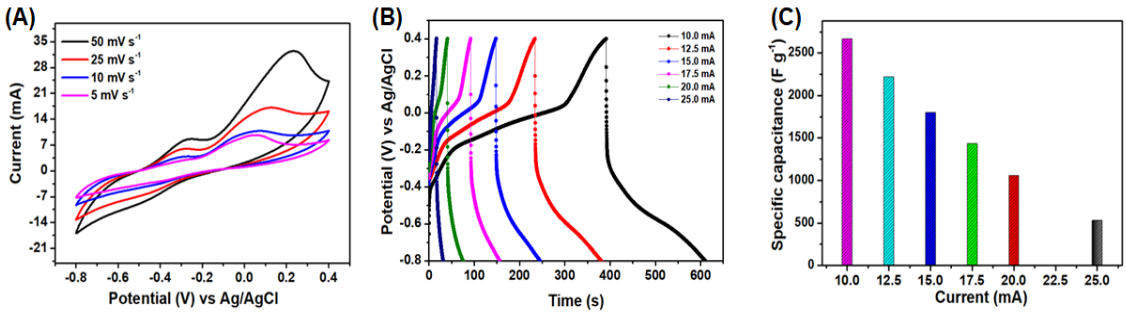

Figure 3.4.5. Electrochemical performances of CWS/Ni in 1 M Li_2SO_4 electrolyte. (A) Cyclic voltammetric profiles of CWS/Ni electrode measured at potential window (−0.2 to 1.4 V) at various scan rate ranging from 5 to 50 mV s^{-1}, (B) Galvanostatic charge-discharge profiles of CWS/Ni electrode measured at potential window (−0.8 to 0.4 V) at various current ranging from 10 to 25 mA, (C) effect of specific capacitance of the CWS/Ni electrode with respect to current.

The mechanism of charge-storage occurred at an electrode can be classified into type A (EDLC, and/or surface pseudocapacitance), type B (intercalation pseudocapacitance (layered), and/or partial redox reaction, type C (Faradaic and/or typical battery type) based on the shape of the CV curves as demonstrated in detail by Prof. Yury Gogotsi and Prof. Reginald M. Penner in their recent editorial note[56]. From Figure 3.4.5(A), the shape of the CV profiles of CWS/Ni electrode closely matched well type-B curves indicating the presence of charge-storage due to the ion-intercalation/de-intercalation (between the interlayers of CWS) capacitance with partial redox process occurred at the electrode [27]. Further, the current range in the CV profiles increased with an increase in the scan rate indicated the occurrence of the diffusion controlled electrochemical process at the CWS/Ni electrode [57,58]. The plot of peak current against the scan rates (as shown in Figure 3.4.6(A) suggested the occurrence of diffusion-controlled reactions during the electrochemical charging and discharging process.

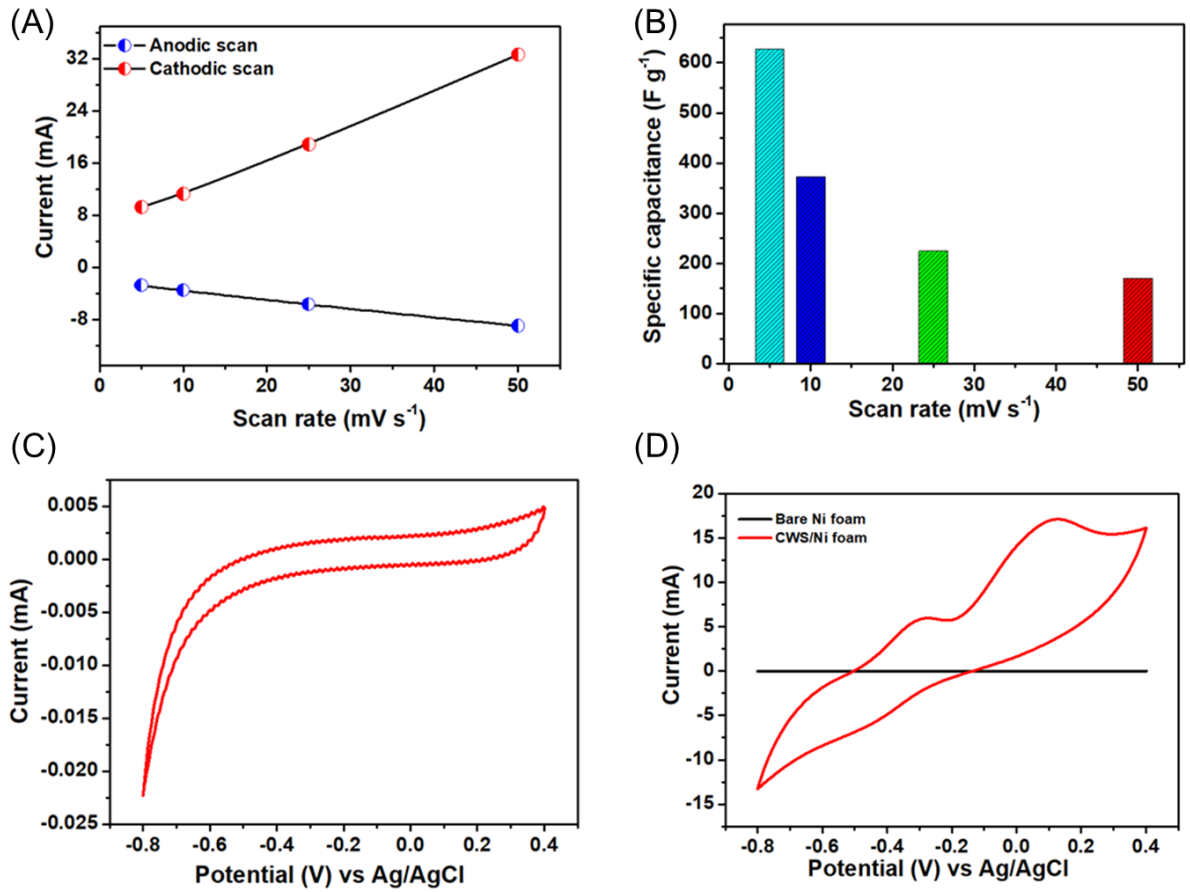

Figure 3.4.6. (A) Plot of peak (anodic and cathodic) current versus the scan rate for the CV data of CWS/Ni electrode, (B) Variation of specific capacitance of CWS/Ni electrode with respect to scan rate. (C) CV profiles of bare Ni foam obtained at a scan rate of 25 mV s^{-1}, (D) comparative CV profiles of bare Ni foam and CWS/Ni foam recorded using scan rate of 25 mV s^{-1}.

The effect of scan rate on the specific capacitance of CWS/Ni electrode (See Figure 3.4.6(B)) shows a high specific capacitance of about 626.7 F g^{-1} (equivalent to a specific capacity of about 208.9 mAh g^{-1} and areal capacitance of 438.68 mF cm^{-2}) obtained at a low scan rate of 5 mV s^{-1}.

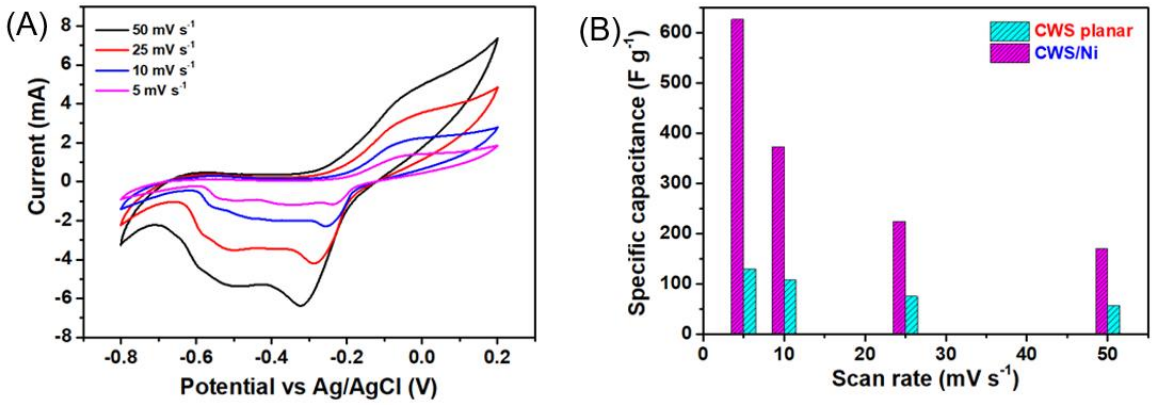

Figure. 3.4.7. (A) CV profiles of planar CWS electrode obtained using different scan rates over an OPW of -0.8 to 0.2 V, and (B) effect of scan rate on the specific capacitance of CWS planar electrode in comparison with CWS/Ni electrode.

To verify the role of nickel foam and the impact of 3D porous structure on the energy-storage properties of CWS/Ni electrode, the electrochemical analysis of bare nickel foam and planar-type CWS electrodes were also studied and compared in this work. The role of nickel foam on the overall specific capacitance of CWS/Ni electrode was analysed via comparing the CV profiles of bare Ni foam (Figure 3.4.6(C)) to that of CWS/Ni electrodes recorded using a scan rate of 25 mV s^{-1} (as shown in Figure 3.4.6(D)). It shows that the contribution of bare Ni foam is almost negligible on the overall specific capacitance of the CWS/Ni electrode. Further, the significance of CWS/Ni electrode was also analyzed via testing the planar type CWS electrode (fabricated using conventional slurry coating method using stainless steel current collectors) in three-electrode configuration. The effect of scan rate on the shape of the CV profiles and the specific capacitance of planar-type CWS electrodes are provided in Figure 3.4.7(A and B). The planar-type CWS electrode shows the Faradaic dominated capacitive behaviour and delivered a specific capacitance of about 130.4 F g^{-1} from the CV profiles recorded at a scan rate of 5 mV s^{-1}. At the same scan rate, the CWS/Ni electrode possess almost 4.8- fold higher specific capacitance which is mainly due to the (i) direct integration of CWS on the nickel foam, (ii) high electroactive surfaces, and (iii) elimination

of insulating polymeric binder, etc. The observed high specific capacitance in binder-free electrode over the planar type electrode is in good agreement with the previous reports available in the literature[35,39].

Figure 3.4.7(B) shows the GCD profiles of CWS/Ni electrode obtained at various current ranges (10 to 25 mA). The GCD profiles indicate the presence of distinct plateau regions (non-linear profiles)[56], demonstrating the pseudocapacitive nature of CWS/Ni electrode and is close in agreement with the CV profiles (Figure 3.4.7(A)). The effect of applied current on the specific capacitance of CWS/Ni electrode is provided in Figure 3.4.7(C). A high specific capacitance (specific capacity/areal capacitance) of 2666.6 F g^{-1} (888.8 mAh g^{-1}/1866.6 mF cm^{-2}) was obtained for the CWS/Ni electrode from the GCD profile obtained at a current of 10 mA. The obtained specific capacitance is higher compared to MoS_2/rGO grown on Ni foam (1071 F g^{-1})[59], Co_9S_8/Ni foam (1775 F g^{-1})[60], Ni_3S_2@β-NiS/Ni foam (1158 F g^{-1})[61] and so on. An increase in the applied current to 25 mA, the CWS/Ni electrode retained a specific capacitance (specific capacity/areal capacitance) of 529.76 F g^{-1} (176.58 mAh g^{-1}/370.8 mF cm^{-2}) suggesting better capacitive behaviour. Table 3.4.1 shows the performance superiority of the CWS/Ni electrode over the recently reported binder-free electrodes based on Ni foam. This superior performance of the CWS/Ni electrode is mainly due to the hierarchical CWS nanostructures grown on Ni foam better electrochemical ion pathways during the electrochemical charging and discharging process compared to the planar type CWS electrodes [62,63]. Further, the CWS/Ni electrode operates in the negative potential window -0.8 to 0.4 V which is an added advantage for supercapacitor devices since only a few materials are reported as negative electrode until now [64]. These studies demonstrated the better electrochemical properties of the CWS/Ni electrode and their ability to serve as a negative electrode for supercapacitor.

Table 3.4.1: Comparison on the specific capacitance of CWS/Ni electrode with the recently reported binder free electrodes based on TMCs, and TMOs.

S.No.	**Electrode**	**Mass loading (per cm^{-2})**	**Specific capacitance (F g^{-1})**	**Reference**
1	Ni_3S_2/Ni	3.5 mg	1691.4 (5 mA cm^{-2})	[65]
2	Ni-Co-Fe-S@NCAsNP	0.7 mg	2159.7 (7 A g^{-1})	[66]
3	$CoSe_2$/CC	1.7 mg	544 (1 mA cm^{-2})	[67]
4	Co_9S_8-NSA/Ni foam	2.8 mg	1098.8 (0.5 A g^{-1})	[68]
5	**$CoNi_2S_4$-rGO/Ni foam**	-	1680 (1 A g^{-1})	[69]
6	$CuCo_2O_4$/ Ni	3.3 mg	1569.9 (0.6 A g^{-1})	[70]
7	Mxene/Ni	0.5 mg	195.7 (2 A g^{-1})	[71]
8	Ni-Co LDH/Ni	0.5 mg	1435.3 (2 A g^{-1})	[71]
9	Mxene/Ni-Co LDH/Ni	1.0 mg	983.6 (2 A g^{-1})	[71]
10	NiTe/NiSe/Ni	2.1 mg	1868 (1 A g^{-1})	[72]
11	Rough CuS/Ni	2.4 mg	1124 (15 mA cm^{-2})	[32]
12	CuS/Ni	2.6 mg	500.1(15 mA cm^{-2})	[32]
13	CuS/Cu	0.3 mg	305 (0.6 mA cm^{-2})	[73]
14	MnO_2/Ni	0.29 mg	649 (1.7 A g^{-1})	[74]
15	MnO_2/FTO	0.1 mg	239 (0.1 mA cm^{-2})	[75]
16	CoS NWs / Ni	1.7 mg	800 (1 A g^{-1})	[76]
17	Co_9S_8 NTs / Ni	1.9 mg	1775 (4 A g^{-1})	[60]
18	WS_2/CC	4.4 mg	212 (4 mA cm^{-2})	[77]
19	WS_2/CFC	-	399 (1 A g^{-1})	[78]
20	CMS/Ni	1.0 mg	2222.5 (25 mA)	[39]
21	CWS/Ni	0.7 mg	2666.6 (10 mA)	This work

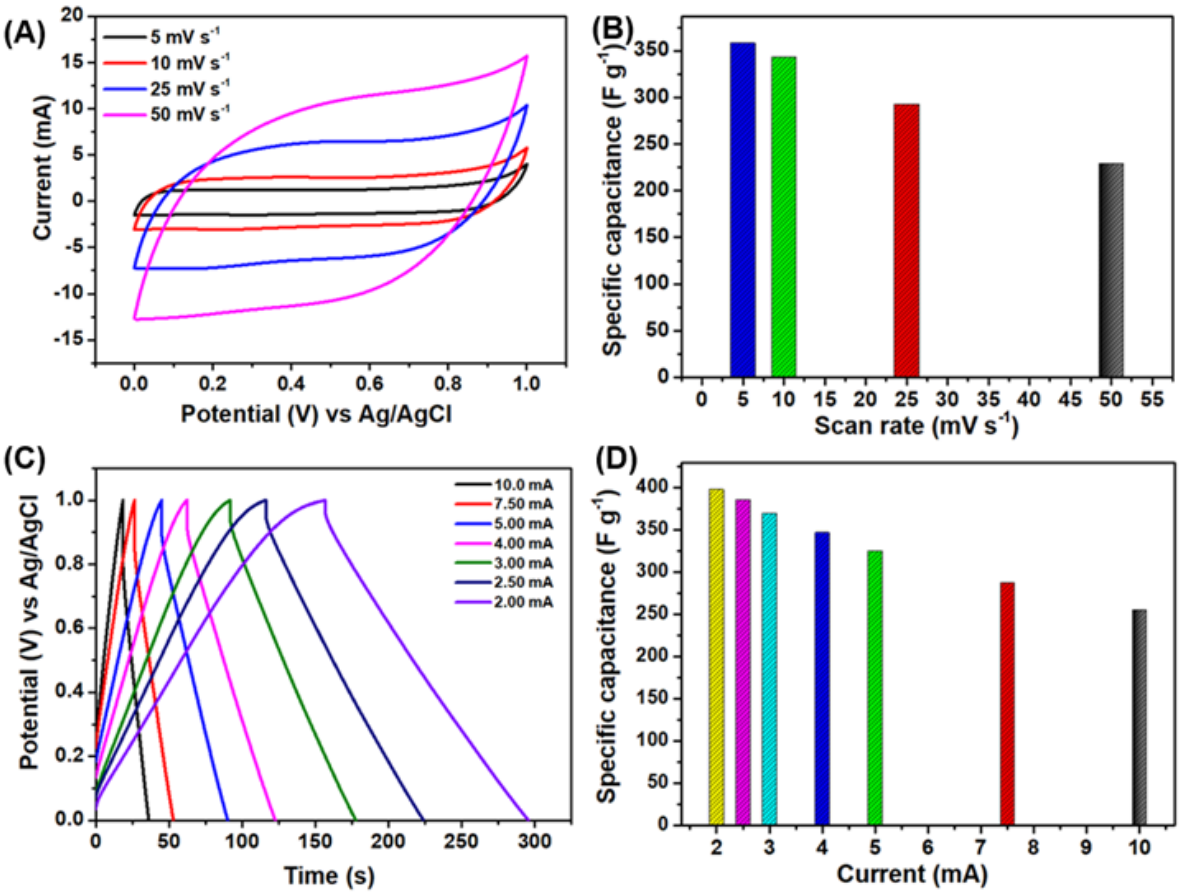

Figure 3.4.8. Electrochemical characterization of graphene electrode (A) Cyclic voltammetry profile measured under various scan rate. (B) Effect of scan rate on specific capacitance. (C) Charge-discharge profiles measured under various current. (D) Effect of current on the specific capacitance of graphene electrode.

To evaluate the device specific properties of the CWS/Ni electrode, asymmetric supercapacitor (ASC) configuration was constructed using graphene as a positive electrode. The electrochemical properties of graphene electrodes using three electrode configurations were evaluated using CV, and GCD analysis and the results are provided in Figure 3.4.8 (A - D). These studies indicated the presence of double layer capacitive properties of graphene electrodes with a specific capacitance of 397.7 F g^{-1} from GCD analysis recorded at a constant discharge current of 2 mA. Prior to the fabrication of the asymmetric supercapacitor, the charge accumulation on each electrode is balanced according to the standard

procedure[79,80]. After mass balancing, the CWS/Ni‖graphene ASC was constructed using a mass ratio of CWS/Ni and graphene of about 1:2. The CV and GCD profiles of the CWS/Ni‖graphene ASC device measured at a various operating voltage from 0.8 to 2.0 V is as shown in Figure 3.4.9 (A and B),. This study clearly indicated that the CWS/Ni‖graphene ASC device could work up to 1.8 V without voltage leap whereas at the higher voltage of 2.0 V there exist a sign of evolution.

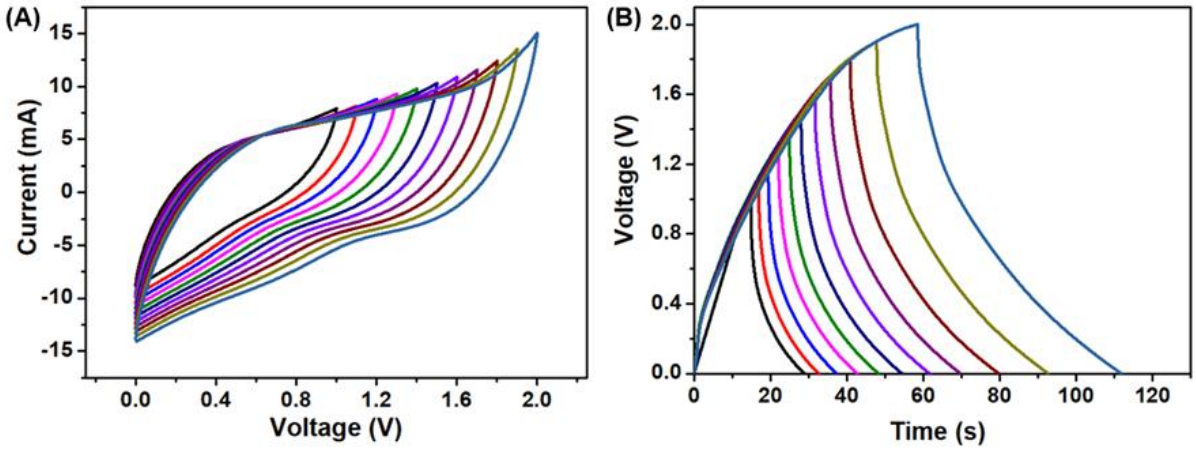

Figure 3.4.9. (A) Cyclic voltammetric profiles of CWS/Ni ‖graphene ASC measured over various operating potential window. (B) Charge-discharge profiles of CWS/Ni ‖graphene ASC measured over various operating potential window.

Figure 3.4.10 (A) shows the CV profiles of the CWS/Ni‖graphene ASC device measured at different rates (from 5 to 100 mV s^{-1}) over the potential window of 0 to 1.8 V. It shows the presence of a quasi-rectangular shaped curve indicating the ideal capacitive properties of the CWS/Ni‖graphene ASC[81]. The CWS/Ni‖graphene ASC device possesses a high specific capacitance of about 74.06 F g^{-1} (155.54 mF cm^{-2}) obtained from the CV profiles recorded at 5 mV s^{-1}. Further, the CWS/Ni‖graphene ASC still holds a specific capacitance of about 21.28 F g^{-1} (44.69 mF cm^{-2}) with an increase in scan rate up twenty-fold, suggesting their better rate capability[15]. Figure 3.4.10 (B) shows the GCD profiles of the CWS/Ni‖graphene ASC device recorded at different applied current ranges

from 0.75 to 5.00 mA. The GCD profiles of CWS/Ni ‖graphene ASC device recorded at high current ranges (7.5 to 30 mA) were provided in Figure S9(A), SI. The GCD profiles revealed the presence of sloppy-symmetric triangular shaped nature as evidence of ion intercalative nature of CWS/Ni ‖graphene ASC[15].

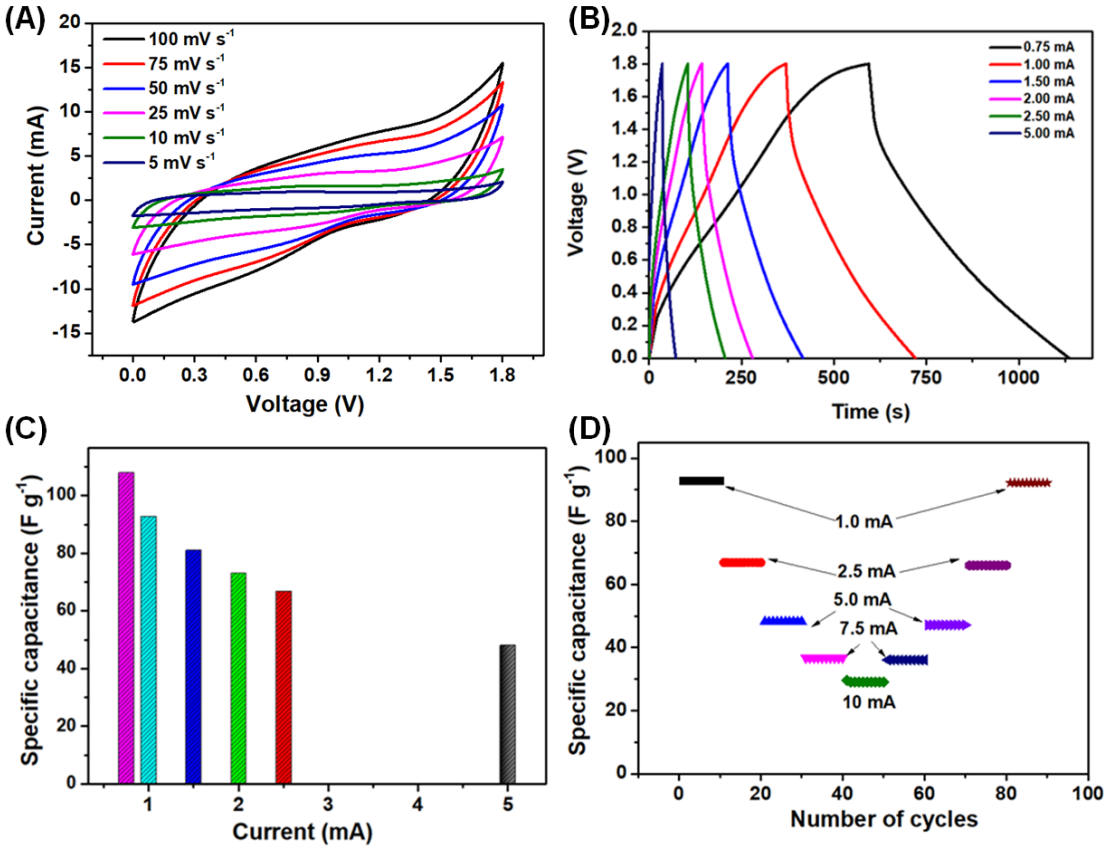

Figure 3.4.10. Electrochemical performances of CWS/Ni‖Graphene ASC in 1 M Li_2SO_4 electrolyte. (A) Cyclic voltammograms measured at operating voltage window (0.0 to 1.8 V) at various scan rate ranging from 5 to 100 mV s^{-1}, (B) Galvanostatic charge-discharge profile measured at potential window (0.0 to 1.8 V) at various current ranging from 0.75 to 5 mA, (C) effect of specific capacitance with respect to current. (D) Rate capability of the CWS/Ni ‖Graphene ASC device.

The effect of applied current ranges on the specific capacitance of CWS/Ni‖graphene ASC is provided in Figure 3.4.10(C) and Figure 3.4.11(B), which shows a high specific capacitance of about 107.93 F g^{-1} (226.67 mF cm^{-2}) was obtained for the

CWS/Ni‖graphene ASC from the discharge profile recorded using 0.75 mA. With an increase in the applied current to 5 mA the CWS/Ni‖graphene ASC delivered a capacitance retention of 44.6 % and still maintains the specific capacitance of 7.94 F g^{-1} (16.67 mF cm^{-2}) at a high current of 30 mA (Figure 3.4.11(B)) suggesting the excellent capacitive nature of the fabricated CWS/Ni‖graphene ASC device.

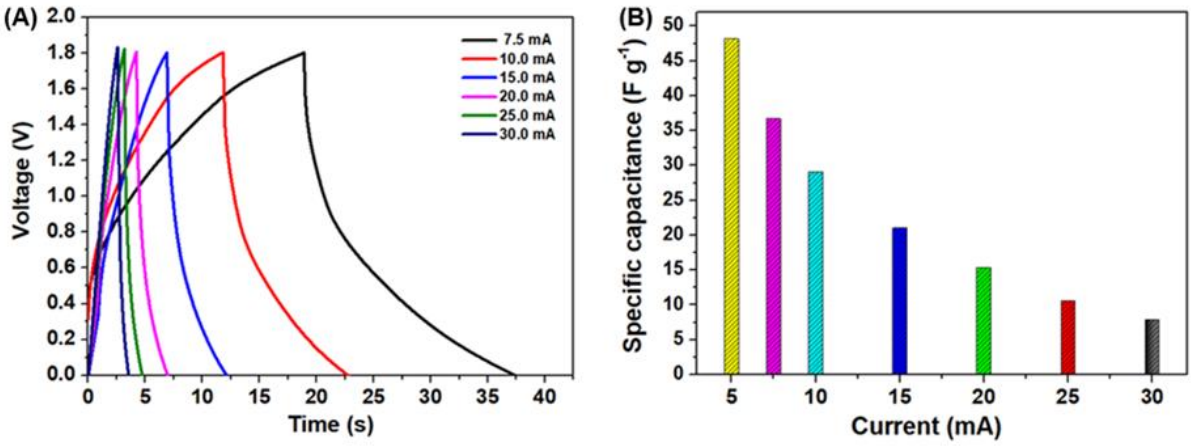

Figure 3.4.11. (A) Charge discharge profiles of CWS/Ni ‖graphene ASC measured at various current ranging from 7.5 to 30 mA. (B) Effect of current on the specific capacitance of CWS/Ni ‖graphene ASC.

Figure 3.4.10 (D) shows the rate capability studies of the CWS/Ni‖graphene ASC device by measuring the specific capacitance progressively over repetitive GCD cycles (ten cycles) via sweeping the current range from low to high (1.00 to 10.00 mA) and vice versa. The CWS/Ni‖graphene ASC device exhibited a very stable specific capacitance even after suffering sudden changes in the level of applied current ranges. After 90 continuous GCD measurements with different levels of applied current ranges, the CWS/Ni‖graphene ASC device still possess a specific capacitance retention of about 99.23 % (to its original capacitance). These studies on the rate capability analysis demonstrated that the CWS/Ni‖graphene ASC device can deliver energy at various levels of loads, which is one of the significant features determining the practical applications of supercapacitor [15,55].

The energy and power density of the CWS/Ni‖graphene ASC was determined from the GCD profiles and is represented in the form of Ragone plot (Figure 3.4.12(A). The CWS/Ni‖graphene ASC possesses a high energy density of 48.57 Wh kg^{-1} (102 µWh cm^{-2}) with a corresponding power density of 321.42 W kg^{-1} (0.675 mW cm^{-2}) obtained from the GCD profile recorded using a current of 0.75 mA. With an increase in current of 30 mA, the CWS/Ni‖graphene ASC still holds an energy density of 3.57 Wh kg^{-1} (7.5 µWh cm^{-2}) whereas the power density increases up to 12857 W kg^{-1} (27 mW cm^{-2}), respectively. The

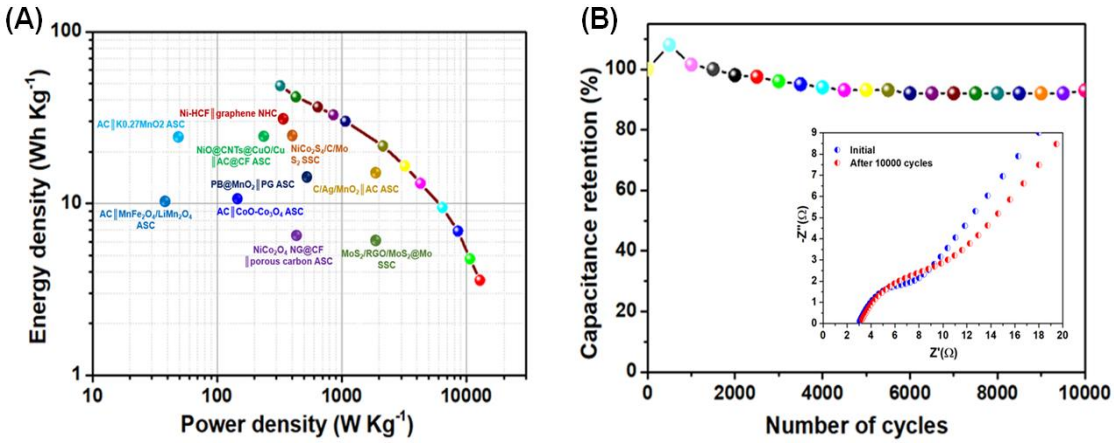

Figure 3.4.12. (A) Ragone plot of CWS/Ni‖Graphene ASC device, (B) cyclic stability of CWS/Ni‖Graphene ASC device over 10,000 cycles of charge-discharge. The inset in the (B) shows the Nyquist plot before and after 10,000 charge-discharge cycles of CWS/Ni‖Graphene ASC device.

energy density and power density of the CWS/Ni‖graphene ASC are quite higher compared to the state of art of asymmetric supercapacitors as evidenced from the Ragone plot. Table 3.4.2 and 3.4.3 shows the comparative performance metrics of the CWS/Ni‖graphene ASC device to that of reported ASCs in gravimetric and areal metrics, respectively, which further highlights the superior performances of CWS/Ni‖graphene ASC device.

Table 3.4.2: Energy/power performance metrics of CWS/Ni‖graphene compared with the reported ASCs devices utilizing TMO/TMC/binary TMC-based binder free electrodes.

S.No.	Device	Energy density ($Wh\ Kg^{-1}$)	Power density ($W\ Kg^{-1}$)	References
1	Ni-HCF‖graphene NHC	39.35	333.3	[79]
2	ND-$CoMoO_4$/NF ‖rGO/NF ASC	26	1832	[82]
3	NiO@CNTs@CuO/Cu‖AC@CF	26.32	219	[83]
4	AC‖$K_{0.27}MnO_2$	26	50	[84]
5	AC‖$MnFe_2O_4$/$LiMn_2O_4$ ASC	10	300	[85]
6	PB@MnO_2‖PG ASC	16.5	550	[86]
7	NiCo2O4 NG@CF ‖ PC	6.61	425	[87]
8	CuS@CD-GOH‖ rGO	28	700	[88]
9	C/Ag/MnO_2 hybrids ‖AC	16.6	1920	[89]
10	CuS ‖AC	15.06	392.9	[90]
11	$Ni(OH)_2$/rGO hydrogel ASC	28	5829	[91]
12	CuS-AC ‖AC	24.88	800	[92]
13	AC‖CoO/Co_3O_4	10.52	140	[93]
14	Co_9S_8-NSA/NF‖AC	20	828.5	[68]
15	CoS@eRG/NF‖AC	20	800	[94]
16	Co_3O_4@$Ni(OH)_2$‖AC	40	346.9	[95]
17	$NiCo_2S_4$@$Co(OH)_2$‖AC	35.89	400	[96]
18	$CoNi_2S_4$/NF‖AC	33.9	409	[97]
19	Ni-Co sulfide ‖AC	25	447	[98]
20	CWS/Ni ‖graphene	48.57	321.42	This work

Table 3.4.3: Arial energy/power performance metrics of CWS/Ni‖graphene compared with the reported ASCs devices.

S.No.	Device	Energy density	Power density	References
1	NiO ‖AC	99 μWh cm^{-2}	0.78 mW cm^{-2}	[99]
2	RuO_2/PEDOT: PSS‖ PEDOT: PSS	0.053 μWh cm^{-2}	147 μW cm^{-2}	[100]
3	CuO‖AC	82 μWh cm^{-2}	1.48 mW cm^{-2}	[101]
4	$NiCo_2O_4$ NG@CF‖porous cabon	9.46 μWh cm^{-2}	608 μW cm^{-2}	[87]
5	$Ni(OH)_2$‖mesoporous carbon	10 μWh cm^{-2}	7.3 mW cm^{-2}	[102]
6	MnO_2/graphene/carbon‖graphene	18.1 μWh cm^{-2}	0.15 mW cm^{-2}	[103]
7	Cobalt carbonate hydroxide‖N-graphene	0.77 μWh cm^{-2}	2.53 mW cm^{-2}	[104]
8	Ni-Co LDH‖ketjen black	14.4 μWh cm^{-2}	312.5 μW cm^{-2}	[105]
9	$Co_{0.85}Se$‖AC	35.65 μWh cm^{-2}	210 μW cm^{-2}	[106]
10	$Ni_{0.76}Co_{0.24}$ LDH‖AC	45.01 μWh cm^{-2}	300 μW cm^{-2}	[107]
11	Ag_3O_4 grafted NiO‖rGO	64.03 μWh cm^{-2}	275 μW cm^{-2}	[108]
12	NC LDH NSs on Ag@CC‖AC	78.8 μWh cm^{-2}	785 μW cm^{-2}	[109]
13	CWS/Ni ‖graphene	102 μWh cm^{-2}	27 mW cm^{-2}	This work

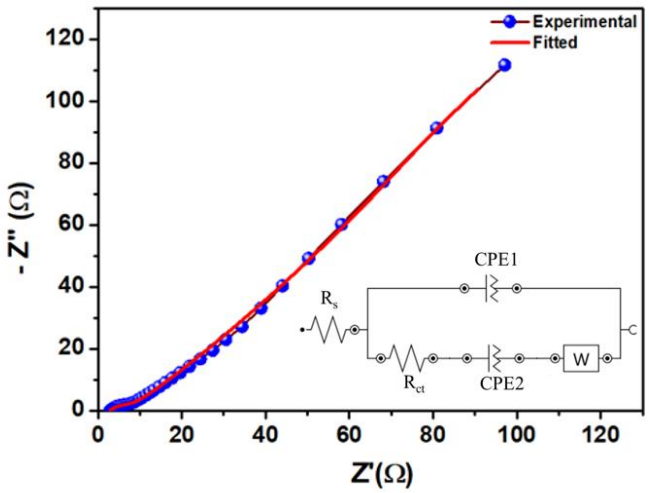

Figure 3.4.13. Nyquist plot of CWS/Ni‖graphene ASC. The inset shows the corresponding equivalent circuit model used for description of EIS.

The Nyquist plot the CWS/Ni‖graphene ASC device is provided in Figure 3.4.13, which can be explained based on an equivalent circuit model (given in the inset of Figure 3.4.13) comprising components such as solution resistance (R_s), charge-transfer resistance (R_{ct}), Constant phase element (CPE_1 and CPE_2) and Warburg impedance (W) [110]. The X-axis intercept obtained at high- frequency region corresponds to the bulk electrolyte solution resistance (R_s), and it is also known as equivalent series resistance (ESR) of the ASC[111]. The diameter of the semicircle observed at the high- frequency range can be related to charge transfer resistance (R_{ct}) which depends on the electrolyte ions accessible area and electrical conductivity of the electrode material[112]. The values of R_s and R_{ct} from the Nyquist plot are determined to be 2.96 Ω and 3.84 Ω respectively. The incorporation of two constant phase elements in the equivalent circuit corresponds to the (i) intercalation pseudocapacitance, and (ii) double layer capacitance raised from CWS/Ni and graphene electrodes in the ASC device, respectively[113]. The presence of the Warburg element in the model circuit related to the frequency dependent ion diffusion kinetics of electrolyte ions to the electroactive surface[113,114]. The electrochemical stability of the CWS/Ni‖graphene ASC SSC over 10,000 cycles of charge-discharge is presented in Figure 3.4.12(B) which showed capacitance retention of about 92.1 % of its initial capacitance. The EIS analysis recorded before and after the cyclic tests and the results are provided in the inset of Figure 3.4.12 (B). The Nyquist plot of the CWS/Ni SSC measured after 10,000 cycles shows an increase in solution resistance (from 2.96 to 3.07 Ω) and charge transfer resistance (from 3.84 to 5.92 Ω,) of CWS/Ni‖graphene ASC, which might be one of the reasons for the observed decay in capacitance over prolonged charge-discharge cycles[115].

3.4.4. Conclusions

The collective findings of this study demonstrated the use of binder free copper tungsten sulfide as a promising candidate as an electrode material with a high specific

capacitance (areal capacitance/ specific capacity) of 2666.6 F g^{-1}(888.8 mAh g^{-1}/1866.6 mF cm^{-2} at a constant applied current of 10 mA. The electrochemical investigation of the CWS/Ni‖graphene ASC suggests the superior charge-storage property with a high specific capacitance (107.9 F g^{-1}/226.67 mF cm^{-2}), high energy density (48.57 Wh kg^{-1}/ 102 μWh cm^{-2}), and excellent cyclic stability over 10000 cycles. Collectively, the experimental finding proved the potential use of CWS/Ni binder free electrode as a high-performance negative electrode towards the development of future generation supercapacitors.

3.4.5 References:

[1] C. Jin, Y. Cui, G. Zhang, W. Luo, Y. Liu, Y. Sun, Z. Tian, W. Zheng, Synthesis of copper-cobalt hybrid oxide microflowers as electrode material for supercapacitors, Chem. Eng. J. 343 (2018) 331–339. doi:10.1016/j.cej.2018.02.117.

[2] L. Hou, R. Bao, Z. Chen, M. Rehan, L. Tong, G. Pang, C. Yuan, Comparative investigation of hollow mesoporous $NiCo_2S_4$ ellipsoids with enhanced pseudo-capacitances towards high-performance asymmetric supercapacitors, Electrochim. Acta. 214 (2016) 76–84. doi:10.1016/j.electacta.2016.08.038.

[3] L. Yu, L. Hu, B. Anasori, Y.-T. Liu, Q. Zhu, P. Zhang, Y. Gogotsi, B. Xu, MXene-Bonded Activated Carbon as a Flexible Electrode for High-Performance Supercapacitors, ACS Energy Lett. (2018) 1597–1603. doi:10.1021/acsenergylett.8b00718.

[4] G. Wang, L. Zhang, J. Zhang, A review of electrode materials for electrochemical supercapacitors, Chem. Soc. Rev. 41 (2012) 797–828. doi:10.1039/C1CS15060J.

[5] H. Hua, S. Liu, Z. Chen, R. Bao, Y. Shi, L. Hou, G. Pang, K.N. Hui, X. Zhang, C. Yuan, Self-sacrifice Template Formation of Hollow Hetero-Ni_7S_6/Co_3S_4 Nanoboxes with Intriguing Pseudo-capacitance for High-performance Electrochemical Capacitors, Sci. Rep. 6 (2016) 20973. doi:10.1038/srep20973.

[6] X.-Y. Yu, L. Yu, X.W.D. Lou, Metal Sulfide Hollow Nanostructures for Electrochemical Energy Storage, Adv. Energy Mater. 6 (2016) 1501333. doi:10.1002/aenm.201501333.

[7] E. Martínez-Periñán, M.P. Down, C. Gibaja, E. Lorenzo, F. Zamora, C.E. Banks, Antimonene: A Novel 2D Nanomaterial for Supercapacitor Applications, Adv. Energy Mater. 8 (2018) 1702606. doi:10.1002/aenm.201702606.

[8] C. Zhan, P. Zhang, S. Dai, D. Jiang, Boron Supercapacitors, ACS Energy Lett. 1

(2016) 1241–1246. doi:10.1021/acsenergylett.6b00483.

[9] H. Xiao, Z.-S. Wu, L. Chen, F. Zhou, S. Zheng, W. Ren, H.-M. Cheng, X. Bao, One-Step Device Fabrication of Phosphorene and Graphene Interdigital Micro-Supercapacitors with High Energy Density, ACS Nano. 11 (2017) 7284–7292. doi:10.1021/acsnano.7b03288.

[10] P. Pazhamalai, K. Krishnamoorthy, V.K. Mariappan, S. Sahoo, S. Manoharan, S.-J. Kim, A High Efficacy Self-Charging $MoSe_2$ Solid-State Supercapacitor Using Electrospun Nanofibrous Piezoelectric Separator with Ionogel Electrolyte, Adv. Mater. Interfaces. 5 (2018) 1800055. doi:10.1002/admi.201800055.

[11] J. Feng, X. Sun, C. Wu, L. Peng, C. Lin, S. Hu, J. Yang, Y. Xie, Metallic Few-Layered VS_2 Ultrathin Nanosheets: High Two-Dimensional Conductivity for In-Plane Supercapacitors, J. Am. Chem. Soc. 133 (2011) 17832–17838. doi:10.1021/ja207176c.

[12] M. Acerce, D. Voiry, M. Chhowalla, Metallic 1T phase MoS_2 nanosheets as supercapacitor electrode materials, Nat. Nanotechnol. 10 (2015) 313–318. doi:10.1038/nnano.2015.40.

[13] C. Zhu, P. Yang, D. Chao, X. Wang, X. Zhang, S. Chen, B.K. Tay, H. Huang, H. Zhang, W. Mai, H.J. Fan, All Metal Nitrides Solid-State Asymmetric Supercapacitors, Adv. Mater. 27 (2015) 4566–4571. doi:10.1002/adma.201501838.

[14] C.J. Zhang, B. Anasori, A. Seral-Ascaso, S.-H. Park, N. McEvoy, A. Shmeliov, G.S. Duesberg, J.N. Coleman, Y. Gogotsi, V. Nicolosi, Transparent, Flexible, and Conductive 2D Titanium Carbide (MXene) Films with High Volumetric Capacitance, Adv. Mater. 29 (2017) 1702678. doi:10.1002/adma.201702678.

[15] K. Krishnamoorthy, P. Pazhamalai, S.-J. Kim, Two-dimensional siloxene nanosheets: novel high-performance supercapacitor electrode materials, Energy Environ. Sci. 11 (2018) 1595–1602. doi:10.1039/C8EE00160J.

[16] X. Xiao, H. Song, S. Lin, Y. Zhou, X. Zhan, Z. Hu, Q. Zhang, J. Sun, B. Yang, T. Li, L. Jiao, J. Zhou, J. Tang, Y. Gogotsi, Scalable salt-templated synthesis of two-dimensional transition metal oxides, Nat. Commun. 7 (2016) 11296. doi:10.1038/ncomms11296.

[17] Y. Ma, C. Hou, H. Zhang, M. Qiao, Y. Chen, H. Zhang, Q. Zhang, Z. Guo, Morphology-dependent electrochemical supercapacitors in multi-dimensional polyaniline nanostructures, J. Mater. Chem. A. 5 (2017) 14041–14052. doi:10.1039/C7TA03279J.

[18] R. Sahoo, A.K. Sasmal, C. Ray, S. Dutta, A. Pal, T. Pal, Suitable Morphology Makes $CoSn(OH)_6$ Nanostructure a Superior Electrochemical Pseudocapacitor, ACS Appl. Mater. Interfaces. 8 (2016) 17987–17998. doi:10.1021/acsami.6b02568.

[19] J. Kunstmann, F. Mooshammer, P. Nagler, A. Chaves, F. Stein, N. Paradiso, G. Plechinger, C. Strunk, C. Schüller, G. Seifert, D.R. Reichman, T. Korn, Momentum-space indirect interlayer excitons in transition-metal dichalcogenide van der Waals heterostructures, Nat. Phys. (2018). doi:10.1038/s41567-018-0123-y.

[20] P. Miró, M. Audiffred, T. Heine, An atlas of two-dimensional materials, Chem. Soc. Rev. 43 (2014) 6537–6554. doi:10.1039/C4CS00102H.

[21] L. Hou, Y. Shi, S. Zhu, M. Rehan, G. Pang, X. Zhang, C. Yuan, Hollow mesoporous hetero-$NiCo_2S_4$/Co_9S_8 submicro-spindles: unusual formation and excellent pseudocapacitance towards hybrid supercapacitors, J. Mater. Chem. A. 5 (2017) 133–144. doi:10.1039/C6TA05788H.

[22] L. Mei, T. Yang, C. Xu, M. Zhang, L. Chen, Q. Li, T. Wang, Hierarchical mushroom-like $CoNi_2S_4$ arrays as a novel electrode material for supercapacitors, Nano Energy. 3 (2014) 36–45. doi:10.1016/j.nanoen.2013.10.004.

[23] P. Zhang, B.Y. Guan, L. Yu, X.W.D. Lou, Formation of Double-Shelled Zinc-Cobalt

Sulfide Dodecahedral Cages from Bimetallic Zeolitic Imidazolate Frameworks for Hybrid Supercapacitors, Angew. Chemie Int. Ed. 56 (2017) 7141–7145. doi:10.1002/anie.201702649.

[24] P. Kulkarni, S.K. Nataraj, R.G. Balakrishna, D.H. Nagaraju, M. V. Reddy, Nanostructured binary and ternary metal sulfides: synthesis methods and their application in energy conversion and storage devices, J. Mater. Chem. A. 5 (2017) 22040–22094. doi:10.1039/C7TA07329A.

[25] Q. Li, Y. Xu, S. Zheng, X. Guo, H. Xue, H. Pang, Recent Progress in Some Amorphous Materials for Supercapacitors, Small. 14 (2018) 1800426. doi:10.1002/smll.201800426.

[26] B.Y. Guan, L. Yu, X. Wang, S. Song, X.W.D. Lou, Formation of Onion-Like $NiCo_2S_4$ Particles via Sequential Ion-Exchange for Hybrid Supercapacitors, Adv. Mater. 29 (2017) 1605051. doi:10.1002/adma.201605051.

[27] X. Hu, W. Shao, X. Hang, X. Zhang, W. Zhu, Y. Xie, Superior Electrical Conductivity in Hydrogenated Layered Ternary Chalcogenide Nanosheets for Flexible All-Solid-State Supercapacitors, Angew. Chemie - Int. Ed. 55 (2016) 5733–5738. doi:10.1002/anie.201600029.

[28] E.A. Pruss, B.S. Snyder, A.M. Stacy, A New Layered Ternary Sulfide: Formation of Cu_2WS_4 by Reaction of WS_4^{2-} and Cu^+ Ions, Angew. Chemie Int. Ed. English. 32 (1993) 256–257. doi:10.1002/anie.199302561.

[29] Q. Jia, Y.C. Zhang, J. Li, Y. Chen, B. Xu, Hydrothermal synthesis of Cu_2WS_4 as a visible-light-activated photocatalyst in the reduction of aqueous Cr(VI), Mater. Lett. 117 (2014) 24–27. doi:10.1016/j.matlet.2013.11.110.

[30] D. Jing, M. Liu, Q. Chen, L. Guo, Efficient photocatalytic hydrogen production under visible light over a novel W-based ternary chalcogenide photocatalyst prepared by a

hydrothermal process, Int. J. Hydrogen Energy. 35 (2010) 8521–8527. doi:10.1016/j.ijhydene.2010.04.170.

[31] S. Kannan, P. Vinitha, K. Mohanraj, G. Sivakumar, Antibacterial studies of novel Cu_2WS_4 ternary chalcogenide synthesized by hydrothermal process, J. Solid State Chem. 258 (2018) 376–382. doi:10.1016/j.jssc.2017.11.005.

[32] Y. Zhang, J. Xu, Y. Zheng, X. Hu, Y. Shang, Y. Zhang, Interconnected CuS nanowalls with rough surfaces grown on nickel foam as high-performance electrodes for supercapacitors, RSC Adv. 6 (2016) 59976–59983. doi:10.1039/C6RA10327H.

[33] S. Ratha, C.S. Rout, Supercapacitor Electrodes Based on Layered Tungsten Disulfide-Reduced Graphene Oxide Hybrids Synthesized by a Facile Hydrothermal Method, ACS Appl. Mater. Interfaces. 5 (2013) 11427–11433. doi:10.1021/am403663f.

[34] F. Chen, H. Wang, S. Ji, V. Linkov, R. Wang, Core-shell structured Ni_3S_2@$Co(OH)_2$ nano-wires grown on Ni foam as binder-free electrode for asymmetric supercapacitors, Chem. Eng. J. 345 (2018) 48–57. doi:10.1016/j.cej.2018.03.152.

[35] S. Xu, G. Wei, J. Li, Y. Ji, N. Klyui, V. Izotov, W. Han, Binder-free $Ti_3C_2T_x$ MXene electrode film for supercapacitor produced by electrophoretic deposition method, Chem. Eng. J. 317 (2017) 1026–1036. doi:10.1016/j.cej.2017.02.144.

[36] W. Zuo, R. Li, C. Zhou, Y. Li, J. Xia, J. Liu, Battery-Supercapacitor Hybrid Devices: Recent Progress and Future Prospects, Adv. Sci. 4 (2017) 1600539. doi:10.1002/advs.201600539.

[37] C. Lamiel, V.H. Nguyen, D.R. Kumar, J.-J. Shim, Microwave-assisted binder-free synthesis of 3D Ni-Co-Mn oxide nanoflakes@Ni foam electrode for supercapacitor applications, Chem. Eng. J. 316 (2017) 1091–1102. doi:10.1016/j.cej.2017.02.004.

[38] H. Hosseini, S. Shahrokhian, Advanced binder-free electrode based on core–shell nanostructures of mesoporous $Co_3V_2O_8$-$Ni_3V_2O_8$ thin layers@porous carbon

nanofibers for high-performance and flexible all-solid-state supercapacitors, Chem. Eng. J. 341 (2018) 10–26. doi:10.1016/j.cej.2018.02.019.

[39] S. Sahoo, K. Krishnamoorthy, P. Pazhamalai, S.-J. Kim, Copper molybdenum sulfide anchored nickel foam: a high performance, binder-free, negative electrode for supercapacitors, Nanoscale. 10 (2018) 13883–13888. doi:10.1039/C8NR03998D.

[40] P. Xu, J. Kang, J.-B. Choi, J. Suhr, J. Yu, F. Li, J.-H. Byun, B.-S. Kim, T.-W. Chou, Laminated Ultrathin Chemical Vapor Deposition Graphene Films Based Stretchable and Transparent High-Rate Supercapacitor, ACS Nano. 8 (2014) 9437–9445. doi:10.1021/nn503570j.

[41] K. Krishnamoorthy, G.-S. Kim, S.J. Kim, Graphene nanosheets: Ultrasound assisted synthesis and characterization, Ultrason. Sonochem. 20 (2013) 644–649. doi:10.1016/j.ultsonch.2012.09.007.

[42] P. Pazhamalai, K. Krishnamoorthy, M.S.P. Sudhakaran, S.J. Kim, Fabrication of High-Performance Aqueous Li-Ion Hybrid Capacitor with $LiMn_2O_4$ and Graphene, ChemElectroChem. 4 (2017) 396–403. doi:10.1002/celc.201600550.

[43] W. Shi, S. Song, H. Zhang, Hydrothermal synthetic strategies of inorganic semiconducting nanostructures, Chem. Soc. Rev. 42 (2013) 5714. doi:10.1039/c3cs60012b.

[44] K. Krishnamoorthy, G.K. Veerasubramani, S. Radhakrishnan, S.J. Kim, One pot hydrothermal growth of hierarchical nanostructured Ni_3S_2 on Ni foam for supercapacitor application, Chem. Eng. J. 251 (2014) 116–122. doi:10.1016/j.cej.2014.04.006.

[45] Q. Wang, R. Gao, J. Li, Porous, self-supported Ni_3S_2/Ni nanoarchitectured electrode operating through efficient lithium-driven conversion reactions, Appl. Phys. Lett. 90 (2007) 143107. doi:10.1063/1.2716308.

[46] S. Ni, X. Yang, T. Li, Fabrication of porous Ni_3S_2/Ni nanostructured electrode and its application in lithium ion battery, Mater. Chem. Phys. 132 (2012) 1103–1107. doi:10.1016/j.matchemphys.2011.12.077.

[47] F. Ozel, E. Aslan, A. Sarilmaz, I. Hatay Patir, Hydrogen Evolution Catalyzed by Cu_2WS_4 at Liquid–Liquid Interfaces, ACS Appl. Mater. Interfaces. 8 (2016) 25881–25887. doi:10.1021/acsami.6b05582.

[48] Z. Cheng, H. Abernathy, M. Liu, Raman Spectroscopy of Nickel Sulfide Ni_3S_2, J. Phys. Chem. C. 111 (2007) 17997–18000. doi:10.1021/jp0770209.

[49] M. Yıldırım, F. Özel, A. Sarılmaz, A. Aljabour, İ.H. Patır, Investigation of structural, optical and dielectrical properties of Cu_2WS_4 thin film, J. Mater. Sci. Mater. Electron. 28 (2017) 6712–6721. doi:10.1007/s10854-017-6365-0.

[50] S. Kannan, P. Vinitha, K. Mohanraj, G. Sivakumar, Antibacterial studies of novel Cu_2WS_4 ternary chalcogenide synthesized by hydrothermal process, J. Solid State Chem. 258 (2018) 376–382. doi:10.1016/j.jssc.2017.11.005.

[51] C.J. Crossland, J.S.O. Evans, Synthesis and characterisation of a new high pressure polymorph of Cu_2WS_4, Chem. Commun. (2003) 2292. doi:10.1039/b306633a.

[52] X. Mao, Y. Xu, Q. Xue, W. Wang, D. Gao, Ferromagnetism in exfoliated tungsten disulfide nanosheets, Nanoscale Res. Lett. 8 (2013) 430. doi:10.1186/1556-276X-8-430.

[53] L. Yang, X. Wu, X. Zhu, C. He, M. Meng, Z. Gan, P.K. Chu, Amorphous nickel/cobalt tungsten sulfide electrocatalysts for high-efficiency hydrogen evolution reaction, Appl. Surf. Sci. 341 (2015) 149–156. doi:10.1016/j.apsusc.2015.03.018.

[54] C.V. V. Muralee Gopi, S. Ravi, S.S. Rao, A. Eswar Reddy, H.-J. Kim, Carbon nanotube/metal-sulfide composite flexible electrodes for high-performance quantum dot-sensitized solar cells and supercapacitors, Sci. Rep. 7 (2017) 46519.

doi:10.1038/srep46519.

[55] X. Xiong, D. Ding, D. Chen, G. Waller, Y. Bu, Z. Wang, M. Liu, Three-dimensional ultrathin $Ni(OH)_2$ nanosheets grown on nickel foam for high-performance supercapacitors, Nano Energy. 11 (2015) 154–161. doi:10.1016/j.nanoen.2014.10.029.

[56] Y. Gogotsi, R.M. Penner, Energy Storage in Nanomaterials – Capacitive, Pseudocapacitive, or Battery-like?, ACS Nano. 12 (2018) 2081–2083. doi:10.1021/acsnano.8b01914.

[57] K.V. Sankar, R.K. Selvan, The ternary $MnFe_2O_4$/graphene/polyaniline hybrid composite as negative electrode for supercapacitors, J. Power Sources. 275 (2015) 399–407. doi:10.1016/j.jpowsour.2014.10.183.

[58] H. Yin, C. Song, Y. Wang, S. Li, M. Zeng, Z. Zhang, Z. Zhu, K. Yu, Influence of morphologies and pseudocapacitive contributions for charge storage in V_2O_5 micro/nano-structures, Electrochim. Acta. 111 (2013) 762–770. doi:10.1016/j.electacta.2013.08.005.

[59] R.N. Bulakhe, V.H. Nguyen, J.-J. Shim, Layer-structured nanohybrid MoS_2@rGO on 3D nickel foam for high performance energy storage applications, New J. Chem. 41 (2017) 1473–1482. doi:10.1039/C6NJ02590K.

[60] J. Pu, Z. Wang, K. Wu, N. Yu, E. Sheng, Co_9S_8 nanotube arrays supported on nickel foam for high-performance supercapacitors, Phys. Chem. Chem. Phys. 16 (2014) 785–791. doi:10.1039/C3CP54192D.

[61] W. Li, S. Wang, L. Xin, M. Wu, X. Lou, Single-crystal β-NiS nanorod arrays with a hollow-structured Ni_3S_2 framework for supercapacitor applications, J. Mater. Chem. A. 4 (2016) 7700–7709. doi:10.1039/C6TA01133K.

[62] Y. Wang, H. Wu, L. Huang, H. Zhao, Z. Liu, X. Chen, H. Liu, Y. Zhang, Hierarchically Porous N,S-Codoped Carbon-Embedded Dual Phase MnO/MnS

Nanoparticles for Efficient Lithium Ion Storage, Inorg. Chem. 57 (2018) 7993–8001. doi:10.1021/acs.inorgchem.8b01156.

[63] J. Mujtaba, H. Sun, G. Huang, K. Mølhave, Y. Liu, Y. Zhao, X. Wang, S. Xu, J. Zhu, Nanoparticle Decorated Ultrathin Porous Nanosheets as Hierarchical Co_3O_4 Nanostructures for Lithium Ion Battery Anode Materials, Sci. Rep. 6 (2016) 20592. doi:10.1038/srep20592.

[64] X.J. Ma, W. Bin Zhang, L. Bin Kong, Y.C. Luo, L. Kang, VO_2: From negative electrode material to symmetric electrochemical capacitor, RSC Adv. 5 (2015) 97239–97247. doi:10.1039/c5ra18758c.

[65] S. Chen, Y. Li, B. Wu, Z. Wu, F. Li, J. Wu, P. Liu, H. Li, 3D meso/macroporous Ni_3S_2@Ni composite electrode for high-performance supercapacitor, Electrochim. Acta. 275 (2018) 40–49. doi:10.1016/j.electacta.2018.04.152.

[66] S. Rahimi, S. Shahrokhian, H. Hosseini, Ternary nickel cobalt iron sulfides ultrathin nanosheets grown on 3-D nickel nanocone arrays-nickel plate current collector as a binder free electrode for fabrication of highly performance supercapacitors, J. Electroanal. Chem. 810 (2018) 78–85. doi:10.1016/j.jelechem.2018.01.004.

[67] T. Chen, S. Li, P. Gui, J. Wen, X. Fu, G. Fang, Bifunctional bamboo-like $CoSe_2$ arrays for high-performance asymmetric supercapacitor and electrocatalytic oxygen evolution, Nanotechnology. 29 (2018) 205401. doi:10.1088/1361-6528/aab19b.

[68] X. Han, K. Tao, D. Wang, L. Han, Design of a porous cobalt sulfide nanosheet array on Ni foam from zeolitic imidazolate frameworks as an advanced electrode for supercapacitors, Nanoscale. 10 (2018) 2735–2741. doi:10.1039/C7NR07931A.

[69] Z. Gao, C. Chen, J. Chang, L. Chen, P. Wang, D. Wu, F. Xu, Y. Guo, K. Jiang, Enhanced cycleability of faradic $CoNi_2S_4$ electrode by reduced graphene oxide coating for efficient asymmetric supercapacitor, Electrochim. Acta. 281 (2018) 394–404.

doi:10.1016/j.electacta.2018.05.194.

[70] W. Liu, Y. Feng, L. Sun, Y. Zhang, G. Wang, L. Zhao, M. Meng, J. Li, K. Liu, Hierarchical $CuCo_2O_4$ nanourchin supported by Ni foam with superior electrochemical performance, J. Alloys Compd. 756 (2018) 68–75. doi:10.1016/j.jallcom.2018.05.026.

[71] H. Li, F. Musharavati, E. Zalenezhad, X. Chen, K.N. Hui, K.S. Hui, Electrodeposited NiCo layered double hydroxides on titanium carbide as a binder-free electrode for supercapacitors, Electrochim. Acta. 261 (2018) 178–187. doi:10.1016/j.electacta.2017.12.139.

[72] B. Ye, M. Huang, Q. Bao, S. Jiang, J. Ge, H. Zhao, L. Fan, J. Lin, J. Wu, Construction of NiTe/NiSe Composites on Ni Foam for High-Performance Asymmetric Supercapacitor, ChemElectroChem. 5 (2018) 507–514. doi:10.1002/celc.201701033.

[73] Y.-K. Hsu, Y.-C. Chen, Y.-G. Lin, Synthesis of copper sulfide nanowire arrays for high-performance supercapacitors, Electrochim. Acta. 139 (2014) 401–407. doi:10.1016/j.electacta.2014.06.138.

[74] A. Kumar, A. Sanger, A. Kumar, Y. Kumar, R. Chandra, Sputtered Synthesis of MnO_2 Nanorods as Binder Free Electrode for High Performance Symmetric Supercapacitors, Electrochim. Acta. 222 (2016) 1761–1769. doi:10.1016/j.electacta.2016.10.161.

[75] K. Jeyasubramanian, T.S. Gokul Raja, S. Purushothaman, M.V. Kumar, I. Sushmitha, Supercapacitive performances of MnO_2 nanostructures grown on hierarchical Cu nano leaves via electrodeposition, Electrochim. Acta. 227 (2017) 401–409. doi:10.1016/j.electacta.2017.01.044.

[76] L. Jinlong, L. Tongxiang, Y. Meng, K. Suzuki, H. Miura, Comparing different microstructures of CoS formed on bare Ni foam and Ni foam coated graphene and their supercapacitors performance, Colloids Surfaces A Physicochem. Eng. Asp. 529 (2017) 57–63. doi:10.1016/j.colsurfa.2017.05.074.

[77] S. Liu, Y. Zeng, M. Zhang, S. Xie, Y. Tong, F. Cheng, X. Lu, Binder-free WS_2 nanosheets with enhanced crystallinity as a stable negative electrode for flexible asymmetric supercapacitors, J. Mater. Chem. A. 5 (2017) 21460–21466. doi:10.1039/C7TA07009H.

[78] X. Shang, J.-Q. Chi, S.-S. Lu, J.-X. Gou, B. Dong, X. Li, Y.-R. Liu, K.-L. Yan, Y.-M. Chai, C.-G. Liu, Carbon fiber cloth supported interwoven WS_2 nanosplates with highly enhanced performances for supercapacitors, Appl. Surf. Sci. 392 (2017) 708–714. doi:10.1016/j.apsusc.2016.09.058.

[79] K. Krishnamoorthy, P. Pazhamalai, S. Sahoo, J.H. Lim, K.H. Choi, S.J. Kim, A High-Energy Aqueous Sodium-Ion Capacitor with Nickel Hexacyanoferrate and Graphene Electrodes, ChemElectroChem. 4 (2017) 3302–3308. doi:10.1002/celc.201700690.

[80] Q. Pan, Y. Liu, L. Zhao, Co_9S_8/Mo_2S_3 nanorods on CoS_2 laminar arrays as advanced electrode with superior rate properties and long cycle life for asymmetric supercapacitors, Chem. Eng. J. 351 (2018) 603–612. doi:10.1016/j.cej.2018.06.131.

[81] S. Vijayan, B. Kirubasankar, P. Pazhamalai, A.K. Solarajan, S. Angaiah, Electrospun Nd^{3+} -Doped $LiMn_2O_4$ Nanofibers as High-Performance Cathode Material for Li-Ion Capacitors, ChemElectroChem. 4 (2017) 2059–2067. doi:10.1002/celc.201700161.

[82] S.H. Kazemi, M. Tabibpour, M.A. Kiani, H. Kazemi, An advanced asymmetric supercapacitor based on a binder-free electrode fabricated from ultrathin $CoMoO_4$ nano-dandelions, RSC Adv. 6 (2016) 71156–71164. doi:10.1039/c6ra05703a.

[83] G. Nagaraju, S.C. Sekhar, J.S. Yu, Utilizing Waste Cable Wires for High-Performance Fiber-Based Hybrid Supercapacitors: An Effective Approach to Electronic-Waste Management, Adv. Energy Mater. 8 (2018) 1702201. doi:10.1002/aenm.201702201.

[84] Q. Qu, L. Li, S. Tian, W. Guo, Y. Wu, R. Holze, A cheap asymmetric supercapacitor with high energy at high power: Activated carbon//$K_{0.27}MnO_2 \cdot 0.6H_2O$, J. Power

Sources. 195 (2010) 2789–2794. doi:10.1016/j.jpowsour.2009.10.108.

[85] Y.P. Lin, N.L. Wu, Characterization of $MnFe_2O_4/LiMn_2O_4$ aqueous asymmetric supercapacitor, J. Power Sources. 196 (2011) 851–854. doi:10.1016/j.jpowsour.2010.07.066.

[86] A.K. Das, R. Bera, A. Maitra, S.K. Karan, S. Paria, L. Halder, S.K. Si, A. Bera, B.B. Khatua, Fabrication of an advanced asymmetric supercapacitor based on a microcubical PB@MnO_2 hybrid and PANI/GNP composite with excellent electrochemical behaviour, J. Mater. Chem. A. 5 (2017) 22242–22254. doi:10.1039/c7ta05134d.

[87] S.T.T. Senthilkumar, N. Fu, Y. Liu, Y. Wang, L. Zhou, H. Huang, Flexible fiber hybrid supercapacitor with $NiCo_2O_4$ nanograss@carbon fiber and bio-waste derived high surface area porous carbon, Electrochim. Acta. 211 (2016) 411–419. doi:10.1016/j.electacta.2016.06.059.

[88] B. De, T. Kuila, N.H. Kim, J.H. Lee, Carbon dot stabilized copper sulphide nanoparticles decorated graphene oxide hydrogel for high performance asymmetric supercapacitor, Carbon N. Y. 122 (2017) 247–257. doi:10.1016/j.carbon.2017.06.076.

[89] X. Cai, H. Bai, Y. Liu, W. Shi, Facile in situ synthesis of Ag and MnO_2 anchored on carbon microtubes for high-performance asymmetric supercapacitor applications, Appl. Mater. Today. 11 (2018) 193–199. doi:10.1016/j.apmt.2018.02.005.

[90] J. Zhang, H. Feng, J. Yang, Q. Qin, H. Fan, C. Wei, W. Zheng, Solvothermal Synthesis of Three-Dimensional Hierarchical CuS Microspheres from a Cu-Based Ionic Liquid Precursor for High-Performance Asymmetric Supercapacitors, ACS Appl. Mater. Interfaces. 7 (2015) 21735–21744. doi:10.1021/acsami.5b04452.

[91] H. Wang, Y. Song, W. Liu, L. Yan, Three dimensional $Ni(OH)_2$/rGO hydrogel as binder-free electrode for asymmetric supercapacitor, J. Alloys Compd. 735 (2018)

2428–2435. doi:10.1016/j.jallcom.2017.11.358.

[92] G. Wang, M. Zhang, L. Lu, H. Xu, Z. Xiao, S. Liu, S. Gao, Z. Yu, One-Pot Synthesis of CuS Nanoflower-Decorated Active Carbon Layer for High-Performance Asymmetric Supercapacitors, ChemNanoMat. (2018). doi:10.1002/cnma.201800179.

[93] M. Pang, G. Long, S. Jiang, Y. Ji, W. Han, B. Wang, X. Liu, Y. Xi, D. Wang, F. Xu, Ethanol-assisted solvothermal synthesis of porous nanostructured cobalt oxides (CoO/Co_3O_4) for high-performance supercapacitors, Chem. Eng. J. 280 (2015) 377–384. doi:10.1016/j.cej.2015.06.053.

[94] J. Shi, X. Li, G. He, L. Zhang, M. Li, Electrodeposition of high-capacitance 3D CoS/graphene nanosheets on nickel foam for high-performance aqueous asymmetric supercapacitors, J. Mater. Chem. A. 3 (2015) 20619–20626. doi:10.1039/C5TA04464B.

[95] X. Bai, Q. Liu, J. Liu, H. Zhang, Z. Li, X. Jing, P. Liu, J. Wang, R. Li, Hierarchical Co_3O_4@$Ni(OH)_2$ core-shell nanosheet arrays for isolated all-solid state supercapacitor electrodes with superior electrochemical performance, Chem. Eng. J. 315 (2017) 35–45. doi:10.1016/j.cej.2017.01.010.

[96] R. Li, S. Wang, Z. Huang, F. Lu, T. He, $NiCo_2S_4$@$Co(OH)_2$ core-shell nanotube arrays in situ grown on Ni foam for high performances asymmetric supercapacitors, J. Power Sources. 312 (2016) 156–164. doi:10.1016/j.jpowsour.2016.02.047.

[97] W. Hu, R. Chen, W. Xie, L. Zou, N. Qin, D. Bao, $CoNi_2S_4$ Nanosheet Arrays Supported on Nickel Foams with Ultrahigh Capacitance for Aqueous Asymmetric Supercapacitor Applications, ACS Appl. Mater. Interfaces. 6 (2014) 19318–19326. doi:10.1021/am5053784.

[98] Y. Li, L. Cao, L. Qiao, M. Zhou, Y. Yang, P. Xiao, Y. Zhang, Ni–Co sulfide nanowires on nickel foam with ultrahigh capacitance for asymmetric supercapacitors,

J. Mater. Chem. A. 2 (2014) 6540–6548. doi:10.1039/C3TA15373H.

[99] F. Luan, G. Wang, Y. Ling, X. Lu, H. Wang, Y. Tong, X.-X. Liu, Y. Li, High energy density asymmetric supercapacitors with a nickel oxide nanoflake cathode and a 3D reduced graphene oxide anode, Nanoscale. 5 (2013) 7984. doi:10.1039/c3nr02710d.

[100] C. (John) Zhang, T.M. Higgins, S.-H. Park, S.E. O'Brien, D. Long, J.N. Coleman, V. Nicolosi, Highly flexible and transparent solid-state supercapacitors based on RuO_2 /PEDOT:PSS conductive ultrathin films, Nano Energy. 28 (2016) 495–505. doi:10.1016/j.nanoen.2016.08.052.

[101] S.M. Cha, G. Nagaraju, S. Chandra Sekhar, J.S. Yu, A facile drop-casting approach to nanostructured copper oxide-painted conductive woven textile as binder-free electrode for improved energy storage performance in redox-additive electrolyte, J. Mater. Chem. A. 5 (2017) 2224–2234. doi:10.1039/C6TA10428B.

[102] X. Dong, Z. Guo, Y. Song, M. Hou, J. Wang, Y. Wang, Y. Xia, Flexible and Wire-Shaped Micro-Supercapacitor Based on $Ni(OH)_2$-Nanowire and Ordered Mesoporous Carbon Electrodes, Adv. Funct. Mater. 24 (2014) 3405–3412. doi:10.1002/adfm.201304001.

[103] Z. Zhang, F. Xiao, S. Wang, Hierarchically structured MnO_2/graphene/carbon fiber and porous graphene hydrogel wrapped copper wire for fiber-based flexible all-solid-state asymmetric supercapacitors, J. Mater. Chem. A. 3 (2015) 11215–11223. doi:10.1039/C5TA02331A.

[104] H. Xie, S. Tang, J. Zhu, S. Vongehr, X. Meng, A high energy density asymmetric all-solid-state supercapacitor based on cobalt carbonate hydroxide nanowire covered N-doped graphene and porous graphene electrodes, J. Mater. Chem. A. 3 (2015) 18505–18513. doi:10.1039/C5TA05129K.

[105] M. Yang, H. Cheng, Y. Gu, Z. Sun, J. Hu, L. Cao, F. Lv, M. Li, W. Wang, Z. Wang, S.

Wu, H. Liu, Z. Lu, Facile electrodeposition of 3D concentration-gradient Ni-Co hydroxide nanostructures on nickel foam as high performance electrodes for asymmetric supercapacitors, Nano Res. 8 (2015) 2744–2754. doi:10.1007/s12274-015-0781-3.

[106] J. Yang, Y. Yuan, W. Wang, H. Tang, Z. Ye, J. Lu, Interconnected $Co_{0.85}Se$ nanosheets as cathode materials for asymmetric supercapacitors, J. Power Sources. 340 (2017) 6–13. doi:10.1016/j.jpowsour.2016.11.061.

[107] X. Wang, X. Li, X. Du, X. Ma, X. Hao, C. Xue, H. Zhu, S. Li, Controllable Synthesis of NiCo LDH Nanosheets for Fabrication of High-Performance Supercapacitor Electrodes, Electroanalysis. 29 (2017) 1286–1293. doi:10.1002/elan.201600602.

[108] I.M. Babu, K.K. Purushothaman, G. Muralidharan, Ag_3O_4 grafted NiO nanosheets for high performance supercapacitors, J. Mater. Chem. A. 3 (2015) 420–427. doi:10.1039/C4TA04586F.

[109] S.C. Sekhar, G. Nagaraju, J.S. Yu, Conductive silver nanowires-fenced carbon cloth fibers-supported layered double hydroxide nanosheets as a flexible and binder-free electrode for high-performance asymmetric supercapacitors, Nano Energy. 36 (2017) 58–67. doi:10.1016/j.nanoen.2017.04.019.

[110] T. Osaka, T. Momma, D. Mukoyama, H. Nara, Proposal of novel equivalent circuit for electrochemical impedance analysis of commercially available lithium ion battery, J. Power Sources. 205 (2012) 483–486. doi:10.1016/j.jpowsour.2012.01.070.

[111] R.B. Rakhi, N.A. Alhebshi, D.H. Anjum, H.N. Alshareef, Nanostructured cobalt sulfide-on-fiber with tunable morphology as electrodes for asymmetric hybrid supercapacitors, J. Mater. Chem. A. 2 (2014) 16190–16198. doi:10.1039/C4TA03341H.

[112] K. Krishnamoorthy, G.K. Veerasubramani, P. Pazhamalai, S.J. Kim, Designing two

dimensional nanoarchitectured MoS_2 sheets grown on Mo foil as a binder free electrode for supercapacitors, Electrochim. Acta. 190 (2016) 305–312. doi:10.1016/j.electacta.2015.12.148.

[113] P. Ilanchezhiyan, G. Mohan Kumar, T.W. Kang, Electrochemical studies of spherically clustered MoS_2 nanostructures for electrode applications, J. Alloys Compd. 634 (2015) 104–108. doi:10.1016/j.jallcom.2015.02.082.

[114] R.B. Rakhi, B. Ahmed, D. Anjum, H.N. Alshareef, Direct Chemical Synthesis of MnO_2 Nanowhiskers on Transition-Metal Carbide Surfaces for Supercapacitor Applications, ACS Appl. Mater. Interfaces. 8 (2016) 18806–18814. doi:10.1021/acsami.6b04481.

[115] Y. Li, Y. Zheng, J. Yao, J. Xiao, J. Yang, S. Xiao, Facile synthesis of nanocrystalline-assembled nest-like NiO hollow microspheres with superior lithium storage performance, RSC Adv. 7 (2017) 31287–31297. doi:10.1039/c7ra05373h.

SUMMARY

- Chapter 3 discusses the energy storage in the view of improving performance metrics using aqueous electrolyte system, the hybrid-ion supercapacitors (HSCs) / asymmetric supercapacitor (ASC) are fabricated using battery-type faradaic nanostructured electrode materials ($LiMn_2O_4$, CuHCF, MnHCF & Cu_2WS_4/Ni) and capacitive type electrode materials (graphene and graphitic carbon).
- The fabricated device such as $LiMn_2O_4$ ‖ graphene, CuHCF ‖ GC and MnHCF ‖ graphene delivers specific energy of about 39, 42, and 44 Wh/kg with the corresponding specific power of 440, 523, and 588 W kg^{-1} respectively.
- Likewise, the CWS/Ni ‖ graphene ASC device also possesses high energy (48 Wh/kg) and power (321 W/kg), due to the direct integration of the electrode material on to the Ni foam which makes the electron-ion transport fast during the electrochemical process.
- The main drawback of this system is that the formation of gel type electrolyte with the neutral electrolyte is difficult. Hence we move on towards the ionic/organic liquid electrolyte based system through which the formation of ionogel is possible for the solid state energy storage system for self-charging applications.

CHAPTER – 4

Synthesis of layered transition metal compounds (TiO_2, siloxene, and HT-siloxene) and fabrication of symmetric capacitor using organic/ionic liquid electrolyte

CHAPTER 4.1 Blue TiO_2 nanosheets as a high-performance electrode material for supercapacitors

Highlights

- A one-pot hydrothermal route was employed for the oxidation of layered titanium diboride (TiB_2) into b-TiO_2 nanosheets.
- The energy storage properties of the b-TiO_2 electrode were examined using aqueous and organic electrolytes.
- The cyclic voltammetry and charge-discharge analysis of b-TiO_2 electrode using 1 M Na_2SO_4 revealed their pseudocapacitive nature with a high specific capacitance ($\sim$19 mF cm^{-2}).
- The b-TiO2 based symmetric supercapacitor (SSC) device using organic liquid (1 M TEABF4) works over a wide operating potential window (3 V) and delivered a high specific capacitance (6.67 F g^{-1} or 3.58 mF cm^{-2}).

4.1.1 Introduction

The use of titanium oxide (TiO_2) nanostructures as an electrode for electrochemical energy storage devices (supercapacitors and batteries) received much attention over other metal oxides (RuO_2, MnO_2, MoO_3, Co_3O_4) mainly due to low cost, highly abundant, environmentally benign, biocompatible, and good chemical stability [1–3]. TiO_2 can exist as several polymorphs such as TiO_2(B), anatase, brookite, and rutile in which the former two possess excellent electrochemical activity over the latter two polymorphs[4]. Extensive research work has been carried out on the supercapacitive properties of TiO_2 via tailoring the surface morphology (nanorods, nanowires, nanotubes), doping, and developing binder-free electrodes, and core-shell/hybrid electrodes to improve their energy and power density[5,6]. However, the performance metrics of TiO_2 based supercapacitors are still low compared to the supercapacitors based on other metal oxides[7]. Thus, improving the electrochemical energy storage properties of TiO_2 might result in the development of low cost and highly efficient supercapacitors.

In general, the electrochemical performance of an electrode can be enhanced via (i) increasing the surface area, (ii) improving the electrical conductivity, and (iii) tailoring the morphology, since all of these three parameters are directly related with the electrochemical activity of the material[8–10]. Further, the emergence of two dimensional materials such as graphene, MXene, siloxene, 2D metal dichalcogenides, and 2D metals created new opportunities on the energy storage devices[11–14]. The development of metal oxides/hydroxides in 2D sheet like morphologies showed better electrochemical properties compared to their conventional counterparts[15,16]. Therefore, tailoring the surface area, intrinsic conductivity and morphology of TiO_2 nanostructures might lead to enhance their electrochemical properties. In this scenario, the chemical approach towards the preparation of electron-rich TiO_2 nanostructures becomes one of the promising ways to improve the

electronic conductivity of TiO_2[17]. Such electron-rich TiO_2 can be referred as blue or black TiO_2 which possess excellent physical and chemical properties (compared to conventional TiO_2) due to their modified structure and composition (such as disordered surface structure and Ti^{3+}/oxygen vacancies) which leads to high conductivity, magnetic properties, and better chemical properties[18–20]. With these structural benefits, the blue/black TiO_2 might possess enhanced electrochemical properties which are not yet studied completely till date. Thus, understanding the electrochemical properties of the blue TiO_2 (b-TiO_2) might provide new opportunities on the energy storage properties of TiO_2. Herein, we aimed to analyze the electrochemical properties of b-TiO_2 with sheet-like nanostructures (prepared via the oxidation of TiB_2 sheets) as a suitable electrode material for high performance supercapacitors using aqueous and organic electrolytes.

4.1.2. Experimental section

4.1.2.1 Preparation of titanium oxide (TiO_2) nanosheets

A facile hydrothermal route has been employed for the preparation of TiO_2 nanosheets using TiB_2 as the starting material[17]. Briefly, 0.5 g of TiB_2 was dissolved in 20 mL of HF and sonicated for 30 minutes, and the mixture solution was transferred to 100 mL Teflon lined stainless steel autoclave for hydrothermal reaction at a temperature of 180 ℃ and kept for 12 h. After completion of the reaction, the reactor was allowed to cool down to room temperature naturally. Then, the blue colored precipitates containing TiO_2 nanosheets were repeatedly washed with DI water and ethanol using centrifugation process to remove residual impurities. The washed TiO_2 nanosheets were dried at 80 ℃ for 12 h and used for further characterization.

4.1.2.2 Electrochemical methods

A working electrode was first prepared by grinding prepared TiO_2 powder, carbon black, and polyvinylidene fluoride (PVDF) with a ratio of 80:15:5 with an appropriate

amount of N-Methyl- 2-pyrrolidone (NMP) in an agate mortar until a uniform slurry was obtained. The slurry was spin coated on a stainless-steel current collector at 200 rpm and then dried at 80 °C for 12 h. The electroactive mass of the TiO_2 sheets on the stainless-steel current collector was determined from the difference between the mass of the current collector before and after TiO_2 sheets loading using a dual-range semi microbalance (AUW-220D, Shimadzu) with an approximation to five decimal places. The mass loading of TiO_2 sheets was about 0.5 mg in each electrode. The TiO_2 SSC device was fabricated in CR2032 coin cell configuration using TiO_2-coated stainless-steel substrates with an area of 1.86 cm^2 as electrodes separated by a Celgard membrane and 1 M $TEABF_4$ in acetonitrile as the electrolyte. The fabricated SSC device was crimped using an electric coin cell crimping and disassembling machine (MTI, Korea). Electrolyte handling and device fabrication were carried out in a glove box with less than 1 ppm of moisture and oxygen. Electrochemical measurements of the TiO_2 SSC device such as CV at different scan rates, galvanostatic CD measurements in different current ranges and EIS analysis in the frequency range from 0.01 Hz to 100 kHz at an amplitude of 10 mV, were performed using an Autolab PGSTAT302N electrochemical workstation.

4.1.3. Results and discussion:

4.1.3.1 Physicochemical characterization

The b-TiO_2 nanostructures were prepared via a one-step hydrothermal method using hexagonal TiB_2 and HF as starting materials[17]. The formation of b-TiO_2 from layered TiB_2 is due to the topochemical deintercalation of boron layers which is similar to that of calcium deintercalation in layered $CaSi_2$[11] and aluminum extraction from Ti_2AlC [21] under acidic conditions. Being a layered material comprising alternating layers of titanium and boron atoms, TiB_2 can react with HF in topochemical pathways which result in the dissolution of boron atoms via releasing hydrogen gas and oxygen vacancies were generated via the H_2

reduction of Ti^{4+} on the surface[17,22]. Figure 4.1.1 shows the change in color from grey (TiB_2) to blue indicating the formation of electron-rich TiO_2 after the hydrothermal reaction.

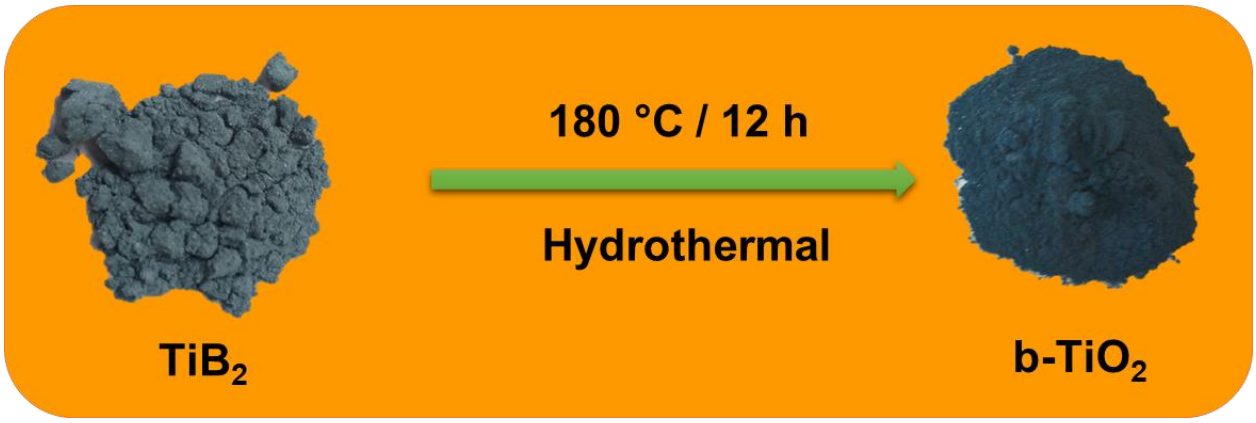

Figure 4.1.1. Digital photographs of TiB_2 and hydrothermally prepared b-TiO_2 powders.

Figure 4.1.2(A) shows the X-ray diffraction pattern of the as-prepared b-TiO_2 in comparison with the TiB_2 powders. It revealed the completer conversion of TiB_2 powders into b-TiO_2, and the observed XRD pattern of b-TiO_2 matched well with the standard diffraction pattern of anatase TiO_2 (JCPDS No: 021-1272)[23]. The significance of color in the blue TiO_2 can be related to their oxygen vacancy, surface disorder, and oxygen deficiency which is confirmed by the use of electron spin resonance spectroscopy, UV-vis and photoluminescence spectroscopic studies. Figure 4.1.2 (B) shows the X-band ESR spectrum of as prepared b-TiO_2 recorded at a temperature of 77 K under the microwave frequency of 9.64 GHz. The ESR spectrum (Fig. 4.1.2(D)) shows the presence of Ti^{3+} centers in the g-region (ranging from 1.87 to 1.99) where Ti^{3+} species generally resonates in the TiO_2 [24].

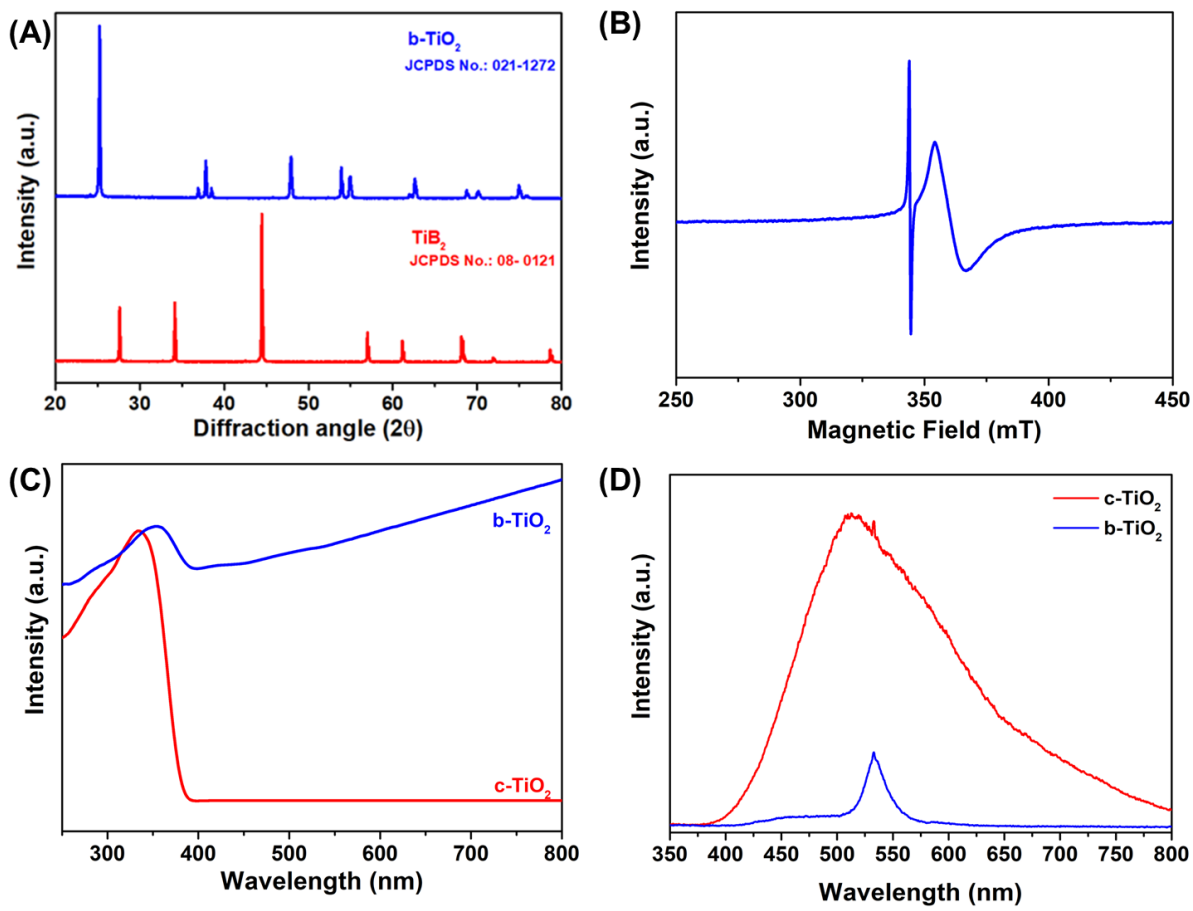

Figure 4.1.2. Physical characterization of the prepared b-TiO_2. (A) X-ray diffraction pattern of the TiB_2(precursor) and b-TiO_2 (prepared). (B) Electron spin resonance spectrum of b-TiO_2. (C) UV-visible (D) Photoluminescence spectrum of commercial anatase TiO_2 and b-TiO_2.

The ESR spectrum revealed the presence of a number of partially overlapping signals which can be amenable to different types of Ti^{3+} centers present in the prepared b-TiO_2. The observed ESR spectrum of b-TiO_2 is matched well with the previous finding on the ESR spectrum of partially reduced TiO_2 demonstrated by Chiesa et al.[17]. The UV-vis spectrum of b-TiO_2 in comparison with commercial anatase TiO_2 (c-TiO_2) is provided in Fig. 4.1.2 (C). The peak observed at 354 nm is related to the intrinsic absorption edge of b-TiO_2 samples which is red-shifted compared to the c-TiO_2 highlighting the presence of increased electron concentration at the b-TiO_2 surface. Further, the UV-vis spectrum of b-TiO_2 shows the

increased absorbance over the region 400 to 800 nm in comparison with the c-TiO_2 [19,25]. This is due to the absorbance of low-energy photon and/or thermal excitations of trapped electrons in localized states of defects and is matched well with the previous findings [19,25–27]. The comparative photoluminescence (PL) spectra of b-TiO_2 and c-TiO_2 are provided in Figure 4.1.2(D). The PL spectra of b-TiO_2 showed the presence of a peak around 510 to 540 nm in comparison to the c-TiO_2 which shows a broad band in the region 400 to 800 nm and the obtained PL spectra are in close agreement with the previous reports[28,29]. The luminescence intensity of b-TiO_2 is two-fold lower compared to the c-TiO_2 indicating that the b-TiO_2 possess low electron-hole recombination rate compared to the c-TiO_2 [30,31]. These studies further confirm the high electronic conductive states of b-TiO_2 in comparison with c-TiO_2.

Figure 4.1.3(A) shows the laser Raman spectrum of the prepared b-TiO_2 nanostructures which revealed the presence of a major sharp band observed at 148.25 cm^{-1} corresponding to the E_g mode of anatase TiO_2 [32]. The three minor bands observed at 396, 517, and 640 cm^{-1} which correspond to the B_{1g}, A_{1g}, and E_g vibrational modes of anatase TiO_2, respectively[19,33]. Figure 4.1.3(B) represents the comparative X-ray photoelectron survey spectrum of TiB_2 and b-TiO_2. The survey spectrum of TiB_2 shows the presence of Ti 2p, B 1s, C 1s and O 1s chemical states at 450 to 470 eV, 180 to 195 eV, 280 to 286 eV and 528 to 534 eV respectively[34]. The presence of O and C peaks in the XPS spectrum are due to interaction with air and carbon contamination on the surface of TiB_2. The XPS spectrum of the TiB_2 precursor is in close agreement with the previous findings of Lim et al. and Mazanek et al. [35,36]. After the hydrothermal process, significant changes in the survey spectrum of b-TiO_2 in comparison with the TiB_2 has been observed. The complete removal of boron layers in the TiB_2 after the hydrothermal reaction has been evident from the survey spectrum of b-TiO_2.

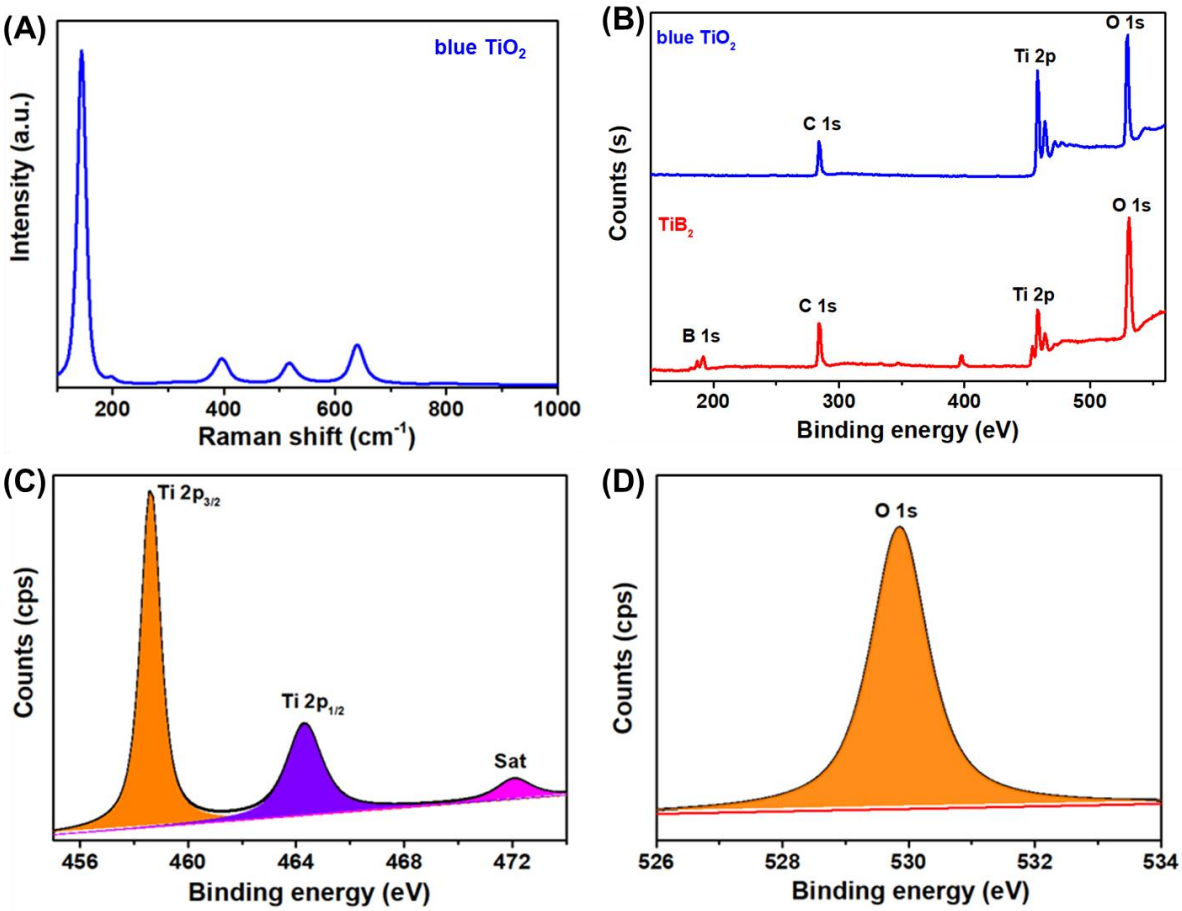

Figure 4.1.3. (A) Laser Raman spectrum of the prepared b-TiO_2. X-ray photoelectron spectroscopy (B) survey spectrum of TiB_2 (precursor) and b-TiO_2 (prepared). (C) core level spectrum of Ti 2p state and (D) core level spectrum of O 1s state of b-TiO_2 respectively.

This study confirms the complete topochemical de-intercalation of boron layers present in the TiB_2 via the hydrothermal process[34]. The core-level spectrum of Ti 2p and O 1s states of elements present in the b-TiO_2 nanostructures were provided in Figure 4.1.3(C and D). Figure 4.1.3(C) revealed the presence of Ti $2p_{3/2}$ and $2p_{1/2}$ states at binding energies 458, and 464 eV respectively. A small satellite peak was observed at 472.2 eV which corresponds to the presence of oxygen defects in the b-TiO_2 nanostructures[19,37]. The Ti 2p core-level spectrum signifies the presence of Ti^{4+} oxidation state with the small contribution of Ti^{3+} which occur due to oxygen deficiency in TiO_2.[38]. Figure 4.1.3(D) shows the O 1s states of b-TiO_2 at 530 eV respectively[19,37]. X-ray photoelectron spectroscopy is widely

used to analyze the chemical composition of a material. The O/Ti atomic ratio of b-TiO_2 nanostructures is found to be 2.47 from XPS analysis. The obtained O/Ti atomic ratio of b-TiO_2 nanostructures in this work is in close agreement with the recent findings of Lin et al. [39]

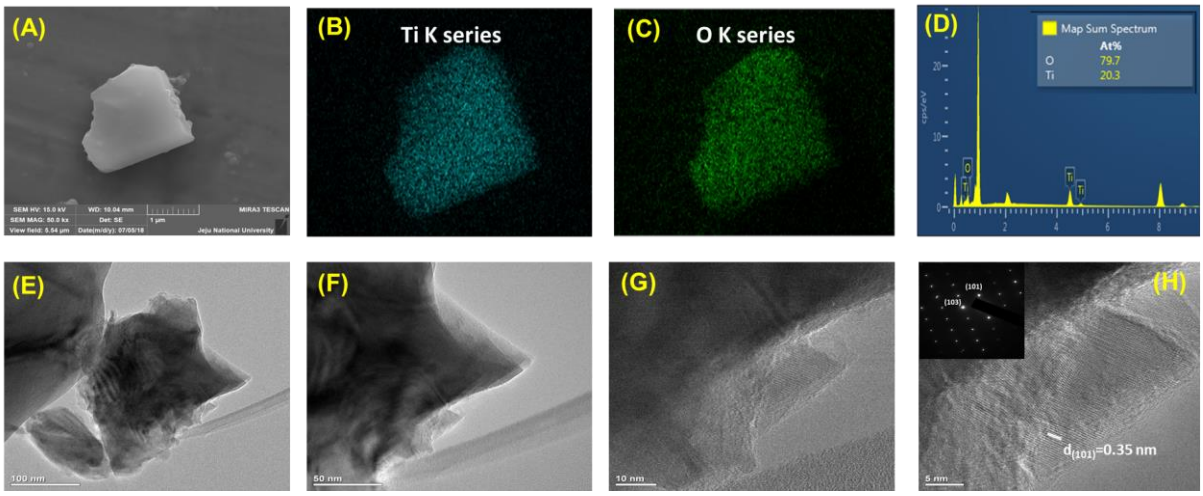

Figure 4.1.4. Surface morphology and elemental analysis of b-TiO_2 nanostructures. (A)FE-SEM micrograph b-TiO_2 nanostructures; (B) elemental mapping of Ti and (C) elemental mapping of O atoms in the b-TiO_2. (D) EDS spectrum of b-TiO_2. (E-H) HR-TEM micrographs of b-TiO_2 measured under various magnifications. The inset in (H) shows the corresponding SAED pattern of the prepared b-TiO_2.

The surface morphology and elemental analysis of b-TiO_2 nanostructures are examined using field emission scanning electron micrograph (FE-SEM) with energy dispersive spectra (EDS) and high-resolution transmission electron microscope (HR-TEM) analyses as shown in Figure 4.1.4 (A-H). The FE-SEM micrograph of b-TiO_2 nanostructures is provided in Figure 4.1.4(A) which revealed the presences of sheets or plate-like nanostructures of b-TiO_2 suggesting the mechanism of formation is due to the topochemical reaction. The elemental mapping elemental mapping images of Ti and O atoms in the b-TiO_2 nanostructures as shown in Figure 4.1.4(B and C) which indicated the homogeneous distributions of Ti and O throughout the b-TiO_2 sheet/plate. The EDS mapping spectrum is

provided in Figure 4.1.4(D) which shows the presence of Ti and O atoms with an O/Ti atomic ratio of about 3.92 present in the b-TiO_2 nanostructures [39,40]. The HR-TEM micrographs of b-TiO_2 obtained under various levels of magnifications are shown in Figure 4.1.4(E-H). The low magnification HR-TEM micrograph of b-TiO_2 (Figure 4.1.4(E) revealed the presence of sheet-like structures with the lateral size ranging from 200 nm in length and 250 nm in breadth. The high-magnification micrograph of b-TiO_2 (Figure 4.1.4(F)) shows the presence of layered b-TiO_2 sheets (with more layers) whereas Figure 4.1.4(G) shows (a magnified portion of Figure 4.1.4(F)) the presence of very thin b-TiO_2 sheets with few layers. Figure 4.1.4(H) shows the lattice fringes of b-TiO_2 sheets with an interplanar spacing of d=0.35 nm which corresponds to the (101) plane of b-TiO_2 and the corresponding SAED pattern (inset of Fig. 4.1.4 (H)) shows the presence of clear diffraction spots suggesting the good crystallinity nature of the prepared b-TiO_2[26].

4.1.3.2 Electrochemical characterization

The electrochemical properties of the b-TiO_2 electrodes in aqueous (half-cell) and ionic liquid (symmetric supercapacitor (SSC)) electrolytes were investigated using cyclic voltammetry (CV), electrochemical impedance spectroscopy (EIS), and galvanostatic charge-discharge (CD) analysis, respectively. Figure 4 shows the electrochemical studies of the b-TiO_2 electrode in the 1 M Na_2SO_4 electrolyte. The CV profile (Figure 4.1.5(A)) shows the presence of quasi-rectangular behavior indicating the pseudocapacitive nature of charge-storage occurred in the b-TiO_2 electrode[41,42]. The CV profiles of b-TiO_2 electrode indicated the presence of pseudocapacitance due to ion-intercalation/de-intercalation phenomenon in addition to the surface capacitance. Thus, in order to examine the contribution of surface and diffusion capacitance on the overall capacitance of b-TiO_2

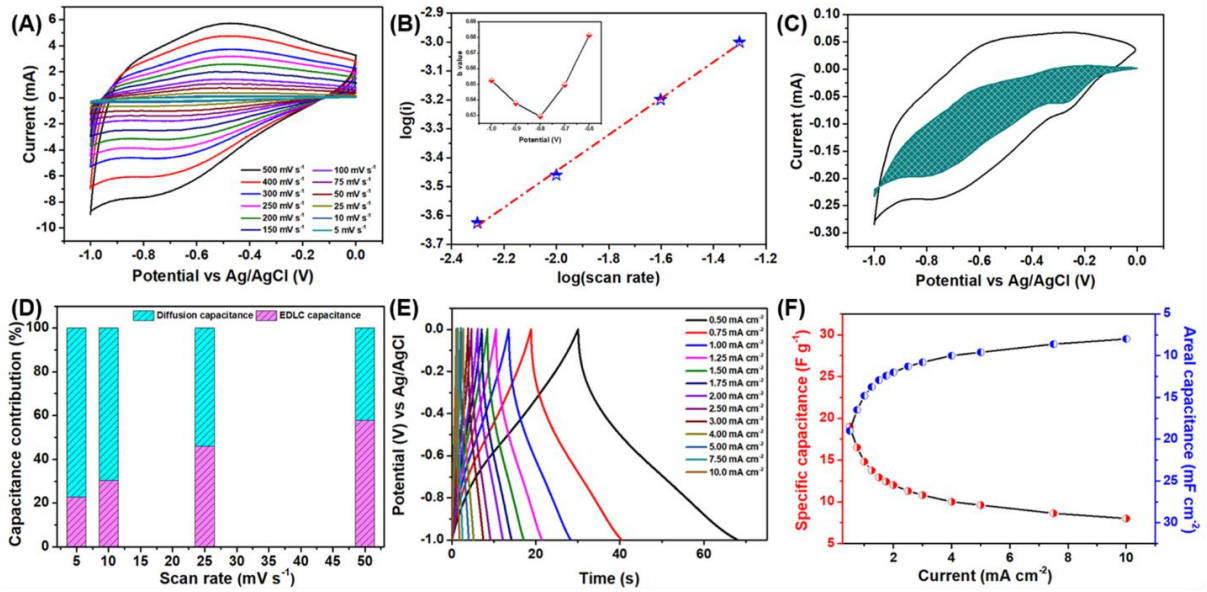

Figure 4.1.5. Electrochemical characterization of the b-TiO_2 electrode via three electrode configurations. (A) CV profiles of the b-TiO_2 electrode measured under various scan rate. (B) Dependence of current on sweep rate. The inset in (B) shows the b-values as a function of potential. (C) CV profile of b-TiO_2 electrode measured at 5 mV s^{-1}. The shaded part reveals the capacitive current at 5 mV s^{-1}. (D) The comparison of the capacitance contribution of the b-TiO2 electrode with various scan rate. (E) galvanostatic CD profiles of the b-TiO_2 electrode measured under various current densities. (F) Effect of current densities on the specific capacitance of the b-TiO_2 electrode.

electrode, Dunn's method has been employed in this study[43]. Figure 4.1.5(B) shows the plot of the slope of log (i) versus log (v) derived in accordance with the power law [14,44]:

$$i = av^b \ldots\ldots\ldots\ldots\ldots\ldots\ldots\ldots\ldots\ldots(1)$$

Here, *"v"* is the scan rate (mV s^{-1}), *"a"* and *"b"* are the adjustable parameters. The *"b"* value can be calculated from the slope of log i versus log v (as shown in the inset of Fig. 4.1.5 (B)). The two well-defined conditions viz (i) *"b=0.5"* as an indication of the diffusion process due to ion-intercalation/de-intercalation, and (ii) *"b=1"* representing the

surface capacitive nature. The contribution of surface and diffusion capacitance on the overall specific capacity can be quantified using the relation[43]:

$$I(V) = k_1 \nu + k_2 \nu^{1/2} \ldots\ldots\ldots\ldots\ldots\ldots\ldots\ldots (2)$$

In equation (2), "k_1 ν" and "k_2 $\nu^{1/2}$"correspond to the contributions from surface capacitance and the diffusion-controlled intercalation/de-intercalation process, respectively. The value of k_1 and k_2 can be obtained from the slope and intercept of the plot between $I(V)/v^{1/2}$ and $v^{1/2}$. Thus, by determining k_1 and k_2 at specific potentials, it is easier to quantify the fraction of the current due to these two types of contributions[43]. The CV curve provided in the Fig. 4.1.5 (C) enable us to determine the total stored charge and the relative contributions associated with both insertion and capacitive contributions. Figure 4.1.5 (D) represents the contribution of surface and diffusion capacitance on the overall capacitance of the b-TiO_2 electrode. It shows that the contribution of diffusion capacitance is increasing from 42.10 to 77.29 % when the scan rate is decreased from 50 to 5 mV s^{-1}. The higher diffusion capacitance obtained at the low scan rate can be explained as follows: at high scan rates, the electrolyte ions faces time constraints which limits the diffusion of electrolyte ions whereas low scan rates provide sufficient time for the electrolyte ions to diffuse into the interior surface of the b-TiO_2 electrode [45]. The presence of sloppy symmetric CD profiles (from Figure 4.1.5(E)) is due to the pseudocapacitive properties of the b-TiO_2 electrode with a high specific capacitance of 19 F g^{-1} (19 mF cm^{-2}) were obtained using the constant current density of 0.5 mA cm^{-2}(Fig. 4(F)). Table 4.1.1 shows the superior performance of the b-TiO_2 electrode (with a specific capacitance of 19 F g^{-1}) with the reported TiO_2 based electrodes in aqueous electrolytes measured using a three-electrode configuration. This superior electrochemical performance of the prepared b-TiO_2 in aqueous electrolyte might be arised from the (i) sheet-like morphology, (ii) improved electrical conductivity, and (iii) oxygen vacant sites of the b-TiO_2.

Table 4.1.1. Performance comparison of b-TiO_2 electrode with the recently reported TiO_2 electrodes for supercapacitor application.

No	Electrode Material	Specific capacitance	Reference
1	TiO_2 NTA	7 mF cm^{-2}	[6]
2	H-TiO_2	3.24 mF cm^{-2}	[1]
3	TiO_2	0.026 mF cm^{-2}	[1]
4	Air TiO_2	0.08 mF cm^{-2}	[1]
5	TiO_2 NTA	0.538 mF cm^{-2}	[46]
6	TiO_2 nanoparticles	0.12 mF cm^{-2}	[43]
7	TiO_2	1.84 mF cm^{-2}	[47]
8	Grass topped ATNT	8.636 mF cm^{-2}	[48]
9	Pristine TiO_2	2.4 mF cm^{-2}	[7]
10	H_2 annealed TiO_2	3.24 mF cm^{-2}	[1]
11	C axis TiO_2	8.21 mF cm^{-2}	[49]
12	Plasma treated TiO_2	7.22 mF cm^{-2}	[50]
13	Black TiO_2	15.6 mF cm^{-2}	[51]
14	TiO_2 NP	0.181 mF cm^{-2}	[52]
15	TiO_2 NT/TI	0.911 mF cm^{-2}	[52]
16	TiO_2 NS	4.5 mF cm^{-2}	[53]
17	TiO_2 NR array	47 μF cm^{-2}	[54]
18	TiO_2/MnO_2	14.36 mF cm^{-2}	[55]
19	TiO_2 NR	60.6 μF cm^{-2}	[5]
20	Large wire like TiO_2	1.29 F g^{-1}	[56]
21	Small wire like TiO_2	2.69 F g^{-1}	[56]
22	Flake-like TiO_2	1.84 F g^{-1}	[57]
23	Flower -like TiO_2	2.62 F g^{-1}	[57]
24	Wire-like TiO_2	3.16 F g^{-1}	[57]
25	**Blue TiO_2**	**19 F g^{-1} (19 mF cm^{-2}) at 0.5 mA cm^{-2}**	**This work**

In order to maximize the energy density of b-TiO_2 SSC, organic liquid ($TEABF_4$) electrolytes were used which can extend the operating potential window (ΔV)[58]. Figure 4.1.6 represents the CV profiles of the fabricated b-TiO_2 SSC device measured at different OPW in the positive regime (0.0 to 3.0 V) at a scan rate of 100 mV s^{-1} which displayed the distorted rectangular shaped curves and also suggested that the b-TiO_2 SSC device can operate at a window of 3.0 V without any sign of evolution.

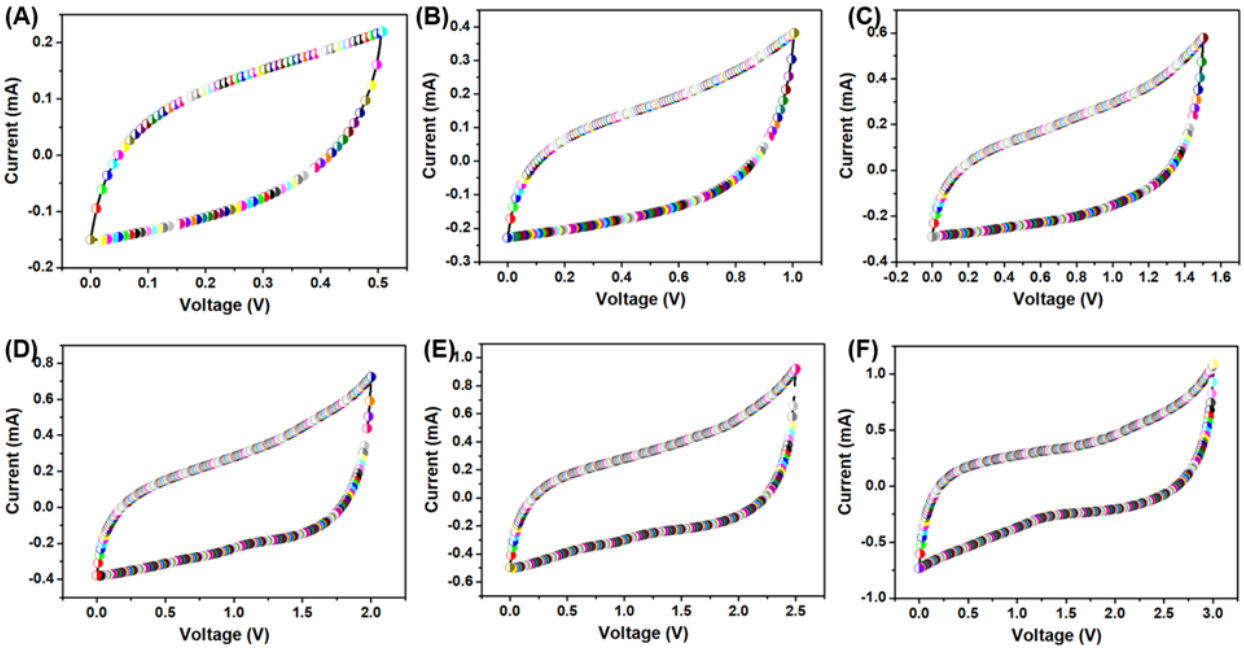

Figure 4.1.6. Cyclic voltammetry curves of b-TiO_2 SSC device over the OPW of 0.0 to +3.0 V measured at a constant scan rate of 100 mV s^{-1}.

Figure 4.1.7(A and B) shows the CV profiles of the b-TiO_2 SSCs using 1 M $TEABF_4$ electrolyte. The presence of typical rectangular shaped curves for all the CV scans at different rates (5 to 1000 mV s^{-1}) indicated the presence of pseudocapacitive nature of charge-storage at the b-TiO_2 via intercalation/de-intercalation phenomenon[59,60]. The effect of scan rate on the specific capacitance of b-TiO_2 is provided in Figure 4.1.7(C). A high specific capacitance of about 6.67 F g^{-1} (equivalent to an areal capacitance of 3.58 mF cm^{-2}) has been obtained for the b-TiO_2 SSCs from the CV profiles recorded at a scan rate of 5 mV s^{-1}. Figure 4.1.7(D-F) represents the EIS analysis of the b-TiO_2 SSCs in the form of Nyquist and Bode plots.

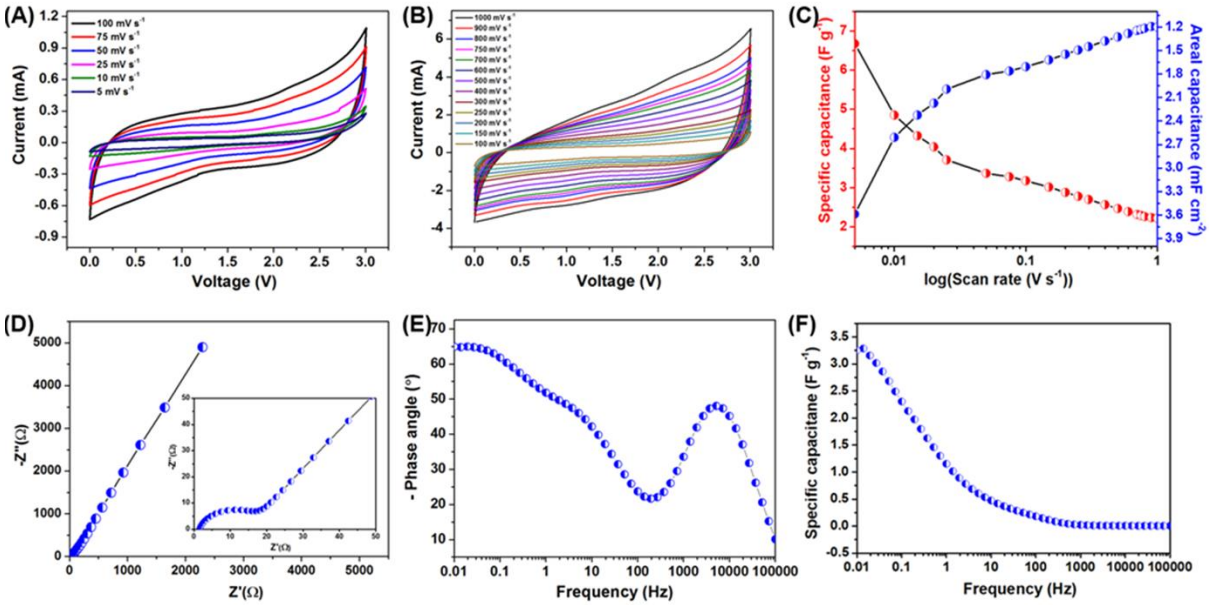

Figure 4.1.7. Electrochemical characterization of the b-TiO_2 symmetric supercapacitor (SSC) device. (A and B) CV profiles of the b-TiO_2 SSC measured under various scan rate (5 to 1000 mV s^{-1}). (C) Effect of scan rate on the specific capacitance of the b-TiO_2 SSC. Electrochemical impedance spectroscopic analysis of the b-TiO_2 SSC (D) Nyquist plot of the b-TiO_2 SSC and the inset shows the enlarged portion of the Nyquist plot. (E) Bode phase angle plot of the b-TiO_2 SSC (F) effect of applied frequency on the specific capacitance b-TiO_2 SSC.

The Nyquist plot of b-TiO_2 SSCs given in Figure 4.1.7(D) shows the presence of three well-defined regions viz high-, mid- and low-frequency region[61]. The high- and mid- frequency region can be used to determine the solution resistance (R_s) or equivalent series resistance (ESR) whereas the low- frequency region directly related to the frequency dependent ion diffusion kinetics of electrolyte ions to the electrode[11]. In order to determine the nature of diffusion kinetics occurred at the electrode surface, the plot between log (Z) vs log (f) (as given in Figure (4.1.8)) was used.

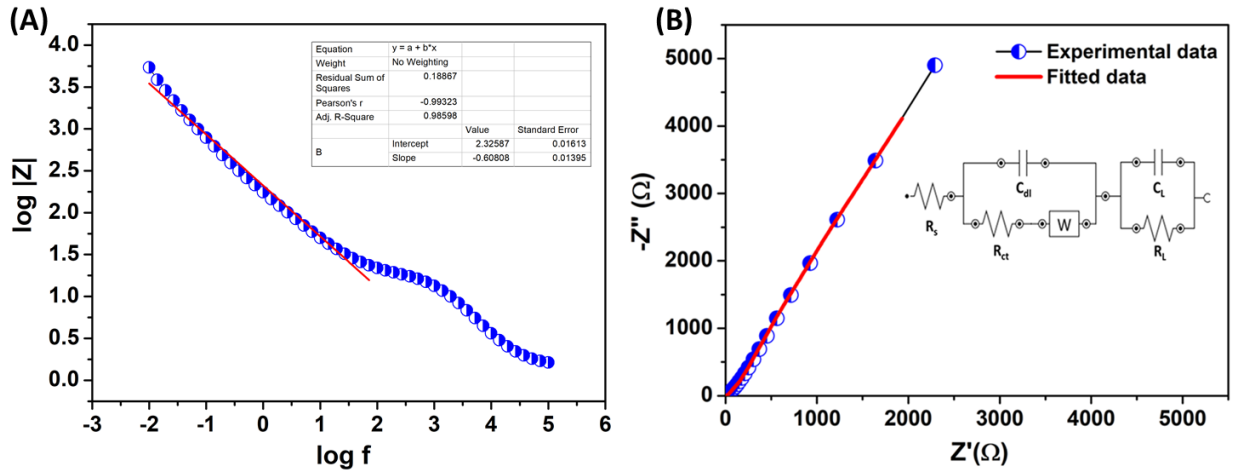

Figure 4.1.8 (A) Plot of log Z against the log f of b-TiO_2 SSC device. (B) Nyquist plot of b-TiO_2 SSC device and the inset in (B) shows the equivalent circuit model of b-TiO_2 SSC device.

The inset in Figure 4.1.8(A) indicated that the slope value obtained at the low-frequency region is about -0.60 (which is closer to the value of -0.5), thus suggesting the presence of Warburg diffusion in this system. An equivalent circuit model used for the description of EIS analysis (as shown in Figure 4.1.8(B)) comprises of solution resistance (R_s), charge-transfer resistance (R_{ct}), leakage resistance (R_L), capacitance (C_{dl} and C_L) and Warburg elements (W) [62]. The X-axis intercept obtained at high- frequency region corresponds to the bulk electrolyte solution resistance (R_s), and it is also known as equivalent series resistance (ESR) of the SSC[11]. The diameter of the semicircle observed at the high-frequency range can be related to charge transfer resistance (R_{ct}) which depends on the electrolyte ions accessible area and electrical conductivity of the electrode material[63]. The values of R_s and R_{ct} from the Nyquist plot are determined to be 1.60 and 15.4 Ω, respectively. The incorporation of two capacitive elements in the equivalent circuit corresponds to the (i) double layer capacitance, and (ii) pseudocapacitance of the electrodes, respectively. The presence of the Warburg element in the model circuit related to the frequency dependent ion

diffusion kinetics of electrolyte ions to the electroactive surface as evident from Figure 4.1.7(D)[64]. The Bode phase angle plot of b-TiO_2 SSCs (Figure 4.1.7(E)) shows that the phase angle at the low- frequency region (0.01 Hz) is about 64.94°, thus, suggesting the pseudocapacitive nature of the b-TiO_2 SSCs[21]. Figure 4.1.7(F) presents the effect of applied frequency on the specific capacitance of b-TiO_2 SSCs. A specific capacitance of about 3.24 F g^{-1} was obtained for the b-TiO_2 SSCs at a low frequency of 0.01 Hz, and the capacitance decreases with respect to an increase in frequency [65].

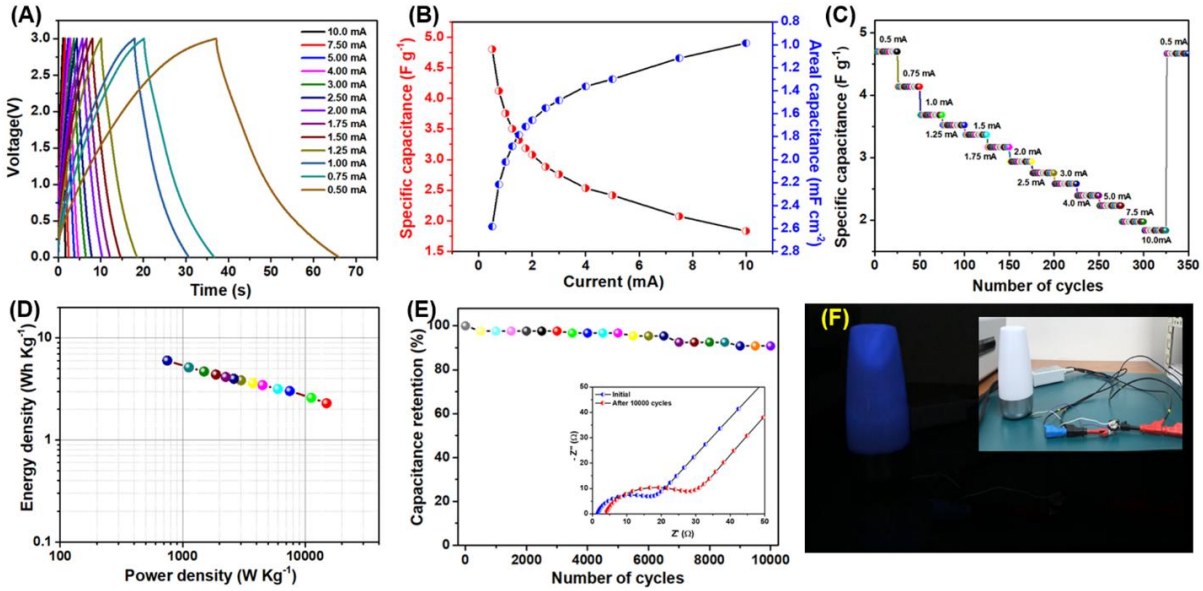

Figure 4.1.9. (A) Galvanostatic CD profiles of the b-TiO_2 SSC device measured at various current range; (B) Effect of discharge current on the specific capacitance of the b-TiO_2 SSC. (C) Rate capability of the b-TiO_2 SSC device. (D) Ragone plot is representing the dependence of the energy density of the b-TiO_2 SSC device on power density. (E) Cycling stability of the b-TiO_2 SSC device over 10000 CD cycles. The inset in (E) shows the Nyquist plot before and after the cyclic stability of b-TiO_2 SSC device. (F) Practical application of the fully charged b-TiO_2 SSC device delivering enough energy to glow a night lamp.

Figure 4.1.9(A) represents the galvanostatic charge-discharge profiles of the b-TiO_2 SSCs obtained using a wide range of constant currents (from 0.5 to 10 mA). The presence of semi-symmetric CD profiles indicated the pseudocapacitive nature of the b-TiO_2 SSCs[53].

The effect of scan rate on the specific capacitance of b-TiO_2 is provided in Figure 4.1.9(B). The b-TiO_2 SSCs possess a high specific capacitance of about 4.80 F g^{-1} (equivalent to an areal capacitance of 2.58 mF cm^{-2}) from the CD profiles recorded using a constant current of 0.5 mA. Figure 4.1.9(C) presents the rate capability of the b-TiO_2 SSC device tested using repetitive cycling at all currents from 0.5 to 10 mA. The b-TiO_2 SSC device holds better capacitance retention while the cycling is switched from low- to high- current range and vice versa, suggesting their superior rate capability[11]. The Ragone plot of the b-TiO_2 SSCs is shown in Figure 4.1.9(D) which shows that the fabricated device holds a high energy density of 6.0 Wh kg^{-1} (areal energy density of 3.22 μWh cm^{-2}) at a corresponding power density of about 750 W kg^{-1} (areal power density of 0.4 mW cm^{-2}), respectively. At a much higher power density of 15,000 W kg^{-1}(areal power density of 8.06 mW cm^{-2}), the b-TiO_2 SSC device holds an energy density of 2.29 Wh kg^{-1}(areal energy density of 1.23 μWh cm^{-2}), suggesting their better capacitive properties. Figure 4.1.9(E) presents the long-term cyclic stability of the b-TiO_2 SSC device over 10,000 cycles of uninterrupted CD analysis recorded using a constant current of 1 mA. The b-TiO_2 SSC retained a specific capacitance of about 90.2 % over 10,000 cycles, demonstrating their better cyclic stability[66]. The Nyquist plot (inset in Fig. 4.1.9 (E)) shows an increase in the solution resistance (from 1.60 Ω to 4.17 Ω) and charge transfer resistance (from 15.4 Ω to 24.4 Ω) after 10,000 cycles of charge-discharge which result in the observed small decay in capacitance of b-TiO_2 SSC device. The Bode phase angle plot (Fig. S9) before and after cyclic stability shows the changes in the phase angle from 64.94° to 63.12°. Figure 4.1.9(F) shows the practical applications of the b-TiO_2 SSC glowing a blue lamp over 10 seconds after charged upto 3 V using a constant current of 0.5 mA.

4.1.4 Conclusion

We prepared b-TiO_2 via reducing TiB_2 in the presence of HF using the hydrothermal route and demonstrated its energy storage properties both in aqueous (three-electrode configuration) and organic electrolyte (symmetric supercapacitor). The electrochemical studies of the b-TiO_2 electrode in aqueous electrolyte showed improved performance compared to the existing TiO_2 electrodes. The symmetric supercapacitor based on b-TiO_2 nanostructures operated over a wide potential range of 3.0 V with a maximum specific capacitance of 4.8 F g^{-1} (2.58 mF cm^{-2}), the high energy density of 6 Wh kg^{-1}, and good rate capability. The b-TiO_2 SSC device delivered a maximum power density of 750 W kg^{-1}, which is higher than those of other 2D electrode materials-based supercapacitors. The b-TiO_2 SSC device showed excellent cycling stability with about 90.2% capacitance retention after 10000 charge-discharge cycles. Considering the achieved electrochemical performance and demonstrated practical application of the b-TiO_2 based SSC device, we strongly believe that b-TiO_2 nanostructures are a promising electrode material for next-generation smart energy storage sectors.

4.1.5 References:

[1] X. Lu, G. Wang, T. Zhai, M. Yu, J. Gan, Y. Tong, Y. Li, Hydrogenated TiO_2 Nanotube Arrays for Supercapacitors, Nano Lett. 12 (2012) 1690–1696. doi:10.1021/nl300173j.

[2] N.M. Ndiaye, B.D. Ngom, N.F. Sylla, T.M. Masikhwa, M.J. Madito, D. Momodu, T. Ntsoane, N. Manyala, Three dimensional vanadium pentoxide/graphene foam composite as positive electrode for high performance asymmetric electrochemical supercapacitor, J. Colloid Interface Sci. 532 (2018) 395–406. doi:10.1016/j.jcis.2018.08.010.

[3] S.B. Kale, A.C. Lokhande, R.B. Pujari, C.D. Lokhande, Cobalt sulfide thin films for electrocatalytic oxygen evolution reaction and supercapacitor applications, J. Colloid Interface Sci. 532 (2018) 491–499. doi:10.1016/j.jcis.2018.08.012.

[4] A. Ramadoss, S.J. Kim, Improved activity of a graphene–TiO_2 hybrid electrode in an electrochemical supercapacitor, Carbon N. Y. 63 (2013) 434–445. doi:10.1016/j.carbon.2013.07.006.

[5] A. Ramadoss, S.J. Kim, Enhanced supercapacitor performance using hierarchical TiO_2 nanorod/$Co(OH)_2$ nanowall array electrodes, Electrochim. Acta. 136 (2014) 105–111. doi:10.1016/j.electacta.2014.05.014.

[6] N.S. Peighambardoust, S. Khameneh Asl, R. Mohammadpour, S.K. Asl, Band-gap narrowing and electrochemical properties in N-doped and reduced anodic TiO_2 nanotube arrays, Electrochim. Acta. 270 (2018) 245–255. doi:10.1016/j.electacta.2018.03.091.

[7] C.C. Raj, R. Prasanth, Review—Advent of TiO_2 Nanotubes as Supercapacitor Electrode, J. Electrochem. Soc. 165 (2018) E345–E358. doi:10.1149/2.0561809jes.

[8] Y. Chen, Z. Liu, L. Sun, Z. Lu, K. Zhuo, Nitrogen and sulfur co-doped porous

graphene aerogel as an efficient electrode material for high performance supercapacitor in ionic liquid electrolyte, J. Power Sources. 390 (2018) 215–223. doi:10.1016/j.jpowsour.2018.04.057.

[9] C. Lu, Y.H. Huang, Y.J. Wu, J. Li, J.P. Cheng, Camellia pollen-derived carbon for supercapacitor electrode material, J. Power Sources. 394 (2018) 9–16. doi:10.1016/j.jpowsour.2018.05.032.

[10] E. Pomerantseva, Y. Gogotsi, Two-dimensional heterostructures for energy storage, Nat. Energy. 2 (2017) 17089. doi:10.1038/nenergy.2017.89.

[11] K. Krishnamoorthy, P. Pazhamalai, S.-J. Kim, Two-dimensional siloxene nanosheets: novel high-performance supercapacitor electrode materials, Energy Environ. Sci. 11 (2018) 1595–1602. doi:10.1039/C8EE00160J.

[12] E. Martínez-Periñán, M.P. Down, C. Gibaja, E. Lorenzo, F. Zamora, C.E. Banks, Antimonene: A Novel 2D Nanomaterial for Supercapacitor Applications, Adv. Energy Mater. 8 (2018) 1702606. doi:10.1002/aenm.201702606.

[13] M. Acerce, D. Voiry, M. Chhowalla, Metallic 1T phase MoS_2 nanosheets as supercapacitor electrode materials, Nat. Nanotechnol. 10 (2015) 313–318. doi:10.1038/nnano.2015.40.

[14] Q. Jiang, N. Kurra, M. Alhabeb, Y. Gogotsi, H.N. Alshareef, All Pseudocapacitive MXene-RuO_2 Asymmetric Supercapacitors, Adv. Energy Mater. 8 (2018) 1703043. doi:10.1002/aenm.201703043.

[15] Z. Hu, X. Xiao, H. Jin, T. Li, M. Chen, Z. Liang, Z. Guo, J. Li, J. Wan, L. Huang, Y. Zhang, G. Feng, J. Zhou, Rapid mass production of two-dimensional metal oxides and hydroxides via the molten salts method, Nat. Commun. 8 (2017) 15630. doi:10.1038/ncomms15630.

[16] K.S. Kumar, N. Choudhary, Y. Jung, J. Thomas, Recent Advances in Two-

Dimensional Nanomaterials for Supercapacitor Electrode Applications, ACS Energy Lett. 3 (2018) 482–495. doi:10.1021/acsenergylett.7b01169.

[17] M. Chiesa, S. Livraghi, E. Giamello, E. Albanese, G. Pacchioni, Ferromagnetic Interactions in Highly Stable, Partially Reduced TiO_2 : The S=2 State in Anatase, Angew. Chemie Int. Ed. 56 (2017) 2604–2607. doi:10.1002/anie.201610973.

[18] G. Liu, H.G. Yang, C. Sun, L. Cheng, L. Wang, G.Q. (Max) Lu, H.-M. Cheng, Titania polymorphs derived from crystalline titanium diboride, CrystEngComm. 11 (2009) 2677. doi:10.1039/b909191m.

[19] G. Liu, H.G. Yang, X. Wang, L. Cheng, H. Lu, L. Wang, G.Q. (Max) Lu, H.-M. Cheng, Enhanced Photoactivity of Oxygen-Deficient Anatase TiO_2 Sheets with Dominant {001} Facets, J. Phys. Chem. C. 113 (2009) 21784–21788. doi:10.1021/jp907749r.

[20] H. Gong, T. Wang, H. Xue, X. Fan, B. Gao, H. Zhang, L. Shi, J. He, J. Ye, Photo-enhanced lithium oxygen batteries with defective titanium oxide as both photo-anode and air electrode, Energy Storage Mater. 13 (2018) 49–56. doi:10.1016/j.ensm.2017.12.025.

[21] K. Krishnamoorthy, P. Pazhamalai, S. Sahoo, S.-J. Kim, Titanium carbide sheet based high performance wire type solid state supercapacitors, J. Mater. Chem. A. 5 (2017) 5726–5736. doi:10.1039/C6TA11198J.

[22] C.Z. Wen, H.B. Jiang, S.Z. Qiao, H.G. Yang, G.Q. (Max) Lu, Synthesis of high-reactive facets dominated anatase TiO_2, J. Mater. Chem. 21 (2011) 7052. doi:10.1039/c1jm00068c.

[23] L. Righini, F. Gao, L. Lietti, J. Szanyi, C.H.F. Peden, Performance and properties of K and TiO_2 based LNT catalysts, Appl. Catal. B Environ. 181 (2016) 862–873. doi:10.1016/j.apcatb.2015.07.008.

[24] M. Chiesa, M.C. Paganini, S. Livraghi, E. Giamello, Charge trapping in TiO_2 polymorphs as seen by Electron Paramagnetic Resonance spectroscopy, Phys. Chem. Chem. Phys. 15 (2013) 9435. doi:10.1039/c3cp50658d.

[25] J. Dong, J. Han, Y. Liu, A. Nakajima, S. Matsushita, S. Wei, W. Gao, Defective Black TiO_2 Synthesized via Anodization for Visible-Light Photocatalysis, ACS Appl. Mater. Interfaces. 6 (2014) 1385–1388. doi:10.1021/am405549p.

[26] Q. Zhu, Y. Peng, L. Lin, C.-M. Fan, G.-Q. Gao, R.-X. Wang, A.-W. Xu, Stable blue TiO_{2-x} nanoparticles for efficient visible light photocatalysts, J. Mater. Chem. A. 2 (2014) 4429. doi:10.1039/c3ta14484d.

[27] J. Qiu, S. Li, E. Gray, H. Liu, Q.-F. Gu, C. Sun, C. Lai, H. Zhao, S. Zhang, Hydrogenation Synthesis of Blue TiO_2 for High-Performance Lithium-Ion Batteries, J. Phys. Chem. C. 118 (2014) 8824–8830. doi:10.1021/jp501819p.

[28] C. Zhang, H. Hua, J. Liu, X. Han, Q. Liu, Z. Wei, C. Shao, C. Hu, Enhanced Photocatalytic Activity of Nanoparticle-Aggregated Ag–Ag_X(X = Cl, Br)@TiO_2 Microspheres Under Visible Light, Nano-Micro Lett. 9 (2017) 49. doi:10.1007/s40820-017-0150-8.

[29] F.J. Knorr, C.C. Mercado, J.L. McHale, Trap-State Distributions and Carrier Transport in Pure and Mixed-Phase TiO_2: Influence of Contacting Solvent and Interphasial Electron Transfer, J. Phys. Chem. C. 112 (2008) 12786–12794. doi:10.1021/jp8039934.

[30] Z. Jiang, W. Wan, W. Wei, K. Chen, H. Li, P.K. Wong, J. Xie, Gentle way to build reduced titanium dioxide nanodots integrated with graphite-like carbon spheres: From DFT calculation to experimental measurement, Appl. Catal. B Environ. 204 (2017) 283–295. doi:10.1016/j.apcatb.2016.11.044.

[31] C. Jin, B. Liu, Z. Lei, J. Sun, Structure and photoluminescence of the TiO_2 films

grown by atomic layer deposition using tetrakis-dimethylamino titanium and ozone, Nanoscale Res. Lett. 10 (2015) 95. doi:10.1186/s11671-015-0790-x.

[32] J. Yan, G. Wu, N. Guan, L. Li, Z. Li, X. Cao, Understanding the effect of surface/bulk defects on the photocatalytic activity of TiO_2: anatase versus rutile, Phys. Chem. Chem. Phys. 15 (2013) 10978. doi:10.1039/c3cp50927c.

[33] T. Ohsaka, F. Izumi, Y. Fujiki, Raman spectrum of anatase, TiO_2, J. Raman Spectrosc. 7 (1978) 321–324. doi:10.1002/jrs.1250070606.

[34] L. Li, F. Qiu, Y. Wang, Y. Wang, G. Liu, C. Yan, C. An, Y. Xu, D. Song, L. Jiao, H. Yuan, Crystalline TiB_2: an efficient catalyst for synthesis and hydrogen desorption/absorption performances of NaAlH4 system, J. Mater. Chem. 22 (2012) 3127. doi:10.1039/c1jm14936a.

[35] V. Mazánek, H. Nahdi, J. Luxa, Z. Sofer, M. Pumera, Electrochemistry of layered metal diborides, Nanoscale. 10 (2018) 11544–11552. doi:10.1039/C8NR02142B.

[36] C.S. Lim, Z. Sofer, V. Mazánek, M. Pumera, Layered titanium diboride: towards exfoliation and electrochemical applications, Nanoscale. 7 (2015) 12527–12534. doi:10.1039/C5NR02692J.

[37] B. Erdem, R.A. Hunsicker, G.W. Simmons, E.D. Sudol, V.L. Dimonie, M.S. El-Aasser, XPS and FTIR Surface Characterization of TiO_2 Particles Used in Polymer Encapsulation, Langmuir. 17 (2001) 2664–2669. doi:10.1021/la0015213.

[38] K. Bapna, D.M. Phase, R.J. Choudhary, Study of valence band structure of Fe doped anatase TiO_2 thin films, J. Appl. Phys. 110 (2011) 043910. doi:10.1063/1.3624775.

[39] T. Lin, C. Yang, Z. Wang, H. Yin, X. Lü, F. Huang, J. Lin, X. Xie, M. Jiang, Effective nonmetal incorporation in black titania with enhanced solar energy utilization, Energy Environ. Sci. 7 (2014) 967. doi:10.1039/c3ee42708k.

[40] L. Kong, Z. Jiang, C. Wang, F. Wan, Y. Li, L. Wu, J.-F. Zhi, X. Zhang, S. Chen, Y.

Liu, Simple Ethanol Impregnation Treatment Can Enhance Photocatalytic Activity of TiO_2 Nanoparticles under Visible-Light Irradiation, ACS Appl. Mater. Interfaces. 7 (2015) 7752–7758. doi:10.1021/acsami.5b00888.

[41] Y. Xia, T.S. Mathis, M.-Q. Zhao, B. Anasori, A. Dang, Z. Zhou, H. Cho, Y. Gogotsi, S. Yang, Thickness-independent capacitance of vertically aligned liquid-crystalline MXenes, Nature. 557 (2018) 409–412. doi:10.1038/s41586-018-0109-z.

[42] M.R. Lukatskaya, S. Kota, Z. Lin, M.-Q. Zhao, N. Shpigel, M.D. Levi, J. Halim, P.-L. Taberna, M.W. Barsoum, P. Simon, Y. Gogotsi, Ultra-high-rate pseudocapacitive energy storage in two-dimensional transition metal carbides, Nat. Energy. 2 (2017) 17105. doi:10.1038/nenergy.2017.105.

[43] J. Wang, J. Polleux, J. Lim, B. Dunn, Pseudocapacitive Contributions to Electrochemical Energy Storage in TiO_2 (Anatase) Nanoparticles, J. Phys. Chem. C. 111 (2007) 14925–14931. doi:10.1021/jp074464w.

[44] V.K. Mariappan, K. Krishnamoorthy, P. Pazhamalai, S. Sahoo, S.-J. Kim, Electrodeposited molybdenum selenide sheets on nickel foam as a binder-free electrode for supercapacitor application, Electrochim. Acta. 265 (2018) 514–522. doi:10.1016/j.electacta.2018.01.075.

[45] B. Huang, W. Wang, T. Pu, J. Li, J. Zhu, C. Zhao, L. Xie, L. Chen, Two-dimensional porous (Co, Ni)-based monometallic hydroxides and bimetallic layered double hydroxides thin sheets with honeycomb-like nanostructure as positive electrode for high-performance hybrid supercapacitors, J. Colloid Interface Sci. 532 (2018) 630–640. doi:10.1016/j.jcis.2018.08.019.

[46] M.S. Kim, T.-W. Lee, J.H. Park, Controlled TiO_2 Nanotube Arrays as an Active Material for High Power Energy-Storage Devices, J. Electrochem. Soc. 156 (2009) A584. doi:10.1149/1.3129682.

[47] H. Zhou, Y. Zhang, Electrochemically Self-Doped TiO_2 Nanotube Arrays for Supercapacitors, J. Phys. Chem. C. 118 (2014) 5626–5636. doi:10.1021/jp4082883.

[48] S. Zhao, Y. Chen, Z. Zhao, L. Jiang, C. Zhang, J. Kong, X. Zhu, Enhanced capacitance of TiO_2 nanotubes topped with nanograss by H_3PO_4 soaking and hydrogenation doping, Electrochim. Acta. 266 (2018) 233–241. doi:10.1016/j.electacta.2018.02.037.

[49] D. Pan, H. Huang, X. Wang, L. Wang, H. Liao, Z. Li, M. Wu, C-axis preferentially oriented and fully activated TiO_2 nanotube arrays for lithium ion batteries and supercapacitors, J. Mater. Chem. A. 2 (2014) 11454–11464. doi:10.1039/C4TA01613K.

[50] H. Wu, C. Xu, J. Xu, L. Lu, Z. Fan, X. Chen, Y. Song, D. Li, Enhanced supercapacitance in anodic TiO_2 nanotube films by hydrogen plasma treatment, Nanotechnology. 24 (2013) 455401. doi:10.1088/0957-4484/24/45/455401.

[51] C. Kim, S. Kim, J. Lee, J. Kim, J. Yoon, Capacitive and Oxidant Generating Properties of Black-Colored TiO_2 Nanotube Array Fabricated by Electrochemical Self-Doping, ACS Appl. Mater. Interfaces. 7 (2015) 7486–7491. doi:10.1021/acsami.5b00123.

[52] M. Salari, S.H. Aboutalebi, K. Konstantinov, H.K. Liu, A highly ordered titania nanotube array as a supercapacitor electrode, Phys. Chem. Chem. Phys. 13 (2011) 5038. doi:10.1039/c0cp02054k.

[53] H.R. Barai, M.M. Rahman, S.W. Joo, Template-free synthesis of two-dimensional titania/titanate nanosheets as electrodes for high-performance supercapacitor applications, J. Power Sources. 372 (2017) 227–234. doi:10.1016/j.jpowsour.2017.10.076.

[54] A. Ramadoss, S.J. Kim, Vertically aligned TiO_2 nanorod arrays for electrochemical supercapacitor, J. Alloys Compd. 561 (2013) 262–267. doi:10.1016/j.jallcom.2013.02.015.

[55] A. Ramadoss, S.J. Kim, Hierarchically structured TiO_2@MnO_2 nanowall arrays as potential electrode material for high-performance supercapacitors, Int. J. Hydrogen Energy. 39 (2014) 12201–12212. doi:10.1016/j.ijhydene.2014.05.118.

[56] U. Nithiyanantham, A. Ramadoss, S.R. Ede, S. Kundu, DNA mediated wire-like clusters of self-assembled TiO_2 nanomaterials: supercapacitor and dye sensitized solar cell applications, Nanoscale. 6 (2014) 8010. doi:10.1039/c4nr01836b.

[57] U. Nithiyanantham, A. Ramadoss, S. Kundu, Supercapacitor and dye-sensitized solar cell (DSSC) applications of shape-selective TiO_2 nanostructures, RSC Adv. 4 (2014) 35659. doi:10.1039/C4RA06226D.

[58] P. Pazhamalai, K. Krishnamoorthy, V.K. Mariappan, S. Sahoo, S. Manoharan, S.-J. Kim, A High Efficacy Self-Charging $MoSe_2$ Solid-State Supercapacitor Using Electrospun Nanofibrous Piezoelectric Separator with Ionogel Electrolyte, Adv. Mater. Interfaces. 5 (2018) 1800055. doi:10.1002/admi.201800055.

[59] J. Han, A. Hirata, J. Du, Y. Ito, T. Fujita, S. Kohara, T. Ina, M. Chen, Intercalation pseudocapacitance of amorphous titanium dioxide@nanoporous graphene for high-rate and large-capacity energy storage, Nano Energy. 49 (2018) 354–362. doi:10.1016/j.nanoen.2018.04.063.

[60] J. Wang, J. Polleux, T. Brezesinski, S. Tolbert, B. Dunn, The Pseudocapacitance Behaviors of TiO_2 (Anatase) Nanoparticles, in: ECS Trans., ECS, 2008: pp. 101–111. doi:10.1149/1.2953511.

[61] K.D. Fong, T. Wang, H.-K. Kim, R.V. Kumar, S.K. Smoukov, Semi-Interpenetrating Polymer Networks for Enhanced Supercapacitor Electrodes, ACS Energy Lett. 2 (2017) 2014–2020. doi:10.1021/acsenergylett.7b00466.

[62] W. Wang, S. Guo, I. Lee, K. Ahmed, J. Zhong, Z. Favors, F. Zaera, M. Ozkan, C.S. Ozkan, Hydrous Ruthenium Oxide Nanoparticles Anchored to Graphene and Carbon

Nanotube Hybrid Foam for Supercapacitors, Sci. Rep. 4 (2015) 4452. doi:10.1038/srep04452.

[63] R.B. Rakhi, N.A. Alhebshi, D.H. Anjum, H.N. Alshareef, Nanostructured cobalt sulfide-on-fiber with tunable morphology as electrodes for asymmetric hybrid supercapacitors, J. Mater. Chem. A. 2 (2014) 16190–16198. doi:10.1039/C4TA03341H.

[64] S. Sahoo, P. Pazhamalai, K. Krishnamoorthy, S.-J. Kim, Hydrothermally prepared α-MnSe nanoparticles as a new pseudocapacitive electrode material for supercapacitor, Electrochim. Acta. 268 (2018) 403–410. doi:10.1016/j.electacta.2018.02.116.

[65] R.B. Rakhi, B. Ahmed, M.N. Hedhili, D.H. Anjum, H.N. Alshareef, Effect of Postetch Annealing Gas Composition on the Structural and Electrochemical Properties of Ti_2CT_x MXene Electrodes for Supercapacitor Applications, Chem. Mater. 27 (2015) 5314–5323. doi:10.1021/acs.chemmater.5b01623.

[66] H. Li, L. Jing, W. Liu, J. Lin, R.Y. Tay, S.H. Tsang, E.H.T. Teo, Scalable Production of Few-Layer Boron Sheets by Liquid-Phase Exfoliation and Their Superior Supercapacitive Performance, ACS Nano. 12 (2018) 1262–1272. doi:10.1021/acsnano.7b07444.

CHAPTER 4.2 Understanding the thermal treatment effect of two dimensional siloxene sheets and the origin of superior electrochemical energy storage performances

Highlights:

- We have demonstrated the dehydrogenation/dehydroxylation of siloxene sheets by thermal annealing at high temperature (HT) and investigated their supercapacitive performances using ionic liquid electrolyte.
- The X-ray diffraction analysis, spectroscopic (FT-IR, laser Raman, and XPS) studies and morphological analysis of HT-siloxene revealed the removal of functional groups at the edges/basal planes of siloxene, and preservation of oxygen interconnected Si_6 rings with sheet-like structures.
- The HT-siloxene symmetric supercapacitor (SSC) operates over a wide potential window (0 to 3.0 V), delivers a high specific capacitance (3.45 mF cm^{-2}), high energy density of about 15.53 mJ cm^{-2} (almost two-fold higher than as-prepared siloxene SSC), low equivalent series resistance (compared to reported silicon based SSCs) with excellent rate capability and long cycle life over 10,000 cycles.

4.2.1. Introduction

The advent of two dimensional materials beyond graphene created new horizons on the development of next-generation energy storage devices[1]. Two dimensional materials such as transition metal dichalcogenides[2], transition metal carbides/nitrides/carbonitrides[3,4], metal organic frameworks[5], and polymers[6] are developed and examined for application as advanced electrode materials for flexible and wearable energy storage devices (batteries and supercapacitors) during this era. Several research works have been focused on development of novel electrode materials and their utilization towards different types of supercapacitors such as (i) aqueous supercapacitors[7], (ii) hybrid ion supercapacitors[8], (iii) colloidal supercapacitors[9], and (iv) non-aqueous supercapacitors[10], respectively. Recent studies demonstrated the possibility of utilizing 2D metals such as boron, germanium, phosphorus as an electrode for supercapacitor devices as an alternative to graphene[11–13]. However, the development of silicon-based materials for high performance supercapacitors are beneficial for ease of integration with the existing silicon technology in the semiconductor industry[14]. Thus, plentiful research is ongoing on the energy storage properties of various silicon materials such as silicon wires, rods, flowers, and sheets, etc[15–18]. In this scenario, silicene, a 2D allotrope of silicon (with sp^3 hybridization) received increasing attention owing to their unique structural and electrical properties[19–21]. Theoretical studies suggested the high possibilities of silicene in various fields including an electronic device, spintronics, ferromagnetism, optoelectronics, sensors, hydrogen storage, catalysis, water splitting, and oxygen reduction reaction, as well as novel electrodes for electrochemical energy storage devices[22–24]. However, experimental findings for many of the above-mentioned theoretical predictions are not yet demonstrated. This is due to the lack of appropriate methods for the preparation of high-quality silicene in bulk scale[19]. High-quality silicene sheets can be grown on the surface of suitable substrates

(silver, iridium, MoS_2) via molecular beam epitaxy method whereas the lateral size of the as-grown silicene is in the range of very few nanometers, thus limits the research on silicene towards functional applications[25,26]. Hitherto, alternative routes are developed recently to obtained silicene-like materials using chemical and electrochemical methods.

Various chemical methods available for the preparation of silicene-like materials are reported viz (i) topotactic transformation of layered calcium silicide in presence of hydrochloric acid results in the formation of siloxene sheets (oxygen functionalized silicene)[27], (ii) iodine mediated liquid oxidation and exfoliation of $CaSi_2$ resulting in the formation of silicene sheets[28], (iii) magnesiothermic reduction of SiO_2 at elevated temperatures resulting in the formation of silicene flowers[29], (iv), electrochemical lithiation and de-lithiation of silicon which resulting in the formation of oxidized silicenes, respectively[30]. All these methods resulted in the formation of silicene sheets functionalized with oxygen in which the oxygen content varies in accordance with the preparation methods employed (such as reaction precursors, reaction temperature, and environment)[27–30]. The silicene-like materials reported being a promising anode material for Li-ion batteries as well as an electrode for high performance supercapacitor devices[31,32]. Our recent work demonstrated that the chemically prepared siloxene sheets as high-performance electrode materials for supercapacitors with a high energy density of 9.82 mJ cm^{-2} (higher compared to the reported silicon-based SCs)[33]. The siloxene sheets with oxidized functional groups on the surfaces of 2D silicon can be considered as analogs to graphene oxides (oxidized graphene, a well know precursor for preparation of chemically derived graphene's). Based on the different structures of siloxene, it can be classified into three major types (i) Weiss siloxene, (ii) chain-like siloxene and (iii) Kautsky-type siloxene[34]. It is expected that the removal of oxidized functional groups in the siloxene sheets can lead to reduced siloxene sheets which might possess higher electronic conductivity. Until now, there are no such

studies has been attempted to investigate the chemical structure of reduced siloxene sheets and their electrochemical properties. Thus, understanding the effect of high-temperature heat treatment (HT) process on the siloxene sheets might provide new insights such as (i) tailoring the functional groups, (ii) preservation of sheet-like structures or not, and (iii) lead to the possible routes for achieving chemically derived silicene or reduced siloxene sheets. Further, the reduced siloxene sheets with improved electronic conductivity (than siloxene sheets) can make them as an ideal candidate for supercapacitor. Therefore, in this work, we aimed to the remove the oxygenated groups from the siloxene sheets via a high-temperature treatment and investigated their chemical nature as well as applications in SCs.

4.2.2 Experimental section

4.2.2.1 Topochemical transformation of $CaSi_2$ into siloxene sheets

In a typical synthesis method, 2D siloxene sheets was prepared via topochemical transformation of calcium silicide in an ice-cold hydrochloric acid[33]. Briefly, to synthesize siloxene sheets, $CaSi_2$ powders (1 g) were stirred in concentrated HCl (100 mL) at 0 °C for 4 days. The transformation from black color to green color confirms the dissolution of calcium in the HCl solution. Upon completion of the reaction, the obtained green colored siloxene sheets was washed with acetone and water. The washed powder was dispersed in water (100 mL) and subjected to ultrasound irradiation for 1 h. Again, the siloxene sheets were washed with water and allowed to dry at 80 °C for 12 h. The as prepared siloxene sheets were denoted as p-siloxene.

4.2.2.2 Thermal annealing of siloxene sheets

Briefly, 1 g of as prepared siloxene sheets was well grounded and annealed at 200 °C for 2 h at a heating rate of 2 °C; and then the temperature was ramped to 900 °C at a heating rate of 10 °C, was kept for 6 h in an Ar atmosphere for the removal of functional groups attached at the edges of the siloxene sheets, followed by cooling to room temperature. A

white greyish powder was formed as a result thermal annealing. The obtained heat treated siloxene powder was collected and used for further characterization. The siloxene sheets prepared via heat treatment were denoted as HT-siloxene sheets.

4.2.2.3 Preparation of electrodes

Initially, the homogeneous slurry of working electrode was prepared by grinding active material (90 wt %) with 5 wt % of carbon black and 5 wt % of PVDF binder dispersed in NMP. Then the prepared slurry was spread onto an aluminum(Al) foil using doctor blade to ensure the uniformity of the electrode thickness. The electrode was dried at 80 °C in a vacuum oven to evaporate the solvent. After complete drying of the electrode coated on Al, it is subjected to be densely pressed by a rolling press machine (WCRP-1015G), and the electroactive mass of the HT-siloxene electrode was calculated from the difference between the mass of the Al foil before and after coating using Dual-range Semi-micro Balance (AUW-220D, SHIMADZU) with an approximation of five-decimal points is approximate ~0.5 mg in each substrate. For the coin cell fabrication, the electrode was cut into a circle shape with a diameter of 14 mm.

4.2.2.4 Fabrication and testing of symmetric supercapacitor device

The symmetric supercapacitor (SSC) device based on p-siloxene and HT-siloxene (HT-siloxene) sheets was fabricated with a CR2032 coin cell configuration with electroactive area of 1.54 cm^2 separated by a Celgard membrane. $EMIMBF_4$ is used as the electrolyte. The fabricated SSC device was crimped using an electric coin cell crimping and disassembling machine (MTI, Korea). All the electrolyte handling and device fabrication were carried out in a glove box with less than 1 ppm of moisture and oxygen. Electrochemical characterization of the SSCs were analyzed using cyclic voltammetry (CV) at various scan rates, EIS analysis in the frequency range from 0.01 Hz to 100 kHz at an amplitude of 10 mV, and galvanostatic charge-discharge (CD) measurements using different current ranges were performed using an

Autolab PGSTAT302N electrochemical workstation. The methods used for determining specific capacitance, energy/power density, and maximal power density of HT-siloxene SSC device is provided with the electronic supporting document.

4.2.3. Results and discussion

4.2.3.1 Physicochemical characterization

Figure 4.2.1 shows the schematic representation of the preparation of reduced siloxene sheets via high-temperature treatment of siloxene sheets (prepared via topochemical reaction of layered calcium disilicide ($CaSi_2$)). A topochemical reaction between the layered $CaSi_2$ with ice-cold HCl results in the de-intercalation of Ca ions from $CaSi_2$ and simultaneous formation of siloxene sheets comprising various functional groups (oxygen interconnected with Si_6 rings, Si-OH, Si-H, and $OSi_2{\equiv}Si–H$ functionalized at the edges and basal planes) as shown in Figure 4.2.1(A and B)[27,33,35]. Upon thermal annealing at a temperature of 900 °C, some of the functional groups attached to the siloxene sheets (Figure 4.2.1 (C)) are decomposed and results in the structure given in Figure 4.2.1 (D).

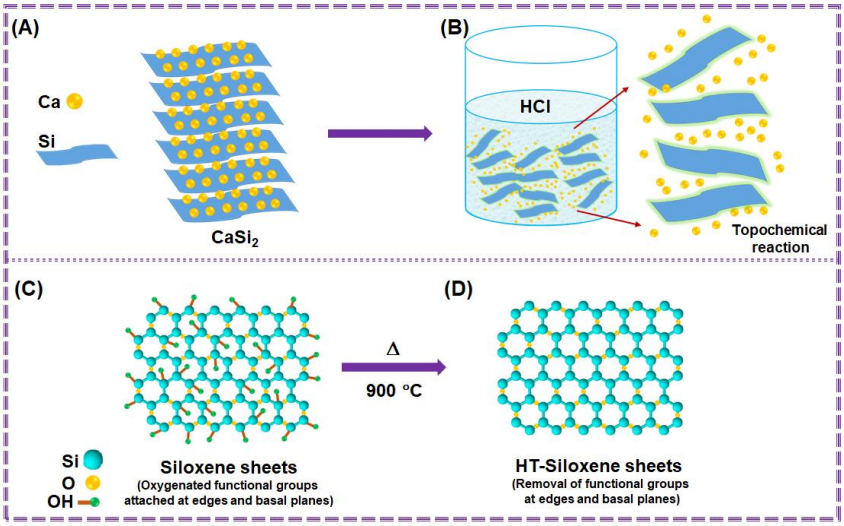

Figure 4.2.1. Schematic representation of the preparation of HT-siloxene sheets. (A-B) Preparation of p-siloxene sheets from $CaSi_2$ via a topochemical reaction, (C) structure of the resulting p-siloxene sheets with oxygenated functional groups. (D) structure of the HT-siloxene sheets after heat treatment of 900 ºC.

Figure 4.2.2 represents the comparative physico-chemical characterization of the p-siloxene and the HT-siloxene sheets. Figure 4.2.2(A) shows the X-ray diffraction (XRD) pattern indicating the presence of two diffraction peaks in the p-siloxene sheets observed at 13.5° and 26° which corresponds to the (001) and (100) planes of bi-dimensional silicon sheets derived from layered calcium disilicide via a topochemical reaction[36]. After thermal treatment, significant changes have been observed in the XRD pattern of HT-siloxene sheets as follows: (i) the peak observed at 13.5° (interlayer spacing of 0.65 nm) was diminished completely, and (ii) the broad peak observed at 26° (interlayer spacing of 0.33 nm) was preserved even after

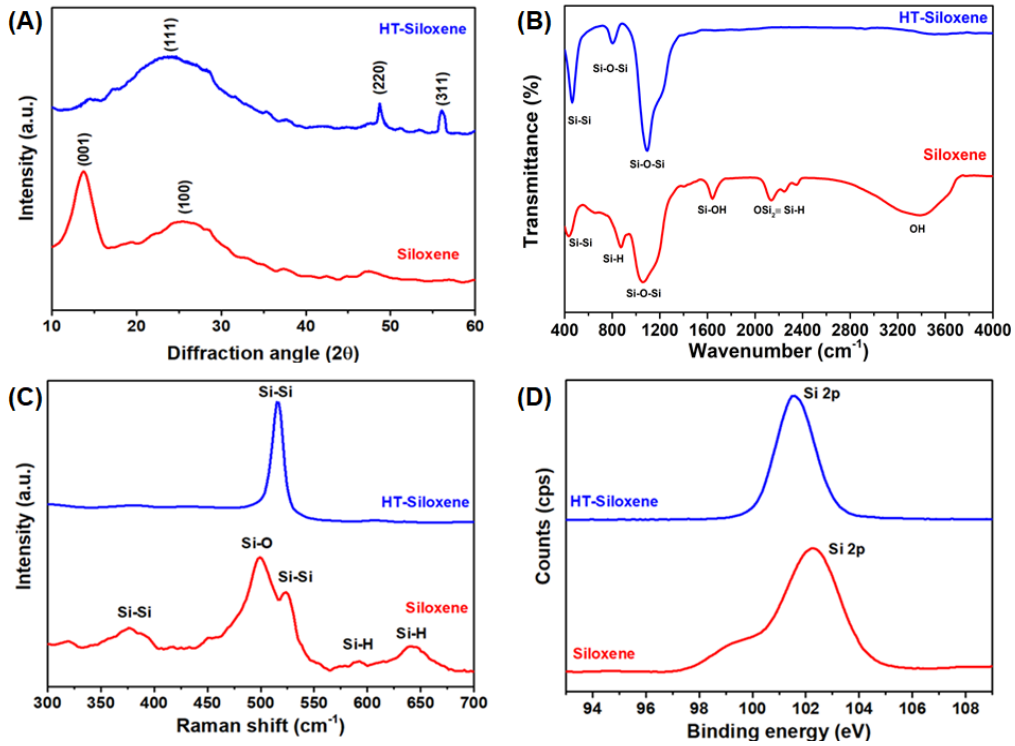

Figure 4.2.2. Physicochemical characterization of p-siloxene and HT-siloxene sheets. (A) X-ray diffraction pattern of the p-siloxene and HT-siloxene sheets. (B) Fourier transform infrared spectrum of p-siloxene and HT-siloxene sheets. (C) Laser Raman spectra of the p-siloxene and HT-siloxene sheets. X-ray photoelectron spectroscopy of the p-siloxene and HT-siloxene sheets (D) Core-level X-ray photoelectron spectra for Si 2p states of p-siloxene and HT-siloxene sheets.

the high temperature treatment. This might be due to the removal of oxygenated functional groups at the edges and basal planes of p-siloxene under HT process[37–39]. This effect is similar to that of thermal reduction of graphene oxide into graphene sheets[39,40]. This suggested that the thermal treatment of p-siloxene sheets resulted in the removal of oxygenated functional groups and the 2D silicon backbone was preserved. This finding is in agreement with the study of Yamanaka et al[27]. The bonding nature of the functional groups present in the p-siloxene and HT-siloxene sheets were examined using Fourier transformed infrared (FT-IR) spectroscopy as shown in Figure 4.2.2(B). The FT-IR spectrum of p-siloxene sheets shows the presence of broad vibration bands observed at 452, 867, 1034, 1639, and 2140 cm^{-1} which correspond to the vibrations raised from the ν(Si–Si), ν(Si–H), ν(Si–O–Si), ν(Si–OH), and ν(OSi_2≡Si–H), respectively[41].

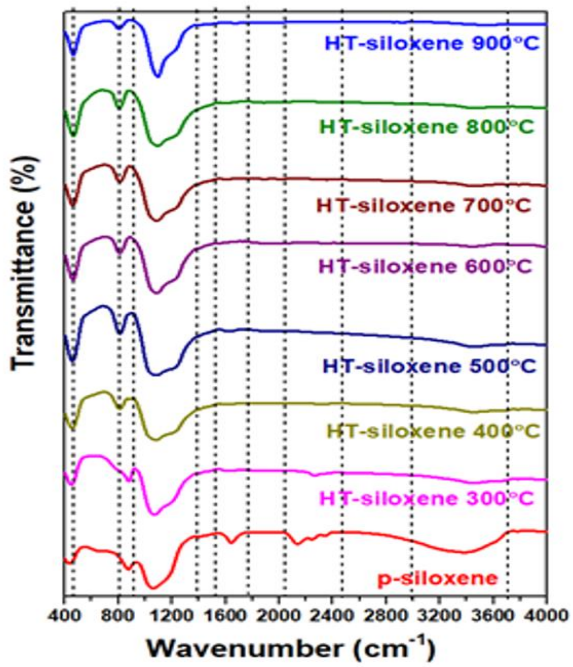

Figure 4.2.3. FT-IR spectrum of p-siloxene sheets thermally treated at various temperatures.

The FT-IR spectrum of p-siloxene treated at various temperatures from 300 to 900 °C is provided in Figure 4.2.3. This study revealed that the dehydrogenation of Si-H groups was occurred at a temperature of 400 °C, whereas the removal of Si-OH and OSi_2≡Si-H groups

were removed at a temperature of 600 °C. Hitherto, the intercalated hydroxyl groups (3100 – 3600 cm^{-1}) has been completely removed at a temperature of 900 °C. This finding is in agreement with the previous study of Yamanaka et al.[37] After the HT process at a temperature of 900 °C , the following changes occurred in the FT-IR spectrum of HT-siloxene as follows: (i) the vibration bands of ν(Si–OH), ν(OSi_2≡Si–H), and ν(Si–H) groups diminished completely suggesting their thermal decomposition at higher temperatures, (ii) The band correspond to ν(Si–O–Si) become broadened due to the thermal shock faced by the oxygen-enriched hexagonal silicon rings which leads to the formation of a new band observed at 805 which corresponds to the ν(Si–O), and (iii) the ν(Si–Si) band (at 452 cm^{-1}) becomes more sharpened after the HT-process.

The crystallinity and bonding nature of the p-siloxene and HT-siloxene sheets were examined using laser Raman spectroscopy as shown in Figure 4.2.2(C). The laser Raman spectrum of p-siloxene sheets shows the presences of two sharp bands two bands at 495 and 525 cm^{-1} attributed to the vibrations of Si–O/Si-OH and Si–Si bonds, respectively[33]. The presence of Si-H bonding (640 and 740 cm^{-1}) in the p-siloxene sheets is also evident from the Raman spectrum. After HT process, the only one sharp band at 516 cm^{-1} was observed in the Raman spectrum of HT-siloxene sheets which corresponds to the vibration raised from symmetric stretching (E_{2g}) modes of Si-Si bonds present in the hexagonal Si_6 rings; this confirms the integrity of the 2D bi-dimensional structure even after HT process. This finding is in close agreement with the previous study on the Raman spectrum of 2D silicon prepared via lithiation and de-lithiation process[30]. Figure 4.2.2(D) shows the core-level spectrum of Si 2p states in the p- siloxene sheets and HT-siloxene sheets which showed significant changes as follows: The core-level spectrum of Si 2p states in p-siloxene sheets can be resolved into two components (i) Si-Si bonding (eV) and Si-O bonding (eV), respectively. After the HT process, the Si-Si component disappeared, and only one peak at 101.5 eV (Si-O

bonding) was observed in the Si 2p core-level spectrum of HT- siloxene sheets. The disappearance of Si-Si peak in the core-level spectrum of HT-siloxene is in agreement with the previous study on the XPS analysis of heat-treated Wohler siloxene sheets[38].

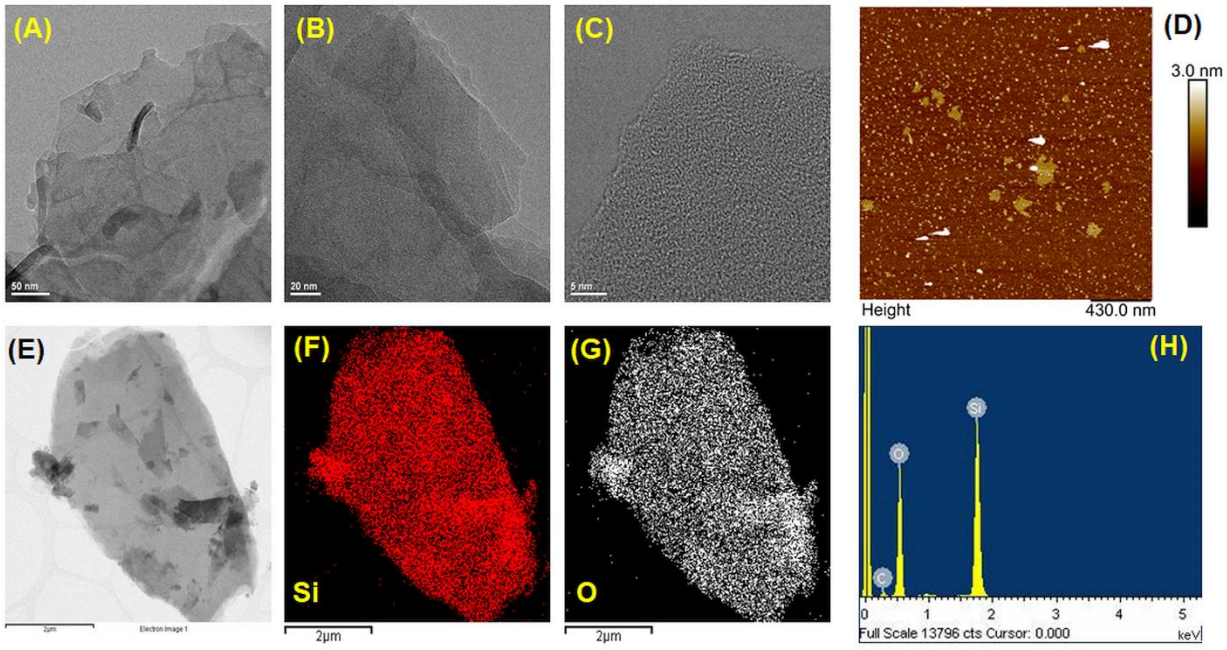

Figure 4.2.4. (A-C) High-resolution transmission electron microscopy (HR-TEM) images, (D) tapping-mode atomic force micrograph of the HT-siloxene sheets, (E-H) overlay image, elemental mapping of Si atoms and oxygen atoms with corresponding EDS mapping table of the HT-siloxene sheets.

Figure 4.2.4(A-G) represents the high-resolution transmission electron microscopic (HR-TEM) images and elemental mapping spectrum of the HT-siloxene. The HR-TEM images revealed the presence of sheet-like morphologies with few layers, suggesting that the HT process did not affect the 2D structure of p-siloxene. The atomic force micrograph (AFM) of the HT-siloxene sheets were provided in Figure 4.2.4(D). Figure 4.2.4 (D) represents the presence of sheet-like morphologies of the HT-siloxene which agrees with the HR-TEM micrographs. The section analysis of the HT-siloxene sheets revealed that the thickness of the sheets is in the range of 0.5 to 0.8 nm suggesting the presence of monolayer and/or bilayers of HT-siloxene sheets[36]. The elemental mapping images of HT-siloxene

sheet (Figure 4.2.4(E-H)) indicates the presence of Si atoms (red-colored) and O atoms (grey-colored) distributed throughout the sheets. The O/Si ratio of the HT-siloxene sheets was found to be 1.17 % determined using Cliff-Lorimer thin ratio section analysis. The O/Si ratio of HT-siloxene is lower compared to that of the p-siloxene sheets (1.49 %)[33] which confirms the decrease in oxygen content after HT-process.

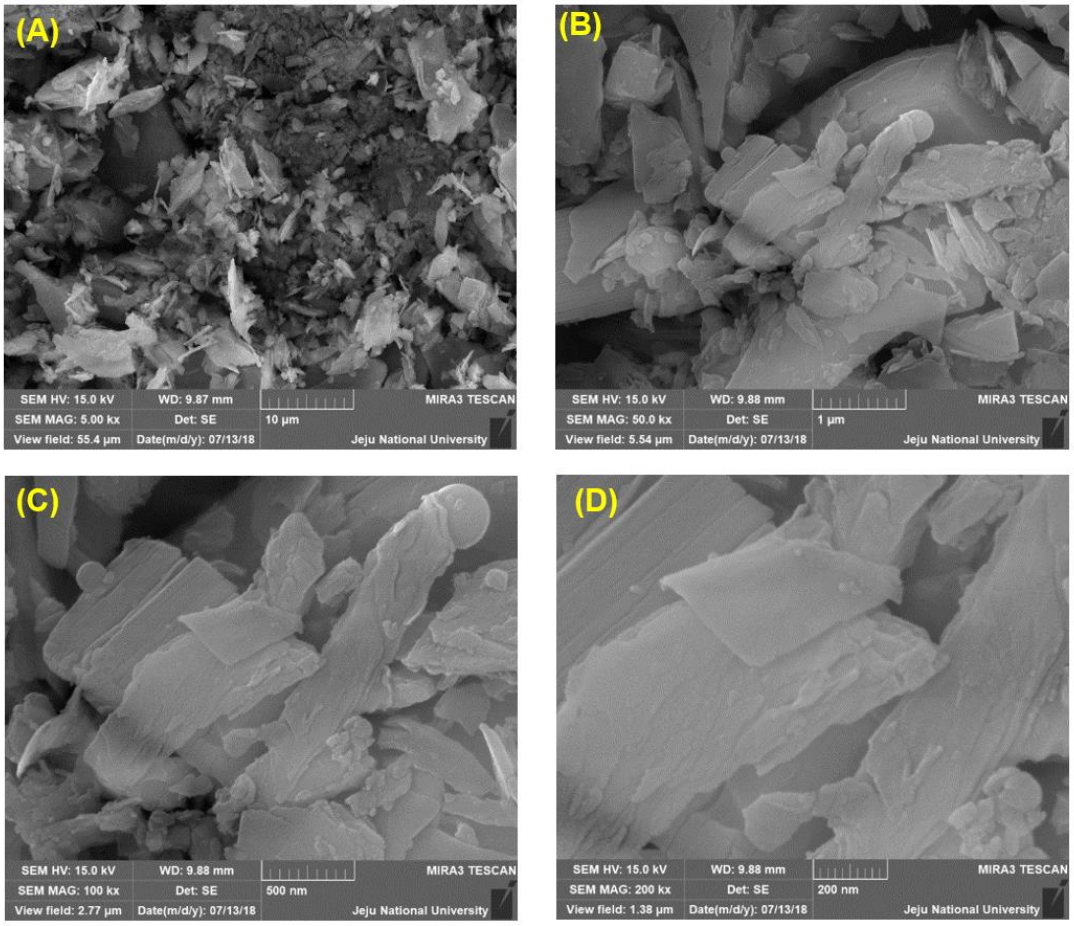

Figure 4.2.5. (A-D) FE-SEM micrograph of the HT-siloxene sheets under various magnifications.

The field emission scanning electron microscopic (FE-SEM) images of the HT-siloxene sheets indicates the presences of sheet-like structures (see Figure 4.2.5(A-D)) and the elemental mapping analysis (see Figure 4.2.6(A-D)) indicates the presence of Si and O atoms in the HT-siloxene sheets. Figure 4.2.7 represents the N_2 adsorption-desorption isotherms of the HT-siloxene sheets indicating the high surface area of about 64.2 m^2 g^{-1}

(which is higher than that of the surface area of siloxene sheets (59.72 m^2 g^{-1})) with an average pore size in the range of 30 to 40 nm respectively.

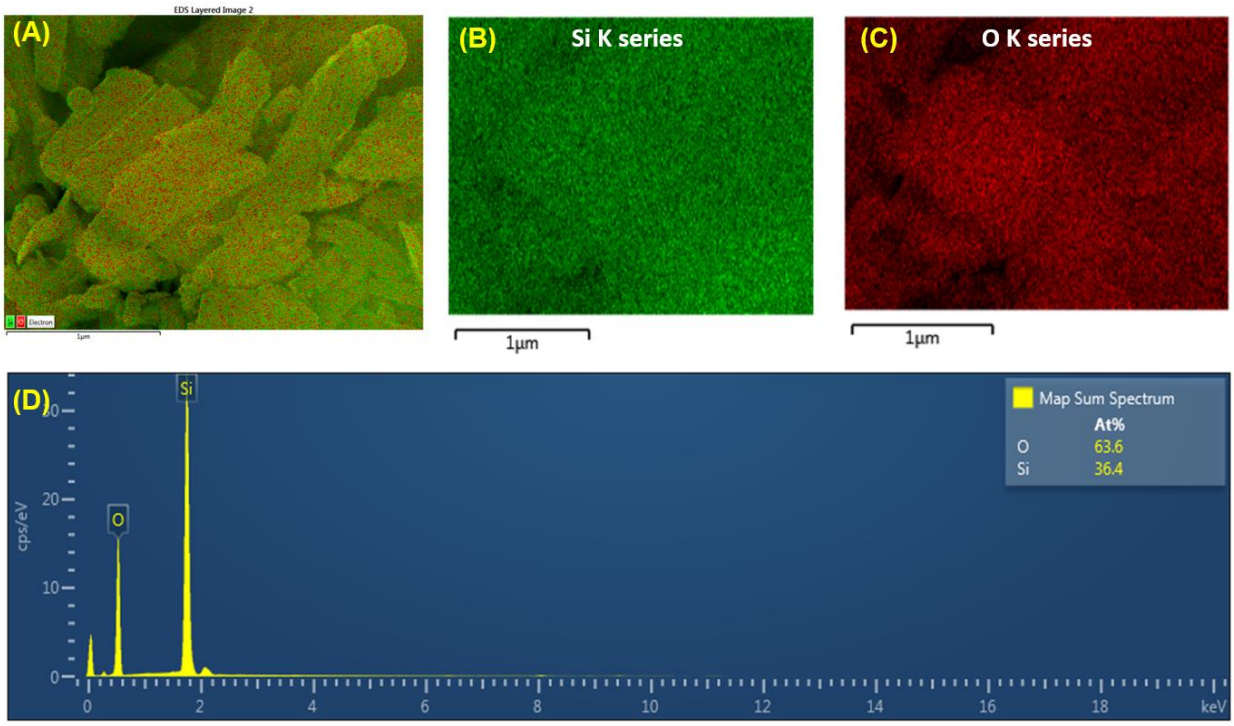

Figure 4.2.6. (A) FE-SEM overlay micrograph and the corresponding elemental mapping of the (B) Si; (C) O and (D) EDS spectrum of HT-siloxene sheets.

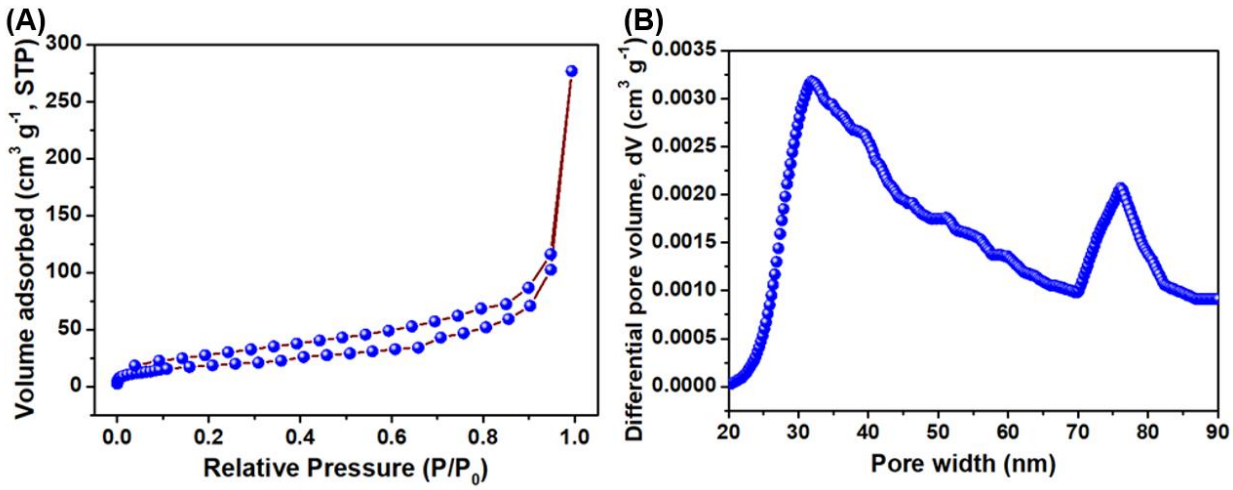

Figure 4.2.7. (A) N_2 adsorption–desorption isotherm and (B) pore size distribution of the prepared HT-siloxene sheets.

These physico-chemical characterizations of HT-siloxene sheets suggested the removal of oxygenated functional groups such as Si-OH and $OSi_2{\equiv}Si–H$ groups at the basal planes and edges of the p-siloxene sheets. The removal of these functional groups might provide distinct electrochemical performances of HT-siloxene sheets compared to the p-siloxene sheets.

4.2.3.2 Electrochemical characterization

The electrochemical energy storage performance of the HT-siloxene sheet as electrodes were characterized via the fabrication of coin-cell type symmetric supercapacitors (SSC) with 1-Ethyl-3-methylimidazolium tetrafluoroborate ($EMIMBF_4$) as electrolyte. Figure 4.2.8 shows the CV profiles of the HT-siloxene SSC measured using a scan rate of 100 mV s^{-1} with different OPWs (0 to 3.0 V) which indicates that the fabricated SSC can operate over a wide OPW of 3.0 V.

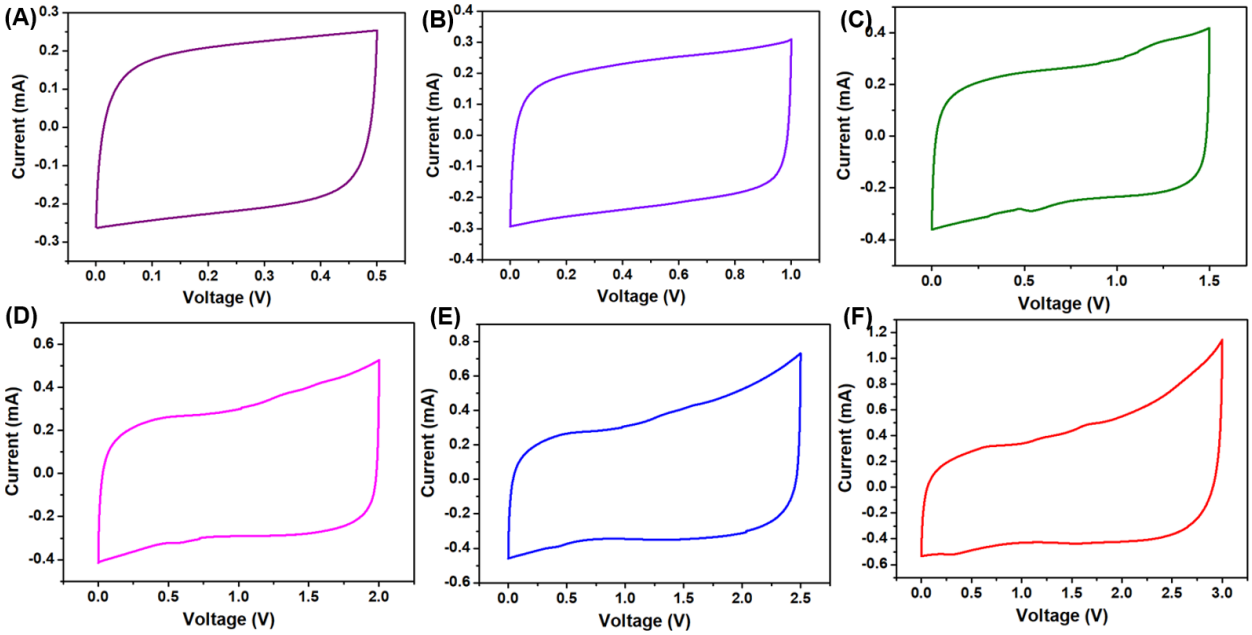

Figure 4.2.8. (A-F) Cyclic voltammetric profiles of HT-siloxene SSC device at various operating potential window recorded at a scan rate of 100 mV s^{-1}.

Figure 4.2.9 shows the comparative CV profiles of the p-siloxene and HT-siloxene sheets based SSCs in $EMIMBF_4$ electrolyte obtained at a scan rate of 100 mV s^{-1}. It shows

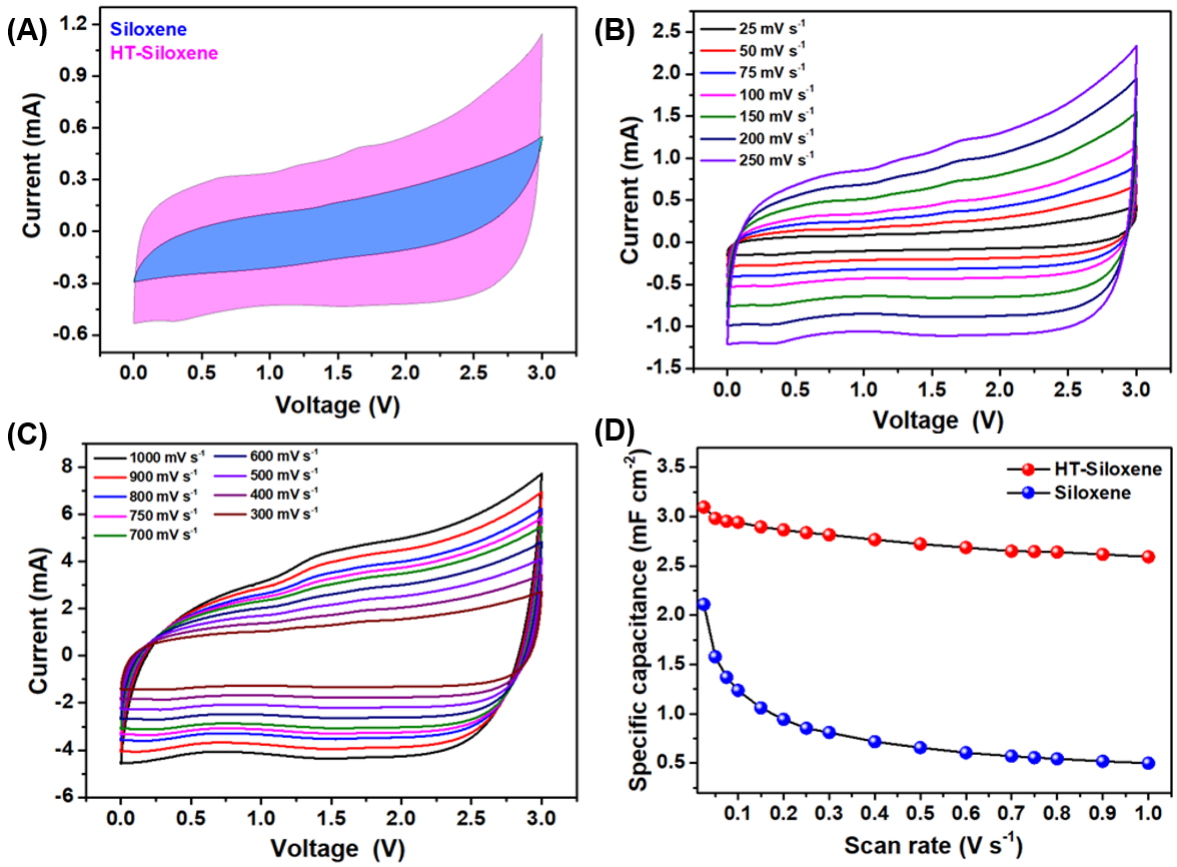

Figure 4.2.9 Electrochemical analysis of the p-siloxene and HT-siloxene-based symmetric supercapacitor (SSC) device (CR2032 coin cell) in 1-Ethyl-3-methylimidazolium tetrafluoroborate ($EMIMBF_4$). (A) Cyclic voltammetric profile of the p-siloxene and HT-siloxene SSCs measured over operating voltage window from 0.0 to 3.0 V using a scan rate of 100 mV s^{-1}. (B-C) Cyclic voltammetric profiles of HT-siloxene SSCs measured using different scan rates from 25 to 1000 mV s^{-1}. (D) Variation of areal specific capacitance of p-siloxene and HT-siloxene SSCs with respect to scan rate.

the presence of quasi-rectangular CV profiles for both SSCs over the operating potential window (OPW) of about 3.0 V. The current range in the CV profiles is higher for the HT-siloxene SSC compared to p-siloxene SSC, thus indicating the superior electrochemical

energy storage performance of the HT-siloxene SSC. The CV profiles of HT-siloxene SSC shows the presence of a small peak observed at a cell voltage of 0.3 V which indicates the conformation change of electrochemical ions inside the micropores of HT-siloxene electrodes during electrochemical charging/discharging cycle[42]. Figure 4.2.9(B and C) shows the CV profiles of the HT-siloxene SSC obtained under different scan rates ranging from 25 to 1000 mV s^{-1}, respectively. The increasing current values and the retained quasi-rectangular nature of the HT-siloxene SSC with an increase in scan rates, suggest the better electrochemical capacitive nature of the HT-siloxene electrodes. The CV profiles of the p-siloxene SSC recorded at different scan rates is also provided (see Figure 4.2.10).

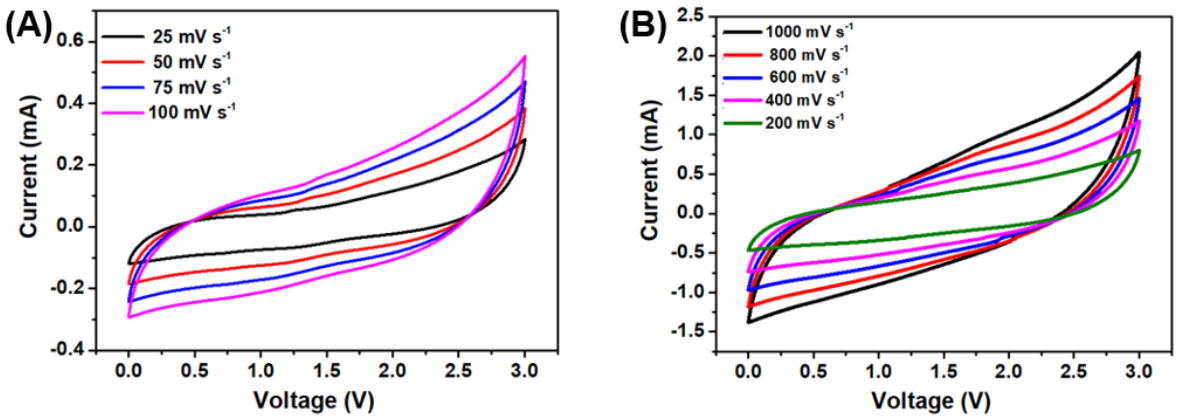

Figure 4.2.10 (A-B) Cyclic voltammetric profiles of p-siloxene SSC measured at various scan rate ranging from 25 to 1000 mV s^{-1}.

The effect of scan rate on the specific capacitance of p-siloxene and HT-siloxene based SSCs are provided in Figure 4.2.9(D). A maximum areal specific capacitance of about 3.09 mF cm^{-2} (equivalent to gravimetric specific device capacitance of 4.76 F g^{-1}) was obtained for the HT-siloxene SSC which is almost 1.47-fold higher compared to the specific capacitance of p-siloxene SSC (2.10 mF cm^{-2} or 3.24 F g^{-1}) obtained using a scan rate of 25 mV s^{-1}. With an increase in scan rate upto ten-fold, the HT-siloxene SSC retains a specific capacitance upto

91.6 % whereas the p-siloxene SSC retains only 40.45 %. Further, increase in scan rate upto 40-fold (1000 mV s^{-1}), the HT-siloxene SSC still retained a specific capacitance of about 83.54 % whereas the p-siloxene SSC retains only 23.68 %. These studies suggested the enhancement of specific capacitance in HT-siloxene based SSCs with superior rate capability compared to p-siloxene SSCs.

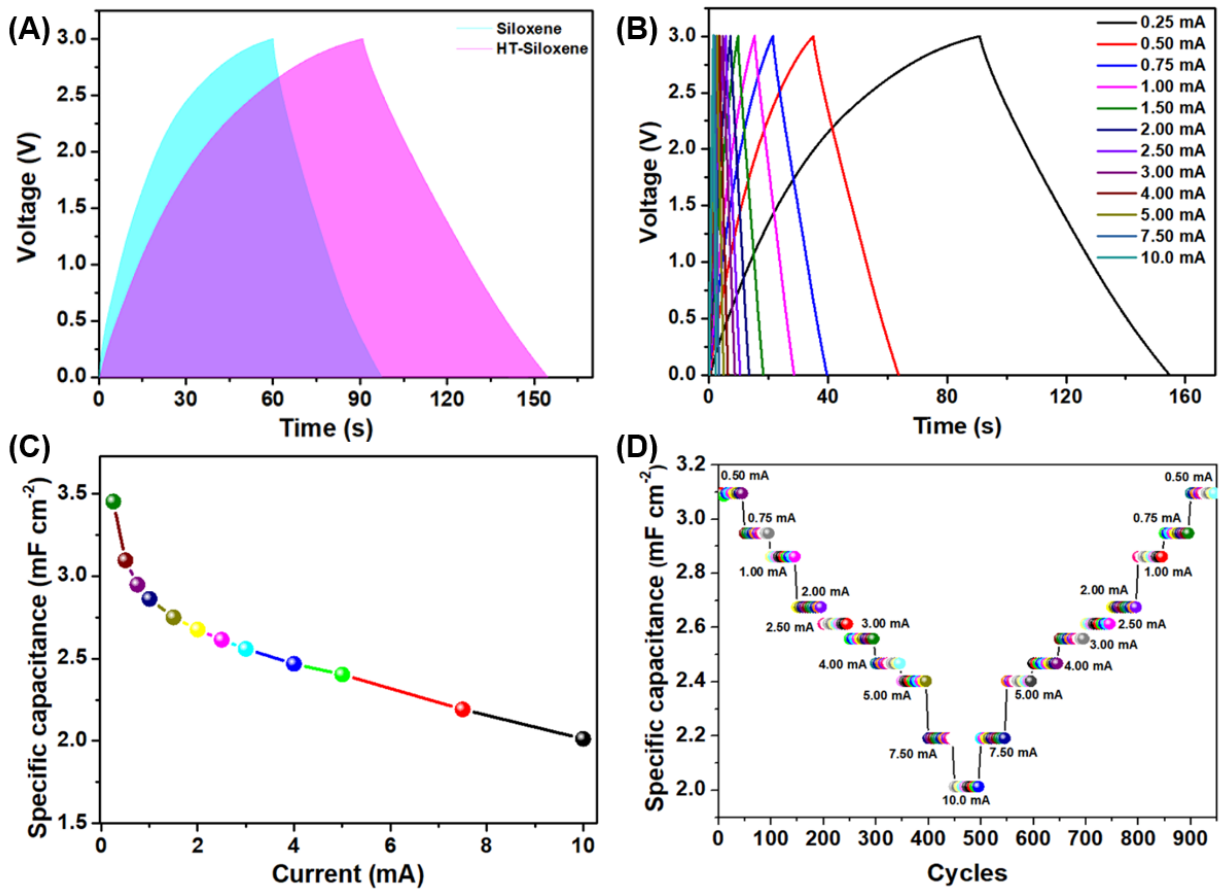

Figure 4.2.11. (A) Galvanostatic charge–discharge profile of the p-siloxene and HT-siloxene SSCs measured using a constant current of 0.25 mA. (B) Charge–discharge profiles of HT-siloxene SSC obtained using various applied current ranges. (C) Effect of discharge current on the specific capacitance of the siloxene and HT-siloxene SSCs ensuring the enhanced electrochemical properties of HT-siloxene. (D) Rate capability studies of the HT-siloxene SSC.

Figure 4.2.11(A) represents the comparative galvanostatic CD profile of p-siloxene and HT-siloxene SSCs recorded using a constant current of 0.25 mA, respectively. It

evidences that the charging and discharging time of the HT-siloxene SSC is quite higher to that of the p-siloxene SSC, thus indicating superior energy storage properties of the HT-siloxene SSC. The CD profiles of HT-siloxene SSC recorded using different applied current ranges are shown in Figure 4.2.11(B) which displayed the presence of quasi-symmetric CD profiles, an indication of predominant charge-storage due to pseudocapacitive nature[43]. The CD profiles of the p-siloxene SSC recorded at different applied current ranges are also provided (see Figure 4.2.12).

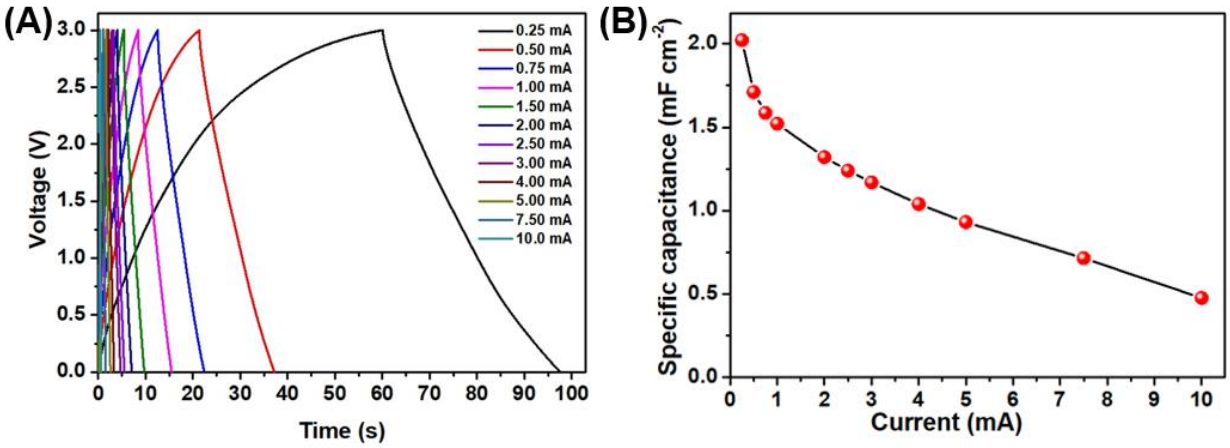

Figure 4.2.12 (A) Galvanostatic CD profiles of p-siloxene SSC measured at various current ranges. (B) Effect of applied current ranges on the specific capacitance of the p-siloxene SSC.

The effect of applied current on the specific capacitance of HT-siloxene SSC is provided in Figure 4.2.11(C). The maximum specific capacitance of 3.45 mF cm^{-2} (equivalent to gravimetric specific device capacitance of 5.31 F g^{-1}) is obtained for the HT-siloxene SSC recorded at a current of 0.25 mA, which is 1.71 times higher than the p-siloxene SSC (specific capacitance of 2.02 mF cm^{-2} (equivalent to gravimetric specific capacitance of 3.11 F g^{-1}) and those of reported SSCs using silicon electrodes in organic electrolyte. The rate capability, cyclic stability, energy and power density are some of the important features which determine the practical applications of a supercapacitor device[33,44]. Figure

4.2.11(D) shows the rate capability of the HT-siloxene SSC which showed better capacitance retention and stable cycling (over 50 cycles) with different applied current ranges from low to high and high to low.

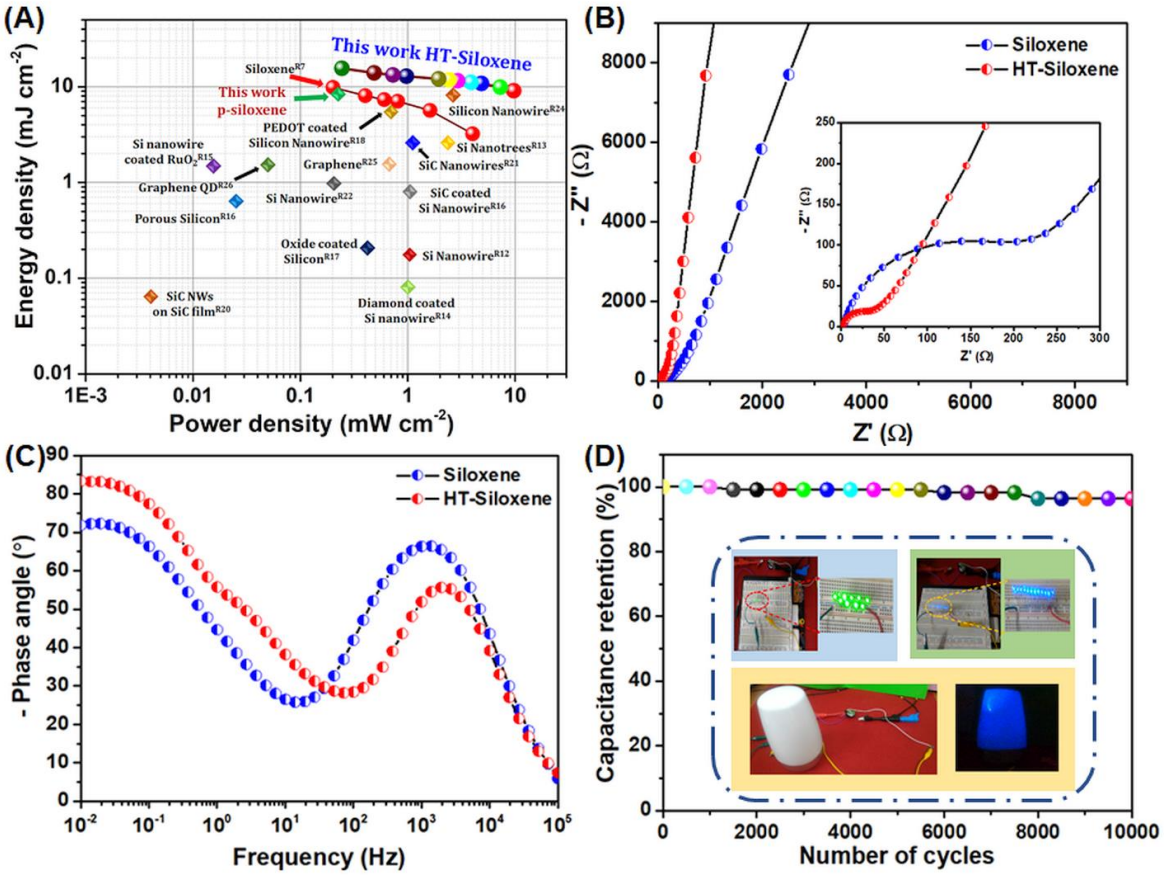

Figure 4.2.13. (A) Ragone plot of the HT-siloxene SSC showing the superior performance metrics over the reported Si-based SSCs.The Electrochemical impedance spectroscopic analysis of the p-siloxene and HT-siloxene SSCs analyzed using (B) Nyquist plot and (C) Bode phase angle plot. (D) Cycling stability of the HT-siloxene SSC over 10,000 continuous charge–discharge cycles. The inset in (D) shows the practical application of fully charged HT-siloxene SSC to glow (i) 10 commercial green LEDs; (ii) glow 12 commercial blue LEDs and (iii) powering a blue LED based night lamp.

This study demonstrated the excellent rate performance of HT-siloxene SSC. The energy/power performance metrics of the HT-siloxene SSC (in comparison with p-siloxene

SSC and other silicon-based SSCs)) is presented in the form of Ragone plot (Figure 4.2.13 (A)). The HT-siloxene SSC possesses a high energy density of about 15.53 mJ cm^{-2} (equivalent to gravimetric energy density of 6.64 Wh Kg^{-1}) with a corresponding power density of 0.24 mW cm^{-2} (equivalent to gravimetric power density of 375 W kg^{-1}) as obtained from the CD profiles using a current range of 0.25 mA, respectively. At the same current range, the p-siloxene SSC possesses an energy density of about 9.09 mJ cm^{-2} or 3.89 Wh Kg^{-1} with a corresponding power density of 0.24 mW cm^{-2} or 375 W kg^{-1}. With an increase in current ranges upto 10 mA, the energy density of p-siloxene and HT-siloxene SSCs are found to be 2.14 and 9.05 mJ cm^{-2} (0.91 and 3.875 Wh kg^{-1}), whereas the power density increases upto 9.74 mW cm^{-2} (equivalent to gravimetric power density of 15000 W kg^{-1}), respectively. Thus, the removal of functional groups in the p-siloxene sheets via thermal treatment results in providing superior energy density without compensating the power density. Further, the Ragone plot also highlights the superior performance metrics of the HT-siloxene with other silicon-based SSCs as well. The energy density of the HT-siloxene SSC is quite higher compared to other SSCs such as silicon nanowires (190 μJ cm^{-2})[45] , diamond coated Si NWs (2.5 mJ cm^{-2})[46], PEDOT coated Si NW (9 mJ cm^{-2})[47], polypyrrole coated Si NW (11 mJ cm^{-2})[15] and polypyrrole coated Si NTr (15 mJ cm^{-2})[15], graphene/Si NW (3.6 mJ cm^{-2})[48] and diamond coated Si NW (11 mJ cm^{-2})[49].

The superior capacitive nature and charge-transfer kinetics of the HT-siloxene SSC over p-siloxene SSC was analyzed in detail using EIS measurements in the frequency range of 0.01 Hz to 100 KHz at an amplitude of 10 mV, and the results are presented in the form of Nyquist and Bode plots. Figure 4.2.13(B) shows the Nyquist plot (plot of real against the imaginary component of the impedance) of p-siloxene and HT-siloxene SSCs. The Nyquist plot of both SSCs revealed the presence of three characteristic regions viz. (i) low-, (ii) intermediate- and (iii) high- frequency regions from which important parameters such as

Warburg line, Knee frequency, and equivalent series resistance (ESR) of the devices[33,50]. At first, the low-frequency region shows the presence of Warburg line (an indication of diffusion controlled reaction) which is closer to the imaginary axis for the HT-siloxene SSC compared to that of the p-siloxene SSC, thus indicating the better capacitance of the former[51]. The knee frequency observed at the intermediate frequency region is about 10 and 100 Hz for the p-siloxene and HT-siloxene SSCs, respectively. The ESR of the p-siloxene and HT-siloxene SSCs can be determined from the low- frequency region (see inset of Figure 4.2.13(B)) which was found to be 3.86 and 2.34 Ω, respectively[52]. The low ESR of the HT-siloxene SSC might be attributed to the removal of oxidized functional groups from the p-siloxene. The ESR of the HT-siloxene SSC is quite lower compared to the reported ESR values of silicon-based SSCs (Si NWs (22 Ω)[45], diamond-coated Si NWs (7 Ω)[46], Si NTs (17 Ω)[53]). A low ESR can results in obtaining maximal power density of a supercapacitor (since $P_{max} = V^2/4ESR$)[44]. The low ESR of HT-siloxene SSC leads to a high maximal power density values of about 627.05 mW cm^{-2} compared to that of p-siloxene SSC (P_{max} = 429.46 mW cm^{-2}). The obtained maximal power density of HT-siloxene SSC is higher compared to the recent works of silicon-based SSCs (Si NWs (182 mW cm^{-2}) [45], diamond-coated Si NWs (321 mW cm^{-2})[46], Si NTs (235 mW cm^{-2})[53], and Si NWs of 20 μm (1.4 mW cm^{-2})[54]). The Bode phase angle plots of the p-siloxene and HT-siloxene SSCs are shown in Figure 4.2.13(C) which indicates the change in phase angle with respect to applied frequency. The phase angle at the low frequency region is often used to characterize the capacitive nature of the device[7]. The phase angle at the low frequency region (0.01 Hz) is found to be 71.85° and 83.38° for the p-siloxene and HT-siloxene SSCs demonstrating the better capacitive nature in the later. The capacitor response frequency (f_o) at the phase angle of -45° was 4.67 Hz for HT-siloxene SSC much higher than that of p-siloxene SSC (0.9668 Hz). Thus, the corresponding time constant ($\tau_o = 1/f_o$) was only 0.214 s for HT-siloxene SSC,

compared to 1.034 s for p-siloxene SSC. The low time constant (time required to discharge all the energy with an efficiency of >50%) strongly suggest that the HT-siloxene SSC possess huge potential for instantaneous delivery of ultra-high power and energy. Figure 4.2.13 (D) shows the capacitance retention of HT-siloxene SSC over 10,000 cycles recorded at a current range of 5 mA. A capacitance retention of 96.3 % of the initial capacitance was obtained for the HT-siloxene SSC, thus demonstrating their better electrochemical stability over prolonged cycles.

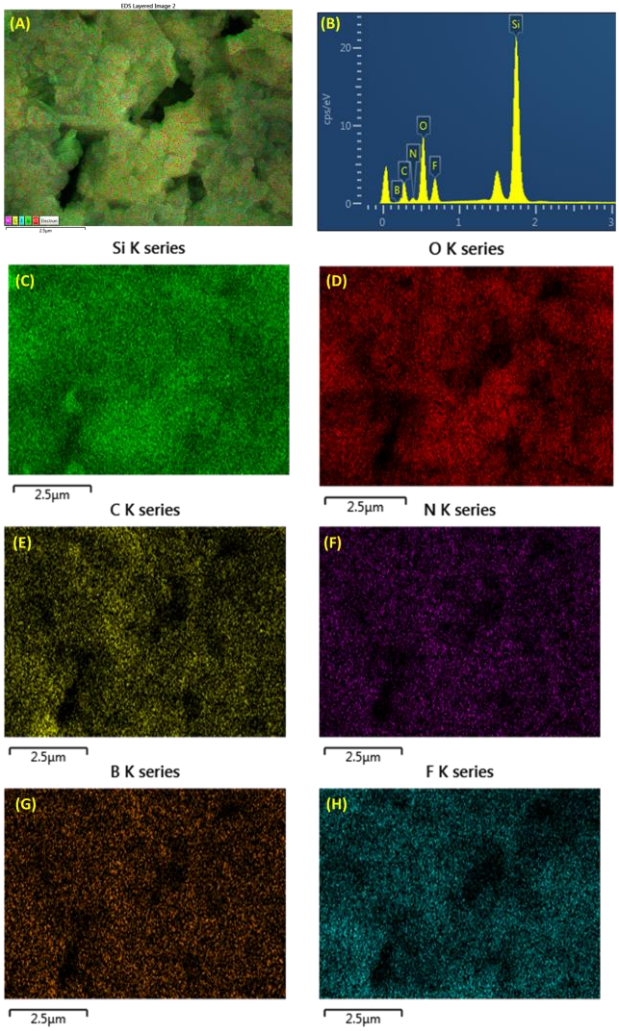

Figure 4.2.14. (A) Field-emission scanning electron overlay image of HT-siloxene sheets after cyclic test. (B) shows the EDS spectra of the elements present in the HT-siloxene sheets after cyclic test. Elemental mapping images (C) Si atom; (D) O atom; (E) F atom; (F) C atom; (G) N atom and (H) B atom present in HT-siloxene sheets after cyclic test.

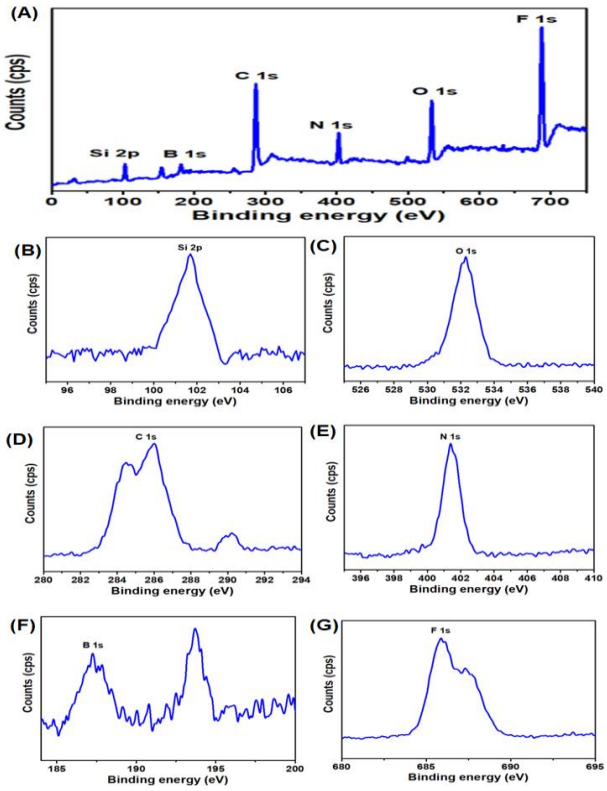

Figure 4.2.15. XPS analysis of HT-siloxene electrode after electrochemical test. (A) survey spectra and core level spectra (B) Si 2p state, (C) O 1s state, (D) C 1s state, (E) N 1s state, (F) B 1s state and (G) F 1s state present in the HT-siloxene electrode after electrochemical test.

The elemental mapping analysis of HT-siloxene electrode after cyclic test (Figure 4.2.14 (C-H)) indicates the presence of Si, O, C, N, B and F atoms distributed throughout the surface of the HT-siloxene electrode. The presence of C, N, B and F elements at the HT-siloxene electrode arises as a result of $EMIMBF_4$ electrolyte ions intercalation/de-intercalation process over prolong CD cycles. Figure 4.2.15 (A) shows the XPS survey spectrum of HT-siloxene electrode after cyclic test which revealed the presence of B 1s, C 1s, N 1s, and F 1s states in addition to the Si 2p and O 1s of the HT-siloxene. The core level spectrum of Si 2p state (Figure 4.2.15 (B)) observed at the binding energy of 101.7 eV was in consistent with the prepared HT-siloxene sheets. The core level spectrum of O 1s state shows the presence of oxygen in the interconnected Si rings of the HT-siloxene sheets[33,38]. Figure 4.2.15 (D-G) shows the core-level spectrum of C 1s, N 1s, B 1s, and F 1s states which

arises from the $EMIMBF_4$ electrolyte used in the HT-siloxene SSC. The binding energy values and spectral features of C 1s, N 1s, B 1s, and F 1s states are well matched with the XPS spectrum of $EMIMBF_4$ electrolyte.[56,57] In spite of having high energy storage capability and long cycle life of the fabricated HT-siloxene SSC, we examined for their use in practical applications. Initially, the HT-siloxene SSC was fully charged upto 3.0 V using a constant current of 0.5 mA, the stored energy in the HT-siloxene SSC can be utilized to power up electronic appliances. The fully charged HT-siloxene SSC is capable of glowing 10 commercial green LED for 15 s, 12 commercial blue LEDs for 25 s and a commercial blue night lamp for 10 s (inset of Figure. 4.2.13 (D)). These practical applications prove the proof of concept for the high-performance HT-siloxene SSC as a promising potency for future generation energy storage sectors.

4.2.3 Conclusion

We have demonstrated the removal of functional groups attached at the edges and basal planes of p-siloxene sheets via thermal annealing process. The chemical and structural analysis of as-prepared HT-siloxene sheets revealed that they are composed of oxygen enriched Si_6 rings with amorphous sheet-like structures. The investigation of HT-siloxene sheets as an electrode for supercapacitors demonstrated the high energy density of 15.53 mJ cm^{-2} (almost 2-fold higher compared to p-siloxene SSC) without compensating the power density. Further, HT-siloxene SSC possesses superior rate capability, low ESR value (compared to that of pristine-siloxene SSC) and better calendar life, thus demonstrating their excellent candidature towards the development of high-performance electrochemical energy storage devices. Future studies via advanced chemical/physical/thermal methods for complete removal of oxygenated functional groups bonded with siloxene sheets might result in the fundamental research development of chemically prepared silicenes and their practical application towards next-generation energy storage devices.

4.2.4 References:

[1] K.S. Kumar, N. Choudhary, Y. Jung, J. Thomas, Recent Advances in Two-Dimensional Nanomaterials for Supercapacitor Electrode Applications, ACS Energy Lett. 3 (2018) 482–495. doi:10.1021/acsenergylett.7b01169.

[2] M. Acerce, D. Voiry, M. Chhowalla, Metallic 1T phase MoS_2 nanosheets as supercapacitor electrode materials, Nat. Nanotechnol. 10 (2015) 313–318. doi:10.1038/nnano.2015.40.

[3] N. Kurra, B. Ahmed, Y. Gogotsi, H.N. Alshareef, MXene-on-Paper Coplanar Microsupercapacitors, Adv. Energy Mater. 6 (2016) 1601372. doi:10.1002/aenm.201601372.

[4] K. Krishnamoorthy, P. Pazhamalai, S. Sahoo, S.-J. Kim, Titanium carbide sheet based high performance wire type solid state supercapacitors, J. Mater. Chem. A. 5 (2017) 5726–5736. doi:10.1039/C6TA11198J.

[5] G. Xu, P. Nie, H. Dou, B. Ding, L. Li, X. Zhang, Exploring metal organic frameworks for energy storage in batteries and supercapacitors, Mater. Today. 20 (2017) 191–209. doi:10.1016/j.mattod.2016.10.003.

[6] W. Liu, M. Ulaganathan, I. Abdelwahab, X. Luo, Z. Chen, S.J. Rong Tan, X. Wang, Y. Liu, D. Geng, Y. Bao, J. Chen, K.P. Loh, Two-Dimensional Polymer Synthesized via Solid-State Polymerization for High-Performance Supercapacitors, ACS Nano. 12 (2018) 852–860. doi:10.1021/acsnano.7b08354.

[7] K. Krishnamoorthy, P. Pazhamalai, S.J. Kim, Ruthenium sulfide nanoparticles as a new pseudocapacitive material for supercapacitor, Electrochim. Acta. 227 (2017) 85–94. doi:10.1016/j.electacta.2016.12.171.

[8] K. Krishnamoorthy, P. Pazhamalai, S. Sahoo, J.H. Lim, K.H. Choi, S.J. Kim, A High-Energy Aqueous Sodium-Ion Capacitor with Nickel Hexacyanoferrate and Graphene

Electrodes, ChemElectroChem. 4 (2017) 3302–3308. doi:10.1002/celc.201700690.

[9] X. Chen, K. Chen, H. Wang, D. Xue, Functionality of $Fe(NO_3)_3$ salts as both positive and negative pseudocapacitor electrodes in alkaline aqueous electrolyte, Electrochim. Acta. 147 (2014) 216–224. doi:10.1016/j.electacta.2014.08.132.

[10] P. Pazhamalai, K. Krishnamoorthy, V.K. Mariappan, S. Sahoo, S. Manoharan, S.-J. Kim, A High Efficacy Self-Charging $MoSe_2$ Solid-State Supercapacitor Using Electrospun Nanofibrous Piezoelectric Separator with Ionogel Electrolyte, Adv. Mater. Interfaces. 5 (2018) 1800055. doi:10.1002/admi.201800055.

[11] Q. Xue, H. Gan, Y. Huang, M. Zhu, Z. Pei, H. Li, S. Deng, F. Liu, C. Zhi, Boron Element Nanowires Electrode for Supercapacitors, Adv. Energy Mater. 8 (2018) 1703117. doi:10.1002/aenm.201703117.

[12] H.S. Im, Y.R. Lim, Y.J. Cho, J. Park, E.H. Cha, H.S. Kang, Germanium and Tin Selenide Nanocrystals for High-Capacity Lithium Ion Batteries: Comparative Phase Conversion of Germanium and Tin, J. Phys. Chem. C. 118 (2014) 21884–21888. doi:10.1021/jp507337c.

[13] X. Chen, G. Xu, X. Ren, Z. Li, X. Qi, K. Huang, H. Zhang, Z. Huang, J. Zhong, A black/red phosphorus hybrid as an electrode material for high-performance Li-ion batteries and supercapacitors, J. Mater. Chem. A. 5 (2017) 6581–6588. doi:10.1039/C7TA00455A.

[14] S. Ortaboy, J.P. Alper, F. Rossi, G. Bertoni, G. Salviati, C. Carraro, R. Maboudian, MnO_x -decorated carbonized porous silicon nanowire electrodes for high performance supercapacitors, Energy Environ. Sci. 10 (2017) 1505–1516. doi:10.1039/C7EE00977A.

[15] D. Aradilla, D. Gaboriau, G.G. Bidan, P. Gentile, M. Boniface, D. Dubal, P. Gómez-Romero, J. Wimberg, T.J.S. Schubert, S.S. Sadki, P. Gomez-Romero, J. Wimberg,

T.J.S. Schubert, S.S. Sadki, An innovative 3-D nanoforest heterostructure made of polypyrrole coated silicon nanotrees for new high performance hybrid micro-supercapacitors, J. Mater. Chem. A. 3 (2015) 13978–13985. doi:10.1039/C5TA03435C.

[16] M.R. Zamfir, H.T. Nguyen, E. Moyen, Y.H. Lee, D. Pribat, Silicon nanowires for Li-based battery anodes: a review, J. Mater. Chem. A. 1 (2013) 9566. doi:10.1039/c3ta11714f.

[17] Y. Cui, Functional Nanoscale Electronic Devices Assembled Using Silicon Nanowire Building Blocks, Science (80-.). 291 (2001) 851–853. doi:10.1126/science.291.5505.851.

[18] R. Xu, G. Wang, T. Zhou, Q. Zhang, H.-P. Cong, Sen Xin, J. Rao, C. Zhang, Y. Liu, Z. Guo, S.-H. Yu, Rational design of Si@carbon with robust hierarchically porous custard-apple-like structure to boost lithium storage, Nano Energy. 39 (2017) 253–261. doi:10.1016/j.nanoen.2017.07.007.

[19] J. Zhao, H. Liu, Z. Yu, R. Quhe, S. Zhou, Y. Wang, C.C. Liu, H. Zhong, N. Han, J. Lu, Y. Yao, K. Wu, Rise of silicene: A competitive 2D material, Prog. Mater. Sci. 83 (2016) 24–151. doi:10.1016/j.pmatsci.2016.04.001.

[20] D. Xue, C. Sun, X. Chen, Hybridization: A Chemical Bonding Nature of Atoms, Chinese J. Chem. 35 (2017) 1452–1458. doi:10.1002/cjoc.201700425.

[21] M.R. Tchalala, M.A. Ali, H. Enriquez, A. Kara, A. Lachgar, S. Yagoubi, E. Foy, E. Vega, A. Bendounan, M.G. Silly, F. Sirotti, S. Nitshe, D. Chaudanson, H. Jamgotchian, B. Aufray, A.J. Mayne, G. Dujardin, H. Oughaddou, Silicon sheets by redox assisted chemical exfoliation, J. Phys. Condens. Matter. 25 (2013) 442001. doi:10.1088/0953-8984/25/44/442001.

[22] A.Y. Galashev, A.S. Vorob'ev, Physical properties of silicene electrodes for Li-, Na-,

Mg-, and K-ion batteries, J. Solid State Electrochem. 22 (2018) 3383–3391. doi:10.1007/s10008-018-4050-8.

[23] A.M. Tokmachev, D. V. Averyanov, O.E. Parfenov, A.N. Taldenkov, I.A. Karateev, I.S. Sokolov, O.A. Kondratev, V.G. Storchak, Emerging two-dimensional ferromagnetism in silicene materials, Nat. Commun. 9 (2018) 1672. doi:10.1038/s41467-018-04012-2.

[24] J. Lv, M. Xu, S. Lin, X. Shao, X. Zhang, Y. Liu, Y. Wang, Z. Chen, Y. Ma, Direct-gap semiconducting tri-layer silicene with 29% photovoltaic efficiency, Nano Energy. 51 (2018) 489–495. doi:10.1016/j.nanoen.2018.06.079.

[25] W. Wei, Y. Dai, B. Huang, Hydrogenation of silicene on Ag(111) and formation of half-silicane, J. Mater. Chem. A. 5 (2017) 18128–18137. doi:10.1039/C7TA03791K.

[26] M. Satta, P. Lacovig, N. Apostol, M. Dalmiglio, F. Orlando, L. Bignardi, H. Bana, E. Travaglia, A. Baraldi, S. Lizzit, R. Larciprete, The adsorption of silicon on an iridium surface ruling out silicene growth, Nanoscale. 10 (2018) 7085–7094. doi:10.1039/C8NR00648B.

[27] M.I. Shoji Yamanaka, Hiroyuki Matsu-ura, New deintercalation reaction of calcium from calcium disilicide. Synthesis of layered polysilane, Mater. Res. Bull. 31 (1996) 307–316. doi:10.1016/0025-5408(95)00195-6.

[28] J. Liu, Y. Yang, P. Lyu, P. Nachtigall, Y. Xu, Few-Layer Silicene Nanosheets with Superior Lithium-Storage Properties, Adv. Mater. 30 (2018) 1800838. doi:10.1002/adma.201800838.

[29] X. Zhang, X. Qiu, D. Kong, L. Zhou, Z. Li, X. Li, L. Zhi, Silicene Flowers: A Dual Stabilized Silicon Building Block for High-Performance Lithium Battery Anodes, ACS Nano. 11 (2017) 7476–7484. doi:10.1021/acsnano.7b03942.

[30] W. Zhang, L. Sun, J.M.V. Nsanzimana, X. Wang, Lithiation/Delithiation Synthesis of

Few Layer Silicene Nanosheets for Rechargeable Li-O_2 Batteries, Adv. Mater. 30 (2018) 1705523. doi:10.1002/adma.201705523.

[31] H. Imagawa, H. Itahara, Stabilized lithium-ion battery anode performance by calcium-bridging of two dimensional siloxene layers, Dalt. Trans. 46 (2017) 3655–3660. doi:10.1039/c6dt03837a.

[32] R. Fu, K. Zhang, R.P. Zaccaria, H. Huang, Y. Xia, Z. Liu, Two-dimensional silicon suboxides nanostructures with Si nanodomains confined in amorphous SiO_2 derived from siloxene as high performance anode for Li-ion batteries, Nano Energy. 39 (2017) 546–553. doi:10.1016/j.nanoen.2017.07.040.

[33] K. Krishnamoorthy, P. Pazhamalai, S.-J. Kim, Two-dimensional siloxene nanosheets: novel high-performance supercapacitor electrode materials, Energy Environ. Sci. 11 (2018) 1595–1602. doi:10.1039/C8EE00160J.

[34] J.R. Dahn, B.M. Way, E. Fuller, J.S. Tse, Structure of siloxene and layered polysilane (Si6H6), Phys. Rev. B. 48 (1993) 17872–17877. doi:10.1103/PhysRevB.48.17872.

[35] S. Li, H. Wang, D. Li, X. Zhang, Y. Wang, J. Xie, J. Wang, Y. Tian, W. Ni, Y. Xie, Siloxene nanosheets: a metal-free semiconductor for water splitting, J. Mater. Chem. A. 4 (2016) 15841–15844. doi:10.1039/C6TA07545B.

[36] H. Nakano, M. Ishii, H. Nakamura, Preparation and structure of novel siloxene nanosheets, Chem. Commun. 2 (2005) 2945. doi:10.1039/b500758e.

[37] S. Yamanaka, H. Matsu-ura, M. Ishikawa, M.I. Shoji Yamanaka, Hiroyuki Matsu-ura, New deintercalation reaction of calcium from calcium disilicide. Synthesis of layered polysilane, Mater. Res. Bull. 31 (1996) 307–316. doi:10.1016/0025-5408(95)00195-6.

[38] J.R. Dahn, B.M. Way, E.W. Fuller, W.J. Weydanz, J.S. Tse, D.D. Klug, T. Van Buuren, T. Tiedje, X-ray diffraction and x-ray absorption studies of porous silicon, siloxene, heat-treated siloxene, and layered polysilane, J. Appl. Phys. 75 (1994) 1946–

1951. doi:10.1063/1.356342.

[39] H. Ubara, T. Imura, A. Hiraki, I. Hirabayashi, K. Morigaki, Structural change from crystalline to amorphous states in siloxene by thermal annealing, J. Non. Cryst. Solids. 59–60 (1983) 641–644. doi:10.1016/0022-3093(83)90665-8.

[40] S. Stankovich, D.A. Dikin, R.D. Piner, K.A. Kohlhaas, A. Kleinhammes, Y. Jia, Y. Wu, S.T. Nguyen, R.S. Ruoff, Synthesis of graphene-based nanosheets via chemical reduction of exfoliated graphite oxide, Carbon N. Y. 45 (2007) 1558–1565. doi:10.1016/j.carbon.2007.02.034.

[41] H. Imagawa, N. Takahashi, T. Nonaka, Y. Kato, K. Nishikawa, H. Itahara, Synthesis of a calcium-bridged siloxene by a solid state reaction for optical and electrochemical properties, J. Mater. Chem. A. 3 (2015) 9411–9414. doi:10.1039/C5TA00321K.

[42] R. Yan, M. Antonietti, M. Oschatz, Toward the Experimental Understanding of the Energy Storage Mechanism and Ion Dynamics in Ionic Liquid Based Supercapacitors, Adv. Energy Mater. 8 (2018) 1800026. doi:10.1002/aenm.201800026.

[43] N. Shpigel, M.R. Lukatskaya, S. Sigalov, C.E. Ren, P. Nayak, M.D. Levi, L. Daikhin, D. Aurbach, Y. Gogotsi, In Situ Monitoring of Gravimetric and Viscoelastic Changes in 2D Intercalation Electrodes, ACS Energy Lett. 2 (2017) 1407–1415. doi:10.1021/acsenergylett.7b00133.

[44] S. Zhang, N. Pan, Supercapacitors Performance Evaluation, Adv. Energy Mater. 5 (2015) 1401401. doi:10.1002/aenm.201401401.

[45] D. Aradilla, P. Gentile, G. Bidan, V. Ruiz, P. Gómez-Romero, T.J.S. Schubert, H. Sahin, E. Frackowiak, S. Sadki, High performance of symmetric micro-supercapacitors based on silicon nanowires using N-methyl-N-propylpyrrolidinium bis(trifluoromethylsulfonyl)imide as electrolyte, Nano Energy. 9 (2014) 273–281. doi:10.1016/j.nanoen.2014.07.001.

[46] D. Aradilla, F. Gao, G. Lewes-Malandrakis, W. Müller-Sebert, P. Gentile, S. Pouget, C.E. Nebel, G. Bidan, Powering electrodes for high performance aqueous micro-supercapacitors: Diamond-coated silicon nanowires operating at a wide cell voltage of 3 V, Electrochim. Acta. 242 (2017) 173–179. doi:10.1016/j.electacta.2017.04.102.

[47] D. Aradilla, G. Bidan, P. Gentile, P. Weathers, F. Thissandier, V. Ruiz, P. Gómez-Romero, T.J.S. Schubert, H. Sahin, S. Sadki, Novel hybrid micro-supercapacitor based on conducting polymer coated silicon nanowires for electrochemical energy storage, RSC Adv. 4 (2014) 26462. doi:10.1039/c4ra03192j.

[48] S. Chatterjee, R. Carter, L. Oakes, W.R. Erwin, R. Bardhan, C.L. Pint, Electrochemical and Corrosion Stability of Nanostructured Silicon by Graphene Coatings: Toward High Power Porous Silicon Supercapacitors, J. Phys. Chem. C. 118 (2014) 10893–10902. doi:10.1021/jp502079f.

[49] D. Aradilla, F. Gao, G. Lewes-Malandrakis, W. Müller-Sebert, D. Gaboriau, P. Gentile, B. Iliev, T. Schubert, S. Sadki, G. Bidan, C.E. Nebel, A step forward into hierarchically nanostructured materials for high performance micro-supercapacitors: Diamond-coated SiNW electrodes in protic ionic liquid electrolyte, Electrochem. Commun. 63 (2016) 34–38. doi:10.1016/j.elecom.2015.12.008.

[50] M.F. El-Kady, R.B. Kaner, Scalable fabrication of high-power graphene micro-supercapacitors for flexible and on-chip energy storage, Nat. Commun. 4 (2013) 1475. doi:10.1038/ncomms2446.

[51] K. Krishnamoorthy, P. Pazhamalai, G.K. Veerasubramani, S.J. Kim, Mechanically delaminated few layered MoS_2 nanosheets based high performance wire type solid-state symmetric supercapacitors, J. Power Sources. 321 (2016) 112–119. doi:10.1016/j.jpowsour.2016.04.116.

[52] C. Choi, K.M. Kim, K.J. Kim, X. Lepró, G.M. Spinks, R.H. Baughman, S.J. Kim,

Improvement of system capacitance via weavable superelastic biscrolled yarn supercapacitors, Nat. Commun. 7 (2016) 13811. doi:10.1038/ncomms13811.

[53] D. Gaboriau, D. Aradilla, M. Brachet, J. Le Bideau, T. Brousse, G. Bidan, P. Gentile, S. Sadki, Silicon Nanowires and Nanotrees : elaboration and optimization of new 3D architectures for high performance on-chip supercapacitors, Soumis à Nano Energy. 6 (2015) 81017–81027. doi:10.1039/C6RA14806A.

[54] F. Thissandier, N. Pauc, T. Brousse, P. Gentile, S. Sadki, Micro-ultracapacitors with highly doped silicon nanowires electrodes, Nanoscale Res. Lett. 8 (2013) 38. doi:10.1186/1556-276X-8-38.

[55] X. Xia, J. Tu, Y. Zhang, X. Wang, C. Gu, X.-B. Zhao, H.J. Fan, High-quality metal oxide core/shell nanowire arrays on conductive substrates for electrochemical energy storage., ACS Nano. 6 (2012) 5531–8. doi:10.1021/nn301454q.

[56] R.K. Blundell, P. Licence, Quaternary ammonium and phosphonium based ionic liquids: a comparison of common anions, Phys. Chem. Chem. Phys. 16 (2014) 15278–15288. doi:10.1039/C4CP01901F.

[57] A. Tõnisoo, J. Kruusma, R. Pärna, A. Kikas, M. Hirsimäki, E. Nõmmiste, E. Lust, In Situ XPS Studies of Electrochemically Negatively Polarized Molybdenum Carbide Derived Carbon Double Layer Capacitor Electrode, J. Electrochem. Soc. 160 (2013) A1084–A1093. doi:10.1149/2.042308jes.

CHAPTER 4.3: Carbothermal conversion of siloxene sheets into silicon-oxy-carbide lamellas: An advanced electrode for high-performance supercapacitors

Highlights:

- This study demonstrates the carbo-thermal preparation of silicon-oxy-carbide (SiOC) lamellas using two dimensional siloxene sheets and alginic acid as precursors.
- The high-resolution transmission electron micrographs and elemental mapping analysis revealed the formation of lamella-like structures with homogenously distributed of Si, O and C atoms in the SiOC lamellas.
- The fabricated SiOC-based symmetric supercapacitors (SSCs) using 1 M $TEABF_4$ electrolyte operates over a wide potential window (3.0 V), delivered a high specific device capacitance (16.71 F g^{-1}), and holds high energy density (20.89 Wh Kg^{-1}), high power density (15,000 W Kg^{-1}), low-equivalent series resistance (compared to other SiOC based SSCs) with excellent cyclic stability and superior rate capability.

4.3.1 Introduction

The rapid growth of renewable energy sources (solar, wind, and mechanical energy harvesting devices) has increased the requirement for sustainable energy-storage technologies in order to meet out the increasing energy demands in the day-to-day life[1]. Supercapacitors (SCs) becomes a prime interest of choice among the other energy storage devices such as lithium- and sodium- ion battery (LIBs and SIBs) due to the high- power density, moderate energy density, and long life-cycle[2]. The synergetic properties of electrode materials and electrolytes plays a vital role in the energy/power performance of a SCs[3,4]. Among the various electrode materials used for SCs, silicon-based electrodes are widely attracting towards micro-capacitor applications with high power density whereas silicon based compounds such as silicon carbide (SiC) and silicon oxy-carbide (SiO_xC_y) ceramics are shown to be a promising electrodes with good energy density[5,6]. Silicon- based ceramics as electrodes for SCs possess the advantage of wide-thermal stability which is an important factor determining the use of SCs in various temperature[7,8]. Earlier studies demonstrated that the electrochemical energy-storage properties of SiOCs is highly dependent on several factors including (i) oxygen functional groups, (ii) free-carbon phase, and (iii) ratio of amorphous/crystalline phase whereas exact role on these factors were not completely understood[9,10]. Recently, silicon oxycarbide (SiOCs) are considered as promising alternative electrodes for SCs, LIBs and SIBs mainly due to their structural advantage comprising (i) glassy SiO_xC_y phase and (ii) free-carbon phase embedded uniformly in the SiOC matrix thereby minimizing the volume changes in the electrodes over prolonged cycles[10,11]. The SiOCs glass-ceramics can be prepared via different methods such as (i) sol-gel method, (ii) carbo-thermal reaction, and (iii) pyrolysis of siloxane- based polymers, respectively which resulted in the formation of various morphologies (particles, irregular shaped powders) and compositions[12,13]. It is well known that size, structure, surface area,

chemical compositions, and porous nature of an electrode materials plays a vital role on the electrochemical energy storage properties. Up-to-date, there are not so many research work has been carried out on the preparation of SiOCs with controlled morphologies. In this work, the siloxene sheets are carbo-thermally converted into SiOC like oxygen enriched silicon oxycarbide (SiOC) lamellas for the first time and their use as novel electrode materials for supercapacitor using organic electrolyte were investigated in detail.

4.3.2. Experimental section

4.3.2.1 Topochemical transformation of $CaSi_2$ into siloxene sheets

In a typical synthesis method, 2D siloxene sheets was prepared via topochemical transformation of calcium silicide in an ice-cold hydrochloric acid[14,15]. Briefly, to synthesize siloxene sheets, $CaSi_2$ powders (1 g) were stirred in concentrated HCl (100 mL) at 0 °C for 4 days. The transformation from black color to green color confirms the dissolution of calcium in the HCl solution. Upon completion of the reaction, the obtained green colored siloxene sheets was washed with acetone and water. The washed powder was dispersed in water (100 mL) and subjected to ultrasound irradiation for 1 h. Again, the siloxene sheets were washed with water and allowed to dry at 80 °C for 12 h. The as prepared siloxene sheets were denoted as p-siloxene.

4.3.2.2 Preparation of silicon-oxy-carbide (SiOC)

A carbothermal reaction was used for the preparation of silicon-oxy-carbide(SiOC). Briefly, 0.4 g of as prepared siloxene sheets and 5 g of sodium alginate was well grounded and annealed at 200 °C for 2 h at a heating rate of 2 °C; and then the temperature was ramped to 900 °C at a heating rate of 10 °C, was kept for 6 h in an Ar atmosphere for the removal of functional groups attached at the edges of the siloxene sheets and to carbonize the biopolymer, followed by cooling to room temperature. A black powder was formed which is washed and used for further characterization. For the preparation of alginate derived carbon,

the above procedure is repeated in absence of siloxene sheets with the same experimental conditions. The prepared silicon-oxy-carbide/ is denoted as SiOC.

4.3.2.3 Preparation of electrodes

Initially, the homogeneous slurry of working electrode was prepared by grinding active material (90 wt %) with 5 wt % of carbon black and 5 wt % of PVDF binder dispersed in NMP. Then the prepared slurry was spread onto an aluminum (Al) foil using doctor blade to ensure the uniformity of the electrode thickness. The electrode was dried at 80 °C in a vacuum oven to evaporate the solvent. After complete drying of the electrode coated on Al, it is subjected to be densely pressed by a rolling press machine (WCRP-1015G), and the electrode was cut into a circle shape with a diameter of 14 mm for the coin cell fabrication.

4.3.2.4 Fabrication of coin-cell type symmetric supercapacitor device

The symmetric supercapacitor (SSC) device based on SiOC was fabricated with a CR2032 coin cell configuration with electroactive area of 1.54 cm^2 separated by a Celgard membrane. A 1 M $TEABF_4$ is used as the electrolyte. The fabricated SSC device was crimped using an electric coin cell crimping and disassembling machine (MTI, Korea). All the electrolyte handling and device fabrication were carried out in a glove box with less than 1 ppm of moisture and oxygen. Electrochemical characterization of the SSCs were analyzed using cyclic voltammetry (CV) at various scan rates, EIS analysis in the frequency range from 0.01 Hz to 100 kHz at an amplitude of 10 mV, and galvanostatic charge-discharge (CD) measurements using different current ranges were performed using an Autolab PGSTAT302N electrochemical workstation.

4.3.3 Results and discussion

4.3.3.1 Physicochemical characterization

The siloxene sheets (prepared via topochemical de-intercalation of calcium from $CaSi_2$[15,16] and alginic acid were used as a silicon and carbon precursor for the preparation

of silicon-oxy-carbide/carbon (SiOC) ceramics. The siloxene sheets (green color) and alginic acid (white) were mixed together at appropriate ratio and thermally treated (carbothermal reaction) at 900 °C which results in the formation of black coloured SiOC ceramics.

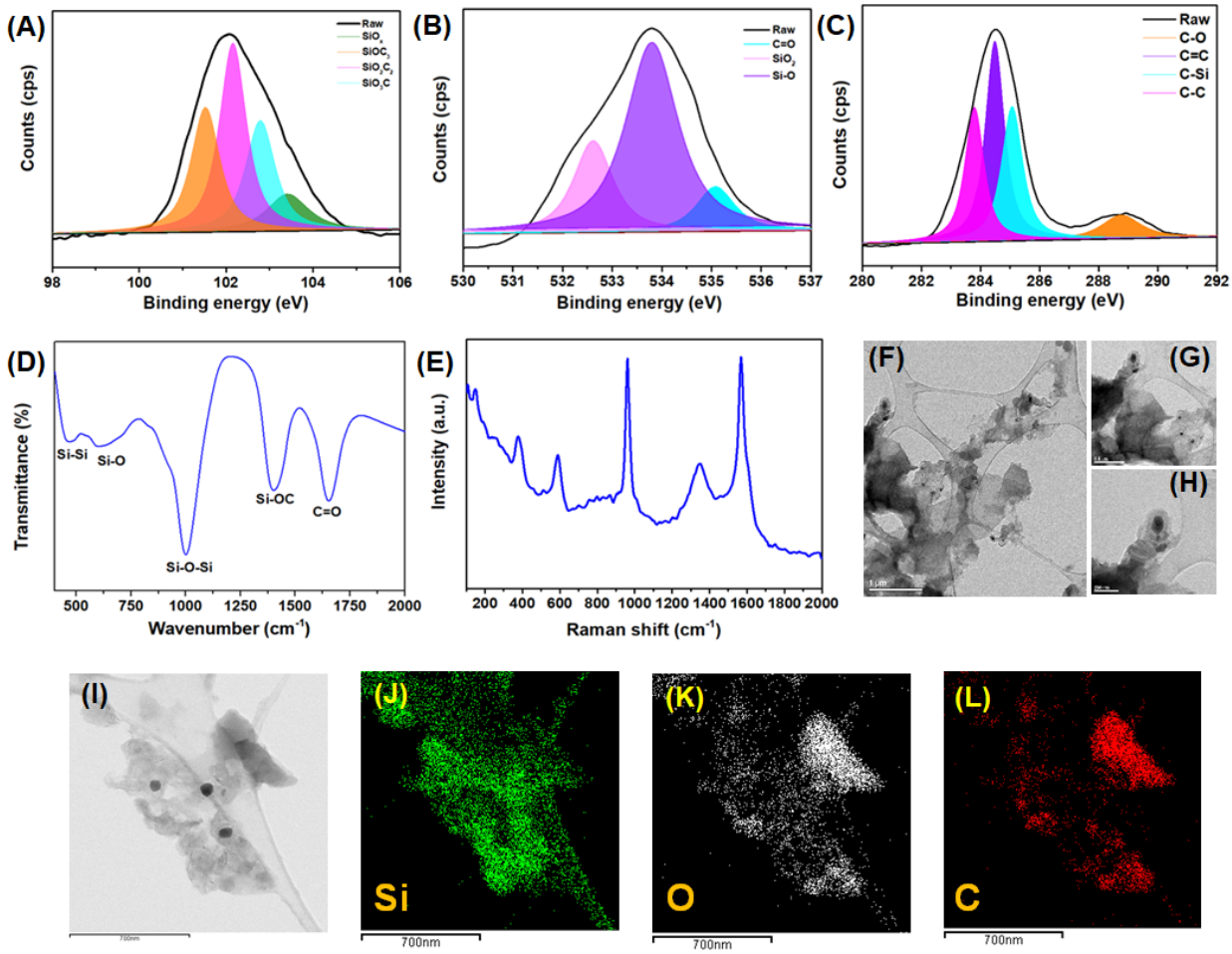

Figure 4.3.1. Physico-chemical characterization of SiOC lamellas. (A-C) The X-ray photoelectron core-level spectrum of (A) Si 2p, (B) O 1s and (C) C 1s states present in SiOC lamellas. (D) Fourier -transformed infrared and (E) Laser Raman spectra of SiOC lamellas. (F-H) High resolution transmission electron micrographs of SiOC lamellas obtained at various magnifications. Elemental mapping analysis of SiOC (I) overlay image, (J) Si atom, (K) O atom and (L) C atom, respectively.

The formation of SiOC hybrids were characterized using X-ray photoelectron spectrum, Fourier transformed infra-red spectroscopy, laser Raman analysis and high-

resolution transmission electron microscopic analysis equipped with elemental mapping analyses, respectively.. In order to understand the chemical states of elements present in the final product, the core-level spectrum of Si, O, and C are analysed as shown in Figure 4.3.1(A-C). The core-level spectrum of Si 2p states is shown in Fig. 4.3.1(A) which can be deconvoluted into four different chemical states such as SiO_3C, SiO_2C_2, $SiOC_3$ and SiO_x at 102.7, 101.8, 101.05 and 103.45 eV respectively[10]. The core-level spectrum of O 1s states (Fig. 4.3.1(B) shows the presence of SiO_2, C=O, and Si-O at binding energies 533.79, 535.05, and 532.56 eV respectively. Figure 4.3.1(C) represents the core-level spectrum of C 1s states shows the presence of C-C, C=C, C-Si, and C-O at 283.76, 284.47, 285.06, and 288.74 eV, respectively[10]. The atomic percentage of SiOC in the final product is in the composition ratio of 22.85:29.22:47.93 (Si:O:C) and is well matched with the previous findings on silicon-oxy-carbide[6]. Figure 4.3.1(D) shows the FT-IR spectrum of the as prepared SiOC powders which shows the presence of vibration bands at 466, 602, 1002, 1409, and 1655 cm^{-1}, corresponds to the vibrations of ν(Si-Si), ν(Si-O_x), ν(Si-O-Si), ν(Si-OC), and ν(C=O), respectively[16–18]. The laser Raman spectrum of the SiOC powders are provided in Figure 4.3.1(E) indicating the presence of bands at 376, 590, 962, 1345, and 1568 cm^{-1}, respectively. The band observed at 376 and 590 cm^{-1} originates from the Si-O_x bonding in the SiOC whereas the band observed at 962 cm^{-1} related to the LO modes of Si-O[6,19]. The other bands 1345 and 1570 cm^{-1} relates to the D and G band of carbon present in the SiOC, respectively[6,19,20]. Figure 4.3.1(F) represents the HR-TEM micrographs of the SiOC powders showing the presence of sheet-like structures with irregular lateral sizes. The high magnification micrograph shown in Figure 4.3.1(G and H) indicates the presence of crumpled edges of the SiOC which might arise due to the effect of high-temperature reaction process. In order to understand the distribution of Si, O and C atoms in the SiOC, the elemental mapping analysis was performed for the SiOC using the HR-TEM micrograph (Figure. 4.3.1

(I)). The elemental maps of C, O and Si atoms are obtained from the micrograph (Figure 4.3.1(I)) provided is Figure 4.3.1 (J-K) respectively. The elemental mapping analysis highlights the homogenous distribution of C, O, and Si atoms in the sheets, suggesting the molecular level transformation of siloxene into SiOC via the carbothermal reaction.

4.3.3.2 Electrochemical characterization

The electrochemical capacitive properties of the prepared SiOC ceramics were analyzed via the fabrication of coin-cell (CR2032) type symmetric supercapacitor (SSC) using 1 M $TEABF_4$ electrolyte. In order to determine the operating potential window (OPW) of the SiOC SSC, the cyclic voltammetry (CV) was performed at different OPWs (from 0.0 to 3.0) recorded using a scan rate of 200 mV s^{-1} as shown in Figure 4.3.2(A). The CV profiles retain a rectangular-shaped curves even at a OPW of up to 3 V, thus, indicating better capacitive properties of the fabricated SiOC SSC with a stable and large OPW in organic-liquid based electrolyte[21]. The specific capacitance of the SiOC SSC increases from 2.51 into 7.02 F g^{-1} with an increase in OPW from 0.5 to 3.0 V. This study highlights the use of SiOC SSC over a high OPW of 3.0 V and further studies are examined in this OPW[22]. Figure 4.3.2(B, C) shows the CV profiles of the SiOC SSC recorded at different scan rates (from 5 to 1000 mV s^{-1}). The presence of rectangular shaped CV profiles from low to high scan rates is evidenced from Figure 4.3.2(B, C) which indicated the ideal capacitive nature of the SiOC SSC[7]. The effect of scan rate on the specific capacitance of SiOC SSC is summarized in Figure 4.3.2(D) which revealed that a high specific device capacitance of about 28.82 F g^{-1} was obtained from the CV profile recorded at a scan rate of 5 mV s^{-1}.

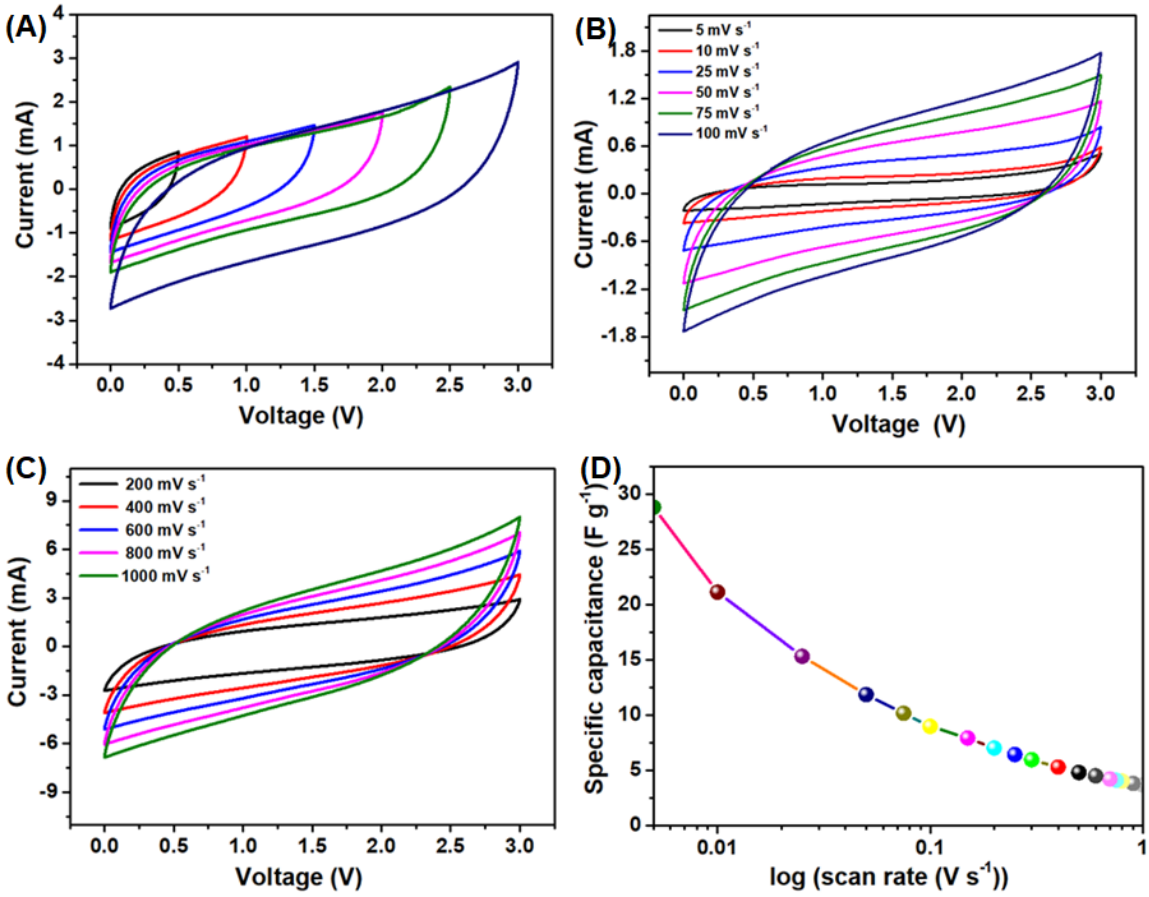

Figure 4.3.2. Electrochemical analysis of the SiOC SSC using 1 M $TEABF_4$. (A) Cyclic voltammetric profiles of the SiOC SSC measured at different operating voltages of 0.0 to 3.0 V using a scan rate of 200 mV s^{-1}. (B-C) Cyclic voltammetric profiles measured at scan rates from 5 mV s^{-1} to 1000m V s^{-1}. (D) Effect of scan rate on the specific capacitance of SiOC SSC.

The galvanostatic charge-discharge (CD) profiles of the SiOC SSC device recorded using a constant applied current of 1 mA was provided in Figure 4.3.3(A) which displayed almost symmetric CD profile. Further, the CD profiles recorded at different levels of applied current ranges are shown in Figure 4.3.3(B) which indicated the retention of symmetric CD profiles from low to high applied current ranges, thus, ensuring the ideal capacitive nature of the SiOC SSC. The effect of applied current range of the specific capacitance of SiOC SSC is shown in Figure 4.3.3(C).

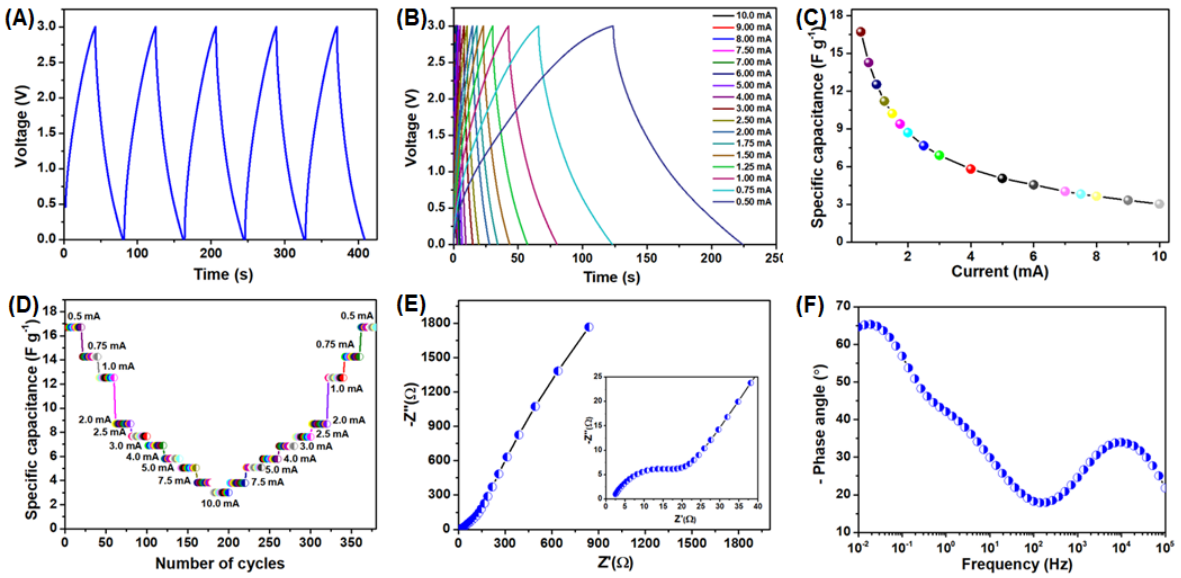

Figure 4.3.3. Electrochemical analysis of the SiOC SSC using 1 M $TEABF_4$. (A) Galvanostatic CD profiles of the SiOC SSC measured at a applied current of 1.0 mA. (B) CD profiles obtained using various applied current ranges from 0.5 to 10 mA. (C) Effect of discharge current on the specific capacitance (D) Rate capability analysis. Electrochemical impedance spectroscopy of SiOC SSC (E) Nyquist plot (F) Bode phase angle plot.

The SiOC SSC delivered a specific capacitance of 16.71 F g^{-1} from the discharge profile recorded using a current range of 0.5 mA. In order to examine the rate capability of SiOC SSC at various load levels, the continuous CD profiles were recorded from low- to high-current range and vice-versa as shown in Figure 4.3.3(D). The effect of various current ranges on the continuous CD measurements displayed an excellent capacitance retention over different current ranges, thus, highlighting the better rate capability of the SiOC SSC[14]. Figure 4.3.3(E) represents the electrochemical impedance spectroscopy (EIS) of the SiOC SSC in the form of Nyquist plot which displayed the presence of typical semi-circle region at high-frequency and linear line at low-frequency region[14]. The equivalent series resistance (ESR) of the SiOC SSC is found to be 2.5 Ω which is low compared to the reported graphene-, MoS_2-, boron- and siloxene-based SSCs using organic electrolytes, thus indicating

the better power capability of the SiOC SSC[14,22–24]. The charge-transfer resistance (R_{ct}) of the SiOC SSC is found to be 17.26 Ω from the enlarged portion of the Nyquist plot (inset of Figure 4.3.3(E)). The Bode phase angle plot shown in Figure 4.3.3(F) revealed that the phase angle at the low-frequency region is about -65°, thus suggesting the pseudocapacitive nature of charge-storage at the SiOC electrodes[25].

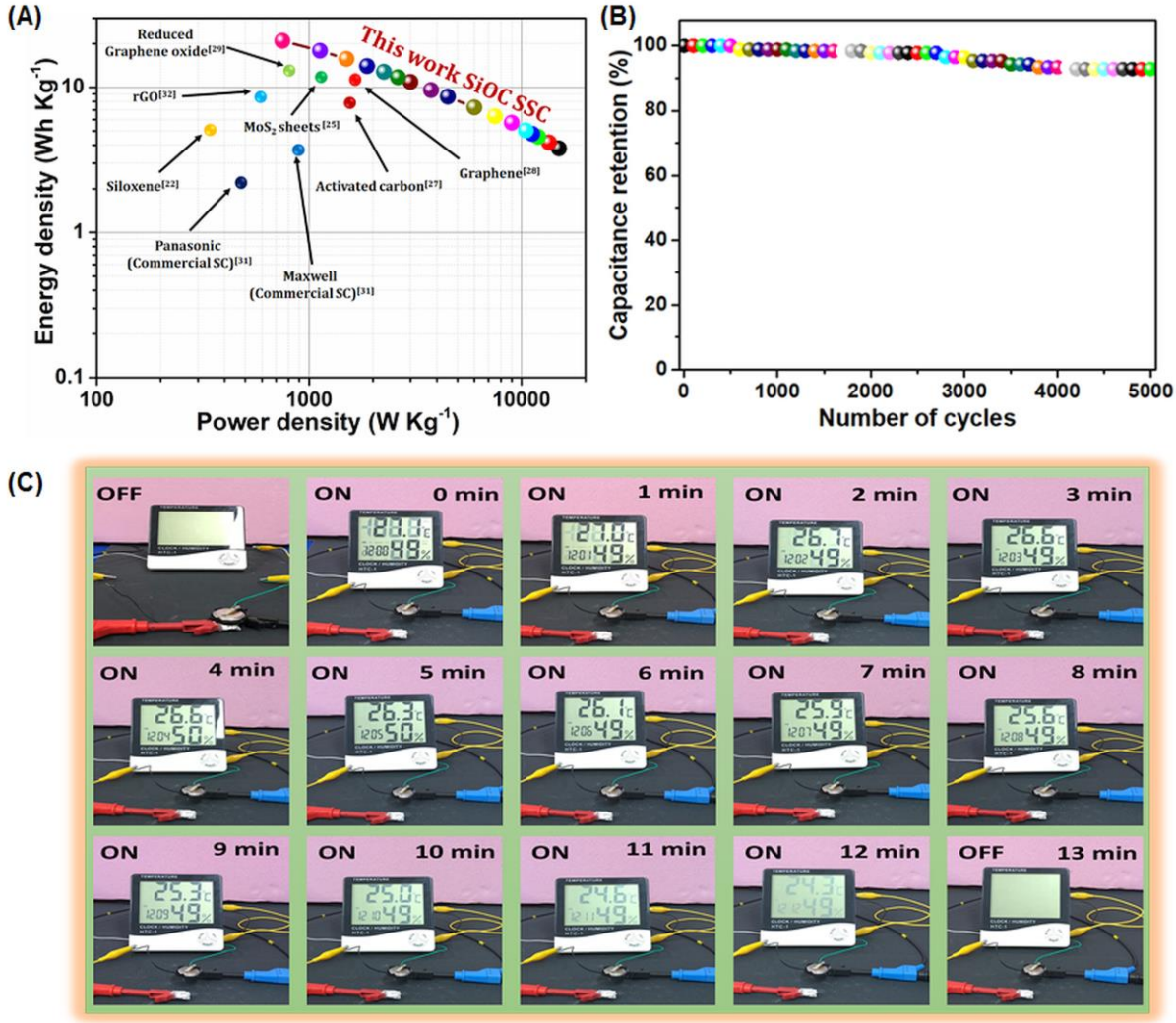

Figure 4.3.4. (A) Ragone plot of the SiOC SSC showing their superior energy/power performances over reported SSCs. (B) Cycling stability of the SiOC SSC over 5000 continuous charge-discharge cycles. (C) Practical application of fully charged SiOC SSC powering a multifunctional electronic display over 720 seconds.

Table 4.3.1: Performance metrics comparison of the SiOC SSC device with the reported SSC utilizing organic/ionic electrolyte.

S. No.	Electrode	Electrolyte	Operating potential window	Energy density (Wh kg^{-1})	Power density (W kg^{-1})	Ref.
1	Activated carbon	Et_4NBF_4/AN	0.0 to 2.3 V	8	1418	[26]
2	Porous carbon	EMI-BF_4	0.0 to 3.0 V	11.4	9800	[24]
3	Graphene sheets	$BMIBF_4$	0.0 to 4.0 V	16.5	1600	[27]
4	Reduced graphene oxide	$[SET_3][TFSI]$-GO	0.0 to 2.5 V	17.7	875	[28]
5	$Ti_3C_2T_x$/MWCNT	Et_4NBF_4	0.0 to 1.8 V	3	-	[29]
6	Siloxene sheets	$TEABF_4$	0.0 to 3.0 V	5.08	375	[14]
7	MoS_2 sheets	$TEABF_4$	0.0 to 3.0 V	18.43	1125	[30]
8	rGO	$LiClO_4$/PC	0.0 to 2.5 V	9.4	678	[31]
9	coPIL-RGO	$BMIMBF_4$/AN	0.0 to 2.5 V	14.7	5400	[32]
10	Maxwell (commercial)	-	2.7 V	4.45	900	[33]
11	Panasonic (commercial)	-	2.5 V	2.3	514	[33]
12	SiOC	$TEABF_4$	0.0 to 3.0 V	20.89	15000	This work

Table 4.3.2: Performance metrics comparison of the SiOC SSC device with the reported Si based SSC.

S. No.	Electrode	Electrolyte	Operating potential window	Energy density (mJ cm^{-2})	Power density (mW cm^{-2})	Ref.
1	Graphene/Si nanowire	$EMIMBF_4$	0.0 to 2.7 V	3.6	1	[34]
2	PEDOT/Si nanowire	$PYR_{13}TFSI$	0.0 to 1.5 V	9	0.8	[35]
3	Diamond/Si nanowire	$Et_3NHTFSI$	0.0 to 4.0 V	15	3	[36]
4	Ppy/Si nanowire	$PYR_{13}TFSI$	0.0 to 1.5 V	11	0.8	[37]
5	Ppy/Si nanotrees	$PYR_{13}TFSI$	0.0 to 1.5 V	15	0.8	[37]
6	PEDOT/D@Si nanowires	$N_{1114}TFSI$	0.0 to 2.5 V	26	1.3	[38]
7	MnO_2/Si nanowires	$PYR_{13}TFSI$/ LiClO4	0.0 to 2.0 V	32	0.4	[39]
8	SiC nanowire	KCl	0.0 to 0.6 V	2.3	1.1	[40]
9	Siloxene	$TEABF_4$	0.0 to 3.0 V	9.82	4.03	[14]
10	SiOC	$TEABF_4$	0.0 to 3.0 V	48.83	9.74	This work

The energy/power density and their ratings, cyclic stability, are very important parameters which determine the practical utilization of any SSC device[41]. The energy/power performance metrics of the SiOC SSC are determined from the CD analysis and present in the form of Ragone plot (Figure 4.3.4(A)). The energy density of SiOC SSC reached upto 20.89 Wh kg^{-1} with a corresponding power density of 750 W kg^{-1}, and still maintains 3.79 Wh kg^{-1} at a power density of 15000 W kg^{-1}, respectively. The energy/power performance metrics of SiOC SSC is also compared with the state of art of supercapacitors using organic/ionic liquid electrolytes as seen in Figure 4.3.4(A) and Table 4.3.1. The energy density of SiOC SSC is higher compared to that of recently reported SSCs made of activated carbon (8 Wh kg^{-1}), porous carbon (11.4Wh Kg^{-1}), graphene (16.5 Wh kg^{-1}), rGO (17.7 Wh

kg^{-1}), rGO (9.4 Wh kg^{-1}), coPIL-RGO (14.7 Wh kg^{-1}), Ti_3C_2Tx/MWCNT (3 Wh kg^{-1}), siloxene (5 Wh kg^{-1})), 2D-MoS_2 (18.43 Wh kg^{-1}) and commercial supercapacitors[14,24,26–29,31–33]. Further, the power density of SiOC SSC reaches upto 15000 W kg^{-1} which indicated their suitability as power source for next generation of vehicles[22]. Table 4.3.1 evidences the superior power performance of the SiOC SSC over the supercapacitor using emerging electrodes such as graphene, rGO, coPIL-RGO, MoS_2, MXene, and siloxene[14,28–32]. Figure 4.3.4(B) represents the excellent cyclic stability with 92 % retention of initial capacitance of SiOC SSC over continuous 5000 CD analysis using an applied current range of 5 mA. Figure 4.3.4(C) presents the real-time application of the SiOC SSC to power a multi-functional electronic display showing the atmospheric temperature and relative humidity. The video of the real time practical demonstration of SiOC SSC is provided in the supporting movie (ESI). The SiOC SSC was initially charged upto 3.0 V using an applied current of 1 mA and the stored energy is delivered to power up the electronic display over 12 min, thus, ensuring the practical applications of the fabricated SiOC SSC.

4.3.4 Conclusion

The significant findings of this study demonstrated an effective method for the preparation of SiOC lamellas using two dimensional siloxene sheets and alginic acid. The formation of SiOC powders and their homogeneous distribution of elements (Si, O, C) were confirmed via spectroscopic, morphological and elemental analysis. The electrochemical studies of the fabricated SiOC SSCs using CV and EIS analysis revealed their ability to operates over a wide potential window (3.0 V) and their good capacitive properties. The CD analysis demonstrated that the SiOC SSC delivered a high specific capacitance (16.71 F g^{-1}), high energy density (20.89 Wh Kg^{-1}), high power density (15,000 W Kg^{-1}), low-equivalent series resistance (compared to other SiC/SiO_xC_y based SSCs), better cyclic stability, and

excellent rate capability. This work demonstrated a new synthetic strategy for the preparation of SiOC derived from 2D siloxene sheets and the exceptional supercapacitive performances of SiOC lamellas which will be useful for the development of high-performance energy storage devices.

4.3.5 References:

[1] M. Zhang, X. Yu, H. Ma, W. Du, L. Qu, C. Li, G. Shi, Robust graphene composite films for multifunctional electrochemical capacitors with an ultrawide range of areal mass loading toward high-rate frequency response and ultrahigh specific capacitance, Energy Environ. Sci. 11 (2018) 559–565. doi:10.1039/C7EE03349D.

[2] Y. Ko, M. Kwon, W.K. Bae, B. Lee, S.W. Lee, J. Cho, Flexible supercapacitor electrodes based on real metal-like cellulose papers, Nat. Commun. 8 (2017) 536. doi:10.1038/s41467-017-00550-3.

[3] C. Zhong, Y. Deng, W. Hu, J. Qiao, L. Zhang, J. Zhang, A review of electrolyte materials and compositions for electrochemical supercapacitors., Chem. Soc. Rev. 44 (2015) 7484–7539. doi:10.1039/c5cs00303b.

[4] N. Kurra, M. Alhabeb, K. Maleski, C.-H. Wang, H.N. Alshareef, Y. Gogotsi, Bistacked Titanium Carbide (MXene) Anodes for Hybrid Sodium-Ion Capacitors, ACS Energy Lett. (2018) 2094–2100. doi:10.1021/acsenergylett.8b01062.

[5] S. Ortaboy, J.P. Alper, F. Rossi, G. Bertoni, G. Salviati, C. Carraro, R. Maboudian, MnO_x -decorated carbonized porous silicon nanowire electrodes for high performance supercapacitors, Energy Environ. Sci. 10 (2017) 1505–1516. doi:10.1039/C7EE00977A.

[6] L. David, R. Bhandavat, U. Barrera, G. Singh, Silicon oxycarbide glass-graphene composite paper electrode for long-cycle lithium-ion batteries, Nat. Commun. 7 (2016) 10998. doi:10.1038/ncomms10998.

[7] M. Kim, H. Ju, J. Kim, Oxygen-doped porous silicon carbide spheres as electrode materials for supercapacitors, Phys. Chem. Chem. Phys. 18 (2016) 3331–3338. doi:10.1039/C5CP06438D.

[8] M. Sarno, S. Galvagno, R. Piscitelli, S. Portofino, P. Ciambelli, Supercapacitor

Electrodes Made of Exhausted Activated Carbon-Derived SiC Nanoparticles Coated by Graphene, Ind. Eng. Chem. Res. 55 (2016) 6025–6035. doi:10.1021/acs.iecr.6b00737.

[9] M. Kim, I. Oh, J. Kim, Influence of surface oxygen functional group on the electrochemical behavior of porous silicon carbide based supercapacitor electrode, Electrochim. Acta. 196 (2016) 357–368. doi:10.1016/j.electacta.2016.03.021.

[10] C. Chandra, J. Kim, Silicon oxycarbide produced from silicone oil for high-performance anode material in sodium ion batteries, Chem. Eng. J. 338 (2018) 126–136. doi:10.1016/j.cej.2018.01.032.

[11] M. Halim, G. Liu, R.E.A. Ardhi, C. Hudaya, O. Wijaya, S.-H. Lee, A.-Y. Kim, J.K. Lee, Pseudocapacitive Characteristics of Low-Carbon Silicon Oxycarbide for Lithium-Ion Capacitors, ACS Appl. Mater. Interfaces. 9 (2017) 20566–20576. doi:10.1021/acsami.7b04069.

[12] M. Weinberger, C. Pfeifer, S. Schindler, T. Diemant, R.J. Behm, M. Wohlfahrt-Mehrens, Submicron-sized silicon oxycarbide spheres as anodes for alkali ion batteries, J. Mater. Chem. A. 3 (2015) 23707–23715. doi:10.1039/C5TA06277B.

[13] M.D. Clark, L.S. Walker, V.G. Hadjiev, V. Khabashesku, E.L. Corral, R. Krishnamoorti, Fast Sol-Gel Preparation of Silicon Carbide-Silicon Oxycarbide Nanocomposites, J. Am. Ceram. Soc. 94 (2011) 4444–4452. doi:10.1111/j.1551-2916.2011.04707.x.

[14] K. Krishnamoorthy, P. Pazhamalai, S.-J. Kim, Two-dimensional siloxene nanosheets: novel high-performance supercapacitor electrode materials, Energy Environ. Sci. 11 (2018) 1595–1602. doi:10.1039/C8EE00160J.

[15] M.I. Shoji Yamanaka, Hiroyuki Matsu-ura, New deintercalation reaction of calcium from calcium disilicide. Synthesis of layered polysilane, Mater. Res. Bull. 31 (1996)

307–316. doi:10.1016/0025-5408(95)00195-6.

[16] R. Fu, K. Zhang, R.P. Zaccaria, H. Huang, Y. Xia, Z. Liu, Two-dimensional silicon suboxides nanostructures with Si nanodomains confined in amorphous SiO_2 derived from siloxene as high performance anode for Li-ion batteries, Nano Energy. 39 (2017) 546–553. doi:10.1016/j.nanoen.2017.07.040.

[17] M.A. Abass, A.A. Syed, C. Gervais, G. Singh, Synthesis and electrochemical performance of a polymer-derived silicon oxycarbide/boron nitride nanotube composite, RSC Adv. 7 (2017) 21576–21584. doi:10.1039/C7RA01545C.

[18] X. Wang, C. Gong, G. Fan, Preparation and mechanical properties of silicon oxycarbide fibers from electrospinning/sol–gel process, Mater. Res. Bull. 46 (2011) 2398–2402. doi:10.1016/j.materresbull.2011.08.052.

[19] F. ROTH, P. WALESKA, C. HESS, E. IONESCU, N. NICOLOSO, UV Raman spectroscopy of segregated carbon in silicon oxycarbides, J. Ceram. Soc. Japan. 124 (2016) 1042–1045. doi:10.2109/jcersj2.16100.

[20] T.S. Perova, J. Wasyluk, S.A. Kukushkin, A. V. Osipov, N.A. Feoktistov, S.A. Grudinkin, Micro-Raman Mapping of 3C-SiC Thin Films Grown by Solid–Gas Phase Epitaxy on Si (111), Nanoscale Res. Lett. 5 (2010) 1507–1511. doi:10.1007/s11671-010-9670-6.

[21] S. Wang, F. Ma, H. Jiang, Y. Shao, Y. Wu, X. Hao, Band gap-Tunable Porous Borocarbonitride Nanosheets for High Energy-Density Supercapacitors, ACS Appl. Mater. Interfaces. 10 (2018) 19588–19597. doi:10.1021/acsami.8b02317.

[22] H. Li, L. Jing, W. Liu, J. Lin, R.Y. Tay, S.H. Tsang, E.H.T. Teo, Scalable Production of Few-Layer Boron Sheets by Liquid-Phase Exfoliation and Their Superior Supercapacitive Performance, ACS Nano. 12 (2018) 1262–1272. doi:10.1021/acsnano.7b07444.

[23] A. Winchester, S. Ghosh, S. Feng, A.L. Elias, T. Mallouk, M. Terrones, S. Talapatra, Electrochemical Characterization of Liquid Phase Exfoliated Two-Dimensional Layers of Molybdenum Disulfide, ACS Appl. Mater. Interfaces. 6 (2014) 2125–2130. doi:10.1021/am4051316.

[24] A. Eftekhari, Supercapacitors utilising ionic liquids, Energy Storage Mater. 9 (2017) 47–69. doi:10.1016/j.ensm.2017.06.009.

[25] K. Krishnamoorthy, P. Pazhamalai, S. Sahoo, S.-J. Kim, Titanium carbide sheet based high performance wire type solid state supercapacitors, J. Mater. Chem. A. 5 (2017) 5726–5736. doi:10.1039/C6TA11198J.

[26] W. Lu, K. Henry, C. Turchi, J. Pellegrino, Incorporating Ionic Liquid Electrolytes into Polymer Gels for Solid-State Ultracapacitors, J. Electrochem. Soc. 155 (2008) A361. doi:10.1149/1.2869202.

[27] Y. Chen, X. Zhang, D. Zhang, Y. Ma, High power density of graphene-based supercapacitors in ionic liquid electrolytes, Mater. Lett. 68 (2012) 475–477. doi:10.1016/j.matlet.2011.11.008.

[28] N. das M. Pereira, J.P.C. Trigueiro, I. de F. Monteiro, L.A. Montoro, G.G. Silva, Graphene oxide – Ionic liquid composite electrolytes for safe and high-performance supercapacitors, Electrochim. Acta. 259 (2018) 783–792. doi:10.1016/j.electacta.2017.10.124.

[29] A.M. Navarro-Suárez, K.L. Van Aken, T. Mathis, T. Makaryan, J. Yan, J. Carretero-González, T. Rojo, Y. Gogotsi, Development of asymmetric supercapacitors with titanium carbide-reduced graphene oxide couples as electrodes, Electrochim. Acta. 259 (2018) 752–761. doi:10.1016/j.electacta.2017.10.125.

[30] P. Pazhamalai, K. Krishnamoorthy, S. Manoharan, S.-J. Kim, High energy symmetric supercapacitor based on mechanically delaminated few-layered MoS_2 sheets in organic

electrolyte, J. Alloys Compd. 771 (2019) 803–809. doi:10.1016/j.jallcom.2018.08.203.

[31] Z. Liu, H. Zhang, Q. Yang, Y. Chen, Graphene/V_2O_5 hybrid electrode for an asymmetric supercapacitor with high energy density in an organic electrolyte, Electrochim. Acta. 287 (2018) 149–157. doi:10.1016/j.electacta.2018.04.212.

[32] L. Mao, Y. Li, C. Chi, H.S. On Chan, J. Wu, Conjugated polyfluorene imidazolium ionic liquids intercalated reduced graphene oxide for high performance supercapacitor electrodes, Nano Energy. 6 (2014) 119–128. doi:10.1016/j.nanoen.2014.03.018.

[33] A. Burke, R&D considerations for the performance and application of electrochemical capacitors, Electrochim. Acta. 53 (2007) 1083–1091. doi:10.1016/j.electacta.2007.01.011.

[34] S. Chatterjee, R. Carter, L. Oakes, W.R. Erwin, R. Bardhan, C.L. Pint, Electrochemical and Corrosion Stability of Nanostructured Silicon by Graphene Coatings: Toward High Power Porous Silicon Supercapacitors, J. Phys. Chem. C. 118 (2014) 10893–10902. doi:10.1021/jp502079f.

[35] D. Aradilla, G. Bidan, P. Gentile, P. Weathers, F. Thissandier, V. Ruiz, P. Gómez-Romero, T.J.S. Schubert, H. Sahin, S. Sadki, Novel hybrid micro-supercapacitor based on conducting polymer coated silicon nanowires for electrochemical energy storage, RSC Adv. 4 (2014) 26462. doi:10.1039/c4ra03192j.

[36] D. Aradilla, F. Gao, G. Lewes-Malandrakis, W. Müller-Sebert, D. Gaboriau, P. Gentile, B. Iliev, T. Schubert, S. Sadki, G. Bidan, C.E. Nebel, A step forward into hierarchically nanostructured materials for high performance micro-supercapacitors: Diamond-coated SiNW electrodes in protic ionic liquid electrolyte, Electrochem. Commun. 63 (2016) 34–38. doi:10.1016/j.elecom.2015.12.008.

[37] D. Aradilla, D. Gaboriau, G.G. Bidan, P. Gentile, M. Boniface, D. Dubal, P. Gómez-Romero, J. Wimberg, T.J.S. Schubert, S.S. Sadki, P. Gomez-Romero, J. Wimberg,

T.J.S. Schubert, S.S. Sadki, An innovative 3-D nanoforest heterostructure made of polypyrrole coated silicon nanotrees for new high performance hybrid micro-supercapacitors, J. Mater. Chem. A. 3 (2015) 13978–13985. doi:10.1039/C5TA03435C.

[38] D. Aradilla, F. Gao, G. Lewes-Malandrakis, W. Müller-Sebert, P. Gentile, M. Boniface, D. Aldakov, B. Iliev, T.J.S. Schubert, C.E. Nebel, G. Bidan, Designing 3D Multihierarchical Heteronanostructures for High-Performance On-Chip Hybrid Supercapacitors: Poly(3,4-(ethylenedioxy)thiophene)-Coated Diamond/Silicon Nanowire Electrodes in an Aprotic Ionic Liquid, ACS Appl. Mater. Interfaces. 8 (2016) 18069–18077. doi:10.1021/acsami.6b04816.

[39] D.P. Dubal, D. Aradilla, G. Bidan, P. Gentile, T.J.S. Schubert, J. Wimberg, S. Sadki, P. Gomez-Romero, 3D hierarchical assembly of ultrathin MnO_2 nanoflakes on silicon nanowires for high performance micro-supercapacitors in Li-doped ionic liquid., Sci. Rep. 5 (2015) 9771. doi:10.1038/srep09771.

[40] L. Gu, Y. Wang, Y. Fang, R. Lu, J. Sha, Performance characteristics of supercapacitor electrodes made of silicon carbide nanowires grown on carbon fabric, J. Power Sources. 243 (2013) 648–653. doi:10.1016/j.jpowsour.2013.06.050.

[41] R. Zhao, M. Wang, D. Zhao, H. Li, C. Wang, L. Yin, Molecular-Level Heterostructures Assembled from Titanium Carbide MXene and Ni–Co–Al Layered Double-Hydroxide Nanosheets for All-Solid-State Flexible Asymmetric High-Energy Supercapacitors, ACS Energy Lett. 3 (2018) 132–140. doi:10.1021/acsenergylett.7b01063.

CHAPTER 5

SYNTHESIS OF LAYERED TRANSITION METAL CHALCOGENIDES (MOS_2, $MOSE_2$ AND RES_2) AND FABRICATION OF SYMMETRIC CAPACITOR USING ORGANIC/IONIC LIQUID ELECTROLYTE

CHAPTER 5.1: HIGH ENERGY SYMMETRIC SUPERCAPACITOR BASED ON MECHANICALLY DELAMINATED FEW-LAYERED MOS_2 SHEETS IN ORGANIC ELECTROLYTE

Highlights:

- Supercapacitive properties of few-layered MoS_2 was examined in organic electrolyte.
- MoS_2 symmetric supercapacitor (SSC) operates over a potential window of 3.0 V.
- MoS_2 SSC device delivered a specific capacitance of 14.75 F g^{-1}.
- MoS_2 SSC device possesses a high energy density of 18.43 Wh kg^{-1}.
- MoS_2 SSC device possess capacitance retention of about 91.2% over 5000 cycles.

5.1.1. Introduction

The energy scarcity due to the depletion of fossil fuels and other natural resources increases day to day with the increase in human population. To overcome the energy crises, the researchers have been focused on the development of efficient energy storage devices which compensates the deficient of energy[1–3]. The energy storage devices have mainly classified into two categories such as batteries (Li-ion battery, Na-ion battery, polymer batteries) and supercapacitors or ultra-capacitors [4–7]. Even though batteries and supercapacitors arise from the synergetic effect between the materials science and electrochemistry, the mechanism of charge-storage in these devices are entirely different thus resulting a high energy density in batteries whereas high power density in supercapacitors[8,9]. Herein, supercapacitors possess the merits of having ultrafast charging rates, long cycle life compared to the batteries. The supercapacitors are classified into mainly three categories based on the mechanism of charge-storage at the electrodes viz. (i) Electrical double layer capacitor (EDLC), (ii) intrinsic pseudocapacitors and (iii) extrinsic pseudocapacitors [10,11]. The charge storage mechanism of EDLC electrode is due to the adsorption/desorption of electrolyte ions over the surface of the electrode whereas, in the pseudocapacitor, the charge storage is due to the reversible faradaic reaction (battery type) and or due to ion intercalation/de-intercalation phenomenon[10,12]. The fundamental mechanism of charge storage in electrode materials of a supercapacitor highly determine their device properties such as specific capacitance, energy/power density, Columbic efficiency, and cycle life[13]. Therefore, recently extensive research is ongoing on using various combination of electrode materials for the fabrication of symmetric, asymmetric, and ion hybrid concepts based supercapacitors during this era[14,15]. These reports suggested the role of electrode materials and understanding their mechanism of charge-discharge is highly significant for the developing high-performance supercapacitors[16].

Among the electrode materials for supercapacitors, carbon-based materials such as activated carbon, graphene and its derivatives are explored as EDLC type[16,17] whereas metal oxides and some polymers possess the pseudocapacitance behavior [18,19]. Due to the high power density of pseudocapacitors over EDLCs[20], electrode materials including transition metal based oxides (RuO_2, MnO_2, Co_3O_4), hydroxides (NiOH, CoOH)[21], and sulfides (MoS_2, VS_2, TiS_2, Ni_3S_2, CuS) [22–26] are extensively studied during this decade. In this scenario, two dimensional layered transition metal chalcogenides (2D TMCs) gained much interest as electrode materials since they possess the merits such as (i) due to the presence mixed valance state of the transition metal, (ii) high electrical conductivity (compared to that of the corresponding metal oxides) and (iii) structural analogue similar to graphene [27,28]. Among the 2D TMCs, molybdenum disulfide (MoS_2) nanosheets become a material of immense interest for electrochemical energy storage devices which is evidenced by the available literature since 2013[29,30]. The electrochemical properties of MoS_2 with different morphology such as sheets, flowers, spheres, particles obtained via a variety of synthetic routes (hydrothermal, sonochemical, microwave, mechanochemical, and liquid phase exfoliation methods) are studied in this era [31,32]. These findings suggested the electrochemical properties of the MoS_2 highly depend on the crystalline nature, phase, layer numbers as well as the lateral size of the sheets[33]. Earlier studies also suggested that the enhanced electrochemical energy storage properties of few-layered MoS_2 compared to bulk MoS_2 [34–37].However, the energy/power density of the MoS_2 supercapacitor reported until now are low compared to the commercial consideration of a supercapacitor device suggested by Andrew Bruke et al.[38]. Therefore, researchers are focusing towards improving the energy density of the MoS_2 supercapacitor device which is an area of huge interest.

Up-to-date, there are two promising strategies widely used for increasing the energy density ($E=0.5\ CV^2$) of the supercapacitor device viz. (i) fabrication of binder free-electrodes,

and (ii) use of ionic or organic electrolytes. The former results in a low mass loading of electrode materials on conductive current collectors (such as Ni foam or carbon cloth), providing more active sites, thus resulting in enhanced specific capacitance [39]. For instance, the specific capacitance of MoS_2 binder-free electrodes is almost two times higher than that of the conventional MoS_2 electrode fabricated by a slurry coating process[40,41]. On the other hand, the use of ionic or organic electrolytes in supercapacitor device directly increase the operating potential window (OPW) to a maximum of 3.0 to 4.0 V, which result in significant enhancement of energy density of the supercapacitor [42,43]. However, only a few works have been carried out on the electrochemical properties of MoS_2 nanosheets in ionic or organic electrolytes as follows [31,44]. Initially, Acerce et al., reported the electrochemical properties of MoS_2 in organic electrolytes using a three-electrode configuration and demonstrated the ion-intercalation/de-intercalation pseudocapacitance in MoS_2 using in-situ X-ray diffraction analysis[34]. K. Pandey et al. reported the electrochemical properties of the MoS_2 electrode using $BMIMPF_6$ as an electrolyte within the bias range of -1.8 to 1.5 V[45]. Both these studies were performed using a three-electrode configuration, and it is well known that symmetric supercapacitor design is highly reliable for analyzing the performance metrics of a supercapacitor for real-time applications. Therefore, in this work, we aimed to investigate the energy-storage properties of few-layered MoS_2 nanosheets (prepared via ball milling process) in tetraethylammonium tetrafluoroborate ($TEABF_4$) electrolyte using the fabrication of symmetric supercapacitor (SSC) device.

5.1.2. Experimental section

5.1.2.1 Preparation of few layered MoS_2

The exfoliation of few layered MoS_2 was prepared via wet milling of bulk MoS_2 using a Pulversitte 6.0 HEBM as reported in our previous work with an increase in milling time[36]. Briefly, 20 g of bulk MoS_2 was dispersed in 50 mL of NMP and allowed to wet

milling for a period of 72 h using tungsten carbide bowl with tungsten carbide balls (ball to powder weight ratio, 10:1) at a speed of 300 rpm. Upon completion of the milling process, the milled MoS_2 powders were washed with ethanol and separated via centrifugation process. The final product was allowed to dry at 80 °C in a hot air oven for 24 h.

5.1.2.2 Fabrication and electrochemical characterization of MoS_2 SSC device

The working electrode (few layered MoS_2) were prepared via grounding the MoS_2, carbon black and PVDF with an appropriate ratio of 85:10:5 using NMP as the solvent in an agate mortar until the formation of uniform slurry[46]. After the slurry formation, the slurry was coated onto a stainless-steel coin cell substrate and allowed to dry at 80 °C for 24 h. The electroactive mass of MoS_2 electrode loaded on the stainless-steel substrate is calculated as the difference between the mass of the substrate before and after coating of the MoS_2 electrode using Dual-range Semi-micro Balance (AUW-220D, SHIMADZU) with approximation of five-decimal points is approximately ~ 0.5 mg in each substrate. The MoS_2 symmetric supercapacitor (SSC) device was fabricated using MoS_2 coated coin type stainless steel electrode, Celgard as a separator, and 0.5 M $TEABF_4$ as the electrolyte. After assembling the components in the CR2032 coin cell case, the coin cell was crimped using Electric Coin Cell Crimping and Disassembling Machine (MTI Korea) in the argon filled glove box to avoid the reaction of electrolyte in the atmosphere. The electrochemical characterization of the fabricated MoS_2 SSC device such as cyclic voltammetry (CV), galvanostatic charge-discharge (CD) and electrochemical impedance spectroscopy (EIS) analysis were performed using an Autolab PGSTAT302N electrochemical workstation.

5.1.3. Results and discussion

5.1.3.1 Physicochemical characterization

The aim of this study is to examine the energy storage properties of few-layered MoS_2 nanosheets in the organic liquid electrolyte. Figure 5.1.1(A) shows the diffraction pattern of

the bulk and few-layered MoS_2 sheets. The sharp diffraction pattern in the bulk MoS_2 corresponds to the bulk 2H-MoS_2(JCPDS -37-1492). From Figure 5.1.1(A), it is clear that the XRD pattern of few-layered MoS_2 shows significant changes compared to bulk MoS_2.

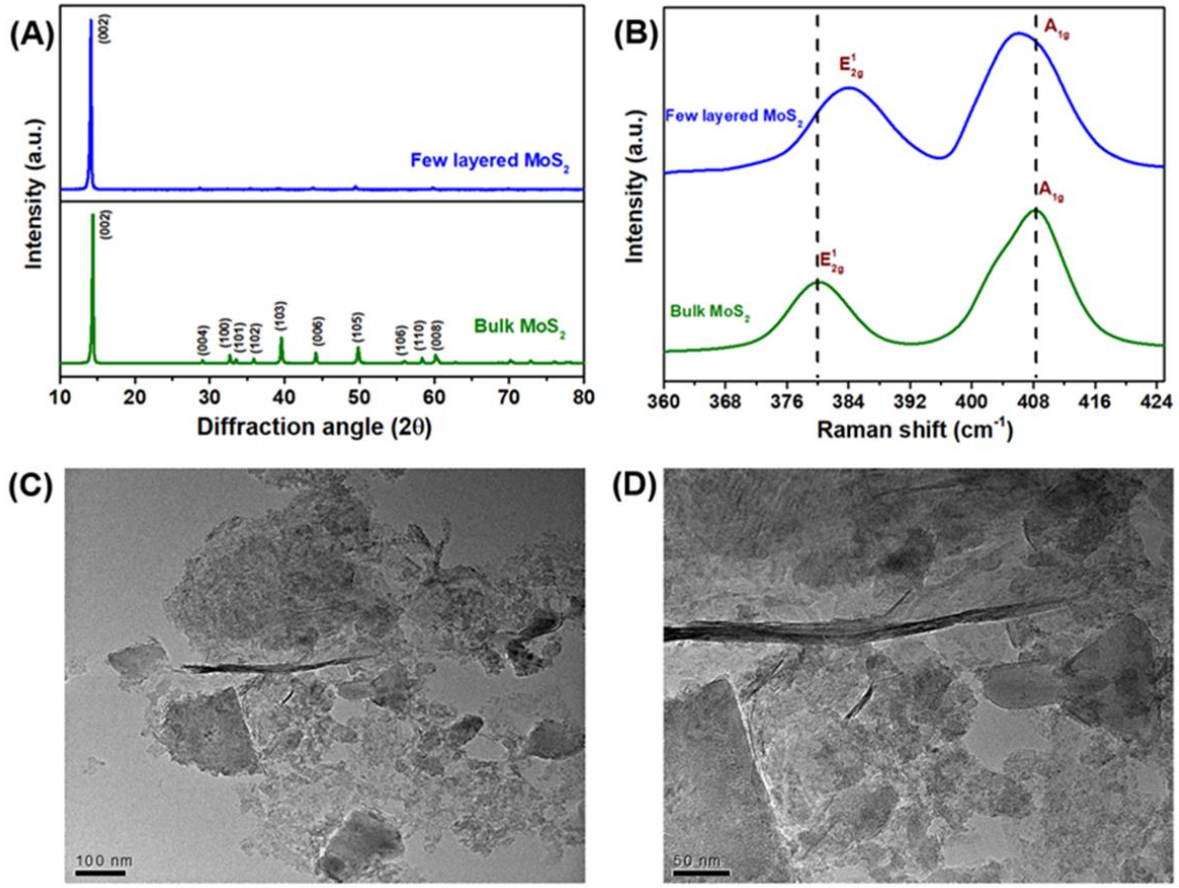

Figure. 5.1.1. Physicochemical characterization of bulk and exfoliated few layered MoS_2. (A) X-ray diffraction spectrum of bulk and exfoliated few layered MoS_2 after 72 h of the milling process. (B) Raman spectrum analysis of bulk and exfoliated few layered MoS_2 which confirms the exfoliation with the shift in the Raman bands of exfoliated few layered MoS_2. The HR-TEM micrograph of the exfoliated few layered MoS_2 (C) low resolution and (D) high resolution depicts the presence of few layers of MoS_2.

The presence of diffraction peak at $2\theta = 14.18°$ is retained in few layered MoS_2, and the other peaks are diminished, thus suggesting the formation of few-layered 1T phase MoS_2 after the ball milling process[36]. This is mainly due to the bifunctional use of NMP such as

dispersant as well as delamination agent for the MoS_2 in the mechanical milling process, and the detailed mechanism of exfoliation is discussed in our recent report [36]. Raman spectroscopy is one of the prominent tools for analysing the structural bonding, crystallinity and associated defect levels in two-dimensional nanostructures[47]. Figure 5.1.1 (B) shows the laser Raman spectrum of the bulk and few-layered MoS_2 sheets. In general, MoS_2 consists of two major bands located at 380 and 408 cm^{-1} corresponding to the E^1_{2g} and A_{1g} modes respectively, and these bands strongly depend on the number of layers and defect levels of the 2D materials[48]. The Raman bands at 408.13 and 380.78 cm^{-1} corresponds to the A_{1g} and E^1_{2g} modes of the bulk MoS_2 sheets[48,49]. The A_{1g} and E^1_{2g} modes of few-layered MoS_2 were observed at 404.97 cm^{-1} and 383.74 cm^{-1}. The observed redshift in the A_{1g} mode is due to a reduction in a number of layers and decrease in the lateral size of the few layered MoS_2 after milling process[36,50].

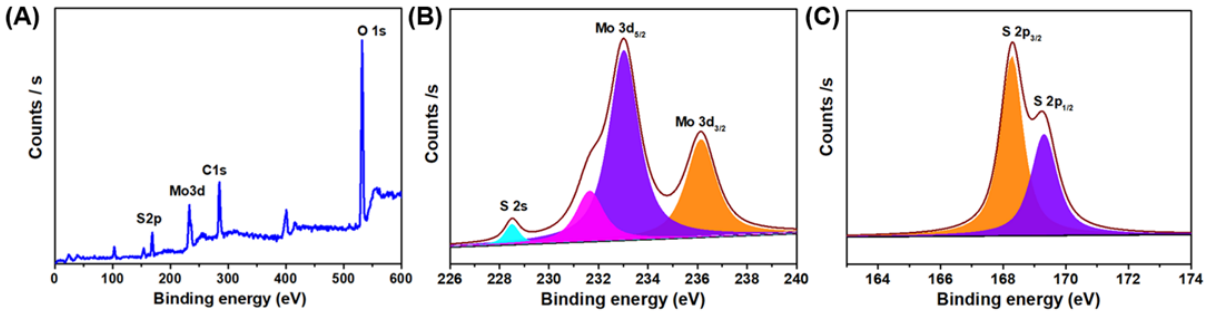

Figure. 5.1.2. X-ray photoelectron spectroscopy of MoS_2 (A) survey spectrum; (B) core level spectrum of Mo atom; (C) Core level spectrum of S atom.

The XPS survey spectrum of the few-layered MoS_2 is shown in Figure 5.1.2 (A), which revealed the presence of states corresponding to Mo, S, C, and O, respectively. The presence of C and O signals were originated from the CO_2 and H_2O impurities as seen in many XPS analysis [51]. Figure 5.1.2 (B) shows the core level spectrum for the Mo 3d state present at 233.15 and 236.2 eV corresponds to Mo $3d_{5/2}$ and Mo 3d $_{3/2}$, respectively[52]. Figure 5.1.2 (C) shows the core level spectrum for the S 2p state present at 168.45 eV which

corresponds to the S $2p_{3/2}$ states of the MoS_2[52]. The observed binding energies of Mo and S components in MoS_2 is in good agreement with the previous studies on the few-layered MoS_2[51]. The HR-TEM micrograph shown in Figure 5.1.1 (C and D) reveals the presence of sheet-like morphology of the few layered MoS_2 with average lateral size in the range of ~100 to 150 nm. The observed lateral size is nearly five times lower compared to that of the bulk MoS_2 (with a lateral size of nearly 700 nm) [36].

The surface area of the electrode materials is one of the important parameter governing the electrochemical energy storage[53]. Further, it is known that milling process

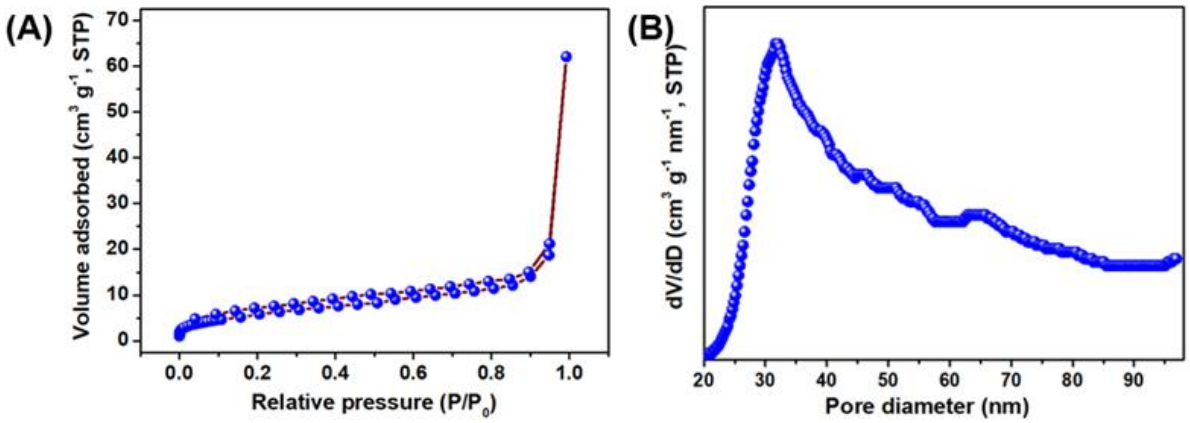

Figure.5.1.3. The surface area analysis of exfoliated few layered MoS_2. (A) N_2 adsorption/desorption isotherm of the exfoliated few layered MoS_2, (B) pore size distribution of the exfoliated few layered MoS_2.

leads to decrease in thickness and lateral size, this can lead to an increase in surface area of the materials[54]. The N_2 adsorption-desorption isotherm and pore size distribution curves of few-layered MoS_2 are provided in the Figure 5.1.3 (A and B). The isotherm curve of the few layered MoS_2 (Figure 5.1.3(A)) can be classified as type IV, revealing the presence of mesoporous nature of the MoS_2. The specific surface area of the few layered MoS_2 is calculated as 20.25 $m^2\ g^{-1}$ and higher than that of bulk MoS_2 sheets (7.943 $m^2\ g^{-1}$) [36]. Figure 5.1.3(B) shows the pore size distribution calculated by HK method indicated that the few layered MoS_2 exhibits the maximum pore size distributed at 30 nm, further confirming

the existence of mesopores and macropores in the few-layered MoS_2 sheets. This study evidences that the few-layered MoS_2 exhibits high surface area with wide pore size distribution, which can facilitate more electroactive sites during the electrochemical reactions.

5.1.3.2 Electrochemical characterization

The energy storage properties of the few layered MoS_2 nanosheets was investigated using symmetric cell configuration (CR2032) using 0.5 M $TEABF_4$ as the electrolyte.

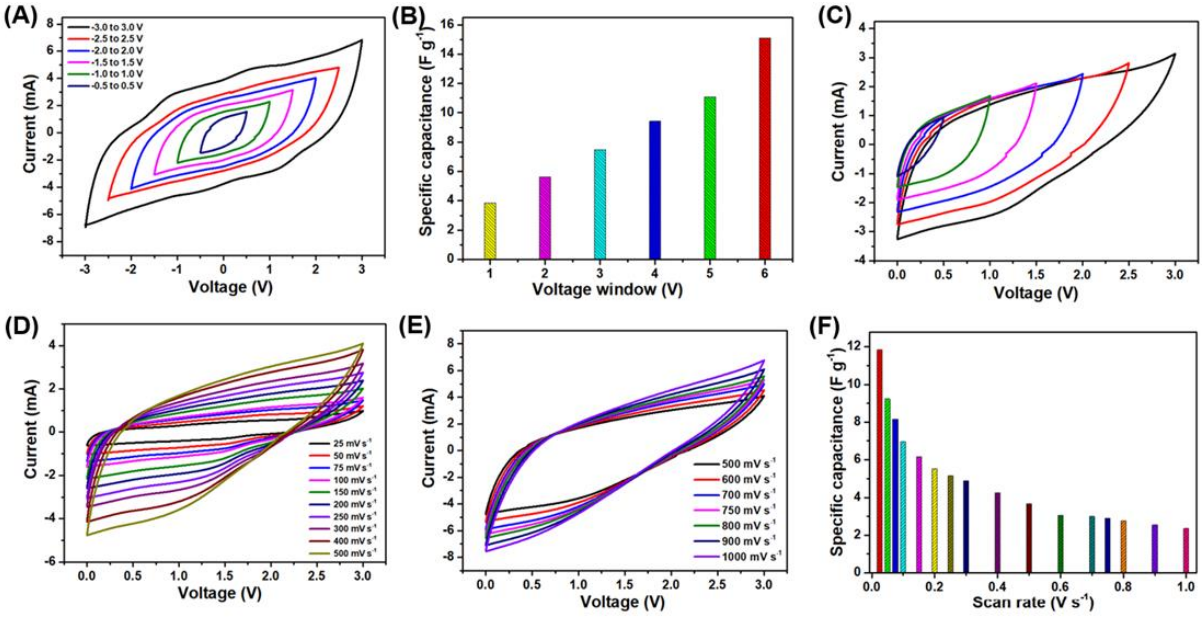

Figure. 5.1.4. Electrochemical characterization of the MoS_2 SSC using 0.5 M $TEABF_4$. (A) Cyclic voltammetric profiles of MoS_2 SSC device measured over the potential region of -3 to 3 V at a scan rate of 250 mV s^{-1}. (B) Effect of specific capacitance with the increase in potential window of MoS_2 SSC device. (C) Cyclic voltammetry profiles of the MoS_2 SSC device over the various potential regime (0 to 3V) measured at a scan rate of 250 mV s^{-1}. (D-E) Cyclic voltammetry profiles of the MoS_2 SSC device over a potential window of 0 to 3 V measured at various scan rates (25 to 1000 mV s^{-1}). (F) the plot of specific capacitance versus scan rates (25 to 1000 mV s^{-1}) for the MoS_2 SSC device.

Figure 5.1.4 (A) shows the CV profiles of MoS_2 SSC device recorded at different operating potential windows (OPWs) from -3.0 to +3.0 V at a scan rate of 250 mV s^{-1}. The CV profiles reveal the quasi-rectangular shaped curves up to a region of -2.0 to +2.0 V whereas with an increase in the OPW from -3.0 to +3.0 V, suggest the presence of ion-intercalation/de-intercalation at the MoS_2 electrodes. Figure 5.1.4(B) shows the specific capacitance of MoS_2 SSC with respect to the various OPWs. It shows a linear increase in specific capacitance with a maximum specific capacitance (15.09 F g^{-1} or 8.11 mF cm^{-2}) at an OPW of ±3.0 V. Winchester et al. reported the electrochemical performance of exfoliated MoS_2-based SSC using Et_4NBF_4 and BMIM-PF_6[55]. In their study, the OPW of MoS_2 SSC is in the range from 1.0 to 1.7 V and from −2.0 to 1.5 V for Et_4NBF_4 and BMIM-PF_6 electrolytes, respectively. Compared to this work, the experimental analysis shown in Figure 5.1.4(B) shows that MoS_2 SSC using $TEABF_4$ electrolyte can work over a wider OPW, thus might possess high energy density. Figure 5.1.4 (C) represents the CV profiles of the MoS_2 SSC device measured at different OPW in the positive regime (0.0 to 3.0 V) at a scan rate of 250 mV s^{-1}. Thus suggested that the MoS_2 SSC device can operate up to a potential window of 3.0 V without any sign of degradation. Figure 5.1.4 (D and E) shows the CV profiles of the MoS_2 SSC device measured over an OPW of 0.0 to 3.0 V measured at various scan rates (25 to 1000 mV s^{-1}). The shape of the CV profiles looks quasi-rectangular nature over the entire OPW indicating the nearly ideal capacitive nature of the MoS_2 SSC device[36]. The charge storage mechanism is attributed to the formation of double layer capacitance and/or intercalation capacitance of the MoS_2 electrode[34,56]. The effect of scan rate on the specific capacitance of MoS_2 SSC device is shown in Figure 5.1.4(F). A specific capacitance of 11.83 F g^{-1} was obtained for the MoS_2 SSC device from CV analysis measured at a scan rate of 25 mV s^{-1}. The MoS_2 SSC device can retain a capacitance of 43.51 % (5.149 F g^{-1}) was achieved with an increase of 10-fold in the scan rate (250 mV s^{-1}) suggesting the better rate capability

of the MoS_2 SSC [57]. The lower specific capacitance of the MoS_2 SSC device obtained at higher scan rate is due to the time constraint of the electrolyte ions transportation to the interior of the MoS_2 electrode[58]. The better electrochemical capacitive properties of the few layered MoS_2 is due to their sheet-like morphology with intrinsic fast ionic conductivity and high surface area (20.25 m^2 g^{-1}) which can facilitate the charge storage via ion-intercalation/de-intercalation mechanism [56].

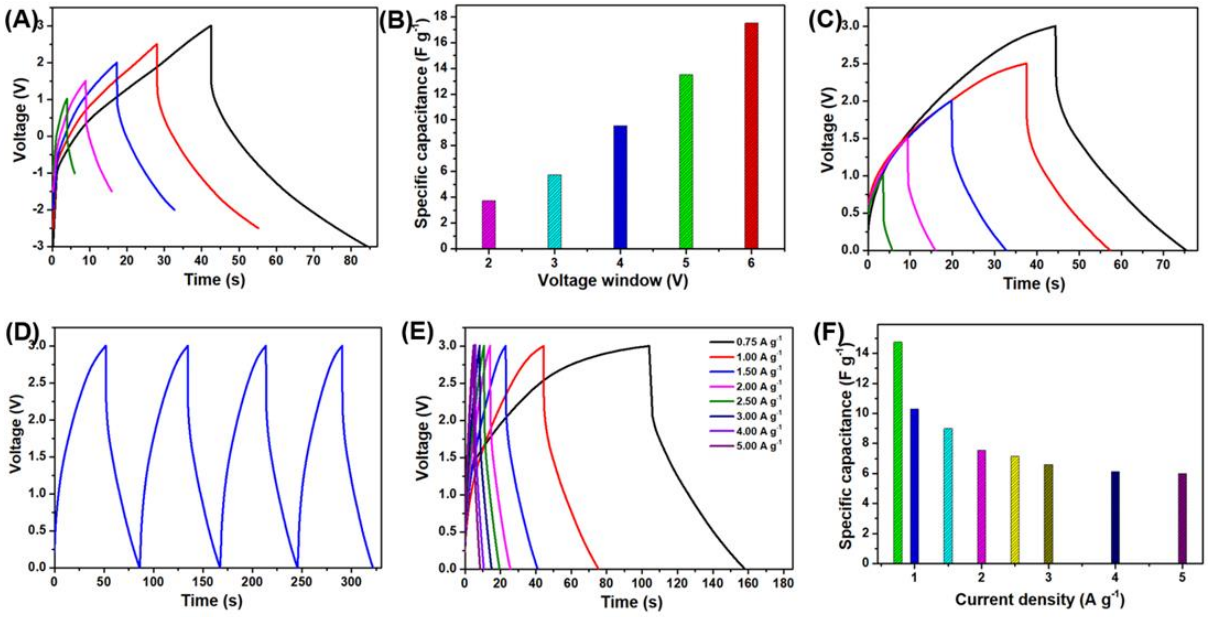

Figure. 5.1.5. Electrochemical characterization of the MoS_2 SSC using 0.5 M $TEABF_4$. (A) Galvanostatic charge-discharge (CD) profiles of MoS_2 SSC device measured over the potential region of -3 to 3 V at a constant current density of 2.5 A g^{-1}. (B) Effect of specific capacitance with an increase in potential window of MoS_2 SSC device. (C) CD profiles of the MoS_2 SSC device over the various potential regime (0 to 3V) measured at a constant current density of 1 A g^{-1}. (D) CD profiles of the MoS_2 SSC device over a potential window of 0 to 3 V measured at various current densities (0.75 to 5.0 A g^{-1}). (F) the plot of specific capacitance versus current densities (0.75 to 5.0 A g^{-1}) for the MoS_2 SSC device.

The galvanostatic CD profiles of the MoS_2 SSC device (shown in Fig 5.1.5 (A)) measured at different OPWs from -3.0 to +3.0 V at a constant current density of 2.5 A g^{-1}. The CD profiles reveal the semi-symmetric triangular curve over the OPW of ±3 V and the plot of specific capacitance of MoS2 SSC against the tested OPWs (-3.0 to +3.0 V) given in Figure 5.1.5(B), shows a linear increase which supports the findings from CV profiles (provided in Figure 5.1.4 (A) and (B)). Figure 5.1.5(C) shows the presence of semi-symmetric CD profiles of MoS_2 SSC device in various OPWs within the range of 0.0 to 3.0 V, respectively. Figure 5.1.5 (D) shows the galvanostatic CD profiles in the positive regime of 0.0 to 3.0 V measured using a constant current density of 1 A g^{-1}. It indicates the presence of semi-symmetric CD profiles as an indication of pseudocapacitive behavior which might arise from the ion-intercalation/de-intercalation phenomenon [36]. Figure 5.1.5 (E) shows the CD profiles of the MoS_2 SSC device measured at various current densities ranging from 0.75 to 5.0 A g^{-1}. The CD curves displayed the presence of semi-symmetric profiles for all the applied current densities. In general, higher current density results in fast charging/discharging time whereas lower current density produces better charging and discharging profiles in the MoS_2 SSC which is clearly noticeable in the Figure 5.1.5 (E). The specific capacitance of 14.75 F g^{-1} was calculated from the CD profile measured at a constant discharge current density of 0.75 A g^{-1}. The variation in the specific capacitance of the MoS_2 SSC device with respect to the current densities is provided in the Figure 5.1.5(F). It showed capacitance retention of 40.67 % of the initial capacitance is retained at a higher current density of 5 A g^{-1} with an increase of almost 6-fold in current density, thus suggesting the better rate capability of the MoS_2 SSC device. The specific capacitance of MoS_2 SSC device is even higher compared to the reported symmetric supercapacitors based on MoS_2 (3.4 F g^{-1})[37], MoS_2-graphene composite (8.12 F g^{-1})[59] and other TMCs [37,46] using aqueous electrolyte. Similarly, the specific capacitance of the MoS_2 SSC device (14.75 F g^{-1}) is quite

higher than symmetric capacitor based on activated carbon (10.5 F g^{-1})[60], and $Ti_3C_2T_x$/MWCNT (7 F g^{-1})[61] using ionic liquid electrolytes.

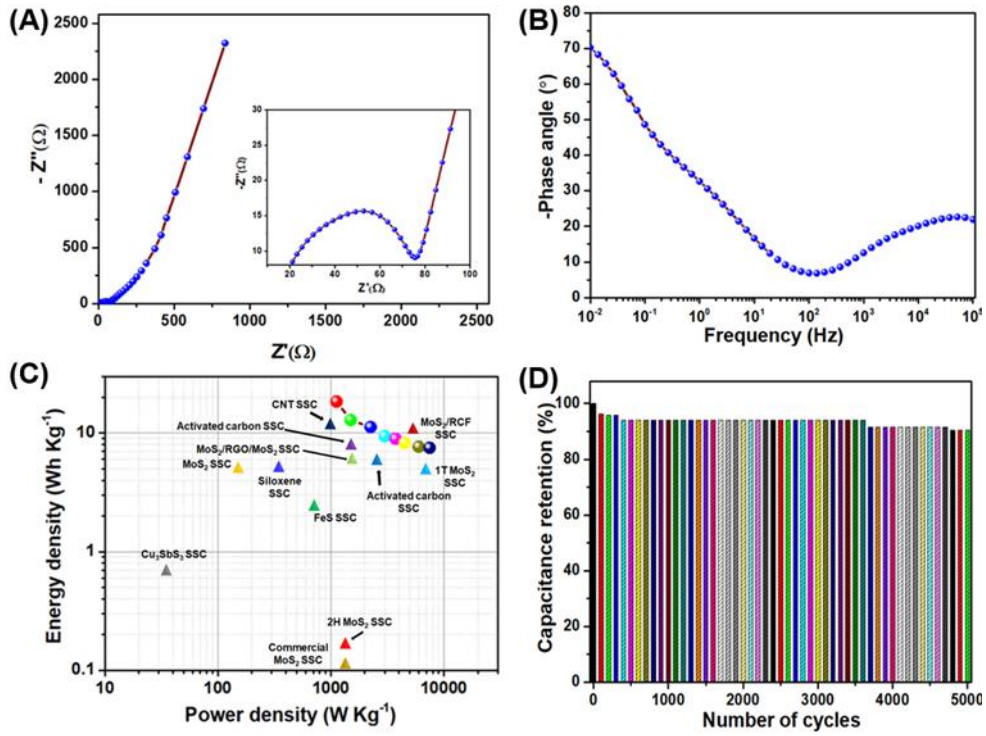

Figure. 5.1.6. Electrochemical impedance spectroscopy of the MoS_2 SSC using 0.5 M $TEABF_4$. (A) Nyquist plot of the MoS_2 SSC device. The inset in (A) shows the enlarged portion of the Nyquist plot representing a small semi-circle at the high-frequency region. (B) Bode phase angle plot of the MoS_2 SSC device. (C) Ragone plot of the MoS_2 SSC device. (D) Cyclic stability of the MoS_2 SSC device measured over 5000 charge-discharge cycles at a constant current density of 1.5 A g^{-1}.

The electrochemical impedance spectroscopy analysis of the MoS_2 SSC device was performed over the frequency 0.01 Hz to 100 kHz at an amplitude of 10 mV s^{-1}, to examine the fundamental charge-transfer kinetics occurred at the electrode/electrolyte interfacial region. The Nyquist plot of MoS_2 SSC device is shown in Figure 5.1.6 (A) and the inset shows the enlarged portion of the Nyquist plot representing the presence of a small semicircle in the high-frequency region and a straight line or Warburg line at the low-frequency region. The transition point between the high and low-frequency region is referred as “knee”

frequency, which is about 138 Hz[36]. The Nyquist plot of the MoS_2 SSC device revealed that it possesses a solution resistance (R_s) of about 21.18 Ω and the charge transfer resistance (R_{ct}) of about 55.15 Ω, respectively. The Warburg line observed at the low-frequency region is almost parallel to the imaginary axis which is related to the frequency dependent ion diffusion kinetics occurred at the MoS_2 electrode[62,63]. THe Bode phase angle plot provided in Figure 5.1.6(B), tails at -70º which reveals the pseudocapacitive nature of the MoS_2. Figure 5.1.6 (C) displays the Ragone plot of the MoS_2 SSC device which shows a high energy density of 18.43 Wh kg^{-1} at a specific power density of 1125 W kg^{-1} obtained at a constant current density of 0.75 A g^{-1}. With an increase of six-fold in the current range, the MoS_2 SSC device delivered an energy density of 7.5 Wh kg^{-1} at a power density of 7500 W kg^{-1}, suggesting a good rate capability of the device. The energy density of MoS_2 SSC device (18.43 Wh kg^{-1}) is higher compared with the MoS_2 based SSC device in aqueous electrolyte such as s-MoS2/CNS (7.4 Wh kg^{-1})[64], f-MoS_2 (8.59 Wh kg^{-1})[64], MoS_2 (5.42 Wh kg^{-1})[65], 1T-MoS_2 (5 Wh kg^{-1})[66] and MoS_2/RGO/MoS_2@Mo (6.22 Wh kg^{-1})[67]. The energy density of MoS_2 SSC device in ionic/organic liquid is also higher compared to the SSCs using ionic liquid electrolytes based on $Ti_3C_2T_x$/MWCNT (3 Wh kg^{-1})[61], interconnected carbon nanosheets (11.4 Wh kg^{-1})[68], activated carbon (10.6 Wh kg^{-1})[69], and three times higher than that of commercial supercapacitors[38]. The power density is even higher than the MoS_2 based symmetric capacitors and other TMCs in aqueous electrolyte such as MoS_2 (1000 W kg^{-1})[70], MoS_2/rGO (159 W kg^{-1})[71], MoS_2 (128 W kg^{-1})[72] and RuS_2 (40 W kg^{-1})[46] respectively. The power density of MoS_2 SSC device (1125 W kg^{-1}) in the ionic liquid electrolyte is higher compared to the other SSC in an ionic liquid such as activated carbon

Table 5.1.1. Summary of electrochemical performance of MoS_2 SSC device with recently reported SSC devices based on metal chalcogenides.

S.No.	SSC device	Energy density (Wh kg^{-1})	Power density (W kg^{-1})	Reference
1	RuS_2	1.51	40	[46]
2	FeS	2.56	726	[73]
3	MnSe	8.60	47.05	[74]
4	$Cu_{12}Sb_4S_{13}$	0.85	320	[75]
5	Cu_3SbS_3	0.7	36	[75]
6	Cu_3SbS_4	0.62	39	[75]
7	MoS_2/RGO/MoS_2@Mo	6.22	1870	[67]
8	MoS_2/RCF	10	5400	[76]
9	1T Mos_2	5	8550	[66]
10	2H MoS_2	0.16	1500	[66]
11	Commercial MoS_2	0.1	1500	[66]
12	MoS_2	5.42	128	[65]
13	MoS_2 sponge	6.15	50	[77]
13	Few layered MoS_2	18.43	1125	This work

Table 5.1.2. Comparison of the energy and power density for the electrode materials with the reported ones using ionic electrolyte.

S.No.	Electrode material	Electrolyte	Energy density (Wh kg^{-1})	Power density (W kg^{-1})	Reference
1	Porous carbon	EMI-BF_4	11.4	9800	[78]
2	CNT fiber	[PYR14] [TFSI]-(PVDF-HFP)	11.4	1000	[79]
3	Activated carbon	Et_4NBF_4/AN	8	1418	[80]
4	Activated carbon	PTFE-[EMIM][Tf_2N]	6	2842	[80]
5	PEDOT	PVdF-HFP-[BMIM][BF_4]	4.25	5000	[81]
6	Si Nanowire	BMI-TFSI	0.23	650	[78]
7	Activated carbon	PYR13-FSI	16	1100	[78]
8	Siloxene	$TEABF_4$	5.08	375	[43]
9	Few layered MoS_2	$TEABF_4$	18.43	1125	This work

(1100 W kg^{-1})[82], and porous carbon nanofiber (400 W kg^{-1})[83]. The superior electrochemical performance of MoS_2 SSC device with recently reported SSC devices using MoS_2, other TMCs and carbon based electrodes are provided in the Table S1 and Table S2 in the supporting information. Figure 5.1.6 (D) shows the cyclic stability test of the MoS_2 SSC device over continuous CD analysis measured using a constant current density of 1.5 A g^{-1}. It

shows a capacitance retention of about 91.2 % of its initial capacitance was retained after 5000 cycles which suggest the better stability of the MoS_2 SSC device. Figure S4 shows the EIS analysis of MoS_2 SSC device measured after 5000 cycles which showed an increase in charge transfer resistance from 55.15 to 98.5 Ω and a small decrease in the phase angle to nearly -60º [68]. This might be a possible reason for the observed capacitance decay after 5000 cycles. Overall, these results demonstrated the promising use of fabricated MoS_2 SSC device in the next generation energy storage sectors.

5.1.4. Conclusion

In conclusion, we demonstrated the energy storage properties of few-layered MoS_2 sheets in the organic liquid electrolyte. Physico-chemical characterizations such as XRD, laser Raman spectroscopy, XPS spectroscopy, and HR-TEM analyses confirmed the delamination of bulk MoS_2 into few-layered MoS_2 sheets via ball milling process. The cyclic voltammetry and electrochemical impedance spectroscopy (using Nyquist and Bode plots) studies revealed the presence of pseudocapacitive nature of charge-storage mechanism in the few layered MoS_2 via ion intercalation/deintercalation phenomenon. The galvanostatic charge-discharge analysis revealed that the fabricated MoS_2 SSC device delivered a specific capacitance of 14.75 F g^{-1} obtained at a constant current density of 0.75 A g^{-1}. Further, the MoS_2 SSC device possesses the high energy of 18.43 Wh kg^{-1} (higher compared to many of the recently reported TMCs, layered nanostructures, and commercial supercapacitors) with a specific power density of 1125 W kg^{-1} and excellent cyclic stability of 91.2 % over 5000 charge-discharge cycles. The collective findings of this study demonstrated the practical use of MoS_2 SSC device towards next-generation energy storage applications.

5.1.5 References

[1] R.R. Salunkhe, Y. V. Kaneti, Y. Yamauchi, Metal–Organic Framework-Derived Nanoporous Metal Oxides toward Supercapacitor Applications: Progress and Prospects, ACS Nano. 11 (2017) 5293–5308. doi:10.1021/acsnano.7b02796.

[2] B. Sathyaseelan, E. Manikandan, I. Baskaran, K. Senthilnathan, K. Sivakumar, M.K. Moodley, R. Ladchumananandasivam, M. Maaza, Studies on structural and optical properties of ZrO_2 nanopowder for opto-electronic applications, J. Alloys Compd. 694 (2017) 556–559. doi:10.1016/j.jallcom.2016.10.002.

[3] A. Venkadesh, S. Radhakrishnan, J. Mathiyarasu, Eco-friendly synthesis and morphology-dependent superior electrocatalytic properties of CuS nanostructures, Electrochim. Acta. 246 (2017) 544–552. doi:10.1016/j.electacta.2017.06.077.

[4] L. Cong, H. Xie, J. Li, Hierarchical Structures Based on Two-Dimensional Nanomaterials for Rechargeable Lithium Batteries, Adv. Energy Mater. 7 (2017) 1601906. doi:10.1002/aenm.201601906.

[5] W. Zhou, L. Lin, W. Wang, L. Zhang, Q. Wu, J. Li, L. Guo, Hierarchial Mesoporous Hematite with “Electron-Transport Channels” and Its Improved Performances in Photocatalysis and Lithium Ion Batteries, J. Phys. Chem. C. 115 (2011) 7126–7133. doi:10.1021/jp2011606.

[6] H. Liu, P. He, Z. Li, Y. Liu, J. Li, A novel nickel-based mixed rare-earth oxide/activated carbon supercapacitor using room temperature ionic liquid electrolyte, Electrochim. Acta. 51 (2006) 1925–1931. doi:10.1016/j.electacta.2005.06.034.

[7] T.-H. Ko, S. Radhakrishnan, M.-K. Seo, M.-S. Khil, H.-Y. Kim, B.-S. Kim, A green and scalable dry synthesis of $NiCo_2O_4$/graphene nanohybrids for high-performance supercapacitor and enzymeless glucose biosensor applications, J. Alloys Compd. 696 (2017) 193–200. doi:10.1016/j.jallcom.2016.11.234.

[8] B.E. Conway, Electrochemical Supercapacitors, Springer US, Boston, MA, 1999. doi:10.1007/978-1-4757-3058-6.

[9] S. Radhakrishnan, H.-Y. Kim, B.-S. Kim, Expeditious and eco-friendly fabrication of highly uniform microflower superstructures and their applications in highly durable methanol oxidation and high-performance supercapacitors, J. Mater. Chem. A. 4 (2016) 12253–12262. doi:10.1039/C6TA04888A.

[10] T. Brousse, D. Belanger, J.W. Long, To Be or Not To Be Pseudocapacitive?, J. Electrochem. Soc. 162 (2015) A5185–A5189. doi:10.1149/2.0201505jes.

[11] X. Cong, C. Cheng, Y. Liao, Y. Ye, C. Dong, H. Sun, X. Ji, W. Zhang, P. Fang, L. Miao, J. Jiang, Intrinsic Charge Storage Capability of Transition Metal Dichalcogenides as Pseudocapacitor Electrodes, J. Phys. Chem. C. 119 (2015) 20864–20870. doi:10.1021/acs.jpcc.5b07004.

[12] G. Nallamuthu, S. Thangavel, K. Kirubakaran, V. Vasudevan, Y. Sivalingam, G. Venugopal, Study of structural and electrochemical properties of $La_2SrV_2O_9$ perovskites prepared using ball-milling, Appl. Surf. Sci. 449 (2018) 468–473. doi:10.1016/j.apsusc.2017.12.187.

[13] S. Padmajan Sasikala, K.E. Lee, J. Lim, H.J. Lee, S.H. Koo, I.H. Kim, H.J. Jung, S.O. Kim, Interface-Confined High Crystalline Growth of Semiconducting Polymers at Graphene Fibers for High-Performance Wearable Supercapacitors, ACS Nano. 11 (2017) 9424–9434. doi:10.1021/acsnano.7b05029.

[14] J. Yan, Q. Wang, T. Wei, Z. Fan, Recent Advances in Design and Fabrication of Electrochemical Supercapacitors with High Energy Densities, Adv. Energy Mater. 4 (2014) 1300816. doi:10.1002/aenm.201300816.

[15] S. Vijayan, B. Kirubasankar, P. Pazhamalai, A.K. Solarajan, S. Angaiah, Electrospun Nd^{3+}-Doped $LiMn_2O_4$ Nanofibers as High-Performance Cathode Material for Li-Ion

Capacitors, ChemElectroChem. 4 (2017) 2059–2067. doi:10.1002/celc.201700161.

[16] P. Sharma, T.S. Bhatti, A review on electrochemical double-layer capacitors, Energy Convers. Manag. 51 (2010) 2901–2912. doi:10.1016/j.enconman.2010.06.031.

[17] R. Ramachandran, M. Saranya, V. Velmurugan, B.P.C. Raghupathy, S.K. Jeong, A.N. Grace, Effect of reducing agent on graphene synthesis and its influence on charge storage towards supercapacitor applications, Appl. Energy. 153 (2015) 22–31. doi:10.1016/j.apenergy.2015.02.091.

[18] A. Afzal, F.A. Abuilaiwi, A. Habib, M. Awais, S.B. Waje, M.A. Atieh, Polypyrrole/carbon nanotube supercapacitorsTechnological advances and challenges, J. Power Sources. 352 (2017) 174–186. doi:10.1016/j.jpowsour.2017.03.128.

[19] P. Pazhamalai, K. Krishnamoorthy, V.K. Mariappan, S. Sahoo, S. Manoharan, S.-J. Kim, A High Efficacy Self-Charging $MoSe_2$ Solid-State Supercapacitor Using Electrospun Nanofibrous Piezoelectric Separator with Ionogel Electrolyte, Adv. Mater. Interfaces. 5 (2018) 1800055. doi:10.1002/admi.201800055.

[20] J. Lim, D.S. Choi, G.Y. Lee, H.J. Lee, S.P. Sasikala, K.E. Lee, S.H. Kang, S.O. Kim, Omnidirectional Deformable Energy Textile for Human Joint Movement Compatible Energy Storage, ACS Appl. Mater. Interfaces. 9 (2017) 41363–41370. doi:10.1021/acsami.7b14981.

[21] G. Wang, L. Zhang, J. Zhang, A review of electrode materials for electrochemical supercapacitors, Chem. Soc. Rev. 41 (2012) 797–828. doi:10.1039/C1CS15060J.

[22] X. Zhang, L. Hou, A. Ciesielski, P. Samorì, 2D Materials Beyond Graphene for High-Performance Energy Storage Applications, Adv. Energy Mater. 6 (2016). doi:10.1002/aenm.201600671.

[23] R. Kumuthini, R. Ramachandran, H.A. Therese, F. Wang, Electrochemical properties of electrospun MoS_2@C nanofiber as electrode material for high-performance

supercapacitor application, J. Alloys Compd. 705 (2017) 624–630. doi:10.1016/j.jallcom.2017.02.163.

[24] X. Fu, P. Ilanchezhiyan, G. Mohan Kumar, H.D. Cho, L. Zhang, A.S. Chan, D.J. Lee, G.N. Panin, T.W. Kang, Tunable UV-visible absorption of SnS_2 layered quantum dots produced by liquid phase exfoliation, Nanoscale. 9 (2017) 1820–1826. doi:10.1039/C6NR09022B.

[25] S. Radhakrishnan, S.J. Kim, Facile fabrication of NiS and a reduced graphene oxide hybrid film for nonenzymatic detection of glucose, RSC Adv. 5 (2015) 44346–44352. doi:10.1039/C5RA01074H.

[26] S. Radhakrishnan, H.-Y. Kim, B.-S. Kim, A novel CuS microflower superstructure based sensitive and selective nonenzymatic glucose detection, Sensors Actuators B Chem. 233 (2016) 93–99. doi:10.1016/j.snb.2016.04.056.

[27] Y.-P. Gao, X. Wu, K.-J. Huang, L.-L. Xing, Y.-Y. Zhang, L. Liu, Two-dimensional transition metal diseleniums for energy storage application: a review of recent developments, CrystEngComm. 19 (2017) 404–418. doi:10.1039/C6CE02223E.

[28] L. Peng, Z. Fang, Y. Zhu, C. Yan, G. Yu, Holey 2D Nanomaterials for Electrochemical Energy Storage, Adv. Energy Mater. (2017) 1702179. doi:10.1002/aenm.201702179.

[29] X. Wang, Q. Weng, Y. Yang, Y. Bando, D. Golberg, Hybrid two-dimensional materials in rechargeable battery applications and their microscopic mechanisms, Chem. Soc. Rev. 45 (2016) 4042–4073. doi:10.1039/C5CS00937E.

[30] G. Zhang, H. Liu, J. Qu, J. Li, Two-dimensional layered MoS_2: rational design, properties and electrochemical applications, Energy Environ. Sci. 9 (2016) 1190–1209. doi:10.1039/C5EE03761A.

[31] J. Theerthagiri, R.A. Senthil, B. Senthilkumar, A. Reddy Polu, J. Madhavan, M.

Ashokkumar, Recent advances in MoS_2 nanostructured materials for energy and environmental applications – A review, J. Solid State Chem. 252 (2017) 43–71. doi:10.1016/j.jssc.2017.04.041.

[32] M.-R. Gao, Y.-F. Xu, J. Jiang, S.-H. Yu, Nanostructured metal chalcogenides: synthesis, modification, and applications in energy conversion and storage devices, Chem. Soc. Rev. 42 (2013) 2986. doi:10.1039/c2cs35310e.

[33] X. Hu, W. Zhang, X. Liu, Y. Mei, Y. Huang, Nanostructured Mo-based electrode materials for electrochemical energy storage, Chem. Soc. Rev. 44 (2015) 2376–2404. doi:10.1039/C4CS00350K.

[34] M. Acerce, D. Voiry, M. Chhowalla, Metallic 1T phase MoS_2 nanosheets as supercapacitor electrode materials, Nat. Nanotechnol. 10 (2015) 313–318. doi:10.1038/nnano.2015.40.

[35] A.H. Loo, A. Bonanni, Z. Sofer, M. Pumera, Exfoliated transition metal dichalcogenides (MoS_2, $MoSe_2$, WS_2, WSe_2): An electrochemical impedance spectroscopic investigation, Electrochem. Commun. 50 (2015) 39–42. doi:10.1016/j.elecom.2014.10.018.

[36] K. Krishnamoorthy, P. Pazhamalai, G.K. Veerasubramani, S.J. Kim, Mechanically delaminated few layered MoS_2 nanosheets based high performance wire type solid-state symmetric supercapacitors, J. Power Sources. 321 (2016) 112–119. doi:10.1016/j.jpowsour.2016.04.116.

[37] M.A. Bissett, S.D. Worrall, I.A. Kinloch, R.A.W. Dryfe, Comparison of Two-Dimensional Transition Metal Dichalcogenides for Electrochemical Supercapacitors, Electrochim. Acta. 201 (2016) 30–37. doi:10.1016/j.electacta.2016.03.190.

[38] A. Burke, R&D considerations for the performance and application of electrochemical capacitors, Electrochim. Acta. 53 (2007) 1083–1091.

doi:10.1016/j.electacta.2007.01.011.

[39] S. Sahoo, C.S. Rout, Facile Electrochemical Synthesis of Porous Manganese-Cobalt-Sulfide Based Ternary Transition Metal Sulfide Nanosheets Architectures for High Performance Energy Storage Applications, Electrochim. Acta. 220 (2016) 57–66. doi:10.1016/j.electacta.2016.10.043.

[40] K. Krishnamoorthy, G.K. Veerasubramani, S. Radhakrishnan, S.J. Kim, Supercapacitive properties of hydrothermally synthesized sphere like MoS_2 nanostructures, Mater. Res. Bull. 50 (2014) 499–502. doi:10.1016/j.materresbull.2013.11.019.

[41] P. Ilanchezhiyan, G. Mohan Kumar, T.W. Kang, Electrochemical studies of spherically clustered MoS_2 nanostructures for electrode applications, J. Alloys Compd. 634 (2015) 104–108. doi:10.1016/j.jallcom.2015.02.082.

[42] C. Zhong, Y. Deng, W. Hu, J. Qiao, L. Zhang, J. Zhang, A review of electrolyte materials and compositions for electrochemical supercapacitors., Chem. Soc. Rev. 44 (2015) 7484–7539. doi:10.1039/c5cs00303b.

[43] K. Krishnamoorthy, P. Pazhamalai, S.-J. Kim, Two-dimensional siloxene nanosheets: novel high-performance supercapacitor electrode materials, Energy Environ. Sci. 11 (2018) 1595–1602. doi:10.1039/C8EE00160J.

[44] W.-J. Zhang, K.-J. Huang, A review of recent progress in molybdenum disulfide-based supercapacitors and batteries, Inorg. Chem. Front. 4 (2017) 1602–1620. doi:10.1039/C7QI00515F.

[45] K. Pandey, P. Yadav, I. Mukhopadhyay, Electrochemical and electronic properties of flower-like MoS_2 nanostructures in aqueous and ionic liquid media, RSC Adv. 5 (2015) 57943–57949. doi:10.1039/C5RA09282E.

[46] K. Krishnamoorthy, P. Pazhamalai, S.J. Kim, Ruthenium sulfide nanoparticles as a

new pseudocapacitive material for supercapacitor, Electrochim. Acta. 227 (2017) 85–94. doi:10.1016/j.electacta.2016.12.171.

[47] P. Paulraj, A. Manikandan, E. Manikandan, K. Pandian, M.K. Moodley, K. Roro, K. Murugan, Solid-State Synthesis of POPD@AgNPs Nanocomposites for Electrochemical Sensors, J. Nanosci. Nanotechnol. 18 (2018) 3991–3999. doi:10.1166/jnn.2018.15219.

[48] R. Suto, G. Venugopal, K. Tashima, N. Nagamura, K. Horiba, M. Suemitsu, M. Oshima, H. Fukidome, Observation of nanoscopic charge-transfer region at metal/MoS_2 interface, Mater. Res. Express. 3 (2016) 075004. doi:10.1088/2053-1591/3/7/075004.

[49] S. Thangavel, S. Thangavel, N. Raghavan, R. Alagu, G. Venugopal, Efficient visible-light photocatalytic and enhanced photocorrosion inhibition of Ag_2WO_4 decorated MoS_2 nanosheets, J. Phys. Chem. Solids. 110 (2017) 266–273. doi:10.1016/j.jpcs.2017.06.005.

[50] H. Li, Q. Zhang, C.C.R. Yap, B.K. Tay, T.H.T. Edwin, A. Olivier, D. Baillargeat, From Bulk to Monolayer MoS_2: Evolution of Raman Scattering, Adv. Funct. Mater. 22 (2012) 1385–1390. doi:10.1002/adfm.201102111.

[51] F. Lan, Z. Lai, R. Yan, Y. Xu, H. Cheng, S. Zhang, J. Chen, Z. Jia, Z. Wang, C. Qi, Epitaxial Growth of Single-Crystalline Monolayer MoS_2 by Two-Step Method, ECS Solid State Lett. 4 (2015) P19–P21. doi:10.1149/2.0041502ssl.

[52] N.M.. Brown, N. Cui, A. McKinley, An XPS study of the surface modification of natural MoS_2 following treatment in an RF-oxygen plasma, Appl. Surf. Sci. 134 (1998) 11–21. doi:10.1016/S0169-4332(98)00252-9.

[53] A. Ambrosi, C.K. Chua, A. Bonanni, M. Pumera, Electrochemistry of Graphene and Related Materials, Chem. Rev. 114 (2014) 7150–7188. doi:10.1021/cr500023c.

[54] R. Aparna, N. Sivakumar, A. Balakrishnan, A. Sreekumar Nair, S. V. Nair, K.R. V. Subramanian, An effective route to produce few-layer graphene using combinatorial ball milling and strong aqueous exfoliants, J. Renew. Sustain. Energy. 5 (2013) 033123. doi:10.1063/1.4809794.

[55] A. Winchester, S. Ghosh, S. Feng, A.L. Elias, T. Mallouk, M. Terrones, S. Talapatra, Electrochemical Characterization of Liquid Phase Exfoliated Two-Dimensional Layers of Molybdenum Disulfide, ACS Appl. Mater. Interfaces. 6 (2014) 2125–2130. doi:10.1021/am4051316.

[56] J.M. Soon, K.P. Loh, Electrochemical Double-Layer Capacitance of MoS_2 Nanowall Films, Electrochem. Solid-State Lett. 10 (2007) A250. doi:10.1149/1.2778851.

[57] M.H. Yang, J.M. Jeong, Y.S. Huh, B.G. Choi, High-performance supercapacitor based on three-dimensional MoS_2/graphene aerogel composites, Compos. Sci. Technol. 121 (2015) 123–128. doi:10.1016/j.compscitech.2015.11.004.

[58] N. Savjani, E.A. Lewis, M.A. Bissett, J.R. Brent, R.A.W. Dryfe, S.J. Haigh, P. O'Brien, Synthesis of Lateral Size-Controlled Monolayer 1H-MoS_2@Oleylamine as Supercapacitor Electrodes., Chem. Mater. 28 (2016) 657–664. doi:10.1021/acs.chemmater.5b04476.

[59] M.A. Bissett, I.A. Kinloch, R.A.W. Dryfe, Characterization of MoS_2–Graphene Composites for High-Performance Coin Cell Supercapacitors, ACS Appl. Mater. Interfaces. 7 (2015) 17388–17398. doi:10.1021/acsami.5b04672.

[60] J. Jiang, High Temperature Monolithic Biochar Supercapacitor Using Ionic Liquid Electrolyte, J. Electrochem. Soc. 164 (2017) H5043–H5048. doi:10.1149/2.0211708jes.

[61] A.M. Navarro-Suárez, K.L. Van Aken, T. Mathis, T. Makaryan, J. Yan, J. Carretero-González, T. Rojo, Y. Gogotsi, Development of asymmetric supercapacitors with

titanium carbide-reduced graphene oxide couples as electrodes, Electrochim. Acta. 259 (2018) 752–761. doi:10.1016/j.electacta.2017.10.125.

[62] K. Jeyasubramanian, M. Nisanthi, V.S. Benitha, N. Selvakumar, Electrochemical Impedance Spectroscopic Analysis of ZnS Nanorod Fabricated Using Butterfly Wings as Biotemplate, Acta Metall. Sin. (English Lett. 28 (2015) 103–109. doi:10.1007/s40195-014-0175-7.

[63] R.B. Rakhi, W. Chen, D. Cha, H.N. Alshareef, Substrate dependent self-organization of mesoporous cobalt oxide nanowires with remarkable pseudocapacitance, Nano Lett. 12 (2012) 2559–2567. doi:10.1021/nl300779a.

[64] T.N.Y. Khawula, K. Raju, P.J. Franklyn, I. Sigalas, K.I. Ozoemena, Symmetric pseudocapacitors based on molybdenum disulfide (MoS_2)-modified carbon nanospheres: Correlating physicochemistry and synergistic interaction on energy storage, J. Mater. Chem. A. 4 (2016) 6411–6425. doi:10.1039/c6ta00114a.

[65] M.S. Javed, S. Dai, M. Wang, D. Guo, L. Chen, X. Wang, C. Hu, Y. Xi, High performance solid state flexible supercapacitor based on molybdenum sulfide hierarchical nanospheres, J. Power Sources. 285 (2015) 63–69. doi:10.1016/j.jpowsour.2015.03.079.

[66] S. Yang, K. Zhang, C. Wang, Y. Zhang, S. Chen, C. Wu, A. Vasileff, S.-Z. Qiao, L. Song, Hierarchical 1T-MoS_2 nanotubular structures for enhanced supercapacitive performance, J. Mater. Chem. A. 5 (2017) 23704–23711. doi:10.1039/C7TA08115D.

[67] Y. Zhang, P. Ju, C. Zhao, X. Qian, In-situ Grown of MoS_2/RGO/MoS_2@Mo Nanocomposite and Its supercapacitor Performance, Electrochim. Acta. 219 (2016) 693–700. doi:10.1016/j.electacta.2016.10.072.

[68] D. Zhou, H. Wang, N. Mao, Y. Chen, Y. Zhou, T. Yin, H. Xie, W. Liu, S. Chen, X. Wang, High energy supercapacitors based on interconnected porous carbon nanosheets

with ionic liquid electrolyte, Microporous Mesoporous Mater. 241 (2017) 202–209. doi:10.1016/j.micromeso.2017.01.001.

[69] X. Zhang, L. Wang, J. Peng, P. Cao, X. Cai, J. Li, M. Zhai, A Flexible Ionic Liquid Gelled PVA-Li_2SO_4 Polymer Electrolyte for Semi-Solid-State Supercapacitors, Adv. Mater. Interfaces. 2 (2015) 1500267. doi:10.1002/admi.201500267.

[70] X. Geng, Y. Zhang, Y. Han, J. Li, L. Yang, M. Benamara, L. Chen, H. Zhu, Two-Dimensional Water-Coupled Metallic MoS_2 with Nanochannels for Ultrafast Supercapacitors, Nano Lett. 17 (2017) 1825–1832. doi:10.1021/acs.nanolett.6b05134.

[71] S. Kamila, B. Mohanty, A.K. Samantara, P. Guha, A. Ghosh, B. Jena, P. V. Satyam, B.K. Mishra, B.K. Jena, Highly Active 2D Layered MoS_2 -rGO Hybrids for Energy Conversion and Storage Applications, Sci. Rep. 7 (2017) 8378. doi:10.1038/s41598-017-08677-5.

[72] C.N.R. Rao, K. Gopalakrishnan, U. Maitra, Comparative Study of Potential Applications of Graphene, MoS_2 , and Other Two-Dimensional Materials in Energy Devices, Sensors, and Related Areas, ACS Appl. Mater. Interfaces. 7 (2015) 7809–7832. doi:10.1021/am509096x.

[73] S.S. Karade, P. Dwivedi, S. Majumder, B. Pandit, B.R. Sankapal, First report on a FeS-based 2 V operating flexible solid-state symmetric supercapacitor device, Sustain. Energy Fuels. 1 (2017) 1366–1375. doi:10.1039/C7SE00165G.

[74] S. Sahoo, P. Pazhamalai, K. Krishnamoorthy, S.-J. Kim, Hydrothermally prepared α-MnSe nanoparticles as a new pseudocapacitive electrode material for supercapacitor, Electrochim. Acta. 268 (2018) 403–410. doi:10.1016/j.electacta.2018.02.116.

[75] K. Ramasamy, R.K. Gupta, H. Sims, S. Palchoudhury, S. Ivanov, A. Gupta, Layered ternary sulfide $CuSbS_2$ nanoplates for flexible solid-state supercapacitors, J. Mater. Chem. A. 3 (2015) 13263–13274. doi:10.1039/c5ta03193a.

[76] C. Zhao, Y. Zhou, Z. Ge, C. Zhao, X. Qian, Facile construction of MoS_2/RCF electrode for high-performance supercapacitor, Carbon N. Y. 127 (2018) 699–706. doi:10.1016/j.carbon.2017.11.052.

[77] S.K. Balasingam, M. Lee, B.H. Kim, J.S. Lee, Y. Jun, Freeze-dried MoS_2 sponge electrodes for enhanced electrochemical energy storage, Dalt. Trans. 46 (2017) 2122–2128. doi:10.1039/C6DT04466B.

[78] A. Eftekhari, Supercapacitors utilising ionic liquids, Energy Storage Mater. 9 (2017) 47–69. doi:10.1016/j.ensm.2017.06.009.

[79] E. Senokos, V. Reguero, L. Cabana, J. Palma, R. Marcilla, J.J. Vilatela, Large-Area, All-Solid, and Flexible Electric Double Layer Capacitors Based on CNT Fiber Electrodes and Polymer Electrolytes, Adv. Mater. Technol. 2 (2017) 1600290. doi:10.1002/admt.201600290.

[80] W. Lu, K. Henry, C. Turchi, J. Pellegrino, Incorporating Ionic Liquid Electrolytes into Polymer Gels for Solid-State Ultracapacitors, J. Electrochem. Soc. 155 (2008) A361. doi:10.1149/1.2869202.

[81] G.P. Pandey, A.C. Rastogi, Solid-State Supercapacitors Based on Pulse Polymerized Poly(3,4-ethylenedioxythiophene) Electrodes and Ionic Liquid Gel Polymer Electrolyte, J. Electrochem. Soc. 159 (2012) A1664–A1671. doi:10.1149/2.047210jes.

[82] V. Chaudoy, F. Tran Van, M. Deschamps, F. Ghamouss, Ionic liquids in a poly ethylene oxide cross-linked gel polymer as an electrolyte for electrical double layer capacitor, J. Power Sources. 342 (2017) 872–878. doi:10.1016/j.jpowsour.2016.12.097.

[83] C. Tran, D. Lawrence, F.W. Richey, C. Dillard, Y.A. Elabd, V. Kalra, Binder-free three-dimensional high energy density electrodes for ionic-liquid supercapacitors, Chem. Commun. 51 (2015) 13760–13763. doi:10.1039/C5CC04359J.

CHAPTER 5.2: TWO-DIMENSIONAL MOLYBDENUM DISELENIDE NANOSHEETS AS A NOVEL ELECTRODE MATERIAL FOR SYMMETRIC SUPERCAPACITORS USING ORGANIC ELECTROLYTE

Highlights

- Energy storage properties of 2H $MoSe_2$ nanosheet was examined in organic electrolyte.
- $MoSe_2$ symmetric supercapacitor (SSC) operates over a potential window of 3.0 V.
- $MoSe_2$ SSC device delivered a specific capacitance of 25.31 F g^{-1}.
- $MoSe_2$ SSC device possesses a high energy density of 20.31 Wh kg^{-1}.
- $MoSe_2$ SSC device possess capacitance retention of about 87 % over 10,000 cycles.

5.2.1. Introduction

Two-dimensional transition metal chalcogenides (TMCs) received increasing attention in the field of energy harvesting and energy storage sectors due to their electronic conductivity, optical properties, and distinct electrochemical properties[1–3]. Recently, 2D TMCs based on sulfides such as vanadium disulfide (VS_2), titanium disulfide (TiS_2), and molybdenum disulfide (MoS_2) has demonstrated as potential candidates for use as electrode materials for supercapacitors, batteries, and hybrid ion capacitors[4,5]. The merits of 2D-TMCs over transition metal oxides and binary metal oxides for energy storage devices is their high electronic conductivity with surface redox properties and high ionic diffusivity compared to their oxide analogs [6]. Increasing efforts are made towards the preparation of single or few layered 2D TMCs via chemical methods as well as exfoliation methods during this decade[7]. The mechanism of charge storage in layered TMCs can be due to (i) electrical double layer capacitance, (ii) pseudocapacitance, and (iii) ion-intercalation capacitance which strongly depends on the electronic conductivity, thickness/layer numbers, and lateral size of the 2D TMCs[8–10]. In our earlier study, the specific capacitance of bulk MoS_2 was increased nearly five-fold after exfoliation into few layered MoS_2 nanosheets in LiOH electrolyte[11]. Due to these interesting properties, the research in the development of TMCs based supercapacitors gained higher attention in this decade. Hitherto, TMCs based on metal sulfides are extensively studied compared to the metal selenides in which the latter is expected to deliver excellent electrochemical properties due to their large anionic polarizability (as well as high ionic diffusivity) arises from the Se^{2-} as similar to that of sulfides [12,13]. Up-to-date, the studies on the electrochemical performances of metal selenides are very limited and only a few reports available in the literature. Therefore, the study on the electrochemical performances of TMCs based on selenides is highly important.

Considering the efforts taken on the metal selenides based electrodes, the performances of cobalt selenides, nickel selenides, and molybdenum selenides has been reported recently [13–16]. Among these materials, $MoSe_2$ is meritorious due to its sheet-like structures with Se-Mo-Se individual nanosheets separated via van der-Waals interactions similar to that of MoS_2, thus providing sufficient space for ion intercalation and de-intercalation process[17]. Recently, researchers focused on understanding the electrochemical properties of $MoSe_2$ sheets for applications in batteries and supercapacitors [18–20]. At first, Carmen et al. demonstrated the enhanced specific capacitance of exfoliated $MoSe_2$ (17 F g^{-1}) compared to bulk $MoSe_2$ (~3 F g^{-1}) using a three-electrode configuration[20]. Later on, Bissett et al. demonstrated the performance of $MoSe_2$ symmetric supercapacitor (without conductive additive) with a specific capacitance of 2.57 F g^{-1}[5]. In order to improve the energy storage properties of $MoSe_2$, researchers carried out different strategies such as developing binder-free electrodes and obtaining high surface area $MoSe_2$ with different morphologies. For instance, Huang et al. demonstrated the enhanced electrochemical properties of hydrothermally grown $MoSe_2$/Ni foam with a specific capacitance of 1114 F g^{-1}[21]. Further, they also demonstrated the use of carbon materials to increase the specific capacitance of $MoSe_2$ such as $MoSe_2$/graphene and porous layered $MoSe_2$/acetylene black binder-free electrodes which delivered a specific capacitance of 1422 and 2020 F g^{-1}, respectively [15,22]. Gao et al. reported a specific capacitance of 243 F g^{-1} for the hydrothermally prepared $MoSe_2$ nanosphere based electrodes[23]. In our recent work, we demonstrated the electrochemically deposited $MoSe_2$ sheets with a specific capacity of 548 mAh g^{-1} (specific capacitance of about 2468 F g^{-1}) [24]. These studies demonstrated the use of $MoSe_2$ electrode for supercapacitors using a three-electrode system, however, two-electrode tests are more ideal for elucidating the electrode materials properties and device performance[25]. A previous study reported that the $MoSe_2$ based symmetric supercapacitor

device (0.5 M H_2SO_4 electrolyte) delivered a specific capacitance of 10.4 F g^{-1} at a current density of 0.1 A g^{-1}[26]. Recently, Qiu et al. reported $MoSe_2$ based solid state supercapacitor (using MoSe2 rods and sheets as two electrode) with enhanced energy-storage properties due to the high operating potential window of 1.4 V [27]. These studies suggested that the morphology, electrode fabrication, and surface area of the $MoSe_2$ highly reflects on their electrochemical capacitive properties.

Another promising way to enhance the energy density of the supercapacitor is the use of ionic or organic electrolytes which can provide a wide voltage window of nearly 3.5 V, thus resulting in the improved energy density of the supercapacitor[28]. For instance, the recent work of Suarez et al. demonstrated that the energy density of graphene-based symmetric supercapacitor is increased from 5 to 16 Wh kg^{-1} from aqueous to ionic liquid electrolyte[29]. Therefore, a study of capacitive properties of $MoSe_2$ using ionic liquid electrolyte will result in enhanced energy storage properties. Up to date, the electrochemical properties of $MoSe_2$ nanosheets are examined only in aqueous electrolytes and gel polymer electrolytes. However, the study on the electrochemical properties of $MoSe_2$ nanosheets in non-aqueous organic electrolytes is not yet studied. In this study, the electrochemical properties of $MoSe_2$ nanosheets in tetraethylammonium tetrafluoroborate/acetonitrile ($TEABF_4$/AN) electrolyte was investigated using the fabrication of symmetric supercapacitor (SSC).

5.2.2. Experimental section

5.2.2.1 Synthesis of molybdenum selenide ($MoSe_2$) nanosheets

A facile hydrothermal process was used for the preparation of $MoSe_2$ nanosheets using sodium molybdate, selenium, and sodium borohydride as the precursors [30]. At first, the 1.24 g of selenium and 0.2 g of sodium borohydride were dissolved in 40 mL of doubly distilled water with constant stirring until the formation of clear red colored solution which

indicated the homogeneous distribution of Se metal in the solution. Then, 1.32 g of sodium molybdate is dissolved in 40 mL of doubly distilled water separately and mixed with the solution containing selenium. The final solution is transferred into 100 mL Teflon-lined stainless-steel autoclave, and the hydrothermal reaction was carried out at 180 °C for 48 h. Upon completion of the reaction, the autoclave is cooled down to room temperature naturally, and the black precipitates of $MoSe_2$ were collected and washed with doubly distilled water followed by absolute ethanol and dried at 70 °C overnight. The obtained powders were further calcinated to 650 °C for 5h at N_2 atmosphere and cooled to room temperature naturally which results in the formation of $MoSe_2$ nanosheets [31–33].

5.2.2.2 Fabrication and electrochemical characterization of $MoSe_2$ SSC

The $MoSe_2$ electrode was prepared by grounding $MoSe_2$ (85 %), carbon black (10 %) and PVDF (5 %) with the appropriate amount of NMP (solvent) in an agate mortar until a uniform slurry was formed. Then, the slurry was coated on to a stainless-steel coin cell substrate (15.4 mm x 0.2 mm) and allowed to dry at 80 °C for 12 h. The electroactive mass of the $MoSe_2$ electrode on to the stainless-steel substrate is calculated from the difference between the mass of the substrate before and after coating of the $MoSe_2$ electrode using Dual-range Semi-micro Balance (AUW-220D, SHIMADZU) with an approximation of five-decimal points is approximate ~0.5 mg in each substrate. The electrolyte solution of 0.5 M $TEABF_4$/AN was prepared by dissolving $TEABF_4$ in acetonitrile solution and used for the electrochemical characterization. The $MoSe_2$ symmetric coin cell supercapacitor (SSC) was fabricated using $MoSe_2$ coated stainless electrode, Celgard as a separator, and $TEABF_4$/AN as the electrolyte. After assembling the electrodes in the CR2032 coin cell case, the coin cell was crimped using Electric Coin Cell Crimping and Disassembling Machine (MTI Korea). The assembling of the symmetric coin cell supercapacitor was done in the argon filled glove box to avoid the reaction of electrolyte in the atmosphere. The electrochemical

characterization of the fabricated $MoSe_2$ SSC such as cyclic voltammetry (CV), galvanostatic charge-discharge (CD) and electrochemical impedance spectroscopy (EIS) analysis was performed using an Autolab PGSTAT302N electrochemical workstation.

5.2.3. Results and discussion

5.2.3.1 Physicochemical characterization

In this work, we prepared the $MoSe_2$ using a simple hydrothermal method followed by calcination at the inert atmosphere.

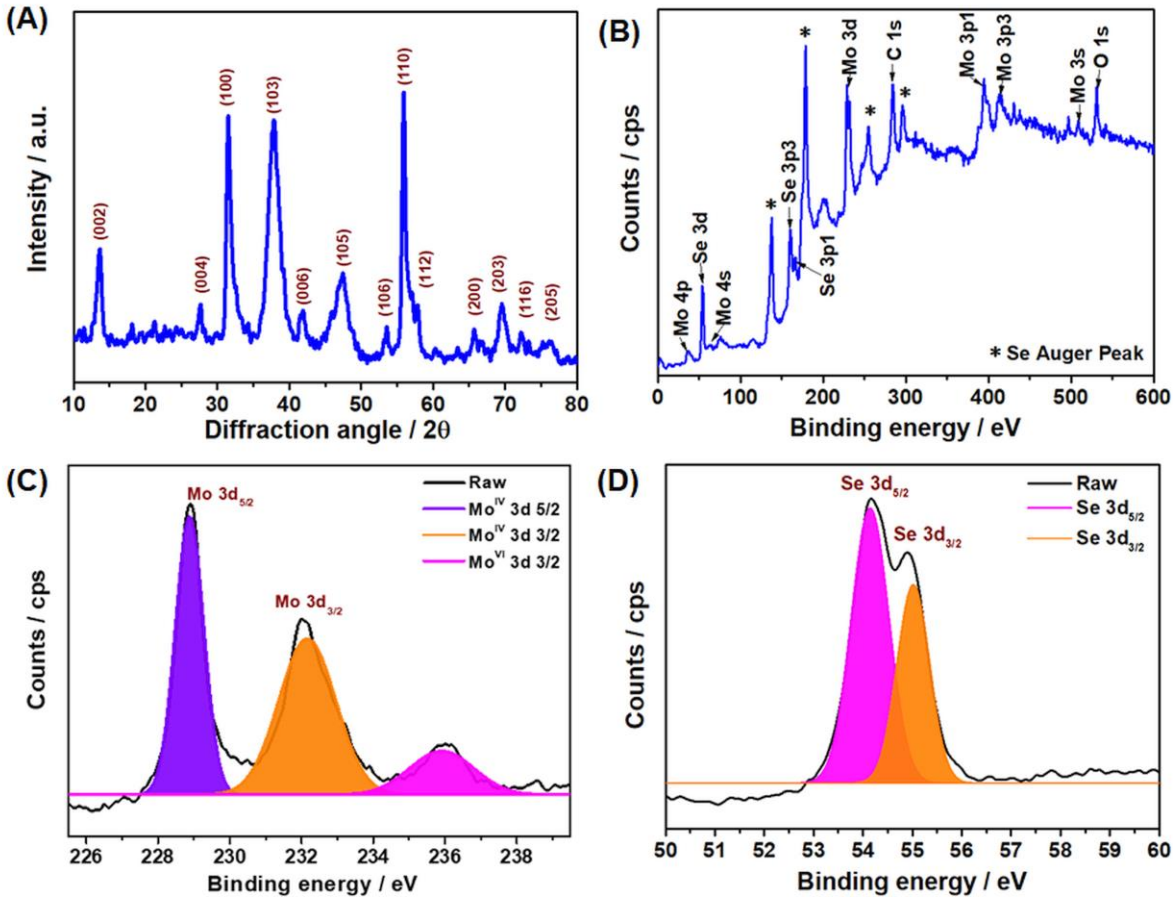

Figure 5.2.1. Physico-chemical characterizations of hydrothermally prepared 2H-$MoSe_2$ nanosheets. (A) X-ray diffraction pattern for the hydrothermally prepared $MoSe_2$ confirms the formation of high crystalline 2H $MoSe_2$. X-ray photoelectron spectroscopy for the $MoSe_2$ nanosheets (B) survey spectrum, (C) high-resolution Mo 3d core-level spectrum and (D) high-resolution Se 3d core-level spectrum.

The hydrothermal reaction between the sodium molybdate and selenium powders in the presence of sodium borohydride results in the formation of amorphous $MoSe_2$ which upon further heat treatment at a temperature of 650 °C results in the formation of crystalline $MoSe_2$ sheets [32,33]. In general, $MoSe_2$ occurs in two major phases such as 2H-$MoSe_2$ and 1T-$MoSe_2$ in which the former possesses semiconducting nature whereas the later behaves like metallic nature[34]. To identify the phase of the obtained $MoSe_2$, we examined the X-ray diffraction analysis, which is a well-known technique used for analyzing the phase of the materials. Figure 5.2.1 (A) represents the X-ray diffraction pattern of the prepared $MoSe_2$ which shows the presence of diffraction peaks at 13.53°, 27.65°, 31.55°, 37.79°, 41.67°, 47.10°, 53.44°, 55.99°, 57.74°, 65.93°, 69.84°, 72.27° and 76.67°, corresponding to the (002), (004), (100), (103), (006), (105), (106), (110), (112), (200), (203), (116) and (205) planes of 2H-$MoSe_2$ with a space group D^4_{6h} (*P63/mmc*) (JCPDS No.29-0914) [18,31,33]. X-ray photoelectron spectroscopy was used to investigate the chemical composition and the oxidation state of the elements present in the $MoSe_2$ nanosheets. The XPS survey spectrum of $MoSe_2$ nanosheets shown in Fig. 5.2.1(B) revealed the presence of oxidation states corresponding to the Mo and Se components in the $MoSe_2$. The presence of C 1s and O 1s signals were originated from the CO_2 and H_2O impurities as seen in previous works[35]. Figure 5.2.1 (C) shows the deconvoluted spectra of Mo 3d, which reveals the presence of two major peaks around the binding energies of 228.9 and 232 eV, corresponds to the Mo^{4+} $3d_{5/2}$ and Mo^{4+} $3d_{3/2}$ states, respectively and a minor peak around 236 eV has been observed which corresponds to the presence of Mo^{6+} $3d_{3/2}$ state. The observed binding energies are in good agreement with the 2H phase of $MoSe_2$[36]. The deconvoluted spectrum of the selenium 3d (Fig. 5.2.1(D)) shows the presence of peaks at 54.1, and 54.89 eV binding energy split into two well-defined peaks corresponds to Se $3d_{3/2}$ and Se $3d_{5/2}$ state,

respectively which confirms the oxidation state of selenium is -2 in the $MoSe_2$ nanosheets[24].

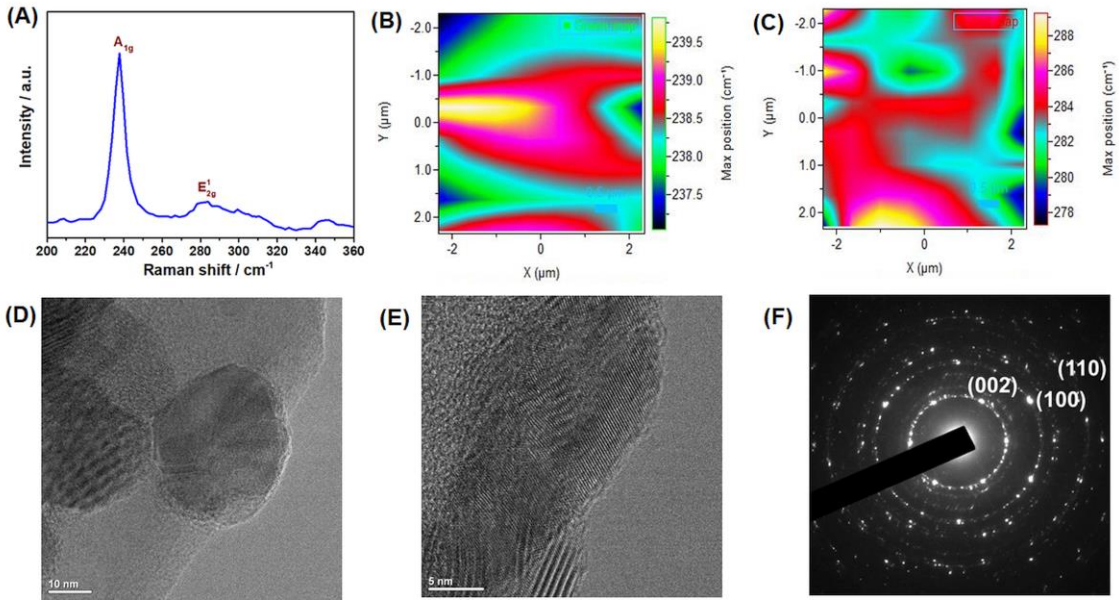

Figure 5.2.2. Laser Raman spectrum and mapping analysis of $MoSe_2$ nanosheets. (A) Raman spectrum of the $MoSe_2$ reveals the two major band of A_{1g} and E^1_{2g} mode in the $MoSe_2$; Raman mapping analysis of the $MoSe_2$ electrodes over the region of 4 × 4 μm and the peak position maps of A_{1g} and E^1_{2g} mode are provided in (B) and (C) respectively. High-resolution transmission electron micrograph of $MoSe_2$ nanosheets depicts the sheet-like structure. (D) shows the low resolution and (E) high-resolution transmission electron micrograph of $MoSe_2$ nanosheets; (F) represents the selected area diffraction pattern of the $MoSe_2$ nanosheets

Laser Raman spectroscopy and mapping is a powerful technique to understand the structural properties of low dimensional materials and can be used for the determination of the number of layers [37,38]. Figure 5.2.2 (A) shows the laser Raman spectrum of the $MoSe_2$ nanosheets indicating the presence of a sharp band at 238 cm^{-1} and a relatively broad weakened band at 282 to 285 cm^{-1}, respectively. The band observed at 238 cm^{-1} is due to the A_{1g} mode which associated with the vibrations (out-of-plane) of selenium atoms in opposite directions, whereas the band observed at 282 to 285 cm^{-1} corresponds to the E^1_{2g} mode in which the vibrations (in-plane) of two selenium atoms with the molybdenum atom[39]. The

peak position of the A_{1g} and E^1_{2g} bands are strongly correlated to the layer numbers in $MoSe_2$ [40]. Therefore, we performed Raman mapping analysis of the $MoSe_2$ electrodes over the region of 4×4 μm, and the peak position maps of A_{1g} and E^1_{2g} modes are provided in Fig 5.2.2 (B) and (C) respectively. In bulk $MoSe_2$, the out of plane A_{1g} mode and in-plane E^1_{2g} mode usually appears at 242 cm^{-1} and 287 cm^{-1} which can vary from 242 to 238 cm^{-1} and 287 to 284 cm^{-1} during the transition from bulk to monolayers[17]. The peak position maps of A_{1g} mode (Fig 5.2.2(B)) shows the presence of mono to few layered $MoSe_2$ corresponding to the peak positions observed from 237.5 to 239.5 indicated by green to red color transition. Further, the peak position map of E^1_{2g} mode (Fig. 5.2.2 (C)) shows the presence of green and red colored spots which correspond to the positions 282 and 285 cm^{-1}, indicating the formation of few-layered $MoSe_2$. The further, the broadened peaks of E^1_{2g} mode suggested the less number of layers and is in good agreement with the previous work of Tongay et al. [17]. The surface morphology of the $MoSe_2$ nanosheets is examined using field emission scanning electron microscope (FE-SEM) and high-resolution transition electron microscopic (HR-TEM) analysis, respectively. The low magnification micrograph (Fig. 5.2.2 (D)) shows the presence of $MoSe_2$ nanosheets overlapped with the adjacent sheets and the high magnification micrographs shown in Fig. 5.2.2 (E) displayed the presence of few-layered $MoSe_2$ nanosheets. Figure 5.2.2 (E) shows the high magnification micrographs indicating the presence of disorders in the presence of $MoSe_2$ which is in agreement with the previous finding of Ambrosi et al. [41]. The SAED pattern given in Fig. 5.2.2 (F) represents the presence of crystalline diffraction spots which corresponds to the hexagonal crystal structure of the $MoSe_2$ nanosheets[42].

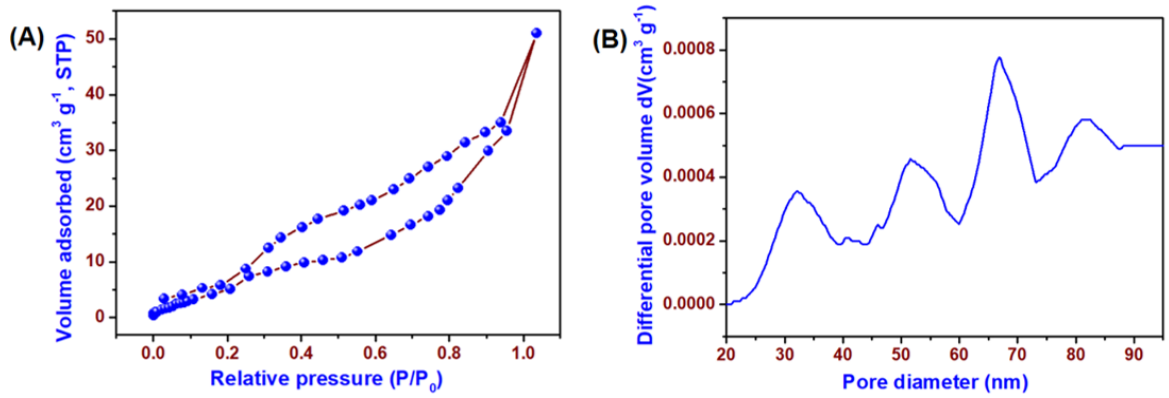

Figure 5.23. Surface area and pore size analysis of $MoSe_2$ nanosheets. (A) The N_2 adsorption-desorption isotherm of the $MoSe_2$ and (B) Pore size distribution in the $MoSe_2$ calculated by HK method.

The surface area of the electroactive material is one of the important parameters which possesses significant influence on the electrochemical properties of the materials[11]. The N_2 adsorption-desorption analysis was measured to study the pore structure, and the specific surface area of the $MoSe_2$ and the adsorption-desorption isotherm and pore size distribution curves are shown in the Fig.5.2.3. From the isotherm curve (Fig. 5.2.3(A)), it has been classified as type IV, revealing the mesoporous structure of the $MoSe_2$. From the N_2 adsorption-desorption isotherm, the specific surface area of the $MoSe_2$ is calculated as 37.836 $m^2\ g^{-1}$ which is closer to the reported values of hydrothermally $MoSe_2$ sheets (33.6 $m^2\ g^{-1}$) and higher than that of bulk and exfoliated MoS_2 sheets[11,35]. Figure 5.2.3(B) shows the pore size distribution calculated by HK method indicated that the $MoSe_2$ exhibits a wide range of pore size distributions from 20 to 80 nm, with the maximum pore size distributed at 66 nm, further confirming the existence of mesopores and macropores in the $MoSe_2$[35]. From the results obtained, it is evident that the $MoSe_2$ exhibits high surface area with a wide range of pore size which facilitates more electroactive sites for the electrochemical reactions.

5.2.3.2 Electrochemical characterization

The electrochemical properties of the $MoSe_2$ nanosheets were investigated using symmetric cell configuration using $TEABF_4$/AN as the electrolyte. Initially, the CV profiles in the various operating potential windows (OPW) from ±0.5 to ±3.0 V (shown in Fig. 5.2.4(A)) using a scan rate of 100 mV s^{-1}, to understand the polarization of the device, and the electrochemical stability of $MoSe_2$ electrodes[4]. It shows quasi-rectangular shaped CV curves up to a region of -2 to +2 V whereas an increase in the voltage window (-3 to 3V) confirms the pseudocapacitive nature of the $MoSe_2$ electrodes via ion intercalation/de-intercalation phenomenon[43]. Further, the obtained current range is increasing with increase in OPW suggesting the ideal capacitive nature of the $MoSe_2$ SSC device.

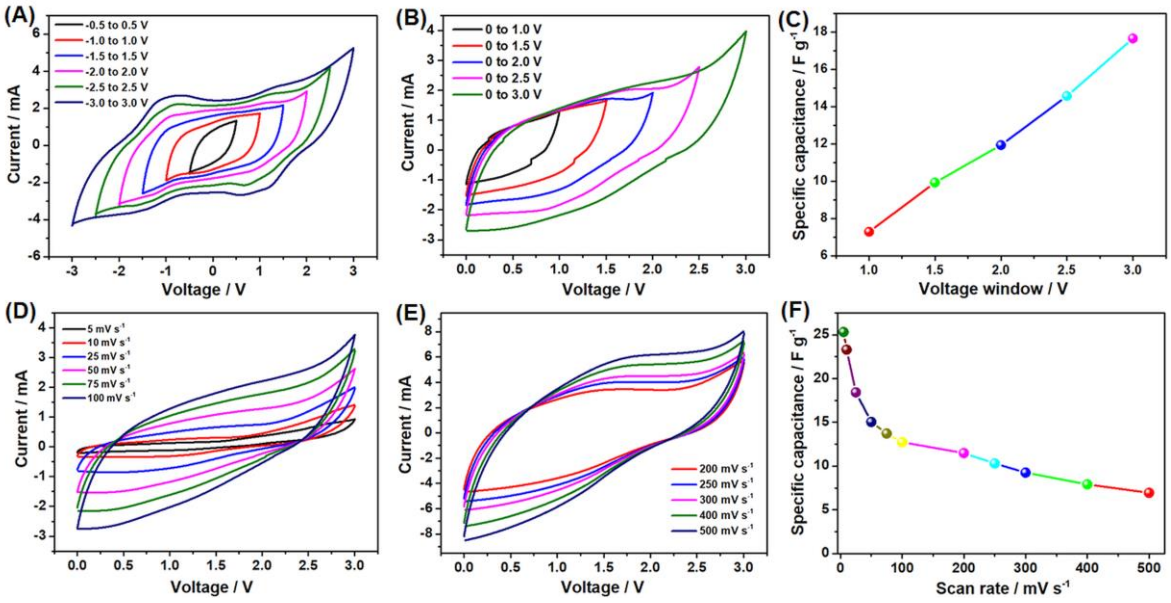

Figure 5.2.4. Electrochemical performances of $MoSe_2$ symmetric supercapacitor (SSC) in 0.5 M $TEABF_4$/AN electrolyte. (A) cyclic voltammetric profiles of $MoSe_2$ SSC measured at different operating voltage window (-3 to +3 V) at a scan rate of 100 mV s^{-1}, (B) CV profiles recorded at different operating voltage windows at a scan rate of 100 mV s^{-1}, (C) Effect of voltage window on the specific capacitance of $MoSe_2$ SSC for the data shown in Fig. (B). (D) and (E) represents the CV profiles measured at different scan rates (0 to 100 mV s^{-1}) and (200 to 500 mV s^{-1}), and (F) represents the plot of scan rate on the specific capacitance.

This study clearly evidences that the $MoSe_2$ SSC device can operate over a potential window of ±3.0 V with excellent electrochemical reversibility without a sign of any evolution. Figure 5.2.4 (B) represents the CV profiles of the fabricated $MoSe_2$ SSC measured at different operating voltage window in the positive regime (0 to 1.0 V, 0 to 1.5 V, 0 to 2 V, 0 to 2.5 V and 0 to 3.0 V) at a scan rate of 100 mV s^{-1} which displayed the distorted rectangular shaped curves and also suggested that the $MoSe_2$ SSC can operate at a window of 3.0 V without any sign of evolution. The plot of specific capacitance against voltage shows a linear increase (Fig. 5.2.4 (C)), thereby suggesting the ideal capacitive behavior [44] The CV profiles of the $MoSe_2$ SSC were measured at various scan rate from 5 - 500 mV s^{-1} is shown in Fig. 5.2.4 (D, E). The shape of the CV profiles looks quasi-rectangular nature indicating the nearly ideal capacitive nature of $MoSe_2$. The increase in the current range of the CV profile with an increase in scan rate from 5 to 500 mV s^{-1} suggests the excellent capacitive property of the $MoSe_2$ SSC[45]. The charge storage mechanism may be attributed to the formation of double layer capacitance and /or intercalation capacitance of the electrode materials. Figure 5.2.4 (F) depicts the relation between the scan rate and specific capacitance of $MoSe_2$ SSC. A specific cell capacitance of 25.31 F g^{-1} was obtained for the $MoSe_2$ SSC from CV analysis measured at a scan rate of 5 mV s^{-1}. The specific capacitance of single $MoSe_2$ electrode was determined as 101.24 F g^{-1} from the device capacitance using the relation ($C_{electrode} = 4 \times C_{cell}$)[46]. The obtained specific cell capacitance of the $MoSe_2$ SSC device is higher compared to the other reported 2D electrode materials based SSC such as Ti_2C M'Xene (4.9 F g^{-1}), Silicon nanowire (0.7 F g^{-1}), exfoliated MoS_2 (2.68 F g^{-1}), MnSe (21.69 F g^{-1}), RuS_2 (17 F g^{-1}), MoS_2 (3.40 F g^{-1}) , WS_2 (3.50 F g^{-1}), and TiS_2 (4.60F g^{-1}) [5,25,47–50]. A capacitance retention of 50.25 % (about was 12.72 F g^{-1}) was achieved for the $MoSe_2$ SSC with an increase of 20-fold in the scan rate (100 mV s^{-1}). The obtained lower specific capacitance at higher scan rate is due to a limitation in mass transport of the electrolyte ions to the interior part of the electrode

material limits the electrochemical reaction, which is in agreement with the previous works on TMCs[51]. Further, the $MoSe_2$ SSC possesses a capacitance of about 6.93 F g^{-1} at a scan rate of 500 mV s^{-1}, thus suggesting the better rate capability of the $MoSe_2$ SSC. This better electrochemical performance of the $MoSe_2$ SSC might be attributed due to the sheet-like morphology of the $MoSe_2$ which can provide sufficient sites of the ion-intercalation and de-intercalation during the electrochemical charging and discharging process.

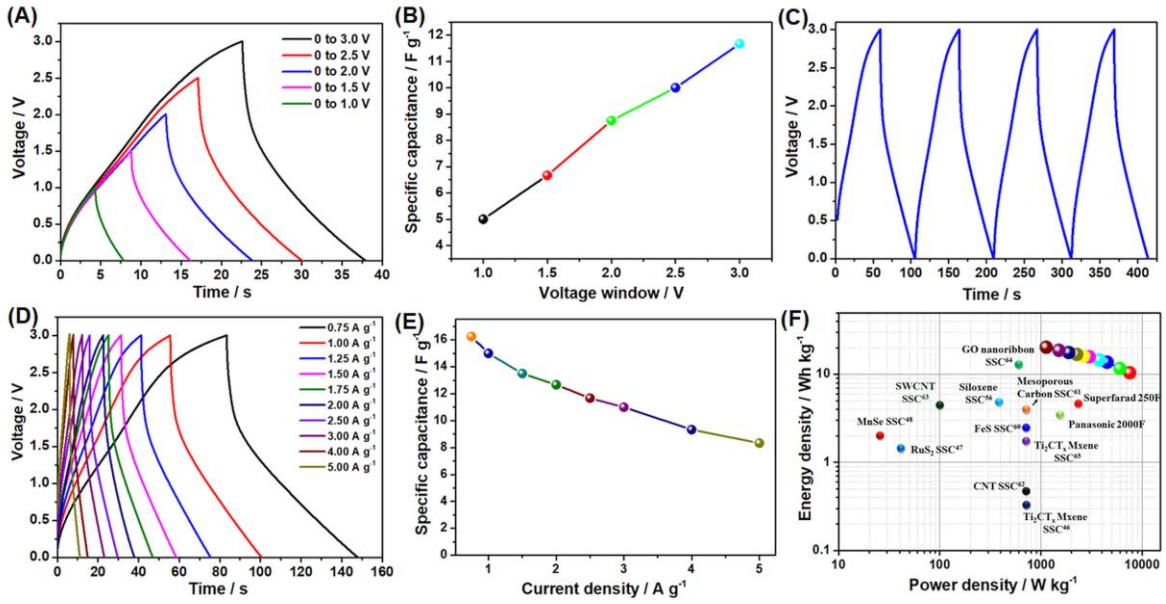

Figure 5.2.5. Electrochemical performances of $MoSe_2$ symmetric supercapacitor (SSC) in 0.5 M $TEABF_4$/AN electrolyte. (A) Galvanostatic CD profiles of $MoSe_2$ SSC measured at different operating voltage windows, (B) Effect of operating voltage windows on the specific capacitance of $MoSe_2$ SSC, (C) shows the CD profiles of $MoSe_2$ SSC measured using a constant current density of 1 A g^{-1}, (D) represents the CD profiles $MoSe_2$ SSC measured under various current densities, (E) Effect of current densities on the specific capacitance of $MoSe_2$ SSC, and (F) shows the Ragone plot of $MoSe_2$ SSC.

Figure 5.2.5 (A) represents the galvanostatic CD profiles of the $MoSe_2$ SSC measured at different operating voltage window (0 – 1 V, 0 - 1.5 V, 0 – 2 V, 0 - 2.5 V and 0 -3.0 V) using a constant current density of 2.5 A g^{-1}. The CD profiles of different operating voltage windows show the presence of semi-symmetric curves supporting the CV profiles shown in

Fig. 5.2.4 (B). The specific capacitance with respect to the voltage window is shown in Fig. 5.2.5 (B) indicated a linear increase in specific capacitance[44], thus, support the observations from CV analysis. Figure 5.2.5 (C) shows the continuous charging and discharging profiles of the $MoSe_2$ SSC obtained at a current density of 1 A g^{-1}. The CD profile exhibits the nearly triangular shaped charge-discharge curves (in agreement with the CV curves) suggesting the ideal capacitive nature of the $MoSe_2$ SSC [52]. Figure 5.2.5 (D) shows the CD profiles of the $MoSe_2$ SSC measured at various current densities ranging from 0.75 to 5.0 A g^{-1}. The CD curves show symmetric behavior over all the current densities measured for the $MoSe_2$ supercapacitor. From the Fig. 5.2.5 (D), it is evident that the high current density results in fast charging and discharging time whereas at the lower current density produced better charging and discharging profiles in the $MoSe_2$ SSC[53]. A specific cell capacitance of 16.25 F g^{-1} was calculated from the CD profile measured at a constant discharge current density of 0.75 A g^{-1} from which the estimated specific capacitance of the single $MoSe_2$ electrode was found to be 65 F g^{-1} respectively[54]. The change in the specific capacitance of the $MoSe_2$ SSC with respect to the current density is provided in the Fig. 5.2.5 (E). At a higher current density of 5 A g^{-1}, the $MoSe_2$ SSC delivered a capacitance of 8.33 F g^{-1} which almost retained 51.26 % of the initial capacitance with an increase of almost 6-fold in current density, thus suggesting the better rate capability of the $MoSe_2$ SSC. Figure 5.2.5 (F) displays the Ragone plot of the $MoSe_2$ SSC in comparison with the reported SSC devices, which shows a high energy density of 20.31 Wh kg^{-1} at a specific power density of 1125 W kg^{-1} when measured at a constant current density of 0.75 A g^{-1}. With an increase of six-fold in current density, the $MoSe_2$ SSC delivered an energy density of 10.42 Wh kg^{-1} at a power density of 7500 W kg^{-1}, suggesting a good rate capability of the $MoSe_2$ SSC. The specific energy density of $MoSe_2$ SSC was comparably higher compared to the reported organic electrolyte based SSCs using electrode materials such as porous carbon (11.4 Wh kg^{-1} in

EMI-BF_4 electrolyte), siloxene (5.08 Wh kg^{-1} in $TEABF_4$ electrolyte), activated carbon (17 Wh kg^{-1} in PTFE-[EMIM][Tf_2N] electrolyte), and RGO-800 (16.7 Wh kg^{-1} in $EMIMBF_4$ electrolyte)[50,55–57]. Table 5.2.1 shows superior performance metrics of the $MoSe_2$ SSC over the recently reported SSC devices and is nearly four-fold higher than that of the commercial supercapacitors[58]. The power density of $MoSe_2$ SSC is higher compared to that of reported SSCs such as $MoSe_2$ (1.4 kW kg^{-1})[27], MoS_2 (128 W kg^{-1})[59], RuS_2 (40 W kg^{-1})[25], MnSe (25 W kg^{-1})[48], FeS (726 W kg^{-1})[60], heat treated Ti_2CTx Mxene (700 W kg^{-1})[47], Siloxene (375 W kg^{-1})[56], ordered mesoporous carbon (800 w kg^{-1})[61], CNT (7000 W kg^{-1})[62], SWCNT (100 W kg^{-1})[63], graphene oxide nanoribbons (807 W kg^{-1})[64] and Ti_2CTx Mxene (700 W kg^{-1})[65] respectively.

Table 5.2.1. Comparison of the energy density for the electrode materials with the reported ones using ionic electrolyte.

S.No.	Electrode material	Electrolyte	Energy density (Wh kg^{-1})	Reference
1	Porous carbon	EMI-BF_4	11.4	[6]
2	CNT fiber	[PYR14] [TFSI]-(PVDF-HFP)	11.4	[7]
3	Biochar monolith	BMI-BF_4	20	[8]
4	Activated carbon	PTFE-[EMIM][Tf_2N]	17	[9]
5	PEDOT	PVdF-HFP-[BMIM][BF_4]	4.25	[10]
6	Si Nanowire	BMI-TFSI	0.23	[6]
7	Activated carbon	PYR13-FSI	16	[6]
8	Siloxene	$TEABF_4$	5.08	[11]
9	$MoSe_2$	$TEABF_4$	20.31	This work

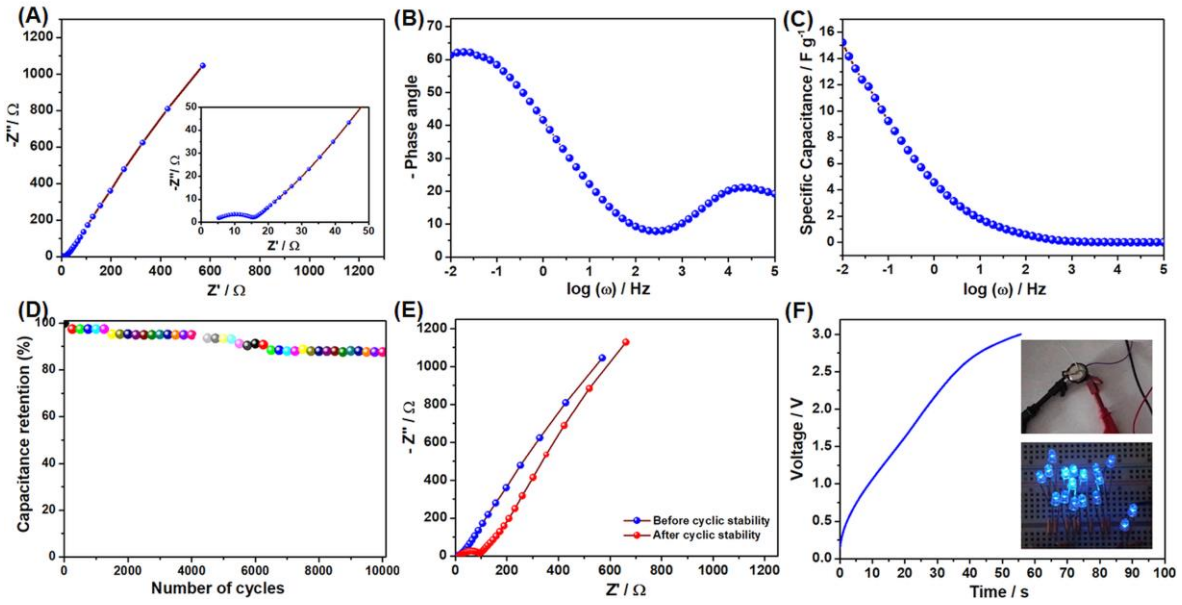

Figure 5.2.6 Electrochemical impedance spectroscopy and cyclic stability analyses of $MoSe_2$ SSC in 0.5 M $TEABF_4$/AN electrolyte. (A) Nyquist plot of $MoSe_2$ SSC, (B) Bode phase angle plots of $MoSe_2$ SSC, (C) variation of specific capacitance of $MoSe_2$ SSC with respect to applied frequency, (D) Cyclic stability of $MoSe_2$ SSC over 10,000 cycles of charge-discharge using cyclic voltammetry, (E) Nyquist plot of $MoSe_2$ SSC measured after cyclic test, (F) shows the practical applications of $MoSe_2$ SSC for glowing 15 blue LEDs.

The electrochemical impedance spectroscopy analysis of the $MoSe_2$ SSC was performed over the frequency 0.01 Hz to 100 kHz at an amplitude of 10 mV, to examine the fundamental charge-transfer kinetics occurred at the electrode/electrolyte interfacial region. The Nyquist plot of $MoSe_2$ SSC is shown in Fig. 5.2.6 (A) represents the presence of a small semicircle at the high-frequency region (arises due to the charge transfer resistance) followed by a straight line or Warburg line at the low-frequency region almost parallel to the imaginary axis (related to the frequency dependent ion diffusion kinetics [66]. The magnified portion of the high-frequency region is shown in the inset of Fig. 5.2.6 (A), which revealed that the $MoSe_2$ SSC possesses a solution resistance (R_s) of about 5.22 Ω and the charge transfer resistance (R_{ct}) of about 10.9 Ω, respectively. The Bode phase plot is shown in Fig.

5.2.6 (B). From the Bode plot, the phase angle tail is about -61.38º which highlights the pseudocapacitive nature of the $MoSe_2$ SSC[25]. Figure 5.2.6 (C) shows the variation of specific capacitance with respect to the applied frequency of the $MoSe_2$ SSC which revealed that a maximum specific capacitance of about 15.23 F g^{-1} at an applied frequency of 0.01 Hz which is closer compared to that of the capacitance value obtained from CD profiles of the $MoSe_2$ SSC. The cyclic life of the supercapacitor device is one of the significant criterion determining theirs for the practical applications[67]. Figure 5.2.6 (D) shows the cyclic stability of $MoSe_2$ SSC over 10000 CV cycles (measured at a scan rate of 50 mV s^{-1}). A capacitance retention of 87.62 % of its initial capacitance has been retained after 10000 cycles which suggest the better stability of the $MoSe_2$ SSC. In order to evaluate the observed small decrease in specific capacitance of ~13 %, we measured the EIS analysis after cyclic tests as given in Fig. 5.2.6 (E). It showed an increase in R_{ct} from 10.9 to 79.25 Ω after 10,000 cycles which might be a possible reason for the observed capacitance decay of 13 % [14]. Figure 5.2.6 (F) demonstrates the practical applications of $MoSe_2$ SSC. Initially, the $MoSe_2$ SSC is charged into 3 V using a current density of 1 A g^{-1} and the stored charge are delivered to drive fifteen blue LEDs connected in parallel for 10 seconds which further highlights their practical application. Overall, these results demonstrated the promising use of fabricated $MoSe_2$ SSC in the next generation energy storage sectors.

5.2.4. Conclusion

In conclusion, we demonstrated the high-performance supercapacitive properties of layered 2H $MoSe_2$ nanosheets in an organic electrolyte ($TEABF_4$/AN). The CV studies confirmed the mechanism of charge-storage in $MoSe_2$ might be due to the intercalation/deintercalation of $TEABF_4$ electrolyte ions and the $MoSe_2$ SSC delivered a device capacitance of 25.31 F g^{-1} at a scan rate of 5 mV s^{-1}. The Bode phase plots of $MoSe_2$ SSC is about -61.38º which highlights the pseudocapacitive nature of the $MoSe_2$ electrodes.

The galvanostatic CD studies demonstrated that the $MoSe_2$ SSC possesses a specific capacitance of 16.25 F g^{-1} with a power density of 7.5 KW kg^{-1} and excellent cyclic stability of 87.62 % over 10,000 cycles. The collective findings of this study demonstrated the practical use of $MoSe_2$ SSC towards portable energy storage applications.

5.2.5 References

[1] M.-R. Gao, Y.-F. Xu, J. Jiang, S.-H. Yu, Nanostructured metal chalcogenides: synthesis, modification, and applications in energy conversion and storage devices, Chem. Soc. Rev. 42 (2013) 2986. doi:10.1039/c2cs35310e.

[2] M. Liu, Z. Wang, J. Liu, G. Wei, J. Du, Y. Li, C. An, J. Zhang, Synthesis of few-layer 1T′-$MoTe_2$ ultrathin nanosheets for high-performance pseudocapacitors, J. Mater. Chem. A. 5 (2017) 1035–1042. doi:10.1039/C6TA08206H.

[3] X. Xu, C.S. Rout, J. Yang, R. Cao, P. Oh, H.S. Shin, J. Cho, Freeze-dried WS_2 composites with low content of graphene as high-rate lithium storage materials, J. Mater. Chem. A. 1 (2013) 14548. doi:10.1039/c3ta13329j.

[4] J. Feng, X. Sun, C. Wu, L. Peng, C. Lin, S. Hu, J. Yang, Y. Xie, Metallic Few-Layered VS_2 Ultrathin Nanosheets: High Two-Dimensional Conductivity for In-Plane Supercapacitors, J. Am. Chem. Soc. 133 (2011) 17832–17838. doi:10.1021/ja207176c.

[5] M.A. Bissett, S.D. Worrall, I.A. Kinloch, R.A.W. Dryfe, Comparison of Two-Dimensional Transition Metal Dichalcogenides for Electrochemical Supercapacitors, Electrochim. Acta. 201 (2016) 30–37. doi:10.1016/j.electacta.2016.03.190.

[6] L. Mei, T. Yang, C. Xu, M. Zhang, L. Chen, Q. Li, T. Wang, Hierarchical mushroom-like $CoNi_2S_4$ arrays as a novel electrode material for supercapacitors, Nano Energy. 3 (2014) 36–45. doi:10.1016/j.nanoen.2013.10.004.

[7] A.H. Loo, A. Bonanni, Z. Sofer, M. Pumera, Exfoliated transition metal dichalcogenides (MoS_2, $MoSe_2$, WS_2, WSe_2): An electrochemical impedance spectroscopic investigation, Electrochem. Commun. 50 (2015) 39–42. doi:10.1016/j.elecom.2014.10.018.

[8] J.M. Soon, K.P. Loh, Electrochemical Double-Layer Capacitance of MoS_2 Nanowall Films, Electrochem. Solid-State Lett. 10 (2007) A250. doi:10.1149/1.2778851.

[9] J.B. Cook, H.-S. Kim, T.C. Lin, C.-H. Lai, B. Dunn, S.H. Tolbert, Pseudocapacitive Charge Storage in Thick Composite MoS_2 Nanocrystal-Based Electrodes, Adv. Energy Mater. 7 (2017) 1601283. doi:10.1002/aenm.201601283.

[10] H.D. Yoo, Y. Li, Y. Liang, Y. Lan, F. Wang, Y. Yao, Intercalation Pseudocapacitance of Exfoliated Molybdenum Disulfide for Ultrafast Energy Storage, ChemNanoMat. 2 (2016) 688–691. doi:10.1002/cnma.201600117.

[11] K. Krishnamoorthy, P. Pazhamalai, G.K. Veerasubramani, S.J. Kim, Mechanically delaminated few layered MoS_2 nanosheets based high performance wire type solid-state symmetric supercapacitors, J. Power Sources. 321 (2016) 112–119. doi:10.1016/j.jpowsour.2016.04.116.

[12] C.-P. Yang, S. Xin, Y.-X. Yin, H. Ye, J. Zhang, Y.-G. Guo, An Advanced Selenium-Carbon Cathode for Rechargeable Lithium-Selenium Batteries, Angew. Chemie Int. Ed. 52 (2013) 8363–8367. doi:10.1002/anie.201303147.

[13] G. Nagaraju, S.M. Cha, S.C. Sekhar, J.S. Yu, Metallic Layered Polyester Fabric Enabled Nickel Selenide Nanostructures as Highly Conductive and Binderless Electrode with Superior Energy Storage Performance, Adv. Energy Mater. 7 (2017) 1601362. doi:10.1002/aenm.201601362.

[14] H. Peng, G. Ma, K. Sun, Z. Zhang, J. Li, X. Zhou, Z. Lei, A novel aqueous asymmetric supercapacitor based on petal-like cobalt selenide nanosheets and nitrogen-doped porous carbon networks electrodes, J. Power Sources. 297 (2015) 351–358. doi:10.1016/j.jpowsour.2015.08.025.

[15] K.-J. Huang, J.-Z. Zhang, J.-L. Cai, Preparation of porous layered molybdenum selenide-graphene composites on Ni foam for high-performance supercapacitor and electrochemical sensing, Electrochim. Acta. 180 (2015) 770–777. doi:10.1016/j.electacta.2015.09.016.

[16] S.R. Marri, S. Ratha, C.S. Rout, J.N. Behera, 3D cuboidal vanadium diselenide embedded reduced graphene oxide hybrid structures with enhanced supercapacitor properties, Chem. Commun. 53 (2017) 228–231. doi:10.1039/C6CC08035A.

[17] S. Tongay, J. Zhou, C. Ataca, K. Lo, T.S. Matthews, J. Li, J.C. Grossman, J. Wu, Thermally Driven Crossover from Indirect toward Direct Bandgap in 2D Semiconductors: $MoSe_2$ versus MoS_2, Nano Lett. 12 (2012) 5576–5580. doi:10.1021/nl302584w.

[18] Y. Liu, M. Zhu, D. Chen, Sheet-like $MoSe_2$/C composites with enhanced Li-ion storage properties, J. Mater. Chem. A. 3 (2015) 11857–11862. doi:10.1039/C5TA02100F.

[19] Z. Zhang, Y. Fu, X. Yang, Y. Qu, Z. Zhang, Hierarchical $MoSe_2$ Nanosheets/Reduced Graphene Oxide Composites as Anodes for Lithium-Ion and Sodium-Ion Batteries with Enhanced Electrochemical Performance, ChemNanoMat. 1 (2015) 409–414. doi:10.1002/cnma.201500097.

[20] C.C. Mayorga-Martinez, A. Ambrosi, A.Y.S. Eng, Z. Sofer, M. Pumera, Transition metal dichalcogenides (MoS_2, $MoSe_2$, WS_2 and WSe_2) exfoliation technique has strong influence upon their capacitance, Electrochem. Commun. 56 (2015) 24–28. doi:10.1016/j.elecom.2015.03.017.

[21] K.-J. Huang, J.-Z. Zhang, Y. Fan, Preparation of layered $MoSe_2$ nanosheets on Ni-foam substrate with enhanced supercapacitor performance, Mater. Lett. 152 (2015) 244–247. doi:10.1016/j.matlet.2015.03.130.

[22] X. Liu, J.-Z. Zhang, K.-J. Huang, P. Hao, Net-like molybdenum selenide–acetylene black supported on Ni foam for high-performance supercapacitor electrodes and hydrogen evolution reaction, Chem. Eng. J. 302 (2016) 437–445. doi:10.1016/j.cej.2016.05.074.

[23] Y.-P. Gao, K.-J. Huang, H.-L. Shuai, L. Liu, Synthesis of sphere-feature molybdenum selenide with enhanced electrochemical performance for supercapacitor, Mater. Lett. 209 (2017) 319–322. doi:10.1016/j.matlet.2017.08.044.

[24] V.K. Mariappan, K. Krishnamoorthy, P. Pazhamalai, S. Sahoo, S.-J. Kim, Electrodeposited molybdenum selenide sheets on nickel foam as a binder-free electrode for supercapacitor application, Electrochim. Acta. 265 (2018) 514–522. doi:10.1016/j.electacta.2018.01.075.

[25] K. Krishnamoorthy, P. Pazhamalai, S.J. Kim, Ruthenium sulfide nanoparticles as a new pseudocapacitive material for supercapacitor, Electrochim. Acta. 227 (2017) 85–94. doi:10.1016/j.electacta.2016.12.171.

[26] S.K. Balasingam, J.S. Lee, Y. Jun, Few-layered $MoSe_2$ nanosheets as an advanced electrode material for supercapacitors, Dalt. Trans. 44 (2015) 15491–15498. doi:10.1039/C5DT01985K.

[27] Y. Qiu, X. Li, M. Bai, H. Wang, D. Xue, W. Wang, J. Cheng, Flexible full-solid-state supercapacitors based on self-assembly of mesoporous $MoSe_2$ nanomaterials, Inorg. Chem. Front. 4 (2017) 675–682. doi:10.1039/c6qi00569a.

[28] C. Zhong, Y. Deng, W. Hu, J. Qiao, L. Zhang, J. Zhang, A review of electrolyte materials and compositions for electrochemical supercapacitors., Chem. Soc. Rev. 44 (2015) 7484–7539. doi:10.1039/c5cs00303b.

[29] A.M. Navarro-Suárez, K.L. Van Aken, T. Mathis, T. Makaryan, J. Yan, J. Carretero-González, T. Rojo, Y. Gogotsi, Development of asymmetric supercapacitors with titanium carbide-reduced graphene oxide couples as electrodes, Electrochim. Acta. 259 (2018) 752–761. doi:10.1016/j.electacta.2017.10.125.

[30] X. Li, C. Liu, T. Wang, W. Wang, X. Wang, Q. Jiang, F. Jiang, J. Xu, Preparation of 2D $MoSe_2$/PEDOT:PSS composite and its thermoelectric properties, Mater. Res.

Express. 4 (2017) 116410. doi:10.1088/2053-1591/aa99f9.

[31] Z. Luo, J. Zhou, L. Wang, G. Fang, A. Pan, S. Liang, Two-dimensional hybrid nanosheets of few layered $MoSe_2$ on reduced graphene oxide as anodes for long-cycle-life lithium-ion batteries, J. Mater. Chem. A. 4 (2016) 15302–15308. doi:10.1039/C6TA04390A.

[32] C. Fan, Z. Wei, S. Yang, J. Li, Synthesis of $MoSe_2$ flower-like nanostructures and their photo-responsive properties, RSC Adv. 4 (2014) 775–778. doi:10.1039/C3RA42564A.

[33] R. Harpeness, A. Gedanken, A.M. Weiss, M.A. Slifkin, Microwave-assisted synthesis of nanosized $MoSe_2$, J. Mater. Chem. 13 (2003) 2603. doi:10.1039/b303740a.

[34] A.L. Friedman, A.T. Hanbicki, F.K. Perkins, G.G. Jernigan, J.C. Culbertson, P.M. Campbell, Evidence for Chemical Vapor Induced 2H to 1T Phase Transition in MoX_2 (X=Se,S) Transition Metal Dichalcogenide Films, Sci. Rep. 7 (2017) 3836. doi:10.1038/s41598-017-04224-4.

[35] J. Yao, B. Liu, S. Ozden, J. Wu, S. Yang, M.-T.F. Rodrigues, K. Kalaga, P. Dong, P. Xiao, Y. Zhang, R. Vajtai, P.M. Ajayan, 3D Nanostructured Molybdenum Diselenide/Graphene Foam as Anodes for Long-Cycle Life Lithium-ion Batteries, Electrochim. Acta. 176 (2015) 103–111. doi:10.1016/j.electacta.2015.06.138.

[36] M. Jiang, J. Zhang, M. Wu, W. Jian, H. Xue, T.-W. Ng, C.-S. Lee, J. Xu, Synthesis of 1T-$MoSe_2$ ultrathin nanosheets with an expanded interlayer spacing of 1.17 nm for efficient hydrogen evolution reaction, J. Mater. Chem. A. 4 (2016) 14949–14953. doi:10.1039/C6TA07020E.

[37] K. Krishnamoorthy, G.K. Veerasubramani, P. Pazhamalai, S.J. Kim, Designing two dimensional nanoarchitectured MoS_2 sheets grown on Mo foil as a binder free electrode for supercapacitors, Electrochim. Acta. 190 (2016) 305–312. doi:10.1016/j.electacta.2015.12.148.

[38] V. Gunasekaran, M.K. Devaraju, S. Yuvaraj, V.J.Y. Surya, V. Singh, K. Karthikeyan, S.J. Kim, Electrical transport properties of two-dimensional MoS_2 nanosheets synthesized by novel method, Mater. Sci. Semicond. Process. 66 (2017) 81–86. doi:10.1016/j.mssp.2017.04.011.

[39] D. Nam, J.-U. Lee, H. Cheong, Excitation energy dependent Raman spectrum of $MoSe_2$, Sci. Rep. 5 (2015) 17113. doi:10.1038/srep17113.

[40] P. Soubelet, A.E. Bruchhausen, A. Fainstein, K. Nogajewski, C. Faugeras, Resonance effects in the Raman scattering of monolayer and few-layer $MoSe_2$, Phys. Rev. B. 93 (2016) 155407. doi:10.1103/PhysRevB.93.155407.

[41] A. Ambrosi, Z. Sofer, M. Pumera, 2H → 1T phase transition and hydrogen evolution activity of MoS_2, $MoSe_2$, WS_2 and WSe_2 strongly depends on the MX_2 composition, Chem. Commun. 51 (2015) 8450–8453. doi:10.1039/C5CC00803D.

[42] Z. Zhang, X. Yang, Y. Fu, K. Du, Ultrathin molybdenum diselenide nanosheets anchored on multi-walled carbon nanotubes as anode composites for high performance sodium-ion batteries, J. Power Sources. 296 (2015) 2–9. doi:10.1016/j.jpowsour.2015.07.008.

[43] A. Chaturvedi, P. Hu, V. Aravindan, C. Kloc, S. Madhavi, Unveiling two-dimensional TiS_2 as an insertion host for the construction of high energy Li-ion capacitors, J. Mater. Chem. A. 5 (2017) 9177–9181. doi:10.1039/C7TA01594A.

[44] M.S. Javed, S. Dai, M. Wang, D. Guo, L. Chen, X. Wang, C. Hu, Y. Xi, High performance solid state flexible supercapacitor based on molybdenum sulfide hierarchical nanospheres, J. Power Sources. 285 (2015) 63–69. doi:10.1016/j.jpowsour.2015.03.079.

[45] B. Xie, C. Yang, Z. Zhang, P. Zou, Z. Lin, G. Shi, Q. Yang, F. Kang, C.-P. Wong, Shape-Tailorable Graphene-Based Ultra-High-Rate Supercapacitor for Wearable

Electronics, ACS Nano. 9 (2015) 5636–5645. doi:10.1021/acsnano.5b00899.

[46] T. Chen, L. Dai, Flexible supercapacitors based on carbon nanomaterials, J. Mater. Chem. A. 2 (2014) 10756. doi:10.1039/c4ta00567h.

[47] R.B. Rakhi, B. Ahmed, M.N. Hedhili, D.H. Anjum, H.N. Alshareef, Effect of Postetch Annealing Gas Composition on the Structural and Electrochemical Properties of Ti_2CT_x MXene Electrodes for Supercapacitor Applications, Chem. Mater. 27 (2015) 5314–5323. doi:10.1021/acs.chemmater.5b01623.

[48] S. Sahoo, P. Pazhamalai, K. Krishnamoorthy, S.-J. Kim, Hydrothermally prepared α-MnSe nanoparticles as a new pseudocapacitive electrode material for supercapacitor, Electrochim. Acta. 268 (2018) 403–410. doi:10.1016/j.electacta.2018.02.116.

[49] M.A. Bissett, I.A. Kinloch, R.A.W. Dryfe, Characterization of MoS_2-Graphene Composites for High-Performance Coin Cell Supercapacitors, ACS Appl. Mater. Interfaces. 7 (2015) 17388–17398. doi:10.1021/acsami.5b04672.

[50] A. Eftekhari, Supercapacitors utilising ionic liquids, Energy Storage Mater. 9 (2017) 47–69. doi:10.1016/j.ensm.2017.06.009.

[51] S. Ratha, C.S. Rout, Supercapacitor Electrodes Based on Layered Tungsten Disulfide-Reduced Graphene Oxide Hybrids Synthesized by a Facile Hydrothermal Method, ACS Appl. Mater. Interfaces. 5 (2013) 11427–11433. doi:10.1021/am403663f.

[52] B.D. Boruah, A. Misra, Polyethylenimine mediated reduced graphene oxide based flexible paper for supercapacitor, Energy Storage Mater. 5 (2016) 103–110. doi:10.1016/j.ensm.2016.05.007.

[53] B. Zhao, D. Chen, X. Xiong, B. Song, R. Hu, Q. Zhang, B.H. Rainwater, G.H. Waller, D. Zhen, Y. Ding, Y. Chen, C. Qu, D. Dang, C.P. Wong, M. Liu, A high-energy, long cycle-life hybrid supercapacitor based on graphene composite electrodes, Energy Storage Mater. 7 (2017) 32–39. doi:10.1016/j.ensm.2016.11.010.

[54] K.V. Sankar, R. Kalai Selvan, Improved electrochemical performances of reduced graphene oxide based supercapacitor using redox additive electrolyte, Carbon N. Y. 90 (2015) 260–273. doi:10.1016/j.carbon.2015.04.023.

[55] W. Lu, K. Henry, C. Turchi, J. Pellegrino, Incorporating Ionic Liquid Electrolytes into Polymer Gels for Solid-State Ultracapacitors, J. Electrochem. Soc. 155 (2008) A361. doi:10.1149/1.2869202.

[56] K. Krishnamoorthy, P. Pazhamalai, S.-J. Kim, Two-dimensional siloxene nanosheets: novel high-performance supercapacitor electrode materials, Energy Environ. Sci. 11 (2018) 1595–1602. doi:10.1039/C8EE00160J.

[57] Z. Lei, Z. Liu, H. Wang, X. Sun, L. Lu, X.S. Zhao, A high-energy-density supercapacitor with graphene-CMK-5 as the electrode and ionic liquid as the electrolyte, J. Mater. Chem. A. 1 (2013) 2313–2321. doi:10.1039/c2ta01040b.

[58] P. Sharma, T.S. Bhatti, A review on electrochemical double-layer capacitors, Energy Convers. Manag. 51 (2010) 2901–2912. doi:10.1016/j.enconman.2010.06.031.

[59] C.N.R. Rao, K. Gopalakrishnan, U. Maitra, Comparative Study of Potential Applications of Graphene, MoS_2, and Other Two-Dimensional Materials in Energy Devices, Sensors, and Related Areas, ACS Appl. Mater. Interfaces. 7 (2015) 7809–7832. doi:10.1021/am509096x.

[60] S.S. Karade, P. Dwivedi, S. Majumder, B. Pandit, B.R. Sankapal, First report on a FeS-based 2 V operating flexible solid-state symmetric supercapacitor device, Sustain. Energy Fuels. 1 (2017) 1366–1375. doi:10.1039/C7SE00165G.

[61] W. Xing, S.Z. Qiao, R.G. Ding, F. Li, G.Q. Lu, Z.F. Yan, H.M. Cheng, Superior electric double layer capacitors using ordered mesoporous carbons, Carbon N. Y. 44 (2006) 216–224. doi:10.1016/j.carbon.2005.07.029.

[62] M. Kaempgen, C.K. Chan, J. Ma, Y. Cui, G. Gruner, Printable Thin Film

Supercapacitors Using Single-Walled Carbon Nanotubes, Nano Lett. 9 (2009) 1872–1876. doi:10.1021/nl8038579.

[63] C. Yu, C. Masarapu, J. Rong, B. Wei, H. Jiang, Stretchable Supercapacitors Based on Buckled Single-Walled Carbon-Nanotube Macrofilms, Adv. Mater. 21 (2009) 4793–4797. doi:10.1002/adma.200901775.

[64] V. Sahu, S. Shekhar, R.K. Sharma, G. Singh, Ultrahigh performance supercapacitor from lacey reduced graphene oxide nanoribbons, ACS Appl. Mater. Interfaces. 7 (2015) 3110–3116. doi:10.1021/am5071706.

[65] R.B. Rakhi, B. Ahmed, D. Anjum, H.N. Alshareef, Direct Chemical Synthesis of MnO_2 Nanowhiskers on Transition-Metal Carbide Surfaces for Supercapacitor Applications, ACS Appl. Mater. Interfaces. 8 (2016) 18806–18814. doi:10.1021/acsami.6b04481.

[66] R.B. Rakhi, W. Chen, D. Cha, H.N. Alshareef, Substrate dependent self-organization of mesoporous cobalt oxide nanowires with remarkable pseudocapacitance, Nano Lett. 12 (2012) 2559–2567. doi:10.1021/nl300779a.

[67] P. Hao, J. Tian, Y. Sang, C.C. Tuan, G. Cui, X. Shi, C.P. Wong, B. Tang, H. Liu, 1D Ni-Co oxide and sulfide nanoarray/carbon aerogel hybrid nanostructures for asymmetric supercapacitors with high energy density and excellent cycling stability, Nanoscale. 8 (2016) 16292–16301. doi:10.1039/c6nr05385h.

CHAPTER 5.3: HIGH PERFORMANCE ELECTROCHEMICAL ENERGY STORAGE DEVICE USING HYDROTHERMALLY PREPARED RHENIUM DISULFIDE NANOSTRUCTURES

Highlights

- Rhenium sulfide (ReS_2) nanostructures has been prepared via hydrothermal method.
- ReS_2 electrode delivers a specific capacitance of 189.28 F g^{-1} at 0.5 mA cm^{-2}.
- ReS_2 symmetric supercapacitor(SSC) operates over a potential window of 0.8 V.
- ReS_2 SSC delivers a cell capacitance of 35.75 F g^{-1} with energy density of 3.17 Wh kg^{-1}.
- ReS_2 SSC device possess a capacitance retention of about 98.3 % over 5000 cycles.

5.3.1. Introduction

Two-dimensional materials become a prior choice in all aspects of science and technology in this decade, after the discovery of graphene in 2004[1,2]. Transition metal dichalcogenides (TMDs) are a series of two-dimensional materials comprising layered metal sulfides, selenides and tellurides[3,4]. Unlike graphene with a semi-metallic nature, these layered TMDs possess a defined band gap which makes them as a viable candidate for applications in various fields such as optoelectronics, field-effect transistors, photocatalysis, and so on [5–9]. Further, the redox chemistry of the transition metal present in TMDs with higher electronic conductivity compared to their oxide counterparts makes them a suitable candidate for electrochemical applications such as electrocatalysis, photo-electrochemistry, electrochemical energy storage devices such as supercapacitors and batteries[10–12]. The research on TMDs as an advanced electrode for supercapacitors received much attention due to the decrease in fossil fuels and the current global energy crisis. A wide range of 2D TMDs (including MoS_2, $MoSe_2$, WS_2, RuS_2, TiS_2, SnS) with different morphologies was examined for their applications as an electrode material for supercapacitors [13–15]. The tunable electrochemical properties of 2D TMDs via thinning of layers from bulk to few-layers, decrease in lateral size, and increase in surface area makes them interesting materials towards energy-storage applications[16,17]. Another important aspect of 2D TMDs relies on their suitability for lightweight and flexible energy storage devices with high areal, and volumetric energy densities[18,19]. Considerable efforts have been carried out to understand the fundamental electrochemistry of TMDs with different exfoliation strategies, engineered surface area, different morphologies via tailored chemical synthetic routes, and various device configurations using hybrid electrode, binder-free electrodes, and different electrolytes (aqueous and ionic liquids) during this decade[20,21].

In this scenario, rhenium disulfide (ReS_2) gained recent attention mainly of its unusual properties (structural, electronic, electro-optical and chemical) which is exceptional among the other TMDs investigated in the recent years[22,23]. The structure of ReS_2 comprises three layers in S-Re-S configuration in which Re and S atoms are covalently bonded with adjacent layers separated via weak van der Waals forces similar to that of other TMDs [24,25]. The anisotropic properties of ReS_2 are shown to be layer independent whereas the properties of other TMDs are known to be highly dependent on the number of layers [26,27]. The merits of ReS_2 over other TMDs is their unique-physico-chemical properties independent of their nature of phases such as 3D bulk counterpart, and 2D structure[26]. Due to these distinguishable and intriguing properties, ReS_2 becomes an emerging material of interest for a variety of applications mainly focused on the energy conversion, and storage sectors[28,29]. Until now, ReS_2 can be prepared via either top-down approaches or bottom-up approaches based on the nature of starting materials. The top-down method such as mechanical exfoliation (similar to graphene or MoS_2), chemical and liquid-phase exfoliation are used for the preparation of mono or few-layered ReS_2 sheets[30,31]. Other preparation methods include the chemical vapour deposition, vapour-transport method, Bridgman method, and wet chemical reactions[32–34]. Among these, chemical methods used for the preparation of ReS_2 is more promising due to the high yield compared to exfoliation techniques which can be useful for various fields. There are few studies available in the literature demonstrating the semiconducting properties of ReS_2 focusing towards application in optoelectronics using the micro-mechanically exfoliated sheets[35,36]. Hitherto, the energy storage properties of ReS_2 is less studied even though its structure and electronic conductivity favour the possibility for electrochemical energy storage applications. Few studies reported the use of ReS_2 sheets hybridized with carbon-based materials as electrode materials for batteries[37–39]. However, the applications of ReS_2 as an electrode material for

supercapacitor is not yet studied. Upto date, there are several chemical methods available reported for the preparation of TMCs such as precipitation, sol-gel, sonochemistry, hydrothermal and microwave irradiation methods. In general, wet-chemical preparation of TMCs with well crystalline and phase purity are quite complicated due to the heterogeneous nature of sulfides and selenides[40]. In this scenario, the hydrothermal method possesses the merits of achieving crystalline TMCs at low-temperature over the other chemical methods which require an additional heat treatment[41]. In particular, the use of the hydrothermal method for ReS_2 can be explained on the basis of recrystallization of metastable precursors (RMP) which is one of the four kinds of basic routes/modes where hydrothermal technology relies on[42]. Therefore, in this contribution, we used hydrothermal method for the preparation of ReS_2 nanostructures and demonstrated their use as novel electrode materials for supercapacitor devices. The electrochemical properties were examined using a three-electrode configuration for understanding the mechanism of charge-storage occurred at the ReS_2 electrode as well as a two-electrode symmetric device configuration (using aqueous and organic electrolytes) to ensure the device properties of ReS_2 for energy storage applications.

5.3.2. Experimental section

5.3.2.1 Preparation of rhenium disulfide (ReS_2) nanostructures

A facile hydrothermal method was employed for the preparation of ReS_2 nanostructures according to the methods available in literature[38,39]. At first, ammonium perrhenate (0.161 g), hydroxylamine hydrochloride (0.125 g), and thiourea (0.205 g) were dissolved in 50 mL of DI water and stirred for 30 min. Then, the mixture solution was transferred to an 80 mL stainless steel autoclave for hydrothermal reaction at a temperature of 240 ℃ and kept for 24 h. After completion of the reaction, the reactor was allowed to cool down to room temperature naturally. Then, the black colored precipitates containing ReS_2

was repeatedly washed with DI water and ethanol using centrifugation process and dried at 80 ℃ for 12 h.

5.3.2.2 Electrochemical studies

The ReS_2 electrode for the electrochemical studies were according to the slurry coating procedure reported in our previous work[43]. Briefly, the active material (ReS_2), carbon black and polyvinylidene difluoride (PVDF) were mixed the ratio of 85:10:5 using N-methyl pyrrolidone (NMP) as solvent and ground well to form the slurry. Then, the prepared slurry was coated on to the pre-cleaned SS substrate (1×1 cm^2) and allowed to dry at 80 ºC overnight. The electroactive mass of the ReS_2 electrode on to the stainless-steel substrate is calculated from the difference between the mass of the substrate before and after coating of the ReS_2 electrode using Dual-range Semi-micro Balance (AUW-220D, SHIMADZU) with an approximation of five-decimal points is approximate ~ 0.7 mg in each substrate. The electrochemical characterization of the ReS_2 electrode was examined using a three-electrode system. Here, the ReS_2 electrode was used as the working electrode, silver/silver chloride as the reference electrode, and platinum as the counter electrode. The ReS_2 symmetric capacitors (two-electrode) were fabricated in the form of a sandwich-type electrode, with an electrolyte-immersed Celgard as the separator. The electrochemical properties were examined via cyclic voltammetry (CV), electrochemical impedance spectroscopy (EIS) and galvanostatic charge-discharge (CD) measurements using an Autolab PGSTAT302N electrochemical workstation. An aqueous solution containing 1 M Li_2SO_4 and 1M $TEABF_4$ was used as an electrolyte.

5.3.3. Results and discussion

5.3.3.1 Physicochemical characterization

In this study, the ReS_2 nanostructure was prepared via a one-pot hydrothermal reaction using ammonium perrhenate and thiourea as rhenium and sulfur sources. The

mechanism of hydrothermal growth of ReS_2 can be explained as follows: During the hydrothermal process, the ReO_4 ions and sulfur ions released from the ammonium perrhenate and thiourea react together leading to the formation of metastable intermediates comprising Re and S initially which later recrystallized into crystalline ReS_2 with an increase in reaction time at desired temperature[42].

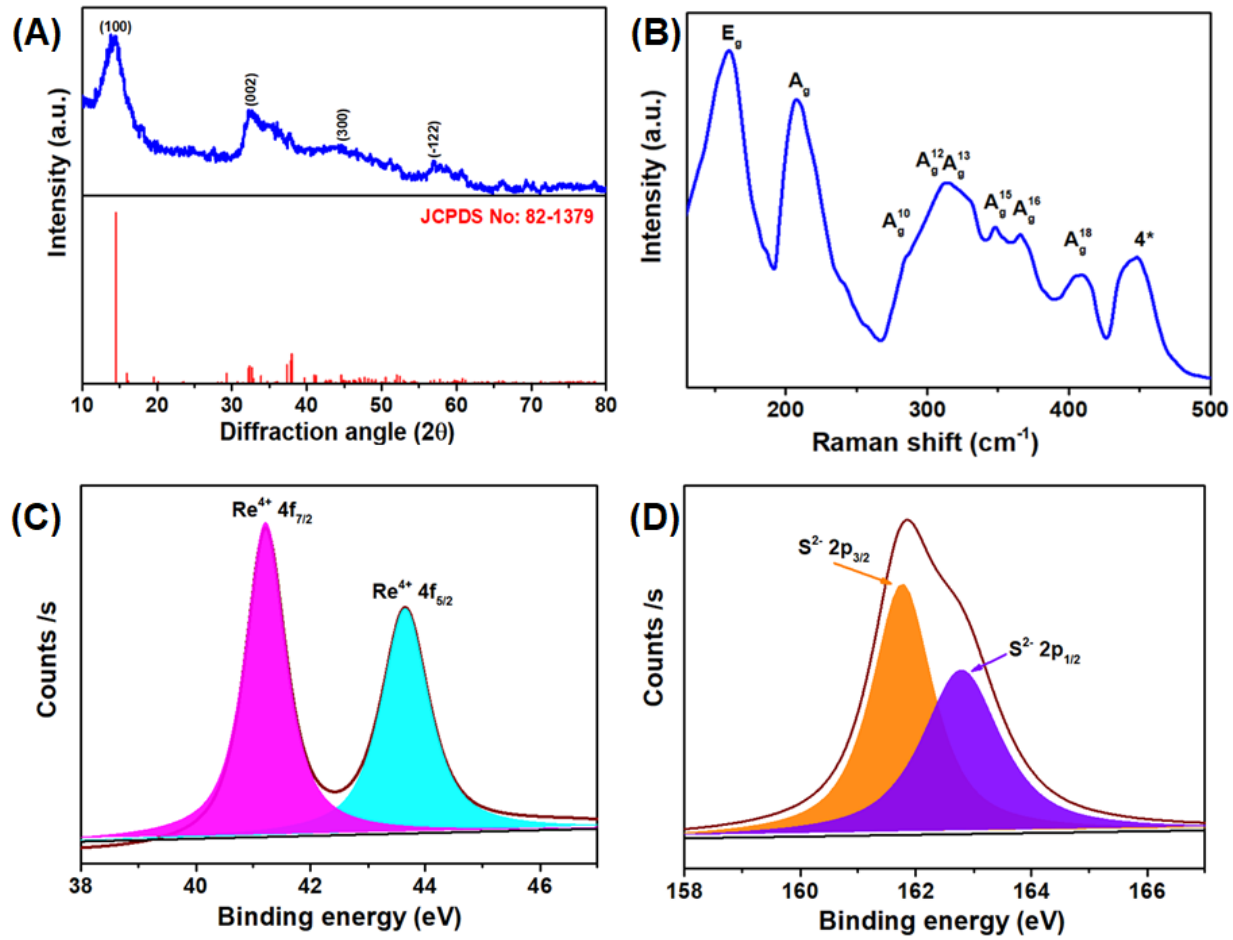

Figure 5.3.1. (A) X-ray diffraction spectrum with the standard diffraction pattern of ReS_2; (B) laser Raman spectrum of the hydrothermally prepared ReS_2 nanostructures. X-ray photoelectron spectroscopy (C) core-level spectrum of Re 4f state and (D) core-level spectrum of S 2p state present in the ReS_2 nanostructures.

Figure 5.3.1(A) shows the X-ray diffraction pattern of the hydrothermally prepared ReS_2 nanostructures. The diffraction peaks observed at 14.45°, 32.56°, 44.64°, and 57.57°, arises from the ((100), (002), (300), and (-122) planes of ReS_2[38,39]. The observed

diffraction pattern is in close agreement with the standard diffraction pattern of ReS_2 (JCPDS No: 82-1379). Raman spectroscopy is used to identify the crystalline and bonding nature of the ReS_2 as shown in Figure 5.3.1(B). It revealed the presence of two characteristic Raman bands at 159.9 cm^{-1} and 207.4 cm^{-1} with some additional bands. The Raman band observed at 159.9 cm^{-1} is associated with the in-plane (E_g) vibrational modes of ReS_2 whereas the band observed at 207.4 cm^{-1} corresponds to the out-of-plane (A_g) vibrational modes of ReS_2. The additional bands observed in the region of 250 to 500 cm^{-1} corresponds to the second order vibration in the ReS_2 nanostructures which are mainly due to the vibration of S atom in ReS_2 and the band (*) at 448 cm^{-1} is due to the symmetric stretching of the central S–S bonds in the ReS_2. The observed Raman spectra are in close agreement with recent studies of ReS_2[38,44].

X-ray photoelectron spectroscopy is used for understanding the chemical and surface states of elements present in the hydrothermally prepared ReS_2[45]. The XPS survey spectrum of ReS_2 indicated the presence of Re and S components at binding energies of about 42 and 162 eV, respectively. Figure 5.3.1(C) presents the core-level spectrum of Re 4f states of ReS_2 which indicated the presence of two characteristic peaks at 41.2 and 43.63 eV, respectively. These peaks are related to the core $4f_{7/2}$ and $4f_{5/2}$ level peaks of the Re^{4+} present in the ReS_2 nanostructures[31]. Figure 5.3.1(D) shows the core-level spectrum of S 2p states of ReS_2 which can be deconvoluted into two peaks. The peaks observed at 161.85 and 163.1 eV for the bonding configurations of S, related to the core $2p_{3/2}$ and $2p_{1/2}$ orbital peaks of S^{2-}, respectively[31]. In addition, the Re and S atomic ratio obtained from XPS analysis is equal to 1:2, thus, indicating the prepared ReS_2 is of good stoichiometric value[38]. The surface morphology of the ReS_2 nanostructures is examined using field emission scanning electron micrograph (FE-SEM) and high-resolution transmission electron micrographs (HR-TEM)

respectively. Figure 5.3.2(A) shows the FE-SEM micrograph of the as-prepared ReS_2 which indicated the presence of agglomerated ReS_2 powders.

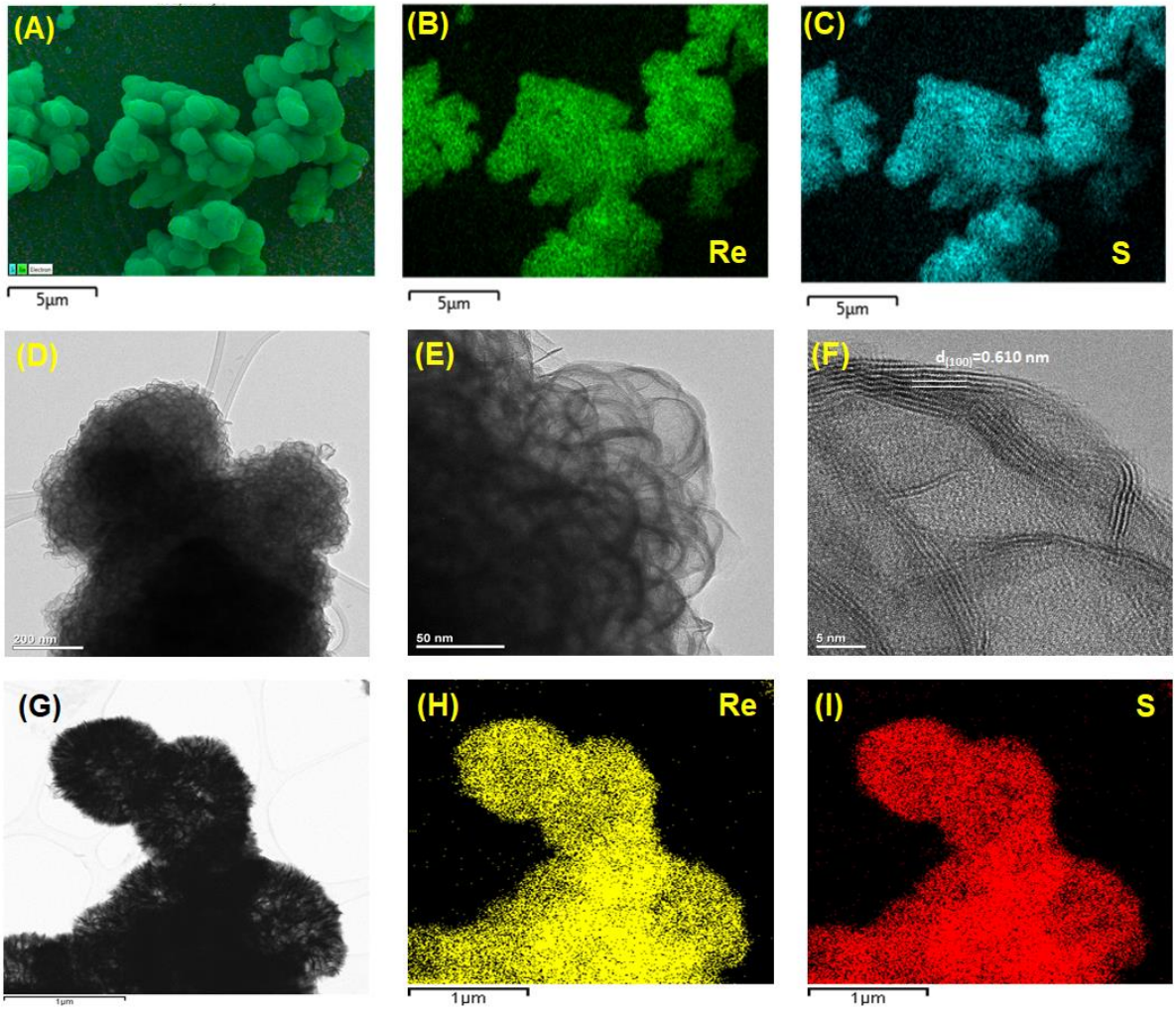

Figure 5.3.2. Surface morphology and elemental analysis of ReS_2 nanostructures (A) overlay field-emission scanning electron micrograph, (B) elemental mapping showing the distribution of Re element, (C) elemental mapping showing the distribution of S element present in the ReS_2 nanostructures respectively. High resolution transmission electron micrograph under various magnification (D) 200 nm; (E) 50 nm; (F) 5 nm. (G) overlay of high-resolution transmission electron micrograph of ReS_2, (H) elemental mapping showing the distribution of Re element, and (I) elemental mapping showing the distribution of S element present in the ReS_2 nanostructures respectively.

Figure 5.3.2(B and C) shows the elemental mapping of Re and S which further confirms the formation of ReS_2.. Figure 5.3.2(D-F) represents the HR-TEM micrographs of the prepared ReS_2 nanostructures obtained under different magnifications. The low magnification micrographs (Fig. 5.3.2(D,E)) revealed the presence of self-aggregated ReS_2 sheets whereas the high-magnification micrograph (Fig. 5.3.2(F)) revealed the presence of crumpled ReS_2 sheets and self-assembly of individual sheets with the adjacent one. The HR-TEM micrograph (Fig. 5.3.2(F)) representing the lattice fringes with an interplanar spacing of d=0.610 nm, corresponds to the (100) plane. Figure 5.3.2 (G-I) shows the HR-TEM elemental mapping of ReS_2 nanostructures which also confirms the uniform distribution of Re and S in the ReS_2.

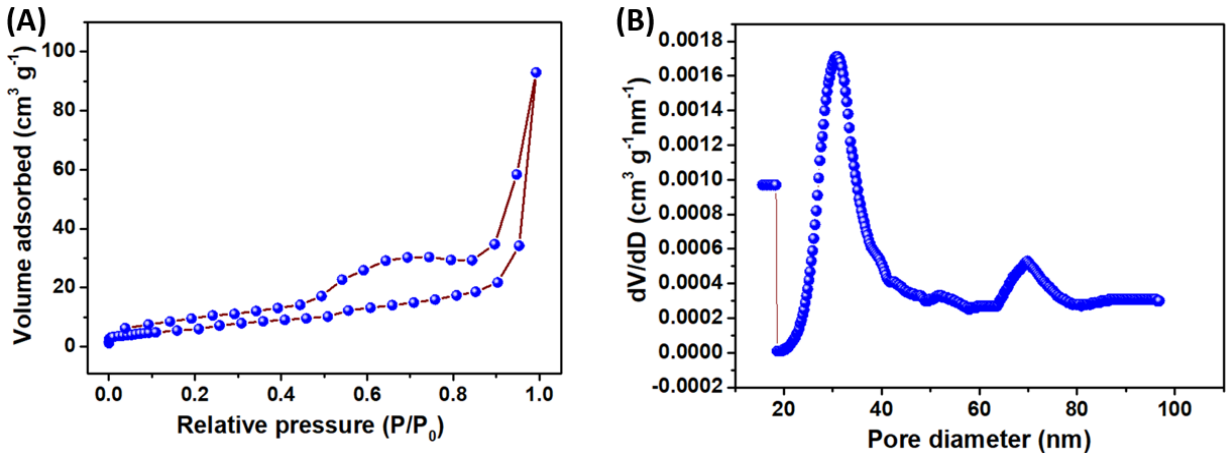

Figure 5.3.3. Surface area analysis of ReS_2 nanostructures (A) N_2 adsorption/desorption isotherm (B) Pore volume distribution.

The specific surface area of the electrode materials plays a crucial role in their electrochemical properties[46,47]. The N_2 adsorption-desorption analysis was performed in order to study the pore structure and the specific surface area of the ReS_2 nanostructures. The adsorption-desorption isotherm and pore size distribution curves are shown in the Fig. 5.3.3 (. From the isotherm curve shown in Fig. 5.3.3 (A) can be classified as type IV (as per IUPAC nomenclature) revealing the presence of a mesoporous structure of ReS_2[46]. The specific

surface area of the ReS_2 is calculated as 26.582 m^2 g^{-1} which are closer to the reported values of hydrothermally $MoSe_2$ sheets (33.6 m^2 g^{-1}) [48]. Figure 5.3.3 (B) shows the pore size distribution calculated by HK method indicated that the ReS_2 exhibits a wide range of pore size distributions from 20 to 80 nm, with the maximum pore size distributed at 30 nm, further confirming the existence of mesopores in the ReS_2[46]. From the results obtained, it is evident that the ReS_2 exhibits high surface area with a wide range of pore size which facilitates more electroactive sites for the electrochemical reactions. These physico-chemical characterizations confirmed the formation of ReS_2 nanostructures and further studies are carried out to understand the usefulness of the prepared ReS_2 nanostructures towards application in energy storage devices.

5.3.3.2 Electrochemical characterization

At first, the electrochemical properties of the ReS_2 electrode were evaluated by three-electrode configuration. Figure 5.3.4 (A) shows the CV profiles of the ReS_2 electrode recorded over a potential of -0.8 to 0.0 V obtained using different scan rates from 5 to 100 mV s^{-1}. The CV profiles show the presence of typical rectangular shaped curves as an indication of good capacitive behaviour. Further, there are no obvious redox peaks has been observed in the CV profiles indicating the absence of charge-storage via any Faradaic process or battery-type mechanism[49]. Thus, the mechanism of charge-storage occurred at the ReS_2 electrode is due to the non-faradaic process attributed to the lithium ion-adsorption/desorption pseudocapacitance at the electrode surface. The possible electrochemical reaction involved in the charge storage of ReS_2 is as follows[8]:

$$(ReS_2)\ \text{surface} + Li^+ + e^- \leftrightarrow (ReS_2 - Li^+)\ \text{surface} \quad \ldots\ldots\ldots\ldots\ldots\ldots\ (1)$$

There is no distortion observed in the shape of the CV curves even at higher scan rates, thus suggesting the good rate capability of the ReS_2 electrode. Figure 5.3.4(B) represents

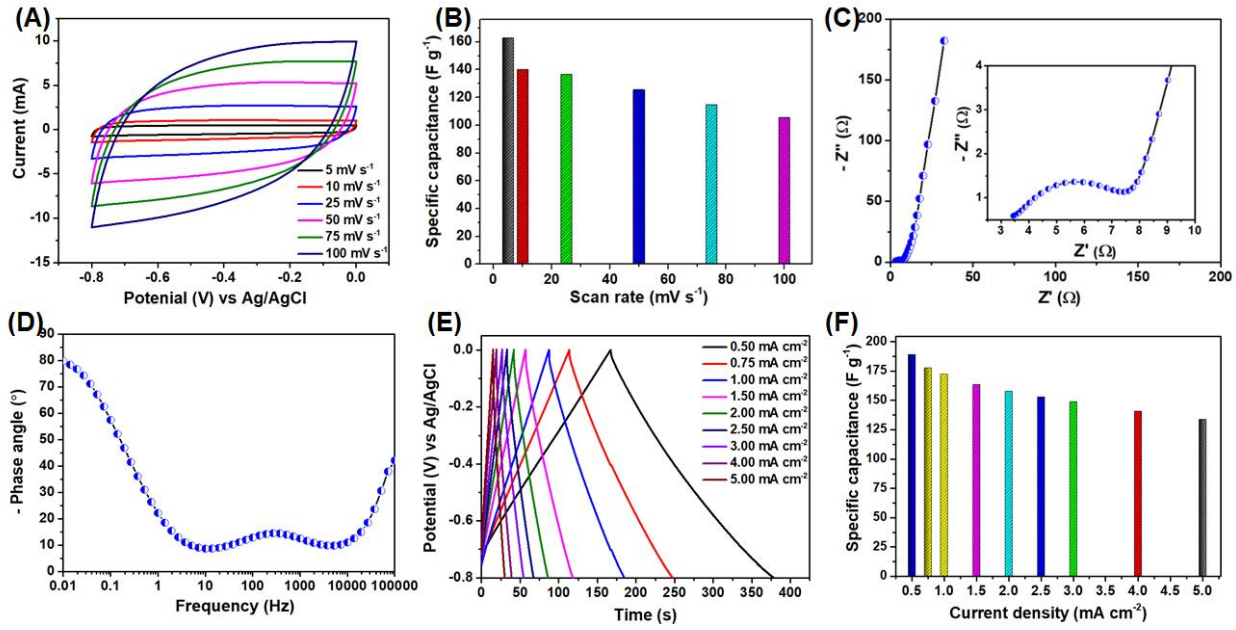

Figure 5.3.4. Electrochemical characterization of the ReS_2 electrode using three-electrode configuration. (A) Cyclic voltammetry profiles of ReS_2 electrode recorded using various scan rate (5 – 100 mV s^{-1}). (B) Effect of scan rate on the specific capacitance of ReS_2 electrode. Electrochemical impedance spectroscopic analysis of ReS_2 electrode represents (C) Nyquist plot (an enlarged portion is provided as an inset) and (D) Bode phase angle plot. (E) CD profiles of the ReS_2 electrode recorded using different current densities (0.50 to 5.00 mA cm^{-2}). (F) Effect of current densities on the specific capacitance of the ReS_2 electrode. A 1 M Li_2SO_4 solution is used as the electrolyte.

the effect of scan rate on the specific capacitance of ReS_2 electrode obtained from the CV analysis. A specific capacitance of about 162.94 F g^{-1} was obtained from the ReS_2 electrode from the CV profiles recorded at a scan rate of 5 mV s^{-1}. The decrease in specific capacitance with an increase in scan rate is attributed to the effect of time constraints of electrolyte ions at different scan rates [47]. The Nyquist plot of ReS_2 electrode is shown in Fig. 5.3.4(C) which shows the presence of a semi-circle region at high frequency followed by a straight line at the low-frequency[50]. The inset of Fig. 5.3.4(C) shows the enlarged portion of the high-

frequency region which indicated that the ReS_2 electrode possesses a solution resistance (R_s) of about 3.2 Ω and a charge-transfer resistance (R_{ct}) of about 4.1 Ω. The straight line observed at low frequencies relates to the frequency dependent ion-diffusion kinetics occurred at the electrolyte/electrode interfacial region [51]. The Bode phase angle plot of the ReS_2 electrode is provided in Fig. 5.3.4(D) which shows the variation of phase angle with respect to the applied frequencies. The phase angle at the low frequency (0.01 Hz) is about 79.86°, indicating the ideal capacitive properties of ReS_2 electrode [43]. It shows that the specific capacitance of ReS_2 electrode decreases with an increase in frequency and a maximum capacitance of about 124.93 F g^{-1} was obtained at a low frequency of about 0.01 Hz. Figure. 5.3.4(E) shows the CD profiles of ReS_2 electrode recorded using different current densities ranging from 0.5 to 5.0 mA cm^{-2}. The nature of CD profiles remains symmetric triangular shaped even at ten-fold increase in current density, thus, highlighted the better rate capability of the ReS_2 electrode[52]. Figure 5.3.4(F) represents the effect of discharge current density on the specific capacitance of ReS_2 electrode. A specific capacitance of about 189.28 F g^{-1} was obtained for the ReS_2 electrode from the discharge profile recorded using a current density of 0.5 mA cm^{-2}. A specific capacitance of about 80.89 % and 70.75 % was retained for the ReS_2 electrode with a five- and ten-fold increase in current density. The excellent capacitance retention indicated the better rate and power capability of the ReS_2 electrode at various loads. The specific capacitance of the ReS_2 electrode (189.28 F g^{-1}) is relatively higher compared to that of the recently reported specific capacitance values of TMDs. The performance of ReS_2 as a negative electrode is also compared with the reported negative electrodes for supercapacitors. Thus, the use of ReS_2 as a negative electrode for supercapacitor using aqueous electrolyte in this study signifies its application on energy storage devices. The Columbic efficiency of the ReS_2 electrode is closer to 100 % suggested the better capacitive properties and electrochemical reversibility of the ReS_2 electrode. The

cyclic stability of ReS_2 electrode over 2000 cycles of continuous charge-discharge analysis using a current density of 5.0 mA cm^{-2}. It showed a capacitance of about 96.45 % of its initial capacitance was retained after cyclic tests, indicating the better cyclic stability of the ReS_2 electrode.

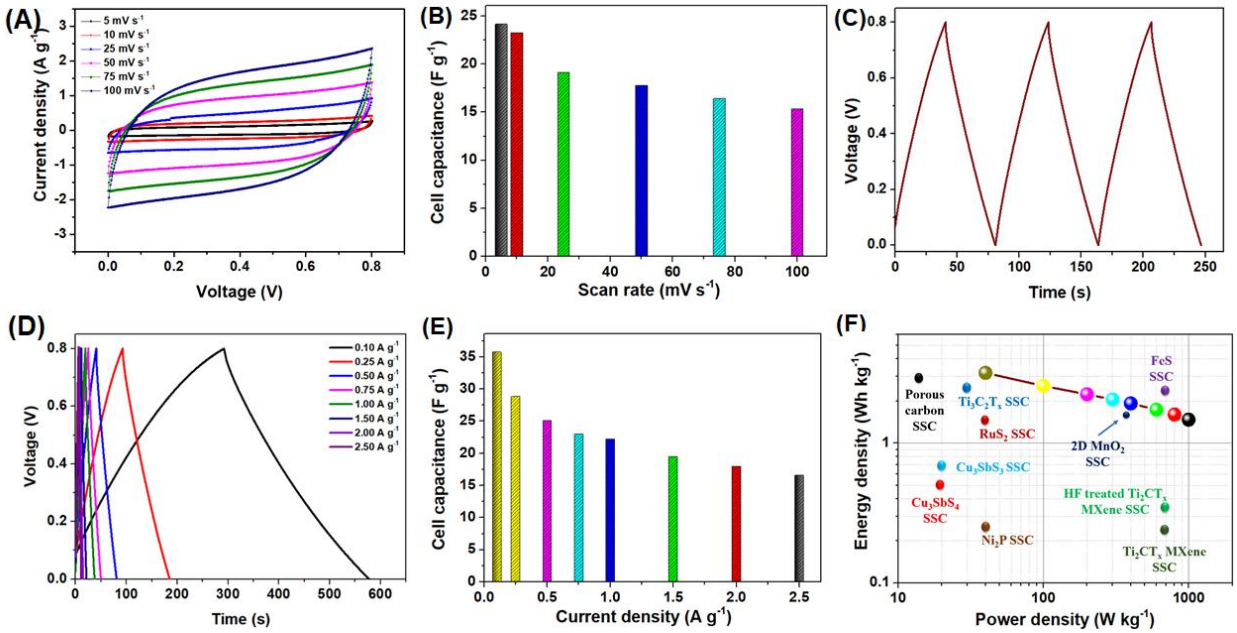

Figure 5.3.5. Electrochemical characterization of ReS_2 symmetric supercapacitor (SSC) device. (A) Cyclic voltammetry profiles of the ReS_2 SSC device recorded using different scan rate (5 – 100 mV s^{-1}), (B) Effect of scan rate on the cell capacitance of the ReS_2 SSC device, (C) continuous CD profile of the ReS_2 SSC device obtained using a constant current density of 0.50 A g^{-1}, (D) CD profiles of the ReS_2 SSC device recorded using different current densities (0.10 – 2.50 A g^{-1}). (E) Effect of current densities on the cell capacitance of the ReS_2 SSC device. (F) Ragone plot of ReS_2 SSC device showing the superior performance of ReS_2 SSC over the reported TMC based SSCs.

The electrochemical studies of the ReS_2 electrode using three-electrode configuration suggested the superior performance of ReS_2 over other TMDs. However, for practical applications, it is highly desirable to examine the electrochemical properties using a full-cell or symmetric device configuration[53]. Therefore, in this study, we fabricated symmetric

supercapacitor (SSC) device using the ReS_2 electrodes and examined their device properties as well. Figure 5.3.5(A) represents the CV profiles of the ReS_2 SSC device recorded over an operating potential window (OPW) from 0.0 to 0.8 V using different scan rates (5 to 100 mV s^{-1}). The CV profiles of ReS_2 SSC device displayed the ideal rectangular behaviour and the current range increase linearly with respect to the scan rate highlighting the better capacitive properties of the ReS_2 SSC device[54]. The rectangular nature of the CV profiles is retained even at high scan rates which indicated the high rate capability of the ReS_2 SSC device[18]. Figure 5.3.5(B) presents the effect of scan rate on the cell capacitance of ReS_2 SSC device which shows a maximum cell capacitance of 24.15 F g^{-1} was obtained at a low scan rate of 5 mV s^{-1}. With an increase in scan rate, the ReS_2 SSC device retained a cell capacitance of about 63.39 %, thus demonstrating their superior rate capability.

Typical CD profile of the ReS_2 SSC device recorded using a current density of about 0.5 A g^{-1} (as shown in Fig. 5.3.5(C)) shows the presence of symmetric triangular curves indicating the ideal capacitive nature of ReS_2 SSC device[43]. The CD profiles of ReS_2 SSC device recorded using different current densities (0.1 to 2.5 A g^{-1}) is provided in Fig. 5.3.5(D). It revealed that the charging and discharging time is low at high current densities and higher at low current densities, which can be explained on the basis of time constraints faced by electrolyte ions to access the electroactive materials at different current densities[55]. The effect of discharge current density on the cell capacitance of ReS_2 SSC device is provided in Fig. 5.3.5(E). A high cell capacitance of about 35.75 F g^{-1} is obtained for the ReS_2 SSC device using a current density of 0.1 A g^{-1}. The Columbic efficiency, energy density, power density, and cyclic stability are some of the important parameters which determine the practical application of a supercapacitor[18,56]. It showed that the Columbic efficiency of the ReS_2 SSC device is above 90 % for all the tested current densities, suggesting the better capacitive properties of ReS_2 SSC device[57]. The energy and power

density of the ReS_2 SSC device is provided in the form of Ragone plot (shown in Fig. 5.3.5(F)). The ReS_2 SSC device possesses a high energy density of about 3.17 Wh kg^{-1} with a corresponding power density of 40 W kg^{-1} obtained at a constant current density of about 0.1 A g^{-1}. With a five-fold increase in current density, the ReS_2 SSC device still holds an energy density of 1.47 Wh kg^{-1} with an increase in power density up to 1000 W kg^{-1}, respectively. The obtained cell capacitance and energy density of ReS_2 SSC device are higher compared to that of the recently reported SSCs as evidenced from the Ragone plot.

The electrochemical impedance spectroscopy of ReS_2 SSC device was analyzed using a Nyquist plot and Bode phase angle plots in order to understand the charge-transfer kinetics and capacitive nature of the fabricated device. The Nyquist plot of the ReS_2 SSC device is shown in Figure 5.3.6(A) which represents a plot of real versus the imaginary component of the impedance as a function of frequency. It revealed the presence of a quasi-semi-circle like a region followed by vertical line while sweeping from high- to low- frequencies. The observed semi-circle demonstrates the presence of a charge-transfer resistance in the ReS_2 SSC device which might be related to the resistance between the electrode and electrolyte, as well as the internal resistance of the electroactive materials, and the contact resistance between the electroactive material and the current collector[18]. The solution resistance (R_s) and charge-

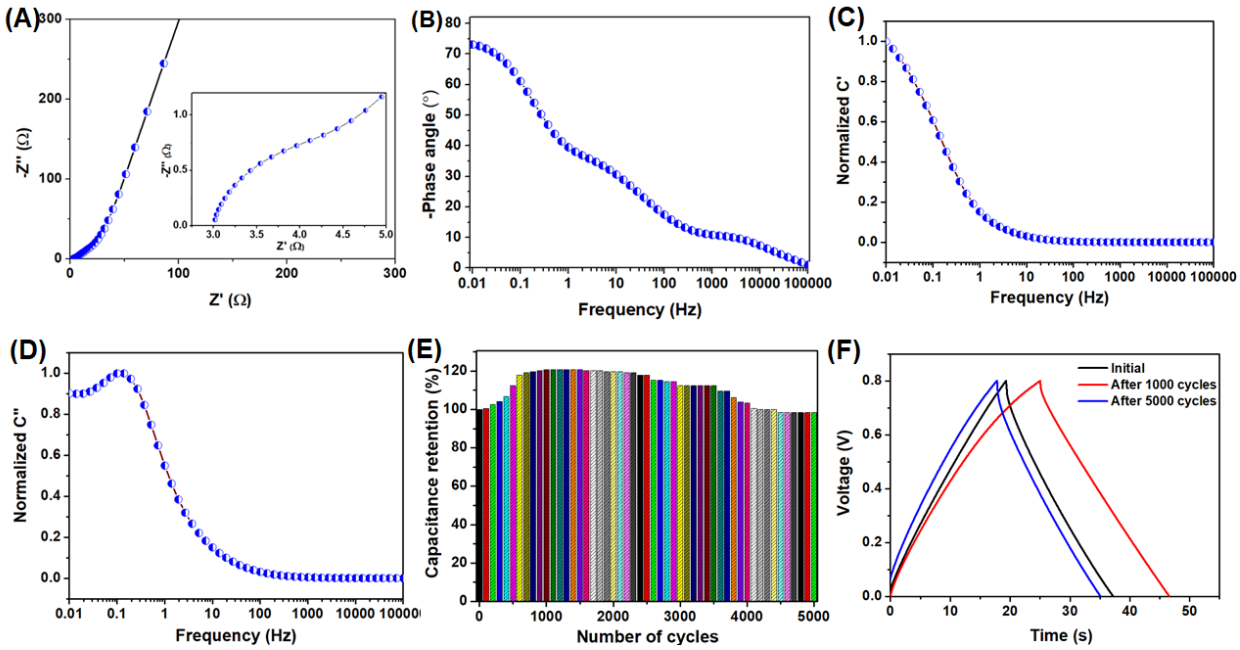

Figure 5.3.6. Electrochemical impedance spectroscopic analysis of ReS_2 SSC device. (A) Nyquist plot of ReS_2 SSC device representing the plot of real against imaginary values of impedance, (B) Variation of phase angle of ReS_2 SSC device with respect to the applied frequency, (C) Plot of real component of capacitance of ReS_2 SSC versus the frequency, and (D) Plot of imaginary component of capacitance versus the frequency of ReS_2 SSC device. (E) Cyclic stability of ReS_2 SSC device over 5000 continuous cycles charge-discharge analysis measured at a current density of 1 A g^{-1}, (F) The charge-discharge profiles of initial, 1000th cycle and the 5000th cycle of ReS_2 SSC device.

transfer resistance (R_{ct}) of the ReS_2 SSC device are found to be 3.01 and 1.1 Ω, respectively. The straight line observed at the low-frequency region indicates the capacitive nature of the ReS_2 SSC device mainly governed by the ion-diffusion controlled electrochemical reactions occurred at the electrode/electrolyte interface[58]. Figure 5.3.6(B) shows the variation of phase angle with respect to the applied frequency which shows that phase angle at the low-frequency region is about -73.14° (almost closer to the phase angle of the ideal capacitor, -90°), thus indicating the nearly capacitive nature of the ReS_2 SSC device[18,57]. The effect

of specific capacitance with respect to applied frequencies revealed that a specific capacitance of about 26.54 F g^{-1} was obtained for the ReS_2 SSC device at a low frequency of about 0.01 Hz. The variation of real and imaginary capacitance of ReS_2 SSC with respect to the applied range of frequencies was provided in Fig. 5.3.6(C and D), respectively. Figure 5.3.6(C) shows that the real capacitance of ReS_2 SSC is higher at low frequencies and it decreases with respect to an increase in frequency, indicating that the ReS_2 SSC behaviours like an ideal capacitor at low frequencies and as a resistor at high frequencies[43]. Figure 5.3.6(D) presents the imaginary component of the capacitance of ReS_2 SSC against the applied frequencies form which it is easier to determine the dielectric relaxation time and capacitor-response frequency of the device. It is evident from Fig. 5.3.6(D) that the imaginary component of capacitance is increasing with respect to frequency (from low to high) reaches a maximum at a certain frequency (related to the dielectric relaxation time) and then decreases with further increase in frequency[43]. The relaxation time of the ReS_2 SSC is found to be about 7.6 seconds. Additionally, only one peak maxima were observed in Fig. 5.3.6(D) which indicates that the charge-storage in the ReS_2 SSC device is mainly due to the pseudocapacitance. The stability of the ReS_2 SSC device is examined over 5000 cycles of continuous charge-discharge obtained using a current density of 1 A g^{-1} as shown in Fig. 5.3.6 (E). It showed an increase in capacitance values during the initial cycles which might be due to the activation process[53] and it became stabilized afterwards. Figure 5.3.6(F) shows the CD profiles of initial, 1000^{th} and 5000^{th} cycles which shows an increase in time for 1000^{th} cycle mainly due to the activation of ReS_2 electrodes and after that, the device becomes highly stable. The ReS_2 SSC device retained about 98.31 % of its initial capacitance, thus, suggesting superior electrochemical stability of the device.

It is well known that the energy density of a supercapacitor can be boosted into several folds with the use of organic electrolytes which can operate over 3 V[2,59].

Therefore, in this study, we also explored the electrochemical performances of ReS_2 SSC device (CR2032 type) using 1 M $TEABF_4$ as electrolytes, and the results are summarized in Figure 6. The CV profiles of the ReS_2 SSC device using organic electrolyte is provided in Fig. 5.3.7(A) which shows that the device can operate over a potential window of 2 V. Figure 5.3.7(B) displays the effect of scan rate on the specific capacitance of ReS_2 SSC device which indicated that a maximum specific capacitance of about 47.92 F g^{-1} was obtained at a low scan rate of 5 mV s^{-1}. The obtained specific capacitance of ReS_2 SSC device using organic electrolyte is almost two-fold higher compared to that of aqueous electrolyte (24.15 F g^{-1}). The CD profiles of ReS_2 SSC device is given in Figure 5.3.7(C) which shows the presence quasi-symmetric nature, suggesting the ideal capacitive properties. A maximum specific capacitance of about 51.40 F g^{-1} was obtained for the ReS_2 SSC device from the discharge profiles obtained using a current density of 0.5 A g^{-1} and the effect of applied current on the specific capacitance of ReS_2 SSC device was provided in Figure 5.3.7 (D). The Ragone plot of ReS_2 SSC device using organic electrolyte was provided in Figure 5.3.7(E) which demonstrates the comparative performance metrics of ReS_2 SSC device with the recently reported SSCs using organic electrolytes. The ReS_2 SSC device delivered an energy density of about energy density of about 28.55 W h kg^{-1} at a constant current density of 0.5 A g^{-1} with a corresponding power density of 500 W kg^{-1}. The energy density of the ReS_2 SSC device decreased from 28.55 to 16.11 Wh kg^{-1}) with an increase of power density from 500 to 10,000 W kg^{-1}) as the galvanostatic discharge current densities increased from 0.5 to 10 A g^{-1}.

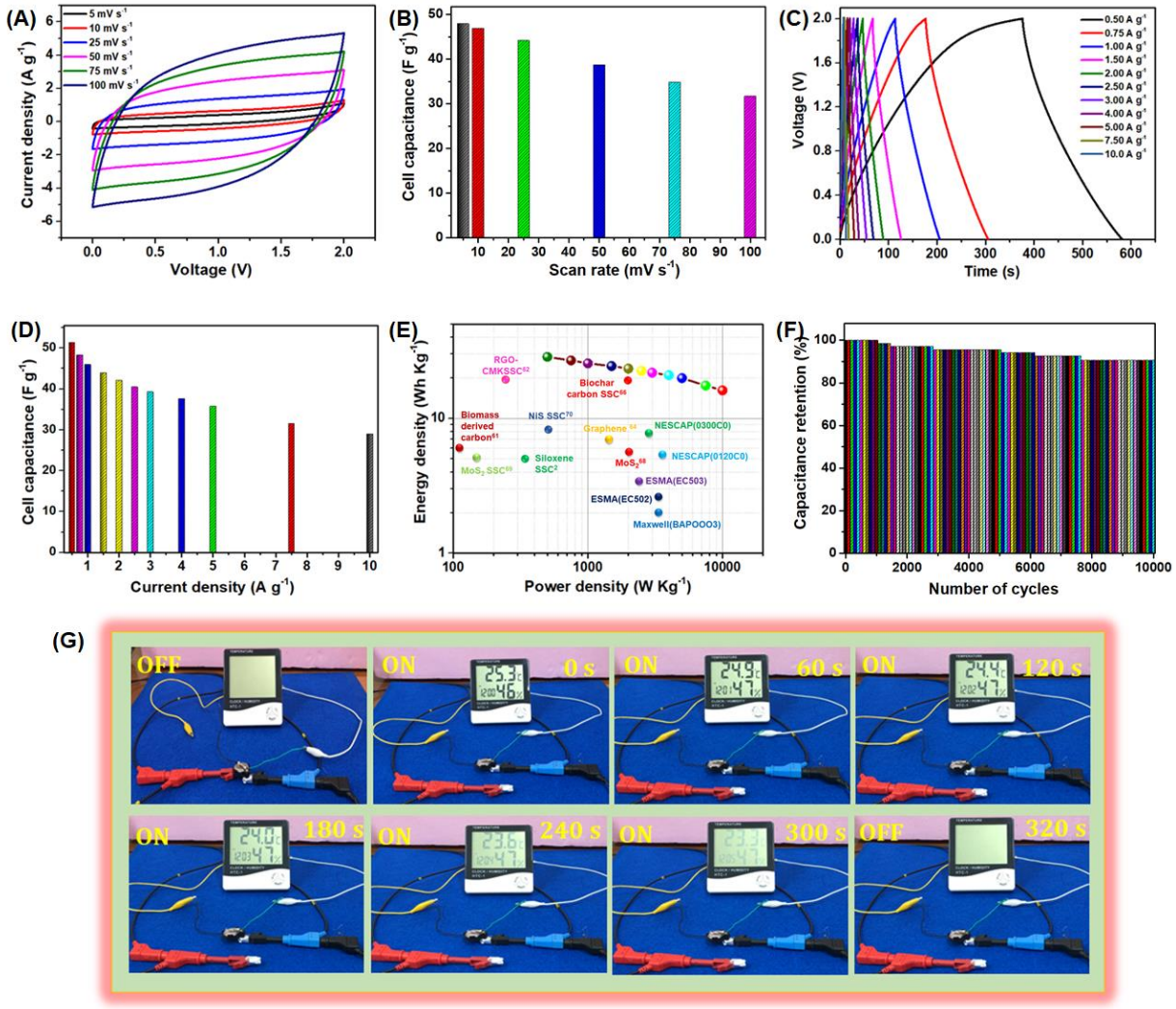

Figure 5.3.7. Electrochemical characterization of ReS_2 symmetric supercapacitor (SSC) device in an organic electrolyte. (A) Cyclic voltammetry profiles of the ReS_2 SSC device recorded using different scan rate (5 – 100 mV s^{-1}), (B) Effect of scan rate on the cell capacitance of the ReS_2 SSC device. (C) CD profiles of the ReS_2 SSC device recorded using different current densities (0.50 – 10 A g^{-1}) (D) Effect of current densities on the cell capacitance of the ReS_2 SSC device. (E) Ragone plot of ReS_2 SSC device showing the superior performance of ReS_2 SSC over the reported SSCs. (F) Cyclic stability of ReS_2 SSC device over 10000 continuous cycles charge-discharge analysis measured at a current density of 5 A g^{-1}. (G) practical application of the ReS_2 SSC device capable of powering the multifunctional electronic display.

The obtained energy density of ReS_2 SSC device is quite higher compared to biomass derived carbon (6.68 Wh kg^{-1})[60] , RGO-CMK (23.1 Wh kg^{-1})[61] , porous activated reduced graphene oxide (26 Wh kg^{-1})[62] , graphene sheets (7.13 Wh kg^{-1})[63], siloxene sheet (5.08 Wh kg^{-1})[2], porous carbon (11.4 Wh kg^{-1})[59], CNT fiber (11.4 Wh kg^{-1})[64], biochar monolith carbon (20 Wh kg^{-1})[65], PEDOT (4.25 Wh kg^{-1})[66], MoS_2 (6.22 Wh kg^{-1})[67] , MoS_2 (5.4 Wh kg^{-1})[68], NiS SSC(9.30 Wh kg^{-1})[69] and activated carbon (16 Wh kg^{-1})[59]. Figure 5.3.7(F) demonstrated the better cyclic stability of the ReS_2 SSC device using organic electrolytes with excellent capacitance retention of about 90.57 % of its initial capacitance.

Further, the practical application of the ReS_2 SSC is examined to evaluate their power delivery capabilities in order to ensure their candidature as a sustainable power sources[70]. Figure 5.3.7 (G) shows the practical application of the ReS_2 SSC device capable of powering the multifunctional electronic display. Initially, the ReS_2 SSC was charged upto 2.0 V using a current range of 1 mA, and the stored energy was delivered to power the multifunctional electronic display for monitoring temperature and relative humidity with respect to time. At the initial stage, the multifunctional electronic display is in OFF condition, and it turns ON after the ReS_2 SSC was connected to the terminals of the multifunctional electronic display. The Figure 5.3.7 (G) shows that the ReS_2 SSC was capable of driving the multifunctional electronic display over a time period of 300 seconds and the electronic supporting movie 1 shows the videos demonstrating the real-time applications of ReS_2 SSC. Collectively, these studies suggested the better electrochemical properties of ReS_2 nanostructures towards the application in supercapacitors.

5.3.4. Conclusions

The key findings of this work demonstrated the electrochemical energy storage (supercapacitive) properties of hydrothermally prepared ReS_2 nanostructures using aqueous and organic electrolytes. The recrystallization of the intermediate precursor's phenomenon

under hydrothermal conditions resulted in the formation of layered ReS_2 nanostructures with good crystallinity and triclinic phase as revealed from the X-ray diffraction analysis, laser Raman spectroscopy. The electrochemical properties of the ReS_2 electrode using three-electrode configuration revealed their potential use as an advanced negative electrode (OPW from 0.0 to -0.8 V) with a high electrode capacitance (189.28 F g^{-1}) which might be competitive to the available few negative electrodes for supercapacitors. Further, the device specific properties of ReS_2 SSC were tested using aqueous and organic electrolytes in this work. The ReS_2 SSC device using aqueous electrolyte delivered a high cell capacitance of 35.75 F g^{-1}, the energy density of 3.17 Wh kg^{-1} with excellent cyclic stability (retention of 98.31 % of initial capacitance) over 5,000 cycles. The performance of ReS_2 SSC using aqueous electrolyte is quite higher and comparable to that of recently explored 2D materials (such as MXenes, RuS_2, layered famatinite, etc.,), thus ensuring that the ReS_2 might be a promising candidate for aqueous electrochemical energy storage devices. The ReS_2 SSC device using organic electrolyte showed their capability to operate over a high OPW of 2.0 V and possesses an excellent energy density (28.55 Wh kg^{-1}) with an outstanding power density of 10,000 W kg^{-1} as well as better cyclic stability (retention of about 90.57 % of initial capacitance) over 10,000 cycles. The remarkable energy/power performance metrics of the ReS_2 SSC using organic electrolyte compared to existing carbon-, and TMC- based SSCs, ensure their significant candidature towards the development of next-generation high performance supercapacitors.

5.3.5 References:

[1] P. Geng, S. Zheng, H. Tang, R. Zhu, L. Zhang, S. Cao, H. Xue, H. Pang, Transition Metal Sulfides Based on Graphene for Electrochemical Energy Storage, Adv. Energy Mater. 8 (2018) 1703259. doi:10.1002/aenm.201703259.

[2] K. Krishnamoorthy, P. Pazhamalai, S.-J. Kim, Two-dimensional siloxene nanosheets: novel high-performance supercapacitor electrode materials, Energy Environ. Sci. 11 (2018) 1595–1602. doi:10.1039/C8EE00160J.

[3] C. Wang, Y. Niu, J. Jiang, Y. Chen, H. Tian, R. Zhang, T. Zhou, J. Xia, Y. Pan, S. Wang, Hybrid thermoelectric battery electrode FeS_2 study, Nano Energy. 45 (2018) 432–438. doi:10.1016/j.nanoen.2018.01.025.

[4] T. Wang, S. Chen, H. Pang, H. Xue, Y. Yu, MoS_2-Based Nanocomposites for Electrochemical Energy Storage, Adv. Sci. 4 (2017) 1600289. doi:10.1002/advs.201600289.

[5] H. Wang, H. Yuan, S. Sae Hong, Y. Li, Y. Cui, Physical and chemical tuning of two-dimensional transition metal dichalcogenides, Chem. Soc. Rev. 44 (2015) 2664–2680. doi:10.1039/c4cs00287c.

[6] J. Du, C. Xia, W. Xiong, T. Wang, Y. Jia, J. Li, Two-dimensional transition-metal dichalcogenides-based ferromagnetic van der Waals heterostructures, Nanoscale. 9 (2017) 17585–17592. doi:10.1039/c7nr06473j.

[7] A. Venkadesh, S. Radhakrishnan, J. Mathiyarasu, Eco-friendly synthesis and morphology-dependent superior electrocatalytic properties of CuS nanostructures, Electrochim. Acta. 246 (2017) 544–552. doi:10.1016/j.electacta.2017.06.077.

[8] J.M. Soon, K.P. Loh, Electrochemical Double-Layer Capacitance of MoS_2 Nanowall Films, Electrochem. Solid-State Lett. 10 (2007) A250. doi:10.1149/1.2778851.

[9] X. Li, J. Wei, Q. Li, S. Zheng, Y. Xu, P. Du, C. Chen, J. Zhao, H. Xue, Q. Xu, H.

Pang, Nitrogen-Doped Cobalt Oxide Nanostructures Derived from Cobalt-Alanine Complexes for High-Performance Oxygen Evolution Reactions, Adv. Funct. Mater. 28 (2018) 1800886. doi:10.1002/adfm.201800886.

[10] X.F. Qiao, J. Bin Wu, L. Zhou, J. Qiao, W. Shi, T. Chen, X. Zhang, J. Zhang, W. Ji, P.H. Tan, Polytypism and unexpected strong interlayer coupling in two-dimensional layered ReS_2, Nanoscale. 8 (2016) 8324–8332. doi:10.1039/c6nr01569g.

[11] J. Ma, X. Guo, Y. Yan, H. Xue, H. Pang, FeO_x-Based Materials for Electrochemical Energy Storage, Adv. Sci. 5 (2018) 1700986. doi:10.1002/advs.201700986.

[12] X. Fu, P. Ilanchezhiyan, G. Mohan Kumar, H.D. Cho, L. Zhang, A.S. Chan, D.J. Lee, G.N. Panin, T.W. Kang, Tunable UV-visible absorption of SnS_2 layered quantum dots produced by liquid phase exfoliation, Nanoscale. 9 (2017) 1820–1826. doi:10.1039/C6NR09022B.

[13] P. Ilanchezhiyan, G. Mohan Kumar, T.W. Kang, Electrochemical studies of spherically clustered MoS_2 nanostructures for electrode applications, J. Alloys Compd. 634 (2015) 104–108. doi:10.1016/j.jallcom.2015.02.082.

[14] C. Wang, H. Tian, J. Jiang, T. Zhou, Q. Zeng, X. He, P. Huang, Y. Yao, Facile Synthesis of Different Morphologies of Cu_2SnS_3 for High-Performance Supercapacitors, ACS Appl. Mater. Interfaces. 9 (2017) 26038–26044. doi:10.1021/acsami.7b07190.

[15] P. Pazhamalai, K. Krishnamoorthy, V.K. Mariappan, S. Sahoo, S. Manoharan, S.-J. Kim, A High Efficacy Self-Charging $MoSe_2$ Solid-State Supercapacitor Using Electrospun Nanofibrous Piezoelectric Separator with Ionogel Electrolyte, Adv. Mater. Interfaces. 5 (2018) 1800055. doi:10.1002/admi.201800055.

[16] X. Cao, C. Tan, X. Zhang, W. Zhao, H. Zhang, Solution-Processed Two-Dimensional Metal Dichalcogenide-Based Nanomaterials for Energy Storage and Conversion, Adv.

Mater. 28 (2016) 6167–6196. doi:10.1002/adma.201504833.

[17] M. Acerce, D. Voiry, M. Chhowalla, Metallic 1T phase MoS_2 nanosheets as supercapacitor electrode materials, Nat. Nanotechnol. 10 (2015) 313–318. doi:10.1038/nnano.2015.40.

[18] K. Krishnamoorthy, P. Pazhamalai, S. Sahoo, S.-J. Kim, Titanium carbide sheet based high performance wire type solid state supercapacitors, J. Mater. Chem. A. 5 (2017) 5726–5736. doi:10.1039/C6TA11198J.

[19] S. Zheng, L. Zheng, Z. Zhu, J. Chen, J. Kang, Z. Huang, D. Yang, MoS_2 Nanosheet Arrays Rooted on Hollow rGO Spheres as Bifunctional Hydrogen Evolution Catalyst and Supercapacitor Electrode, Nano-Micro Lett. 10 (2018) 62. doi:10.1007/s40820-018-0215-3.

[20] E. Kovalska, C. Kocabas, Organic electrolytes for graphene-based supercapacitor: Liquid, gel or solid, Mater. Today Commun. 7 (2016) 155–160. doi:10.1016/j.mtcomm.2016.04.013.

[21] A. Ambrosi, Z. Sofer, M. Pumera, Lithium intercalation compound dramatically influences the electrochemical properties of exfoliated MoS_2, Small. 11 (2015) 605–612. doi:10.1002/smll.201400401.

[22] M. Gehlmann, I. Aguilera, G. Bihlmayer, S. Nemšák, P. Nagler, P. Gospodarič, G. Zamborlini, M. Eschbach, V. Feyer, F. Kronast, E. Młyńczak, T. Korn, L. Plucinski, C. Schüller, S. Blügel, C.M. Schneider, Direct Observation of the Band Gap Transition in Atomically Thin ReS_2, Nano Lett. 17 (2017) 5187–5192. doi:10.1021/acs.nanolett.7b00627.

[23] O.B. Mohammed, H.C.P. Movva, N. Prasad, A. Valsaraj, S. Kang, C.M. Corbet, T. Taniguchi, K. Watanabe, L.F. Register, E. Tutuc, S.K. Banerjee, ReS_2-based interlayer tunnel field effect transistor, J. Appl. Phys. 122 (2017) 245701.

doi:10.1063/1.5004038.

[24] Y.C. Lin, H.P. Komsa, C.H. Yeh, T. Björkman, Z.Y. Liang, C.H. Ho, Y.S. Huang, P.W. Chiu, A. V. Krasheninnikov, K. Suenaga, Single-Layer ReS_2: Two-Dimensional Semiconductor with Tunable In-Plane Anisotropy, ACS Nano. 9 (2015) 11249–11257. doi:10.1021/acsnano.5b04851.

[25] L.S. Hart, J.L. Webb, S. Murkin, D. Wolverson, D.-Y. Lin, Identifying light impurities in transition metal dichalcogenides: the local vibrational modes of S and O in $ReSe_2$ and $MoSe_2$, Npj 2D Mater. Appl. 1 (2017) 41. doi:10.1038/s41699-017-0043-1.

[26] M. Rahman, K. Davey, S.Z. Qiao, Advent of 2D Rhenium Disulfide (ReS_2): Fundamentals to Applications, Adv. Funct. Mater. 27 (2017) 1606129. doi:10.1002/adfm.201606129.

[27] L. Hart, S. Dale, S. Hoye, J.L. Webb, D. Wolverson, Rhenium Dichalcogenides: Layered Semiconductors with Two Vertical Orientations, Nano Lett. 16 (2016) 1381–1386. doi:10.1021/acs.nanolett.5b04838.

[28] M. Mao, C. Cui, M. Wu, M. Zhang, T. Gao, X. Fan, J. Chen, T. Wang, J. Ma, C. Wang, Flexible ReS_2 nanosheets/N-doped carbon nanofibers-based paper as a universal anode for alkali (Li, Na, K) ion battery, Nano Energy. 45 (2018) 346–352. doi:10.1016/j.nanoen.2018.01.001.

[29] F. Qi, Y. Chen, B. Zheng, J. He, Q. Li, X. Wang, B. Yu, J. Lin, J. Zhou, P. Li, W. Zhang, 3D chrysanthemum-like ReS_2 microspheres composed of curly few-layered nanosheets with enhanced electrochemical properties for lithium-ion batteries, J. Mater. Sci. 52 (2017) 3622–3629. doi:10.1007/s10853-016-0500-9.

[30] H. Jang, C.R. Ryder, J.D. Wood, M.C. Hersam, D.G. Cahill, 3D Anisotropic Thermal Conductivity of Exfoliated Rhenium Disulfide, Adv. Mater. 29 (2017) 1700650. doi:10.1002/adma.201700650.

[31] T. Fujita, Y. Ito, Y. Tan, H. Yamaguchi, D. Hojo, A. Hirata, D. Voiry, M. Chhowalla, M. Chen, Chemically exfoliated ReS_2 nanosheets, Nanoscale. 6 (2014) 12458–12462. doi:10.1039/c4nr03740e.

[32] N. Al-Dulaimi, D.J. Lewis, X.L. Zhong, M. Azad Malik, P. O'Brien, Chemical vapour deposition of rhenium disulfide and rhenium-doped molybdenum disulfide thin films using single-source precursors, J. Mater. Chem. C. 4 (2016) 2312–2318. doi:10.1039/c6tc00489j.

[33] B. Jariwala, D. Voiry, A. Jindal, B.A. Chalke, R. Bapat, A. Thamizhavel, M. Chhowalla, M. Deshmukh, A. Bhattacharya, Synthesis and Characterization of ReS_2 and $ReSe_2$ Layered Chalcogenide Single Crystals, Chem. Mater. 28 (2016) 3352–3359. doi:10.1021/acs.chemmater.6b00364.

[34] S. Shen, Y. Chao, Z. Dong, G. Wang, X. Yi, G. Song, K. Yang, Z. Liu, L. Cheng, Bottom-Up Preparation of Uniform Ultrathin Rhenium Disulfide Nanosheets for Image-Guided Photothermal Radiotherapy, Adv. Funct. Mater. 27 (2017) 1700250. doi:10.1002/adfm.201700250.

[35] Y.L. Li, Y. Li, C. Tang, Strain engineering and photocatalytic application of single-layer ReS_2, Int. J. Hydrogen Energy. 42 (2017) 161–167. doi:10.1016/j.ijhydene.2016.11.097.

[36] M. Hafeez, L. Gan, H. Li, Y. Ma, T. Zhai, Large-Area Bilayer ReS_2 Film/Multilayer ReS_2 Flakes Synthesized by Chemical Vapor Deposition for High Performance Photodetectors, Adv. Funct. Mater. 26 (2016) 4551–4560. doi:10.1002/adfm.201601019.

[37] Q. Zhang, S. Tan, R.G. Mendes, Z. Sun, Y. Chen, X. Kong, Y. Xue, M.H. RÃ¼mmeli, X. Wu, S. Chen, L. Fu, Extremely Weak van der Waals Coupling in Vertical ReS2Nanowalls for High-Current-Density Lithium-Ion Batteries, Adv. Mater. 28

(2016) 2616–2623. doi:10.1002/adma.201505498.

[38] F. Qi, J. He, Y. Chen, B. Zheng, Q. Li, X. Wang, B. Yu, J. Lin, J. Zhou, P. Li, W. Zhang, Y. Li, Few-layered ReS_2 nanosheets grown on carbon nanotubes: A highly efficient anode for high-performance lithium-ion batteries, Chem. Eng. J. 315 (2017) 10–17. doi:10.1016/j.cej.2017.01.004.

[39] F. Qi, Y. Chen, B. Zheng, J. He, Q. Li, X. Wang, J. Lin, J. Zhou, B. Yu, P. Li, W. Zhang, Hierarchical architecture of ReS_2/rGO composites with enhanced electrochemical properties for lithium-ion batteries, Appl. Surf. Sci. 413 (2017) 123–128. doi:10.1016/j.apsusc.2017.03.296.

[40] G. Huang, T. Chen, Z. Wang, K. Chang, W. Chen, Synthesis and electrochemical performances of cobalt sulfides/graphene nanocomposite as anode material of Li-ion battery, J. Power Sources. 235 (2013) 122–128. doi:10.1016/j.jpowsour.2013.01.093.

[41] I. Uzcanga, I. Bezverkhyy, P. Afanasiev, C. Scott, M. Vrinat, Sonochemical Preparation of MoS_2 in Aqueous Solution: Replication of the Cavitation Bubbles in an Inorganic Material Morphology, Chem. Mater. 17 (2005) 3575–3577. doi:10.1021/cm0501766.

[42] W. Shi, S. Song, H. Zhang, Hydrothermal synthetic strategies of inorganic semiconducting nanostructures, Chem. Soc. Rev. 42 (2013) 5714. doi:10.1039/c3cs60012b.

[43] K. Krishnamoorthy, P. Pazhamalai, S.J. Kim, Ruthenium sulfide nanoparticles as a new pseudocapacitive material for supercapacitor, Electrochim. Acta. 227 (2017) 85–94. doi:10.1016/j.electacta.2016.12.171.

[44] J. Borowiec, W.P. Gillin, M.A.C. Willis, F.S. Boi, Y. He, J.Q. Wen, S.L. Wang, L. Schulz, Room temperature synthesis of ReS_2 through aqueous perrhenate sulfidation, J. Phys. Condens. Matter. 30 (2018) 055702. doi:10.1088/1361-648X/aaa474.

[45] N.S. Arul, D. Mangalaraj, R. Ramachandran, A.N. Grace, J.I. Han, Fabrication of CeO_2/Fe_2O_3 composite nanospindles for enhanced visible light driven photocatalysts and supercapacitor electrodes, J. Mater. Chem. A. 3 (2015) 15248–15258. doi:10.1039/C5TA02630J.

[46] J. Aliaga, T. Zepeda, J. Araya, F. Paraguay-Delgado, E. Benavente, G. Alonso-Núñez, S. Fuentes, G. González, Low-Dimensional ReS_2/C Composite as Effective Hydrodesulfurization Catalyst, Catalysts. 7 (2017) 377. doi:10.3390/catal7120377.

[47] R. Ramachandran, C. Zhao, D. Luo, K. Wang, F. Wang, Morphology-dependent electrochemical properties of cobalt-based metal organic frameworks for supercapacitor electrode materials, Electrochim. Acta. 267 (2018) 170–180. doi:10.1016/j.electacta.2018.02.074.

[48] J. Yao, B. Liu, S. Ozden, J. Wu, S. Yang, M.-T.F. Rodrigues, K. Kalaga, P. Dong, P. Xiao, Y. Zhang, R. Vajtai, P.M. Ajayan, 3D Nanostructured Molybdenum Diselenide/Graphene Foam as Anodes for Long-Cycle Life Lithium-ion Batteries, Electrochim. Acta. 176 (2015) 103–111. doi:10.1016/j.electacta.2015.06.138.

[49] T. Brousse, D. Belanger, J.W. Long, To Be or Not To Be Pseudocapacitive?, J. Electrochem. Soc. 162 (2015) A5185–A5189. doi:10.1149/2.0201505jes.

[50] S. Vijayakumar, S. Nagamuthu, K.-S. Ryu, $CuCo_2O_4$ flowers/Ni-foam architecture as a battery type positive electrode for high performance hybrid supercapacitor applications, Electrochim. Acta. 238 (2017) 99–106. doi:10.1016/j.electacta.2017.03.178.

[51] L. Wang, X. Zhang, Y. Ma, M. Yang, Y. Qi, Supercapacitor Performances of the MoS2/CoS2Nanotube Arrays in Situ Grown on Ti Plate, J. Phys. Chem. C. 121 (2017) 9089–9095. doi:10.1021/acs.jpcc.6b13026.

[52] J. Qi, Y. Chang, Y. Sui, Y. He, Q. Meng, F. Wei, Y. Zhao, Y. Jin, Facile Construction

of 3D Reduced Graphene Oxide Wrapped Ni_3S_2 Nanoparticles on Ni Foam for High-Performance Asymmetric Supercapacitor Electrodes, Part. Part. Syst. Charact. 34 (2017) 1700196. doi:10.1002/ppsc.201700196.

[53] M.D. Stoller, R.S. Ruoff, Best practice methods for determining an electrode material's performance for ultracapacitors, Energy Environ. Sci. 3 (2010) 1294. doi:10.1039/c0ee00074d.

[54] K.J. Huang, J.Z. Zhang, G.W. Shi, Y.M. Liu, Hydrothermal synthesis of molybdenum disulfide nanosheets as supercapacitors electrode material, Electrochim. Acta. 132 (2014) 397–403. doi:10.1016/j.electacta.2014.04.007.

[55] K.-J. Huang, J.-Z. Zhang, K. Xing, One-step synthesis of layered CuS/multi-walled carbon nanotube nanocomposites for supercapacitor electrode material with ultrahigh specific capacitance, Electrochim. Acta. 149 (2014) 28–33. doi:10.1016/j.electacta.2014.10.079.

[56] S. Zhang, N. Pan, Supercapacitors Performance Evaluation, Adv. Energy Mater. 5 (2015) 1401401. doi:10.1002/aenm.201401401.

[57] K. Krishnamoorthy, P. Pazhamalai, G.K. Veerasubramani, S.J. Kim, Mechanically delaminated few layered MoS_2 nanosheets based high performance wire type solid-state symmetric supercapacitors, J. Power Sources. 321 (2016) 112–119. doi:10.1016/j.jpowsour.2016.04.116.

[58] C. Zhang, Y. Huang, S. Tang, M. Deng, Y. Du, High-Energy All-Solid-State Symmetric Supercapacitor Based on Ni_3S_2 Mesoporous Nanosheet-Decorated Three-Dimensional Reduced Graphene Oxide, ACS Energy Lett. 2 (2017) 759–768. doi:10.1021/acsenergylett.7b00078.

[59] A. Eftekhari, Supercapacitors utilising ionic liquids, Energy Storage Mater. 9 (2017) 47–69. doi:10.1016/j.ensm.2017.06.009.

[60] Y. Gong, D. Li, C. Luo, Q. Fu, C. Pan, Highly porous graphitic biomass carbon as advanced electrode materials for supercapacitors, Green Chem. 19 (2017) 4132–4140. doi:10.1039/C7GC01681F.

[61] Z. Lei, Z. Liu, H. Wang, X. Sun, L. Lu, X.S. Zhao, A high-energy-density supercapacitor with graphene-CMK-5 as the electrode and ionic liquid as the electrolyte, J. Mater. Chem. A. 1 (2013) 2313–2321. doi:10.1039/c2ta01040b.

[62] L.L. Zhang, X. Zhao, M.D. Stoller, Y. Zhu, H. Ji, S. Murali, Y. Wu, S. Perales, B. Clevenger, R.S. Ruoff, Highly Conductive and Porous Activated Reduced Graphene Oxide Films for High-Power Supercapacitors, Nano Lett. 12 (2012) 1806–1812. doi:10.1021/nl203903z.

[63] W. Liu, X. Yan, J. Lang, C. Peng, Q. Xue, Flexible and conductive nanocomposite electrode based on graphene sheets and cotton cloth for supercapacitor, J. Mater. Chem. 22 (2012) 17245. doi:10.1039/c2jm32659k.

[64] E. Senokos, V. Reguero, L. Cabana, J. Palma, R. Marcilla, J.J. Vilatela, Large-Area, All-Solid, and Flexible Electric Double Layer Capacitors Based on CNT Fiber Electrodes and Polymer Electrolytes, Adv. Mater. Technol. 2 (2017) 1600290. doi:10.1002/admt.201600290.

[65] J. Jiang, High Temperature Monolithic Biochar Supercapacitor Using Ionic Liquid Electrolyte, J. Electrochem. Soc. 164 (2017) H5043–H5048. doi:10.1149/2.0211708jes.

[66] G.P. Pandey, A.C. Rastogi, Solid-State Supercapacitors Based on Pulse Polymerized Poly(3,4-ethylenedioxythiophene) Electrodes and Ionic Liquid Gel Polymer Electrolyte, J. Electrochem. Soc. 159 (2012) A1664–A1671. doi:10.1149/2.047210jes.

[67] Y. Zhang, P. Ju, C. Zhao, X. Qian, In-situ Grown of MoS_2/RGO/MoS_2@Mo Nanocomposite and Its supercapacitor Performance, Electrochim. Acta. 219 (2016)

693–700. doi:10.1016/j.electacta.2016.10.072.

[68] M.S. Javed, S. Dai, M. Wang, D. Guo, L. Chen, X. Wang, C. Hu, Y. Xi, High performance solid state flexible supercapacitor based on molybdenum sulfide hierarchical nanospheres, J. Power Sources. 285 (2015) 63–69. doi:10.1016/j.jpowsour.2015.03.079.

[69] W. Li, S. Wang, L. Xin, M. Wu, X. Lou, Single-crystal β-NiS nanorod arrays with a hollow-structured Ni_3S_2 framework for supercapacitor applications, J. Mater. Chem. A. 4 (2016) 7700–7709. doi:10.1039/C6TA01133K.

[70] S.E. Moosavifard, J. Shamsi, M.K. Altafi, Z.S. Moosavifard, All-solid state, flexible, high-energy integrated hybrid micro-supercapacitors based on 3D LSG/$CoNi_2S_4$ nanosheets, Chem. Commun. 52 (2016) 13140–13143. doi:10.1039/C6CC07053A.

SUMMARY

- Chapter 4 and 5 discuss the preparation of layered materials involved various methodologies such as hydrothermal preparation (blue TiO_2, $MoSe_2$, ReS_2), topochemical de-intercalation reaction (2D silicon sheets), and mechanomilling assisted exfoliation process (MoS_2).
- Different layered materials such as metal oxide (blue TiO_2), two-dimensional transition metal chalcogenides (MoS_2, ReS_2, $MoSe_2$), layered siloxene and their derivatives (siloxene, heat-treated siloxene, silicon oxy carbide lamellas) were examined as novel electrode materials for symmetric supercapacitors (SSCs) using organic electrolyte ($TEABF_4$).
- Further, for the fabrication of self-charging power cell, the choice of electrode material is evaluated. The electrical conductivity of $MoSe_2$ sheets is higher than MoS_2, and ReS_2 sheets with the advantage of large anionic polarizability (and high ionic diffusivity) arise from the Se^{2-} as compared to that of S^{2-} in MoS_2 and ReS_2. Thus, $MoSe_2$ SSC is used for further studies for the fabrication and performance evaluation of self-charging supercapacitor cell (SCSPC) device using ionogel electrolyte and electrospun PVDF fibres for the first time was discussed in the chapter 6.

CHAPTER 6

SELF-CHARGING SUPERCAPACITOR POWER CELL: ENERGY CONVERSION AND STORAGE

A HIGH EFFICACY SELF-CHARGING $MoSe_2$ SOLID-STATE SUPERCAPACITOR USING ELECTROSPUN NANOFIBROUS PIEZOELECTRIC SEPARATOR WITH IONOGEL ELECTROLYTE

Highlights:

- A new type of SCSPC device is fabricated comprising 2D molybdenum di-selenide ($MoSe_2$) as an energy storing electrode with polyvinylidene fluoride-co-hexafluoropropylene/ tetraethylammonium tetrafluoroborate (PVDF-co-HFP/$TEABF_4$) ion gelled polyvinylidene fluoride/sodium niobate (PVDF/NaNbO3) as the piezopolymer electrolyte.
- The fabricated SCSPC delivers a specific capacitance of 18.93 mF cm^{-2} with a specific energy of 37.90 mJ cm^{-2} at a specific power density of 268.91 μW cm^{-2} obtained at a constant discharge current of 0.5 mA.
- The $MoSe_2$ SCSPC device can be charged up to a maximum of 708 mV under a compressive force of 30 N in 100 s, and the mechanism of charge-storage is discussed in detail.
- The experimental findings of this work demonstrate the high efficiency of the fabricated $MoSe_2$ SCSPC device, which can provide new insights for developing sustainable power sources for the next generation wearable electronic applications.

6.1. Introduction

The self-charging power system has become imperative research in the field of energy harvesting and storage due to the depletion of the available fossil fuels for the use in day to day life.[1–5] Self-charging power system consists of two significant compartments viz. (i) Energy harvesting and (ii) energy storage in which the former generates the energy while the latter is used to store the generated energy.[6,7] Renewable energy sources such as solar, wind and hydropower, mechanical energy (piezoelectric/triboelectric nanogenerator) and electrochemical energy (fuel cells) are used as energy harvesting system whereas batteries and supercapacitors are used an energy storing system in the design of self-charging power system.[8–12] Renewable power sources based self-charging power system such as coupling of the solar cell/photovoltaics with the electrochemical energy storage are commercialized for making use of the photon energy into useful energy.[13,14] Hitherto, the utilization of biomechanical energy for the self-charging system is still in research level, and further efforts are needed to be undertaken for practical applications. The concept of self-charging and/or self-powered system for harvesting and storing mechanical and/or biomechanical energy become plausible after the research findings of Prof. Z. L. Wang and co-workers for the first time when they designed a self-powered system using nanogenerator and supercapacitor in 2012.[2] Up-to-date two different types of self-charging power cell have been reported such as (i) external powering and (ii) internally integrated the system.[8,15–17] In the former case, the mechanical energy harvester is externally connected to the energy storage device using a rectifier whereas the latter uses an all-in-one integrated system which will be beneficial for several applications in portable and wearable devices due to their miniaturized size.[18,19] The pulsating alternating current output of nanogenerator is the major concern for the practical application of NG based self-charging power cells (SCPCs) due to their low energy

conversion efficiency.[7,20] Therefore, the design and development of high-performance self-charging power cell with high energy conversion efficiency are highly essential.

In this scenario, integrated self-charging supercapacitor power cell (SCSPC) utilizing supercapacitor as energy storage device attracts much attention compared to batteries mainly due to the fast charging rates of a capacitive type electrode; it can scavenge/store the piezo-electrochemically generated energy rapidly compared to that of the battery type electrode. Considering the efforts taken until now on the supercapacitors based SCSPC, only a few reports are available in the literature. Initially, our group used the effectiveness of ZnO nanorod/PVDF composite thin film based separator in the self-charging capacitor using MnO_2 electrodes which charged about 110 mV in 300 s.[21] Later on, Song et al. demonstrated a similar work with enhanced self-charging properties using PVDF separator with carbon cloth electrodes which charged about 100 mV in 40 s.[22] In these two works, polymer gel electrolyte using polyvinyl alcohol as a matrix with aqueous electrolytes are used in the construction of SCPC. Further, the SCPC device demonstrated by Parida et al. using PMMA/$LiClO_4$ as an electrolyte which showed a self-charging of about 75 mV in 40 s using PVDF-TrFE as the separator with carbon nanotubes as energy storage electrodes. [23] All these three devices utilized symmetric supercapacitor device configuration by replacing a commercial polymeric separator with a piezoelectric polymer separator made of PVDF and their hybrids. Recently, Maitra et al. reported SCPC in the asymmetric configuration using a natural bio-piezoelectric separator (derived from fish swim bladder) which self-charged up to 150 mV in 80 s.[24] It is clearly evident from these studies that still a lot of efforts are highly needed to improve the self-charging performance of the integrated device which highly depends on the piezo-electrochemical energy conversion process. This can be possibly achieved by examining the SCPC system with different kind of electrode materials, electrolytes, and piezopolymer separator with exceptional properties.[25]

Considering the structural design and essential requirements of an SCPC device, it comprises of an electrode material for energy storage with piezoelectric energy harvesting separator impregnated with the electrolyte for driving the generated power into energy stored via a highly debatable piezo-electrochemical process.[26] Among the electrode materials, MnO_2, carbon, carbon nanotube, NiCoOH/CuO-Cu, rGO/CuO are used in SCPC device, and it is well known that the mechanism of charge storage in these materials is different such as electric double layer capacitance, pseudocapacitance, and Faradic capacitance.[21–24] Further, different types of piezo-polymer separator such as solvent cast PVDF thin films, porous PVDF, porous PVDF-TrFE, and bio-piezoelectric separator from fish swim bladder are used to date. Among the electrolytes, mostly PVA based polymer gel electrolyte (aqueous) is coated on the piezo-polymer separator.[21–24] One of the possible reason for low power to energy conversion process in the SCPC devices might be the use of aqueous electrolyte (H_3PO_4, H_2SO_4, KOH) which might hinder the generated piezoelectric output of the separator since they possess a limited operating potential window of about 1.2 V.[27] On the other hand, the organic electrolytes possess a wide potential window of about 3.0 V with the advantage of being non-aqueous nature which may provide better piezo-electrochemical process, yet, such a study is not performed till date.

In this work, we focused on improving the porous nature of the PVDF film incorporated with the piezoelectric semiconductor material through electrospinning process and also the usage of ionic liquid-based ionogel electrolyte to increase the performance and charging rate of the supercapacitor. Herein, we used the electrospun PVDF/$NaNbO_3$ nanofibrous mat as the piezo separator, PVDF-co-HFP based ionogel as the electrolyte, and 2D-$MoSe_2$ nanosheets as the electrode material for the fabrication of the novel self-charging supercapacitor and investigated its performance metrics in detail.

6.2. Experimental section

6.2.1. Preparation of sodium niobate

A simple hydrothermal technique was employed for the preparation of sodium niobate cubes. [1] Briefly, an aqueous solution of 240 mM sodium hydroxide was prepared in 60 ml of DI water. 3.76 mM of niobium oxide was added to the sodium hydroxide solution and stirred for 1 h until complete dissolution. The prepared solution was then transferred to the 100 ml Teflon lined stainless steel autoclave and kept at 150 °C for 10 h. After the completion of the hydrothermal reaction, the obtained product was centrifuged with doubly distilled water for several times and dried at 80 °C in a hot air oven. The final product was annealed further at 600 °C for 12 h to obtain pure sodium niobate cubes.

6.2.2 Electrospinning of PVDF/$NaNbO_3$ nanofibers for energy harvesting:

The PVDF/$NaNbO_3$ nanofibers were prepared using the Electrospinning system (NanoNC; Model: ESR200R2, South Korea). Briefly, the PVDF polymer solution was prepared by dissolving 10 wt.% of PVDF in 70:30 (v/v) ratio of dimethylacetamide and acetone followed by the addition of 10 wt.% of the $NaNbO_3$ cubes (hydrothermally prepared according to reported work,[28] Section S1 (Supporting Information)) and the entire mixture was allowed to stirring vigorously for 48 h to form white colored viscous solution. After that, the obtained viscous solution was loaded on to a 15 mL syringe with a stainless-steel needle size of 21 G at a flow rate of 0.5 mL h^{-1} under a constant DC voltage of 15 KV with the tip to collector distance of 10 cm to obtain PVDF/$NaNbO_3$ nanofibrous mat. The electrospun energy harvesting PVDF/$NaNbO_3$ nanofibrous mat obtained was dried at 60 °C for 24 h. The piezoelectric properties of the PVDF/$NaNbO_3$ nanofibrous mat with aluminum as top and bottom electrodes was measured under various external mechanical forces with the aid of a linear motor (E1100), and the output voltage was measured using Keithley Electrometer (Model no: 6514).

6.2.3 Preparation of molybdenum diselenide ($MoSe_2$) nanosheets for energy storage:

A hydrothermal method has been employed for the preparation of $MoSe_2$ nanosheets using sodium molybdate, selenium, and sodium borohydride as the precursors.[50,51] Initially, a stoichiometric amount of selenium (1.24 g) was dissolved in the 40 mL solution containing sodium borohydride (0.2 g) and stirred until the formation of a red colored solution. Subsequently, a stoichiometric amount of sodium molybdate (1.32 g) was dissolved in 40 mL of doubly distilled water separately and mixed with the solution containing selenium and sodium borohydride. Finally, the mixed solution is transferred into 100 mL Teflon-lined stainless-steel autoclave, and the hydrothermal reaction was carried out at 180 °C for 48 h. Upon completion of the reaction, the autoclave is cooled down to room temperature naturally, and the black precipitates of $MoSe_2$ were collected and washed with doubly distilled water followed by absolute ethanol and dried at 70 °C overnight. Further, the obtained powders were calcined at 650 °C for 5 h under Ar atmosphere and cooled to room temperature naturally which results in the formation of well crystalline $MoSe_2$ nanosheets.

6.2.4 Preparation ionogel electrolyte:

The ionogel electrolyte was prepared using PVDF-co-HFP and $TEABF_4$ as reported in the literature.[52] Briefly, 1 g of PVDF-co-HFP is dissolved in 10 mL of 70:30 (v/v) ratio of dimethylacetamide and acetone using vigorous stirring to form a homogeneous solution. To the obtained solution, 1 g of $TEABF_4$ was added and allowed to vigorous stirring under heat until a transparent gel was formed.

6.2.5 Fabrication and testing of $MoSe_2$ self-charging supercapacitor power cell (SCSPC) device:

The $MoSe_2$ electrodes for the SCSPC device were prepared using a slurry coating method as reported in our previous work. [53] Briefly, the electroactive material ($MoSe_2$), carbon black and PVDF in the ratio of 85:10:5 was ground using NMP as a dispersant in an

agate mortar until a uniform slurry was formed. Then, the slurry was coated on to a stainless-steel coin cell substrate (15.4 mm x 0.2 mm) and allowed to dry at 80 °C for 12 h. The $MoSe_2$ SCSPC device was fabricated using $MoSe_2$ coated stainless electrode, PVDF/$NaNbO_3$ as a piezo separator with PVDF-co-HFP/$TEABF_4$ as the ionogel electrolyte. After assembling the electrodes in the CR2032 coin cell case, the coin cell was crimped using electric coin cell crimping and disassembling machine (MTI Korea). The assembling of the symmetric SCSPC device was done in the argon filled glove box to avoid the reaction of electrolyte in the atmosphere. The electrochemical performance of the fabricated $MoSe_2$ SCSPC device such as cyclic voltammetry (CV), galvanostatic charge-discharge (CD) and electrochemical impedance spectroscopy (EIS) analysis was performed using an Autolab PGSTAT302N electrochemical workstation. The self-charging behavior of the $MoSe_2$ SCSPC device was measured under an external mechanical force applied to the $MoSe_2$ SCSPC device with the aid of a linear motor (E1100).

6.3. Results and discussion

6.3.1 Physicochemical characterization of Energy harvester material

The X-ray diffraction pattern (Figure 6.1) of the hydrothermally prepared $NaNbO_3$ which shows the presence of sharp diffraction peaks matched well with the standard diffraction pattern of $NaNbO_3$ (JCPDS no.: 82-0606).[28] The diffraction peaks obtained at 22.94°, 32.75°, 46.8°, 52.67°, 58.11°, 68.2°, 72.85°, and 77.41° corresponds to the (020), (121)/(002), (040), (141), (042), (004), (024)/(143), and (204) planes of the $NaNbO_3$ cubes with a space group of *P21ma*.

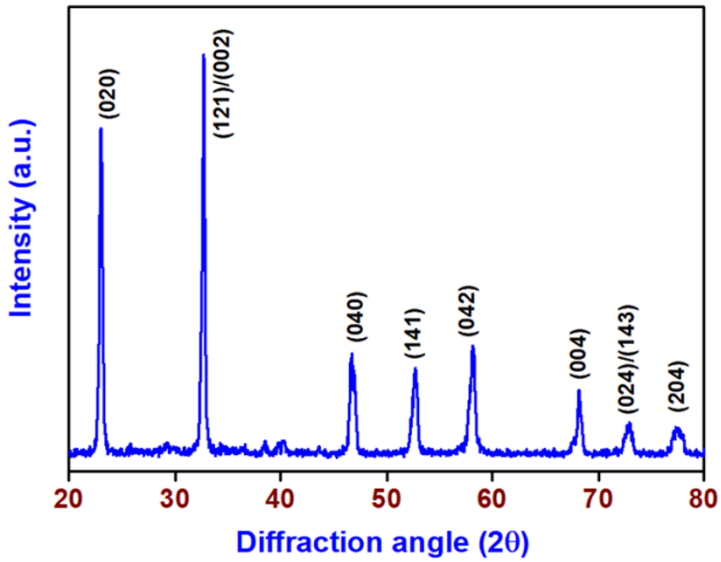

Figure 6.1. X-ray diffraction pattern of the prepared $NaNbO_3$ nanocubes

The laser Raman spectrum of the bare PVDF and $NaNbO_3$/PVDF fibrous mat is provided in Figure 6.2 (A). The Raman spectrum of the bare electrospun PVDF nanofibrous mat indicated the presence of major vibrational bands observed at 795, 838, and 880 cm^{-1} respectively.[29] The bands observed at 795 and 880 cm^{-1} corresponds to the α phase of PVDF whereas the prominent band observed at 838 cm^{-1} correspond to the β phase of PVDF.[30] The origin of β phase in the electrospun PVDF nanofibrous mat is due to the electrical poling during the spinning process under a constant DC voltage of 15 KV. The prepared $NaNbO_3$ shows all the characteristics vibrational bands of ferroelectric $NaNbO_3$ cubes and well matched with the reported literature.[31,32] The Raman spectrum of the $NaNbO_3$/PVDF nanofibrous mat shows the bands observed at 115, 140, 175, 198, 224, 246, 276, 428, 571, 612, and 870 cm^{-1} all corresponds to the band vibration of ferroelectric $NaNbO_3$ cubes.[32] The presence of a band at 615 cm^{-1} (ν_1) accompanied by a shoulder at around 571 cm^{-1} (ν_2) confirms the orthorhombic perovskite structure of the $NaNbO_3$ cubes present in the piezo-polymer-separator.[28] Further, the vibration bands due to PVDF are not observed in the Raman spectrum of the $NaNbO_3$/PVDF nanofibrous mat since the strong vibration bands arise from crystalline $NaNbO_3$ cubes overwhelms the weak vibrations bands from the PVDF.

This is in agreement with the previous studies on the Raman spectrum of nanomaterial impregnated polymer nanocomposites.[33]

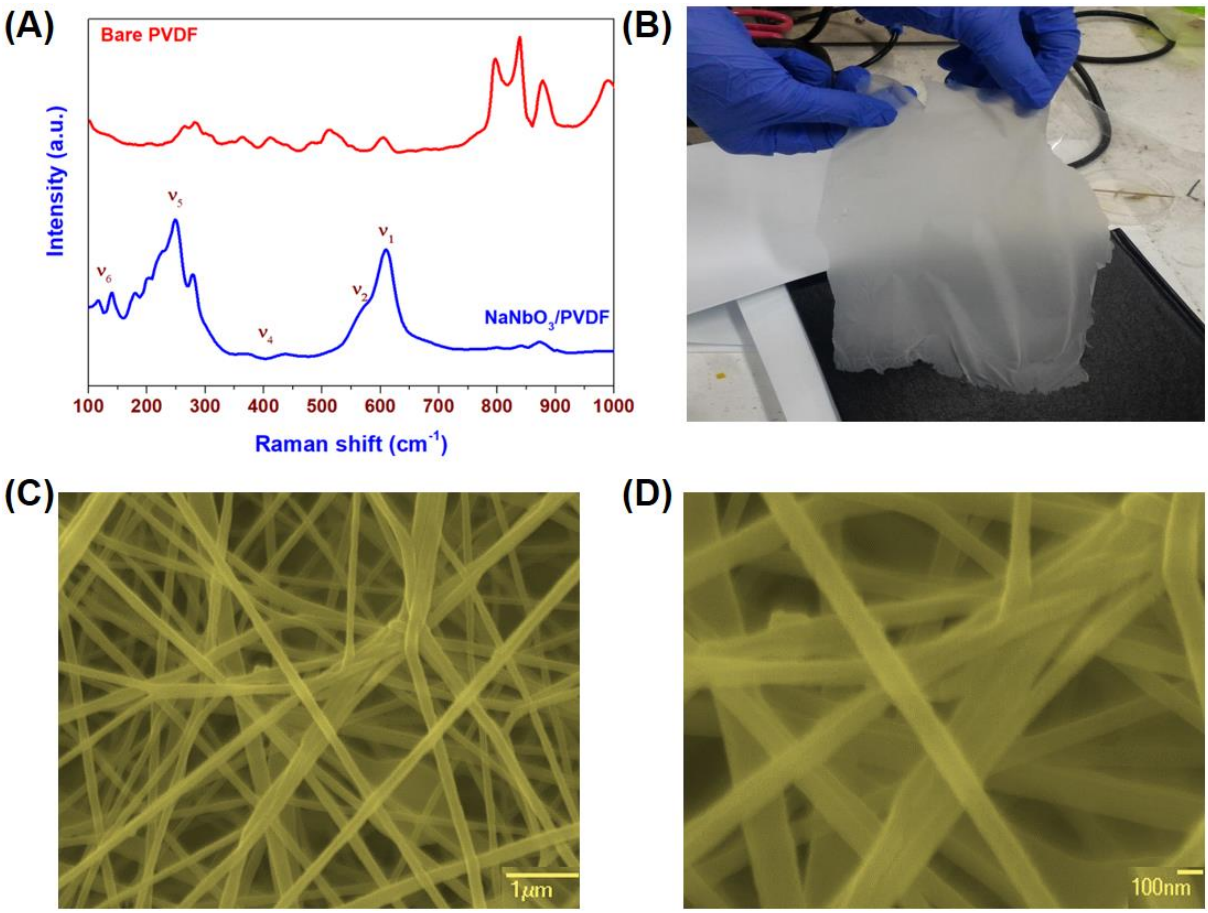

Figure 6.2. Physico-chemical characterization of the prepared $NaNbO_3$ cubes. (A) laser Raman spectra for the electrospun bare PVDF and $NaNbO_3$/PVDF nanofibrous separator, (B) Digital photograph of the electrospun $NaNbO_3$/PVDF nanofibrous separator, FE-SEM micrograph of the electrospun $NaNbO_3$/PVDF (C) low-resolution image, and (D) high-resolution image.

The $NaNbO_3$ cubes are used to prepare a piezo polymer-separator for the SCSPC device by impregnating $NaNbO_3$ cubes in a PVDF matrix followed by electrospinning. The digital micrograph of the freestanding electrospun $NaNbO_3$/PVDF fibrous mat (approximately 10×12 cm^2) is shown in Figure 6.2 (B). The FE-SEM micrograph shown in

Figure 6.2(C and D) shows the formation of the $NaNbO_3$/PVDF nanofibrous mat with a diameter of 500 nm.

6.3.2 Energy harvester analysis

Figure 6.3 shows the piezoelectric characteristics of the electrospun $NaNbO_3$/PVDF nanofibrous separator in comparison with the bare PVDF fibers using aluminum as the top and bottom electrode given in the inset of Figure 6.3(A).

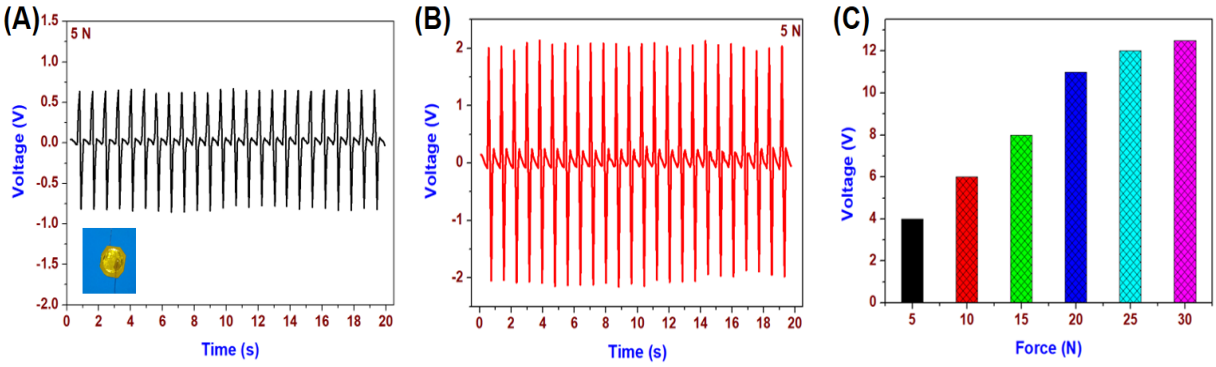

Figure 6.3. Piezoelectric characterization of the electrospun PVDF and $NaNbO_3$/PVDF nanofibrous separator. (A) open circuit voltage profile of the bare PVDF nanogenerator under a compressive force of 5 N. Inset of (A) shows the digital micrograph of the piezoelectric nanogenerator using $NaNbO_3$/PVDF nanofibrous separator with aluminum as top and bottom electrode, (B) open circuit voltage of the electrospun $NaNbO_3$/PVDF nanofibrous separator under compressive force of 5 N, and (C) comparison of the open circuit voltage (Voc) of the $NaNbO_3$/PVDF device under various compressive force.

The comparative piezoelectric characteristics of the bare and $NaNbO_3$/PVDF using a periodic force of 5 N is given in Figure 6.3 (A and B). The open circuit voltage (V_{oc}) of the bare electrospun PVDF nanofibrous separator shows a peak to peak voltage of about 1.2 V under a force of 5 N. Under the applied compressive force, the piezoelectric field is generated across the compressive and tensile surface of the nanofibrous mat which results in the output voltage of 1.2 V. Figure 6.3 (B) represents the piezoelectric response of the electrospun

$NaNbO_3$/PVDF nanofibrous mat which shows a significant improvement in the piezo output compared to the bare PVDF.

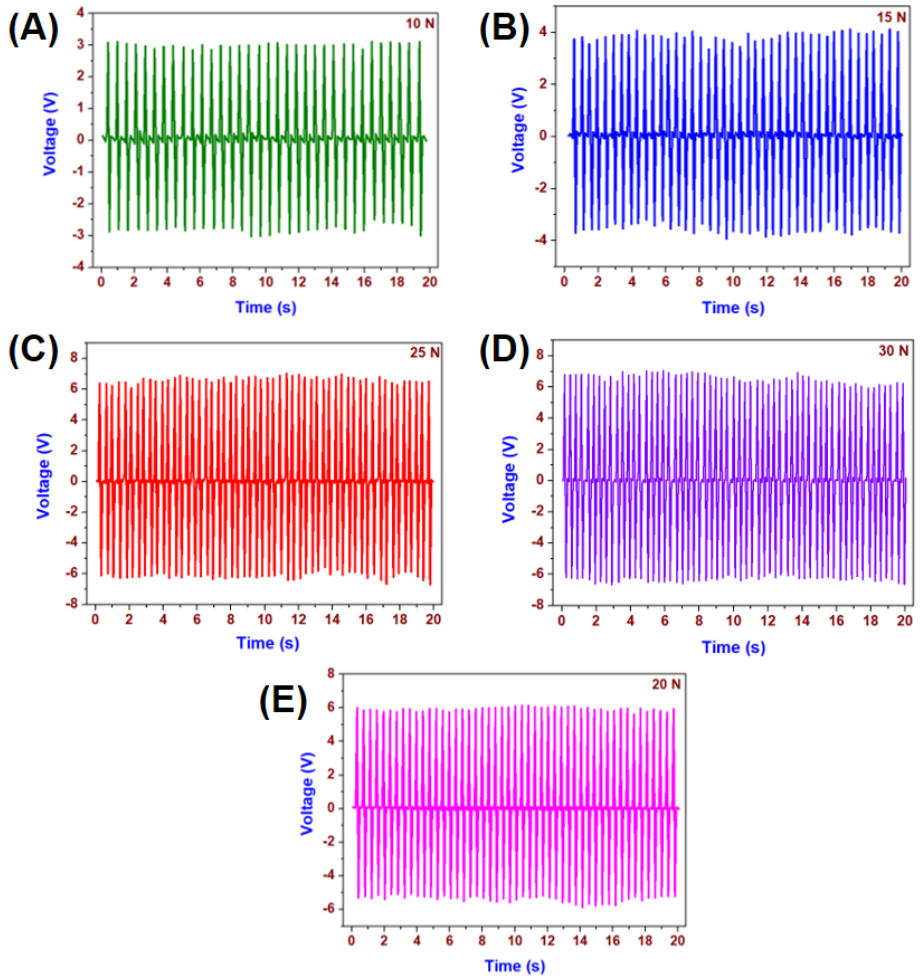

Figure 6.4. (A-E) Piezoelectric open circuit voltage of the electrospun $NaNbO_3$/PVDF nanofibrous separator under various compressive force ranging from 10 to 30 N.

A peak to peak voltage of about 4 V has been achieved for the $NaNbO_3$/PVDF nanofibrous mat. The improved piezo-response of the composite mat is attributed due to the presence of crystalline $NaNbO_3$ in the piezopolymer fibers.[34,35] Figure 6.4 (A-E) represents the piezo-response of the $NaNbO_3$/PVDF nanofibrous separator measured under various applied compressive forces from 10 to 30 N. It clearly evidences that the output piezo-voltage is highly depended on the applied compressive force and directly proportional to it. Figure 6.3 (C) shows the effect of compressive force on the piezo-response of the $NaNbO_3$/PVDF

nanofibrous separator. It shows that the output voltage of $NaNbO_3$/PVDF nanofibrous separator is increased about 3-fold with an increase in five-fold compressive force.

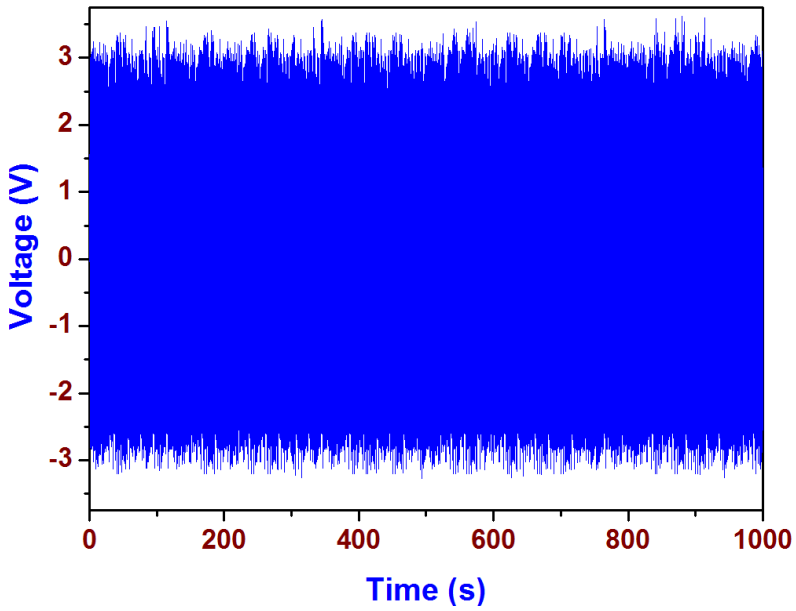

Figure 6.4. Output voltage of piezo-polymer separator under 10 N compressive force demonstrating the stability of the separator

Figure 6.4 shows the mechanical stability of the $NaNbO_3$/PVDF nanofibrous separator at a compressive force of 10 N for 1000 seconds. It showed that the initial peak to peak voltage of the separator is retained after 1500 cycles, thus, suggesting the better mechanical stability of the $NaNbO_3$/PVDF nanofibrous separator. These results highlight that the electrospun $NaNbO_3$/PVDF nanofibrous separator enhanced piezoelectric output will be a promising candidate as a piezo-polymer separator in the fabrication of SCSPC.

6.3.3 Physicochemical characterization of Energy storage material

Figure 6.5 (A) shows the X-ray diffraction pattern of the hydrothermally prepared $MoSe_2$ nanosheets. The presence of sharp diffraction peaks at 13.53°, 27.65°, 31.55°, 37.79°, 41.67°, 47.10°, 53.44°, 55.99°, 57.74°, 65.93°, 69.84°, 72.27° and 76.67°, which corresponds to the (002), (004), (100), (103), (006), (105), (106), (110), (112), (200), (203), (116) and (205) planes of 2H-$MoSe_2$ with a space group D^4_{6h} (*P63/mmc*) (JCPDS No.29-0914).[36]

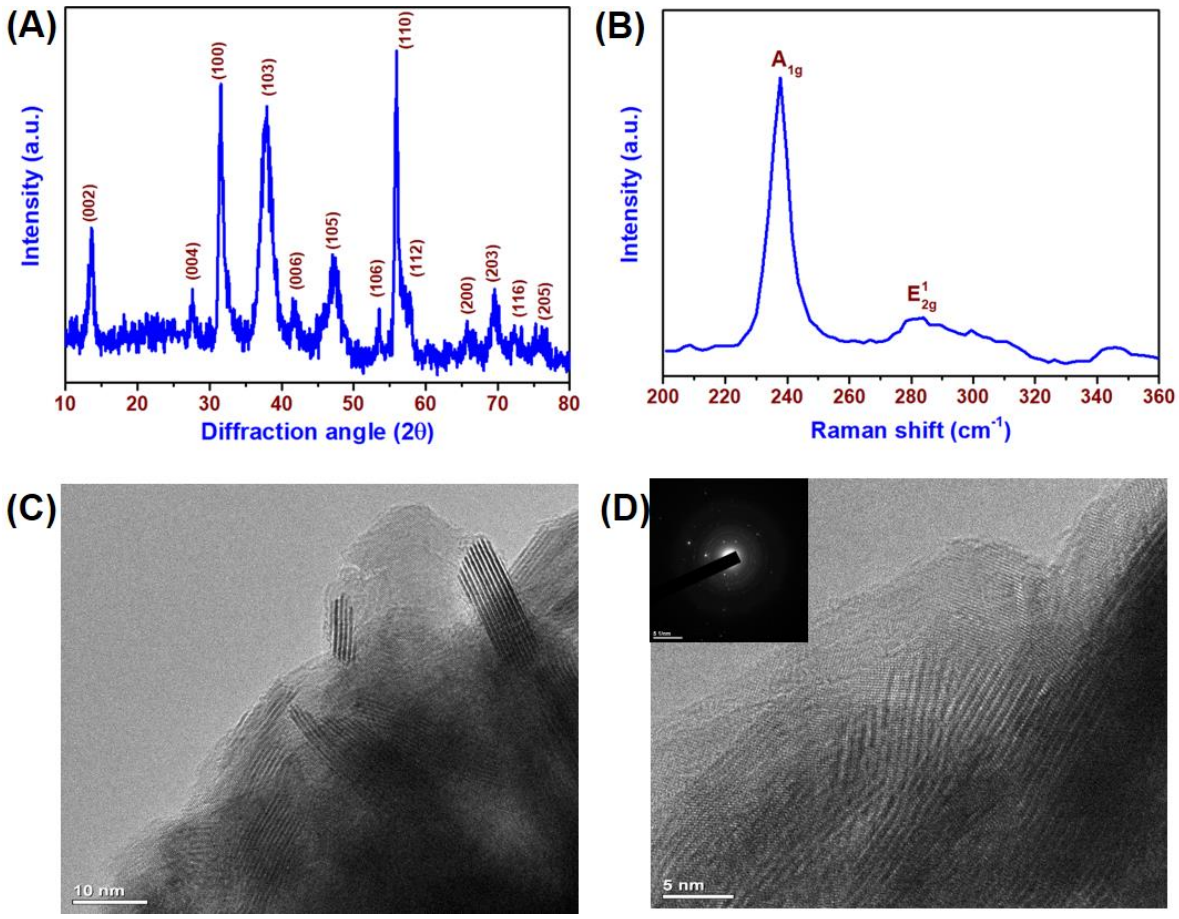

Figure 6.5. Physicochemical characterization of the prepared $MoSe_2$. (A) X-ray diffraction pattern of the $MoSe_2$ nanosheets. (B) laser Raman spectrum of the $MoSe_2$ nanosheets. (C-D) Low and high-resolution HR-TEM images and inset in (D) shows the SAED pattern of the $MoSe_2$ nanosheets.

The laser Raman spectrum of the $MoSe_2$ sheets is given in Figure 6.5 (B) which shows the presence of a sharp band at 238 cm^{-1} and a relatively broad weakened band in the region 282 to 285 cm^{-1}, respectively. The band observed at 238 cm^{-1} is due to the A_{1g} mode which associated with the vibrations (out-of-plane) of selenium atoms in opposite directions, whereas the band observed at 282 to 285 cm^{-1} corresponds to the E^1_{2g} mode in which the vibrations (in-plane) of two selenium atoms with the molybdenum atom.[37] The observed Raman bands of $MoSe_2$ nanosheets is in good agreement with the previous findings. The surface morphology of the prepared $MoSe_2$ nanosheets was examined using FE-SEM and

HR-TEM analysis. Figure 6.5(C and D) represents the HR-TEM micrographs of the $MoSe_2$ with different magnifications which showed the presence of sheet-like $MoSe_2$ overlapping with each other. The high magnification micrograph is shown in Figure 3 (D) represents the few layered $MoSe_2$ sheets with little disorder arise due to the heat treatment at a high temperature which is in agreement with the earlier report by Ambrosi et al.[38] The SAED pattern of $MoSe_2$ sheets is provided in the inset of Figure 6.5 (D) which shows the presence of crystalline diffraction spots corresponds to the hexagonal crystal structure of the $MoSe_2$ nanosheets.[39]

6.3.4 Electrochemical characterization of Energy storage

The SCSPC device was fabricated using the prepared $MoSe_2$ nanosheets as electrode material with PVDF-co-HFP/$TEABF_4$ ion gelled PVDF/$NaNbO_3$ as the piezopolymer separator. Initially, the energy storage and power delivering capabilities of the fabricated $MoSe_2$ SCSPC device has been examined using cyclic voltammetry, galvanostatic charge-discharge analysis, and electrochemical impedance spectroscopy. At first, we recorded the CV profiles in the various operating potential window (OPW) from ± 0.5 to ± 3.0 V (shown in Figure 6.6(A)) using a scan rate of 100 mV s^{-1}, to understand the polarization of the device, and the electrochemical stability of $MoSe_2$ electrodes.[40] The shape of the CV profiles shown in Figure 6.6(A) revealed the quasi-rectangular nature with the tested operating potential windows from ± 0.5 to ± 3.0 with little sign of evolution at higher potentials (as observed by the current leap at a potential above ± 2.0 V). Further, the obtained current range is increasing with increase in OPW suggesting the ideal capacitive nature of the $MoSe_2$ SCSPC device. This study clearly evidences that the $MoSe_2$ SCSPC device can operate over a potential window of ±2.0 V with excellent electrochemical reversibility without a sign of any evolution.

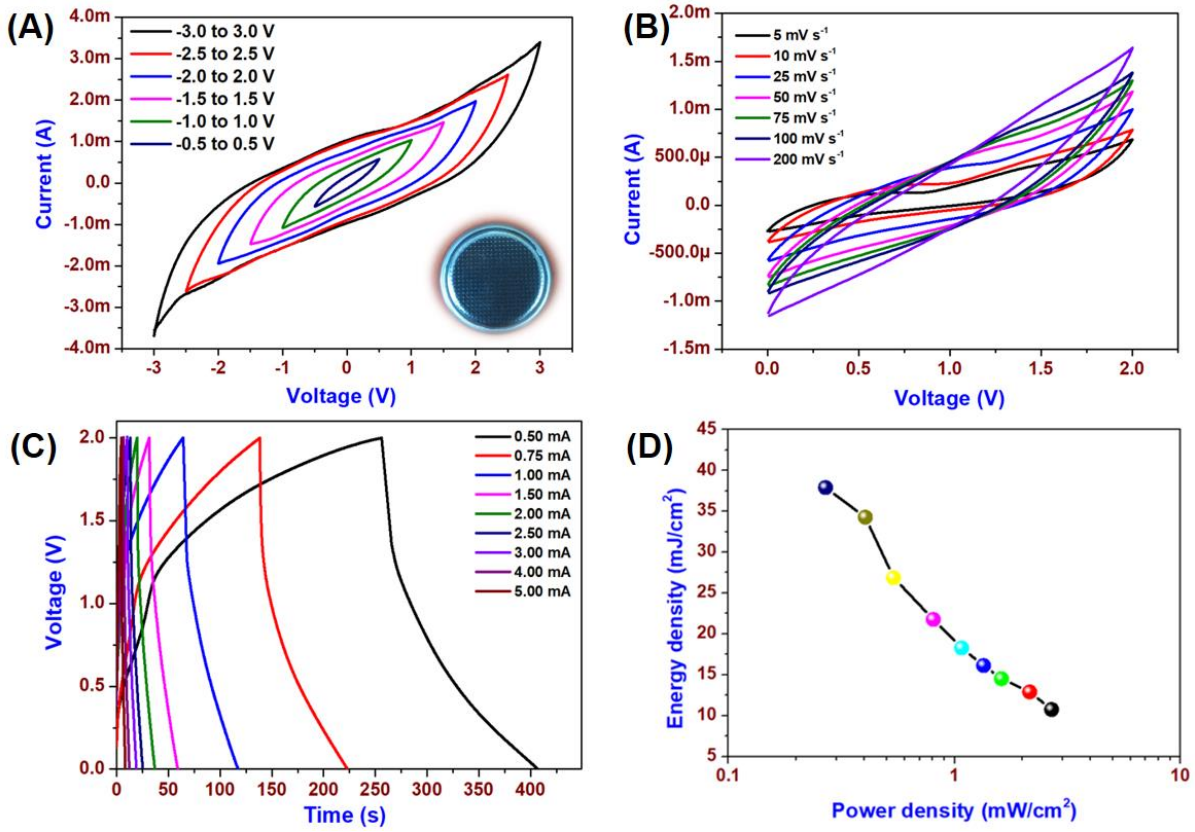

Figure 6.6. Electrochemical characterization of the $MoSe_2$ SCSPC device. (A) Cyclic voltammetry profiles of the $MoSe_2$ SCSPC device with different operating potential windows (± 0.5 to ± 3.0 V) measured at a scan rate of 100 mV s^{-1}. (B) Cyclic voltammetry profiles of the $MoSe_2$ SCSPC device measured at an operating voltage of 0 to 2.0 V measured at the various scan rate. (C) Galvanostatic charge-discharge profile of the $MoSe_2$ SCSPC device measured at various current ranging from of 0.5 to 5 mA. (D) Ragone plot for the $MoSe_2$ SCSPC device.

Figure 6.6 (B) shows the CV curve of the $MoSe_2$ SCSPC device with the OPW of 0.0 to 2.0 V measured at different scan rate from 5 to 200 mV s^{-1}. The CV curve shows the quasi-rectangular shape curve with small redox peak appears which suggest the pseudocapacitive nature of the $MoSe_2$ electrodes via ion intercalation/de-intercalation phenomenon. [41] The shape of the CV curves maintains the quasi-rectangular behavior at all the scan rates suggesting the ideal capacitive nature of the $MoSe_2$ electrode. The increase in the current

range of the CV profile with an increase in scan rate from 5 to 200 mV s^{-1} suggests the excellent capacitive property of the $MoSe_2$ SCSPC device. The charge storage mechanism might be attributed as a combination of double layer capacitance and/or intercalation capacitance of the $MoSe_2$ electrode materials.[42,43] A specific capacitance of 22.76 mF cm^{-2} was obtained for the $MoSe_2$ SCSPC device from CV analysis measured at a scan rate of 5 mV s^{-1}. The $MoSe_2$ SCSPC device delivered a specific capacitance of 2.98 mF cm^{-2} when the scan rate is increased to 100 mV s^{-1}. Higher scan rates resulted in low specific capacitance for the $MoSe_2$ SCSPC device which is due to the restriction in mass transport of the electrolyte ions to the inner part of the electrode materials and is in agreement with the reported literature.[44] The electrochemical impedance spectroscopy analysis of the $MoSe_2$ SCSPC device was performed over the frequency 0.01 Hz to 100 kHz at an amplitude of 10 mV, to examine the fundamental charge-transfer kinetics occurred at the electrode/electrolyte interfacial region. Figure 6.7 (A) shows the Nyquist plot of $MoSe_2$ SCSPC device which represents the presence of three characteristic regions viz (i) high frequency, (ii) intermediate frequency and (iii) low-frequency regions.[45] The equivalent series resistance (*ESR*) of the $MoSe_2$ SCSPC device is about 8.43368 Ω from the Nyquist plot, and the high-frequency region shows the presence of a small semicircle corresponding to the charge transfer resistance (of about 589 Ω) of the electrode-electrolyte interface. The observed higher charge-transfer resistance is due to the use of ionogel electrolyte which possesses high resistance compared to the ionic liquid electrolyte.[46]

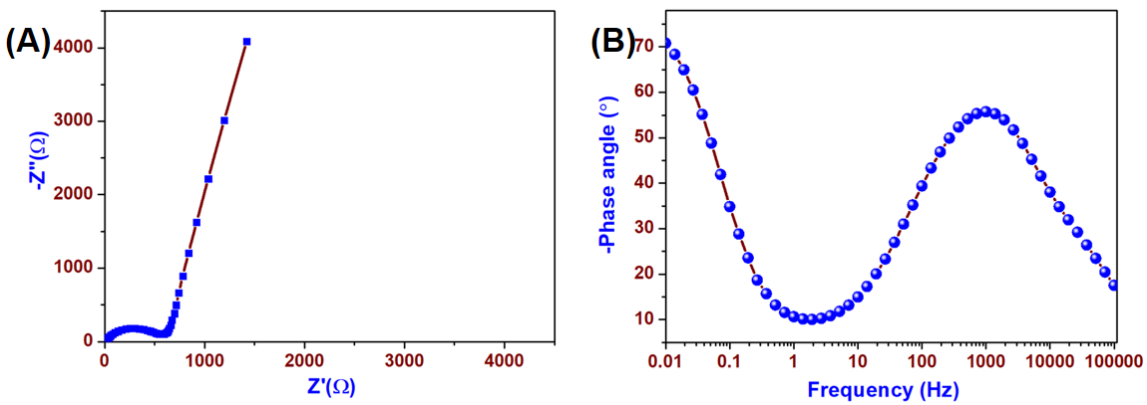

Figure 6.7. (A) The Nyquist plot and (B) Bode phase angle plot of the $MoSe_2$ SCSPC device.

The intermediate frequency region shows the transition point between the high and low-frequency region, and it is denoted as "Knee frequency" which is found to be about 1.38 Hz Ω. The high-frequency region shows the presence of a straight line or Warburg line at the low-frequency region almost parallel to the imaginary axis (related to the frequency dependent ion diffusion kinetics).[47,48] The Bode phase angle plot is given in Figure 6.7 (B) shows that the phase angle at the tail is about -70.83 º which highlights the pseudocapacitive nature of the $MoSe_2$ SCSPC device. The galvanostatic charge-discharge analysis was performed for the $MoSe_2$ SCSPC device measured over the potential window of 0 to 2 V using a constant current of 2.5 mA is shown in Fig S9 (A). The CD profiles display nearly triangular shaped charge-discharge curves which are in agreement with the CV curves suggesting the ideal capacitive nature of the $MoSe_2$ SCSPC device. Figure 6.6 (C) shows the CD profiles of the $MoSe_2$ SCSPC device measured at various current ranging from 0.5 to 5.0 mA. The CD curves show symmetric behavior over all the current ranges measured for the $MoSe_2$ SCSPC device. It is evident from the Figure 6.6 (C) that the high current results in fast charging and discharging time whereas at the lower current produced better charging and discharging profiles in the $MoSe_2$ SCSPC device. The specific capacitance of 18.93 mF cm^{-2} was calculated from the CD profile measured at a constant discharge current of 0.5 mA. At a

higher current of 5 mA, the $MoSe_2$ SCSPC device delivered a capacitance of 5.37 mF cm^{-2} with an increase of almost 10-fold in current, thus suggesting the better rate capability of the $MoSe_2$ SCSPC device. Figure 6.6 (D) represents the Ragone plot of the $MoSe_2$ SCSPC device which shows a high energy density of 37.90 mJ cm^{-2} at a specific power density of 268.91 µW cm^{-2} obtained using at a constant current of 0.5 mA. With an increase of ten-fold in current range, the device delivered an energy density of 10.75 mJ cm^{-2} at a power density of 2.68563 mW cm^{-2}, suggesting a good rate capability of the device.

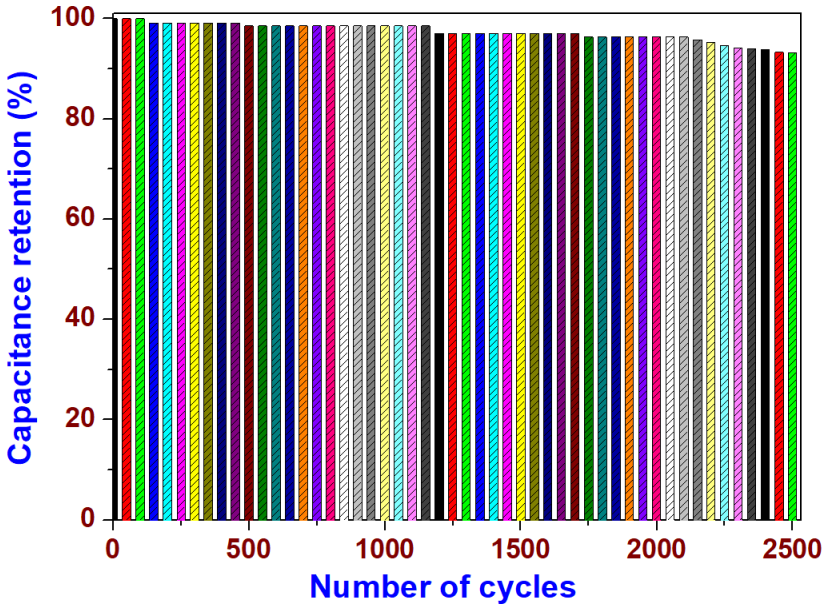

Figure 6.8. Cyclic stability of the $MoSe_2$ SCSPC device

The $MoSe_2$ SCSPC device were examined for their cyclic performance and it retained almost 91 % of its initial capacitance over 2500 cycles (Figure 6.8).

6.3.5 Self-charging characteristics

The self-charging performance of the $MoSe_2$ SCSPC device with PVDF-co-HFP/$TEABF_4$ ion gelled PVDF/$NaNbO_3$ as the piezopolymer separator sealed in 2016 stainless steel coin cell is evaluated under the applied periodic compressive force. When the $MoSe_2$ SCSPC device is subjected to a compressive force of 5 N, the potential of the SCSPC device increases from 109 to 319 mV in a duration of 100 s (shown in Figure 6.9 (A)).

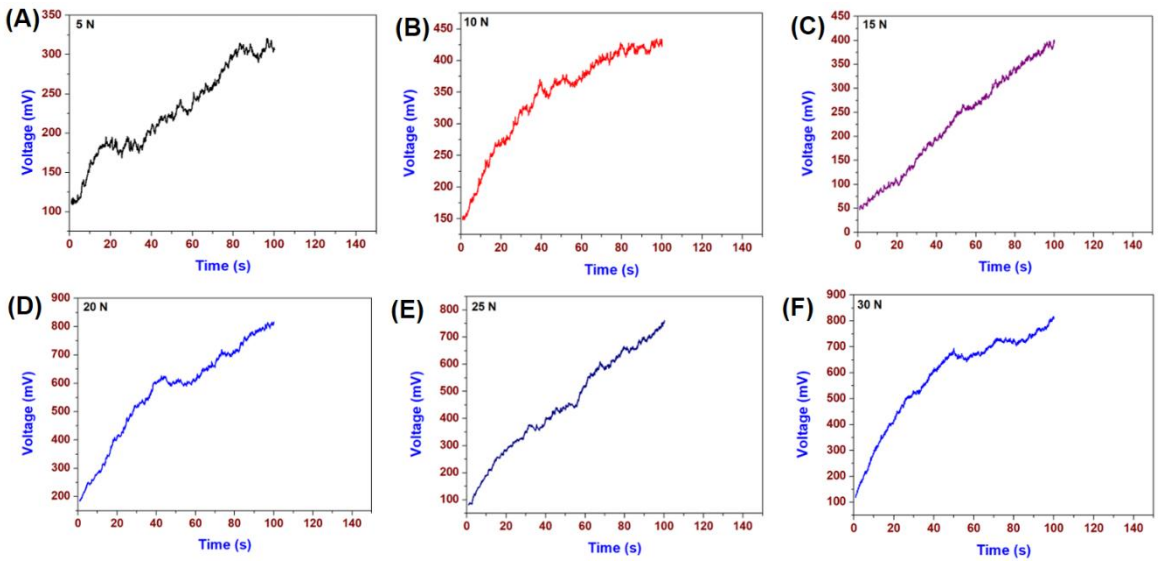

Figure 6.9. (A-F) The self-charging behavior of the fabricated $MoSe_2$ SCSPC device subjected to various applied compressive force ranging from 5 to 30 N for a time period of 100 s.

The SCSPC device charged to a voltage of 210 mV under a compressive stress of 5 N. After the self-charging process, the device is discharged to its original state via discharging using a constant discharge current. Figure 6.9 (B-F) (Supporting Information) shows the self-charging behavior of the $MoSe_2$ SCSPC device under various applied compressive forces. When the applied compressive force of 10, 15, 20, 25 and 30 N is applied, the $MoSe_2$ SCSPC device charged to 280, 355, 633, 680, and 708 mV in 100 s respectively. The increase in the applied compressive force enhances the self-charging performance of the SCSPC device which is due to the piezoelectric output increases with increase in the force/strain applied.[49] Figure 6.10 (A) shows the self-charging behavior of the $MoSe_2$ SCSPC device with a semilinear charging voltage plateau. The voltage of the $MoSe_2$ SCSPC device increases from 85 to 680 mV under an applied compressive force of 25 N within 100 s, and the device was discharged at a constant current of 0.5 mA. The comparison of the charging voltage against

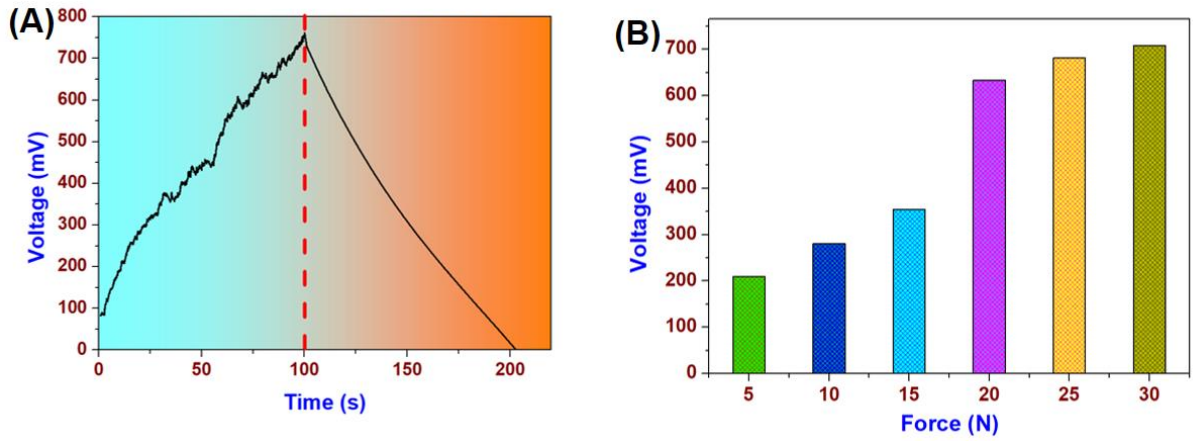

Figure 6.10. (A) Self-charging profile of the $MoSe_2$ SCSPC device under an applied compressive force of 25 N charged for 100 seconds and discharged at a constant current. (B) Comparison of the charging voltage of the $MoSe_2$ SCSPC device under various applied compressive force.

the applied compressive force is provided in Figure 6.10 (B). It is evident that the charging voltage of the SCSPC device is directly proportional to the applied compressive force to the SCSPC device. Under an applied compressive force of 5 N the device is charged to 210 mV whereas, at the higher compressive force of 30 N, the device charged to 708 mV under constant time duration of 100 s.

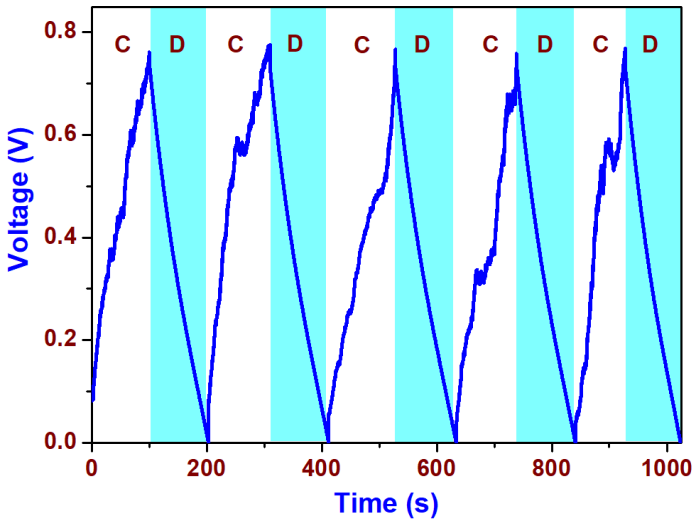

Figure 6.11. Self-charging performance of $MoSe_2$ SCSPC device over 5 consecutive cycles using a compressive force of 25 N.

This result indicates the self-charging process of the SCSPC is directly related to inputting mechanical energy applied to the SCSPC device. The voltage of the SCSPC increases under increasing compressive force, and with no applied force, then there is no charging process occurred.[16] Figure 6.11 showed the self-charging behavior of the fabricated SCSPC device subjected to a compressive force of 25 N and discharged at a constant discharge current of 0.5 mA over five consecutive cycles. It showed that the device maintains the consistent self-charging capability of the $MoSe_2$ SCSPC device over repeated cycles under a compressive force of 25 N.

The working mechanism of the SCSPC devices based on battery and supercapacitors are still under debate, and it can be explained on the basis of piezo-electrochemistry with the use of Nernst equation (relation between electrolyte ions and electrode potential). The self-charging performance of the $MoSe_2$ SCSPC device is more likely due to the piezoelectric driven electrochemical process occurred at the interfacial surface between the electrospun PVDF/$NaNbO_3$ nanofibrous mat (gelled with PVDF-co-HFP/$TEABF_4$ ionogel) and the 2D $MoSe_2$ electrodes under applied compressive force, as shown in Figure 6.12 (A). At the initial stage, the SCSPC device is at the equilibrium state due to the absence of electrochemical reaction between the electrode and electrolyte (as shown in Figure 6.12 (A)). Figure 6.12 (B) shows the state of the SCSPC under a compressive force is applied on to the device which results in the generation of piezoelectric potential across the PVDF/$NaNbO_3$ mat. This, in turn, results in the re-distribution of electrolyte ions (TEA^+ and BF_4^- ions) followed by the accumulation of charge at the electrode surface which is based on the Nernst equation.[22] Further, the presence of porous nature in the electrospun nanofibrous piezo-polymer separator also provide ionic conduction pathways for the migration of ions on the electrode surface due to the generated piezo potential under compressive force. This process results in the storage of energy at the $MoSe_2$ electrode surface via a combination of both double layer capacitance

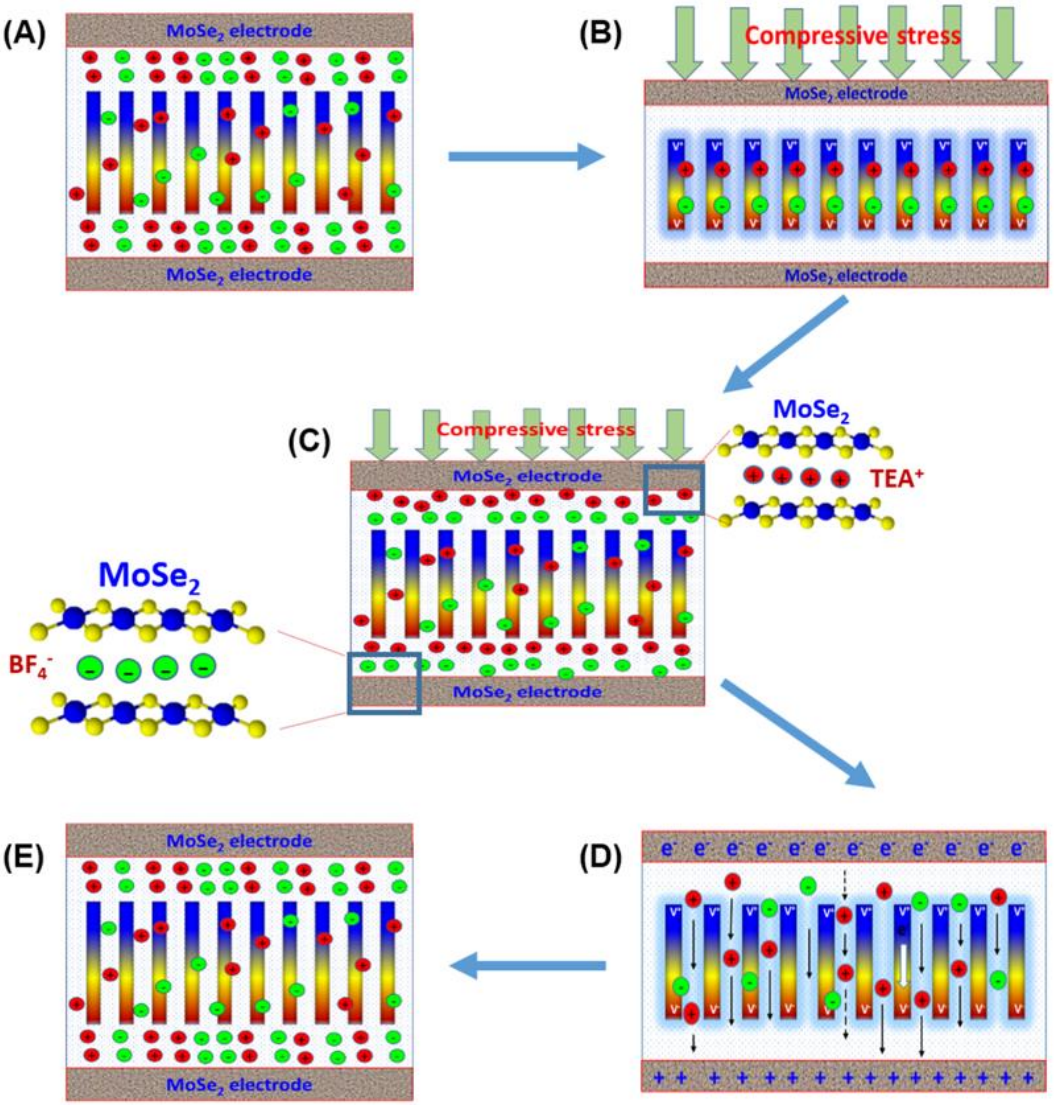

Figure 6.12. Schematic illustration for the working mechanism of the self-charging of $MoSe_2$ SCSPC device. (A) The initial state of the $MoSe_2$ SCSPC device with no applied compressive force. (B) With an applied compressive force to the $MoSe_2$ SCSPC device, the $NaNbO_3$/PVDF creates a piezoelectric potential which drives the migration of electrolyte ions. (C) the electrolyte ions drive towards the electrode and electrochemical intercalation of ions in the $MoSe_2$ electrode. (D) An equilibrium state has been reached between the piezoelectric potential created and the electrochemical reaction of the $MoSe_2$ SCSPC device. (E) Completion of one self-charging cycle with the compressive force applied is released, and the piezoelectric potential disappeared, and the electrolyte ions reach the equilibrium state.

and pseudocapacitance due to ion intercalation and de-intercalation process as seen in Figure 6.12 (C). When the compressive force is removed from the SCSPC, the piezoelectric field in the PVDF/$NaNbO_3$ disappears, and a number of electrolyte ions migrate back to the electrode, and the distribution of ions reaches the balance point again as shown in Figure 6.12 (D and E). The whole self-charging process is completed, and the mechanical energy is converted and stored as electrochemical energy in the SCSPC.[21] When the compressive force is applied again repeatedly on the SCSPC device again, the self-charging process is repeated. Keeping the mechanistic investigation aside and considering the performance of the fabricated SCSPC device, it showed enhanced piezo-electrochemical performance comparatively with the reported works on supercapacitors which might be attributed to the non-fluidity, stable chemical/physical characteristics, and considerable piezoelectric output of the solid piezo-ionogel electrolyte with nanofibrous web-like structure.

6.4. Conclusion

In conclusions, we demonstrated the fabrication of SCSPC device using $MoSe_2$ electrodes PVDF-co-HFP/$TEABF_4$ ion gelled electrospun PVDF/$NaNbO_3$ nanofibrous mat based piezo-polymer separator. The fabricated SCSPC device is capable of harvesting the mechanical energy simultaneously and storing them as electrical energy with excellent self-charging performance compared to the reported SCSPC. The better performance of the fabricated SCSPC devices might be due to the three factors (i) intercalative type $MoSe_2$ energy storing electrode, (ii) porous and nanofibrous web-like structured electrospun PVDF/$NaNbO_3$ mat and (ii) the use of ionogel electrolyte. The collective experimental findings demonstrated that the fabricated SCSPC device is capable of converting the mechanical energy into electrical energy with high charging rates which can be suitable for the development of next-generation self-powered systems for portable electronics applications.

6.5 References

[1] L. Yuan, X. Xiao, T. Ding, J. Zhong, X. Zhang, Y. Shen, B. Hu, Y. Huang, J. Zhou, Z. L. Wang, *Angew. Chemie - Int. Ed.* **2012**, *51*, 4934.

[2] X. Xue, S. Wang, W. Guo, Y. Zhang, Z. L. Wang, *Nano Lett.* **2012**, *12*, 5048.

[3] X. Xiao, T. Li, P. Yang, Y. Gao, H. Jin, W. Ni, W. Zhan, X. Zhang, Y. Cao, J. Zhong, L. Gong, W.-C. Yen, W. Mai, J. Chen, K. Huo, Y.-L. Chueh, Z. L. Wang, J. Zhou, *ACS Nano* **2012**, *6*, 9200.

[4] P. Yang, X. Xiao, Y. Li, Y. Ding, P. Qiang, X. Tan, W. Mai, Z. Lin, W. Wu, T. Li, H. Jin, P. Liu, J. Zhou, C. P. Wong, Z. L. Wang, *ACS Nano* **2013**, *7*, 2617.

[5] P. Pazhamalai, K. Krishnamoorthy, S. -J. Kim, *Int. J. Hydrogen Energy* **2016**, *41*, 14830.

[6] X. Pu, M. Liu, L. Li, C. Zhang, Y. Pang, C. Jiang, L. Shao, W. Hu, Z. L. Wang, *Adv. Sci.* **2015**, *3*, 1.

[7] X. Pu, L. Li, H. Song, C. Du, Z. Zhao, C. Jiang, G. Cao, W. Hu, Z. L. Wang, *Adv. Mater.* **2015**, *27*, 2472.

[8] K. Dong, Y.-C. Wang, J. Deng, Y. Dai, S. L. Zhang, H. Zou, B. Gu, B. Sun, Z. L. Wang, *ACS Nano* **2017**, 11, 9490.

[9] J. Luo, F. R. Fan, T. Jiang, Z. Wang, W. Tang, C. Zhang, M. Liu, G. Cao, Z. L. Wang, *Nano Res.* **2015**, *8*, 3934.

[10] Y. Song, X. Cheng, H. Chen, J. Huang, X. Chen, M. Han, Z. Su, B. Meng, Z. Song, H. Zhang, *J. Mater. Chem. A* **2016**, *4*, 14298.

[11] X. Cao, Y. Jie, N. Wang, Z. L. Wang, *Adv. Energy Mater.* **2016**, *6*, 1600665.

[12] K. Krishnamoorthy, P. Pazhamalai, S. Sahoo, J. H. Lim, K. H. Choi, S. -J. Kim, *ChemElectroChem* **2017**, *4*, 3302.

[13] R. Liu, J. Wang, T. Sun, M. Wang, C. Wu, H. Zou, T. Song, X. Zhang, S.-T. Lee, Z. L.

Wang, B. Sun, *Nano Lett.* **2017**, *17*, 4240.

[14] A. P. Cohn, W. R. Erwin, K. Share, L. Oakes, A. S. Westover, R. E. Carter, R. Bardhan, C. L. Pint, *Nano Lett.* **2015**, *15*, 2727.

[15] L. Xing, Y. Nie, X. Xue, Y. Zhang, *Nano Energy* **2014**, *10*, 44.

[16] X. Xue, P. Deng, S. Yuan, Y. Nie, B. He, L. Xing, Y. Zhang, *Energy Environ. Sci.* **2013**, *6*, 2615.

[17] E. Jacques, G. Lindbergh, D. Zenkert, S. Leijonmarck, M. H. Kjell, *ACS Appl. Mater. Interfaces* **2015**, *7*, 13898.

[18] H. Guo, M. H. Yeh, Y. C. Lai, Y. Zi, C. Wu, Z. Wen, C. Hu, Z. L. Wang, *ACS Nano* **2016**, *10*, 10580.

[19] Y. Yao, T. Jiang, L. Zhang, X. Chen, Z. Gao, Z. L. Wang, *ACS Appl. Mater. Interfaces* **2016**, *8*, 21398.

[20] X. Pu, L. Li, M. Liu, C. Jiang, C. Du, Z. Zhao, W. Hu, Z. L. Wang, *Adv. Mater.* **2016**, *28*, 98.

[21] A. Ramadoss, B. Saravanakumar, S. W. Lee, Y.-S. Kim, S. -J. Kim, Z. L. Wang, *ACS Nano* **2015**, *9*, 4337.

[22] R. Song, H. Jin, X. Li, L. Fei, Y. Zhao, H. Huang, H. Lai-Wa Chan, Y. Wang, Y. Chai, *J. Mater. Chem. A* **2015**, *3*, 14963.

[23] K. Parida, V. Bhavanasi, V. Kumar, J. Wang, P. S. Lee, *J. Power Sources* **2017**, *342*, 70.

[24] A. Maitra, S. K. Karan, S. Paria, A. K. Das, R. Bera, L. Halder, S. K. Si, A. Bera, B. B. Khatua, *Nano Energy* **2017**, *40*, 633.

[25] G. Wang, L. Zhang, J. Zhang, *Chem. Soc. Rev.* **2012**, *41*, 797.

[26] H. He, Y. Fu, T. Zhao, X. Gao, L. Xing, Y. Zhang, X. Xue, *Nano Energy* **2017**, *39*, 590.

[27] C. Zhong, Y. Deng, W. Hu, J. Qiao, L. Zhang, J. Zhang, *Chem. Soc. Rev.* **2015**, *44*, 7484.

[28] J. H. Jung, M. Lee, J.-I. Hong, Y. Ding, C.-Y. Chen, L.-J. Chou, Z. L. Wang, *ACS Nano* **2011**, *5*, 10041.

[29] E. H. Abdelhamid, O. D. Jayakumar, V. Kotari, B. P. Mandal, R. Rao, V. M. Naik, R. Naik, A. K. Tyagi, *RSC Adv.* **2016**, *6*, 20089.

[30] T. G. Mofokeng, A. S. Luyt, V. P. Pavlović, V. B. Pavlović, D. Dudić, B. Vlahović, V. Djoković, *J. Appl. Phys.* **2014**, *115*, 84109.

[31] E. R. Camargo, M. Popa, M. Kakihana, *Chem. Mater.* **2002**, *14*, 2365.

[32] Z. X. Shen, X. B. Wang, S. H. Tang, M. H. Kuok, R. Malekfar, *J. Raman Spectrosc.* **2000**, *31*, 439.

[33] C. Dagdeviren, M. Papila, *Polym. Compos.* **2009**, *31*, 1003.

[34] M. Choi, G. Murillo, S. Hwang, J. W. Kim, J. H. Jung, C.-Y. Chen, M. Lee, *Nano Energy* **2017**, *33*, 462.

[35] J. Wu, D. Xiao, J. Zhu, *Chem. Rev.* **2015**, *115*, 2559.

[36] Z. Zhang, Y. Fu, X. Yang, Y. Qu, Z. Zhang, *ChemNanoMat* **2015**, *1*, 409.

[37] D. Nam, J.-U. Lee, H. Cheong, *Sci. Rep.* **2015**, *5*, 17113.

[38] A. Ambrosi, Z. Sofer, M. Pumera, *Chem. Commun.* **2015**, *51*, 8450.

[39] Z. Zhang, X. Yang, Y. Fu, K. Du, *J. Power Sources* **2015**, *296*, 2.

[40] J. Feng, X. Sun, C. Wu, L. Peng, C. Lin, S. Hu, J. Yang, Y. Xie, *J. Am. Chem. Soc.* **2011**, *133*, 17832.

[41] Y. Qiu, X. Li, M. Bai, H. Wang, D. Xue, W. Wang, J. Cheng, Y. Xi, L. Chen, D. Zhao, T. Yu, *Inorg. Chem. Front.* **2017**, *4*, 675.

[42] X. Liu, J.-Z. Zhang, K.-J. Huang, P. Hao, *Chem. Eng. J.* **2016**, *302*, 437.

[43] K.-J. Huang, J.-Z. Zhang, Y. Fan, *Mater. Lett.* **2015**, *152*, 244.

[44] L. Kong, C. Zhang, S. Zhang, J. Wang, R. Cai, C. Lv, W. Qiao, L. Ling, D. Long, D. S. Su, H. Zhu, F. Kang, H. Zhu, *J. Mater. Chem. A* **2014**, *2*, 17962.

[45] K. Krishnamoorthy, P. Pazhamalai, S. Sahoo, S.-J. Kim, *J. Mater. Chem. A* **2017**, *5*, 5726.

[46] R. Muchakayala, S. Song, J. Wang, Y. Fan, M. Bengeppagari, J. Chen, M. Tan, *J. Ind. Eng. Chem.* **2017**, DOI:10.1016/j.jiec.2017.10.009.

[47] R. B. Rakhi, W. Chen, D. Cha, H. N. Alshareef, *Nano Lett.* **2012**, *12*, 2559.

[48] K. Krishnamoorthy, P. Pazhamalai, S. -J. Kim, *Electrochim. Acta* **2017**, *227*, 85.

[49] Y. Qiu, X. Li, M. Bai, H. Wang, D. Xue, W. Wang, *Inorg. Chem.* **2017**.

[50] R. Harpeness, A. Gedanken, A. M. Weiss, M. A. Slifkin, *J. Mater. Chem.* **2003**, *13*, 2603.

[51] Z. Luo, J. Zhou, L. Wang, G. Fang, A. Pan, S. Liang, *J. Mater. Chem. A* **2016**, *4*, 15302.

[52] C. Yang, M. Sun, X. Wang, G. Wang, *ACS Sustain. Chem. Eng.* **2015**, *3*, 2067.

[53] K. Krishnamoorthy, P. Pazhamalai, G. K. Veerasubramani, S. -J. Kim, *J. Power Sources* **2016**, *321*, 112.

CHAPTER-7

Conclusions and Future Work

7.1. Conclusions

This chapter describes the general conclusions of overall thesis and future directions of this work.

- In this thesis, the chapter 1 discuss regarding the general concepts about the energy storage and harvesting parameters and the chapter 2 provides the materials, experimental section and the characterization and fabrication technique of supercapacitors.
- Chapter 3 discusses the energy storage in the view of improving performance metrics using aqueous electrolyte system, the hybrid-ion supercapacitors (HSCs) / asymmetric supercapacitor (ASC) are fabricated using battery-type faradaic nanostructured electrode materials ($LiMn_2O_4$, CuHCF, MnHCF & Cu_2WS_4/Ni) and capacitive type electrode materials (graphene and graphitic carbon).
- The fabricated device such as $LiMn_2O_4$ ‖ graphene, CuHCF ‖ GC and MnHCF ‖ graphene delivers specific energy of about 39, 42, and 44 Wh/kg with the corresponding specific power of 440, 523, and 588 W kg^{-1} respectively.
- Likewise, the CWS/Ni ‖ graphene ASC device also possesses high energy (48 Wh/kg) and power (321 W/kg), due to the direct integration of the electrode material on to the Ni foam which makes the electron-ion transport fast during the electrochemical process.
- Chapter 4 and 5 discuss another systematic way to improve the performance metric is to develop electrode materials made of layered/sheet-like structures which can provide superior electrochemical active sites with the use of the ionic/organic electrolyte.

- In this aspect, the preparation of layered materials involved various methodologies such as hydrothermal preparation (blue TiO_2, $MoSe_2$, ReS_2), topochemical de-intercalation reaction (2D silicon sheets), and mechanomilling assisted exfoliation process (MoS_2).
- Different layered materials such as metal oxide (blue TiO_2), two-dimensional transition metal chalcogenides (MoS_2, ReS_2, $MoSe_2$), layered siloxene and their derivatives (siloxene, heat-treated siloxene, silicon oxy carbide lamellas) were examined as novel electrode materials for symmetric supercapacitors (SSCs) using organic electrolyte ($TEABF_4$).
- Chapter 4 discuss the areal performance metrics are widely used for silicon- and TiO_2- based SSCs whereas gravimetric performance metrics are used for TMC- based SSCs. The specific energy and specific power in areal metrics of TiO_2 and 2D silicon based SSCs were in the order of TiO_2 (3.22 μWh cm^{-2}) > siloxene (2.52 μWh cm^{-2}) > HT-siloxene (4.31 μWh cm^{-2}) for specific energy and TiO_2 (8.06 mW cm^{-2}) > siloxene (9.75 MWh cm^{-2}) > HT-siloxene (9.75 mW cm^{-2}) for specific power.
- The novel preparation of silicon oxy carbide lamellas derived from siloxene and alginate carbon has been reported. The electrochemical analysis of silicon oxy carbide SSC device possesses specific energy (~20.8 Wh/kg) with a maximum specific power (15 kW/kg) which can be applicable for the regenerative braking system.
- The analysis of performance metrics of these SSCs demonstrated that the high specific energy is in the order of MoS_2 (18.43 Wh/kg) > $MoSe_2$ (20.31 Wh/kg) > ReS_2 (28.55 Wh/kg) and the specific power is in the order of MoS_2 (7.5 kW/kg) > $MoSe_2$ (7.5 kW/kg) > ReS_2(10 kW/kg). Based on these findings, $MoSe_2$ electrodes and supercapacitors possess the advantage of high OPW (3.0V) with high specific energy (20.31 Wh/kg) and power density (7.5 kW/kg).

- ❖ Further, for the fabrication of self-charging power cell, the choice of electrode material is evaluated. The electrical conductivity of $MoSe_2$ sheets is higher than MoS_2, and ReS_2 sheets with the advantage of large anionic polarizability (and high ionic diffusivity) arise from the Se^{2-} as compared to that of S^{2-} in MoS_2 and ReS_2. Thus, $MoSe_2$ SSC is used for further studies for the fabrication and performance evaluation of self-charging supercapacitor cell (SCSPC) device using ionogel electrolyte and electrospun PVDF fibres for the first time.
- ❖ Chapter 6 discuss the SCSPC device fabricated using $MoSe_2$ electrodes (as energy storage electrode), electrospun nanofibrous PVDF/$NaNbO_3$ mats (porous piezo-polymer separator), and PVDF-co-HFP/$TEABF_4$ (ionogel electrolyte). The individual electrochemical performance of SCSPC showed their ability to work over an OPW of 2.0 V and delivered high specific energy (37900 µJ cm^{-2}) and specific power (2685 µW cm^{-2}).
- ❖ The individual electromechanical performance of electrospun nanofibrous PVDF/$NaNbO_3$ mats showed a high voltage (~12 V) when subjected to a mechanical force (30 N). The self-charging properties of the $MoSe_2$ SCSPC was examined via monitoring the charge stored in the SCSPC under various range of applied force (compressive).
- ❖ The SCSPC was charged up to 0.7 mV subjected to a maximum force of 30 N. The achieved performance metrics of $MoSe_2$ SCSPC is five- fold higher compared to state of art of SCSPCs.
- ❖ The key findings ensure the conversion of mechanical energy into useful energy using the $MoSe_2$ SCSPC device, thus highlighting their impact towards the development of future-generation self-powered devices for flexible/portable/wearable electronics.

7.2. Suggestions for the Future Work

Forever increasing R&D efforts are going on in the study of energy harvesting and energy storage devices. In the present study, enhancement on energy storage capacity was achieved by designing novel architecture electrode materials with the combination of both EDLC and pseudo-capacitance. Further, for the first time, we have fabricated and demonstrated the self-charging supercapacitor power cell using ionogelled electrospun piezoelectric membrane as a separator and electro-active 2D TMC as a positive and negative electrode. However, the preserve of both EDLC and pseudo-capacitance in the final product is the key for the ultimate performance of a supercapacitor.

- Therefore, it is suggested that the design of a suitable hybrid electrode configuration with optimized charge storage capacity in a two-electrode cell perhaps with a good research direction towards commercialization of advanced materials in supercapacitors.
- To improve the self-charging performance of the SCSPC for sustainable self-powered device operation, finding new nanostructured materials with higher redox reactions with better charging behavior as well as better piezoelectric separator would provide a significant improvement to the future SCSPC devices.

APPENDIX A: List of Publications

1. **Parthiban Pazhamalai,** K. Krishnamoorthy, S. Sahoo, V. K. Mariappan, S.-J. Kim, "Copper tungsten sulfide anchored on Ni-foam as a high-performance binder free negative electrode for asymmetric supercapacitor". **Chemical Engineering Journal** 359 (2019) 409-418. **I.F. 6.735**
2. **Parthiban Pazhamalai**, K. Krishnamoorthy, S. Sahoo, S.-J. Kim, "Two-dimensional molybdenum diselenide nanosheets as a novel electrode material for symmetric supercapacitors using organic electrolyte". **Electrochimica Acta** 295 (2019) 591-598. **I.F. 5.116**
3. **Parthiban Pazhamalai**, K. Krishnamoorthy, V. K. Mariappan, S.-J. Kim, "Blue TiO_2 nanosheets as a high-performance electrode material for supercapacitors". **Journal of Colloid and Interface Science** 536 (2019) 62-70. **I.F. 5.09**
4. V. K. Mariappan, K. Krishnamoorthy, **Parthiban Pazhamalai**, S. Sahoo, S.-J. Kim, "Nanostructured ternary metal chalcogenide-based binder-free electrodes for high energy density asymmetric supercapacitors". **Nano Energy** 57 (2019) 307-316. **I.F. 13.120**
5. **Parthiban Pazhamalai**, K. Krishnamoorthy, S. Manoharan, S.-J. Kim, "High energy symmetric supercapacitor based on mechanically delaminated few-layered MoS2 sheets in organic electrolyte". **Journal of Alloys and compounds** 771 (2019) 803-809. **I.F. 3.779**
6. **Parthiban Pazhamalai,** K. Krishnamoorthy, S. Sahoo, V. K. Mariappan, S.-J. Kim," Understanding the thermal treatment effect of two dimensional siloxene sheets and the origin of superior electrochemical energy storage performances". **ACS Applied Materials and Interface** 2018 (Just accepted) **I.F. 8.097**

7. K. Krishnamoorthy, **Parthiban Pazhamalai**, S.-J. Kim, “Two-dimensional siloxene nanosheets: Novel high-performance supercapacitor electrode materials”. **Energy & Environmental Science** 11 (2018) 1595-1602 **I.F. 30.67**
8. **Parthiban Pazhamalai**, K. Krishnamoorthy, S. Sahoo, S.-J. Kim, “High-energy aqueous Li-ion hybrid capacitor using metal organic framework mimic insertion-type copper hexacyanoferrate and capacitive-type graphitic carbon electrodes”. **Journal of Alloys and compounds** 765 (2018)1041-1048. **I.F. 3.779**
9. S. Sahoo, K. Krishnamoorthy, **Parthiban Pazhamalai**, S.-J. Kim, “Copper molybdenum sulfide anchored nickel foam: A high performance, binder-free, negative electrode for supercapacitor”. **Nanoscale** 10 (29) (2018) 13883-13888. **I.F. 7.233**
10. V. K. Mariappan, K. Krishnamoorthy, **Parthiban Pazhamalai**, S. Sahoo, S.-J. Kim, “Layered famatinite nanoplates as an advanced pseudocapacitive electrode material for supercapacitor applications”. **Electrochimica Acta** 275 (2018) 110-118. **I.F. 5.116**
11. S. Sahoo, **Parthiban Pazhamalai**, K. Krishnamoorthy, S.-J. Kim, “Copper molybdenum sulfide: A novel pseudocapacitive electrode material for electrochemical energy storage device”. **International Journal of Hydrogen Energy** 43 (27) (2018) 12222-12232. **I.F. 4.229**
12. **Parthiban Pazhamalai**, K. Krishnamoorthy, V. K. Mariappan, S. Sahoo, S. Manoharan, S.-J. Kim, “A high efficacy self-charging $MoSe_2$ solid state supercapacitor using electrospun nanofibrous piezoelectric separator with ionogel electrolyte”. **Advanced Materials and Interface** 5 (2018) 1800055. **I.F. 4.834**
13. **Parthiban Pazhamalai**, K. Krishnamoorthy, V. K. Mariappan, S.-J. Kim, “Fabrication of high energy Li-ion hybrid capacitor using sonochemically prepared manganese hexacyanoferrate and graphene electrodes in aqueous system”. **Journal of Industrial and Engineering Chemistry** 64 (2018) 134-142. **I.F. 4.841**

14. K. Krishnamoorthy, **Parthiban Pazhamalai**, J. H. Lim, K. H. Choi, S.-J. Kim, "Mechanochemical reinforcement of graphene sheets into alkyd resin matrix for the development of electrically conductive paints". **ChemNanoMat** 4(6) (2018) 568-574 **I.F. 3.173**
15. V. K. Mariappan, K. Krishnamoorthy, **Parthiban Pazhamalai**, S. Sahoo, S.-J. Kim, "Electrodeposited molybdenum selenide sheets on nickel foam as a binder-free electrode for supercapacitor application". **Electrochimica Acta** 265 (2018) 514-522. **I.F. 5.116**
16. S. Sahoo, **Parthiban Pazhamalai**, K. Krishnamoorthy, S.-J. Kim, "Hydrothermally prepared α-MnSe nanoparticles as a new pseudocapacitive electrode material for supercapacitor". **Electrochimica Acta** 268 (2018) 403-410. **I.F. 5.116**
17. S. Manoharan, S. Sahoo, **Parthiban Pazhamalai**, S.-J. Kim, "Supercapacitive properties of activated carbon electrode using ammonium-based proton conducting electrolytes", **International Journal of Hydrogen Energy** 43 (3) (2018) 1667-1674. **I.F. 4.229**
18. K. Krishnamoorthy, **Parthiban Pazhamalai**, S. Sahoo, J. H. Lim, K. H. Choi, S.-J. Kim, "High-energy aqueous metal organic framework-based Li-ion capacitor with copper hexacyanoferrate and graphitic carbon electrodes", **ChemElectroChem** 4 (12) (2017) 3302-3308. **I.F. 4.446**
19. V. Shobana, K. Balakrishnan, **Parthiban Pazhamalai**, A. Subramania, "Electrospun Nd^{3+} doped $LiMn_2O_4$ nanofibers as high-performance cathode materials for Li-ion capacitors", **ChemElectroChem** 4 (8) (2017) 2059-2067. **I.F. 4.446**
20. K. Krishnamoorthy, **Parthiban Pazhamalai**, S.-J. Kim, "Ruthenium sulfide nanoparticles as a new pseudocapacitive material for supercapacitor", **Electrochimica Acta** 227 (2017) 85-94. **I.F. 5.116**

21. **Parthiban Pazhamalai**, K. Krishnamoorthy, M. S. P. Sudhakaran, S.-J. Kim, "Fabrication of High-Performance Aqueous Li-Ion Hybrid Capacitor with $LiMn_2O_4$ and Graphene", **ChemElectroChem** 4 (2) (2017) 396-403. **I.F. 4.446**
22. K. Krishnamoorthy, **Parthiban Pazhamalai**, S. Sahoo, S.-J. Kim, "Titanium carbide sheet based high performance wire type solid state supercapacitors", **Journal of Materials Chemistry A** 5 (12) (2017) 5726-5736. "*Article featured as **2017 Journal of Materials Chemistry A HOT Papers**"* **I.F. 9.931**
23. G. K. Veerasubramani, K. Krishnamoorthy, **Parthiban Pazhamalai**, S.-J. Kim, "Enhanced electrochemical performances of graphene based solid-state flexible cable type supercapacitor using redox mediated polymer gel electrolyte", **Carbon** 105 (2017) 638-648. **I.F. 7.082**
24. **Parthiban Pazhamalai**, K. Krishnamoorthy, S.-J. Kim, "Hierarchical copper selenide nanoneedles grown on copper foil as a binder free electrode for supercapacitors", **International Journal of Hydrogen Energy** 41 (33) (2016), 14830-14835. **I.F. 4.229**
25. K. Krishnamoorthy, **Parthiban Pazhamalai**, G. K. Veerasubramani, S.-J. Kim, "Mechanically delaminated few layered MoS_2 nanosheets based high performance wire type solid-state symmetric supercapacitors", **Journal of Power Sources** 321(2016) 112-119. **I.F. 6.945**
26. K. Krishnamoorthy, G. K. Veerasubramani, **Parthiban Pazhamalai**, S.-J. Kim, "Designing two dimensional nanoarchitectured MoS_2 sheets grown on Mo foil as a binder free electrode for supercapacitors", **Electrochimica Acta** 190 (2016) 305-312. **I.F. 5.116**
27. V. Shobana, **Parthiban Pazhamalai**, K. Balakrishnan, "Lithium based battery-type cathode material for hybrid supercapacitor", **Journal of Chemical and Pharmaceutical Research** 7 (2) (2015) 207-212.

List of paper submitted

1. **Parthiban Pazhamalai**, K. Krishnamoorthy, S. Sahoo, V. K. Mariappan, S.-J. Kim, "Energy storage properties of amorphous MoS_3 and crystalline MoS_2 nanosheets in ionic liquid electrolyte".
2. **Parthiban Pazhamalai**, K. Krishnamoorthy, S. Sahoo, V. K. Mariappan, S.-J. Kim, "High performance electrochemical energy storage device using hydrothermally prepared rhenium disulfide nanostructures".
3. **Parthiban Pazhamalai,** K. Krishnamoorthy, S. Sahoo, V. K. Mariappan, S.-J. Kim," Carbothermal conversion of siloxene sheets into silicon-oxy-carbide lamellas: An advanced electrode for high-performance supercapacitors".

APPENDIX-B: Conference Presentations

1. **Parthiban Pazhamalai**, K. Balakrishnan, A. Subramania "Synthesis, characterization & electrochemical supercapacitor performances of electrospun $LiAl_{0.3}Mn_{1.7}O_4$ nanofibers", International Conference on Nanoscience and Technology-2014 (ICONSAT-2014), Panjab University, Chandigarh. **(Poster presentation)**
2. K. Balakrishnan, **Parthiban Pazhamalai**, A. Subramania "Neodymium doped lithium manganese oxide nanofibers as electrode material for li-ion supercapacitors", International Conference on Emerging Materials and Applications-2014(ICEMA-2014), IIT Roorkee Saharanpur Campus, Saharanpur (UP). (**Oral presentation)**
3. K. Krishnamoorthy, **Parthiban Pazhamalai**, G. K. Veerasubramani, S.-J. Kim, "High performance wire type solid-state symmetric supercapacitors using mechanically delaminated few layered MoS_2 nanosheets", International Conference on Electronic Materials and Nanotechnology for Green Environment-2016(ENGE-2016), Jeju, Korea. **(Poster presentation)**
4. **Parthiban Pazhamalai**, K. Krishnamoorthy, S.-J. Kim, "Development of high performance aqueous Li-ion hybrid capacitor", International Conference on Electronic Materials and Nanotechnology for Green Environment-2016 (ENGE-2016), Jeju, Korea. **(Poster presentation)**
5. **Parthiban Pazhamalai**, K. Krishnamoorthy, S. Sahoo, S.-J. Kim, "Biopolymer derived graphitic carbon nanoparticles as an electrode for supercapacitor", The 19th Korean MEMS Conference-2017, Jeju, Korea. **(Poster presentation)**
6. **Parthiban Pazhamalai**, S. Sahoo, K. Krishnamoorthy, V. K. Mariappan, S. Manoharan, S.-J. Kim, "Development of polymer based self-charging supercapacitor", The 4th International Conference on Advanced Electromaterials (ICAE 2017), Jeju, Korea. **(Poster presentation).**

7. **Parthiban Pazhamalai**, K. Krishnamoorthy, S. Sahoo, V. K. Mariappan, S. Manoharan, S.-J. Kim, "Development of high-energy aqueous sodium ion capacitors using metal hexacyanoferrate and graphene", The 4th International Conference on Advanced Electromaterials (ICAE 2017), Jeju, Korea. **(Poster presentation).**
8. S. Sahoo, **Parthiban Pazhamalai**, K. Krishnamoorthy, S. Manoharan, V. K. Mariappan, S.-J. Kim "A Facile and Template-Free Synthesis of α-MnSe Microspheres as electrodes for high performance supercapacitor", The 4th International Conference on Advanced Electromaterials (ICAE 2017), Jeju, Korea. **(Poster presentation).**
9. V. K. Mariappan, **Parthiban Pazhamalai**, S. Sahoo, S. Manoharan, K. Krishnamoorthy, S.-J. Kim, "Duo-facet molybdenum selenide as a binder free electrode for supercapacitor application", The 4th International Conference on Advanced Electromaterials (ICAE 2017), Jeju, Korea. **(Poster presentation).**
10. **Parthiban Pazhamalai**, K. Krishnamoorthy, S. Sahoo, V. K. Mariappan, S. Manoharan, S.-J. Kim, "Development of high-energy aqueous Li-ion capacitors using metal hexacyanoferrate", The 10th International Conference on Advanced Materials and Devices (ICAMD 2017), Jeju, Korea. **(Poster presentation).**
11. **Parthiban Pazhamalai**, K. Krishnamoorthy, S. Sahoo, S.-J. Kim, "Preparation of graphene based conductive paint", The 10th International Conference on Advanced Materials and Devices (ICAMD 2017), Jeju, Korea. **(Poster presentation).**
12. S. Sahoo, **Parthiban Pazhamalai**, K. Krishnamoorthy, S. Manoharan, V. K. Mariappan, S.-J. Kim "Electrochemically deposited FeS as new electrode material for supercapacitors", The 10th International Conference on Advanced Materials and Devices (ICAMD 2017), Jeju, Korea. **(Poster presentation).**
13. S. Manoharan, S. Sahoo, **Parthiban Pazhamalai**, K. Krishnamoorthy, V. K. Mariappan, S.-J. Kim, "Ammonium based proton conducting electrolytes for supercapacitor

applications", The 10th International Conference on Advanced Materials and Devices (ICAMD 2017), Jeju, Korea. **(Poster presentation)**.

14. **Parthiban Pazhamalai**, K. Krishnamoorthy, S. Sahoo, V. K. Mariappan, S. Manoharan, S.-J. Kim, "Cobalt hexacyanoferrate as the intercalative type electrode for Li-ion capacitors", The 20th Korean MEMS Conference-2018, Jeju, Korea. **(Poster presentation)**
15. V. K. Mariappan, K. Krishnamoorthy, **Parthiban Pazhamalai**, S. Sahoo, S. Manoharan, Suk-Jun Ko, and S.-J. Kim, "Layered famatinite nanoplates as an advanced pseudocapacitive electrode material", The 20th Korean MEMS Conference-2018, Jeju, Korea. **(Poster presentation)**
16. S. Sahoo, **Parthiban Pazhamalai**, K. Krishnamoorthy, S. Manoharan, V. K. Mariappan, Nam-Jin Kim, and S.-J. Kim, "Electrochemically deposited FeS nanosheet arrays as electrode material for high performance supercapacitors", The 20th Korean MEMS Conference-2018, Jeju, Korea. **(Poster presentation)**
17. **Parthiban Pazhamalai**, K. Krishnamoorthy, S. Sahoo, V. K. Mariappan, S. Manoharan, S.-J. Kim, "Development of self-charging supercapacitor using polymer composites", 4th International Conference on Nanogenerators and Piezotronics (NGPT 2018), Seoul, Korea. **(Poster presentation)**
18. **Parthiban Pazhamalai**, K. Krishnamoorthy, V. K. Mariappan, S.-J. Kim, "Mechanical energy harvesting using free-standing carbyne prepared via dehydrohalogenation of PVDF", 4th International Conference on Nanogenerators and Piezotronics (NGPT 2018), Seoul, Korea. **(Poster presentation)**
19. S. Sahoo, K. Krishnamoorthy, **Parthiban Pazhamalai**, S.-J. Kim, "Binary metal sulfide-based supercapacitors for self-powered Nanosystems", 4th International Conference on Nanogenerators and Piezotronics (NGPT 2018), Seoul, Korea. **(Poster presentation)**

20. V. K. Mariappan, K. Krishnamoorthy, **Parthiban Pazhamalai**, S.-J. Kim, “Self-charging supercapacitor based on Carbyne”, 4th International Conference on Nanogenerators and Piezotronics (NGPT 2018), Seoul, Korea. **(Poster presentation)**
21. **Parthiban Pazhamalai**, Ananthakumar Ramadoss, Saravanakumar Balasubramaniam, K. Krishnamoorthy, S.-J. Kim, “Toward High-Performance Self-Charging Supercapacitor Power Cell”, 4th International Conference on Nanogenerators and Piezotronics (NGPT 2018), Seoul, Korea. **(Invited Talk)**
22. **Parthiban Pazhamalai**, K. Krishnamoorthy, S. Sahoo, S.-J. Kim, “Two-dimensional titanium carbide sheets based high performance flexible wire type solid state supercapacitors”, The 19th International Symposium on the Physics of Semiconductors and Applications (ISPSA 2018), Jeju, Korea **(Oral Presentation)**
23. **Parthiban Pazhamalai**, K. Krishnamoorthy, S.-J. Kim, “Development of high-performance solid state self-charging supercapacitor”, The 19th International Symposium on the Physics of Semiconductors and Applications (ISPSA 2018), Jeju, Korea **(Poster presentation)**
24. S. Sahoo, **Parthiban Pazhamalai**, V. K. Mariappan, S.-J. Kim, “Copper molybdenum sulfide: a novel pseudocapacitive electrode material for electrochemical energy storage device”, The 19th International Symposium on the Physics of Semiconductors and Applications (ISPSA 2018), Jeju, Korea. **(Poster presentation)**
25. V. K. Mariappan, K. Krishnamoorthy, **Parthiban Pazhamalai**, S.-J. Kim, “Free-standing, Flexible conducting carbyne: A novel electrode material for supercapacitor applications”, The 19th International Symposium on the Physics of Semiconductors and Applications (ISPSA 2018), Jeju, Korea. **(Poster presentation)**
26. K. Krishnamoorthy, S. Sahoo, **Parthiban Pazhamalai**, S.-J. Kim, “Copper molybdenum sulfide anchored on nickel foam: binder-free electrodes for high-performance symmetric

supercapacitors", The 23th Annual Joint Workshop on Advanced Electronic Technology and Application, Jeju, Korea. **(Poster presentation)**

27. **Parthiban Pazhamalai**, K. Krishnamoorthy, S. Sahoo, S.-J. Kim, "Two-dimensional molybdenum diselenide nanosheets as high-performance symmetric supercapacitor in organic electrolyte", International Conference on Electronic Materials and Nanotechnology for Green Environment-2018(ENGE-2018), Jeju, Korea. **(Poster presentation)**
28. K. Krishnamoorthy, **Parthiban Pazhamalai**, S.-J. Kim, "Ruthenium sulfide: A new pseudocapacitive electrode material for supercapacitor application", International Conference on Electronic Materials and Nanotechnology for Green Environment-2018(ENGE-2018), Jeju, Korea. **(Poster presentation)**
29. S. Sahoo, **Parthiban Pazhamalai**, K. Krishnamoorthy, S.-J. Kim, "Direct Growth of Copper molybdenum sulfide Nanostructures on Nickel Foam as High-Performance Binder-Free Negative Electrodes for Supercapacitors", International Conference on Electronic Materials and Nanotechnology for Green Environment-2018(ENGE-2018), Jeju, Korea. **(Poster presentation)**
30. V. K. Mariappan, **Parthiban Pazhamalai**, K. Krishnamoorthy, S.-J. Kim, "Preparation of carbyne/Ni using chemical dehydrohalogenation process: A novel binder-free electrode for supercapacitor application", International Conference on Electronic Materials and Nanotechnology for Green Environment-2018(ENGE-2018), Jeju, Korea. **(Poster presentation)**
31. S. Manoharan, **Parthiban Pazhamalai**, K. Krishnamoorthy, S.-J. Kim, "A solid proton conducting electrolyte leading towards self-charging supercapacitor", International Conference on Electronic Materials and Nanotechnology for Green Environment-2018(ENGE-2018), Jeju, Korea. **(Poster presentation)**

DECLARATION

I, **Parthiban Pazhamalai**, hereby declare that the thesis entitled "**Development of Advanced Nanostructured Electrode Materials for High-Performance Supercapacitors and Self-Charging Power Cell**", submitted to Jeju National University, in the partial fulfillment of the requirements for the award of the **Degree of Doctor of Philosophy in the Department of Mechatronics Engineering** is a record of original and independent research work done and published by me during the period March 2015 to February 2019 under the supervision and guidance of **Prof. Sang -Jae Kim**, Department of Mechatronics Engineering, Jeju National University. This thesis is based on out publication in reputed journals and it has not been formed for the award of any other Degree/ Diploma/ Associateship/Fellowship to any candidate of any university.

Parthiban Pazhamalai